Studies of Hydrothermal Processes in Crater Lake, OR

Robert W. Collier, Jack Dymond and James McManus
College of Oceanography
Oregon State University
Corvallis, OR 97331

In Collaboration With:

H. Phinney, D. McIntire, G. Larson, M. Buktenica	Oregon State University
C. R. Bacon, C. H. Nelson, J. H. Barber, Jr.	U.S.G.S., Menlo Park
D. Karl	U. Hawaii
J. Lupton	U.C. Santa Barbara
M. Watwood, C. Dahm	U. of New Mexico
A. Soutar, R. Weiss	U. C. San Diego
C. G. Wheat	U. of Hawaii

Submitted to:

The National Park Service, PNW Region
Seattle, WA

May 31, 1991

Cooperative Agreement No. CA 9000-3-0003
Subagreement No. 7
CPSU, College of Forestry, OSU

~~Data~~ Ref.
OSU College of Oceanography Report # 90 - 7

Studies of Hydrothermal Processes in Crater Lake, OR

Robert W. Collier, Jack Dymond and James McManus
College of Oceanography
Oregon State University
Corvallis, OR 97331

In Collaboration With:

H. Phinney, D. McIntire, G. Larson, M. Buktenica	Oregon State University
C. R. Bacon, C. H. Nelson, J. H. Barber, Jr.	U.S.G.S., Menlo Park
D. Karl	U. Hawaii
J. Lupton	U.C. Santa Barbara
M. Watwood, C. Dahm	U. of New Mexico
A. Soutar, R. Weiss	U. C. San Diego
C. G. Wheat	U. of Hawaii

Submitted to:

The National Park Service, PNW Region
Seattle, WA

May 31, 1991

Cooperative Agreement No. CA 9000-3-0003
Subagreement No. 7
CPSU, College of Forestry, OSU

OSU College of Oceanography Report # 90 - 7

Executive summary

Significant Observations

Measurements of temperature and salt content within the South Basin of Crater Lake show surprising variations over distances of a few meters. These thermal and salinity gradients can only be maintained by a continuing input of anomalous fluids.

Communities of bacteria, which produce impressive mat features on rock outcrops and sediment surfaces, mark sites of deep lake venting. The mats have internal temperatures which are more than 15°C higher than lake bottom water. These communities apparently use the abundant reduced iron in the advecting fluids to fuel their metabolism. Although there were no visible indications of fluid flow through or from the mats, fluid advection is necessary in order to provide the continuous input of reduced chemical species which is required for the survival of these prolific bacterial communities. The temperature gradients within the mats indicate that the advection rates are as high as 100 meters per year. Consequently, the bacterial mats are visual markers of thermally and chemically enriched fluid venting.

Pools of saline water, with major element contents that are approximately ten times greater than background lake values, have been discovered in two widely separated areas of the lake. Sediment pore water compositions from some South Basin cores are similar to those of the pools. The pore water measurements define non-linear gradients which indicate vertical fluid advection rates of up to two meters/year. These measurements as well as the major element compositions suggest that the fluids advecting through the sediments, the brine pools, and the bacterial mats are derived from a similar source. Results from chemical geothermometry determinations suggest that this source equilibrated with silicate rocks at temperatures ranging from 40 to 165 °C.

Sampling of the mat fluids, the brine pools, and sediment pore waters has dramatically increased the known range of anomalous water compositions within Crater Lake. In the most anomalous fluids manganese is enriched by as much as a million times and ^{222}Rn is enriched 100,000 times over typical lake values. Helium-3, perhaps the most distinctive indicator of a magmatic source, is enriched 500 times over values for waters in equilibrium with the atmosphere. Striking depletions of ^{14}C in pool fluids and the deep lake waters indicate a magmatic source of "dead carbon" is entering the deep lake. Rare earth element concentrations in lake and sediment pore waters have an abundance pattern which indicate a hydrothermal source. Isotopic compositions of hydrogen in the saline pools clearly show that these anomalous fluids are highly modified lake water and could not have originated outside the lake.

The enhanced salt content of the anomalous fluids enables us to account for the bulk composition of the lake by elucidating the sources of chemical species which were previously unexplained by known water sources such as precipitation and caldera springs. We have identified a third source—a hydrothermal component—as the major influence on lake composition. Using sensitive analytical methods, we have monitored the active accumulation of heat and salt in the deep lake that results from this source. Various mass balance models indicate that a net heat flow of 15 to 30 megawatts (MW) is carried into the lake by thermal fluids. The calculated flow rates for a thermally and chemically enriched fluid are approximately 200-400 liters/second—roughly two billion gallons per year.

Conclusions

As a result of the past three years of field studies and our interpretation of these and other data from the literature, we conclude that there <u>are</u> inputs of hydrothermal fluids into the bottom of Crater Lake. The dissolved materials associated with these thermally and chemically enriched fluids, coupled with the overall hydrologic balance, control the observed chemical composition of the lake. Because the hydrothermal input dominates the flux of most dissolved chemicals into Crater Lake, the hydrothermal process is highly significant. Furthermore, the geothermal inputs have a direct effect on the density structure of the deep lake, and therefore can profoundly affect the rate of heat transport and the redistribution of dissolved salts and nutrients within the body of the lake.

Table of Contents

VII. Appendices

List of Figures

List of Figures (continued)

List of Plates

List of Tables

List of Figures (Appendices)

List of Figures (Appendices) - continued

List of Tables (Appendices)

I Introduction

Crater Lake sits within the caldera of Mt. Mazama, a center of volcanism in the Oregon Cascades for more than 400,000 years (Bacon and Lanphere, 1990). The morphology of the lake is largely a consequence of a climactic eruption that occurred 6845 ± 50 years ago; however, intercaldera volcanism took place as recently as 4000 years ago (Bacon and Lanphere, 1990). The volcanic morphology provides a basin for what is now the deepest lake in the United States (approximately 590 meters). The volcanic terrain strongly limits the nutrient fluxes into the lake, mostly because the lake covers 78% of the total drainage area. Consequently, the lake is highly oligotrophic and one of the clearest lakes in the world.

Our studies of Crater Lake began as an attempt to understand the important physical and chemical characteristics of the lake and the processes which produced some unusual sediment compositions. As we have reported in the past (Collier and Dymond, 1988a; Collier and Dymond, 1989; Dymond et al., 1989; Dymond and Collier, 1990; Collier et al., 1990), a number of these features are consistent with hydrothermal inputs to the lake. Given the location of the lake directly above a relatively recent and major magmatic source (Bacon and Druitt, 1988), thermal spring input to the lake would not be surprising. Such a source was first suggested by Van Denburgh (1968), who noted the relatively high sulfate and chloride content of Crater Lake as compared to nearby Davis Lake, and suggested that these two constituents " .... may have been contributed to the lake by thermal springs or fumaroles, probably located below the present lake level. Such springs and fumaroles are a common expression of hydrothermal activity at a site of volcanic eruptions." Van Denburgh did not state whether he thought hydrothermal input was active today. Simpson (1970a) showed that the deep lake had strong gradients in both ^{14}C and the stable carbon isotopes, ^{12}C and ^{13}C. These gradients were consistent with a source of carbon having an isotopic composition similar to magmatic sources. Simpson also constructed a mass balance model which indicated that only a fraction of the ionic content of Crater Lake could be accounted for by known inputs. He suggested the missing source was the result of "fumarole or hot spring activity near the bottom," and he estimated fluxes from this proposed source.

More recently Williams and Von Herzen (1983) measured high conductive heat flow in certain areas of the lake's sedimented bottom. In one of these areas of high heat flow, they also documented anomalous near-bottom temperatures. This study reinforced earlier work describing the deep temperature structure of the lake as hyperadiabatic (Neal et al., 1971; 1972). On the basis of the heatflow pattern and the water column measurements, Williams and Von Herzen (1983) suggested that there is thermal spring input to the deep lake.

Studies of Crater Lake water composition have provided further support for hydrothermal hypotheses. Thompson et al. (1990) pointed out that Crater Lake has high boron and lithium contents compared to local meteoric water; these elements are typically enriched in thermal waters of volcanic origin. In addition, they showed that Cl/Li ratios in Crater Lake waters are very similar to those observed in hot springs from volcanic sources but that these ratios are outside the range of values observed in Mt. Mazama cold springs. Nathenson (1990a) demonstrated that a hydrologic model which incorporated precipitation, cold springs, evaporation, and seepage could not account for the major element content of Crater Lake. He suggested thermal springs provide the missing input and, based on geochemical mass balance models, he constrained the input of thermal waters to range between 80 and 1900 liters/second. Nathenson points out that this inflow can easily provide the convective heat flux estimated by Williams and Von Herzen (1983). Nathenson's

lower estimate of hydrothermal flux overlaps that of Sorey (1985) who suggested a thermal-spring discharge into the lake of 30 - 150 liters/second.

Evidence of hydrothermal sources to the lake have not gone unchallenged. La Fleur (1987; 1990) argues against any hydrothermal inputs to the lake and suggests that underestimated evaporation rates, fumarolic inputs, and weathering of Mazama ash could account for the anomalous composition of the lake. He suggests that conductive heating rather than convective inputs accounts for the temperature anomalies. La Fleur (1990) proposes that deep springs from caldera wall aquifers can account for the anomalous fluids observed during our 1989 field program.

The question of whether there are hydrothermal sources to Crater Lake has important implications for understanding the lake ecology. For example, the relatively rapid mixing that has been suggested for Crater Lake (Simpson, 1970b; Volchok et al., 1970) may be a consequence of hydrothermal inputs to the bottom of the lake. If this is true, temporal variability in this source could impact the nutrient cycling and the plant productivity of the lake. In 1987, in response to the requirement of Public Law 99-591 for identification of significant thermal features in national parks, the Park Service initiated a three-year program to evaluate possible hydrothermal sources to Crater Lake. The research, which is part of a 10-year Limnological Study of Crater Lake, is designed to: (1) define the thermal and chemical variability in the deep lake, (2) examine the data for evidence of a hydrothermal source, (3) design and carry out a program that would find possible venting sites and sample any associated fluids, and (4) evaluate alternative mechanisms to explain the observed thermal and chemical variability.

This report summarizes the field programs and laboratory analyses which have been carried out from 1987 to the present. The results for the 1987 and 1988 field programs also have been reported in Collier and Dymond (1988a); Collier and Dymond (1988b); Collier and Dymond 1989; Dymond et al., 1989; Dymond and Collier, 1990; and Collier et al., (1990). During the summer of 1989, our research group spent approximately 35 days at the lake in an expanded program that included the use of the research submersible, Deep Rover. In order to provide a comprehensive report, results from the previous publications and reports are included here; however, we place greater emphasis on the 1989 field program in this report because those results have not been reported until now.

A draft of this report was completed on October 26, 1990 and submitted to a peer review committee chaired by Dr. Charles Goldman. We have considered the evaluations and recommendations of the review committee in this final report of the research. In addition we have responded to reviews of the draft report by the U.S. Bureau of Land Management and the California Energy Company.

Acknowledgements

We take this opportunity to acknowledge and thank the many people who have helped to make this research effort possible. Gary Larson, our co-PI for the project, provides the important link to the U.S. Park Service and has collaborated on our research efforts for many years. Particular thanks goes to James Milestone and Mark Buktenica, Park personnel who worked for many months prior to the submersible operations to provide the necessary logistical support for the research. Their outstanding efforts and selfless commitment during the field programs are also greatly appreciated. The assistance of Robert Benton, Superintendent of Crater Lake National Park, and other Park

personnel was critical to the smooth operations that we experienced during this very complex program. Can-Dive, Inc. not only provided the submersible, but also kept it functioning so that we were able to carry out the complete dive program with no lost time. Jim English and Steve Fuzessery were superb with their sub-operations. Deep Ocean Engineering, Inc. provided us with ROV equipment and expertise. They made available a state-of-the-art ROV, which was used as a safety backup for the submersible. The vision and energy of Silvia Earle and Graham Hawkes inspired us to move forward with the manned-vehicle concept at the beginning of our project. Rodney Moore was a superb ROV pilot and an able submersible technician - a true "sub"-human. The field and analytical efforts of the OSU research team were outstanding. We especially thank Roberta Conard, Chris Moser, Pat Collier, Brad Beeson, William Rugh, Dick Kovar, Chi Meredith, and Jim Robbins. Continuing discussions, field assistance, and other analytical expertise were provided by Charles Bacon (USGS), John Lupton, (UC Santa Barbara), C. Goeff Wheat (U. of Hawaii), Hans Nelson and John H. Barber (USGS), Bruce Robison (MBARI), Dave McIntire (OSU), Dave Karl (U. of Hawaii), and Ray Weiss (SIO). We also thank Sarah Hoffman for editing this manuscript.

Primary funding for this project has been provided by the U.S. National Park Service (Pacific NW Region, Cooperative Agreement # 9000-3-0003, subagreement #7). Additional support was provided by the OSU College of Oceanography, the OSU Foundation, the US Geological Survey, and the National Geographic Society.

II. Methods

II.1. General

In Figure 1 we show the major bathymetric features of the lake and the location of what we will refer to as the "Detailed Study Area" throughout the text. The Detailed Study Area was a focus of our research operations during the 1987, 1988, and 1989 field seasons. Much of our surface ship sampling has been conducted within this region, and most of the submersible dives that had a hydrothermal focus were carried out within this area. We began our hydrothermal studies here because of the previously reported high heat flow and water column anomalies in this general region (Williams and von Herzen, 1983).

During the summer of 1987, our research group spent 20 days at Crater Lake, during which time we performed extensive sampling operations and made thermal and chemical measurements from the surface research vessel. These measurements formed the basis for preliminary mapping of sites with the most anomalous near-bottom water temperatures and salt contents. The 1987 field program also introduced the use of a remotely operated vehicle (ROV) for making detailed observations of the bottom of Crater Lake. Seven ROV deployments were made which provided information on the sediment thickness, the presence of benthic plants and animals, and the existence of unusual precipitates and crusts which were in marked contrast to the normal buff-colored sediments that blanket much of the bottom.

The hydrothermal field program for 1988 was based on three separate expeditions to the lake. In early July, eight days were used to recover and redeploy a sediment trap mooring, establish our navigational stations, carry out several hydrocasts, make numerous CTD casts, and prepare for a major submersible program. In August. our 25 day field program focused on using the

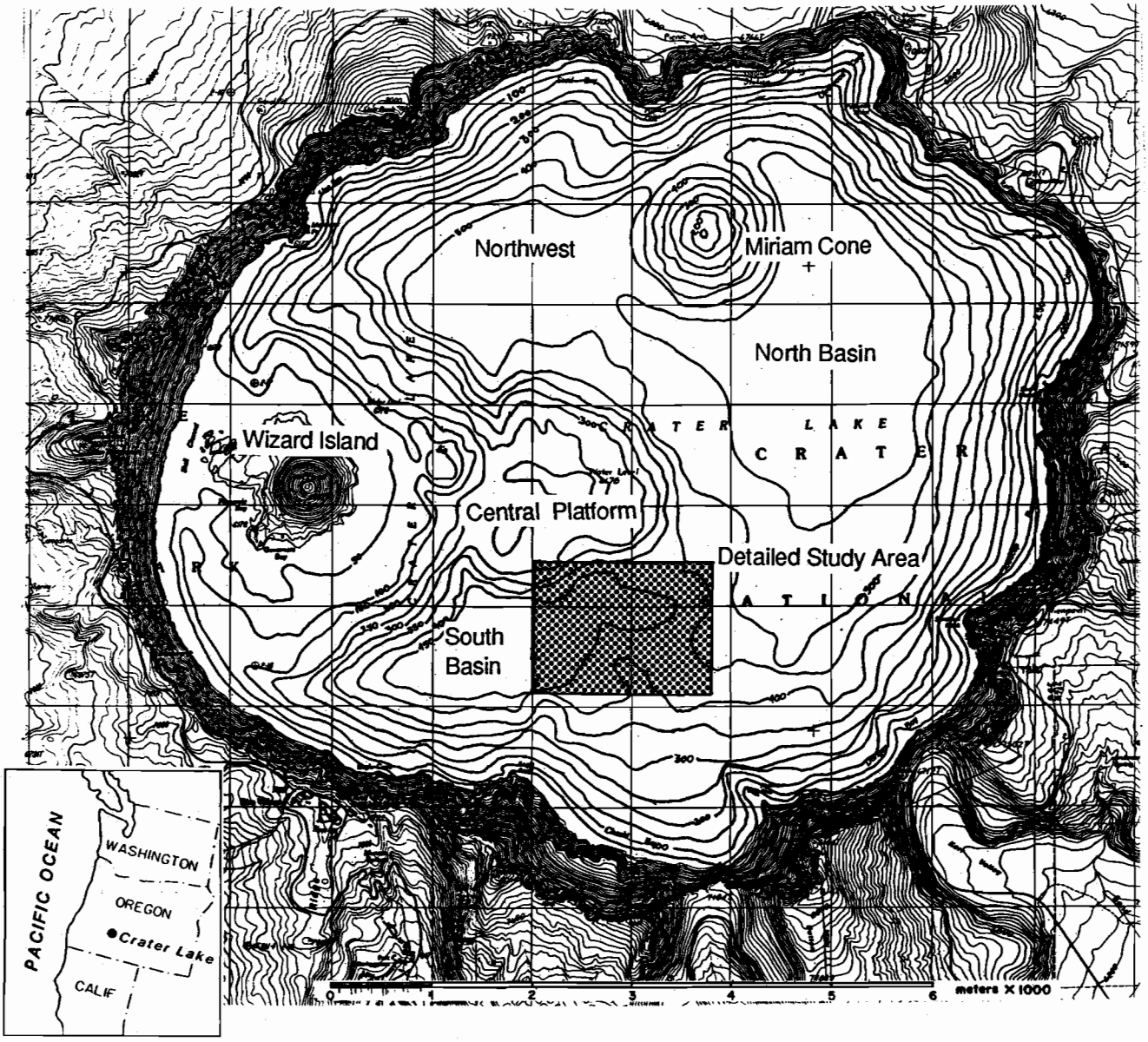

Figure 1. Topographic/bathymetric map of Crater Lake, OR (42°56'N, 122°07'W). The caldera lake, which is the center piece of Crater Lake National Park, has a surface water elevation of 1883 meters and a maximum depth of 594 meters--the deepest lake in the United States. The only access (other than by helicopter to Wizard Island) is a switch-back trail which descends the steep caldera walls rising an average of 300 meters above the lake surface. The major geologic features are noted on the map. The dotted rectangle denotes the Detailed Study Area which was also the focus of previous hydrothermal investigations (Collier and Dymond 1988a; Collier and Dymond 1989). The bathymetry, from Byrne (1965), has been projected onto the USGS 7.5-minute quadrangles for Crater Lake East and West (provisional, 1985).

submersible, Deep-Rover, to locate, observe, and sample geological, geochemical, and biological features in the deep lake that had been hitherto inaccessible. Although much of our efforts were directed toward the submersible operations, we also carried out bathymetric surveying, conducted hydrocasts, made CTD (conductivity, temperature, and depth) measurements, and collected cores during this period. In September we returned to the lake to recover and redeploy the sediment trap mooring and carry out additional CTD measurements and hydrocasts.

The 1989 field programs involved frequent sampling and surface ship measurements throughout the season of normal lake access (June-September) as part of the Ph.D. research of James McManus. Deep-Rover was again used throughout the month of August for expanded survey work, detailed sampling, and the deployment of a number of instruments which would better define the spatial and temporal variations in the anomalous fluids that were discovered during the 1988 field program. In addition to this major effort, we introduced an extensive coring program which was the basis for compositional studies of sediment pore fluids in different parts of the lake.

II.2. Bathymetry

It was necessary to construct a more detailed bathymetric map for the Detailed Study Area than the one for the entire lake bottom published by Byrne, 1962. Twenty navigated transects of the area were used to construct the new map (Figure 2). A 50 kHz echo sounder, which incorporated a 22° transducer, was used to determine the depths. Since the CTD (see below) produced a visible trace on our fathometer record when attached to the research wire during water sampling, the depth measurements could be calibrated against the pressure recorded by the CTD. Depths shown on the new map were also verified with the CTD pressure record collected during the submersible dives. However, the wide cone of the transducer signal tends to obscure sharp changes in slope. Therefore, the true depths of areas where there are steep slopes are probably deeper than the measured depth because the first reflection received may be from adjacent, shallower lake floor. Navigation for the transects was obtained with a microwave ranging system (Motorola Mini-Ranger III) that used shore stations on Eagle Point and Phantom Ship. The precision of the navigation, based on repeated ranges to the same location, is $\pm$ 5 meters.

II.3. Remotely Operated Vehicle (ROV)

A remotely operated vehicle built by Deep Ocean Engineering, Inc., San Leandro, CA, was used to obtain the first video images of the bottom of Crater Lake during the 1987 field program. The vehicle, known as Watchdog, was engineered for tethered operation at depths of 500 feet. Because of the voltage losses due to the exceptionally long cable (1700 feet), a special transformer was required to drive the instrument. With this small modification the ROV operated normally and with only slight loss of power at depths of approximately 1600 feet. The "live" video image quality was very good; however, because of intermittent electronic noise some of the recorded videos were of very poor quality. Seven separate deployments of the ROV provided 12 hours of imagery which covered more than three kilometers of lake bottom. The general locations of these deployments are listed in Appendix H. Deep Ocean Engineering, Inc. also provided an ROV for the 1988 and 1989 field seasons. This vehicle, a Phantom IV, was a backup rescue vehicle and was not used for bottom surveying or sampling.

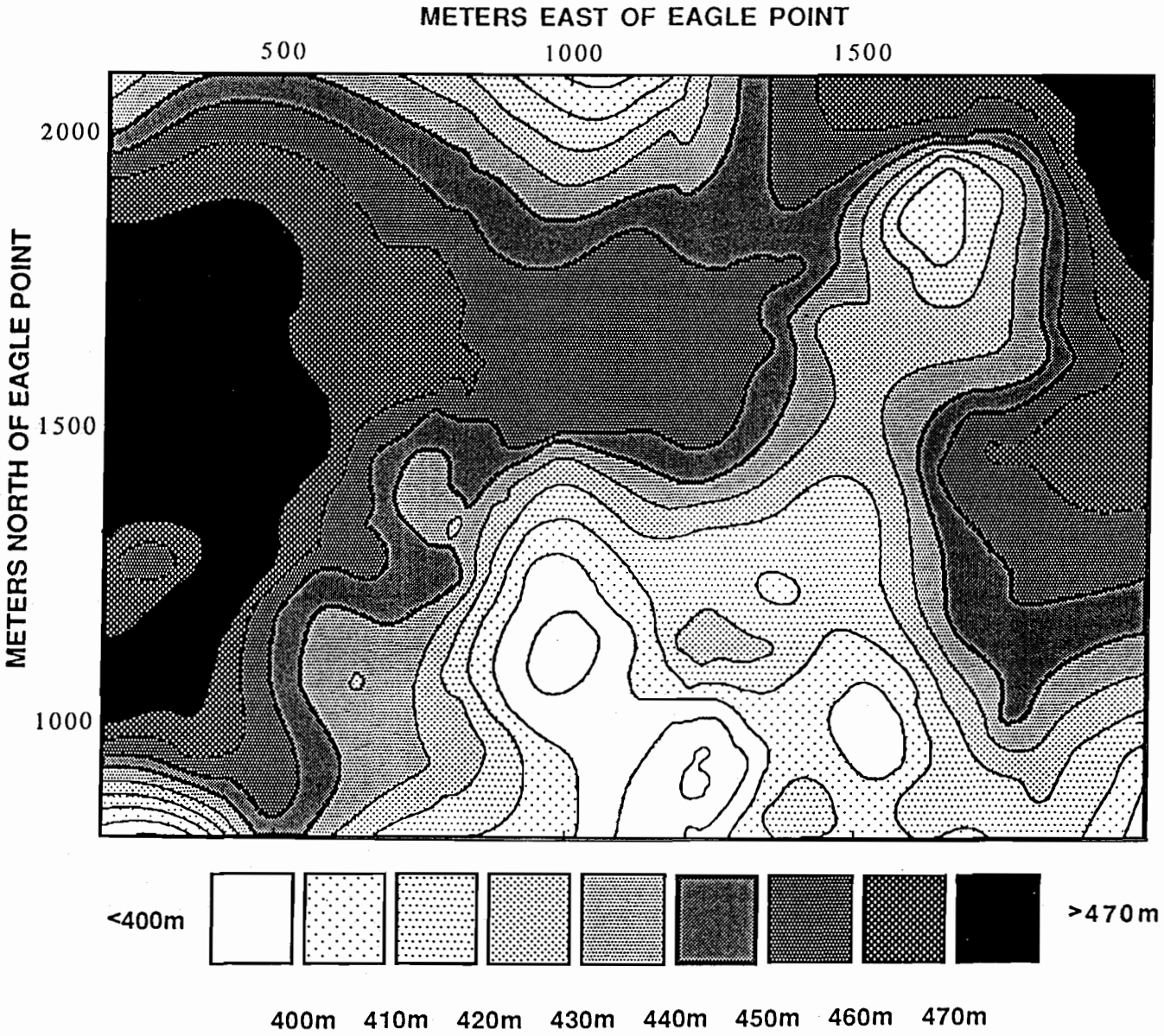

Figure 2. A bathymetric chart constructed for the detailed study area. The contour interval is 10 meters. Darker tones indicate greater depths.

II.4. Manned-Submersible Operations

A one person submersible, Deep Rover (Plates 1 and 2), was chosen as the manned submersible for this research because of its relatively light weight, easy operation and maneuverability, operating depth of 3000 feet, and the external manipulators capable of handling diverse scientific sampling gear. Deep Rover's weight of approximately 3000 kilograms made helicopter transport to the lake feasible. The submarine, which is owned and operated by Can-Dive Inc. in Vancouver, BC., has a spherical acrylic hull that maximizes operator visibility. The propulsion and control system is designed for easy use by non-professional operators. Deep Rover's electric motors were powered by batteries and typically provided five hours of operations before requiring a 12 hour recharge. An air-ballast system controlled buoyancy and allowed descents and ascents of approximately 20 minutes in each direction.

A total of 21 dives were made during the August 1988 expedition. Table H1 (Appendix H) lists the general location and purpose of each dive. Four of the dives were devoted to pilot training or systems checks. Four of the dives were funded by the USGS using the survey sites and goals defined by Dr. Charles Bacon. A summary of results of these dives are described in Appendix C. Dives 180 and 181 were funded by Deep Ocean Engineering, the designers of the submersible. On dive 180 Graham Hawkes, chief designer of Deep Rover, evaluated the systems and performance of the submarine and collected video observations and a sample from the caldera wall. Dive 181 was primarily a biological dive, to observe and sample the attached algae on the south facing caldera wall. Dr. Gary Larson describes the results of the biological dives in Appendix B. The remaining 11 dives were located within the Detailed Study Area and were dedicated to searching for evidence of hydrothermal inputs to the lake, sampling the near-bottom waters, and collecting sediments and other materials from the bottom.

Twenty-six dives were made during the August 1989 field program (Appendix H). Of the science dives, thirteen were funded by the NPS hydrothermal program, five were funded by the USGS and were under the direction of Dr. Charles Bacon, and five were biological dives funded by a grant from the National Geographic Society. The results of the USGS program are discussed in Appendix C. The biological program results appear in Appendix B. All but one of the hydrothermal dives were conducted within the Detailed Study Area. These dives not only added much more detail to the surveys of thermal features such as bacterial mats, iron-rich crusts, and near-bottom temperature anomalies, but they also allowed us to sample and deploy instruments in specific thermal features. The deployed instruments (temperature probe, Benthic Barrel, TTT probe, box core, and peepers) are discussed in the section below, entitled "Submersible Sampling and Photography".

Navigation.

The navigation techniques varied over the three field seasons. For all three years a microwave ranging system (Motorola Mini-Ranger) was used to locate the surface vessel for all water casts, CTD lowerings, and ROV operations. During 1988, we used long-baseline acoustic navigation for submersible positioning. In 1989 our navigation was based on a short-baseline acoustic navigation system. Because the steep caldera walls and the frequently glassy surface produce a difficult acoustic environment, neither long-baseline nor short-baseline navigation were without problems.

The microwave ranging system has a precision of $\pm$ 5 meters for the surface vessel location. The location of the bottom sampler, instrument, or ROV is less certain because of the angle introduced in the wire by drift or movement of the surface vessel.

A long-baseline acoustic navigation system was used in 1988 to position both the boat and the submersible. Unfortunately, problems with the navigation system, contracted from Oceano Instruments, greatly reduced the accuracy and reliability of the submersible navigation. During several dives, the acoustic system failed to locate the submersible for periods of an hour or more. Large, inconsistent errors in positioning frustrated efforts to survey the study area and made relocating important features tedious and time-consuming. A greater reliance on the microwave ranging system and on dead-reckoning partially compensated for these difficulties in the field. We have refined this dead-reckoning navigation with the support of dive logs and bathymetry to produce track lines for most of the dives within the Detailed Study Area.

The track lines for nine dives in the Detailed Study Area are shown in Collier and Dymond (1989). The errors in these lines cannot be estimated directly and will vary depending on the quality of surface-to-submersible communications and the complexity of the track line. In general, the early and late portions of the dives may have navigation errors on the order of $\pm$10 meters but mid-dive periods, far removed from any geodetic reference points, may have errors ranging from 50-100 meters.

Prior to the 1989 field season we enlisted the help of the USGS to refine the geodetic position of our microwave ranging stations. Navigation for the 1989 submersible program was significantly improved, but not without problems. We chose a Trackpoint II system (Land and Sea Surveys) which was integrated with microwave positioning and gyro compass data for the surface vessel. The short-baseline system differs from long-baseline approaches in that no bottom-moored transponders are used for reference. Consequently, line-of-site problems that are inherent in long-baseline navigation are much diminished. In general, this system provided good tracking of the submersible during transects; however, there were periods when the position fixes were noisy. Re-occupation of positions sometimes resulted in discrepancies of 10 to 50 meters.

Video and Photographic Recording.

Lighting for the deep lake operations was provided by several 250 and 500 watt incandescent lights and a 1500 Watt-sec strobe. These lights, although adequate for close-in sampling and observations, did not allow us to take full advantage of the exceptional clarity of the lake. Typically, only a swath 5 to 10 meters across our path was adequately lighted to allow detailed observations.

By making some assumptions about submersible speed and this 5-10 m visual swath, we have estimated the percentage of the bottom covered by our observations with Deep Rover. The 39 science dives had an average bottom time of 4 hours, and typical speeds were 0.5 knots. This results in 144 kilometers of track. For a 10 m swath we observed 1.4×10^6 m^2 of lake bottom. Because of track crossing and sampling stops, we estimate that the observations are only 50% efficient. Consequently, we have covered approximately 7×10^5 m^2 of the bottom. Of this, 63% was spent in the Detailed Study Area and 37% was divided between biology and USGS dives. The total lake area is 53 km^2. Consequently, we covered approximately 1.4% of the lake floor with Deep Rover. Within the South Basin, the site of the thermal anomalies within the water column, our dive tracks covered less than 25% of the bottom.

Plate 1. Deep Rover being towed to dive site within the submarine tender. Photo by Steve Nehl, The Oregonian newspaper.

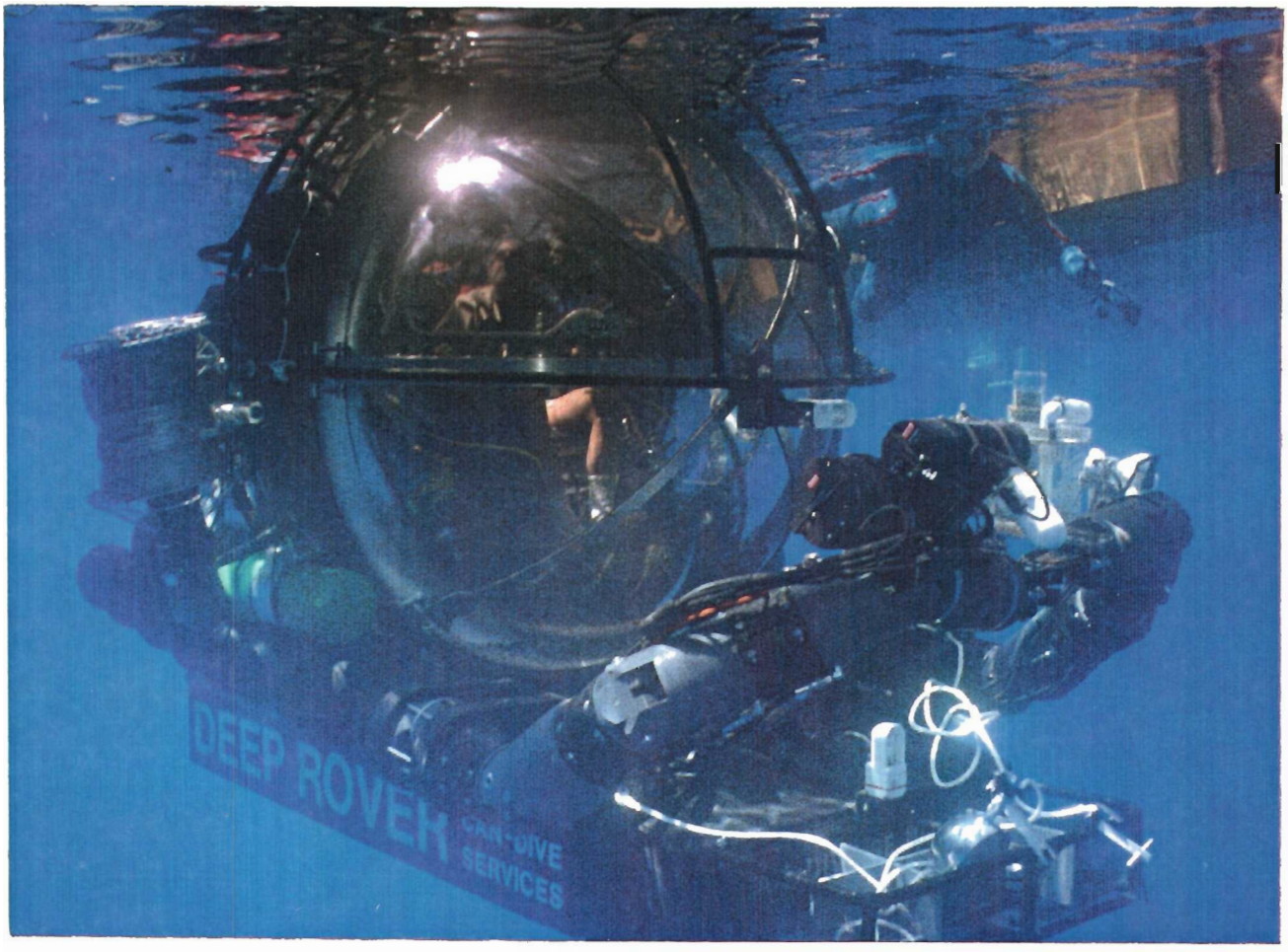

Plate 2. Deep Rover just after launch. Note the basket of "tools" at the front of the sub. The mechanical arms are folded above the basket. The water sampler and pumping system are visible just behind the port arm. Photo by Steve Nehl, The Oregonian newspaper.

Still photography was accomplished with a Photo-Sea camera system. The camera and strobe were mounted on the starboard arm of Deep Rover. With this system the aperture is fixed at the surface; thus the exposure is sensitive to the brightness of and the distance to the subject. Some of the dives were photographed in stereo. Fujichrome 400 film, with a camera aperture of f. 5.8, was used on most dives.

Both internal and external video cameras were used. The external video camera, which provided the highest quality images, was also located on the starboard arm of the submersible. It was connected to an internal 8 mm video recorder. The internal camera was located above the pilot's left shoulder and provided a broader but somewhat degraded visual perspective through the acrylic hull.

Sampling of Rocks, Crusts and Sediments.

The submersible was equipped with a forward sample basket (shown in Plate 2) which served both to carry sampling and measurement tools and as a receptacle for retrieving rock and sediment samples. Sampling of rocks and crusts could be accomplished by picking up specimens with the mechanical arm and dropping them into the basket. In 1988 we used a small push core to take two cores within the Detailed Study Area. For the 1989 field program we developed a submersible-deployed coring apparatus based on the small Soutar box-corer designed by Andrew Soutar of Scripps Institute of Oceanography. The device, which was positioned forward of the submersible, could be released upon command by the pilot using the same hydraulic pin retraction technique used for the Benthic Barrel (see below). The corer would free-fall to the sediments and at the same time release a buoyant package which carried a recovery line to the surface. With this system we were able to position cores with a accuracy of 1 to 2 meters on the bottom. The cores were approximately 30 centimeters in length, undisturbed, and very high quality. Box core locations for the Detailed Study Area are shown in Figure 3.

Temperature Probe.

A device for measuring temperatures within sediments and bacterial features was attached to the wrist mechanism of Deep Rover's mechanical arm. This configuration brought the probe into vertical position with a simple wrist-rotate motion, thereby allowing easy insertion with shoulder motion. The temperature measuring device was a custom-built, fully-immersible thermistor probe connected by a neoprene jacketed cable to a matching precision thermometer inside the submersible. This Yellow Springs Instruments thermistor probe was constructed of a 60-cm-long, 1/4"-diameter stainless steel tube sealed and rounded at one end with three Series 400 thermistors epoxy-potted and evenly spaced within the tube at 20 cm, 40 cm, and at 60 cm, the end of the tube. Thus, with the thermistor probe fully inserted up to the neoprene-jacketed cable connection, the three thermistors would record temperatures at 20 cm 40 cm, and 60 cm below the surface. These recorded temperature values were manually read out inside the submersible on an Omega Model 5830 Thermistor Thermometer with a measurement resolution of 0.01°C and an absolute accuracy of ±0.2°C . The temperature data were also logged on a data channel by the video recorder and through communication with the surface vessel. To ensure reliable, consistent temperature readings, the thermistor thermometer was recalibrated against known resistance values periodically throughout the sampling program.

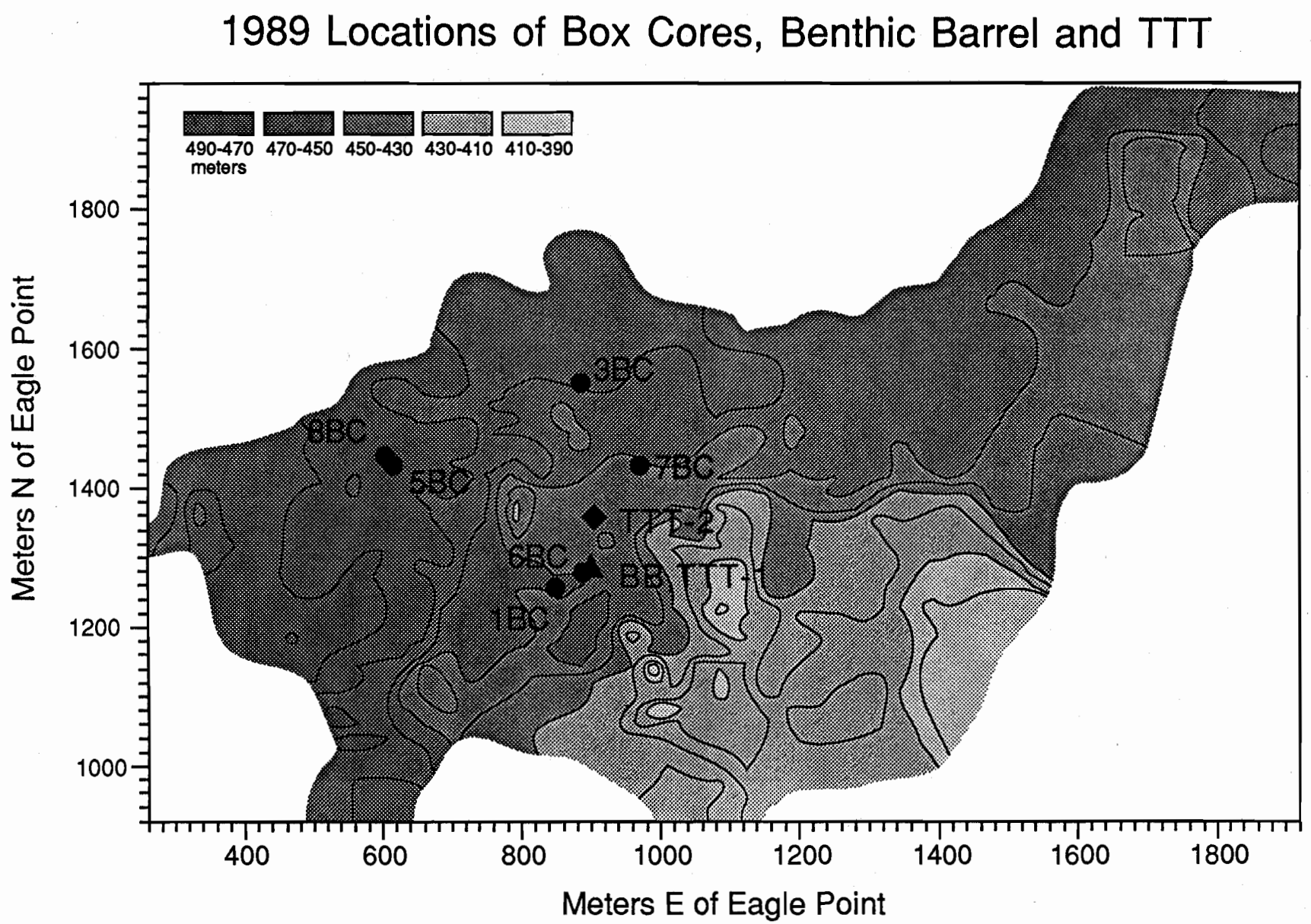

Figure 3. Box core locations in the Detailed Study Area. Bathymetry determined by near-bottom CTD measurements.

Benthic Barrel.

The "Benthic Barrel" consisted of a large, upright 55-gallon polyethylene barrel completely open at the bottom end and vented by a 2.5-cm-diameter hole on top. The barrel lid was removable with an O-ring seal and retaining ring, and the open bottom edge of the barrel was fitted with a 25-cm-wide silicone rubber skirt to ensure a tight seal over the vent site. When placed on the sediment, the barrel enclosed 0.26 m^2 of the bottom surface area. The internal volume of the chamber, initially flooded with ambient lake water, was slowly replaced by vented fluids. Inside the barrel, six 2-liter General Oceanics Niskin water sampling bottles were mounted vertically around an internal polycarbonate plastic frame. At predetermined intervals, the open bottles were sequentially tripped and closed by a microprocessor-controlled motor housed in an anodized aluminum pressure case. In this way, the water in each bottle represents a time-series sample of the *in situ* water which had exchanged with the sediment and advected into the barrel during its deployment. The barrel was suspended from a frame at the front of the submersible. Retraction of a hydraulically controlled pin dropped the barrel and its attached flotation device onto a desired spot. Recovery was accomplished when the submersible pilot actuated a pull-pin release to detach a small anchor, thus allowing the Benthic Barrel to float to the surface. The deployment site for the Benthic Barrel is shown in Figure 3.

Recording Sediment Temperature Probe.

The sediment temperature probe ("TTT") consisted of a Sea-Bird Electronics SeaCat SBE 19 Profiler housed in a 4-inch-diameter pressure case with a 24-inch-long, 1/4-inch-diameter stainless steel tube projecting from one end. Epoxy-potted inside the tube, three temperature-sensitive thermistors were connected to three separate data channels inside the profiler. The SeaCat pressure case and its projecting temperature probe were then suspended vertically in a sliding bracket connected to three vertical plastic rods attached to a weighted base plate.

Immediately before a dive, while the submersible was at the surface, the temperature probe and weighted frame were suspended from the mechanical arm of the submersible. In this upright configuration, the profiler would slide to the top of the vertical rods so that the end of the thermistor probe was safely held above a 2-inch -diameter hole drilled into the base plate. Later, as the submersible placed the weighted base plate and frame on the lake bottom and released the profiler, the upright pressure case and thermistor probe slid down the frame allowing the thermistor probe to project through the hole and penetrate the sediment surface to a depth of 35 centimeters. Fully inserted in the sediment, the deep thermistor was 35 cm below the sediment surface, the middle thermistor was 5 cm below the surface, and the top thermistor was 5 cm above the sediment in the bottom water. Once deployed, the SeaCat Profiler and thermistor probe automatically recorded sediment/bottom water temperature profiles two times a second and stored those data in solid-state memory. The SeaCat thermistors were accurate to within ±0.01°C with a resolution of 0.001°C over a temperature range from -5°C to +35°C. The deployment sites for the TTT are shown in Figure 3.

Interstitial Pore Water Samplers - "Peepers".

Peeper samplers were constructed of polycarbonate plastic and were used to sample the small-scale structure of dissolved species in sediment interstitial pore waters. The sampler worked by allowing a small, contained quantity of water to come into equilibrium with the surrounding *in situ* water through a dialysis membrane. The sampler was constructed from two overlain sheets of

five-inch-wide polycarbonate plastic assembled with nylon machine screws to avoid any metallic contamination. Side-by-side oval compartments (1 cm high x 4.5 cm wide) were milled through the thin cover sheet and into the half-inch-thick backing plate at two centimeter intervals down the length of the samplers. A plastic T-handle was added to the top of the peeper, and the bottom edge was bevelled to allow the sampler to slice into the sediment while causing only a minimal disturbance of the interstitial pore waters.

A peeper sampler was prepared by filling the compartments with degassed distilled water and carefully laying a piece of dialysis membrane over the full compartments so as to exclude any air bubbles. The thinner cover sheet was then laid over the membrane, holes were poked for the nylon screws, and the cover sheet was screwed down tight. The entire sampler was then allowed to equilibrate in a closed bath of distilled water under a nitrogen atmosphere where the sampler lost most of its dissolved gases by equilibration. Immediately before the submersible left the surface at the start of a dive, the peepers were transferred to a similar sheath of degassed water in the submersible's basket. As soon as the submersible arrived on the bottom, the peeper was deployed using the sub's articulated arm. The peepers were left in the sediments to equilibrate for approximately one week before recovery. The locations of peeper deployments within the Detailed Study Area are shown in Figure 4.

II.5. Water Temperature, Conductivity, and Light Transmission

CTD Instrumentation.

A profiling instrument package was deployed on a hydrographic wire and was also carried on the submersible in order to measure the conductivity, temperature, and light transmissivity as a function of depth in the water column. This instrument package, which we will refer to as a "CTD", was a SEACAT® model SBE19 (Sea-Bird Electronics, Inc.) coupled to a 25-cm path-length beam transmissometer (Sea Tech, Inc.). The CTD records all data internally (2 scans per second of all sensors for up to 4 hours) and was also monitored in real-time through a special conducting hydrographic cable attached to the computer on the research boat or onboard the submersible. This instrument was specifically modified by the manufacturer to optimize conductivity measurements in the fresh water system of Crater Lake. The CTD has a temperature resolution of better than 0.001°C; the conductivity resolution is 4×10^{-5} Siemens/meter (0.4 µmhos/cm); and the pressure resolution is 0.5 decibars.

In this report the conductivity data is presented in the accepted SI unit of conductivity: Siemens/meter. This unit can be converted to the common limnologic units of µmho/cm by the following relationship: 1 siemen/meter = 10,000 µmhos/cm. However, it should also be noted that the CTD records conductivity at *in situ* temperatures - not at 25°C, as is conventional for reporting the conductivity of discrete samples. Therefore, our data cannot be directly compared to general tabulations of lake conductivities (e.g., data in Thompson et. al., 1987). There is a major temperature effect on conductivity; for example 15°C surface water and 3.6°C deep water have conductivities of 0.010 and 0.007 siemens/meter, respectively. Using rigorous physical chemical models, this temperature effect can only be corrected to 25°C for a few simple electrolytes such as KCl (Harned and Owen, 1958). Tabulations of single-ion specific conductances and functions describing their change in conductance with increasing concentration exist, but the temperature effects on these functions have not been determined for each ion and cannot be predicted from "first principles" (Conway, 1952; Robinson and Stokes, 1959). The most accurate alternative,

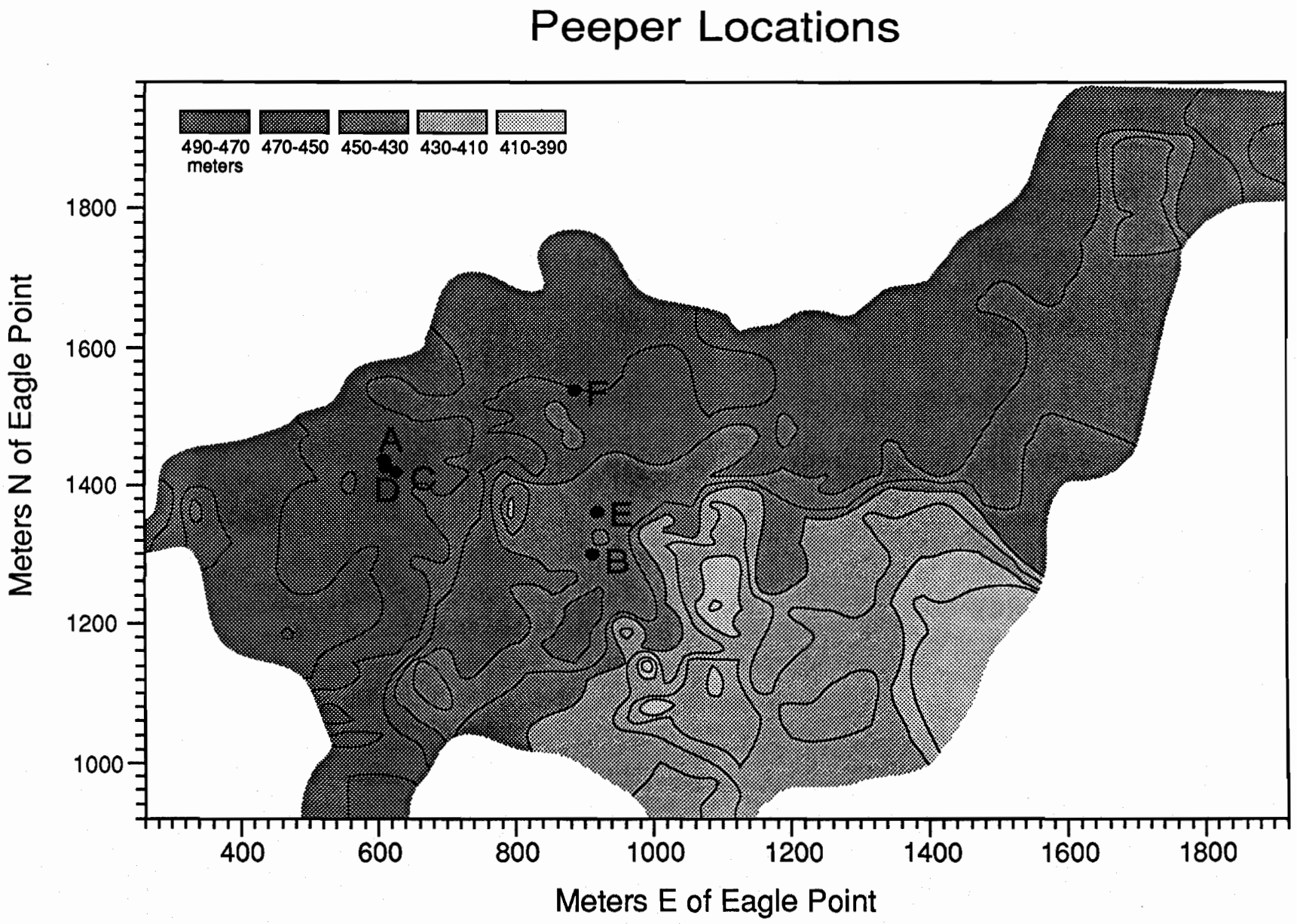

Figure 4. "Peeper" deployments in the Detailed Study Area.

which we have chosen for our work, is a complete temperature calibration of the instrument using the actual ionic composition of Crater Lake water. We believe that the precision and accuracy necessary for computations of density in the deep lake justify this effort.

The CTD was recalibrated for temperature and conductivity at the OSU calibration facility in January 1988 and May 1989. Conversion of pressure (decibars) to depth (meters) is carried out by the integration of water densities down through the water column. The depths are effectively equal to 1.02 times the pressure. All the physical properties derived from the measurement of temperature, conductivity, and pressure were calculated using an equation of state for water adapted for application to lakes (Chen and Millero, 1986). The temperatures of specific water samples collected from the hydrographic wire were estimated from the CTD record for the same hydrocast. Similar estimates for submersible-collected samples were attempted using the on-board CTD record. The separation of the CTD sensor from the water sampler on the sub, coupled with a lack of control between the time base of the dive-logs and CTD-logs, made accurate determination of these water sample temperatures difficult.

Thermistor Chain Mooring.

Three recording thermistor chains were deployed on a single mooring within the North Basin area from 2 September 1989 until 10 July 1990 to monitor details of the water column temperature profile. Each thermistor chain was 100 meters long with 11 thermistors spaced every ten meters along its length. Two of the three thermistor chains were placed end-to-end to monitor water temperatures within the bottom 200 meters of the water column. The third chain sampled the upper water column thermal stratigraphy between 50 and 150 meters depth. Each thermistor chain was connected to an Aanderra TR-2 Temperature Profile Recorder which logged data on a 1/4-inch reel-to-reel magnetic tape at one hour intervals. Each hourly measurement cycle consisted of 12 data channels in sequence, a fixed reference reading in channel 1 to monitor the performance of the instrument and 11 channels of temperatures. The instruments were also calibrated before deployment and again after recovery in a high-precision, temperature-controlled water bath to ensure reliable and reproducible data during their ten month deployment. The results from this thermistor mooring deployment are presented in Appendix A.

II.6. Current measurements

For 16 days, from 22 August 1989 until 7 September 1989, an InterOcean S4 current meter was deployed within the Detailed Study Area (X=585m; Y=1478m, relative to Eagle Point) at 468 meters depth on a mooring in 475 meters of water. The S4 current meter sampled current velocity, current direction, pressure, and temperature data every 30 minutes during its deployment. Unlike other current meters, the spherical S4 instrument contains no moving parts except for the sensing element in its flux-gate magnetometer. Its velocity sensor consisted of a toroidal coil, two orthogonal sets of electrodes, and associated electronic circuitry. The coil produced a high-frequency modulated magnetic field in the region surrounding the current meter. The movement of water through this field induced a potential difference in the associated electrical field that was sensed by the orthogonal electrodes. The velocity information, compass output and other sensor data were then processed by an internal computer and stored in solid-state memory.

II.7. Water Samples

Water samples from throughout the water column were collected from the NPS research boat using the standard 1/8" stainless steel hydrographic wire. Various oceanographic water samplers were mounted on the wire, depending on the sample requirements for individual chemical analyses. Typically, 5-liter or 30-liter Niskin®-type samplers (General Oceanics) were used. Some of the sampling for trace-metal analyses used teflon-coated 5- and 20- liter GoFlo®-type (General Oceanics) samplers. In order to avoid contamination and preserve the integrity of each sample, great care was taken in each step of collection, preservation and analysis (Bruland et al., 1979). These hydrocast locations are shown in Figure 5.

Water sampling on the submersible was accomplished with Niskin-type samplers designed and owned by Dr. Bruce Robison, Monterey Bay Research Institution. These all-plastic samplers held five liters of water. They were tripped with solenoids operated by the submersible pilot. Early in the dive program, paired water samplers were carried in the sample basket and were lifted out and into place with the mechanical arm prior to tripping. This allowed the sampler to be placed relatively accurately in relation to specific features (such as the bacterial mats that are discussed below). The basket placement, however, subjected the samples to jostling and possible leakage during submersible recovery. Consequently, for most of the later dives, the water bottles were mounted on the port side of the submersible, just forward of the acrylic hull. The locations of submersible-collected water samples are shown in Figure 6.

A pumping system was developed to collect water from certain thermal-chemical features with a minimum of lake water admixture. Bruce Robison's large volume filtration pump was attached to the downstream end of a five-liter Go-Flo bottle. A plastic tube and nozzle which could be directed into these features was attached to the upstream end of the water bottle. A sample was obtained by pumping fluid into the bottle for approximately one minute to flush out the ambient water; then the opening and closing valves were tripped.

II.8. Chemical Analyses of Water Samples

All water samples for ionic analyses were filtered through an acid-cleaned, 0.4μm polycarbonate filter (Nuclepore®) under a clean atmosphere. Samples for major and trace cation analyses were acidified to pH2 with sub-boiled redistilled HCl. All samples were subsequently stored in the dark at 4°C until analysis.

The cations, Na, K, Ca, Mg and Li, were analyzed directly by flame atomic absorption spectrophotometry using a Perkin Elmer model-5000 spectrophotometer. All samples and standards were matrix adjusted with CsCl to suppress ionization interferences. Calcium analyses included $LaCl_3$ as a releasing agent to suppress interferences from dissolved silicon. The instrumental setup involved for each element generally followed Perkin Elmer (1982) or EPA (1979) methods. Each individual sample was analyzed two to four times, where each "analysis" is the average of three separate three-second instrument readings. The instrument is recalibrated ("resloped") between each sample.

Standard additions methods were applied to some samples to verify the absence of matrix interferences between samples and standards. Replicate analyses of approximately 10% of the total number of samples were performed during each analysis sequence to check the overall precision.

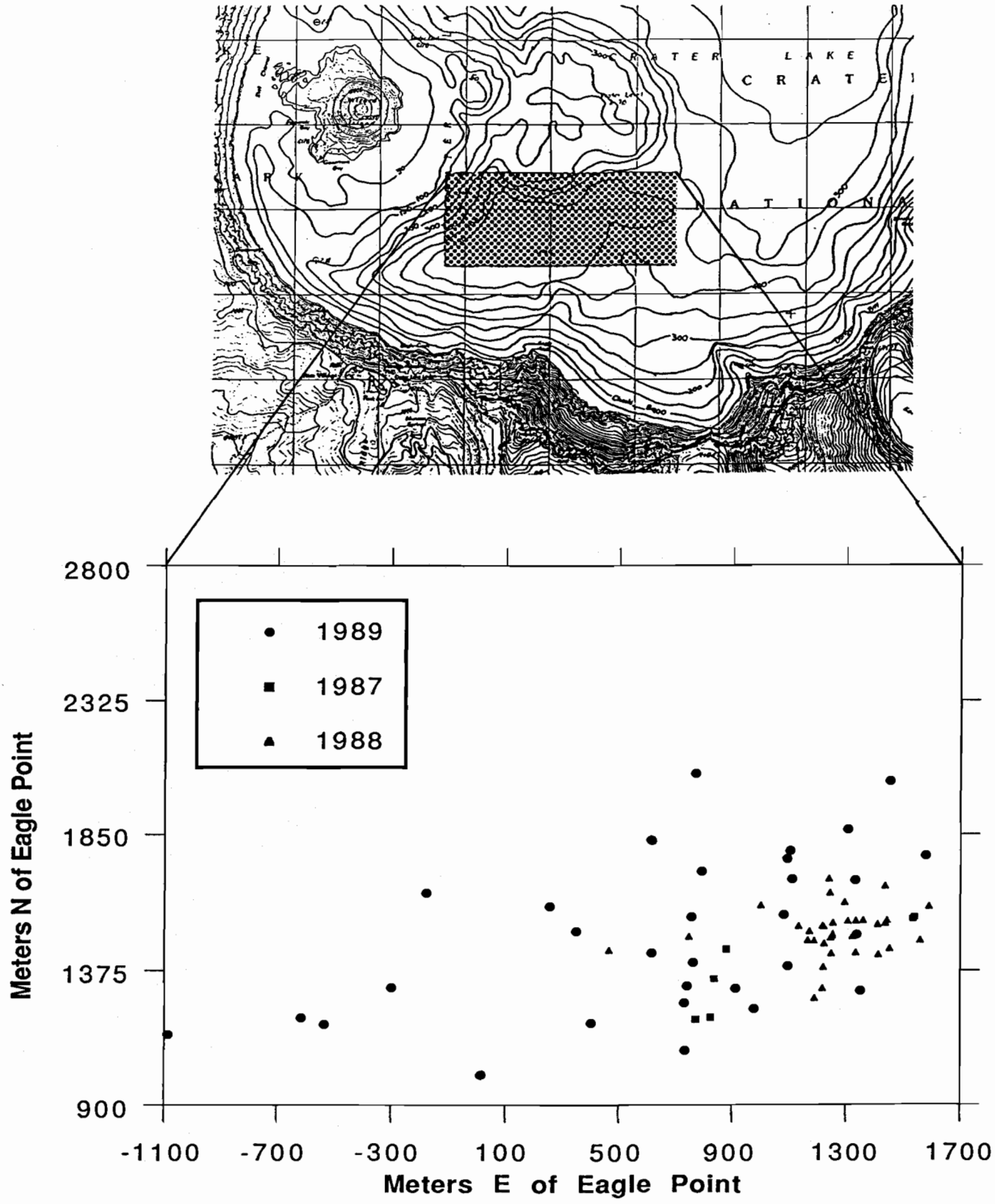

Figure 5. Hydrocast locations in the Detailed Study Area.

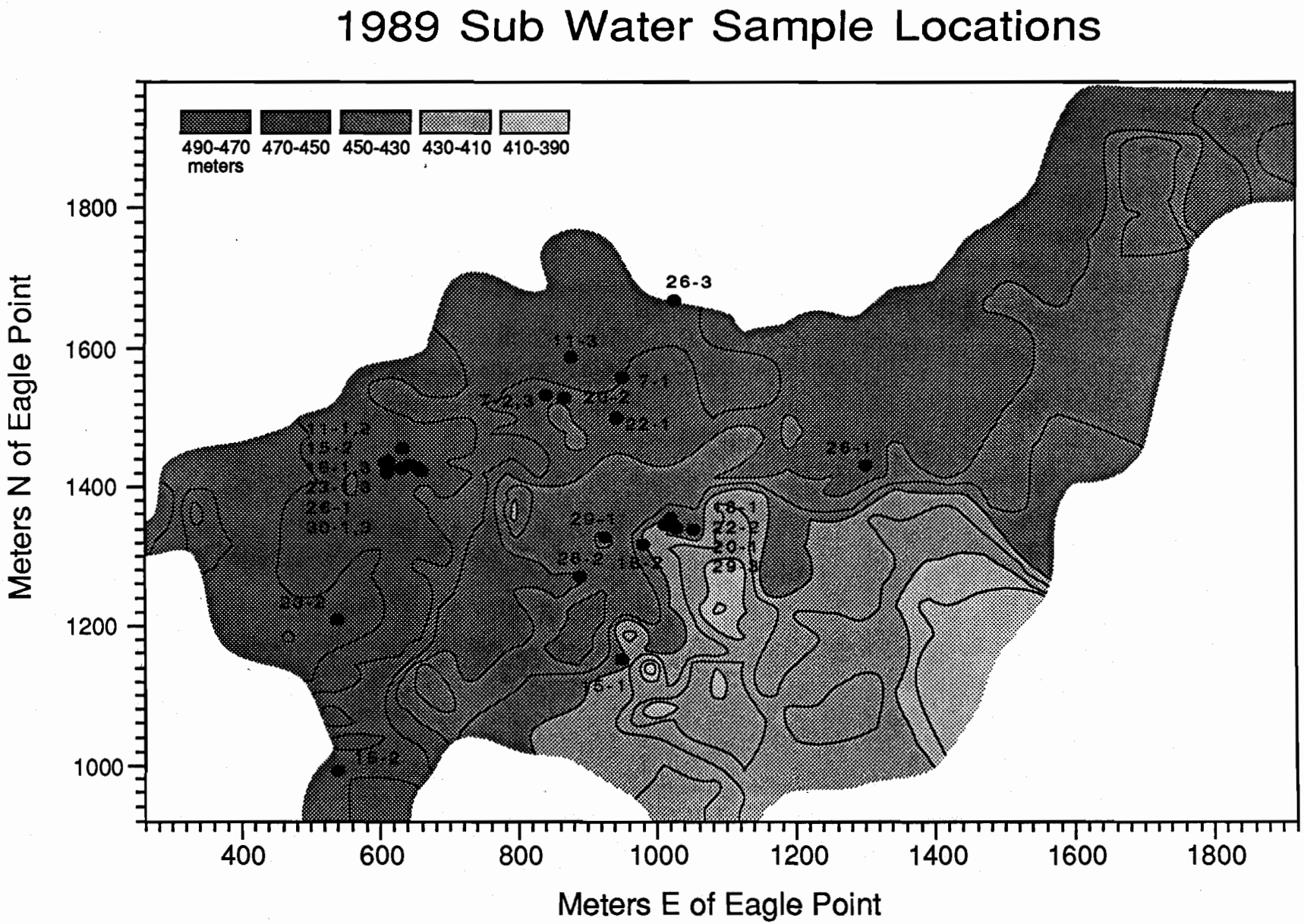

Figure 6. 1989 submersible water sample locations. The numbers refer to the dive number. Thus, 7-1 refers to CD207-1; 30-3 refers to CD230-3; etc.

These repetitive analyses are critical to achieving the maximum precision which is necessary for interpreting the small changes in concentrations present in Crater Lake. Based on replicate measurements, the precision of the major cation analyses is better than ±0.5% (0.2% for Mg, 0.3% for Ca, 0.4% for Na and K). For quality control, preserved samples from earlier data sets (e.g. 1987) are rerun along with new samples (e.g. 1988). The accuracy of the analyses can be traced to certified single-element standards and our results are consistent with other published and unpublished analyses (Thompson et al., 1987; Larson, 1987). Manganese was determined with a precision of approximately 5% by Zeeman-corrected atomic absorption spectrophotometry with graphite furnace atomization.

Silicate concentrations were determined as silicic acid by a colorimetric molybdenum blue method using an Alpkem rapid flow analyzer with a precision of 0.3%. pH values were measured on gas-tight samples in a thermostatted system at 25.0°C using low-ionic strength electrodes and buffers. Alkalinities were determined in the same system by full Gran titrations using a microburet. Due to the low ionic strength of lake water (i.e. as compared to seawater), the precision of the alkalinity determination is only about 3-4%. Sulfate and chloride analyses were determined by ion chromatography and have a precision of 2% and 1% respectively. Overall charge balance calculations for a typical sample agree to within 4% (i.e. Σcations = 1.08 meq and Σanions = 1.11 meq) and are probably constrained by the accuracy of the bicarbonate determination (pH, Alk.).

Radon-222 (^{222}Rn) and radium-226 (^{226}Ra) were measured using the procedures developed in Mathieu (1977). Water from the sampler was transferred to evacuated 20-liter glass bottles. Radon was stripped by bubbling helium through the sample and collected on an activated charcoal column at dry ice temperature. The column was heated and the radon transferred to an evacuated ZnS-coated scintillation cell. This cell was placed in a photomultiplier-tube counting system calibrated with ^{226}Ra standards. ^{226}Ra is measured in a similar fashion except that the water sample is kept sealed in the 20-liter bottles for two weeks to allow ^{222}Rn to achieve radioactive equilibrium with dissolved ^{226}Ra. Counting errors for both analyses are always less than 10%.

Several samples of lake water, brines and porewaters were analyzed at MIT using a VG Inductively-Coupled Plasma Mass Spectrometer. This state-of-the-art instrument allowed us to carry out a sensitive, semi-quantitative elemental analysis covering the majority of the periodic table, thus confirming that we have characterized most of the major chemical components in these samples. We also completed a high-precision isotope-dilution analysis for REE, Ba, Sr, Rb, U, and Cs.

II.9. Sediment, Crust, and Mat Analyses

Samples were prepared for analysis by freeze-drying the wet solids and then pulverizing the dried material with an agate mortar and pestle. Atomic absorption spectrophotometry (AAS) was used to determine concentrations of Li, Na, Mg, Al, Si, K, Ca, Ti, Mn, Fe, Ni, Cu, Zn, and Ba in the sediments, crusts, and bacterial mats using the dissolution and analytical procedures outlined in Dymond et al. (1984). The same techniques were used to analyze samples of USGS standard rocks. A comparison of our results with the standard values demonstrates that there are no systematic errors in our methods.

In most cases, splits of the samples were analyzed for a suite of elements (Cr, Fe, As, Sb, Ba, REE's, Hf, Th and U) by instrumental neutron activation analysis. For elements measured by both techniques, the data agree to within 10%. Samples were also analyzed for C, N, and S using an automated Carlo Erba CNS analyzer. In cases where sufficient material was available, phosphorus was measured colorimetrically.

For the "spire" sample (see the Solid Phase Geochemistry section) a quantitative microprobe transect was made to define the small-scale spatial variability in this unusual material. The sample was vacuum-impregnated with epoxy, polished, carbon coated, and quantitatively analyzed with a Cameca electron microprobe calibrated with rock and alloy standards. Porosity variations and imperfect surfaces result in lower precision for these samples than is typical for microprobe analyses. Precision of the major elements is estimated to be 5% and for minor elements 10% to 20%.

II.10. Additional Chemical Analyses

In addition to the water and sediment analyses that have been carried out at Oregon State University, we have distributed samples for analysis to the following people: Dr. Charles Bacon, US Geological Survey (rock samples); Dr. David Karl, University of Hawaii (microbiological investigations); Dr. Gary Klinkhammer, Oregon State University (rare earth measurements in lake fluids); Dr. John Lupton, University of Santa Barbara (helium isotope and tritium analyses); Drs. Clifford Dahm and Maribeth Watwood of the University of New Mexico (microbiological investigations); Dr. Marvin Lilley, University of Washington (methane analysis); Dr. Dale Pillsbury, Oregon State University (moored thermistors and current meters); Dr. Peter Schlosser, Columbia University (^{14}C analyses); Dr. Ray Weiss, University of California, San Diego (Chlorofluorocarbon measurements); Dr. Goeff Wheat, University of Hawaii (pore water studies).

III Results

III.1. Major Features Observed with the Submersible

The use of the remotely operated vehicle (ROV) and the manned submersible, Deep Rover (Plates 1 and 2), enabled us not only to make detailed measurements and obtain high-quality samples, but they also gave us unparalleled observational opportunities. Features normally isolated by more than 500 meters of water and engulfed in darkness could be studied and photographed with relative ease. This technology has revealed geological features and biological communities that were previously unknown. In effect the work has brought to light the subaqueous portions of Crater Lake National Park.

We have used pressure measurements obtained from the CTD carried by Deep Rover to develop a detailed bathymetry for the Detailed Study Area (Figure 7). Although the spatial coverage of the Detailed Study Area is not so systematic as those provided by the echo sounding transects which produced Figure 2, these data provide much more detailed depth information than that of the relatively broad-beamed echo sounder. A few of the most important thermal-chemical features observed within the Detailed Study Area are shown on a three dimensional perspective version of this bathymetric map (Figure 8).

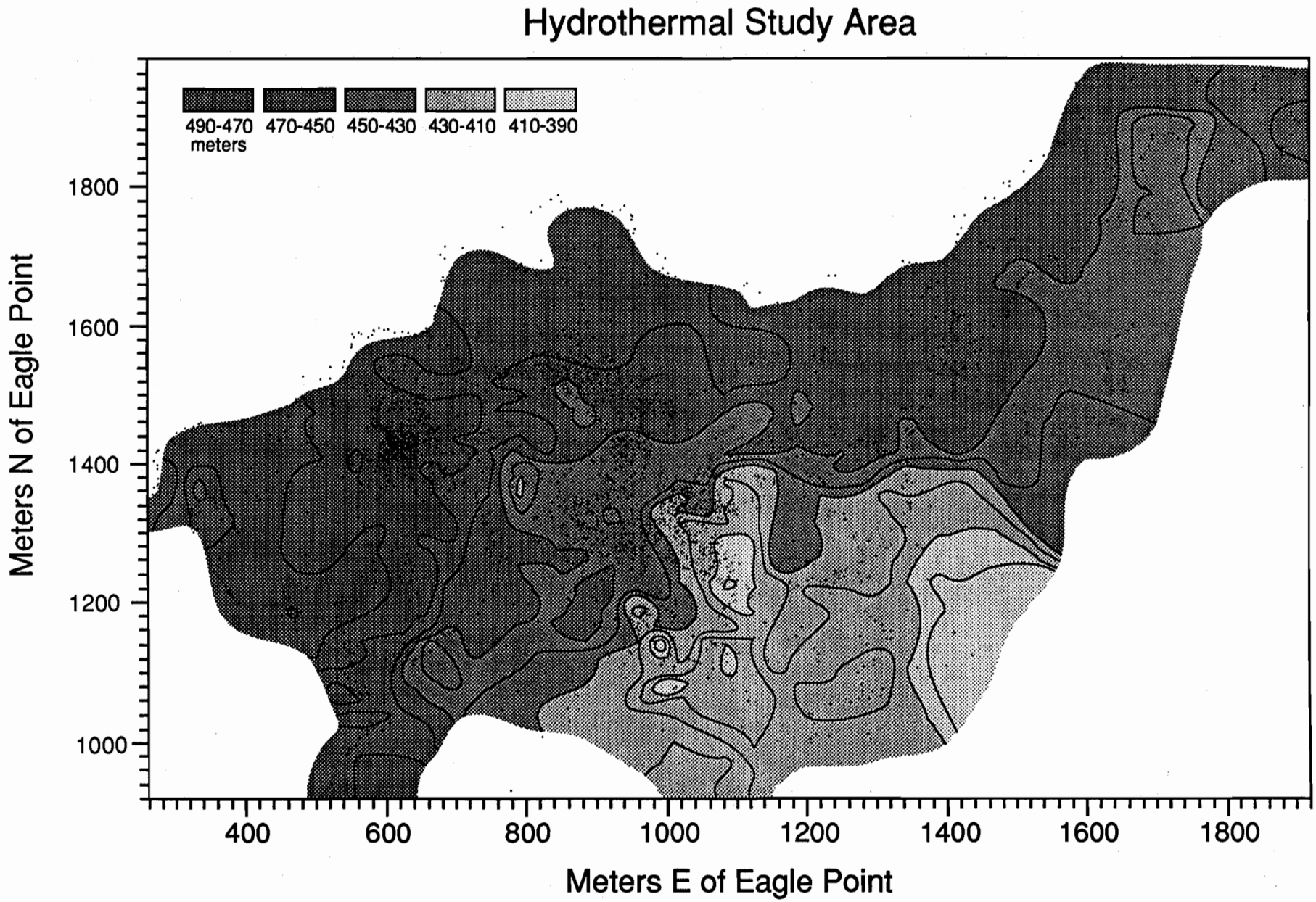

Figure 7. Detailed bathymetry as defined by nearbottom CTD data collected during Deep Rover dives.

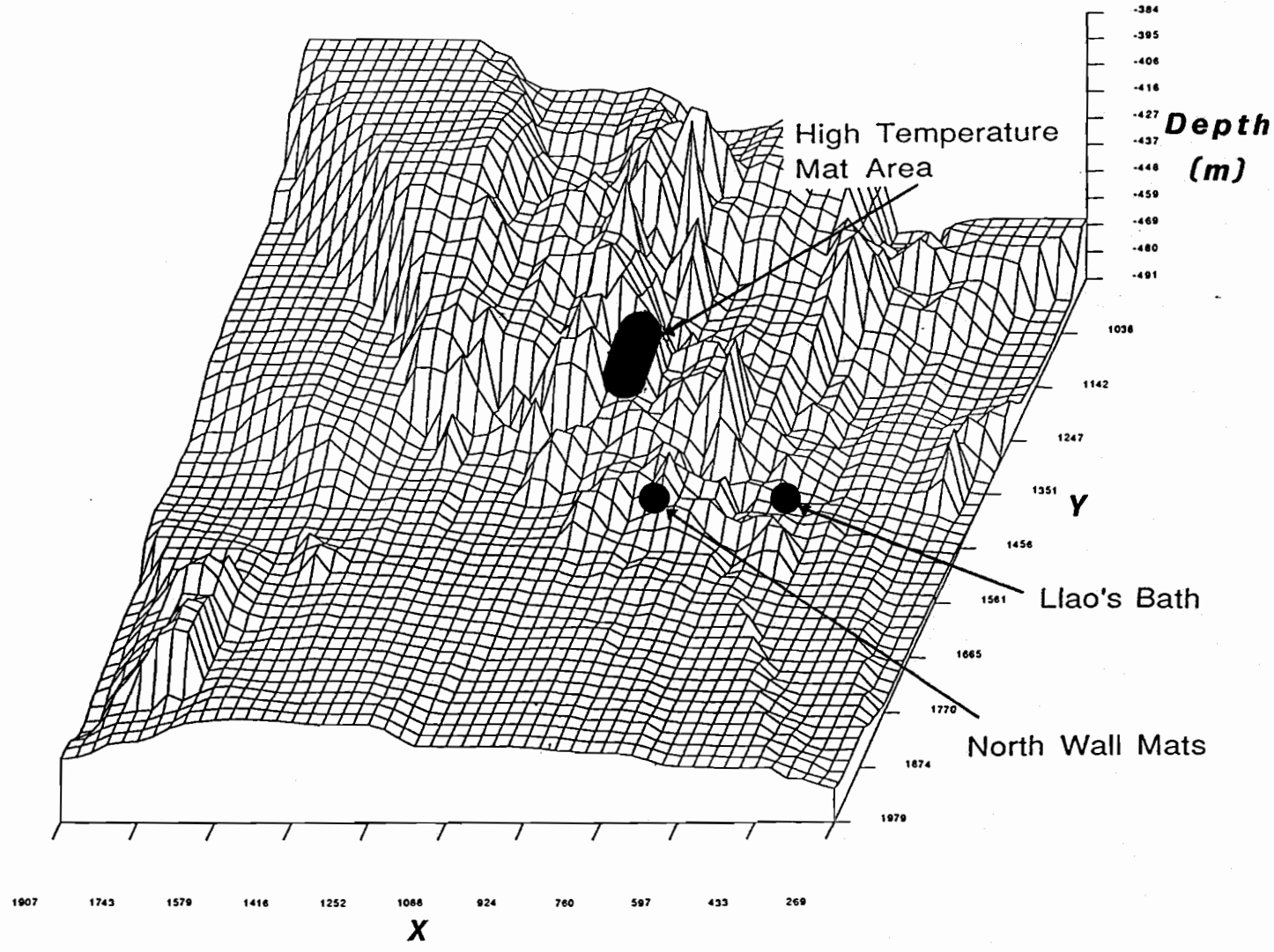

Figure 8. Detailed bathymetry from Figure 7 shown in a three dimensional perspective "mesh" map. Locations for "high temperature bacterial mats", "north wall bacterial mats", and the "Llao's Bath/brain mat complex" are shown. **This view is looking south.**

Iron-Rich Crusts.

Sediment crusts and pebbles which appeared to be iron-rich were discovered on certain parts of the lake floor during the 1987 ROV studies. During the first manned submersible studies, it was possible to collect samples of these features and to photograph them in greater detail. These crusts were found to occur in three forms: (1) pavements of multicolored (ochre to dark brown) crusts that covered dimensions up to 10 meters (Plate 3); (2) fields of pebbles with a similar range of colors as the intact pavements; they appeared to be broken-up equivalents of the pavements; (3) multiple ochre-colored sediment layers that were visible in areas of sediment slumping on steep slopes (Plate 4); sampling revealed the layers were partially-indurated iron-rich crusts.

Bacterial Mats.

The discovery of communities of bacteria which form mats of various sizes and morphologies was one of the most exciting observations made with Deep Rover during the 1988 field season (Dymond et al., 1989). Several of the mat types and forms are shown in Plates 5 to 7. The more detailed surveys carried out in 1989 revealed many bacterial mat locations within the Detailed Study Area. Although we were able to take samples of the mats and document the temperatures at only a few locations, our existing data document a wide range of sizes, morphologies, and temperatures. Temperatures recorded by inserting a 60-centimeter probe into the mats ranged from 4.3°C to 18.9°C.

Prior to the 1989 studies, we had observed the mats only within the Detailed Study Area. Near the end of the 1989 field program, however, we discovered a large area of bacterial mats on the northeast side of the lake off shore from Palisades Point. These newly discovered mats form structures which are 10 to 20 meters long and several meters across (Plate 8). It is noteworthy that the Palisades Point bacterial mats appear to only occur at or near the break in slope between the steep caldera wall and the relatively flat basin floor. When the dive was continued upslope for 500 meters beyond the bacterial mats, no other bacterial communities were found.

Pools.

Pools of saline water, which fill small depressions in the lake bottom, were discovered during the 1989 submersible program. All the pools were located in relatively flat, sedimented areas. They have a very sharp interface with the overlying lake water which is apparently maintained by the density contrast between the overlying waters and the pool water. Samples taken from the pools have salt contents as much as ten times higher than the overlying lake waters. Pools were discovered in three general localities. These are separated from each other by distances of 300 meters to six kilometers. Within each of the three major areas, a number of pools exist.

The first pool discovered, which we named Llao's Bath after the legendary Klamath Indian spirit of the lake (Clark, 1953), received the most detailed study. This pool is located in a sedimented area of low relief about 300 meters west of the steep cliff faces in the center of the Detailed Study Area, in the same locality where many bacterial mats were observed during the 1988 and 1989 diving program (Figures 8 and 9). Llao's Bath is an oval pool three to four meters long by one to one and a half meters wide (Plate 9). The pool is surrounded by sediments on three sides. A rounded outcrop approximately 1.5 m in diameter rises upward from the northwestern edge of the pool (Plate 10). Although the sediments surrounding Llao's Bath have very low slopes down to the edge, the depth within the pool increased sufficiently rapidly that the bottom could not be seen.

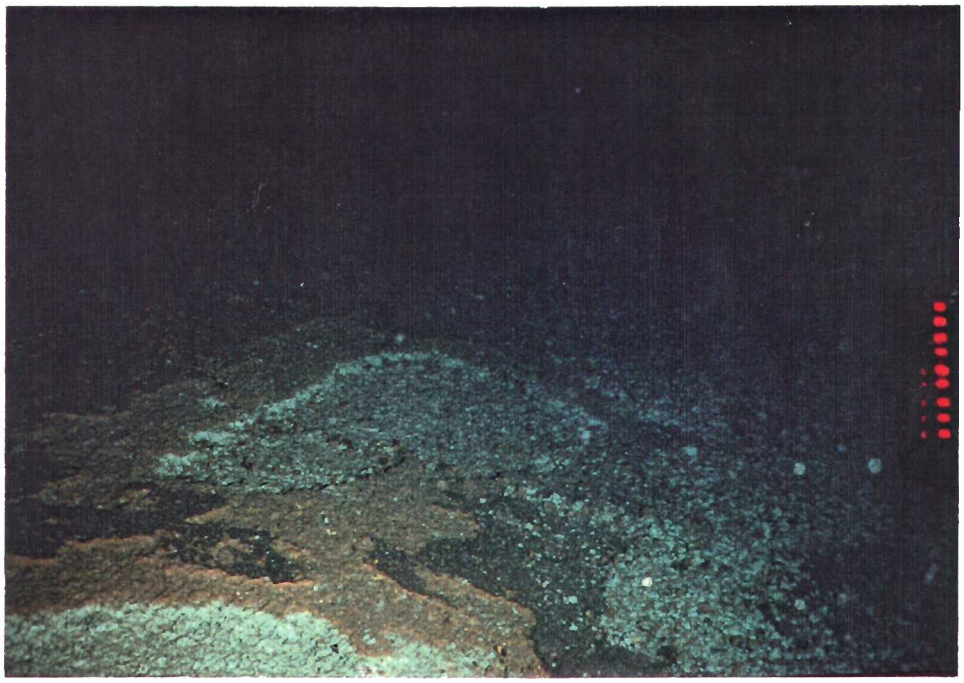

Plate 3. Underwater photograph showing a pavement of metal-rich crusts observed on dive 178. The ochre layers are iron rich. The field of view is approximately five meters on a side; however, the full extent of this particular encrusted sediment covers an area of least 30 by 30 meters.

Plate 4. Exposed sedimentary layering within the Detailed Study Area. Ochre colors reflect iron-rich layers. These downdropped exposures of semi-consolidated sediments are relatively common and appear to be the expressions of small-scale normal faults. This fault, located in the high temperature mat area, strikes N40°E with approximately one meter vertical separation (the high side is to the top of the photo).

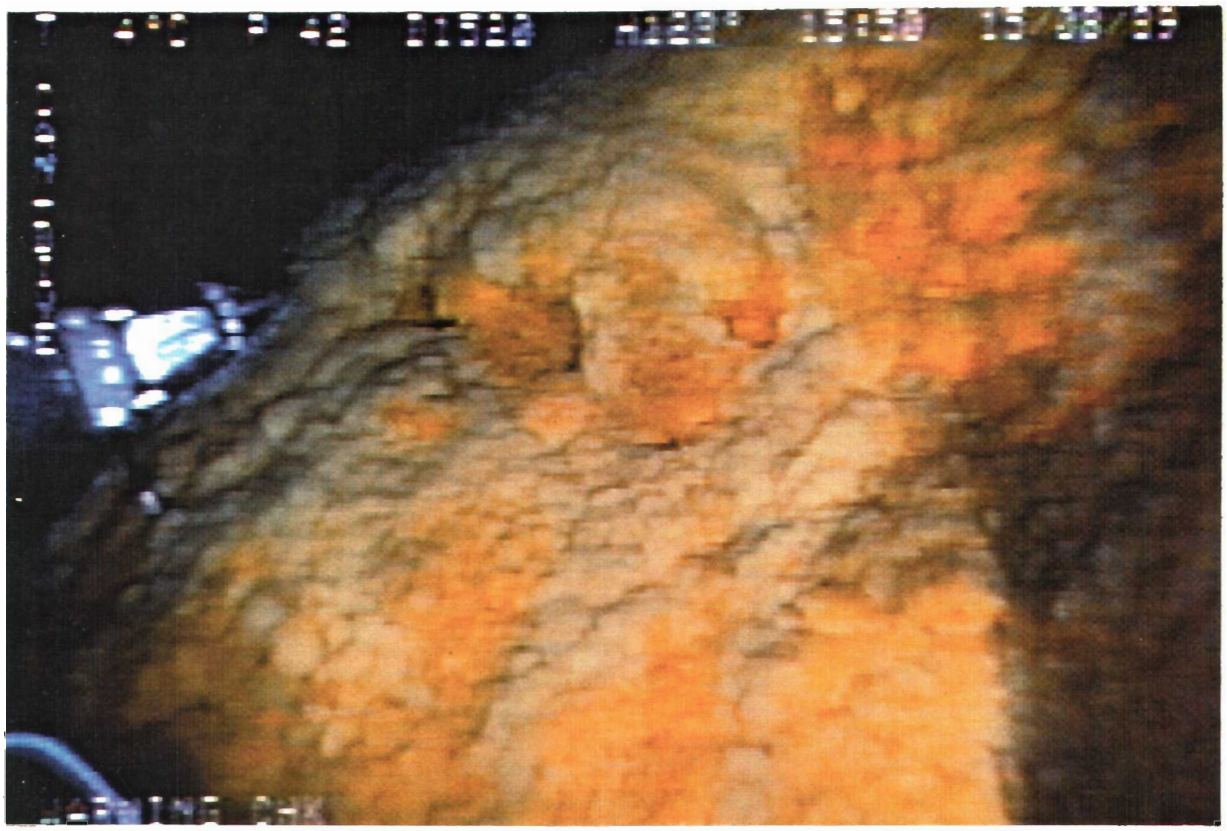

Plate 5. Bacterial mat from CD207. This is the same mat observed and sampled during CD179 in 1988. Note the temperature probe insertion on the left side of the photo. Field of view is about three meters across.

Plate 6. Bacterial mat on flat-lying sediments. The mat is about 1.5 meters across.

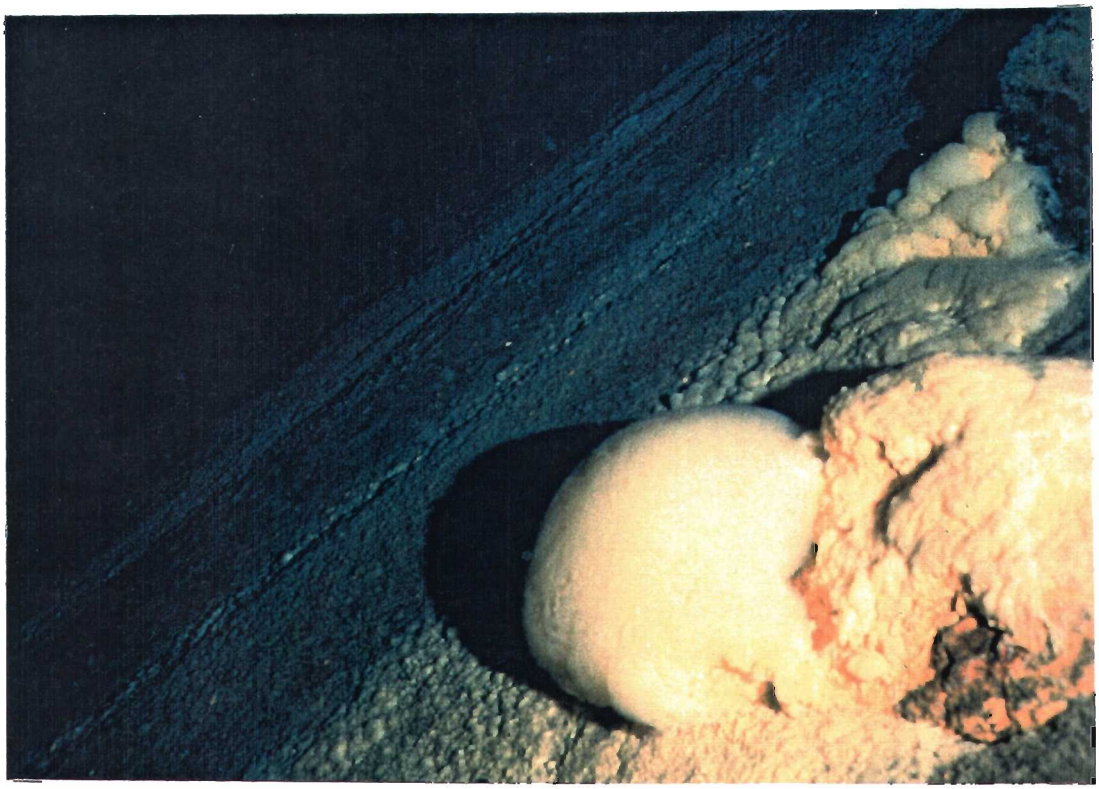

Plate 7. Bacterial mat on a steep surface. This mat, nicknamed the "basketball mat", was observed and sampled during CD 218. Although it has unusual morphology, its location on a steep surface and its relatively small size are typical of mats found in the area of the warmest water temperatures in the central part of the detailed study area.

Plate 8. Elongated bacterial mat in the Palisades Point area (CD 227).

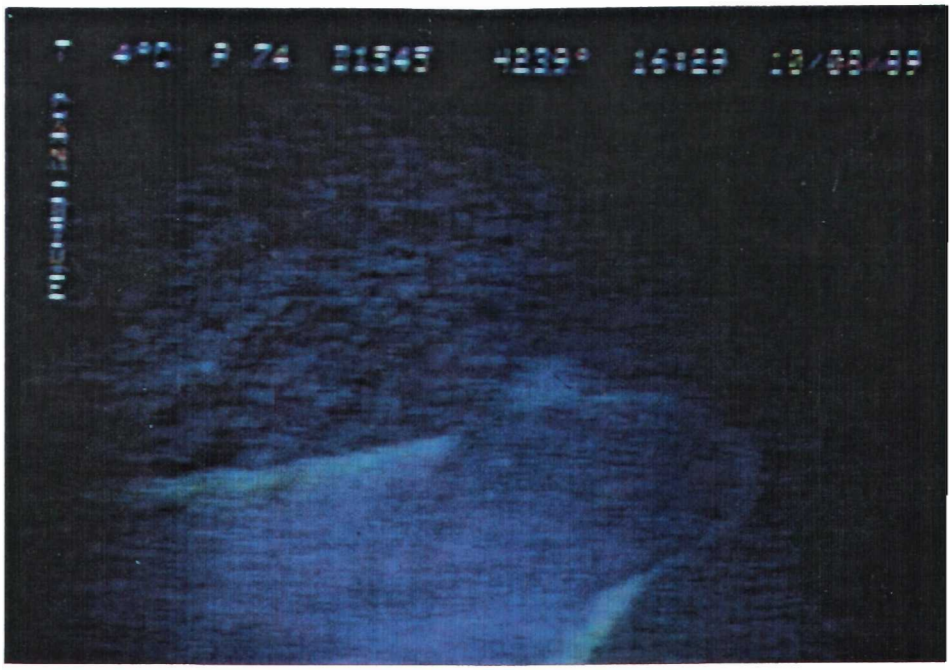

Plate 9. View of the northern end of Llao's Bath. The lighter blue in the center of the photo is the saline water of the pool. A rocky outcrop extends into the back side of the pool. Note the light-colored bacterial growth along the edge of the pool. The bacteria is attached to the sediments and to the outcrop.

Plate 10. Close-up of the rocky outcrop at the edge of Llao's Pool. Note the bacterial growth at the pool/rock interface.

Plate 11. "Brain mat" bacterial growth just to the west of Llao's Bath. Field of view is approximately three meters across, although the feature covers an area at least ten meters across. Small pools of saline water occur within each of the convolutions.

Plate 12. Closeup of the brain mat. Bacterial accumulation at this site.is approximately 50 centimeters thick.

Plate 13. One of the larger pools from the Palisades Point area (CD 228). This pool is more than five meters across. Small stream-like features with delta-like structures suggest that flow from left to right has occurred in the past, although no flow could be detected at the time of the observations.

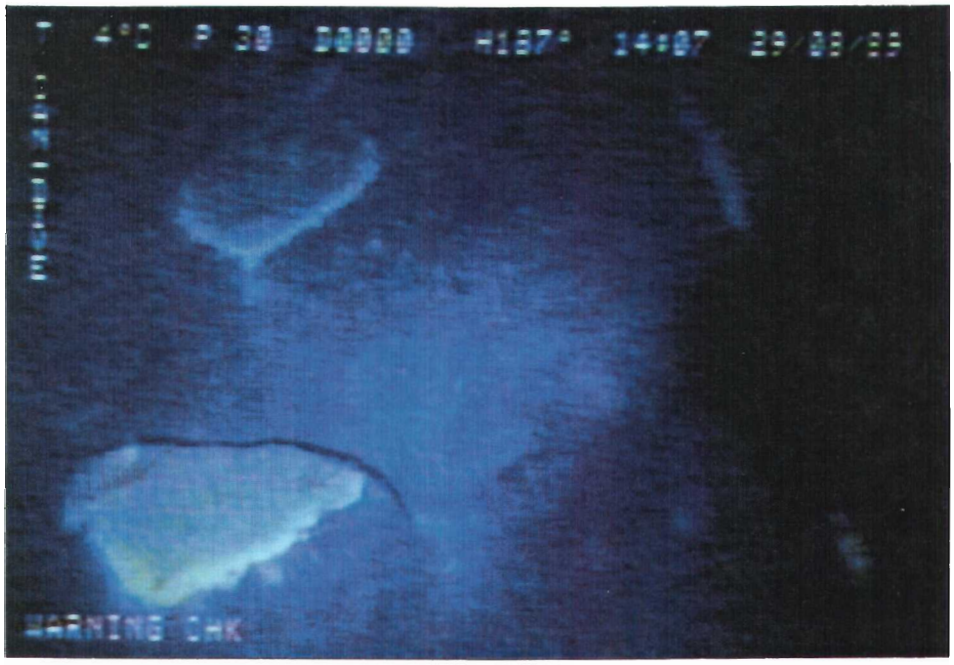

Plate 14. Another of the larger pools in the Palisades Point area (CD 228). Note the islands in the middle of the pool.

Plate 15. One of the stream-like features within the Palisades Point area (CD 227). This channel or rill flows downhill from its origin under the boulder (upper part of the photo).

Plate 16. An example of the siliceous spires that were discovered at the base of the slope below Skell Head. This view shows the tops of some adjacent spires which are 10 to 12 meters tall.

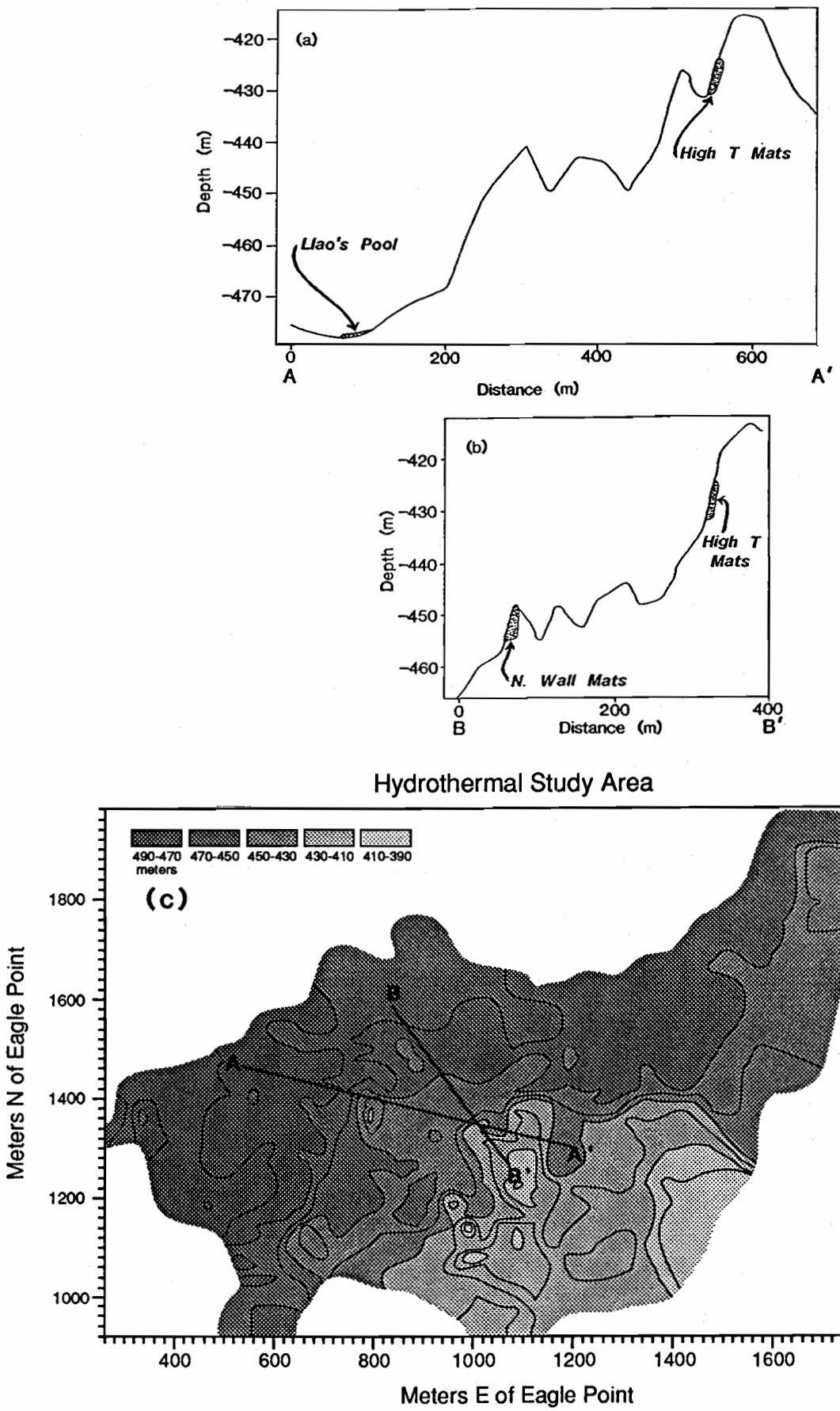

Figure 9. (a) Topographic cross section A-A' drawn from Llao's Bath to the high temperature bacterial mats. (b) Topographic cross section B-B' from the north wall mats to the high temperature bacterial mats. (c) Map of Detailed Study Area showing locations of cross-sections, A-A' and B-B'.

A thin bacterial coating, 10-20 centimeters wide, rimmed the margin of the pool. This bacterial rim was one to two centimeters thick. Although no distinctive inlet or outlet was apparent, the southern edge of the pool had a 20-40 centimeters wide and somewhat thicker bacterial covering. There were linear features in the bacterial rim which suggested that there has been overflow at this section of the pool. A slightly elevated, sedimented area extended to the west of the pool. On this gentle rise and within 10 meters of Llao's Bath we observed an extensive area of bacterial mats with associated saline pools. This area was termed the "brain mat" because of the convoluted morphology of the colony (Plate 11). The convolutions were defined by small (20-100 cm) elongated pools which were surrounded by thick (>50 cm) masses of bacteria (Plate 12). Other pools, both larger and smaller than Llao's Bath, were observed within 50 meters of the Llao's Bath/brain mat complex.

A second area of pools was discovered 300 meters southwest of Llao's Bath. It consisted of several pools, only a few centimeters deep and 10 to 30 cm in diameter, which filled small depressions on a sedimented bottom. These small pools were not sampled.

The third pool area was discovered a few meters downslope from the bacterial mats on the northeast side of the lake near Palisades Point. Many pools (approximately 20 individual features) were observed within an area 50 meters across by 100 meters long. The pool site is within the flat-lying sedimented area at the break in slope at the base of the caldera wall. Several of these pools, which we will refer to as the Palisades Point pools, were larger than any of those found within the Detailed Study Area. The largest Palisades Point pools had maximum dimensions of approximately 15 meters across. Islands, embayments, and delta-like features were observed within these pools (Plates 13 and 14). A striking aspect of these pools was that stream-like features or rills entered from their upslope side. The rills had a dendritic pattern which indicated downslope flow. Many of the dendritic features appeared to originate beneath an outcrop on the slopes (Plate 15). These channels were two to five centimeters across and one to two centimeters deep. Although no fluid flow was observed, erosional features clearly indicated flow had occurred at an earlier time. Bacterial colonies were observed along the sides of the pools and along the rills.

Temperature measurements from both Llao's Bath and the Palisades Point pools were 4.5°C to 5.5°C, respectively. These temperatures are significantly lower than those measured in many of the bacterial mats and in certain sedimented areas.

The geographic relationship between the pools and the bacterial mats in the Detailed Study Area is shown in Figure 9 (a,b, and c), which shows transects from the high temperature bacterial mats to the north wall mats and Llao's Bath.

Spires.

Precipitate spires over 10 meters high were discovered at the eastern margin of the lake below Skell Head (Plate 16). These structures have a morphology and chemistry which is of subaqueous precipitation from hydrothermal solutions. The spires have a composition similar to many siliceous sinter deposits which form around continental hot springs. Silica and iron dominate the composition, but there are also strong enrichments of arsenic, phosphorus, and antimony. However, the deposits are morphologically unlike the broad mounds that characterize most subaerial siliceous deposits; the narrow, elevated forms indicate subaqueous formation. These deposits were located at the base of the slope between the steep caldera wall and the relatively flat

sedimented basin. Although these tall structures were only observed in one location, smaller chimney-like features were observed in two other locations in the Detailed Study Area.

III.2. Distribution of Temperature, Salt, and Physical Properties.

General.

The vertical distribution of temperature in the lake was discussed by Neal et al. (1972), who presented the first detailed high-precision measurements of the complete water column. The general features they described were the strong seasonal thermocline in the upper 100 meters, a decrease in temperature to a minimum value of 3.53°C at mid-depth (295 meters), and an increase in temperature below this point to values as high as 3.69°C. The average temperature of the sediments below these profiles was 3.80°C. Neal et al. (1972) postulated that the stability of this hyperadiabatic deep water column was maintained by an increase in dissolved ions or suspended sediments with depth. Their field methods, however, did not include any way of directly testing this hypothesis. The history of temperature measurements in the lake was reviewed by Williams and Von Herzen (1983) in a paper presenting detailed water column temperatures and sediment heatflow analyses. Their research mapped several areas of the lake bottom with very high heatflow and provided a detailed documentation of deep lake warming. They hypothesized that the vertical structure and horizontal heterogeneity of several deep profiles could be directly attributed to convection from active thermal springs. According to Williams and Von Herzen (1983) these springs appear to provide a warm "dense" water layer that is "ponding" in the South Basin.

Temperature and Density Structure.

Details of data collected in 1987 and 1988 have been discussed in Collier and Dymond (1988a and 1989, respectively) and in Collier et al. (1990), but we review that data here. The high-precision CTD data collected in 1987, 1988, and 1989 allow us to refine the general descriptions of Neal et al. (1972) and Williams and Von Herzen (1983). Furthermore, we have made the first detailed measurements of *in situ* conductivity, which enabled us to calculate salinities and densities at different lake depths. The data set focuses on the magnitude and areal extent of the thermal anomalies in the deep lake and provides the first significant evidence of high dissolved salt content associated with the increases in temperature. Figure 10 shows the full water column distribution of temperature and density at the east end of the South Basin. These data are based on direct measurements from the CTD package as well as on calculated quantities derived from the equation of state applicable to this lake water (Chen and Millero, 1986).

The data collected late in the summer of 1987 documents the fully developed seasonal thermocline in the upper 100 meters (Figure 10a) and the associated decrease in density within this stable warm surface water layer (Figure 10b). Below 100 meters depth, the density of the water is very nearly homogeneous with a total change of less than 4 ppm (Figure 10b, 10c). When the seasonal thermocline erodes and is cooled during the winter, storms drive significant mixing from above. As first noted by Williams and Von Herzen (1983), any significant heating from below by conductive and/or convective inputs may drive convection and mixing of these deep waters with shallower waters. Rapid mixing is indeed suggested by the vertically-homogeneous tritium data of Simpson (1970b), and by dissolved oxygen concentrations which are near-saturation throughout the water column. Additional data on the rate of vertical exchange are presented in Appendix A and G. Data from the two thermistor chain moorings deployed in the South Basin of Crater Lake also

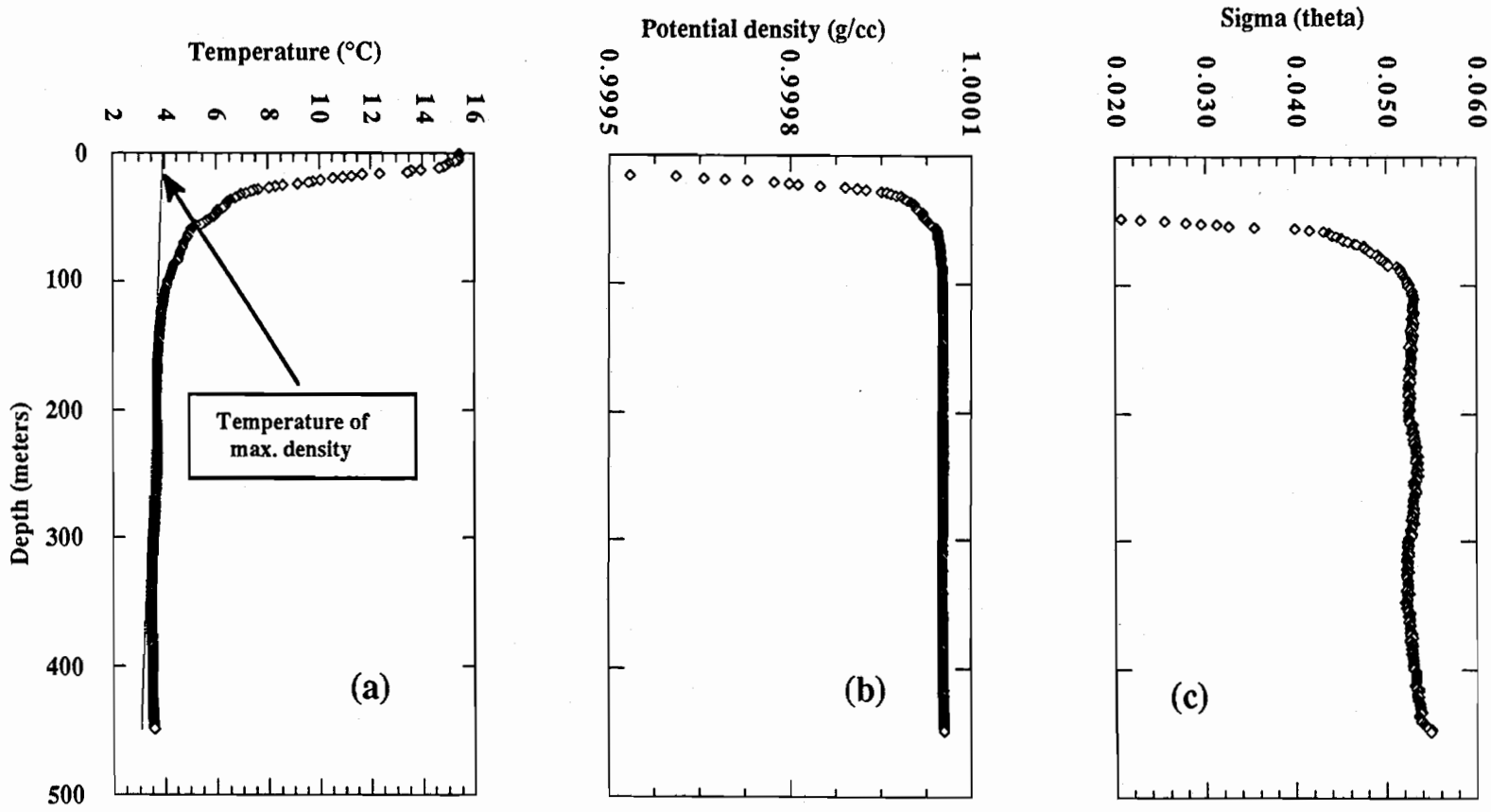

Figure 10. CTD data from. a water column profile in the east end of the south basin (Collier and Dymond, 1988a and 1989). All calculated physical properties are based on the equation of state for limnologic waters developed by Chen and Millero (1986).
(a) Vertical distribution of temperature (°C) as a function of depth. The solid line indicates the temperature of maximum density for Crater Lake water at the *in situ* pressure.
(b) Potential density vs. depth. The potential density is the density of a water parcel moved adiabatically to a common reference pressure - in this case to the lake surface. This parameter is critical in considering the stability of the water column and the rate of turbulent mixing. It can be seen that the water column below 100 meters has a nearly uniform density.
(c) Sigma (θ) vs. depth. This parameter, derived from b, is defined as Sigma (θ) = (potential density - 1) x 1000.

document both surface and deep lake processes. The data set from these chains are presented and described in Appendix A. In these appendices we establish constraints on the overall mixing rates. A well-constrained estimate of mixing rate is critical for estimating the overall rates of input for heat, hydrothermal chemicals, and other materials to the deep lake. For the purposes of the heat and material balance models discussed in this report, we will use a vertical exchange (or deep-water "renewal") rate of two years.

Deep Lake Distributions.

Figure 11 shows expanded plots of the CTD record for the lower 100 meters of the water column at the east end of the South Basin. The scales for temperature (a), salinity (b), and potential density (c) have been significantly expanded over those in Figure 10. The major feature apparent in Figure 11a is the increase in temperature with depth. The slow increase, which begins below 300 meters depth, is seen throughout the lake and appears to reflect the net effect of conductive and convective heat inputs. For example, the light dotted line shown in Figure 11 illustrates the temperature structure in the North Basin.

The adiabatic increase in temperature with depth can be calculated from the equation of state (Chen and Millero, 1986); the resulting average is 3.2×10^{-6} °C/meter. This is an insignificant portion of the observed temperature increase (Figure 11a). The general warming observed throughout the lake below 350 meters (e.g: the North Basin profile shown in Figure 11a) has a gradient of 3.3×10^{-4} C°/meter which is 100 times larger than the adiabatic gradient, thus the use of the term *hyperadiabatic* to describe the temperature distribution in the water column. The gradient seen near the bottom of the South Basin study area is approximately 1×10^{-2} C°/meter, 3400 times larger than the adiabatic gradient. These "sharp" gradients in temperature, such as that seen at 430 meters in Figure 11a, are horizontally heterogeneous and are sometimes followed by a complete reversal in the temperature, suggesting a locally unstable system. Consistent with the interpretations of Williams and Von Herzen (1983) and Collier and Dymond (1988a and 1989), we attribute these features to the active input of thermally and chemically enriched water.

Figure 12a shows a vertical integration of the "excess heat" contained within a portion of the Detailed Study Area. The "excess heat" is defined as the heat content of water with temperatures greater than water at the equivalent depths in the North Basin. That is, the values for each given depth in the North Basin profile, shown as the dotted line in Figure 11a, are subtracted from the values at the equivalent depth in the South Basin. A graph of "excess heat", using data from the 1987 field season, was originally presented in Collier and Dymond (1988a). Figure 12a is a new plot which also incorporates the data collected during our 1988 and 1989 field program.

From the same CTD data, we have also generated a plot of "excess salt" in the South Basin profile from the Detailed Study Area (Figure 12b). The calculation is the same as for "excess heat" That is, the North Basin salinity profile has been subtracted from the South Basin salinity profiles).

The local maxima in integrated heat and salt which occur in the center of the eastern-most portion of Figure 12 are immediately downslope from the highest temperature bacterial mats discovered during the program. The high values on the west end of the plot are primarily a function of the accumulation of warm salty waters in the deeper portions of the South Basin (to the west). Note that this calculation method focuses only on the localized anomalies seen in the South Basin which are above and beyond the general heating effect observed throughout the rest of the deep lake.

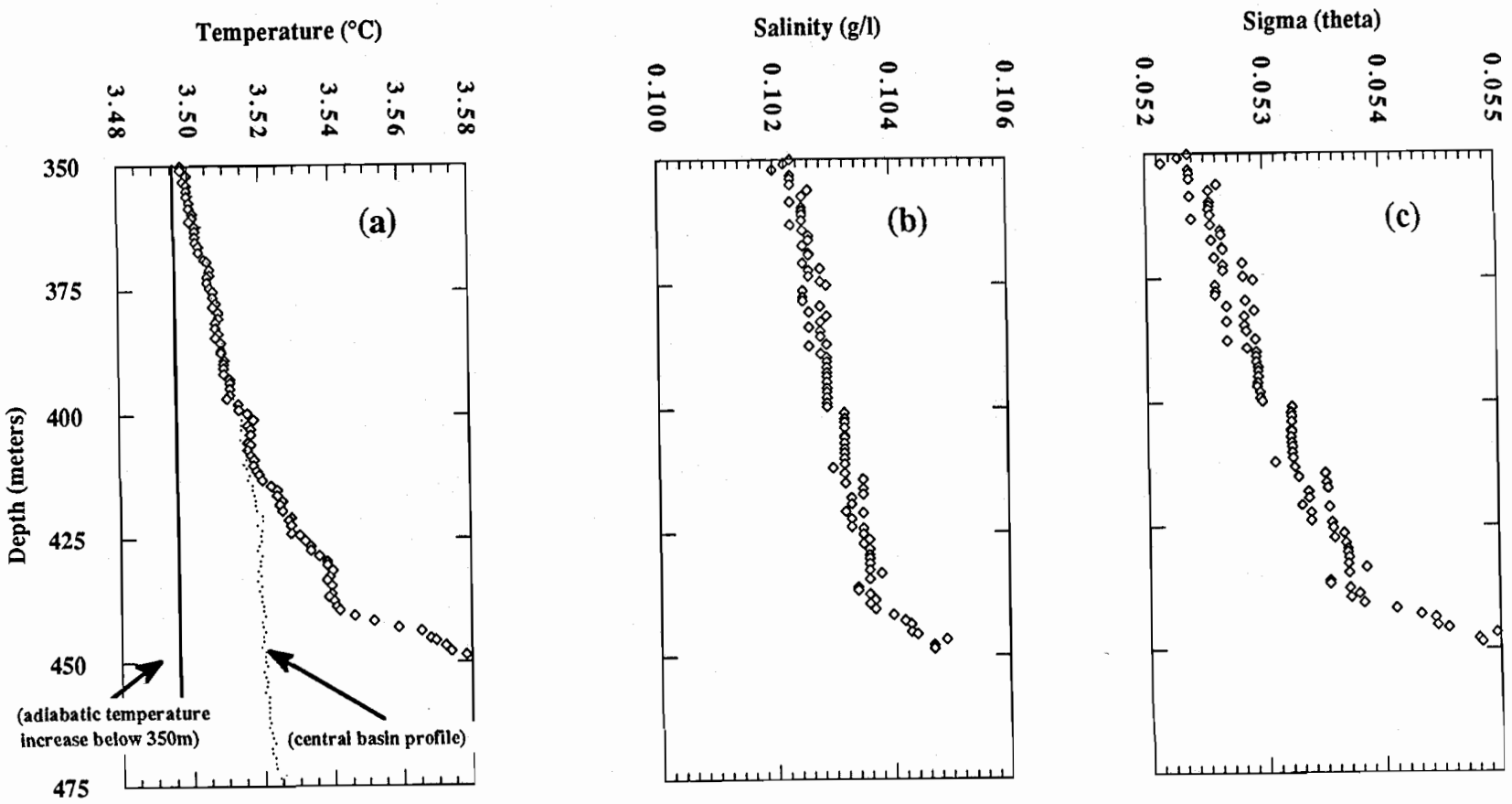

Figure 11. Expanded plots of the CTD data shown in Figure 10 which focus on the bottom 100 meters of the water column. (a) Plot of temperature vs. depth. Three major features are shown: (1) the adiabatic increase in temperature, starting from the minimum temperature in the water column (350 meters), accounts for less than one millidegree of warming (the adiabatic gradient over this interval averages 3.2×10^{-6}°C/meter); (2) the general warming below 350 meters, which is seen throughout the lake, has a gradient which is two orders of magnitude larger (3.3×10^{-4}°C/meter) and is thus *hyperadiabatic*; (3) the gradient seen near the bottom of the thermal study area is approximately 1×10^{-2}°C/meter - a gradient which is 3400 times larger than the adiabatic increase. The depths of discrete water samples taken along with the CTD cast are noted along the side of (a) for reference.
(b) *In Situ* salinity (grams/liter) vs. depth.
(c) Sigma (θ) vs. depth. Note that the total dynamic range in density is less than 2 grams/kg. from 350 meters to 440 meters.

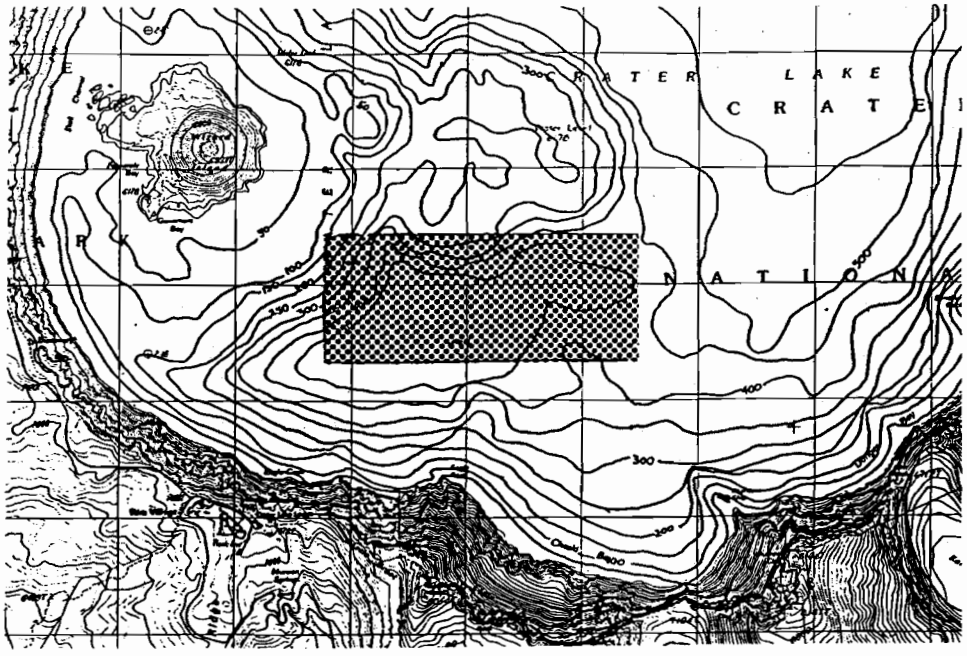

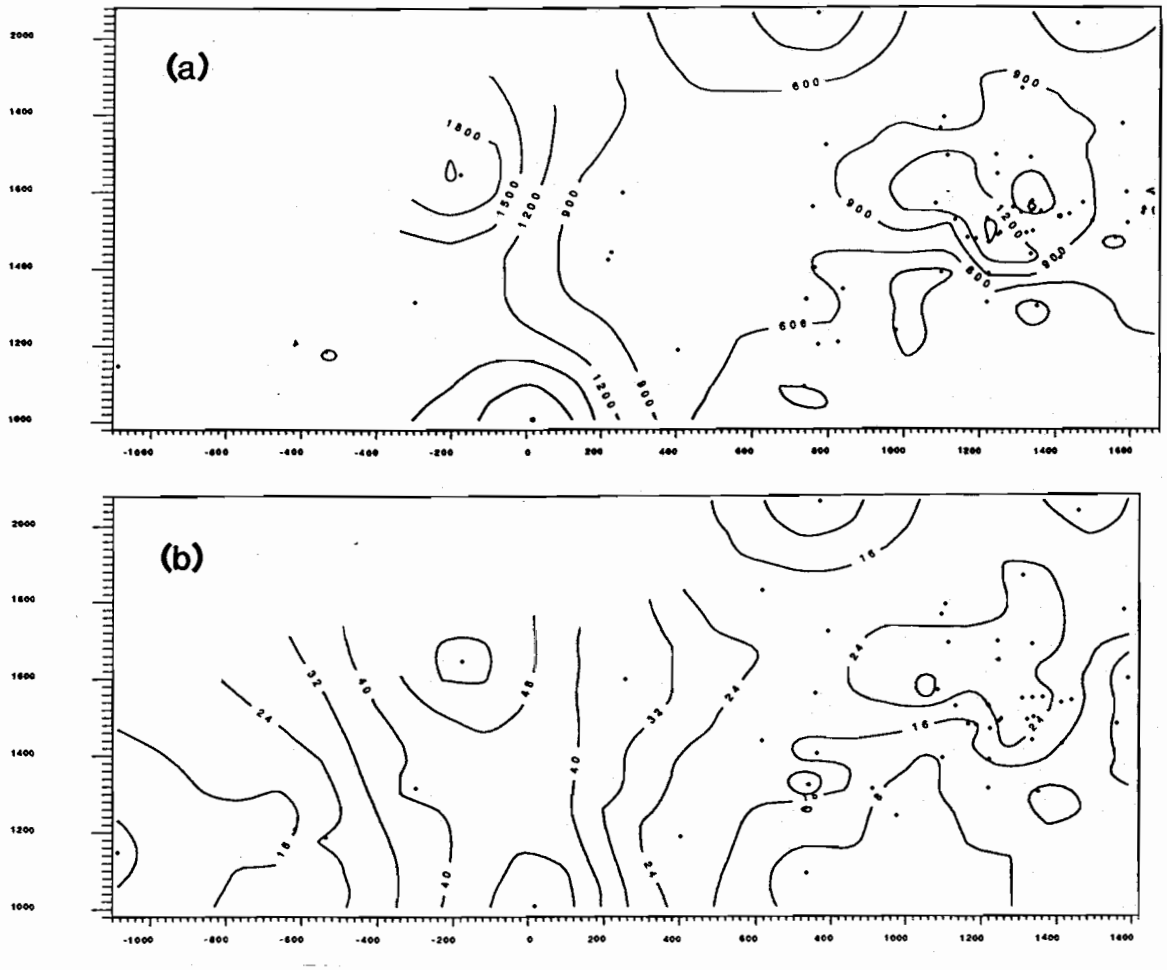

Figure 12. Contour plots of the total water column "anomaly" for heat (a) and salt (b) from 1987-1989 CTD casts (integrated vertically, kcal/m^2)

The temperature and the salinity anomalies are clearly correlated. The net effect of the coupled temperature and salinity increase is that the potential density (Figure 11c) increases very slightly with depth, and therefore the deep water is stable. Both Neal et al. (1972) and Williams and Von Herzen (1983) hypothesized that the lake should have an increase in dissolved solids in order to counteract the effect of the measured temperature increase. However, the total increase in density (less than 2 ppm in 100 meters) produces only a very weak stratification. The static stability, E, an expression of the density gradient normalized to the absolute density, is only 2×10^{-8} m^{-1}. The Brunt-Väisälä frequency, *N*, is 1×10^{-4} cycles/sec. *N* is also related to the density gradient and can be thought of as the frequency of oscillation of a water parcel displaced vertically from its equilibrium position in the water column (Ruttner, 1974; Pond and Pickard, 1978). If the observed temperature increase is due to hydrothermal inputs, the increase in salinity suggests that the input of warm water may carry enough dissolved salts to stabilize the fluid relatively near the lake bottom.

Near-Bottom Measurements of Physical Properties With the Submersible.

As discussed in the Methods Section, the Deep Rover submersible is equipped with a CTD instrument. During the dives, this allowed us to collect data on the temperature and salinity of the bottom one to three meters of water in the lake. Figures 13 and 14, showing the data from dives CD187 and CD182, document the spatial variability of the CTD data in the Detailed Study Area.

Dive CD187 covered a relatively small area in the west-central part of the Detailed Study Area. Total temperature variations during the dive were 0.19°C. Figure 13 shows that these correlate well with significant conductivity variations. A region of consistent thermal and conductivity anomalies was observed during the last 40 minutes of the dive. A small bacterial mat was observed to be growing on the sediment surface in this area of anomalous water. The temperature and conductivity record of this dive provides clear evidence of strong spatial variability in the bottom waters of the Detailed Study Area. Some of the largest anomalies observed were limited to areas a few tens of meters across. Even the consistent large anomalies observed late in the dive were only 100 meters from areas of relatively low temperatures measured earlier in the dive.

The highest temperatures and conductivity anomalies detected during the entire 1988 dive program were observed during dive CD182. The maximum temperatures, measured 1.4 hours into the dive, reached a value of 4.1°C, (off scale on Figure 14). With respect to the coolest waters in the Detailed Study Area, this represents an anomaly of more than 0.5°C. These relatively large anomalies are located in a region of anomalous sediment. Mottled dark brown sediments were frequently observed, and in some places very fine, dark brown to black precipitates covered the bottom (see dive notes on Figure 14 and in Appendix H).

Figures 15 and 16 show contour maps of the near-bottom temperature and salinity measurements from the 1989 field program. These contour maps show several regions of anomalously warm and salty waters, which are separated from each other by areas of cooler and less salty waters. One warmer water area is near many of the bacterial mats, although there is not always a one-to-one correlation between mat sightings and near-bottom temperatures. Areas of saltier waters are often located near the pool sites as well as near some of the bacterial mats. These locations, which also correlate with the integrated water column maxima (Figure 12), are closely associated with the high-temperature mat area (Figure 8).

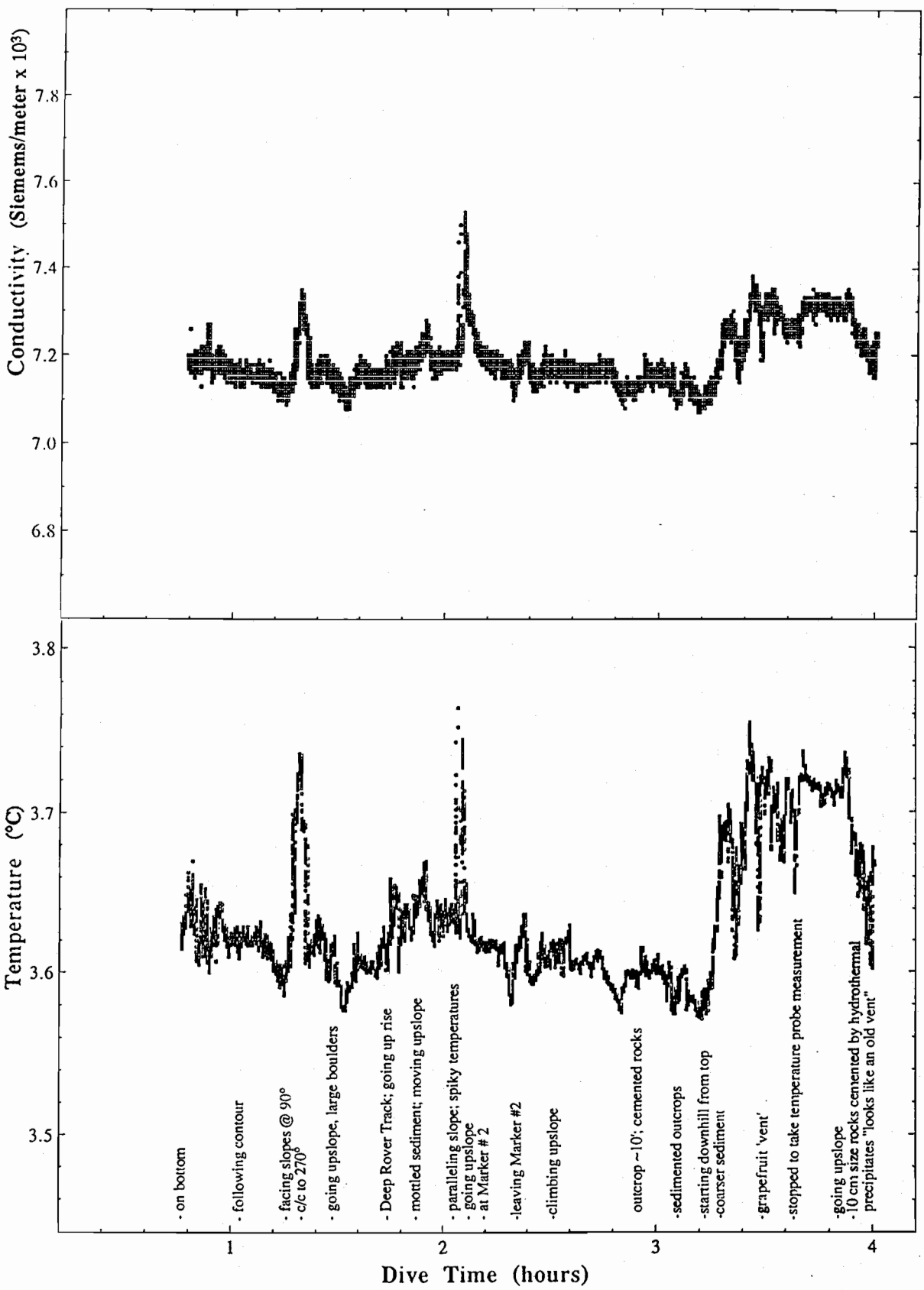

Figure 13. Conductivity (upper panel) and temperature (lower panel) measured with the CTD during CD187. Dive time in hours, shown on the x-axis, was measured from the time the submersible left the surface. The annontated descriptions made during submersible operations are shown along the x-axis.

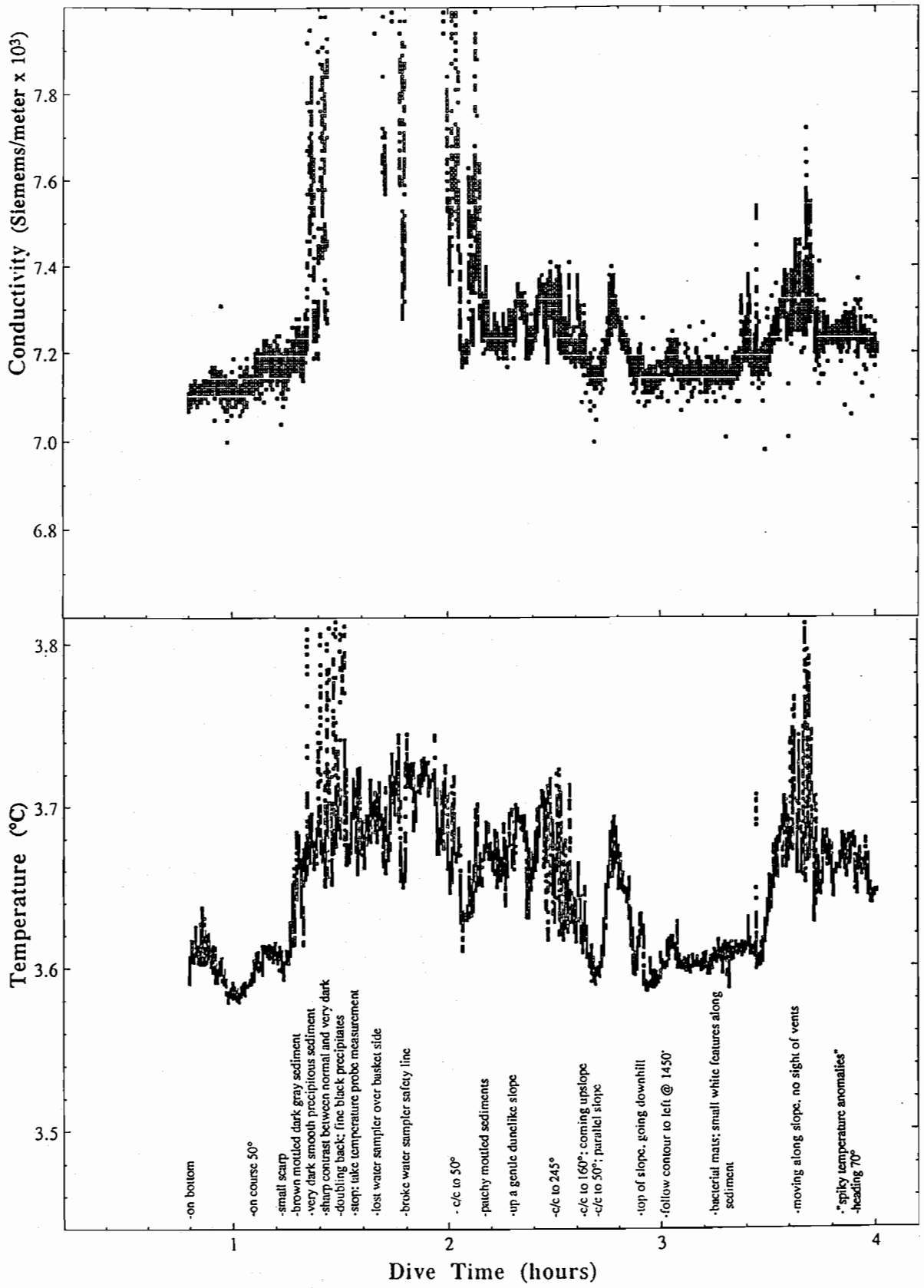

Figure 14. Conductivity (upper panel) and temperature (lower panel) measured with the CTD during CD182. Dive time in hours, shown on the x-axis, was measured from the time the submersible left the surface. The annontated descriptions made during submersible operations are shown along the x-axis.

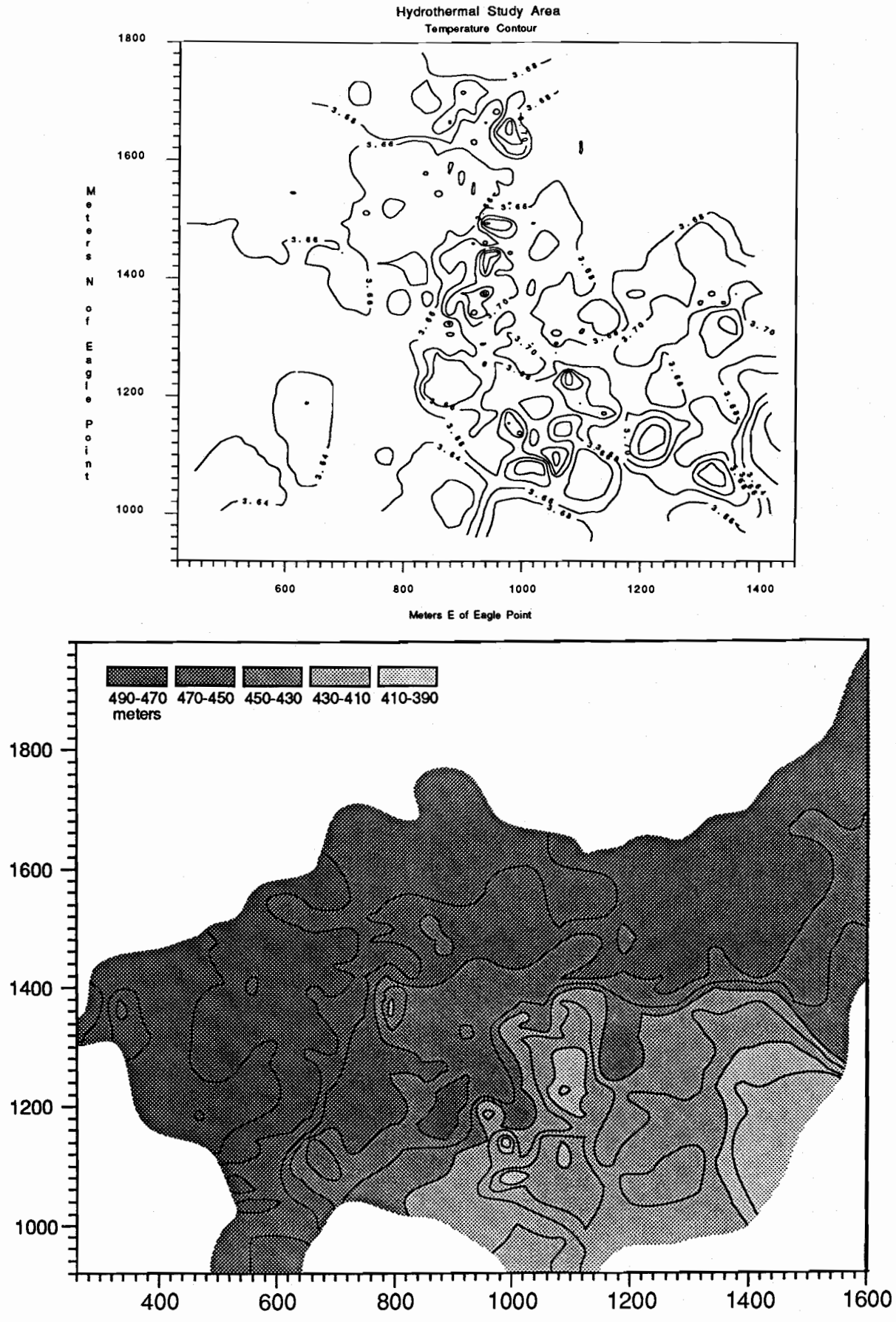

Figure 15. Contour map of near-bottom temperatures (Top) as recorded by the CTD on Deep Rover for dives CD207-CD222. Detailed Study Area bathymetry is included for reference (Bottom).

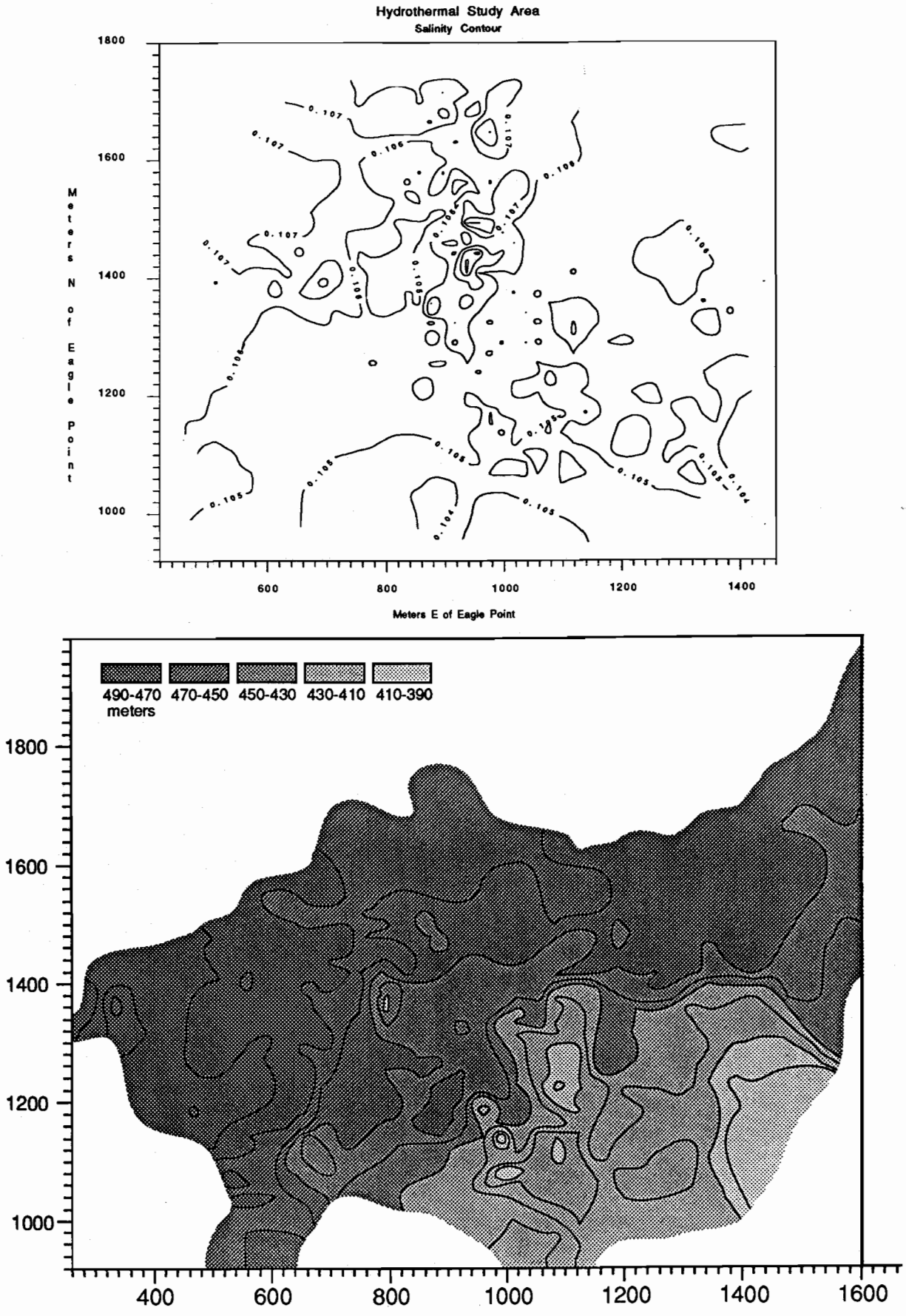

Figure 16. Contour map of near-bottom salinities (Top) as recorded by the CTD on Deep Rover for dives CD207-CD222. Detailed Study Area bathymetry is included for reference (Bottom).

The relationship between temperature and salinity (T-S) is often used in analyzing water masses because both quantities are essentially conservative during mixing and because they can be measured *in situ* with a very high degree of precision (Hutchinson, 1957). The relationship between salinity and temperature during dives CD216, CD218, CD222, and CD223 is shown in Figure 17. These data document mixing between four end-members detected during the 1989 dive program. The largest thermal anomalies measured during the dives are associated with two different fluid end-members, (a) and (c) in Figure 17. The middle "arm" of the data set [(c) in Figure 17] represents a fluid with the highest temperatures and salinities measured by the CTD during the dives (~3.83°C and ~0.112g/l respectively). This fluid is apparently mixing with water along a line extending to background water (~3.65°C and 0.105g/l). Samples from other dives all fall somewhere between the T-S "arms" of CD216 [(b) in Figure 17] and CD218 [(a) in Figure 17].

The locations where bottom waters have a high heat/salt ratio typically correspond to areas having hydrothermal features with elevated temperatures. For example, the paths for dives CD218 and CD220 were near bacterial mats with temperatures in excess of 15°C. The dive track logs presented in Appendix H of this report show that these end-members are spatially separated from the samples of higher heat/salt ratios obtained in the eastern half of the Detailed Study Area and those of lower heat/salt ratios [(b) in Figure 17] located in the western half of the Detailed Study Area. Additional T-S data is presented in Appendix A along with a longer discussion of the physical mixing of these end-members.

Near-Bottom Current Measurements.

In the South Basin near Llao's Pool, currents within approximately one meter of the lake bottom were measured with an S4 electromagnetic current meter. The flow rates of the measured currents range between 0 and 2.0 cm/sec. The current directions were generally in the northwest direction with a series of current reversals (Figure 18). Although the northwest flow *may* represent a downslope density flow, the data set is too poorly constrained to speculate further on the cause for the observed current.

III.3. The Chemistry of Crater Lake Waters

Introduction.

Despite its remote location, the lake has been studied by many limnologists and oceanographers since the turn of the century. A summary of the earlier chemical studies of Crater Lake by the U.S. Geological Survey can be found in a USGS water supply paper by Phillips (1968) and in Van Denburgh (1968). More recent research efforts by the USGS are described by Thompson et al. (1987), Thompson et al. (1990), Nathenson (1990a) and Nathenson and Thompson (1990). In 1969, a group of investigators determined the fission-produced radioisotopic inventory in the lake (Volchok et al., 1970; Simpson, 1970a,b). Water chemistry and biological data collected as part of the on-going 10-year limnological program at the park are reported within the annual reports for this project (e.g., Larson, 1988). In general, all these investigators have reported that the lake is well-mixed with respect to the major ion concentrations. The radioisotope distributions also suggested a rapid vertical mixing rate of less than ten years, meaning that over a ten-year period, there is complete overturn and mixing throughout the Crater Lake water column.

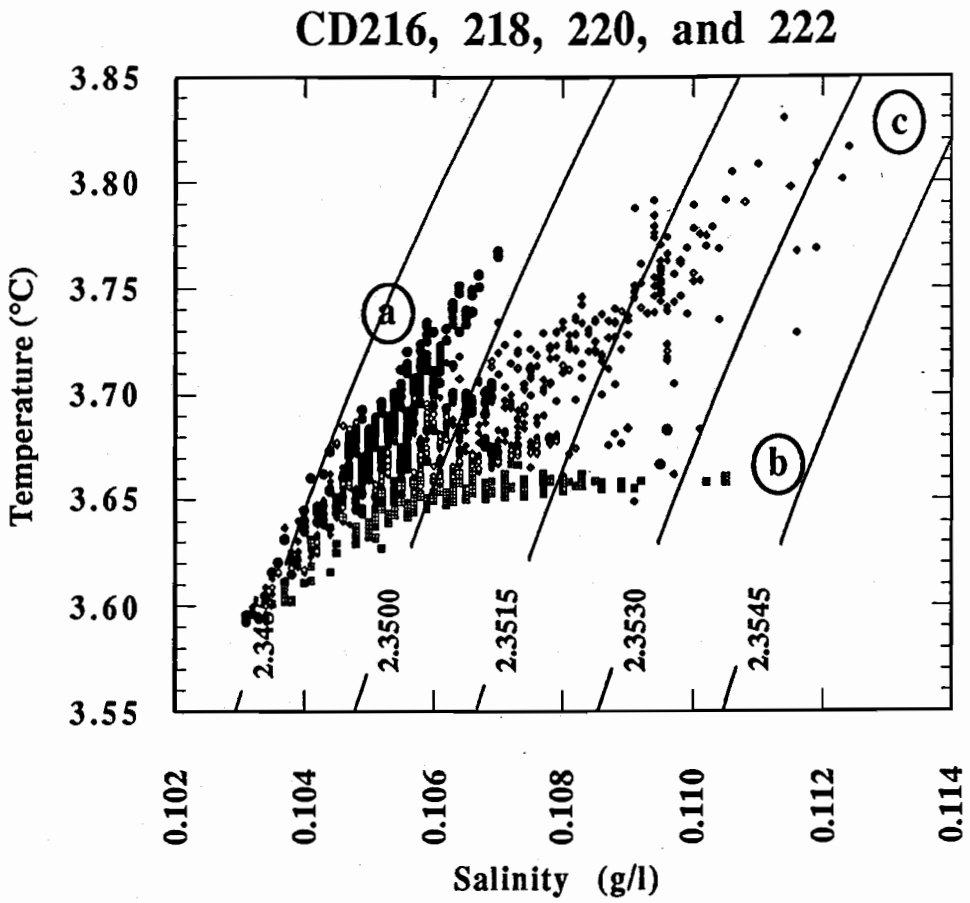

Figure 17. The relationship between temperature and salinity (T-S) for dives CD216, CD218, CD220, and CD222. This type of plot can be used to evaluate the T-S relationships between end members detected during the dive(s). The samples from all the dives lie between the (a) "arm" of T-S points and the (b) "arm" of T-S points. The upper arm (a) represents a fluid of high heat to salt ratio, and the lower arm represents a fluid of low heat to salt ratio. The curves represent isopycnals (lines of constant density calculated at a constant pressure) for pressure of 435 db.

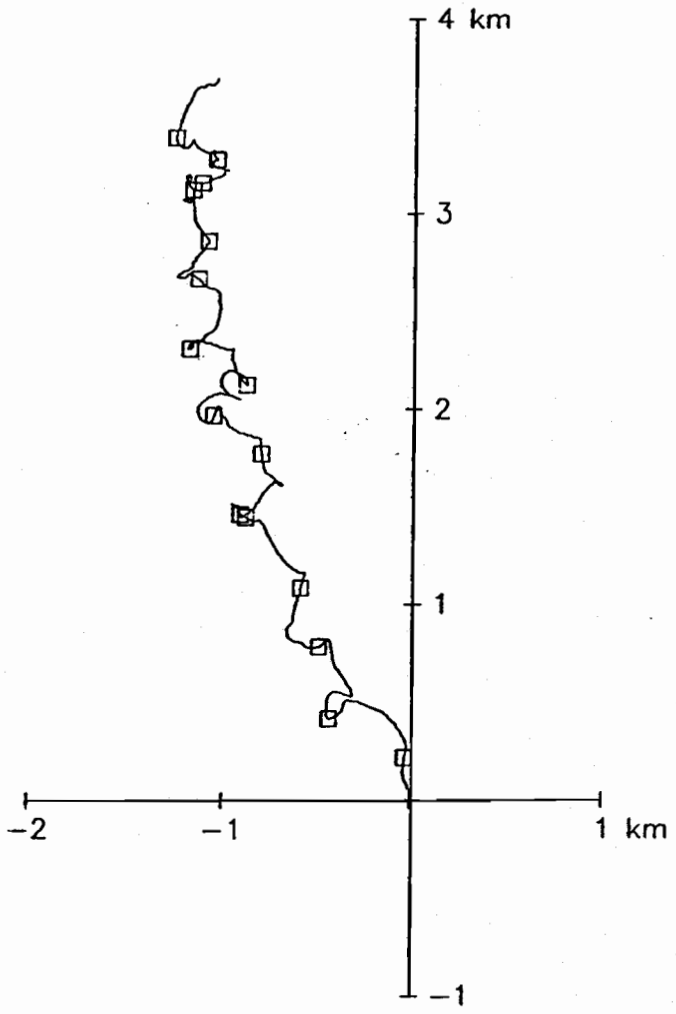

Current from Crater Lake S4 deployment

Figure 18. Progressive vector diagram from a current meter deployed at a depth of 475 meters for 15 days in the South Basin (placed ~ 1 meter above the bottom). This diagram shows the displacement or "path" of a parcel of water if it moved downstream with the velocity observed at the fixed position of the current meter. Since this meter was located near the bottom of the South Basin below the sill depth, this diagram cannot be strictly interpreted in this manner (the diameter of the basin is less than the length of the track plotted). It does demonstrate a nearly constant flow on the order of 1 cm/sec to the north-northeast throughout the deployment. This flow is generally *away* from the source of thermally and chemically enriched water and may suggest a down-slope density flow. Each box on the figure represents the end of a 24-hour sampling period.

Distributions of Dissolved Ions with Depth

The distributions of ions in Crater Lake are approximately homogeneous, in parallel with the deep lake temperature. The cations are dominated by sodium with a significant contribution from calcium; their sum accounts for 75% of the total (Figure 19). Bicarbonate ion (HCO_3^-) is the dominant anion comprising more than 50% of the anion budget in the lake. However, a closer examination reveals slightly elevated concentrations of all ions at depth. Figure 20 shows the vertical distribution of sodium, magnesium, potassium, calcium, silicate, and manganese from samples collected within the Detailed Study Area. The concentration of these dissolved ions increases with depth in the South Basin and this increase correlates with the increase in temperature and total salt measured by the CTD (Figure 11). This is consistent with a common carrier of the signals - warm, salty fluids. While these data alone do not constrain a specific source location, character, or temperature, the horizontal and vertical complexity of the temperature and salinity variations must be actively maintained by the input of anomalous fluids in order to counteract the effects of rapid vertical mixing processes with a characteristic ventilation rate of two years (see Appendices A and G). Thus, although the absolute values of enrichments are small, they provide very significant information about deep lake processes.

The increase of magnesium in the bottom water of the South Basin is shown in Figure 20a. The increased magnesium concentration indicates mixing of the warm, salty end-member fluid. The magnesium content of the Crater Lake warm, salty end-member can be contrasted with the character of marine hydrothermal fluids which are always depleted in magnesium due to the greenschist facies metamorphism of oceanic basalt by seawater (Edmond et al., 1979). However, this depletion is relative to the seawater concentration of magnesium which is 500 times higher than that in Crater Lake. Indeed, magnesium has been shown to increase in many continental hydrothermal systems of low-to-intermediate temperatures which are supplied by relatively pure waters (Mariner et al., 1980, 1982; Fournier and Potter, 1979). Hurst and Dibble (1981) documented an increase in magnesium concentration in Ruapehu Crater Lake (New Zealand) which was associated with lake water interaction with hot andesitic materials. Also, the concentrations of magnesium in Paulina and East Lake (within Newberry Crater) are elevated due to hot spring inputs (Phillips, 1968; Johnson et al., 1985).

However, detailed comparisons of concentrations of elements in hydrothermally-influenced lakes must be done with caution because the concentrations are primarily controlled by the ratio of hydrothermal to total water in the system - not by the existence or absence of hot springs. For instance, East Lake and Paulina Lake which occupy a single volcanic crater to the northeast of Crater Lake, are separated only by water-permeable lava and ash flows. Both lakes have known hot springs with measured temperatures up to 48°C at their outflow, yet their bulk lake water compositions are very different. While the concentrations of some cations are quite high in Paulina Lake compared to Crater Lake (e.g. Ca, Mg), the concentrations of sulfate and chloride are a factor of two higher in Crater Lake than in Paulina.

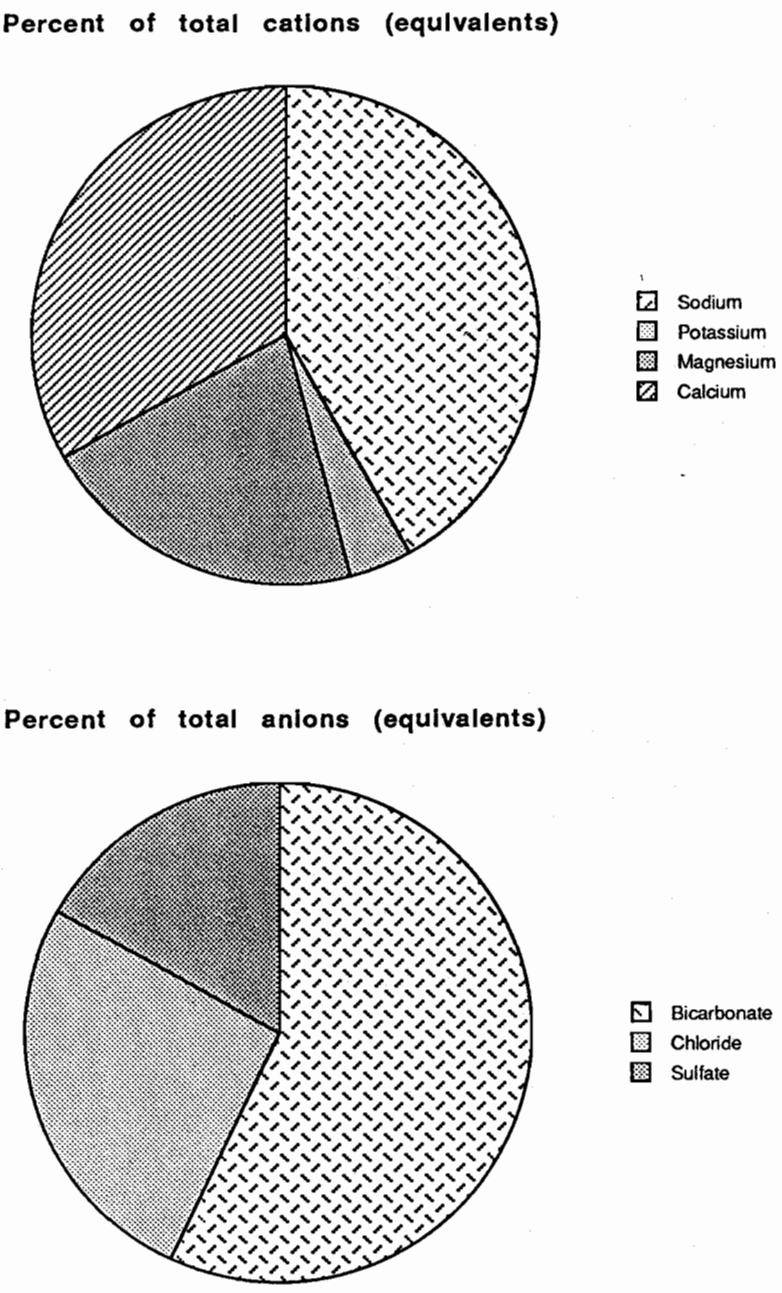

Figure 19. Pie diagram of major cations and anions contained in bulk Crater Lake water.

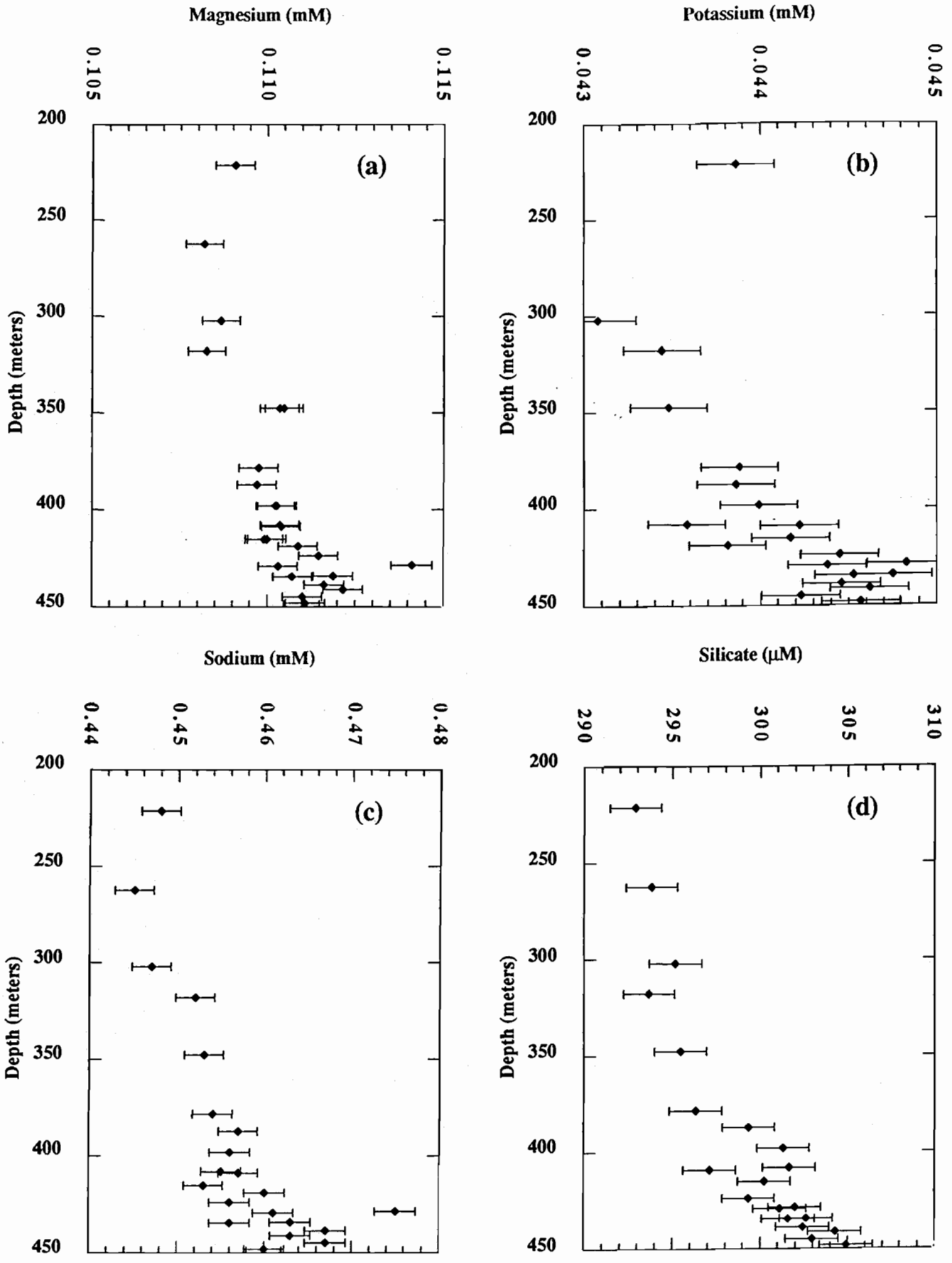

Figure 20. The concentration of various ions as a function of depth in the south basin: (a) magnesium; (b) potassium; (c) sodium; (d) silicate.

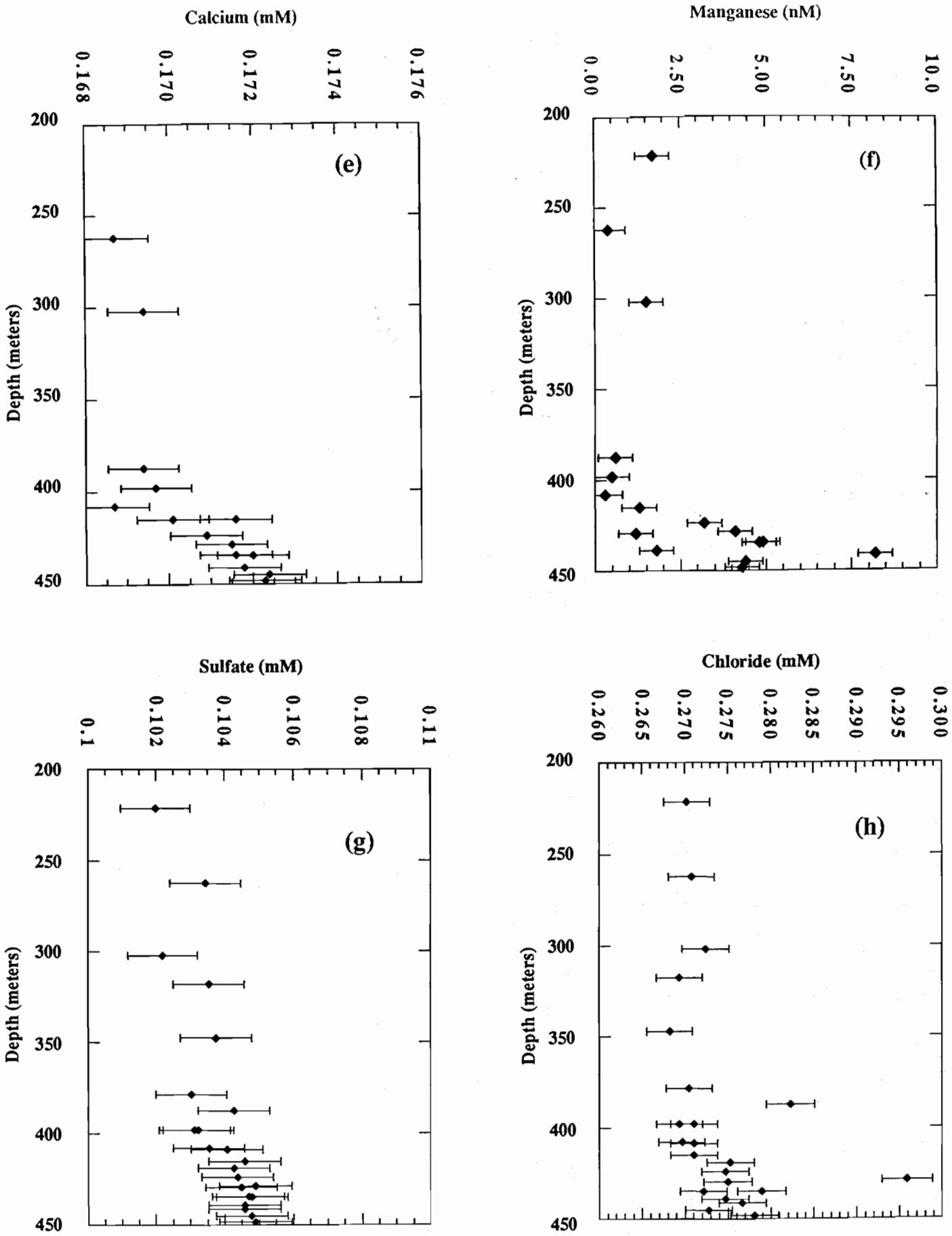

Figure 20 continued. The concentration of various ions as a function of depth in the south basin: (e) calcium; (f) manganese; (g) sulfate; (h) chloride.

The Distribution of CO_2 in the Water Column

Throughout this report we refer to the total CO_2 (ΣCO_2) of the system which is defined as:

$$\Sigma CO_2 = [H_2CO_3^*] + [HCO_3^-] + [CO_3^{-2}]$$

where:

$$[H_2CO_3^*] = [CO_{2\,(aq.)}] + [H_2CO_3^\circ]$$

and we refer to $H_2CO_3^*$ as carbonic acid, HCO_3^- as bicarbonate, and CO_3^{-2} as the carbonate ion.

Samples were collected in a 100 ml, gas-tight syringe directly from the sample bottle and were kept cold until analysis. For analysis, the samples were brought to room temperature and then transferred to a closed titration flask (Edmond, 1970). The sample temperature was maintained at 25 ± 0.5°C using a circulating water bath. Once the electrode had stabilized, the initial pH of the samples was measured, after which 0.425 grams of purified KCl were added to the flask (volume = 56.95 ml) to increase the ionic strength of the solution, and the pH was measured again. The addition of the KCl stabilizes the potentiometric readings and yields more precise pH values than the measurements at low ionic strength. All results are corrected for the ionic strength effects of the added salt (Stumm and Morgan, 1981). The titration alkalinity of the sample was determined using a Gran titration procedure (Gran, 1952; Dryssen and Sillen, 1967; Edmond, 1970). The ΣCO_2 is calculated from the pH and titration alkalinity of the sample (Stumm and Morgan, 1981).

The vertical distributions of pH, ΣCO_2, HCO_3^-, and $H_2CO_3^*$ are presented in Figure 21. At the pH of the lake (Figure 21a), the ΣCO_2 is dominated by the bicarbonate ion (Figure 21b). In parallel with the other ions (Figure 20) and temperature, the bicarbonate ion and ΣCO_2 concentrations increase with depth. Also the pH decreases slightly with depth (Figure 21a) and the concentration of $H_2CO_3^*$ increases with depth (Figure 21c). These data document that the fluids entering the deep lake are enriched in ΣCO_2 compared to bulk lake water.

III.4. Ion-Ion Systematics

The covariation of ions in a system is useful for interpreting the sources of inputs. That is, by plotting the concentrations of different ions against each other, we can compare changes in their ratios which allow us to categorize the relative importance of different sources and processes.

Figure 22 shows the relationship between chloride and sodium in all classes of lake samples including submersible-collected near-bottom samples, representative sediment pore waters, cold springs around the caldera wall and water column samples within the deep lake (>200 meters). The water from the cold springs has very low sodium and essentially zero chloride. This water is derived from rainfall, and thus is considered meteoric (atmospheric) water. However, the water samples from within the lake are clearly enriched in these ions with respect to all cold springs within the caldera walls and to atmospheric inputs (Larson, unpublished data; Reilly et al., 1989). To a first order approximation, the lake water can be viewed as a mixture of meteoric waters, of thermally and chemically enriched springs which contain various enriched source fluids (or "end-members"), and of upward-advecting porewaters (Appendix F).

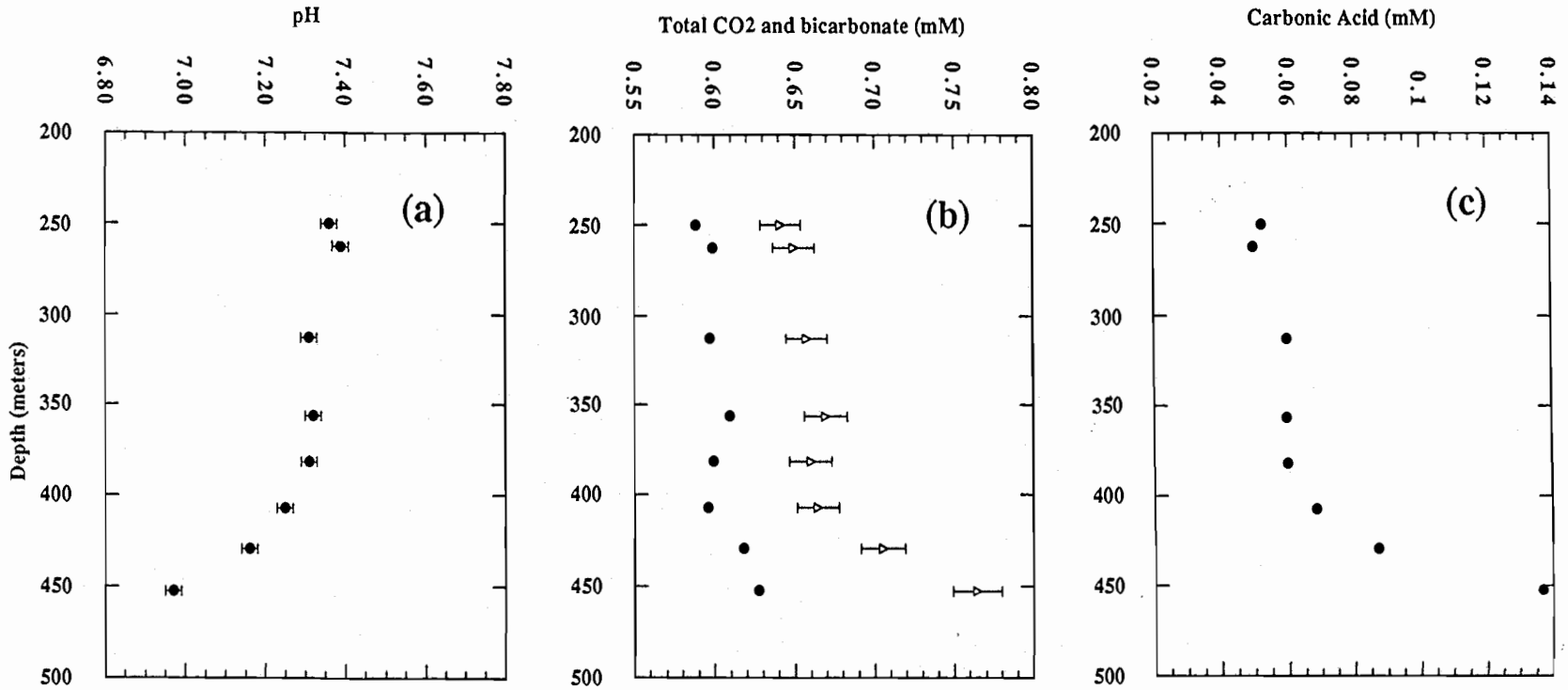

Figure 21. (a) Depth versus pH. (b) The concentration of ΣCO_2 (open circles) and bicarbonate (filled circles) as a function of depth. (c) The concentration of carbonic acid as a function of depth. ΣCO_2 and pH are measured and bicarbonate and carbonic acid concentrations are calculated quantities.

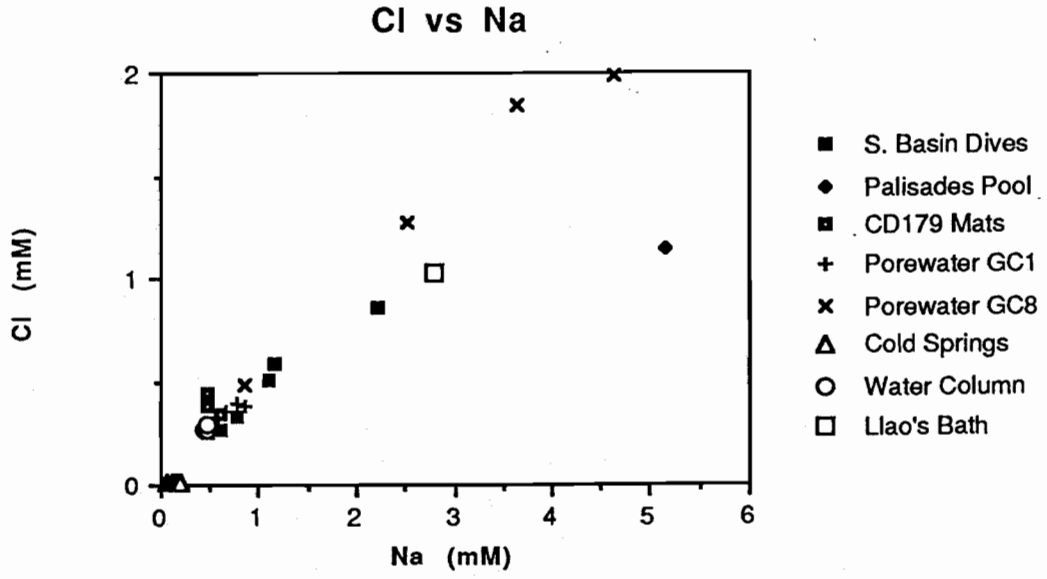

Figure 22. The concentration of chloride (Cl) vs. sodium (Na) in all the hydrologic components of the Crater Lake system - near bottom dive samples, porewater samples, caldera springs, and water column samples.

The sodium and chloride ions in cold spring waters seem to be little affected by the major secondary chemical reactions that could be occurring within the caldera sediments or wall rocks as the spring water enters the lake floor. The ratio of Na to Cl in andesites is approximately 44 (Nathenson, 1990a), while the ratio in the cold spring waters (Figure 22) is two. Clearly, the source of these ions cannot be congruent dissolution of andesites which have very low chloride. This is further documented by the low chloride in all the caldera springs (Figure 22 and Thompson et al., 1990). Therefore, another source of sodium and chloride ions is required to explain their elevated concentrations in Crater Lake.

The Crater Lake bulk water column samples generally fall along a mixing line between caldera spring water and pore waters (Figure 22). One major exception to this is from the Palisade Pool brines where the Na/Cl ratio is significantly higher than all other chemically enriched samples from the Lake. This compositional difference is seen in other ions as well (see below).

Figure 23 shows the relationship between the cations, sodium and magnesium, in the lake system. Figure 23a shows that the sodium/magnesium ratio is approximately 2 in all the near-bottom submersible samples. The chemistry of these samples is primarily controlled by the composition of the two pool areas. Figure 23b expands the plot to include the cold springs which, again, are much lower in concentration than the lake water. Figure 23b clearly shows that the cold springs samples define a separate population of data points. Figure 23c expands the plot even further to show the systematic variations of Mg vs. Na within the water column and in the near-bottom submersible samples which contain a high fraction of lake water. This relationship can be seen as dilution of an average input composition with pure water (meteoric input).

Figure 24 presents the calcium and sodium data. Again, the composition of the lake cannot be accounted for by any combination of the major meteoric inputs (atmosphere and cold springs). The meteoric inputs are depleted in sodium,and the Ca/Na ratios in the springs can be quite different than those of the lake. Crater Lake differs from all the other Cascade lakes in the concentrations of both ions (Collier and Dymond, 1989). These other High Cascade lakes lie in geochemically similar volcanic terrain and should receive similar precipitation and low-temperature weathering inputs to those entering Crater Lake. In fact, since most of these lakes have a larger relative drainage basin (compared with lake surface area), the low-temperature weathering inputs to these lakes should be more significant than at Crater Lake. The only end-members sampled that can account for Crater Lake's high concentration and ratios of Na and Ca are the thermally and chemically enriched fluids sampled by the submersible and collected from sediment pore waters (See Appendix F). The lake water composition appears to lie on a mixing line between the "Llao's bath" fluids and the meteoric waters, although there are clearly other end-members which also contribute. The calcium-sodium relationships seen in Figure 24 show considerably more diversity than the Na-Cl relationships shown in Figure 23. We attribute this to secondary chemical reactions of Ca which do not affect the primary sodium and chloride relationships seen in Figure 23. More details of these systematics will be discussed below in terms of the geochemical mass balances in the lake.

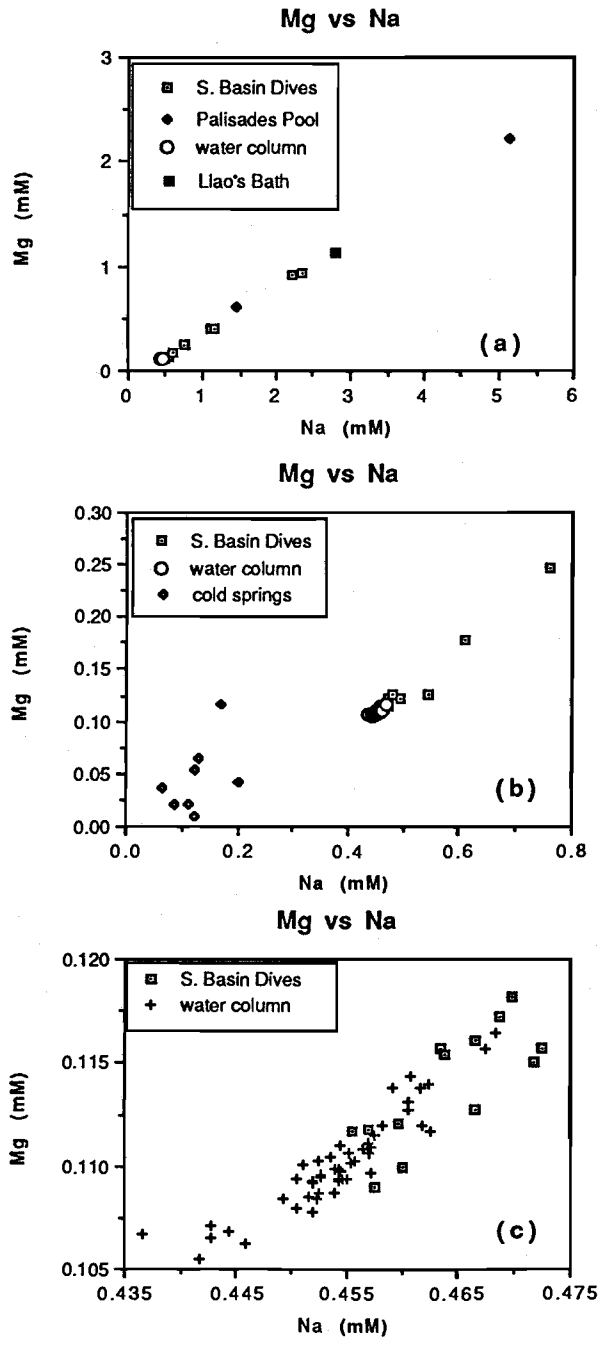

Figure 23. Magnesium (Mg) vs. Sodium (Na) in Crater Lake and associated waters: (a) Mg vs. Na in the south basin dive samples, palisades pool, and the water column; (b) An expanded scale of Mg vs. Na for south basin dive samples, the water column, and the caldera springs; (c) An expanded scale of Mg vs. Na for the water column samples and some of the south basin dive samples.

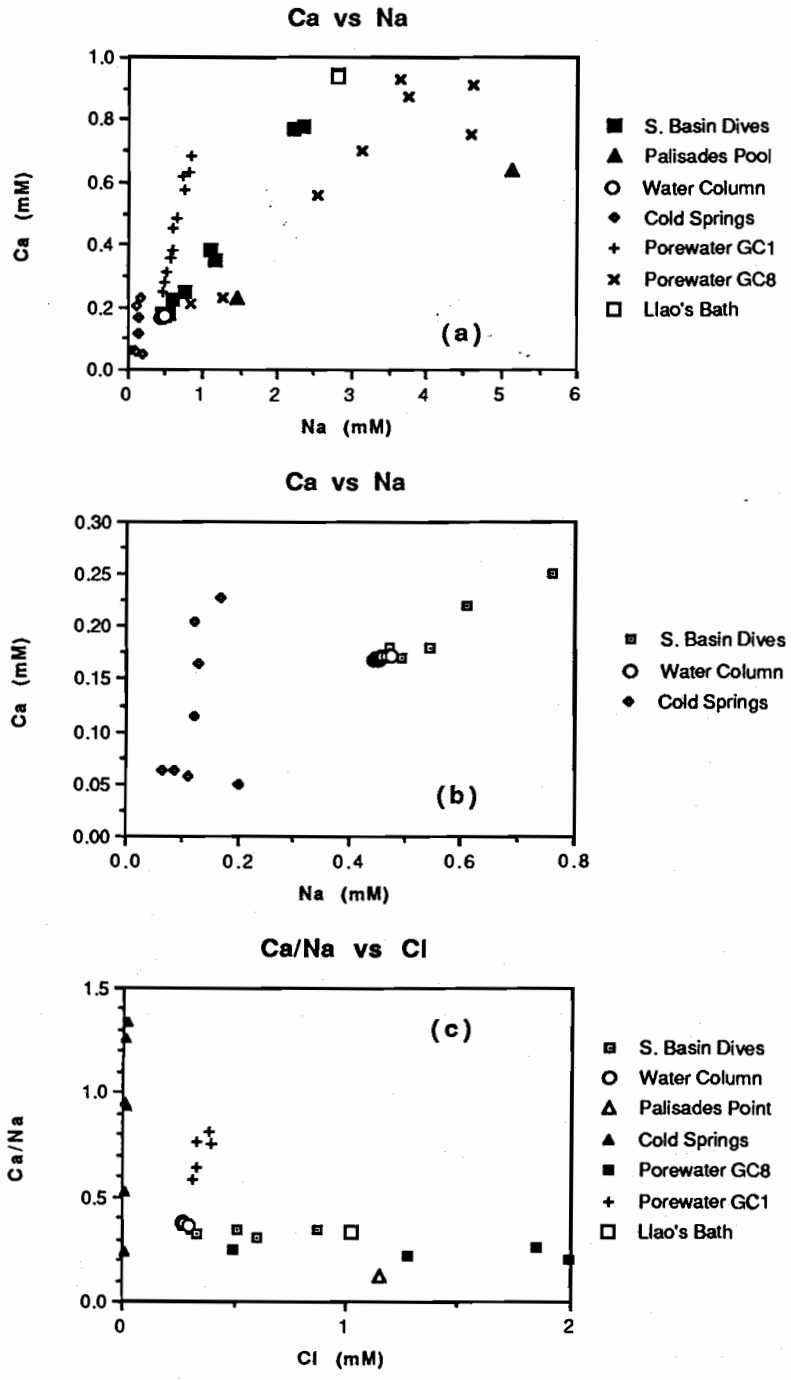

Figure 24. (a) The concentration of calcium (Ca) vs. sodium (Na) in the south basin dive samples, palisades pool, water column, caldera springs, and porewaters. (b) An expanded scale of Ca vs. Na in some of the south basin dive samples, water column samples, and caldera springs. (c) Ca/Na vs. Cl in the south basin dive samples, water column samples, palisades pool, caldera springs, and porewaters.

III.5. Helium Concentrations and Isotopic Ratios

In an earlier publication (Lupton et al., 1987), we reported Crater Lake data which documented enrichments of helium with a mantle isotopic ratio ($R = {}^3He/{}^4He = 7.1$) in deep lake waters. These data are rigorous evidence for injection of magmatic volatiles into the deep lake. Although ^3He anomalies have been one of the most consistent and valuable tracers of hydrothermal activity in the oceans (Lupton et al., 1980; Lupton and Craig, 1985), it might be possible that helium is being transmitted as a volatile into the deep lake rather than within a hydrothermal fluid (La Fleur, 1990). Such a process may have occurred at Lake Monoun and Lake Nyos in Cameroon where deep lake CO_2 injections led to a lethal gas burst (Sigurdsson, 1987). The mantle-like $^3He/^4He$ values in Lake Nyos (Sano et al., 1987; 1990) may be a consequence of gaseous inputs of helium that accompanied the volatile CO_2 injection. In this section of the report, we review the current Crater Lake helium data in an attempt to distinguish between volatile and hydrothermal sources.

Water Column Samples.

The first helium isotopic measurements were made in 1985, and measurements were repeated in 1987, 1988, and 1989. The earlier data were reported in Lupton et al. (1987), Collier and Dymond (1988a,b), and Collier and Dymond (1989) and are tabulated in Appendix I. The depth distribution of ^3He in the North and South Basins as measured in 1989 is shown in Figure 25. Although these data show that the highest He values occur in the South Basin, significant enrichments also occur in the North Basin. The depth distribution pattern from 1989 is consistent with the pattern defined by measurements made in previous years. The water samples obtained near the bottom of the Detailed Study Area contain five to six times more ^3He than air-saturated fresh water (lake surface at 1882 meters elevation and 4°C).

In addition to the mantle source for ^3He discussed above, it is also the stable daughter product of the decay of tritium (^3H or T; half life = 12.33 years). The distribution of ^3H in Crater Lake was previously discussed by Simpson (1970b) and its use in other closed basin lake hydrologic studies has been discussed by Herczeg and Imboden (1988). When a water parcel is isolated from the atmosphere, the decay of the ^3H in that water produces excess ^3He. The systematics of this closed system tritium-helium model are commonly used to estimate the time since a parcel of water was last in contact with the atmosphere (Jenkins, 1988). In our case, in order to evaluate the geothermal input of ^3He, we need to examine the fraction of the total ^3He in Crater Lake that may be derived from ^3H decay.

The primary input of "bomb" ^3H, which dominates the total input to Crater Lake over the last three decades, occurred between 1962-1967 (Simpson, 1970b). The average ^3H content of Crater Lake in 1967 was 24 T.U. (T.U. = a concentration equivalent to 1 ^3H atom per 10^{18} ^1H atoms in water) and the concentration of ^3H at the time we collected our ^3He samples (1987) was certainly less than or equal to this value. The characteristic time of vertical mixing of Crater Lake water averages about 2 years and the "oldest" water, located at the bottom of the basins, is about 3 years old (Appendix A & G). If water is isolated on the bottom of the lake for 3 years, the decay of ^3H [@ 24 T.U.] will produce 9×10^{-15} cc ^3He/gram of water. This is approximately 3.6% of the total ^3He found in the bottom water of Crater Lake (Figure 25). Therefore, the ^3He concentration in this rapidly-mixing lake is essentially unaffected by ^3H decay. Although we do not have current measurements completed for the actual concentration of ^3H in the lake in 1987, it is more likely that radioactive decay has reduced this concentration by as much as a factor of 3 since 1967 and the ^3H contribution to ^3He would be even smaller. From another perspective, if this process made a

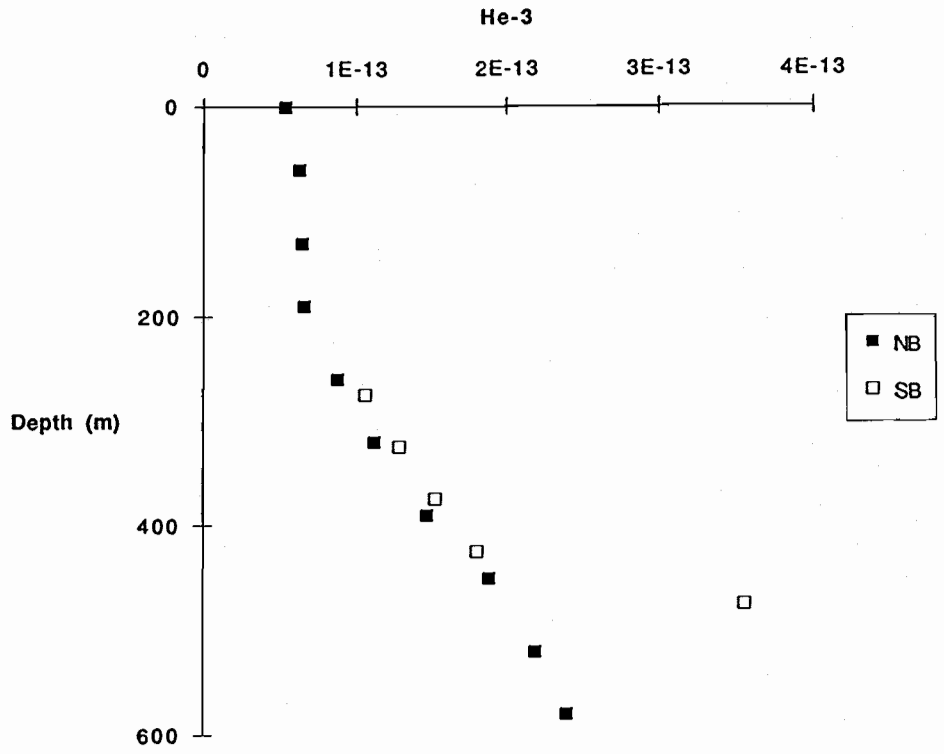

Figure 25. Helium-3 concentration of Crater Lake water as a function of depth. NB and SB refer to North Basin and South Basin, respectively. Concentration units are cubic centimeters of gas at standard temperature and pressure (STP) per gram.

significant contribution to the ^3He in the "older" waters of the lake, we would see a change in the observed $^3He/^4He$ ratio with depth, yet we observe a constant isotopic ratio in the helium added to the deep lake water (Figure 26).

As noted above, the concentrations of the helium isotopes (^3He and ^4He) exhibit a remarkable correlation in deep lake values (Figure 26). This relationship define a two end-member mixture between the atmospheric helium near the surface of the lake ($R = R_{atm} = 1.39 \times 10^{-6}$) and the mantle-enriched helium with $R/R_{atm} = 7.1$. The Crater Lake deep water ratio is similar to values in Lassen Peak hot springs (7.2), Mt. Hood fumaroles (7.2), Mt. Baker fumaroles (7.6), and hydrothermal plumes at the Galapagos Spreading Center (7.8) and the East Pacific Rise (8.0) (Lupton et al., 1987; 1980; Poreda, 1983; Poreda and Craig, 1989).

Because helium exchanges rapidly with the atmosphere in well-mixed surface waters, the process injecting this mantle-derived helium into the deep lake must occur faster than the deep lake exchanges with the atmosphere. Simpson (1970b) estimated that this mixing takes place with a characteristic time of one year. Assuming that all of this excess helium would be stripped from the lake over this same time scale, Lupton et al. (1987) calculated that the total ^3He flux into the lake is 1.8×10^{22} atoms of ^3He/year. Our current "best estimate" for the time scale of deep-lake renewal (i.e., the "ventilation" rate) is two years (Appendix A and G). This slower mixing rate reduces the flux estimate to 9×10^{21} atoms of ^3He/year.

As shown for the 1987 data set (Lupton et al., 1987), the concentration of ^3He correlates well with the increase in temperature observed in the South Basin (Figure 27a). The slope of this relationship is 1.5×10^{-12} cc ^3He/gram°C. This value is similar to the helium-heat ratio seen in marine hydrothermal systems (Lupton et al., 1989), but it is 50 times lower than the ^3He/heat ratio accumulating in the hypolimnion of Lake Nyos, Cameroon (Sano et al., 1990). This ratio can be combined with the ^3He flux estimate (Lupton et al., 1987) to arrive at an estimate of the convective heat input into Crater Lake, which is 2.9×10^7 joules/sec or 29 megawatts. This value can be compared with a heat flux of 14 - 28 megawatts derived from the heat flow data of Williams and Von Herzen (1983) [669-1381 MW/m^2 x the area of their heatflow survey, roughly 21 km^2]. This is at the lower end of a range of heat fluxes estimated by Nathenson (1990a). Also shown in Figure 27(b-f) are the excellent correlations between ^3He concentrations and the dissolved ion concentrations in the South Basin. These correlations support the hypothesis of a common carrier of these signals — thermal waters with high total dissolved ions which also carry dissolved gases of magmatic origin. If the helium is carried into the deep lake in another form such as a non-condensable gas phase, then other independent processes must be combined to create the observed correlations of helium with temperature and dissolved ions.

The measurements of helium concentrations in caldera wall springs provide another test of the hypothesis of non-condensible gas input. If helium is migrating in a gaseous form through Mt. Mazama from a deep magmatic source (La Fleur, 1990), it would dissolve in any ground water source as well as in the deep Crater Lake water. Consequently, the R/R_{atm} in these waters should be similar. During the 1989 field season, we collected two water samples from springs near lake level in the Chaski Slide area. The sampling was done at the source of springs, which directly vented from caldera wall rocks, in order to minimize sampling artifacts from atmospheric equilibration. The helium isotopic composition from the caldera springs is atmospheric, not mantle composition. This is shown in Figure 26, where the cold spring samples fall along the atmospheric line, distinctly different from the mantle line where the lake samples fall. The absolute abundance of helium in the cold springs is also low. The data from the cold spring samples are

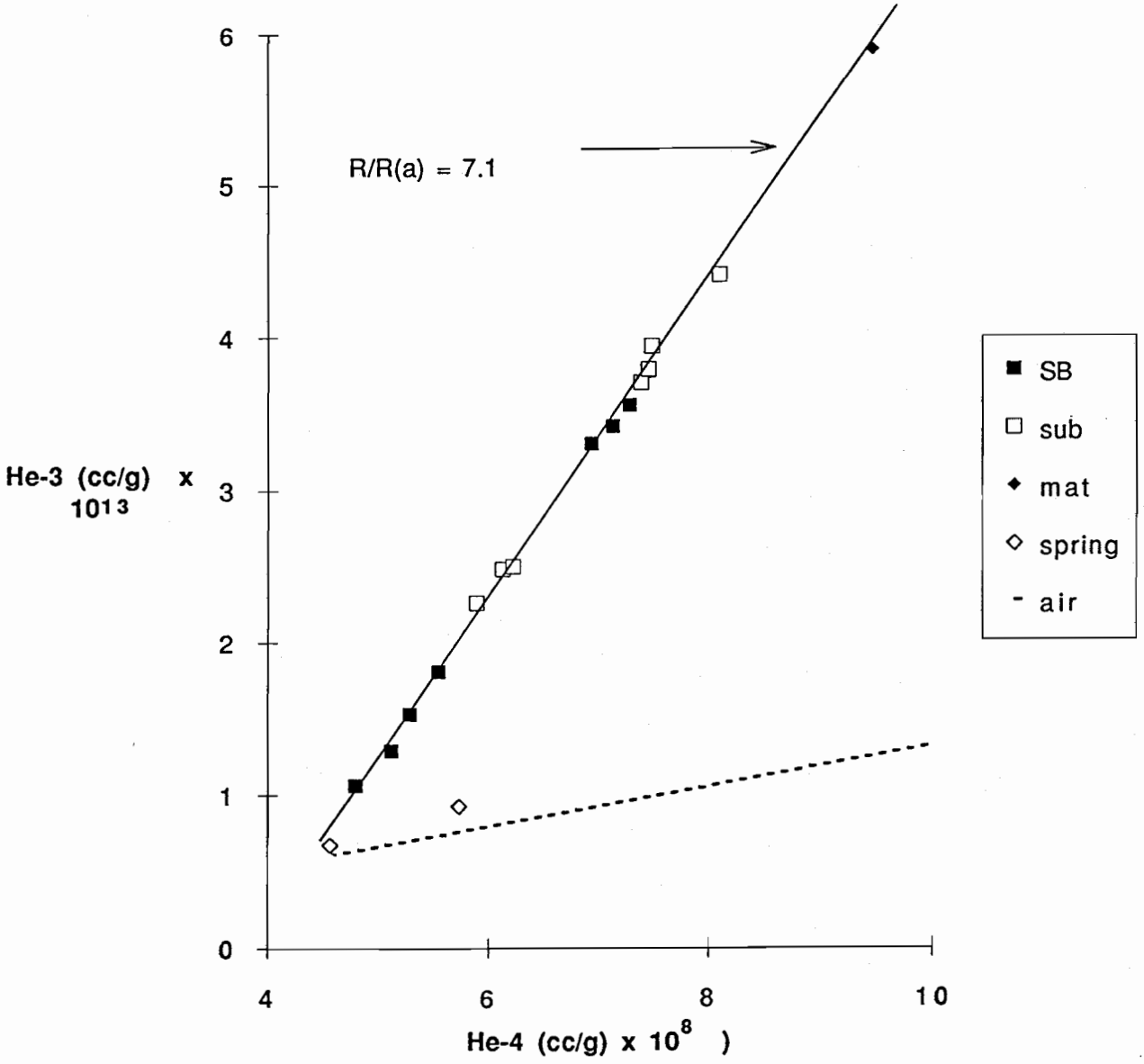

Figure 26. The relationship between the concentration of ^3He and ^4He in Crater Lake samples collected in 1989. The R/Ra is the comparative value of the ratio of ^3He /^4He in a sample relative to the ratio in the atmosphere (Ra = 1.39×10^{-6}). The ratio of 7.1 is a typical mantle value. The dashed line shows the atmospheric ratio (1.0). Samples which equilibrate with an atmospheric source, such as the cold spring waters, should fall along this line.

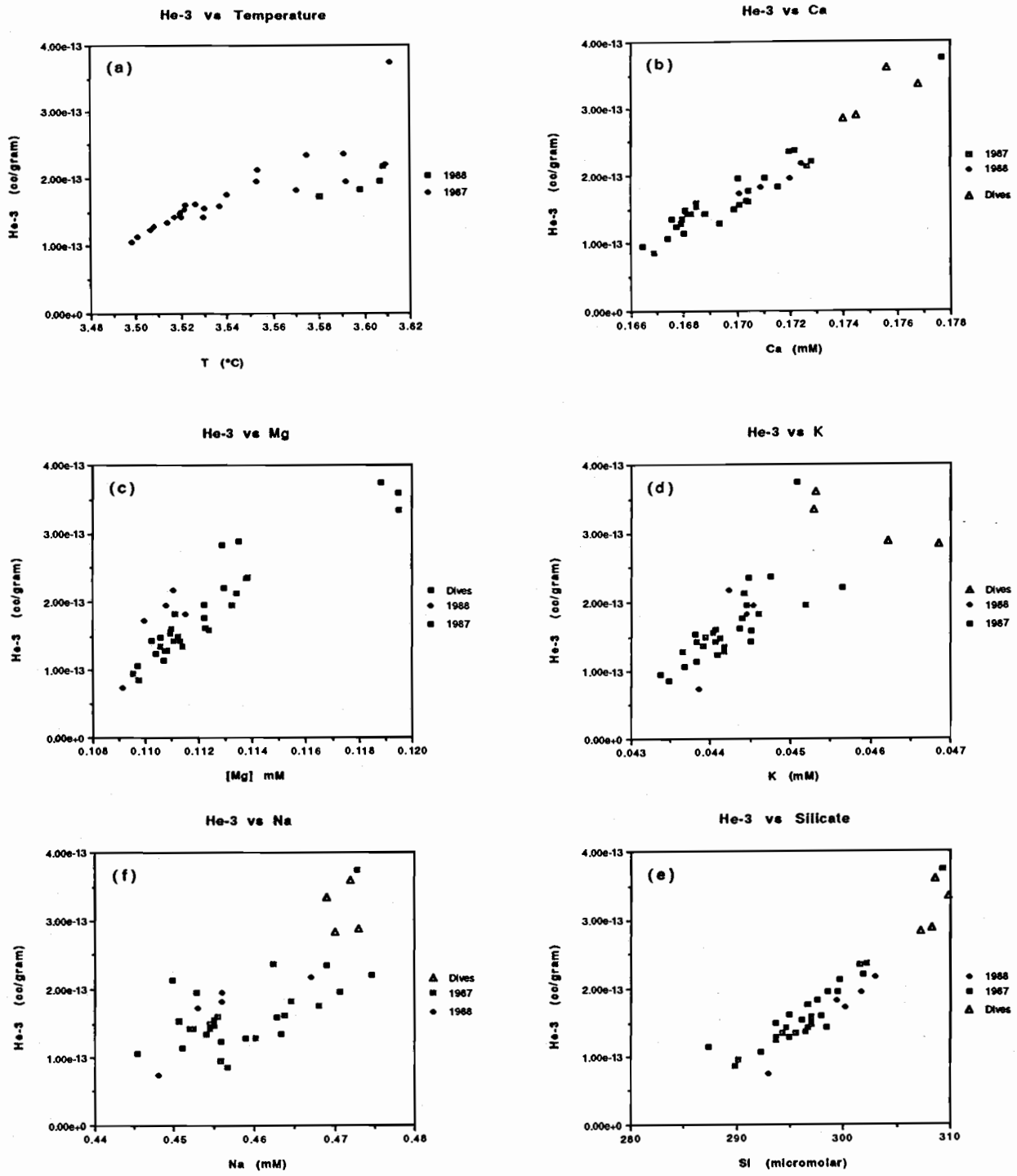

Figure 27. The concentration of He-3 vs. (a) temperature and (b-f) dissolved ions in Crater Lake. These plots include data from 1987 and 1988 and therefore show the excellent agreement between the two years' data sets. The slope of the He-temperature relationship (a) is approximately 1.5 x 10^{-12} cc He3/gram°C. The helium data are unpublished results provided by Dr. J. Lupton, UC Santa Barbara.

consistent with equilibration of these waters with an atmospheric source; magmatic contributions to these cold springs are insignificant. Therefore, we conclude that the non-condensible gas hypothesis cannot explain the observed helium distribution in the lake.

Submersible Samples.

The 1989 data extend the observed helium enrichments in the lake by more than a factor of 100. Thus, the most helium-enriched sample from Llao's Bath is 500 times enriched over what would be expected if these were in equilibrium with atmospheric helium (Figure 28). These enrichments maintain the same mantle isotopic ratio that is observed in the less chemically enriched deep-lake waters. Even the Palisades Point samples, whose elemental composition is significantly different from the pool brines and mat samples of the South Basin (Figures 22, 23, and 24), have the same mantle isotopic composition.

The extreme enrichments observed in the pools and mats are also correlated with major ion concentrations in the fluid (Figure 29a,b). In this case, Palisades Point does not fall on the same correlation line with South Basin samples, providing more evidence for a distinct fluid source for these samples.

In addition to the ionic species shown in Figure 27(b-f) for the 1989 samples, we were able to obtain measurements of ΣCO_2. The correlation between this variable and ^3He in deep lake waters is also very good (Figure 30a). The correlation extends to the very high concentrations of both ΣCO_2 and ^3He measured in the pools and mats (Figure 30b). The trend seen in Figure 30a appears to be derived from a single source input with a $CO_2/^3He$ ratio of 4×10^{10} atom/atom. This is well within the range reported for these gases from other subduction zone volcanics (Marty and Jambon, 1987) and is about ten times higher than ratios in MORB and 1000 times higher than the atmospheric ratio. The high flux of dissolved CO_2 (primarily in the form of bicarbonate ion) into Crater Lake which is implied by this relationship is also consistent with the observation by Nathenson and Thompson (1990) that there is a significant source of CO_2 available in the region which drives weathering reactions.

These correlations might lead one to the erroneous conclusion that ^3He is being carried into the lake with CO_2 in a gas phase. At the alkaline pH's measured in the pool brines, mat waters and pore waters, the ΣCO_2 is dominantly composed of bicarbonate ion. This carbonate species is a reaction product of interactions between silicate rocks and CO_2-rich (acidic) solutions. Thus, the excess ΣCO_2 (and alkalinity) found in the mats and pools is not entering the lake in the form of a non-condensible gas phase.

Summary - Helium Systematics.

The correlations between ^3He, temperature, major cations, and ΣCO_2 indicate that helium fluxes to the lake are carried by thermally and chemically enriched fluids and not as non-condensible gases. The low ^3He abundances and the atmospheric isotopic ratios observed in caldera spring waters are also contrary to the non-condensible gas hypothesis.

If the concentrations of helium measured in the Llao's Bath/brain mat complex represent the enrichments found in venting fluids, we can compute the rate of flow of enriched fluid entering the lake. Dividing the estimate for the ^3He input to the lake (9×10^{21} atoms/year) by the concentration of ^3He in our most enriched sample from the South Basin (2.71×10^{-11} cc/g), shows that an

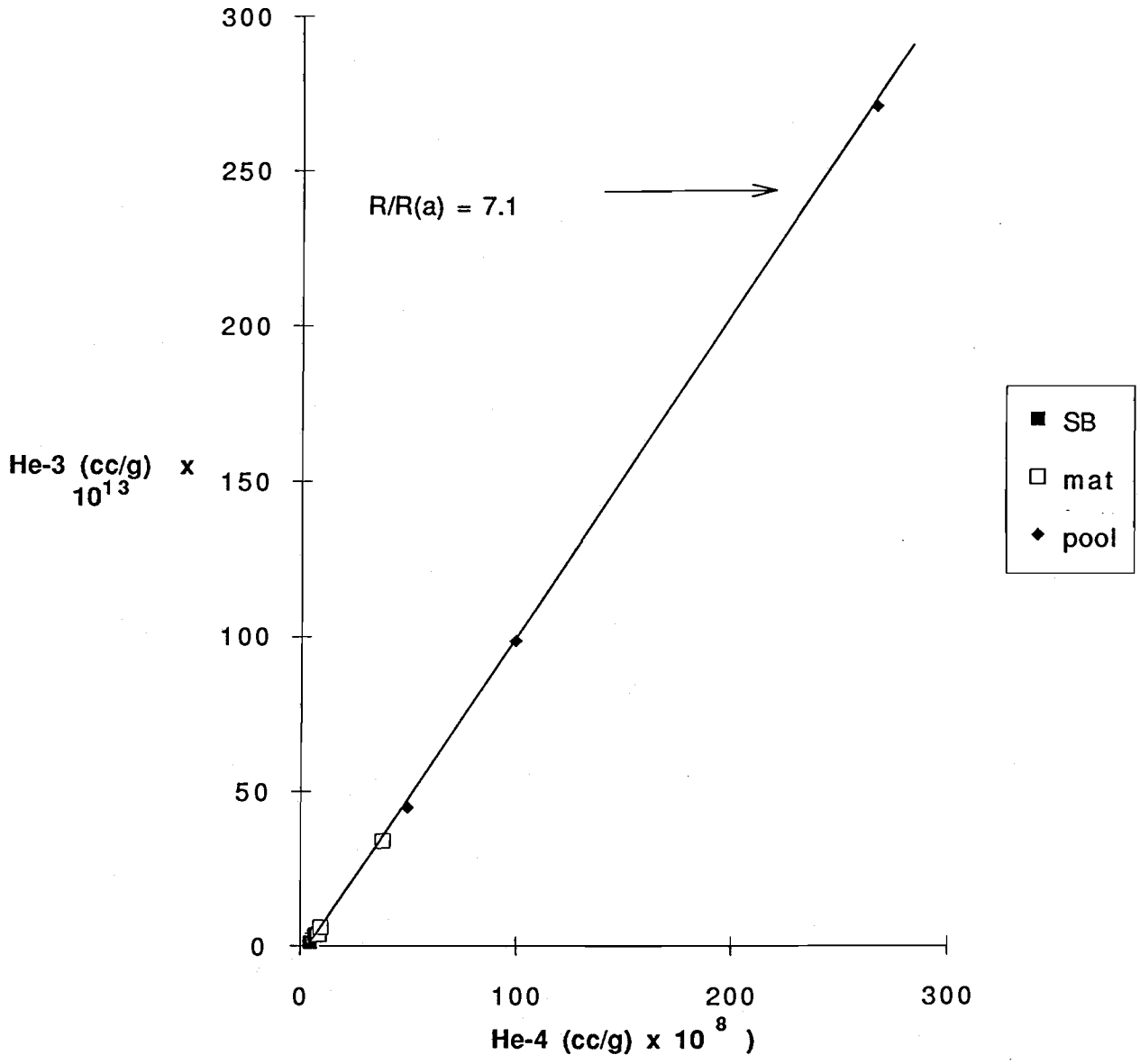

Figure 28. ^{3}He and ^{4}He in Crater Lake samples collected by submersible in 1989. Note the expanded scale relative to Figure 2. South Basin (SB) deep water samples are in the lower left corner. Llao's Bath is the pool sample in the upper right corner.

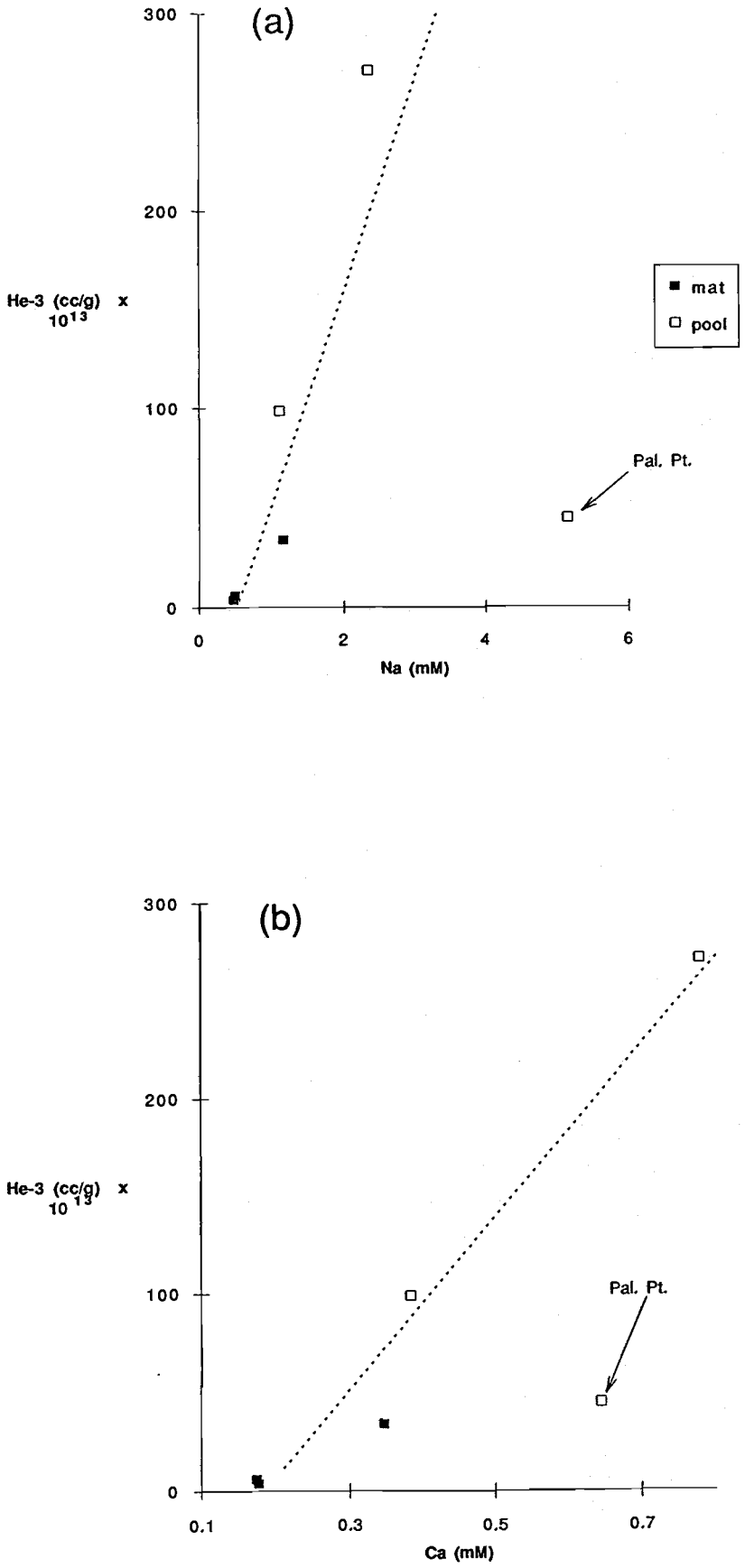

Figure 29. (a) The relationship between ^3He and Na contents in mat and pool samples. Note that the Palisades Point (Pal.Pt.) samples have a very distinct relationship. (b) ^3He vs. Ca for the same sample set.

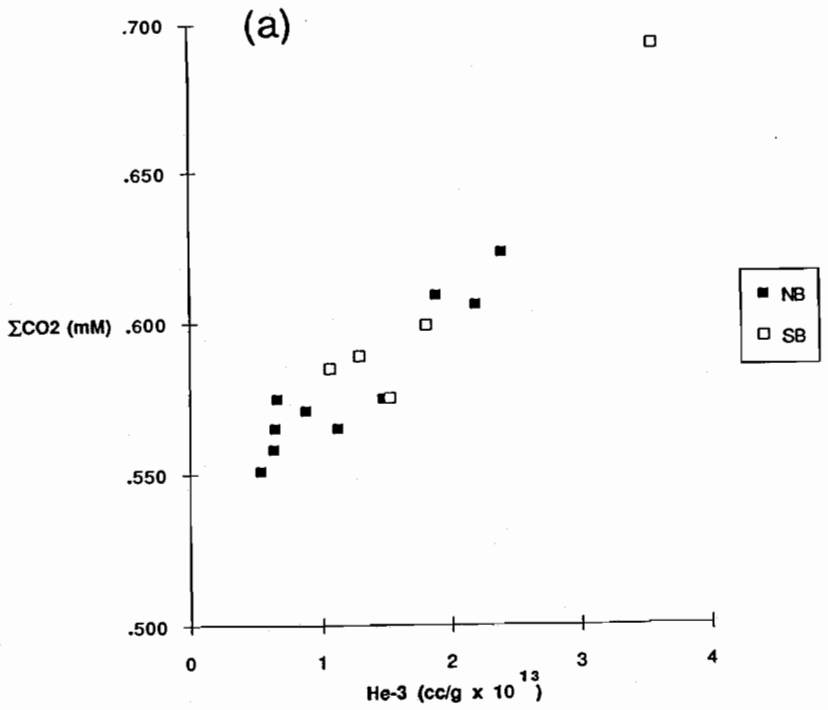

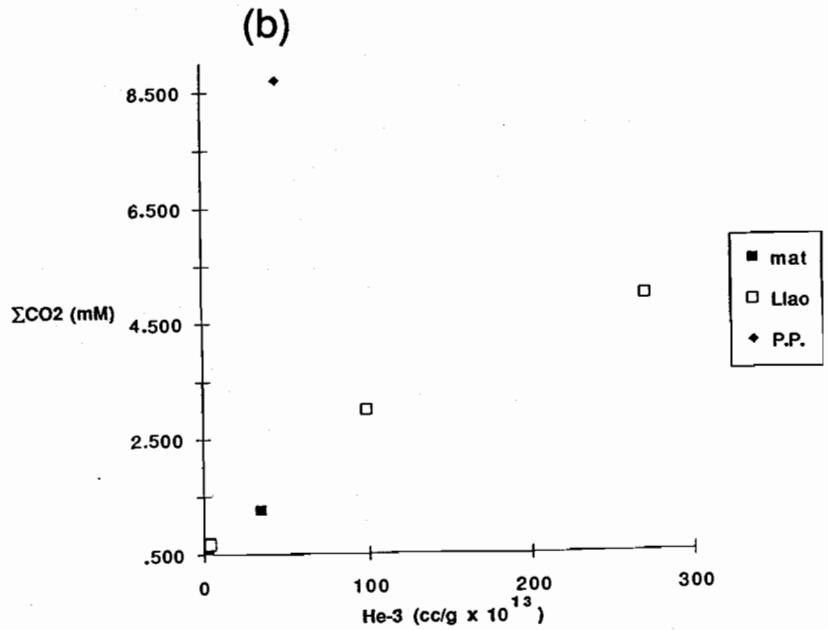

Figure 30. (a) $\Sigma CO2$ vs. ^3He in deep lake samples. NB and SB refer to North Basin and South Basin respectively. (b) $\Sigma CO2$ vs. ^3He in mat and pool samples. Note the expanded scale. Again, Palisades Point (P.P.) has a very different relationship compared to the other samples.

annual flow of 1.2×10^{10} liters of enriched fluid is required to supply the ^3He flux into the lake. This corresponds to approximately 400 liters/second. As we will discuss in more detail in the Geochemical Modeling section below, this rate is comparable to that estimated by a variety of other independent techniques. Assuming the helium-temperature relationship as discussed above (1.5×10^{-12} cc ^3He/gram°C) and a concentration of 2.71×10^{-11} cc ^3He/g in the end-member fluid, we calculate that the temperature of the fluid is 18°C as it enters the lake. This temperature is very similar to the highest measurements recorded in bacterial mat communities.

III.6. Dissolved Oxygen

As part of our on-going research efforts we have collected time-series oxygen data from the summer of 1988 through the summer of 1990. Collection of oxygen data began in July 1988 and samples were also collected during August and September of 1988. During 1989, monthly samples were collected from early April through August with more intensive sampling during our submersible program. Our data demonstrate two fundamental observations relevant to the biogeochemical cycling and physics of the lake: (1) to a first approximation the lake is near saturation with respect to dissolved oxygen; (2) there appears to be partial ventilation of the hypolimnion during each of the study intervals.

In order to assess the effect of the active input of thermally and chemically enriched fluids on the dissolved oxygen concentrations in the deep lake, we will examine the problem with respect to both the bulk water column and spatial scales in close proximity to the inputs of the enriched fluids.

Water Column Oxygen and Mixing.

Figure 31 demonstrates that there is very little observable change in the oxygen budget from July to September and that the entire water column is near saturation with respect to atmospheric oxygen at all times. This is consistent with a low particulate carbon flux and the lake's status as an oligotrophic system. Likewise, to a first approximation, there is little horizontal heterogeneity in the deep-lake oxygen budget between the North (deep) Basin and the South Basin.

Between September 1988 and April 1989, the hypolimnion of Crater Lake was partially mixed with oxygen rich water as is evinced by a net increase in the dissolved oxygen content measured at 550 meters of nearly 10 μM (Table 1 and Appendix A). This reaeration process was again repeated during 1990 as indicated by an increase in deep lake dissolved oxygen in July 1990 as compared to January 1990. In order to quantitatively constrain the mixing between September 1988 and April 1989 we first assume that the dissolved oxygen measurements taken in April will be made up of a mixture of air-saturated water (328.5 μM) and a deep lake endmember whose concentration is 297.4 μM (value for September, Table 1). Under these assumptions, the 307.0 μM April value is comprised of 31% air-saturated water and 69% deep-lake water. However, neither the September data nor the April data are likely to represent true endmembers for the minimum or the maximum in the deep lake dissolved oxygen budget during their respective years; therefore, an appropriate upper limit to this change in dissolved oxygen in terms of physical mixing is necessary.

The time series of oxygen data from April to January suggests a deep lake dissolved oxygen consumption rate of 0.04 μmoles/liter/day. Although oxygen consumption is unlikely to be

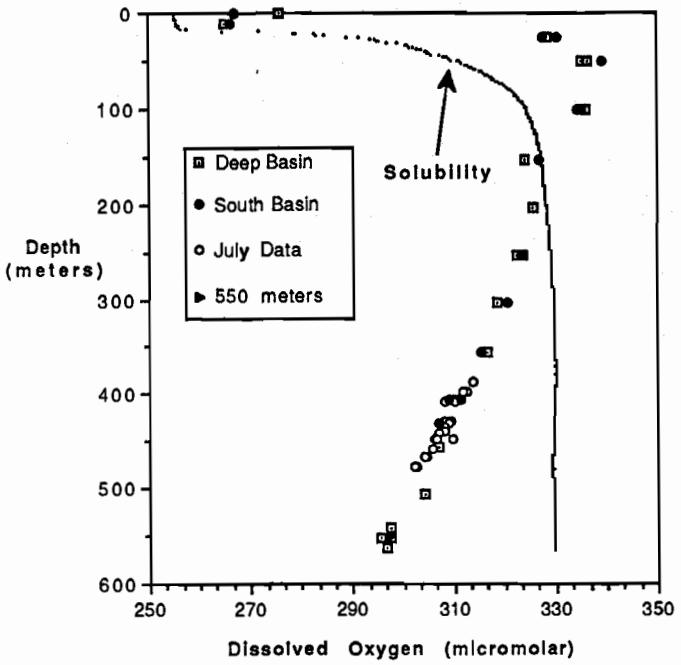

Figure 31. Dissolved Oxygen vs. Depth for samples taken in July and September 1988. Filled circles and open boxes represent September data and open circles represents July South Basin data (no north basin samples were collected in July). Since we calculate oxygen consumption over time at 550 meters, we have indicated this point on the graph.

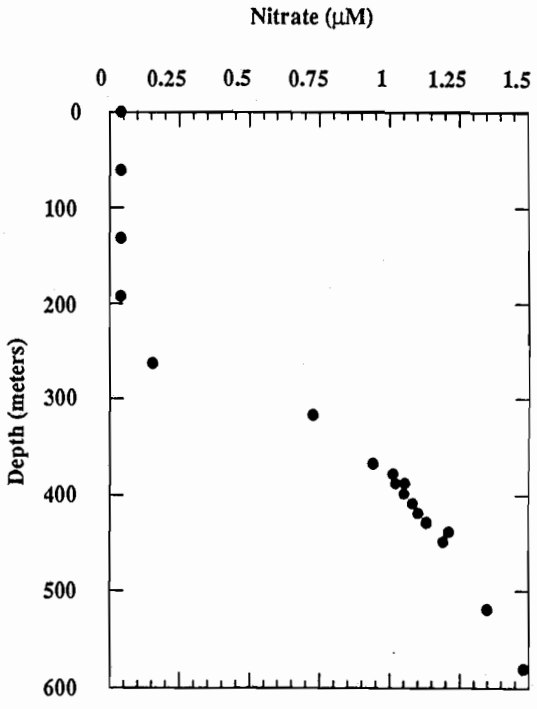

Figure 32. Nitrate vs. Depth for samples collected in August 1989. Samples include data from both the North Basin and South Basin.

constant from year to year or even within the same year we will use this rate as a first order approximation of the oxygen consumption at 550 meters.

Table 1. Dissolved Oxygen at 550 meters

Month	Dissolved Oxygen (μM)	Time (days)
September '88	297.4	NA
April '89	307.0	0
May '89	302.2	37
June '89	302.6	83
July '89	301.8	104
August '89	300.8	128
January '90	294.0	290

Assuming 1 January as the date of the minimum in deep lake dissolved oxygen, we take the September 1988 dissolved oxygen value of 297.4 and subtract 4.1 μM (0.04 μmoles/liter/day times 103 days) yielding an estimated oxygen minimum, at 1 January 1989, of 293.3 μM. Assuming that 1 February 1989 is the date of the maximum in deep lake dissolved oxygen, then we add 2.5 μM (0.04 μmoles/liter/day times 62 days) to the April value, giving 309.5 μM as the maximum in dissolved oxygen at 550 meters for 1989. Based on this second set of assumptions, there was a net increase in dissolved oxygen of 16.2 μM O_2 at 550 meters. Therefore, assuming an air-saturated dissolved oxygen value of 328.5 μM, a minimum dissolved oxygen value of 293.3 μM at 550 meters, and a reaerated hypolimnion with a predicted dissolved oxygen content, measured at 550 meters, of 309.5 μM, we obtain a deep lake mixture which is composed of 46% air-saturated water and 54% deep-lake water. Based on our percent exchange (31-46%) of surface water with deep water, we would expect a deep lake ventilation rate ranging from 2.5 to 3.5 years. Our data are insufficient for the same kind of approximations for the 1990 data; however, the data indicate that some exchange has occurred. As discussed in Appendix A this process is likely to be variable from year to year and a more comprehensive model which might account for interannual variability would need to include meteorological data as well as water column chemistry data.

The Oxygen Budget and the Influence of Hydrothermal Activity.

The stoichiometry of the oxygen-nitrate relationship with depth suggests that a simple Redfield oxidation model of organic matter decomposition is insufficient to explain the observed relationship (i.e. the ΔO_2:ΔNO_3 ratio is ~37 as opposed to 8.6 which is expected by Redfield stoichiometry). This suggests that there may be some other chemical oxidation process(es) influencing the distribution of dissolved oxygen in the deep lake. Figure 32 presents the nitrate distribution versus depth for August 1989 (for additional data consult Larson, 1986-90). Nitrate is depleted in the upper 250 meters followed by an increase from 250-350 meters, after which the nitrate increases slowly with depth. This profile is representative of a typical summer profile (Larson, 1986-1990). Because the slope of the dissolved nitrate concentration versus depth is greater between 250 and 350 meters than between 350 meters and the lake bottom, and because this is not the case with dissolved oxygen, the oxygen to nitrate relationship deviates from linearity in this depth range. The O_2:NO_3 relationship also deviates from linearity near the sources of active inputs of thermally and chemically enriched fluids.

Data from our intensive sampling of dissolved oxygen in the Detailed Study Area during our August 1989 field program suggest that the active input of thermally and chemically enriched fluids may affect the spatial distribution of dissolved oxygen in this basin. Strong correlations were found between temperature and dissolved oxygen and salinity and dissolved oxygen (Figure 33 a and b). This could be a result of three processes: (1) The dilution of deep lake water by anoxic water from the thermal springs. (2) The active input of reduced chemical species from the thermal springs (i.e. Fe^{2+}, Mn^{2+}, CH_4, etc.). (3) The higher density of the water along the sediment-water interface, due to the input of dissolved salts, will tend to inhibit exchange of bottom water with the surrounding water.

The dilution of deep lake water, assuming a minimum deep-lake volume of 4×10^9 m^3 (the volume below 500 meters), with an anoxic fluid that enters the lake at a rate of 63×10^5 m^3/yr (200 liters/second; see later discussion and Appendix A for fluid input rates) would cause a change in dissolved oxygen of approximately 0.1%. Therefore, dilution with zero oxygen water has a negligible effect on the overall oxygen budget of Crater Lake; however, on spatial scales very close to the source of anoxic inputs it is possible that dilution will affect the local dissolved oxygen value.

There is some difficulty in constraining the amount of oxygen consumption due to the introduction of reduced inorganic species. We do not know the exact composition of the reduced end-member fluid; however, based on pore water compositions and the compositions of the pool samples (see later discussion on pool compositions) our data indicate that, in terms of reduced chemical species, the incoming fluid is an iron and manganese rich fluid. Therefore, we will assume that these two elements constitute a large portion of the reduced species. Table 2 presents four redox reactions that we considered.

Table 2. List of redox reactions

$Fe^{2+} + 3/2H_2O + 1/4O_2 = FeOOH(s) + 2H^+$
$Mn^{2+} + 1/4O_2 + 3/2H_2O = \beta MnOOH + 2H^+$
$CH_4 + 2O_2 = CO_2 + 2H_2O$
$H_2S(g) + 2O_2 = SO4^{2-} + 2H^+$

Samples of subsurface thermally and chemically enriched springs recovered during the 1989 field program contained up to 33 μM dissolved iron, 24 μM dissolved manganese, and 900 μM sulfate. Because of atmospheric equilibration prior to filtration and acidification, these iron and manganese measurements are lower limits at best. Sediment pore-water samples taken near suspected sources of active input of reduced fluids have dissolved iron and manganese concentrations as high as 200 μM and 100 μM respectively. The pore water values may be a more realistic upper limit for the metal concentrations entering the deep lake. We assume iron and manganese enter the lake in a reduced form (Table 2) and that exposure to deep lake water will oxidize these species according to the reactions given above.

Since both manganese and iron consume oxygen in the same proportions, we combine their concentration to yield 300 μM iron and manganese. Consequently, the metal:O_2 consumption ratio

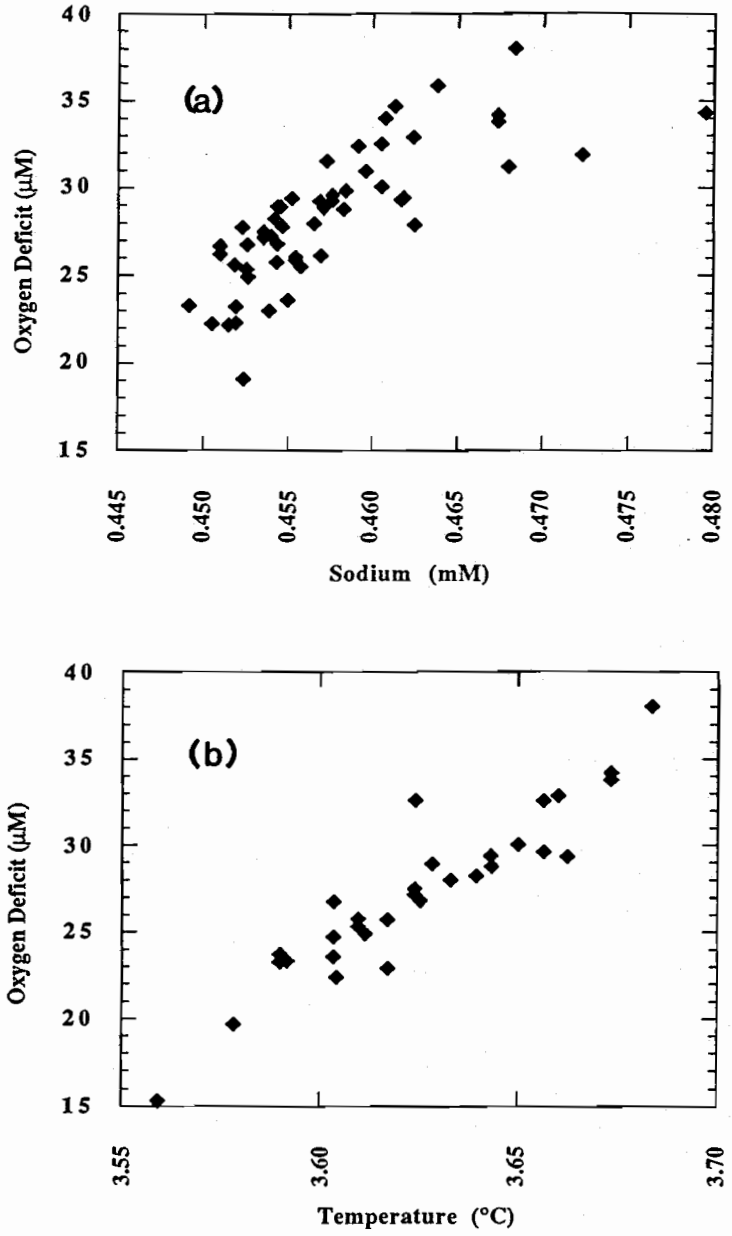

Figure 33. (a) Oxygen Deficit vs. Temperature for hydrocast samples from depths below 400 meters in the south basin in Crater Lake; (b) Oxygen Deficit vs. Sodium for hydrocast samples from depths below 400 meters in the south basin. Oxygen Deficit is the difference between the atmospheric saturation value at ~200 meters (328.5 µM) and the measured dissolved oxygen content.

is 4:1 which will require 75 μM O_2 for the oxidation of 300 μM Fe and Mn. Hence, with a fluid input rate of 63 x 10^8 liters/year, the Fe and Mn will consume 4.7 x 10^{11} μmoles of O_2/year. In the deep lake (volume equivalent to a depth > 500 meters) this corresponds to a consumption of 0.12 μM O_2 per year. Therefore, iron and manganese account for between 2 and 5% of the measured change in dissolved oxygen of the deep lake.

Although sulfate measured in the pool samples and the pore waters was found to be as high as 900μM, we do not expect that all the dissolved sulfate in the lake entered the lake as H_2S(g). Two reasons for suspecting that H_2S(g) is not the primary sulfur species are: (1) The oxidation of H_2S(g) generates one mole of H^+ for every mole of O_2 consumed but the pH of the deep lake and the pore waters is generally too close to neutral (between 6 and 8) for this reaction to be occurring. (2) There was no strong characteristic sulfide odor and even at H_2S(g) concentrations <10 μM we would be able to smell the sulfides in the pore waters and in the pool samples.

We have only a few methane samples to constrain the input of this constituent. Our results indicate that the deep water column methane concentration is between 10 and 30 nM; likewise, dive samples CD215 S1, CD215 S2, CD216 S1 and CD216 S2 ranged between 8 and 23 nM. Water immediately above a box core from a pool had approximately 6 μM methane, indicating that there is some methane present in the reduced fluid.

Assuming concentrations of 10 μM for H_2S(g) and CH_4, and assuming a consumption stoichiometry of 2 moles of O_2 for each mole of H_2S(g) and CH_4 (Table 2), then 40 μM O_2 will be consumed by the incoming fluid. From the mass balance arguments above, this will be less than 2% of the total oxygen deficit.

Circumstantial evidence suggests that the oxygen budget is dominated by the oxidation of organic matter. This conclusion is largely based on the observation of a linear dissolved oxygen to nitrate relationship in the deep lake and on the observation that the active input of reduced fluids cannot account for the observed change in deep lake oxygen. It is beyond our data set to reconcile the discrepancy between the observed ΔO_2:ΔNO_3 relationship and that predicted based on a traditional stoichiometric relationship. There are two distinct possibilities which could explain our inability to balance the O_2 budget: (1) The ΔO_2:ΔNO_3 relationship in Crater Lake is not defined by a traditional 'Redfield' stoichiometric model. (2) We may have drastically underestimated the concentration of reduced species entering the lake.

Small-Scale Variations in Bottom Water O_2 Distribution.

The greater depletion of dissolved oxygen near the sediment-water interface in the South Basin compared to the North Basin may be due to a combination of density effects and local oxygen consumption. Correlations between temperature and salinity with the oxygen deficit suggest a dependence of the oxygen deficit on the active input of saline fluids (Figure 33). As mentioned above, these fluids have enhanced concentrations of reduced chemical species which consume some of the dissolved oxygen in the South Basin. Also, the dilution of deep lake water by anoxic water may cause a net lowering of the dissolved oxygen content very close to the fluid source. An additional influence that these fluids have on the distribution of dissolved oxygen is to increase the stability (density) of near-bottom waters by addition of salts. Consequently, the consumption of oxygen due to the decomposition of organic matter and the local input of reduced fluids can proceed to a greater degree in fluids nearer the source than in bulk deep-lake waters.

Measurements of pool samples (CD230 S1 and CD228 S1) indicate that the pools are anoxic. The minor oxygen contents found in the samples are probably due to bottom water entrainment at the time of collection and not from dissolved oxygen in the pools. The oxygen content of CD223 S1 is quite low relative to the bottom water values listed in Table 3. but this is not surprising since it was collected immediately above a pool. A plot of the oxygen deficit (where the oxygen deficit is the saturation value, 328.5 μM, minus the measured value) versus sodium shows that sample CD230 S3 lies along a line between the Llao's Bath low oxygen-high-sodium end-member and deep lake water (Figure 34). This observation suggests that we were unable to sample these bacterial mat fluids without a large amount of bottom water entrainment. Also Figure 34 demonstrates that there are two trends of dissolved oxygen deficit versus salinity; (1) the deep lake trend which is dominated by a combination of factors which includes the oxidation of organic matter with decreasing oxygen, and (2) a dilution and inorganic oxidation trend which runs from the deep lake to Llao's Bath.

Table 3. Dissolved oxygen and sodium concentrations in submersible samples.

Sample or Dive	DO (μM)	O_2 deficit * (μM)	Sodium (mM)	Comments
CD230 S1	17.7	310.8	2.36	"Llao's" Bath
CD228 S1	17.5	311.0	5.14	Palisades Point Pool
CD223 S1	228.2	100.3	1.109	Above "Llao's" Bath
CD230 S3	279.2	49.3	0.608	Bacterial mat
CD216 S3	294.2	34.3	0.480	Bacterial mat
CD223 S3	294.6	33.9	nm	Above pool
CD229 S2	240.7	87.8	nm	Bottom water
CD230 S2	293.8	34.7	0.461	Bottom water
CD228 S2	297.3	31.2	0.468	Bottom water
CD226 S2	292.6	35.9	0.464	Bottom water
CD222 S2	296.6	31.9	0.472	Bottom water

** The O_2 deficit is defined as the atmospheric saturation value in the upper waters (328.5 μM) minus the observed O_2 value. nm denotes not measured.*

The effect of reduced fluids on the distribution of dissolved oxygen close to the source of fluid input will obviously be much larger than for the bulk water column. If we assume that the enriched fluids enter the lake over an area one tenth the size of the Detailed Study Area and use the oxygen consumption estimates from above (75 μM O_2 for iron and manganese and 40 μM O_2 for methane and sulfate combined), then for a bottom layer 1 meter deep (i.e. 0.3 x 10^6 m^3),we obtain an oxygen consumption rate of 6.6 μM/day. Likewise, we will dilute this volume with anoxic waters by 5.8% per day. Although these calculations are oversimplified, they do make the point that on small spatial scales, near the source of the (thermally and chemically) enriched fluid inputs we should observe heterogeneity in the oxygen distribution.

Therefore, it appears that the influence of anoxic water dilution on the oxygen budget is minimal for the bulk lake; however, it provides heterogeneity in the deep lake on spatial scales of meters. Likewise, the consumption of oxygen by reduced inorganic species accounts for < 5% of the total

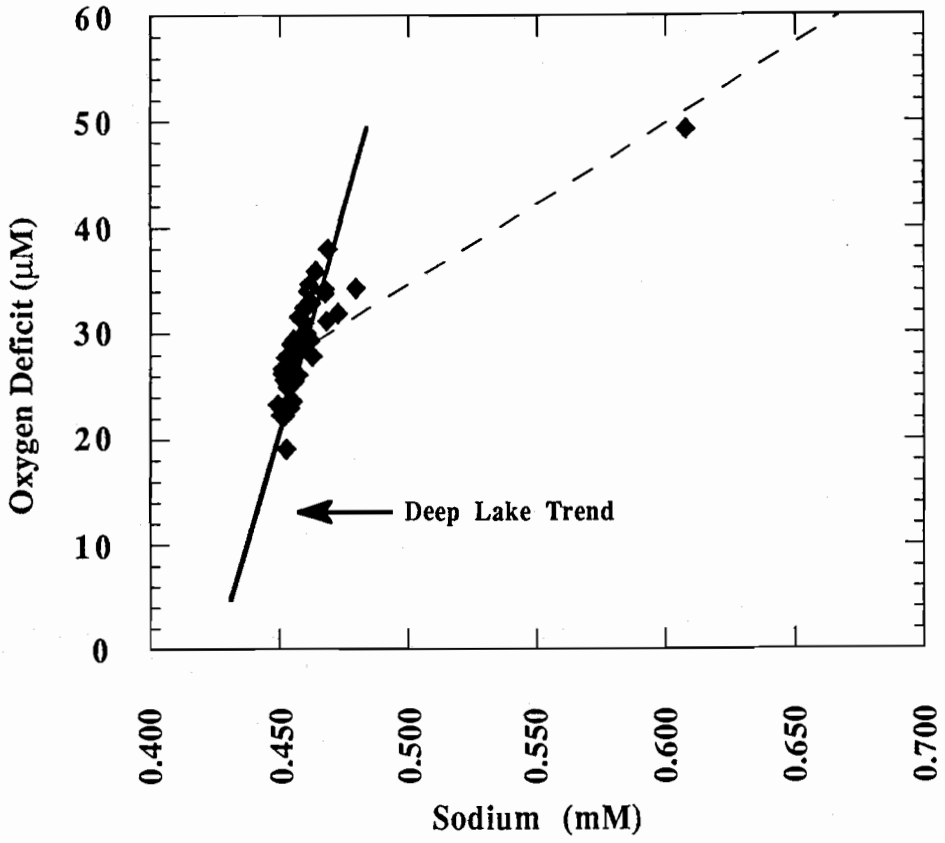

Figure 34. Oxygen Deficit for all samples, including submersible samples, vs. sodium. The dashed line extends to the Llao's Bath sample (310.8 µM oxygen deficit and 2.36 mM Na) and the solid line represents the trend in the deep lake hydrocast samples.

consumption for the bulk lake, although, it is probably greater on local scales in the South Basin. In accord with this concept, the dissolved oxygen content for the deep north basin (NPS station 13) at the time Table 3 samples were collected was approximately 300 μM whereas in the South Basin the values were 5 to 15 μM lower. This suggests that the active inputs of thermally and chemically enriched fluids may not be influencing the waters of the deeper north basin to the same degree as the South Basin, again consistent with the South Basin being the dominant source of reduce saline fluids. Ultimately, the stabilizing force provided by denser bottom waters causes the effectiveness of deep lake mixing to decrease with depth, which is consistent with the mixing models presented in Appendix A and the ages of deep water as revealed through CFC data (Appendix G). For 1989-1990 this mixing corresponded to an effective exchange of surface (well-aerated water) with deep water of approximately 40%. If this exchange was consistent from year to year, it would take 2.5 to 3.5 years to ventilate the deep lake.

III.7. Radon-222

One of the most effective tracers of hydrothermal input to the oceans has been ^{222}Rn, a daughter product of ^{238}U decay. Radon, like helium, is a noble gas, which means that it does not enter into chemical reactions during its movement through geochemical systems. Because of its relatively short half-life (3.8 days) measurements are made at sea to give real-time data (Rosenberg et al., 1988). Although hydrothermal fluids are strongly enriched in ^{222}Rn over normal ocean waters (Dymond et al., 1983), it is not an unequivocal indicator of hydrothermal inputs because there are other sources of the isotope. Diffusive inputs from sediments can be a significant source of ^{222}Rn (Broecker et al., 1968; Kadko, 1981). In addition, ^{222}Rn is enriched in all ground waters, thermal or non-thermal, as a result of α-recoil injection from the surfaces of uranium-bearing solids (Asikainen, 1981). Consequently, in the analyses of Crater Lake waters, this tracer can not distinguish between hydrothermal and non-thermal ground water inputs.

Despite these complicating factors, measurement of this isotope is important because the 3.8 day half life adds a temporal component that does not exist with nonradioactive tracers. One possible analytical technique is the evaluation of variability in the $^{222}Rn/^{3}He$ values, which because both isotopes are noble gases, should decrease according to the radon half life upon injection into bottom water. If there is input of hydrothermal fluid into the deep lake, the rates of dispersion could be evaluated by studies of this isotope pair (Kadko et al.,1990). Similarly, ^{222}Rn/Na can be used as a nonreactive pair. Our previous studies have demonstrated that Na and ^{3}He contents of the deep lake waters are correlated. Consequently, it is reasonable to expect that ^{222}Rn and Na will be venting into the lake at a constant ratio which will decay with the 3.8 day half life of ^{222}Rn.

In addition, the radioactive decay of ^{222}Rn is useful for estimating the flux of hydrothermal elements and heat into the lake. Estimates of the total inventory of ^{222}Rn within the lake can be used to determine the flux of radon into the lake. A similar approach has been used to define the hydrothermal input of radon and other tracers at a major hydrothermal system on the Juan de Fuca Ridge (Rosenberg et al., 1988).

In Figure 35, we have plotted measured ^{222}Rn contents of Crater Lake as a function of sampling depth. The data include only samples recovered during 1989; however, all previous radon measurements of the water column resulted in a similar pattern (Collier and Dymond, 1989). The significant features of this plot are the high values that occur between 400 and 470 meters depth. Above and below this depth, the radon contents decrease to the values expected from the decay of

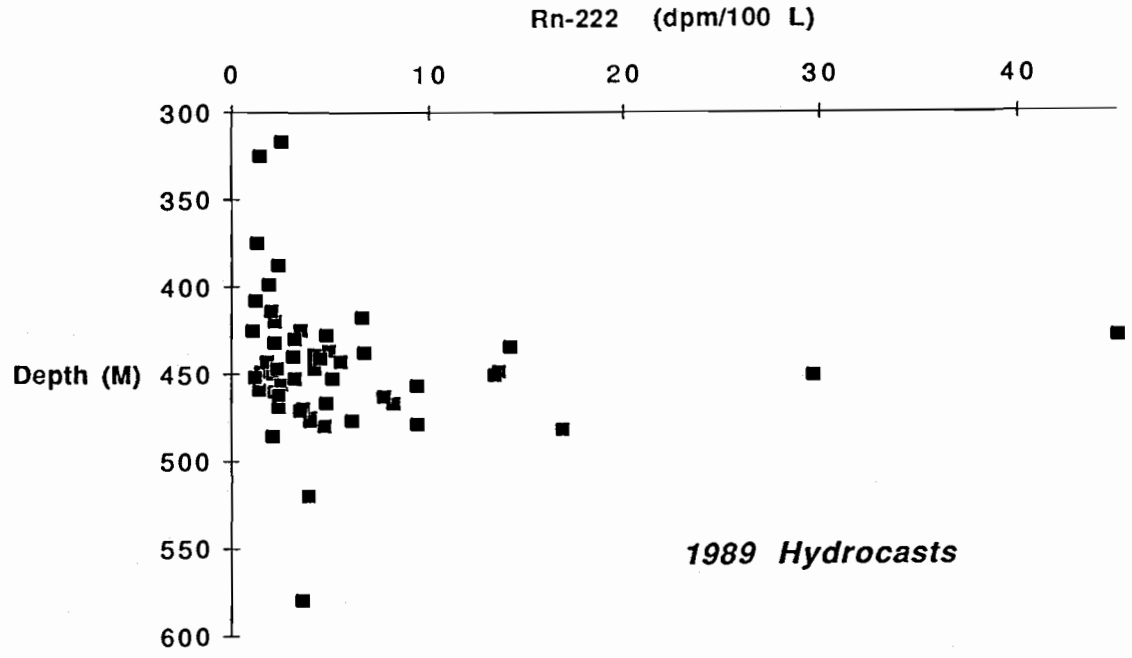

Figure 35. Radon-222 concentrations vs. depth for 1989 hydrocast samples. The strong increase in ^{222}Rn at approximately 450 meters depth is the same pattern that was determined by measurements made in 1985-1988.

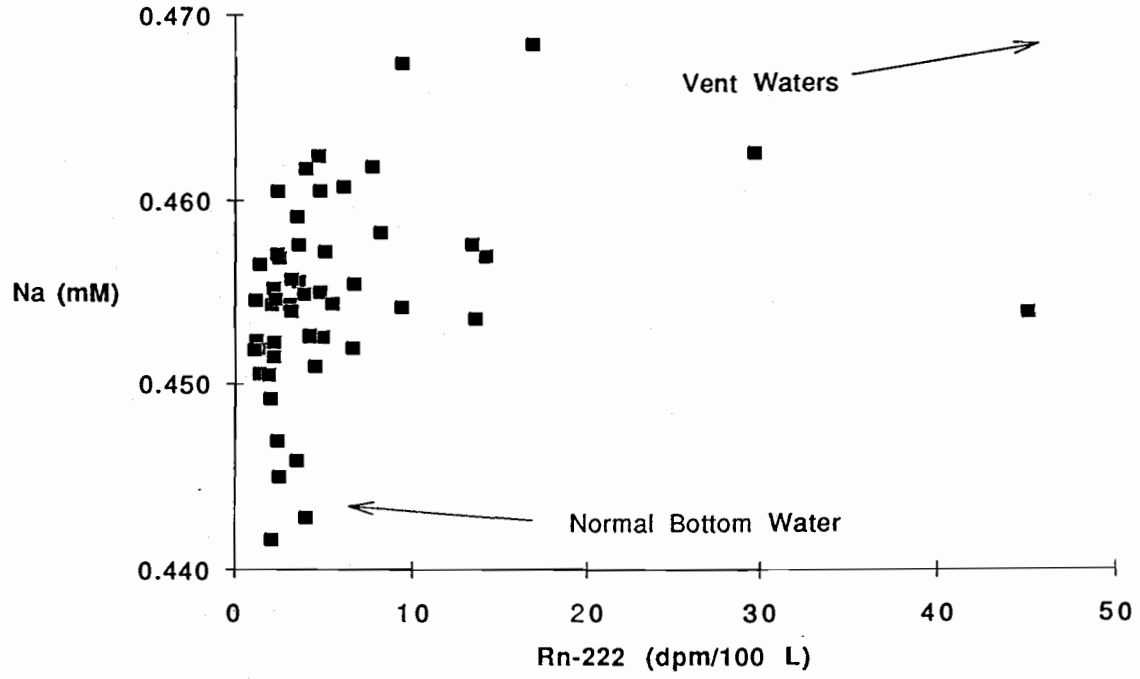

Figure 36. Radon-222 concentrations vs. sodium contents for 1989 hydrocast samples.

dissolved radium-226 (^{226}Ra). The depth maximum for ^{222}Rn is consistent with sources that occur at approximately 450 meters depth. Radium-226 was measured on selected samples in order to define the amount of ^{222}Rn supplied by the decay of this parent isotope. Because of the low values of radium in the lake waters, its measurement by in-growth of ^{222}Rn (Mathieu, 1977) is relatively imprecise. Bottle blanks in general have on the order of 50% of the measured activity, and the overall counting errors are large. Thus, within our precision, the radium content of the hydrocast samples appears to be constant everywhere in the lake. The mean ^{226}Ra for 15 water column samples is 2.4±1.3 dpm/100 liters. This value is similar to the lowest ^{222}Rn values measured in our water samples. Decay rates of ^{226}Ra as low as 1.1 dpm/100 liters were measured on several samples, and we suspect this is the best estimate for the radium-supported ^{222}Rn . Consequently, the high ^{222}Rn values which occur between 400 and 470m are clearly not the result of decay of dissolved ^{226}Ra.

The diffusive inputs of radon from sediment pore waters to the bottom waters appear to be small. This is demonstrated by the fact that near-bottom samples from the North Basin do not have ^{222}Rn values that are significantly above values supported by the decay of ^{226}Ra. Since both the North Basin and the South Basin are covered with sediment, similar rates of ^{222}Rn diffusion are expected in each area unless the sediments in the South Basin are strongly enriched in radium compared to those in the North Basin. Although we have not measured the radium contents of the lake sediments, the major-element abundances and some minor-element abundances in sediments from the two basins are essentially identical, except for some very localized areas of the South Basin which are strongly enriched in iron and believed to be influenced by precipitation from hydrothermal fluids (Dymond et al., 1987).

In addition, we experimentally determined the radon diffusion rates from cores collected in the two basins, following the procedures of Kadko (1981). A sealed core of the sediment and the overlying waters was stripped of its ^{222}Rn contents after 5 to 9 days. The ^{222}Rn values measured in this way were close to detection limits for cores from both the North and South Basins, and therefore, sediment sources cannot account for the high values measured in the water-column samples from some areas of the South Basin.

The ^{222}Rn /Na values measured in the hydrocast samples vary strongly (Figure 36). These variations can be accounted for by time-dependent mixing of lake waters which have a significant component of fluids with a subsurface origin. The samples with the lowest Na and ^{222}Rn values represent the normal lake bottom waters which do not have a strong signal from a bottom source (hydrothermal or cold springs). Conversely, samples enriched in Na and ^{222}Rn show evidence for such a source. Rapid mixing of these two sources would result in a linear array of data points. The observed data, however, has a strong curvature, which is a consequence of ^{222}Rn decay during the mixing process.

Estimates of Radon-222 Inventory.

During the submersible operations in August 1990, 13 hydrocasts were made within the South Basin Detailed Study Area. At each station, radon samples were obtained from the three to five 30-liter water samples collected within the bottom 150 meters. Radon measurements of these samples result in a near-bottom profile of ^{222}Rn (Figure 37). From this profile, we have computed the integrated radon at each sampling site. A map of the integrated ^{222}Rn contours is shown in Figure 38. The integrated ^{222}Rn was computed by assuming a background ^{226}Ra-supported value of 1.1 dpm/100 liters. The measured values were extrapolated to this background value and to the

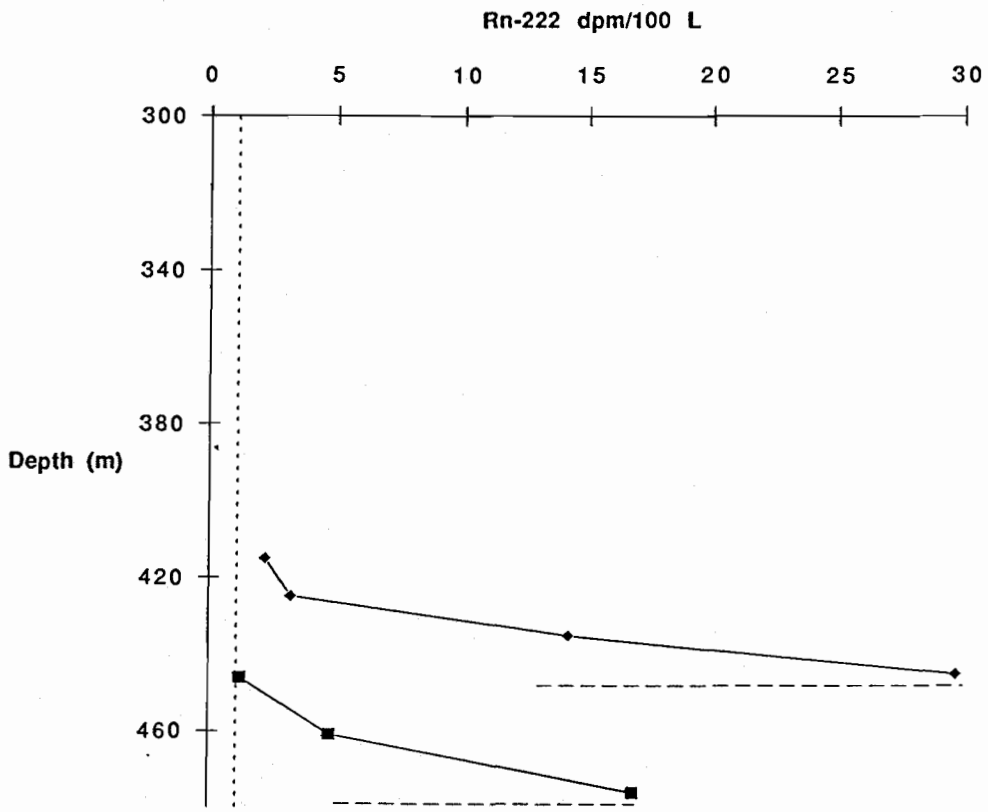

Figure 37. ^{222}Rn contents vs. depth for two profiles within the detailed study area. The vertical dashed line marks the amount of ^{222}Rn which is supplied by the decay of dissolved ^{226}Ra in the water; in effect this is the background level of ^{222}Rn , i.e.,without any inputs from bottom sources.

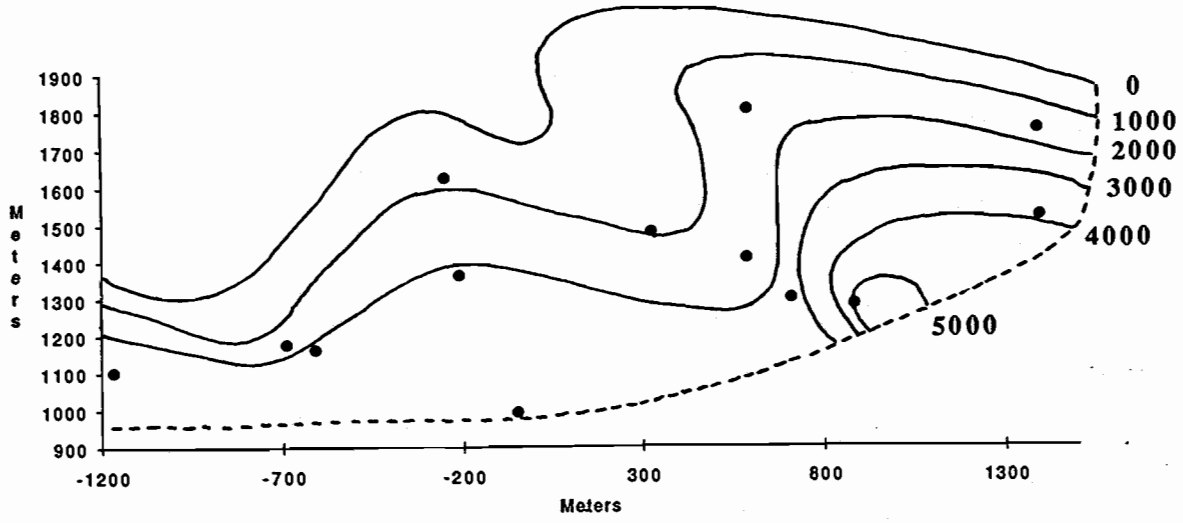

Figure 38. The integrated ^{222}Rn contents in units of dpm per square meter for the detailed study area. High values occur in the southern part of the area, particularly in the vicinity of the high temperature mats.

depth of the bottom. In general, at depths shallower than 400 meters, the ^{222}Rn is derived solely from the decay of ^{226}Ra.

The results of these calculations indicate that the integrated ^{222}Rn values from the sampling sites vary by more than a factor of five (Figure 38) . There is a general south to north decrease in the integrated ^{222}Rn contents across the sampled area. Unfortunately, our sampling pattern did not extend far enough to the south to define the southern extent of the high values. The two highest values are both from relatively shallow sites located on the slopes of the presumed landslide/debris flow that occurs on the southern margin of the Detailed Study Area. From the contoured values of integrated radon we have computed the total radon inventory of the area to be 1.7×10^9 dpm. Assuming the computed inventory is maintained by continuous inputs, the value also represents the number of radon atoms which are injected into the area from all sources each minute. It is difficult to define the errors in this estimate, but the constraints on the contouring suggest that it represents a minimum value for the ^{222}Rn inventory. The contouring is well constrained within the sampling locations, however, we have not made broadly spaced measurements on the margins of the detailed survey area that allow us to estimate the extent of the area with low integrated ^{222}Rn values. The lack of broader sampling is particularly problematic for the southern part of our survey, where we have not constrained the full extent of the areas with the highest integrated radon values. Extending the boundaries of areas with excess radon would have resulted in a larger ^{222}Rn inventory.

If we assume the ^{222}Rn flux comes from a fluid source with a radon content equivalent to the highest value that we measured in any of our hydrocasts (45 dpm/100 liters), an influx of 8000 liters per sec of fluid would be required. This number is approximately an order of magnitude higher than the estimates for hydrothermal fluxes of Reilly et al. (1989) and Nathenson (1990a). As will be discussed below, the samples collected from near bacterial mats and from saline pools have radon contents 100-200 times higher than our most enriched hydrocast samples. If input of mat and pool fluids dominates the radon flux, the required volume of fluid input would be reduced correspondingly (to as low as 40 liters/sec).

Radon and Radium in Submersible Samples.

Because the submersible provides the ability to position samples near the bottom and in known relationship to sites of venting, the ^{222}Rn measurements collected in this way are much higher than those collected with surface hydrocasts. The 1988 submersible samples collected near a bacterial mat extended the amount of ^{222}Rn enrichment observed in the detailed study by more than a factor of six (approximately 200 dpm/100 liters) over our earlier data. The 1989 submersible program collected a number samples with even higher ^{222}Rn contents (Appendix I).

The most enriched samples were found in the pools. Two samples from Llao's Bath differed by more than a factor of three (9961 and 3063 dpm/100 liters); however, the higher value was collected by pumping fluid into a sampler. This sampling procedure should have less bottom water dilution and therefore provides a better measure of the pool composition. This assertion is supported by the higher major element concentrations in the pumped sample.

Samples collected by the submersible in the vicinity of bacterial mats were also strongly enriched in ^{222}Rn, with values ranging from 373 to 1887 dpm/100 liters. Since the highest values generally correlate with Na and other major element contents, this range probably represents varying degrees

of dilution. However, the mixing of mat water with older deep lake waters whose ^{222}Rn contents have decayed would result in lower ^{222}Rn contents and lower ^{222}Rn /Na values.

Radon-222 Constraints on Pool Formation and Exchange Rates.

It is noteworthy that the Palisades Point pool sample, which was also collected by pumping, has 15 times lower ^{222}Rn content than Llao's Bath. Because there is evidence that the Palisades Point pools fill by gravity flow from variable distances upslope, it is tempting to account for the low ^{222}Rn through mixing with normal lake waters. The concentrations of sodium and other major elements in the Palisades Point pool, however, are approximately two times higher than those measured in Llao's Bath (Figure 39), indicating that mixing alone cannot account for their relatively low ^{222}Rn contents.

It is possible that the difference in ^{222}Rn contents between the Llao's Bath brines and the Palisades Point brines reflects a greater mean age of the Palisades point water. For example, if the Palisades Point pool had the same initial ^{222}Rn that we measured in Llao's Bath, our data coupled with the 3.8-day half-life imply that the Palisades Point pool water has a mean age approximately 15 days older than Llao's Bath. This difference in mean age could be a consequence of either time-variable inputs which fill the two pools episodically or continuous fill which results in lower steady-state concentrations of ^{222}Rn in the Palisades Point pool.

To evaluate either case, it is necessary to have an estimate of the ^{222}Rn content of the fluid which enters the pool. The content of ^{222}Rn in any ground water (thermal or non-thermal) is largely controlled by the uranium content of the rock which is in contact with the water. The time since the water has been isolated from atmospheric exchange (degassing) as little effect. This follows from the fact that the relatively short half life of ^{222}Rn results in rapid achievement of a balance between input from recoil and loss by decay (Dymond et al., 1983). Although we cannot unequivocally define the initial values for the pool waters, we can provide some reasonable estimates from which to compute the maximum ages for waters in Llao's Bath. Radon-222 measurements of Annie Springs, a major spring near the southern border of the Park, may provide a good estimate of subsurface waters from the Cascades. Six measurements made in 1988 averaged 93,000 ± 34,000 dpm/100 liters. We suspect the variation reflects sampling artifacts caused by atmospheric exchange. Consequently, the highest value measured, 140,000 dpm/100 liters, is probably the best estimate. Ground water values of ^{222}Rn as large as 10^6 dpm/100 liters have been measured in arkosic aquifers (Krishnaswami et al., 1982), which undoubtedly have much higher uranium contents than Cascade volcanics. Accepting the Annie Springs' ^{222}Rn measurements as an initial ^{222}Rn value would mean that Llao's Bath waters are less than 15 days old. Even a value of 10^6 dpm/100 liters, clearly a conservative estimate, would require the Llao's Bath waters to be less than 30 days old. These estimates are upper limits to the age of Llao's Bath fluids. As we stated in the previous paragraph, this episodic input model would imply that Palisades Point water filled within 30 to 45 days prior to sampling. The fluids entering the pool could have lower radon contents if there had been mixing of lake water with the fluids prior to entering the pool.

In contrast, for a continuous input model, the ^{222}Rn content of the pool can be described as a balance between input and decay plus outflow:

$$(R_i \times C_i) = (R_o \times C_o) + D$$

where R_i and R_o equal the rate of fluid input and output respectively. At steady state these rates are equal. C_i and C_o are the concentrations of ^{222}Rn in the inflowing and outflowing waters. The last term in the equation, D, is the loss of ^{222}Rn by radioactive decay. To determine the decay loss of ^{222}Rn it is necessary to determine the total inventory of ^{222}Rn in the pool. This requires an estimate of the volume of the pool. We estimate the dimensions of the pool to be 3 to 4 meters long and 1 to 1.5 meters wide. Although we could not see the bottom, based on the slopes of the pool margins, we estimate the average depth at 0.5 to 1.0 meters. These dimensions suggest that the pool contains 1500 to 4000 liters of fluid. We measured 100 dpm/l (i.e. 10,000 dpm/100 L) of ^{222}Rn in Llao's Bath. Thus, the total inventory of radon in the bath is 1.5×10^5 to 6×10^5 dpm, which is the number of atoms lost from the pool each minute due to decay. Substituting these estimates and R_i for R_o and rearranging, the above equation becomes:

$$R_i = (1.5 \times 10^5 \text{ to } 6 \times 10^5 \text{ dpm}) / (C_i - C_o)$$

We assume that the ^{222}Rn activity of the inlet fluid is the same as that measured at Annie Springs (1400 dpm/l), and that of the outlet is the measured activity in the pool (100 dpm/l). Thus, the equation solution indicates an inflow rate of 15 to 60 ml per minute. Although a similar calculation for the Palisades Point pool could be made, the highly irregular shape of that pool precludes a sufficiently accurate estimate of the volume to make such a calculation worthwhile. Nonetheless, we can say that if continuous input of fluid results in the lower ^{222}Rn measured in the Palisades Point pool, the ratio of pool volume to fluid input must be higher in this pool compared to Llao's Bath.

A major implication of the estimated inflow/outflow rate for Llao's Bath is that it is sufficiently slow that the flow probably could not be visually observed. The rate is also approximately 10^5 times smaller than previous estimates of the fluid inputs from geothermal sources to the lake (Sorey, 1985; Nathenson, 1990a). Thus, the estimated continuous inflow to Llao's Bath could not be a significant contribution to the salt balance that is required in these models. It is probable, however, that Llao's Bath is only a small fraction of the total reservoir of saline fluids which make up the Llao's Bath/Brain Mat complex. Samples of fluids from pools within the Brain Mat have salt contents very similar to Llao's Bath; it is possible that the general area is underlain by a saline reservoir of fluids with high salt content and that Llao's Bath is one of the larger extrusions of that reservoir. If this is the case, the ^{222}Rn inventory and the flow rate required to maintain that inventory would be correspondingly larger.

There is no firm basis for choosing between the episodic and continuous input models. Because we have no physical models that explain episodic inflow, continuous flow seems inherently more satisfactory. Nonetheless, we did observe flow channels entering the Palisades Point pools. Since no flow could be observed in these channels during our submersible dives, these features suggest that the flow is episodic or has very recently ceased. Perhaps only through time-series measurements of temperature and salt content at the pools can we resolve the process which brings the salty fluid into the pools.

Determination of $^{222}Rn/^{3}He$ values provides some estimate of the relative ages of different water samples. These values range from 1.5 to 9.8×10^9 dpm/cm^3 in samples taken from pools and mats to values from 0.1 to 0.25×10^9 dpm/cm^3 in South Basin bottom water. This range may be due to heterogeneity of source, to mixing between venting fluids and "older" lake waters, or to aging effects of pool waters. The low bottom water ratios are easily explained by advection and the mixing of venting fluids. All three factors, however, could influence the ratios measured in

pools and mats. It may be significant that the highest ratio was observed in a bacterial mat sample. It is possible that the mats have a more vigorous input of crustal fluid sources, whereas slower pool fluid inputs result in a significantly longer residence time to produce measurable decay of ^{222}Rn. A mean age of approximately 10 days longer for the pools would account for the difference in the $^{222}Rn/^{3}He$ values measured in mats and pools.

Radium-226 Measurements.

Radium-226 values of submersible samples vary by more than a factor of 500 (1.5 to 877 dpm/100 L). The lowest values are similar to the background lake values of ^{226}Ra (approximately 1.1 dpm/100 L). The high radium values may be significant with regard to the question of whether the mat and pool samples have a geothermal origin. Unlike ^{222}Rn, it is generally thought that ^{226}Ra concentrations in geothermal fluids reflect high-temperature alteration of rocks by the fluids and not α-decay (Krishnaswami and Turekian 1982; Dymond et al. 1983). In this regard, radium is similar to its chemical analogue, barium; it is well known that Ba is readily leached from rocks by hydrothermal solutions (Mottl and Holland, 1978). Thus, the very high ^{226}Ra values indicate fluids modified by high temperature water-rock interactions.

Nonetheless, the few barium measurements on submersible samples suggest that the extent of radium enrichment indicated by our data is excessive. Figure 40 suggests that samples collected at bacterial mats have high ^{226}Ra and relatively low Ba contents. In contrast, samples collected from the pools have high barium contents and relatively low ^{226}Ra contents. Because these elements are expected to have similar geochemical behavior, we believe the high ^{226}Ra in the pools is a sampling artifact. Submersible samples of mat fluids often contain large quantities of bacterial material. While the fluid samples are filtered for the barium analyses, filtration of the larger samples required for radium analyses is not feasible. Consequently, it is possible that bacterial mat solids within the samples chosen for ^{226}Ra provide a significant contribution to what we have assumed to be the dissolved ^{226}Ra content. Because the pool samples are relatively free of particulate debris, their contribution to the ^{226}Ra contents is small. Consequently, we suspect that the pool enrichments of ^{226}Ra, which are a factor of 50 to 100 over background lake values are more representative of the enrichments from vent sources on the bottom.

III.8. Lakefloor Temperature Data

Submersible Temperature Probe.

As discussed in the Methods Section, we used a temperature probe attached to the starboard manipulator to determine the internal temperatures of sediments, mats, and pools. Variations in temperature with depth inside these features were determined using three thermistors contained within the probe; these thermistors were 20 cm apart. Because of uncertainties in the depth of the probe penetration, these measurements are not particularly useful for estimating the rates of advection of fluids. In some cases the probe encountered hard layers or rocks and could not be inserted the full 60 centimeters. Sometimes, particularly for the bacterial mats, the surfaces were so soft that over-penetration of up to 10 centimeters occurred. Whenever possible, the voice logs and the video record of the operation were used to correct the depth of insertion.

While the absolute depth of the temperature measurement has an uncertainty, the distance between temperature measurements is fixed (20 centimeters). However, even the thermal gradients

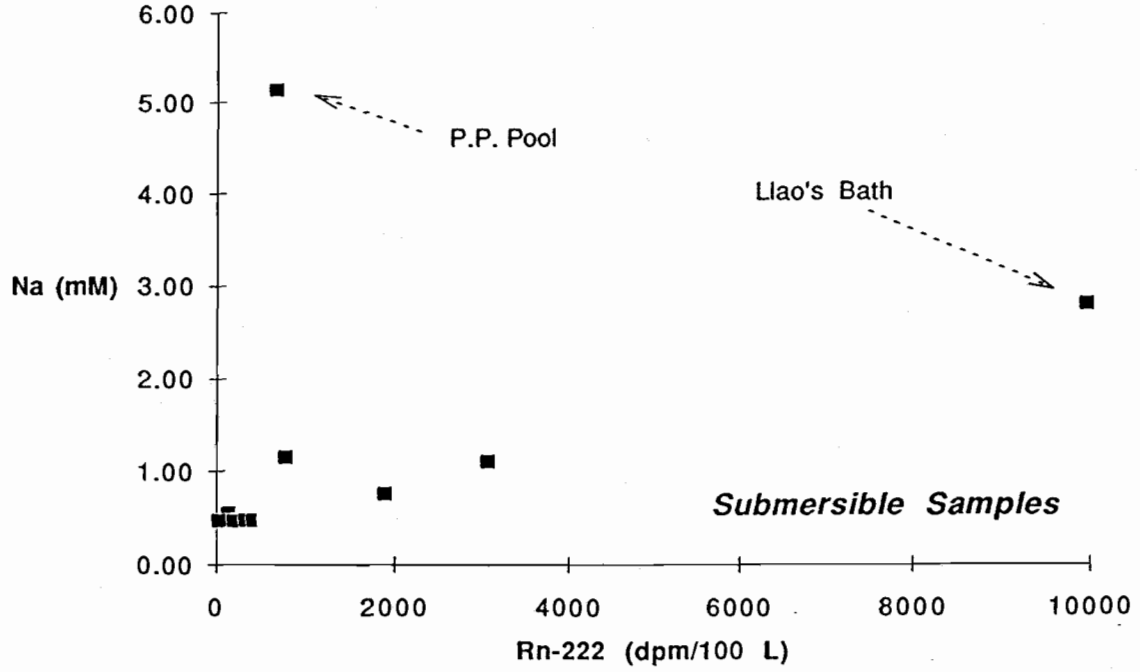

Figure 39. Sodium concentrations vs. ^{222}Rn for submersible samples. Note the much lower ^{222}Rn contents for the Palisades Point Pool (NE Pool).

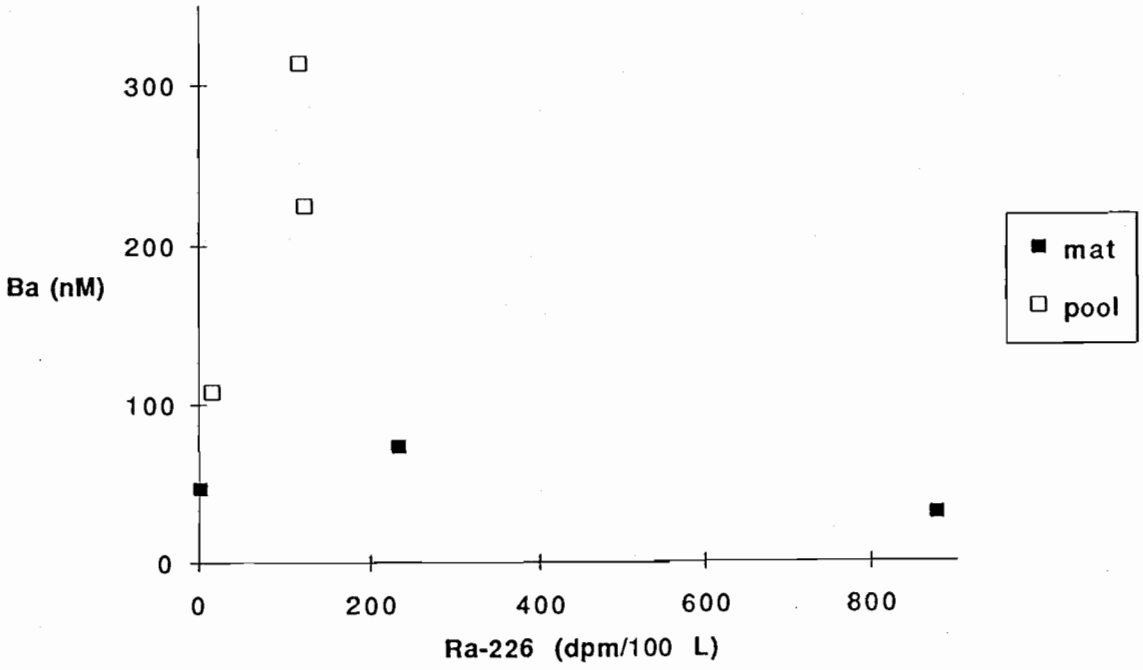

Figure 40. Barium concentrations vs. ^{226}Ra for mat and pool samples. Note the very different relationships for mats and pools.

estimated from intra-thermistor comparisons can be disturbed by non-vertical probe insertions. If the probe does not enter the mat or sediment vertically, an influx of cold bottom water along the probe can occur. Although this problem was minimized by inserting the probe through vertical motion of the manipulator from the shoulder, nevertheless, the arc of the shoulder movement introduced a non-vertical component to the insertion. The effects of this non-vertical component and of any resulting cold-water influx would be to lower the measured temperatures and to increase the inferred gradients between thermistors. However, the thermal gradient between the shallowest thermistor and the bottom water would be decreased by leakage of bottom water along the thermistor probe.

Uncertainties in the depth of penetration and the possibility of lake water seepage along the probe limit the precision of advection rates computed from the measured gradients. Since seepage will cause the computed advection rates to be minimum values, we include the rates estimated by Goeff Wheat (University of Hawaii) as semi-qualitative constraints on the advective flow in various parts of the lake (Table 4). Wheat's modeling assumes that only advection and diffusion processes influence the temperature profile. He assumes a constant thermal conductivity (2×10^{-3} cm^2/sec; Williams and Von Herzen, 1983). In addition, he assumes a uniform bottom temperature of 3.74°C; however, the bottom water temperature was not measured at every site and varies by about 0.2°C over the study area.

The highest temperatures were measured in the bacterial mats (Figure 41) where a maximum temperature of 18.9°C was obtained. This temperature and several single point measurements greater than 15°C were measured in the vicinity of a west-facing cliff near the center of the Detailed Study Area. In this area the mats were generally less than 20 cm thick and underlain by rocks or impenetrable crusts, thus making deeper insertions impossible. The measured maximum temperature varied by more than a factor of two over distances of less than 50 meters in this general area. Two of the mats (Central and North Wall) had nearly isothermal conditions and relatively high temperatures (>7°C). The "brain" mat (near Llao's Bath) was the coolest mat investigated (6°C). Table 4 shows that advection rates in the mats are typically in the range of ten's of meters per year, but one of the mats from the high temperature mat area had a rate of approximately 100 meters per year.

Sediments from two sites had temperatures greater than 10°C at depths of 50-60 centimeters (Figure 42). One of these relatively warm sediments was within 50 meters of the warmest bacterial mat and within 100 meters of the Benthic Barrel and the "Sea-Cat thermal probe" (TTT). The other warm sediment site, however, was located near the Palisades Point pool/bacterial mat complex. The coolest sediments were located in a low-relief, sedimented area in the central portion of the Detailed Study Area and west of the the most prominent mats and pools. Table 4 shows that the advection rates range from values near zero to more than 50 meters per year in the Palisades Point area. The data collected near the Benthic Barrel and the TTT site suggest that there is no advection. However, because the TTT measurements (see next section) indicate advection rates of 25 to 45 meters per year, we suspect that the upper thermistors on the submarine probe were affected by seepage of lake water. This interpretation is compatible with the relatively high temperature (10.2°C) measured by the deepest thermistor at this site

We measured the temperatures of Llao's Bath and one of the Palisades Point pools (Figure 43). The data show that the temperatures of these saline water sources are relatively low. Although the salt content of these waters is approximately 10 times greater than background lake values, their temperatures are only one to two degrees warmer.

Table 4. Submersible temperature data and advection/diffusion model estimates of fluid advection rates.

Sample Type/ Dive	Depth (cm)	Temperature °C	Advection Rate m/y	Comments
Sediment				
CD 222	30	5.55		
	50	6.35	~10	
	70	6.92		
CD 223	15	3.80		
	35	4.05	0	
	55	4.24		
CD 226	20	5.3		
	40	7.9	0	probable seepage at 20 and 40 cm
	60	10.2		
CD 228	2	4.6		
	22	10.2	50 to 70	
	42	10.8		
Mats				
CD 207	30	7.56		
	50	7.76	25 to 45	
	70	8.1		
CD 215	10	9.0	> 100	
	30	9.6		
CD 226	10	7.5		
	30	11.08	20 to 25	
	50	12.9		
CD 228	15	5.6		
	35	7.15	~15	
	55	8.11		
CD 230	20	4.84		
	40	5.75	10 to 25	possible seepage
	60	6.0		

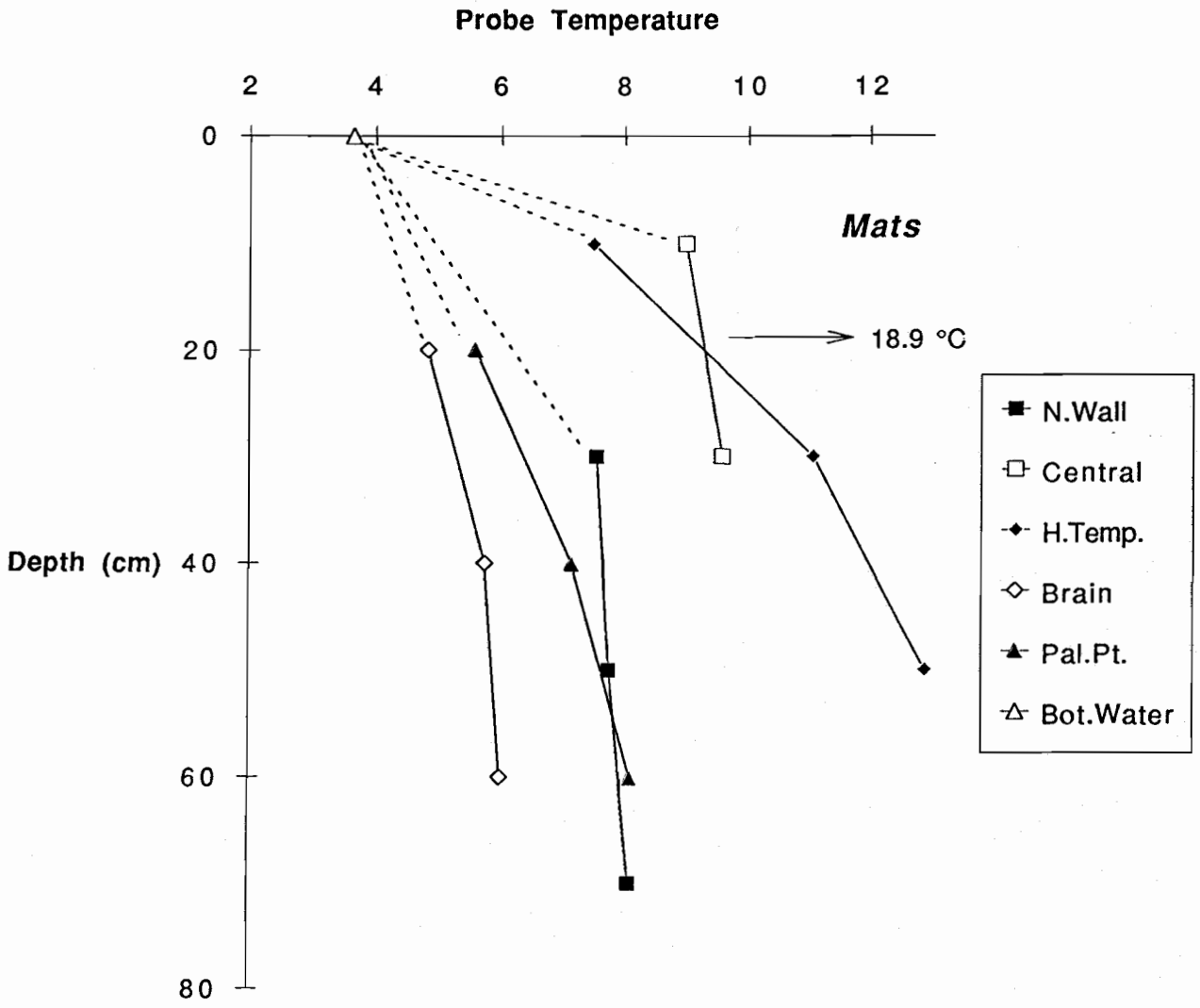

Figure 41. Submersible temperature probe measurements made in bacterial mats at different lake locations. Sites with only one or two temperature-depth measurements had thin mats underlain by rocks that prevented greater penetration of the temperature probe.

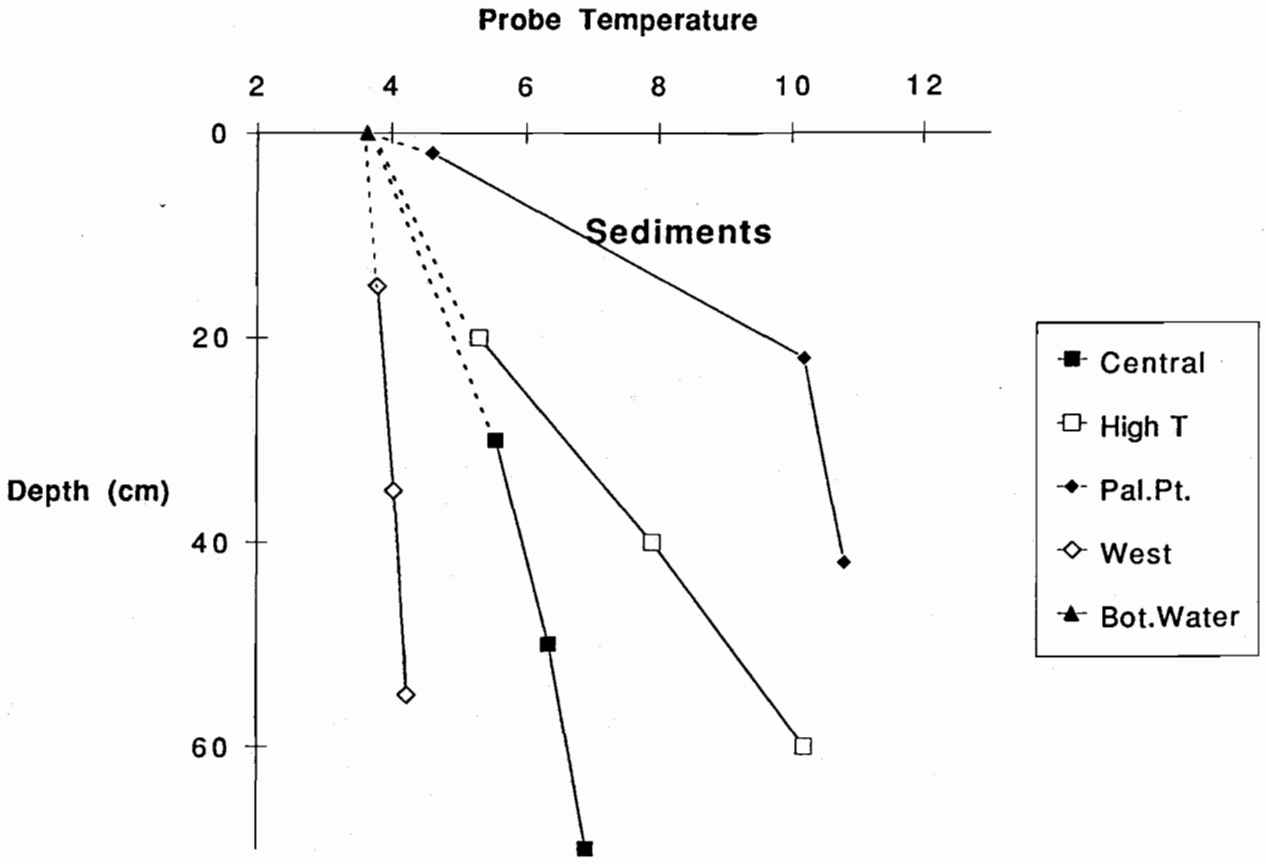

Figure 42. Submersible temperature probe measurements made in sediments at different lake sites.

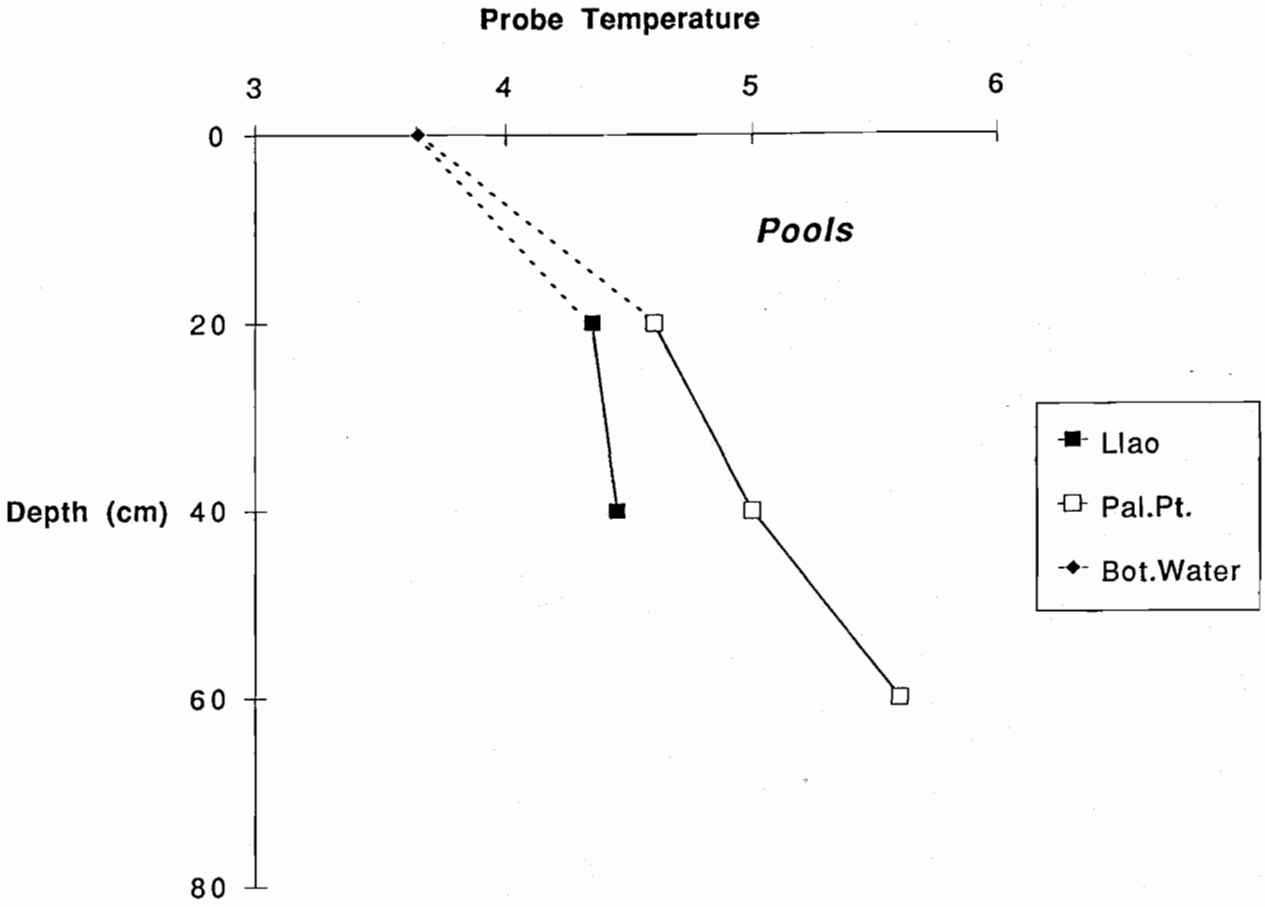

Figure 43. Pool temperatures determined with the submersible temperature probe.

Taken altogether, the temperature probe measurements show considerable variation in mat and pool temperatures over a range of spatial scales. The observation that warm sediments (>10°C) are found on essentially opposite sides of the lake demonstrates that the thermal anomalies have a lake-wide scale. On the other hand, measurements 50 to 100 meters apart have maximum temperatures which can differ by a factor of two. These observations suggest that venting of the anomalous fluids is highly localized. The pools, which have highly anomalous salt contents and relatively small thermal anomalies, may reflect the importance of conductive heat loss during and after the venting of these saline fluids.

Sediment Temperature Profiles.

Time series measurements of sediment temperatures were made at two sedimented sites near the high temperature bacterial mats (see Figure 3 for locations). As discussed in the Methods section, the instrument we used, a SeaCat TTT, has an internal data recorder and three vertically-arrayed, high precision thermistors which can be inserted into the sediments. The instrument is designed so that the uppermost thermistor records bottom water temperatures a few centimeters above the sediment-water interface.

The SeaCat TTT sediment temperature probe was deployed for a seven day period from 24 August 1989 until 31 August 1989. The submersible deployed the instrument in its frame on the lake bottom. The variations of temperature with depth were collected by three thermistors contained within the probe - the deep thermistor was 35 cm below the sediment surface, the middle thermistor was 5 cm below the sediment surface, and the top thermistor monitored the bottom water temperature 5 cm above the bottom. The SeaCat profiler automatically logged these bottom water-sediment temperature profiles two times a second. It has an accuracy of $\pm$0.01°C and a resolution of 0.001°C.

An example of the intercalibrated accuracy of the thermistor data can be seen in Figure 44. All three thermistors (Deep, Middle, and Top) registered identical temperatures during the submersible's descent to the lake bottom. Only after initial penetration of the sediment by the probe did the temperature readings of the three thermistors diverge in response to the thermal gradients within the sediment.

The sediment temperature probe was initially deployed next to the Benthic Barrel on 24 August 1989 during Dive CD222. The barrel was deployed earlier at that site (Dive CD217 - 17 August 1989) and was still collecting time-series samples of *in situ* vent water that had advected from the sediment. Also, a box core (BC6) had already been recovered only 20 meters away and an interstitial sediment pore water sampler (Peeper B) had already been left there on 19 August 1989 during Dive CD218. It was hoped that the thermal gradient data recorded by the sediment temperature probe would compliment the data from the other experiments. Three days later, the sediment temperature probe was moved (27 August 1989 - Dive CD226) to an adjacent, heavily mottled, sedimented area about 30 meters away where higher bottom water and sediment temperatures had been recorded.

The results of the TTT Sediment Temperature Probe deployment are shown in Figure 45. In Area #1 immediately next to the Benthic Barrel, the Deep thermistor registered 5.61°C at 35 cm depth, while 30 cm shallower, at 5 cm depth, the Middle thermistor recorded 4.36°C. Bottom water temperatures at that time were fluctuating between 3.7°C and 4.1°C. It is remarkable how stable the sediment temperatures were over this time period of more than three days.

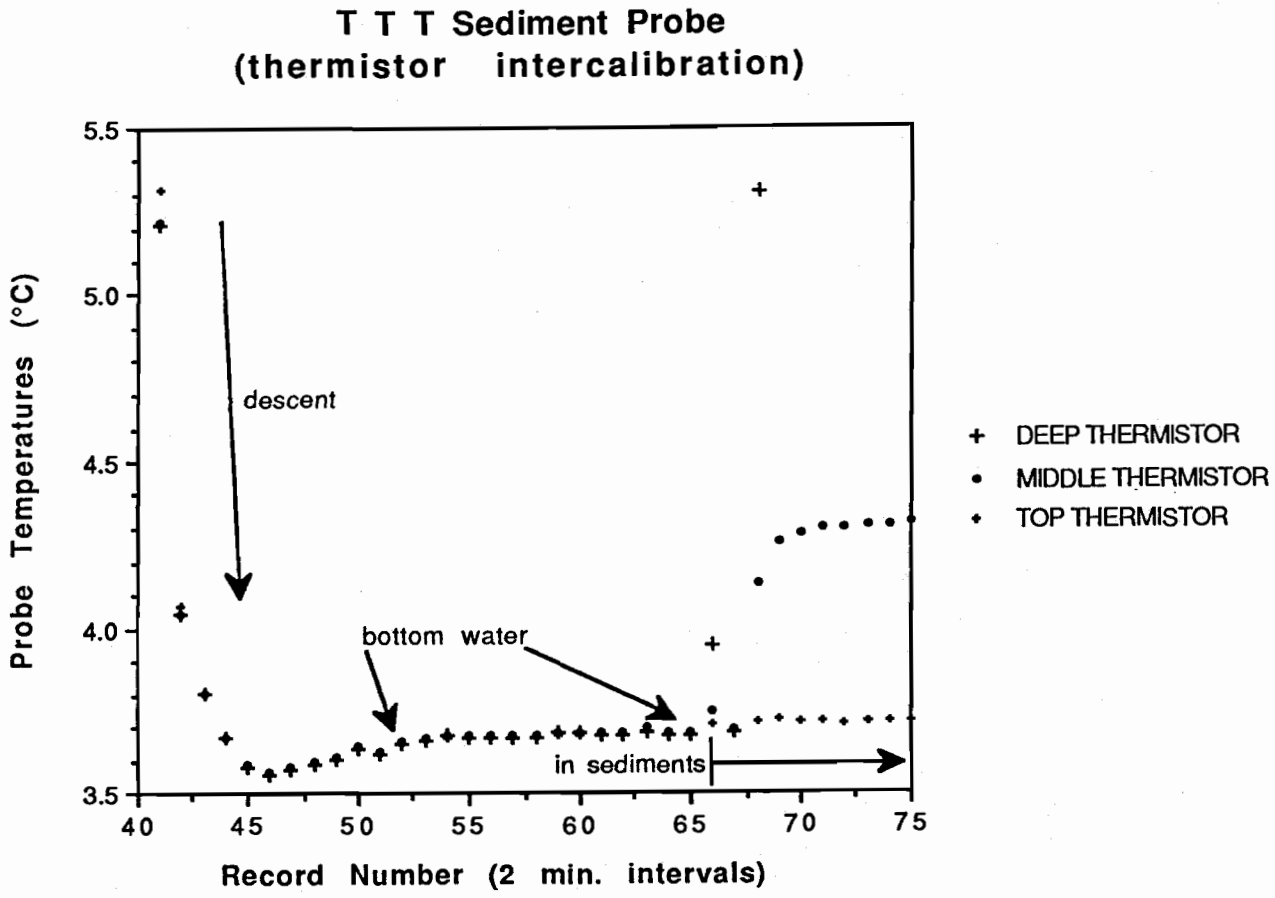

Figure 44. Illustration of the intercalibration accuracy of the Deep, Middle, and Top Thermistors in the SeaCat TTT Sediment Temperature Probe. All three thermistors showed exactly the same water temperatures until the probe was inserted into the sediment.

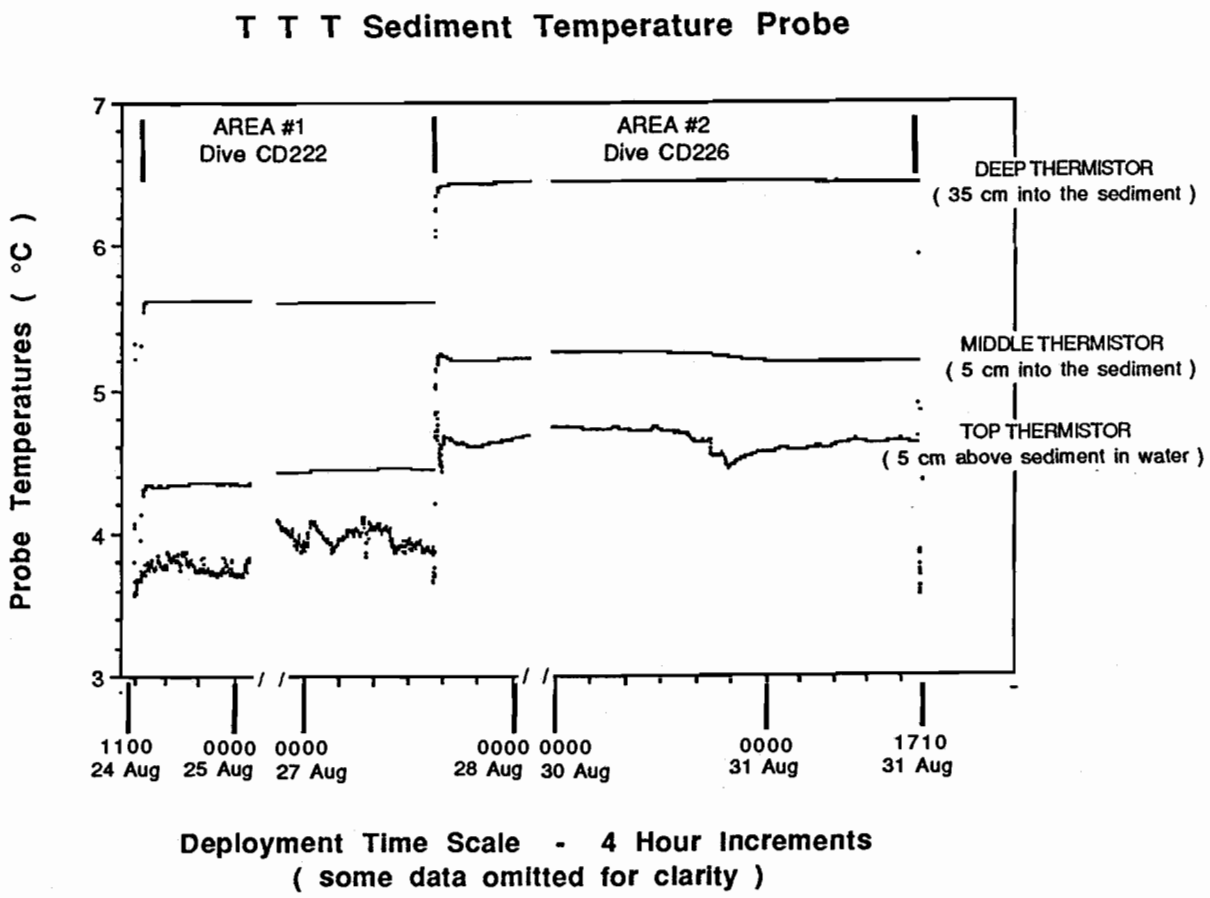

Figure 45. Seven day time-series record of TTT Sediment Temperature Probe. Sedimentary thermal gradients were recorded at both Area #1 and Area #2. Note the omission of data for 25-26 August and 28-29 August 1989 in order to improve the clarity of the record.

The thermal gradient in Area #2 shows higher temperatures than Area #1 at equivalent depths, and this supports the contention that a crusted sedimentary surface is indicative of an area of warmer, more rapidly-advecting interstitial pore water. The Deep thermistor, 35 cm below the crusty, mottled sediment in Area #2, registered 6.45°C; the Middle thermistor recorded 5.25 C. Both values are approximately 0.80°C higher than those of the equivalent Area #1 sediments. The Top thermistor in Area #2 shows an anomalously high and stable temperature value unlike what one would expect from a bottom water temperature record. One can only assume that the temperature probe settled at least 5 cm deeper into the soft sediments at Area #2, effectively covering the Top thermistor and shielding it from direct bottom water temperatures.

Advection-diffusion modeling of these data can be accomplished by assuming a constant coefficient of thermal diffusion, 2×10^{-3} cm^2/sec, (Williams and Von Herzen, 1983). The calculated advection rates are 3.5 meters per year at the first deployment and 4.0 meters per year for the second site (Goeffrey Wheat, personal communication). These estimates for vertical advection in the sediments lie between those determined from by pore fluid composition (Appendix F) and the measurements by the submersible temperature probe.

We believe that the range in estimated advection rates reflects horizontal heterogeneity, which will be reflected in any sample or measurement taken in close proximity to a thermal or advecting feature, such as a bacterial mat. Thus, gravity coring from the surface vessel has very limited precision in terms of knowing the relationship to specific features (realistically not better than ±50 meters). Therefore, calculations based upon measurements of these cores resulted in the lowest advection rates. The TTT was placed in a general area of elevated sediment temperatures and mottled sediments, but the deployment of this device could not be guided by detailed sediment temperature information. Box cores, which could be placed with a precision of ±2 meters from mat features associated with sediments, recorded advection rates of a few meters per year, similar to those of the TTT. Temperature measurements, made by inserting the temperature probe into known thermal-chemical features, provided estimates of advection rates in the range of 10 to 100 meters per year.

III.9. Bacterial mats

1988 Observations.

During the 1988 field season Deep Rover dives discovered bacterial colonies which covered portions of the bottom in six locations (Table 5). The mats observed during that year are gelatinous, low-density features (Plate 5), 15 to 300 cm in diameter and 2 to 15 cm thick. Some of the largest mats were draped over steep rock outcrops (Plate 5 and 7); however, smaller mats lay directly upon sediments (Plate 6). Rusty-brown colors within the mats suggest that iron oxidation may be important in mat formation. The sediments near the mats are dark and contrast strongly with the normal buff sediments that cover most of the bottom. At some sites, many individual mats were observed.

The mats discovered in 1988 were all within 500 m of each other and were either on or near the scarp that extends across the Detailed Study Area with a NE-SW orientation. Several of the mats were found in the relatively flat, sedimented sites at the base of the scarp. Some of the largest mats, however, were found draped over the cliff face, 15 meters above the base of the slope. A schematic drawing of the mats first observed during dive CD179 in 1988 is shown in Figure 46. The mat on the right was the largest mat observed and extends from a dome-like mass down the cliff as a continuous feature for more than 10 meters.

Table 5. Bacterial Mat Temperatures and Descriptions, 1988

Dive	Measured Temperature °C	Description
179	5.70	Three large mats draped on a cliff face; two mats are 2-3 m across; one mat is 2 m wide and 10-15 m long; small mats are attached to sediment at base of slope (see Figure 46).
182	9.52	One mat 3 m in diameter on a sloping, sedimented surface; mat thickness is 2-4 cm ; sediment is discolored.
183a	5.70	Three mats, 20-40 cm in diameter, on discolored sediment associated with outcrops
183b	4.30	Four mats, 10-30 cm in diameter, on thin sediments with outcrops.
183c	n.d.	One mat 15 cm by 30 cm, on discolored sediments.
187	n.d.	One mat, 30 cm in diameter, on discolored sediments.

Microscopic Evaluations.

Scanning electron microscopy has shown that these bacterial colonies are composed of the genera *Gallionella* and *Leptothrix* (Dymond et al., 1989; Plates 17 and 18). The sheath-forming *Gallionella* is generally considered to be a chemolithoautotroph (Erlich, 1981) as it requires a source of reduced iron (Hanert, 1981) and will grow in the absence of significant organic carbon (Wolfe, 1964). It is not necessarily thermophilic since it has been found in low temperature springs, wells, and drainages (Hanert, 1981), but this genus has been observed in thermal springs with temperatures up to 47°C (Hanert, 1973). Because of the accumulations of ferric hydroxide and manganese dioxide on the sheaths of *Leptothrix*, these bacteria are thought to oxidize ferrous and manganous ions (Mulder and Deinema, 1981). An autotrophic metabolism for *Leptothrix* has not been demonstrated, but like *Gallionella*, it seems to thrive in environments which provide a gradient between reduced and oxidized forms of iron and manganese. *Leptothrix* is also not a thermophilic form, but it has been observed in the recently discovered thermal springs on Loihi Seamount, the most eastward extension of Hawaiian-chain volcanism. There, thick mats similar to the Crater Lake communities surround vents with temperatures that range between 15 and 30°C (Karl et al., 1988).

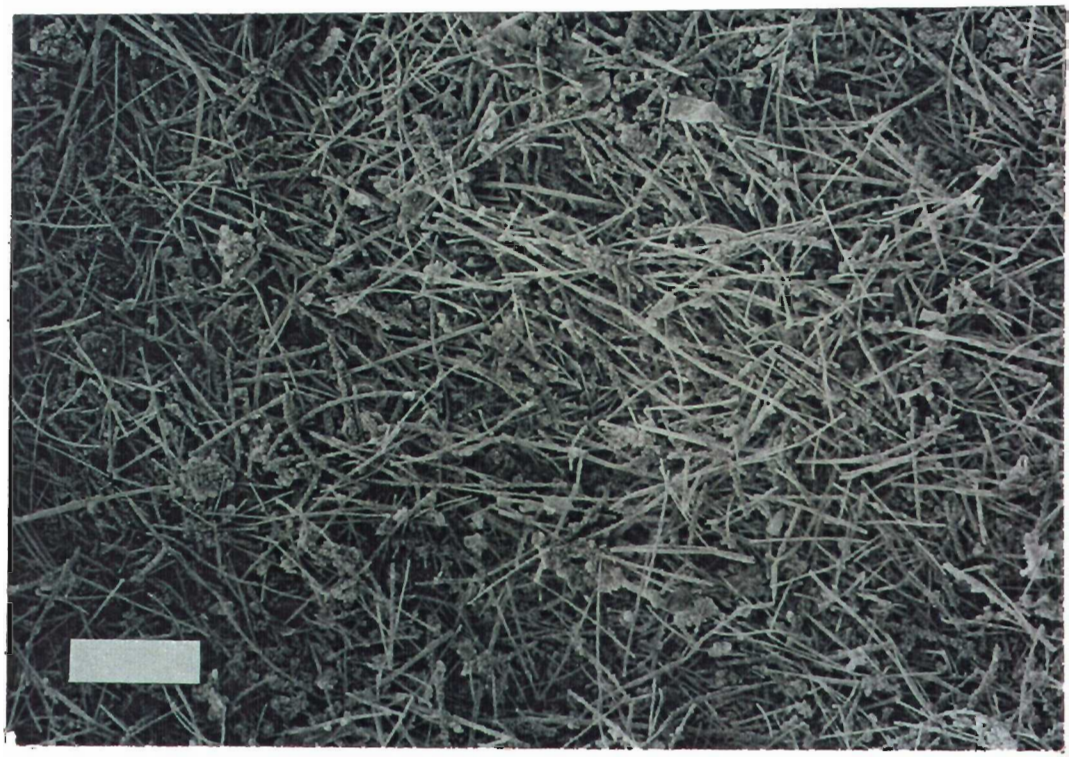

Plate 17. A low-power scanning electron micrograph of the bacterial mat from CD 179. These are iron-oxidizing, sheath-forming bacteria of the genera, *Gallionella* and *Leptothrix*. The scale-bar is 100 μm in length.

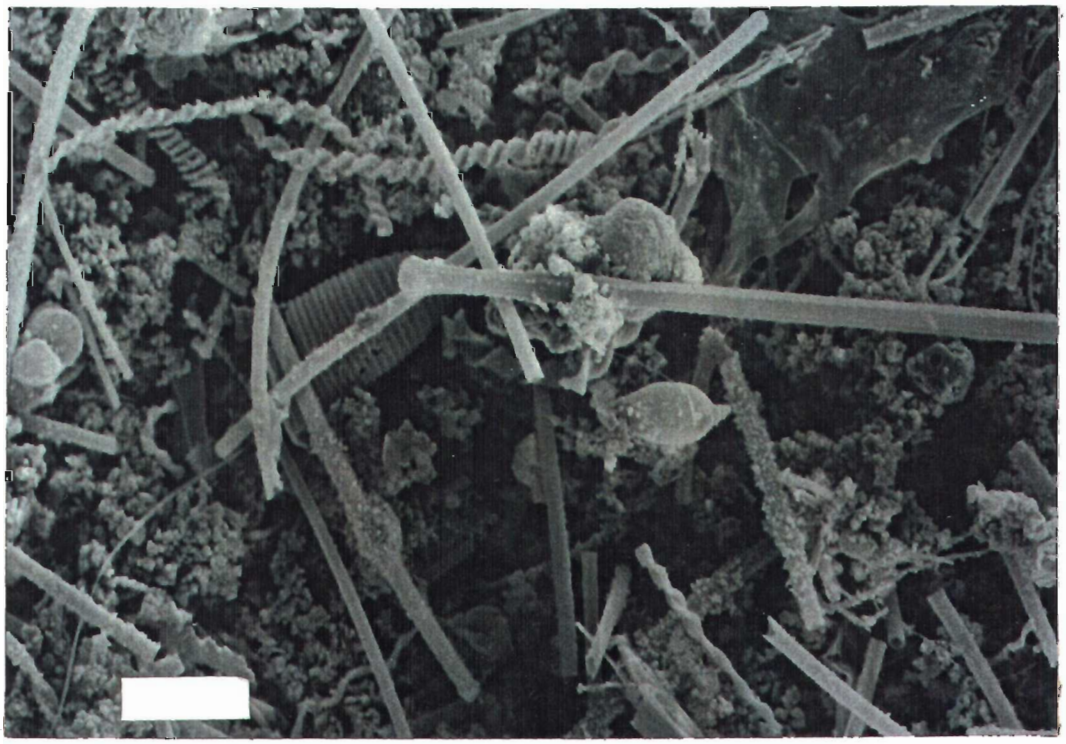

Plate 18. A higher power scanning electron micrograph of the bacterial mat from CD 179. The scale-bar is 10 μm in length. The genus, *Gallionella*, are the forms with twisted sheaths; *Leptothrix* are the straight sheaths. The ribbed, dome-like form in the center is thought to be a protozoa. This form is seen on many of the SEM photos. The tube-like form in the center-right with a blunt end is part of a diatom.

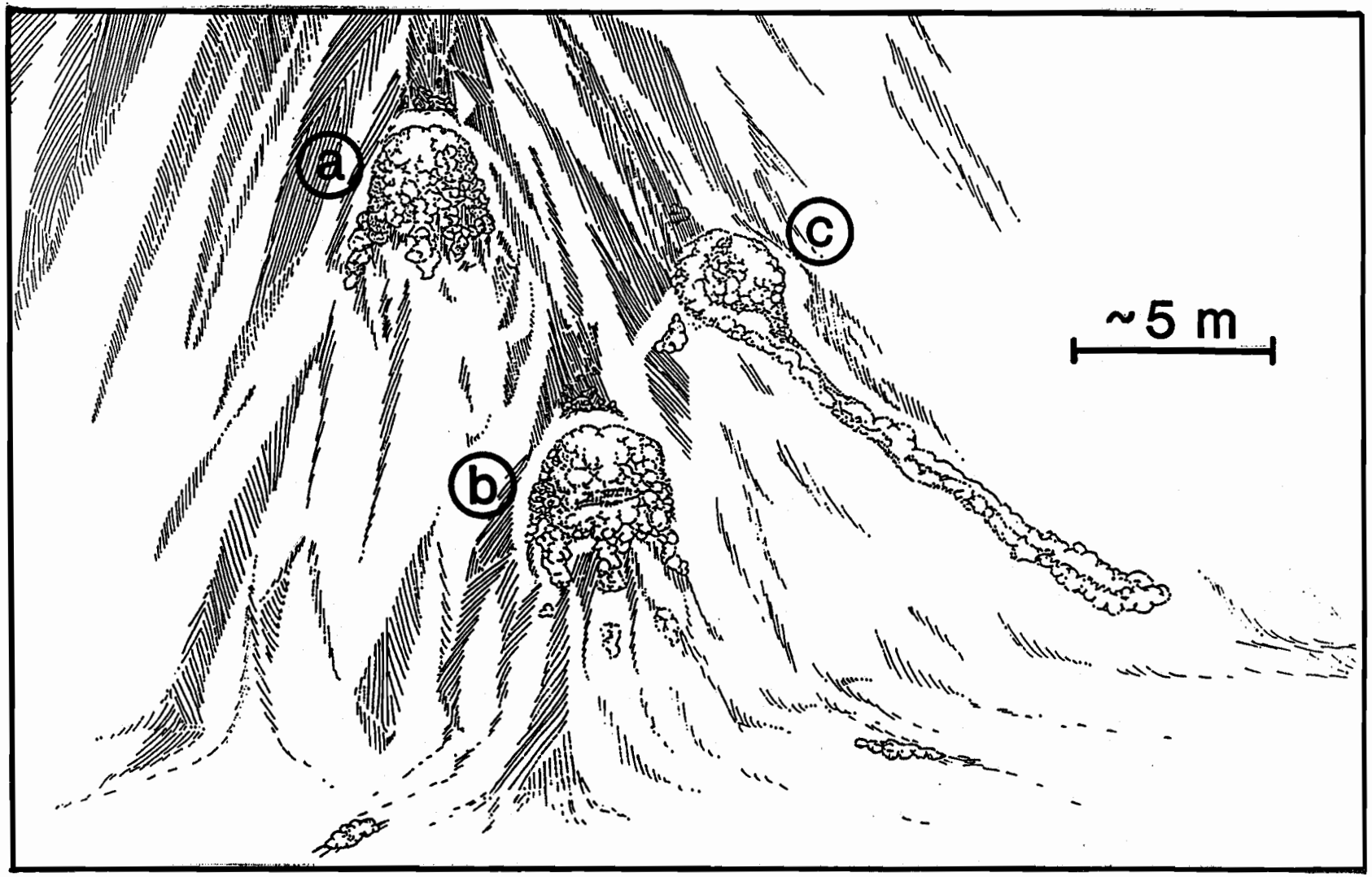

Figure 46. A schematic drawing of bacterial mats first observed during CD 179 in 1988. These features are now known as the North Wall mats. The letters "a", "b", and "c" identify the three principal mats at this site. These mats appear to be attached to rocky cliff faces. Mat "c" extends down the cliff face an additional 10 m below the primary structure. This extension appears to be actively growing and not simply a consequence of pieces that roll down the slope. Small mats are growing on sediments at the base of the slope. The sediments along the base of the slope are darker and mottled compared to typical lake sediments. Drawing by Kathryn Brooksforce.

Environmental Settings of the Bacterial Features.

The 1989 dive program greatly expanded the number of bacterial mats observed on the bottom of Crater Lake (Figure 47). More than 30 mat locations were defined during the program, and many of these contained multiple mat structures. Within the Detailed Study Area there are three primary sites with multiple bacterial features:

(1) the mat area discussed above that was discovered in 1988 on CD 179; we will refer to this feature as the North Wall mats because they are located on the northernmost cliff face, on what appears to be part of the Chaski Slide.
(2) A 300-meter band of mats with a general N-S trend within the central part of the Detailed Study Area; because these mats were often associated with the warmest temperatures, we refer to them as the high temperature mats.
(3) Spectacular colonies adjacent to Llao's bath and other saline pools, 400 meters west of the high temperature mats; because of the thick undulating nature of these mats, we refer to them as the brain mats.

A high priority for the 1989 submersible program was to revisit the large bacterial mat colony that was observed and sampled on CD 179 during the 1988 field season (the North Wall mats). This was re-visited during the first 1989 hydrothermal dive (CD 207) and during several other dives that summer. Although one of the bacterial mats had been significantly dispersed during the submersible sampling in 1988, it appeared to have regained its original form by the 1989 visit. This is proof that the bacterial mats are dynamic biological communities which can quickly reestablish themselves. It is probable that the size and morphology of this particular community are in balance with the flow of warmer and chemically enriched fluids that must be occurring at this site.

Although the maximum temperature recorded in 1988 for the North Wall mat was 5.70°C, temperatures as high as 10.0°C were measured in 1989. The higher temperature may be is a consequence of chance probing into the mat structure in a spot where there is less mixing with cold bottom waters rather than a generalized temperature increase in the venting fluids. Temperature measurements in other portions of the mat revealed values similar to those made in 1988 (Figure 41). Water samples taken at this site in 1989 had major element enrichments similar to those observed in 1988 (approximately twice the background lake values).

The high temperature mats are located along the west facing slope that marks the western boundary of the shallow topography extension formed by Chaski Slide. The mats are found primarily between 440 and 420 meters depth. The slope is not constant, but instead consists of a number of steps with heights ranging from 5 to 10 meters and separated by more level, sedimented sections. The steps may reflect the original topography of Chaski Slide or may be the result of more recent faulting. The mats primarily occur on the step portions of the slope where sediments are thin or absent. In some more rare cases, however, the mats were observed on flat-lying sediments (e.g., see Plate 6). The level, sedimented portions of the slope are the sites of discolored, mottled sediments, which have dark brown to dark grey colors instead of the more typical buff to tan colors of lake bottom sediments.. Temperature probing into these sediments revealed maximum temperatures of over 10°C (Figure 42), and the temperatures commonly fell in the range of 6°C to 8°C. These mottled sediments were also the location for the deployment of the Benthic Barrel experiment and the time series temperature probe (See preceeding section). Maximum temperatures measured in the bacterial mats were 18.9°C , with a number of values greater than 15°C recorded (Figure 41).

The mats observed at the high temperature site typically did not have dimensions as large as those observed at the North Wall site. Most commonly the high temperature mats were a meter across and 10 to 20 centimeters thick. The patchy nature suggests that fluid venting on the cliff faces is heterogeneous. The patches occurred in a variety of forms (e.g., see Plate 7). As will be

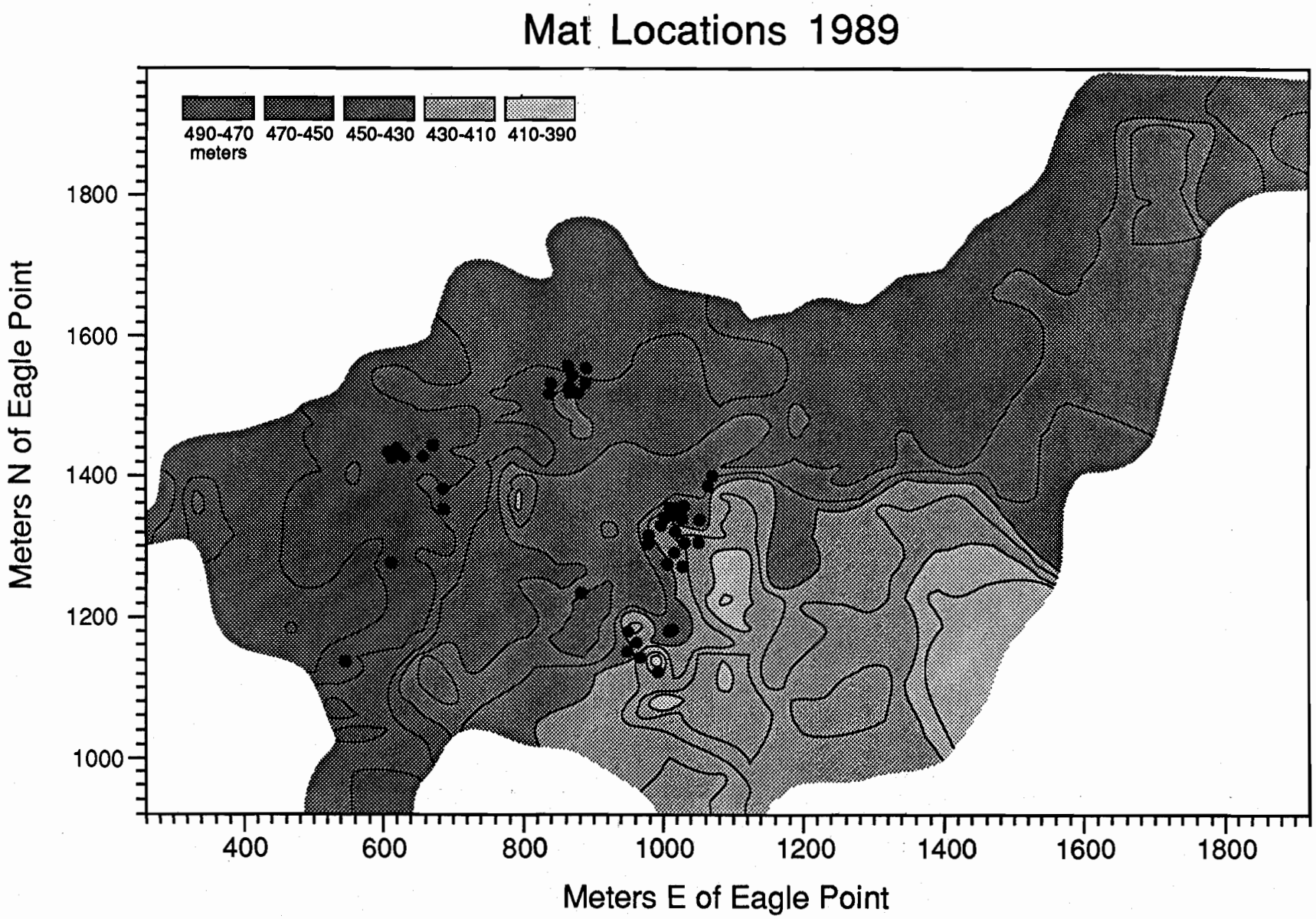

Figure 47. Bacterial mat locations in the detailed study area which we observed in 1989.

discussed in the Solid Phase Geochemistry Section, the mats in this area have exceptionally high arsenic contents (as much as 9600 ppm) and fractionated rare earth element (REE) contents which suggest the influence of hydrothermal fluids on their composition.

Bacterial communities in the saline pools area ranged from spectacular mats with associated small pools to no more than thin coatings on the sediments and rocks adjacent to the pools. The brain mat bacterial community is several tens of meters across in both both length and width and possibly 50 centimeters thick (Plates 11 and 12). It is intimately associated with saline pools, as these fluids fill indentations within the mats. A schematic drawing of the pool/mat complex is shown in Figure 48. In one small pool within the brain mat, the bacteria appeared to be growing across the pool's surface, like algal scum floating on a pond. In most pools, however, the surfaces were clean. One of the larger pools, Llao's bath, had very little associated bacteria, only a thin layer on sediments at the edge of the pool. One end of Llao's Bath had a broader, thicker bacterial growth, as though it was fed by continuous or intermittent overflows from the pool. Since this is a low-relief, sedimented area, the mats frequently grew on sedimented surfaces in contrast to the north wall or high temperature mat areas.

The maximum temperatures measured within the brain mat were 6.0°C. These are among the lowest temperatures measured within bacterial mats from anywhere in the lake (Figure 41). These are approximately 1.5 °C warmer than the temperature measured at the nearby Llao's Bath.

The three primary bacterial mat areas discussed above all had numerous bacterial features and mats. In the region 100 to 300 meters south of the Llao's Pool/brain mat complex, four scattered bacterial sites were also observed but not sampled (Figure 47). One of these sites was associated with small, shallow pools . A second site had numerous colonies growing on a rocky cliff face.

In addition to the many bacterial occurrences discovered within the Detailed Study Area, the 1989 field program found a major bacterial community on the far side of the lake near Palisades Point, approximately six kilometers from the locations noted above. These bacterial features were first discovered on a biological dive (CD227) designed to define the algal depth limitations. Consequently, they were only photographed, and no samples or temperatures were measured until dive CD228 returned to the site.

Much of the bacterial growth observed at the Palisades Point location is in the form mat structures which are of 20 to 30 meters long by five meters (Plate 8). They are elongated in the downslope direction. These strips of bacteria were set in a gentle (~ 20°), sedimented slope with numerous outcrops and large boulders (Figure 49). The bacterial structures were located within 50 to 100 meters of the break in slope which separated the basin floor from the caldera wall. On the flat-lying sediments at the break of slope, there were a number of saline pools. Another distinct feature of the area was the presence of small channels or rills which, because they were always located quasi-parallel to the slope, appeared to be erosional in origin. The rills formed dendritic patterns, many originating from beneath boulders and outcrops. Although they had all the features of stream channels, no flow could be observed during the submersible dives. They "flowed" into the elongated mat structures and also into pools. Some channels connected pools and had deltaic structures at points of entry. Minor amounts of bacteria could be observed along the rills and the sedimented edges of the pools.

The temperatures measured within the Palisades Point bacterial growths were as high as 8.1°C (Figure 41). However, higher temperatures (10.8°C) were measured in sediments between a mat and a rock from which flow channels drained. The highest temperature measured in the nearby pools was 5.6°C.

Figure 48. The Llao's Bath and brain mat complex. Llao's Bath is in the foreground. Note the bacterial community which extends away from the left side of the pool. The brain mat is in the background. The dark areas within the mat mark small pools that are located in the convolutions of the mat structure. Llao's pool is 3-4 meters long. **This view is looking west.** Drawing by Kathryn Brooksforce.

Figure 49. The Palisades Point mat and pool complex. Mats have flow lines emanating from them which extend downslope in the background. Many stream-like features extend into and away from these mats. Some of the channels enter pools on the level, sedimented surface in the foreground. The entire field of view of this drawing is approximately 75 meters across. Drawing by Kathryn Brooksforce.

Chemical Composition of Bacterial Samples.

The bulk chemical composition was determined on mats from the four major bacterial locations by our dives (Table 6). Iron is the most abundant element and, as FeOOH, can account for more than 70% of the mass of the mat material. Significant amounts of silicon and phosphorus are also present. Although the SEM photographs (Plates 17 and 18) show that the mats are predominantly composed of sheath-forming bacteria, organic carbon makes up only about 2% of the material. Probably, that most of the bacteria shown in Plates 17 and 18 are remnant sheaths rather than living bacteria. Analyses of the organic fraction show that the extractable lipids are simple fatty acids (B. Simoneit, personal communication). Sterols and other indicators of phytoplankton, zooplankton, or local terrigenous sources are absent. These data are consistent with fresh organic matter of microbial origin.

Although there are general similarities in the composition of the bacteria from different sites, there are also some significant differences. Aluminium content varies by more than an order of magnitude (Table 6). These variations most likely reflect the differences in contamination by typical Crater Lake sediments which are dominantly composed of detrital aluminosilicate materials. Thus, the Palisades Point sample, which has the highest Al content (3.26 %), probably contains nearly 40% aluminosilicate material. This contamination could either result from accidental inclusion of settling aluminosilicate particulates or from the intermixing of underlying sediments during the sampling process with the submersible. The aluminosilicate contamination primarily enhances the measured Si content and decreases the measured iron content of the samples, although it would also affect the content of minor elements which were primarily associated with either the mat or the aluminosilicates.

There are other variations between samples which cannot be accounted for by aluminosilicate contributions. In the five samples, arsenic and antimony contents vary by approximately a factor of 30. Manganese varies by approximately a factor of 40. Because we have multiple samples from only one location (the brain mat), it is difficult to say whether these variations reflect site-to-site differences in vent fluid composition and bacterial metabolisms or inter-site variability. There may well be intra-site differences in the fluid composition. The very high As and Sb contents of the high temperature mat, for example, may reflect the more rapid venting and higher As and Sb contents of what are the warmest fluids detected. These fluids may have a stronger hydrothermal signal. Variations in the numbers of manganese-oxidizing bacteria at different sites could also account for the differences in observed manganese. The two samples from the brain mat, however, show that even relatively close samples can differ in composition. One sample has significantly higher Mn and Zn, while the other has higher arsenic.

Biological and Biochemical Studies.

For the 1989 field program we enlisted the help of Dr. David Karl of the University of Hawaii to undertake microbiological studies. Dr. Karl is a renowned marine microbiologist who has worked extensively on hydrothermal systems and most recently with the Loihi Seamount bacterial colonies which are also iron oxidizing systems (Karl et al., 1988; Karl et al., in press). Dr. Karl was not able to personally participate in the field program, but he provided our research group with equipment and detailed sampling instructions in order to collect bacteria and other materials. From the various samplings of bacterial mats and fluids we provided: 1) live and preserved bacterial mats collected from a variety of sites for direct microscopy and pure culture isolation; (2) unpreserved, frozen bacterial mats for chemical, isotopic and enzymatic (carboxylase) determinations; and (3) frozen porewaters for measurement of DOC, DON, DOP and specific organic constituents (amino acids and nucleic acids). No formal funding for this work was provided from the Park Service or other agencies. Despite the lack of funding, significant work has been completed. He provided a report on his results so far which is reproduced in unedited form in Appendix E.

Table 6 . Bacterial mat compositions

Dive Number	179	218	230	216	228
Area	North Wall	High Temp.	Brain Mat	Brain Mat	Palisades Pt.
Elements					
C	2.44	—	1.86	3.47	4.21
N	0.97	—	0.22	0.37	0.42
Al	0.21	1.76	1.44	2.31	3.26
Si	7.18	8.58	12.2	14.5	16.19
P	1.37	—	1.09	0.20	1.84
S	0.27	—	0.17	0.13	0.12
Ca	0.78	1.26	1.33	1.23	2.05
Cr	10	29	14	18	22
Fe	38.0	28.7	34.1	28.7	18.3
Mn	137	1470	150	3272	6190
Cu	—	52	26	48	87
Zn	—	33	19	35	59
As	3250	9600	1710	355	6139
Sb	2.7	21	0.6	0.6	1.1
Ba	320	570	380	378	716
La	4.6	8.0	5.4	7.0	12.1
Pb	—	49	50	58	55
Th	nd	1.1	0.85	1.4	2.2
U	1.7	nd	1.3	1.8	1.2

Values are in weight per cent, except for Cr, Mn, Cu, Zn, As, Sb, Ba, La, Pb,Th and U, which are in ppm.

"nd" means below the detection limit. — means not measured; the lack of measurement is a consequence of insufficient sample sizes.

Dr. Karl's bacterial culture experiments document the the presence of the *Leptrothrix* and *Gallionella* genera. Since all samples tested positive for *Gallionella*, an obligate autotroph, at least one of the forms within the bacterial community requires a continuous input of a reduced chemical species, in this case ferrous iron. The lack of growth of the sulfur-oxidizing autotrophs may suggest that sulfur is not an important source of energy. This would be consistent with the low sulfur contents of the bacteria material (Table 6). Sediment pore waters in locations with a strong advective signal have both high and low sulfate zones which are compatible with an upward advection of reduced sulfur species followed by sulfate oxidation. As suggested in Karl's report, the positive evidence of autotrophic growth indicated by the cultural experiments is not necessarily contradictory to the enzymatic measurements. Although the autotrophic enzyme, RuBPCase, was not observed, this could be the result of the low numbers of viable cells in communities such as this and of the need for more sensitive detection limits.

We have estimated how much heat is supplied to the mats by bacterial metabolism (Dymond and Collier, 1989). Assuming that the heat produced by oxidation of all dissolved ferrous ions in mat fluids is retained within the mat, an upper limit to the metabolic heat production can be computed. Using this closed system assumption, the increase in temperature is strictly a function of the concentration of iron in the fluids. An appropriate reaction is:

$$Fe^{2+} + 3/2H_20 + 1/4O_2 = FeOOH\,(s) + 2H^+$$

The enthalpy of this reaction is -9.2 kcal/mole (Garrels and MacKenzie, 1967). Assuming an upper limit of 1.0 millimolar iron (Mariner et al., 1980), the conversion of all the dissolved iron to solid form would add approximately 9 calories of heat to each liter of water. Thus, the reaction would raise the temperature of that water by less than 0.01 degrees, an insignificant amount compared to the measured temperatures of the mats (>10°C) or the estimated temperatures based on chemical geothermometers (>100°C).

Summary.

The bacterial mats are visible indicators of sites where thermally and chemically enriched fluids are venting into the lake. The environmental settings for these venting fluids are variable, and these variations result in site-to-site differences in sizes and morphologies of the bacterial communities. Despite the distinct morphologies, all the vent-related communities appear to have iron-oxidation as a major component of their metabolism. This requires a continuous supply of reduced iron from the venting fluids. The energy from this exothermic reaction cannot account for the measured internal temperatures of the bacterial features. High temperature interactions (>100°C) of water with rocks can supply the iron andthe other ions observed in the fluids. Site-to-site variations in the bulk composition of the bacterial communities probably reflect variations in the advecting fluid composition.

III.10. Solid-Phase Geochemistry

General.

Three components can describe the overall composition of Crater Lake sediments (Dymond and Collier, 1990): (1) aluminosilicate debris eroded from the caldera walls; (2) biogenic debris produced by biological activity in the upper levels of the lake; (3) iron and manganese oxyhydroxide precipitates.

The aluminosilicate debris has high aluminum contents compared to the other two sources, and it also has characteristic elemental ratios (e.g., Fe/Al = 0.4 ± 0.2, and Si/Al = 3.0 ± 2.0. The biogenic debris has high contents of Si (in the form of opal) and of organic matter; in general, this source has relatively low concentrations of most major and minor elements. The iron and manganese oxyhydroxide precipitates occur only in certain areas, which indicates that the precipitates do not form by the redox-driven diffusion of iron within the sediment column (Dymond and Collier, 1990). Because carbon burial drives oxidation-reduction reactions, localized mobilization and precipitation would require heterogeneities in surface primary productivity and/or sedimentation rates on an unreasonably small scale. A variety of elemental characteristics define the three end-members (e.g., see Figure 50).

Crusts and Mats.

The composition of the oxyhydroxide precipitate component is similar to lakefloor deposits observed and sampled with Deep-Rover (Dymond and Collier, 1990). For example, lithified crusts (Plates 3 and 19) and pebbles, rich in iron and depleted in Al, covered portions of the bottom in a number of locations . In some areas, sediment slumping and small faults revealed sub-surface, iron-rich layers (Plate 4). Iron oxyhydroxides with no discernible crystallographic characteristics in X-ray diffraction measurements dominate the composition of these crusts. However, Figure 51 shows that they also have strong enrichments in silicon, arsenic (Figure 52), phosphorus, and antimony. These enrichments are too large to be accounted for by contamination from volcanogenic debris (Table 7).

Bacterial mats, which blanket cliffs (Plates 5 and 7) and grow as patches on sediments (Plate 6), have major element compositions similar to the sediment precipitates and also to the hydrothermal oxides observed in the oceans (Dymond et al., 1989). Because of their compositional similarity, Dymond and Collier (1990) suggested that the bacterial mats, lithified crusts, and pebbled surfaces are depositional forms from distinct stages of a hydrothermal system. The bacterial mats are hypothesized to thrive under a continuous source of reducing compounds provided by fluids which advect through rock outcrops and the sedimented lake floor. Precipitation within conduits of a hydrothermal system will eventually block the flow and stop the venting at a given site. When this occurs, the bacterial mat may be transformed from a gelatinous, living system to a lithified crust. The breakup of the crusts into pebbles could occur by collapse of depositional sites which had been elevated by the excess pore pressure accompanying hydrothermal venting. From this perspective, the crusts are in effect fossilized bacterial mats. Microscopic examination of several crust samples reveals iron-encrusted, sheath-like forms very reminescent of the living bacterial communities. The 1990 research program added greatly to the number of known bacterial mat locations (Figure 47).

The enrichment of phosphorus, arsenic, and antimony observed in the crusts and bacterial mats (Tables 6 and 7) can be accounted for in part through coprecipitation and scavenging of these elements by the iron oxyhydroxides. Phosphorus, arsenic, and antimony are oxyanions in aqueous solution which are strongly attracted to the positively charged surfaces of the amorphous iron material. This process accounts for the abundance of similar oxyanions and the REE elements on iron-rich precipitates found within seawater hydrothermal plumes (Trefry and Metz, 1989; Feely et al., 1990; German et al., 1990).

Because there is abundant phosphorus in the deep lake, the observed phosphorus enrichments in mats and crusts could be explained by scavenging of dissolved phosphorus in normal lake water. For arsenic and antimony, however, the explanation is less likely. We don't know how much arsenic and antimony are in Crater Lake waters. In general, however, arsenic and antimony concentrations in surface waters from volcanic terrains are very low compared to concentrations in thermal springs (Onishi, 1969) and hydrothermal fluids (Ellis and Mahon, 1977). It is more likely that solid-phase arsenic and antimony enrichments result from high concentrations of these

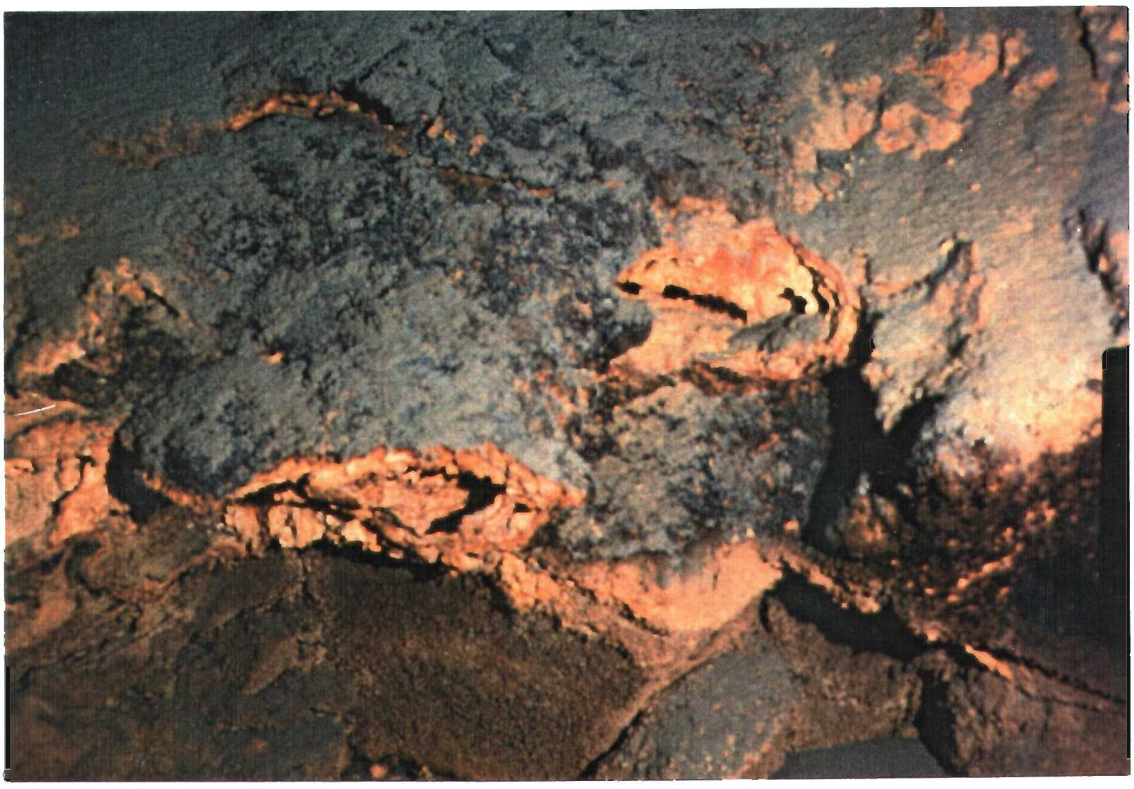

Plate 19. Iron rich crusts with a light dusting of sediments. These crusts are found near the top of a steep rocky outcrop in a position similar to that of many bacterial mats.

Plate 20. A short, spire-like feature discovered south of Llao's Bath (CD 223). The spire is approximately 40 centimeters in height.

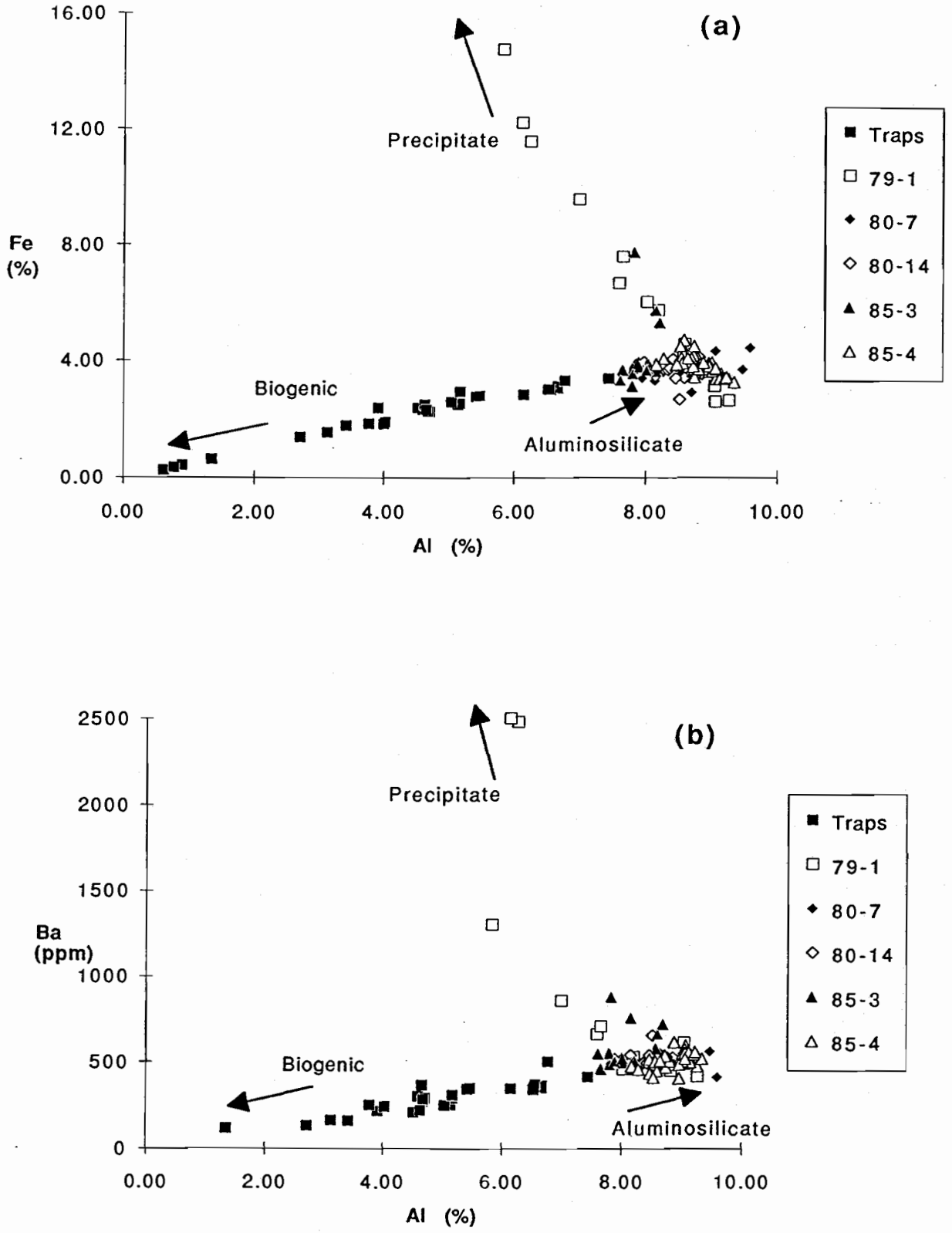

Figure 50. (a) Concentration of aluminum vs. the concentration of iron in sediment core and sediment trap samples. (b) Barium vs. iron for the same samples. Both plots are taken from Dymond and Collier (1990).

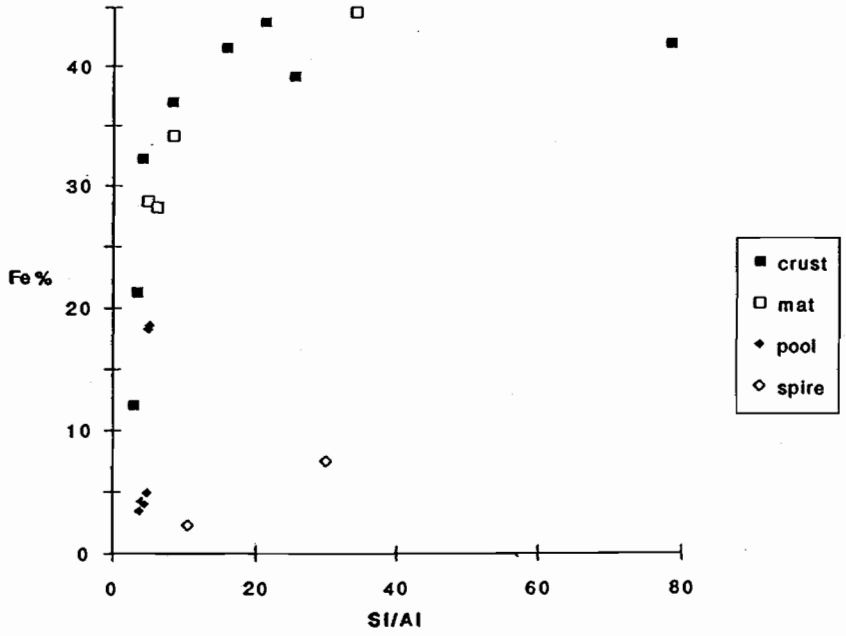

Figure 51. Concentration of iron vs. the Si/Al ratio in samples from the various thermochemical features in the lake. "Crust" refers to iron-rich crusts, "mat" refers to bacterial mats, "pool" refers to sediments recovered from the bottom of saline pools, and "spire" refers to the siliceous spires near Skell Head.

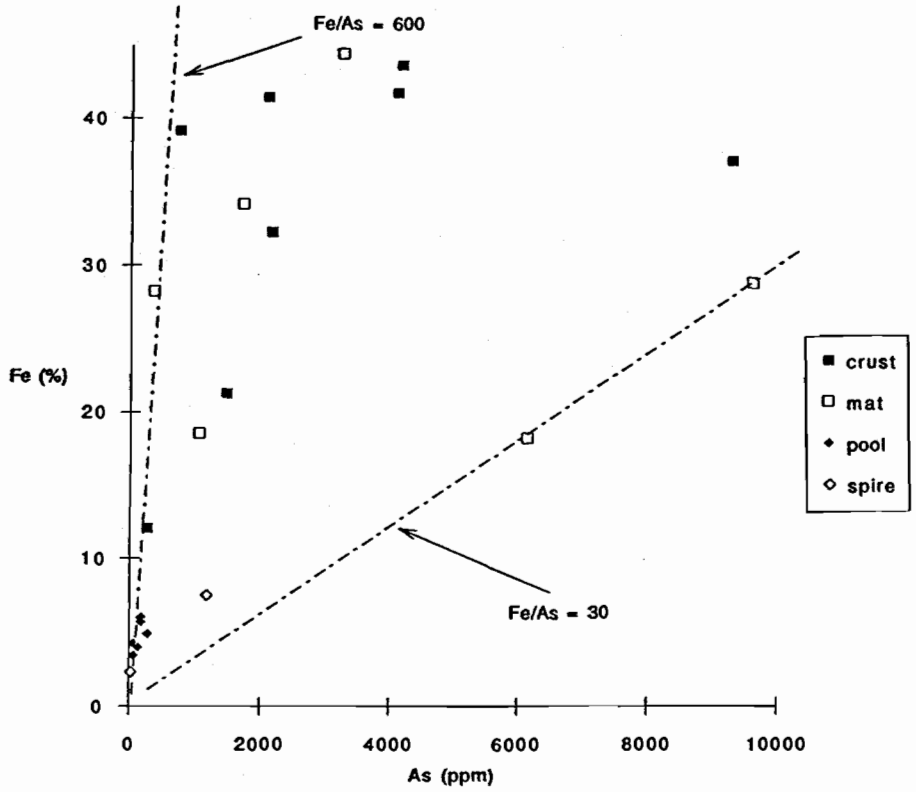

Figure 52. Iron vs. arsenic for various types of solid samples from the lake. The symbols are the same as those used in the previous figure.

Table 7. Crater Lake crust and spire compositions

	Dive Number				
	220	223	213	230	216
Sample Type	Fe-crust	Fe-Crust	Spire	Si-Crust	Pool
Elements					
C	0.42	0.49	0.32	0.19	2.58
N	0.1	0.09	0.08	0.04	0.3
Al	0.080	0.83	1.3	3.61	6.7
Si	6.29	6.97	38.7	38.3	26.6
P	1.61	2.81	0.19	0.03	0.15
S	nd	nd	nd	nd	2.1
Ca	0.66	1.3	-	1.4	2.33
Cr	9.1	11.4	9.3	19	38.7
Mn	1844	1732	260	230	460
Fe	41.70	36.90	7.52	2.33	6.00
Cu	17	21	45	51	89
Zn	10	27	32	32	82
As	4100	9280	1181	30	180
Sb	2.7	11.6	61	0.3	0.6
Ba	305	540	145	225	490
La	3.8	7.6	3.2	8.6	16.3
Pb	52	48	39	34	53
Th	nd	0.3	0.7	1.6	3.2
U	2.00	1.50	0.5	1	1.8

Values are in weight per cent, except for Cr, Mn, Cu, Zn, As, Sb, Ba, Ce, Pb, Th, and U, which are ppm.

"nd" means below the detection limit.

elements in the fluids from which the mats and crust formed rather than from coprecipitation of these elements in normal lake waters.

This inference is supported by data which indicates that the scavenging by iron oxyhydroxides can be described by the distribution coefficients for particulate and dissolved constituents (Honeyman et al., 1988; Feely et al., 1990). This means that the enrichments of elements like phosphorus and arsenic in oxyhydroxides are primarily a function of the concentration in solution. It is noteworthy that the relationship between Fe and arsenic abundances in the Crater Lake samples is somewhat variable. Although there is a significant correlation between the abundances of the two elements in mats and crusts, the Fe/As values vary from 30 to more than 600 (Figure 52). This observation may reflect a similar variability in the arsenic concentrations in the fluids from which the mats and crust form.

Spires.

In addition to new mat discoveries, the 1990 submarine program discovered solid-phase deposits with distinct forms and compositions. One of the most spectacular deposits is a group of spires that were observed and sampled along the eastern margin of the lake. The spires have a narrow, conical shape; they rise from a base approximately one to three meters across and terminate in narrow (4-6 cm) pinnacles 10-12 meters above the bottom (Plate 16). The morphology of these features is neither volcanic nor erosional; they appear to have formed by precipitation from aqueous solutions.

A sample six cm in diameter and ten cm long was collected from near the top of one of the spires. The sample is composed of low-density material which in cross section exhibits alternating reddish-brown and white-to-buff bands; the bands range from less than a millimeter to a centimeter in thickness. Bulk analyses of this material have shown that it is much richer in Si than any Crater Lake precipitate samples that we have studied previously. The bulk material contains 38.7% Si, or approximately 83% SiO_2. This composition resembles the siliceous sinter or geyserite that precipitates from hot springs (Elder, 1981). The spire deposit is enriched in iron, but the elemental relationships among Si, Fe, and minor elements are generally distinct from those observed in either the Fe-rich crusts discussed above or the bacterial mats (e.g., Figures 51 and 52).

An X-ray microprobe traverse across a section of the spire sample reveals strong variations in the iron and silicon contents and some distinct interelemental relationships. The outermost layer of the sample contains approximately 40% Fe (Figure 53a) and 12% Si (Figure 53b), similar to the bacterial mats and iron-rich crusts. At approximately two millimeters from the margin, the Fe content decreases abruptly and silica dominates the composition. Continuing into the sample there are alternating Fe-rich and Si-rich bands which varyi in thickness from 0.1 to 1.0 mm. We suggest that these compositional variations reflect changes in the composition of fluids from which these deposits precipitated. The high silica contents of this deposit suggest deposition from fluids that have higher dissolved Si contents than any of the currently analyzed fluids, either from the pools or from within bacterial mats. Because the solubility of Si is strongly dependent on temperature, the compositional data imply that the spires are deposits of a previously active hydrothermal system with exit temperatures that were higher than any of the known sources of anomalous fluids found in Crater Lake during our field program. Alternating Fe-rich and Si-rich bands may indicate variable fluid compositions and/or temperatures of the venting.

The arsenic content of the bulk spire sample is approximately 1200 ppm (Table 7, but microprobe measurements document large variations over a transect from the outer edge toward the center of the sample (Figure 53c). Arsenic values greater than 1% are somewhat higher than the highest values observed in our bulk analyses of crusts and mats (Figure 52). Measurements of antimony in this sample reveal similar elevated values in the bulk sample (>60 ppm) and large variations

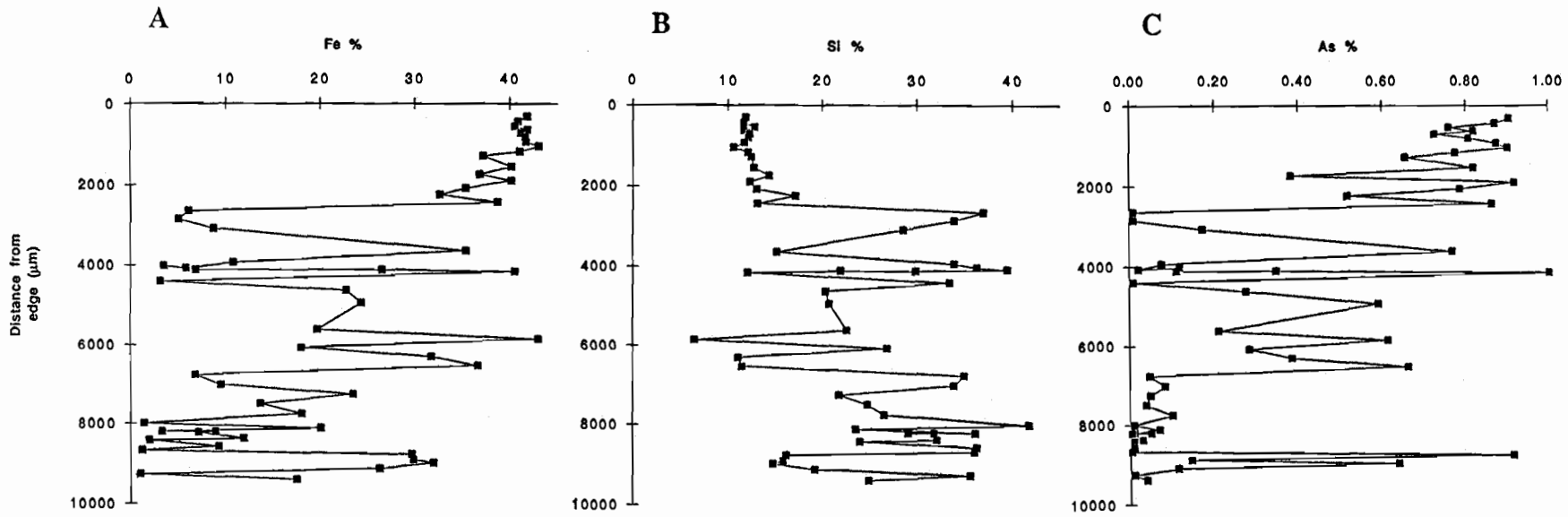

Figure 53. Quantitative microprobe scan across the siliceous spire sample from below Skell Head. (a) The iron concentration vs. distance from the outer surface. (b) Silicon concentrations for the same sample. (c) Arsenic concentrations in the same sample.

along the microprobe transect. The highest As and Sb concentrations are generally found in samples with high iron contents. However, as in crusts and mats, the Fe/As and the Fe/Sb values show significant variations over the transect. The high and variable abundances of As and Sb support the hypothesis of precipitation from a hydrothermal source.

The tall, chimney-like morphology is unlike the typical siliceous sinter deposits that occur around subaerial hot springs; these deposits are typically broad mounds (Don White, personal communication). The morphology is more akin to submarine black-smoker chimneys. It is probable that spire morphology is characteristic of subaqueous precipitation. Fluids exiting from a subaqueous vent are not controlled by the same gravitational forces which result in downslope flow, lateral spreading of fluids, and broad zones of precipitationin subaerial systems. Taken all together, the spire chemistry and morphology indicate subaqueous precipitation from a hydrothermal spring. No active flow was noted; it appears the hydrothermal activity is currently quiescent. The age of the deposit is unknown, but the spires appear to have their pristine form. No broken or fallen spires were noted. The fact that the deposits are located at the base of the caldera wall, the general location of frequent downslope debris flows and turbidites, suggests that these structures are not thousands of years old. Because the spires have steep surfaces, the lack of sediment cover (Plate 16) does not constrain the age of the deposits. An attempt to measure the ^{228}Ra and ^{226}Ra contents of this material was unsuccessful because the concentrations were too low to determine if these isotopes were in radioactive equilibrium with their parent thorium and uranium isotopes. Consequently, the age of formation of the deposits is unknown.

Although nothing with the sizable dimensions and exact morphology of the spires has yet been observed in other parts of the lake, several other deposits either have similar features or compositions that warrant comparison with the spire samples. One of these was observed within a few tens of meters from the bacterial mat sample where 18.9°C temperatures were recorded. There, small protuberances (approximately 20-30 cm) were attached to the same sloping surface on which the bacterial mats were growing. We were unable to collect a sample of these features, but the color and morphology suggest they may be compositionally similar to the spire samples.

At another site, approximately 200 meters south of Llao's Bath, a protuberance on a sedimented sloping surface was observed (Plate 20). Although chimney-like, the morphology of this feature differs from either the large or small spire-like forms discussed above. Its friable texture made it easy to break loose, and we recovered a sample which is listed in Table 7 as an iron crust from dive CD 223. The general composition of this material is similar to other iron-rich crusts. It is an amorphous iron-oxyhydroxide with significant concentrations of Si. Minor element contents, as in most crusts, are low except for As; this sample has the highest As concentration of any bulk solid sample analyzed (9300 ppm). ^{228}Ra and ^{226}Ra activities in this small spire were measured by gamma counting; both isotopes are present in excess of the ^{232}Th and ^{238}U activities. Because the half-life of ^{228}Ra is 5.7 years, excess ^{228}Ra activity indicates that this spire formed less than 30 years ago.

A crust of unusual composition was recovered from the edge of Llao's Bath. A rock outcrop covered by a one centimeter thick crust extends into this pool (Plate 10). A sample of this coating was recovered with the submersible; it has a very high silica content and is similar to the bulk spire sample from the eastern margin of the lake (Table 7). This crust, however, has lower abundances of iron and arsenic.

The precipitates, like many iron-rich precipitates, are composed mainly of material which is crystallographically amorphous to X-rays. The spire sample has the typical broad amorphous silica spectrum, with possibly some cristobalite present (Figure 54a). There are also peaks from very minor amounts of feldspar and quartz, probably from cemented aluminosilicate debris from the caldera wall. The iron-rich crusts are highly amorphous (Figure 54b).

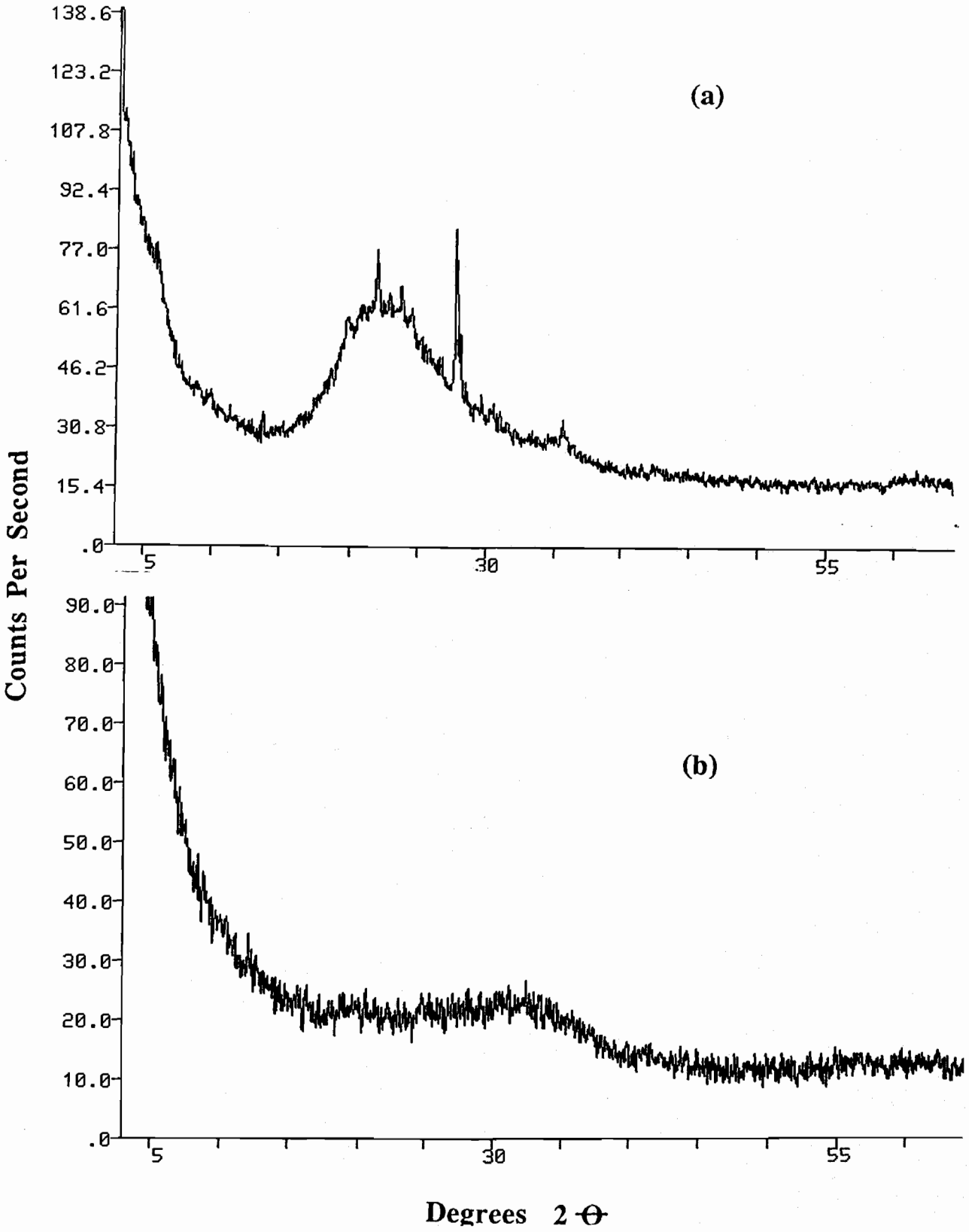

Figure 54. X-ray diffraction scan of: (a) CD213 spire sample. The broad peak near 20 ° 2θ is amorphous silica with some christobalite present; minor quartz (26.6 °) and feldspar peaks (28 °) are also present. (b) Iron-rich crust from CD220. This sample, which was collected from the North Wall bacterial mat discovered in 1988, exhibits no crystalline phases. Both samples were scanned at very slow rates (0.2 ° 2θ) and point averaging was used to enhance the signal to noise ratio.

Pool Sediments.

Solid samples from the pools were obtained either by box coring from the submarine or by pumping water and suspended particles into the water bottle. The pool samples were composed of very black mud. The aluminium content of the pool samples, which range from four to five percent, indicate that volcanic aluminosilicate debris comprises 50 to 60 percent of the sample. However, there are small iron and silica enrichments over normal caldera wall material. Arsenic and minor metals also appear to be slightly enriched over typical Crater Lake sediments.

The pool sediments have significant enrichments of sulfur and carbon (Table 7). Because the pools are essentially anoxic, sulfide precipitation is possible and the preservation of organic matter might also be enhanced. Abundant organic matter and the presence of sulfides can account for the black color of the mud.

Sediment Core Analyses.

The solid-phase chemical composition was determined on samples from two submersible-deployed box cores, BC6 and BC8. Both cores were recovered within the Detailed Study Area. BC6 is from the Benthic Barrel site, a low relief, sedimented area which has elevated sediment temperatures (approximately 8°C at 75 centimeters sediment depth) and mottled sediments. BC8 was recovered a few meters from the "brain mat", a bacteria/pool complex that lies 10-20 meters west of Llao's Bath. Pore water analyses and advection-diffusion modeling suggest that significant advection of fluids is occurring at both sites. Approximately 200 cm/year of upward pore water flow is occurring at the BC6 site (Appendix F), while 100 cm/year is estimated at the BC8 site.

Both cores have compositional variations which cannot be explained by deposition of the biogenic or aluminosilicate components of Crater Lake sediments. Iron varies from 4% to nearly 10% in BC6 and from 4% to nearly 25% in BC8 (Figure 55a). Large ranges in concentration are also observed for Mn (Figure 55b) and As (Figure 55c). The strong enrichment of Mn within the upper two centimeters of both cores suggests that this is a steady-state pattern resulting from advection of manganese-rich pore waters and precipitation within a surface oxic zone. Pore water measurements document high dissolved iron concentrations below approximately 10 cm in both cores (Figure 56), indicating iron reduction below this depth. Steady state diffusion and advection with oxic precipitation above 10 centimeters could account for the increase in solid iron which is found at 5 to 10 centimeters depth in each core. However, the strong increase in Fe and As at 18 centimeters depth in BC8, indicates a deviation from purely steady-state diffusion/advection and precipitation effects.

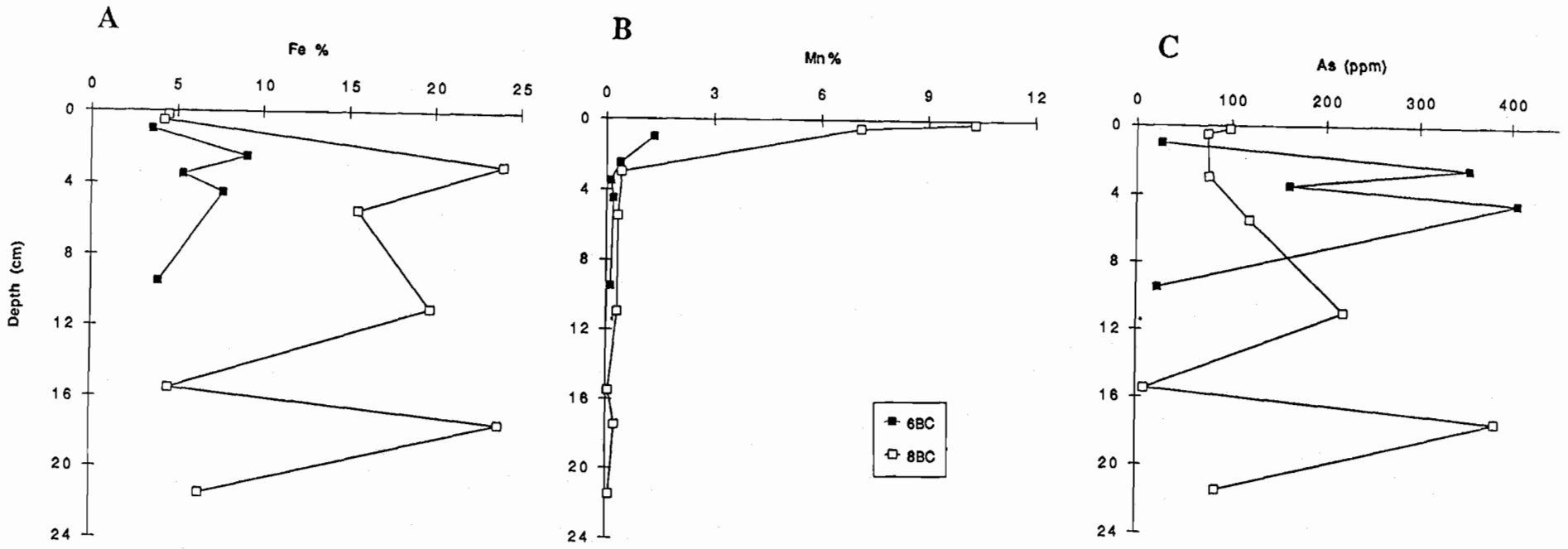

Figure 55. Downcore variations in the concentrations of iron (A), manganese (B), and arsenic (C) in two box cores from the detailed study area. BC6 was cored near the high temperature mats. BC8 was cored near the Llao's Bath/brain mat complex. (A) Iron vs depth. (B) Manganese vs depth. (C) Arsenic vs depth.

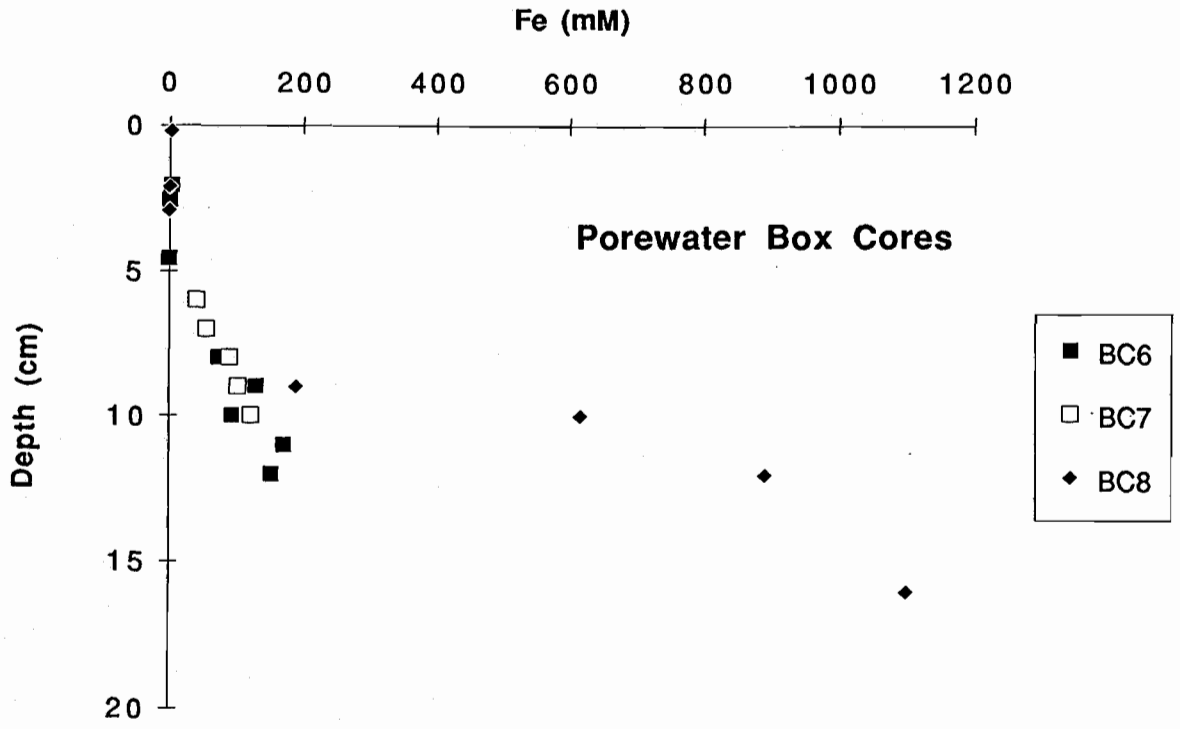

Figure 56. Pore water iron concentrations as a function of depth. Core locations have been previously shown in Figure 3. All three cores (BC6,BC7,BC8) indicate high dissolved iron concentrations below 10 centimeters depth in the sediments.

IV. Discussion

IV.1. Geological Setting of Features in the Detailed Study Area

Regional Setting.

Mount Mazama is a major site of Quaternary volcanism in the volcanic arc known as the Oregon Cascade Range. This volcanism is linked to the subduction and melting of the Juan de Fuca Plate beneath the North American Plate. The central Oregon segment of the Cascades, which includes Mount Mazama, has the highest regional rates for volcanic extrusion found in the entire 1200 km range of the Cascades (Sherrod and Smith 1990). Large areas of high regional conductive heat flow coincide with this magmatic activity (Blackwell et al., 1982; Blackwell et al., 1990; Ingebritsen et al., 1989). Moreover, the total convective discharge of thermal waters in the Oregon segment of the Cascades is the highest measured within the volcanic arc (Mariner et al., 1990).

The dramatic physiographic setting of Crater Lake is a consequence of the relatively recent volcanism of Mount Mazama. Although the major explosive eruption which led to caldera collapse and the formation of the Crater Lake basin occurred 6845 ± 50 years ago, Mount Mazama has been an eruptive center for approximately 400,000 years (Bacon and Lanphere, 1990). Within a few hundred years after the climactic eruption, andesitic outpourings within the caldera produced Wizard Island, Miriam Cone, and the so-called Central Platform on the east side of Wizard Island (Bacon and Druitt, 1988; Nelson et al., 1988). The most recent activity within the mountain is thought to be a small rhyodacite dome extruded on the east flank of Wizard Island approximately 4,000 years ago (Bacon and Lanphere, 1990).

Because of the relatively recent volcanism of Mount Mazama, thermal springs and/or other modes of hydrothermal activity might reasonably be expected. Such features could be driven by the residual heat of cooling intrusive bodies within the mountain or a residual magma chamber. On the basis of gravity data, Williams and Finn (1985) infer a dense mass of intrusive material a few kilometers below the floor of Crater Lake. Fumaroles and thermal springs are found near the crests of some other nearby volcanoes, for example, Mt. Hood (Steele et al., 1982) and Newberry Crater (Mariner et al., 1990). In general, however, the majority of the Cascade thermal springs are found away from the central axis of the volcanic arc (Blackwell et al., 1982; Ingebritsen et al., 1989). In addition, the upper 200 to 1000 meters of young volcanic crust in the high Cascades is nearly isothermal (and therefore has low conductive heat flow). These observations have led to the proposal that ground water circulation away from the crest of the high Cascades transports heat east and west to lower elevations where it is discharged in thermal springs (Ingebritsen et al., 1989).

The hydraulic effects hypothesized for the high Cascades are expressed on a more local scale by a numerical simulation of the hydraulic system under Crater Lake and Mount Mazama (Sammel and Benson, 1987). Although the model is not based on measured geothermal gradients or permeabilities in the crust beneath Crater Lake, it indicates that the regional ground-water flow field will transport fluids away from the lake. Nonetheless, several variations of Sammel and Benson's 1987 model exhibit a convective upflow of warm water into the lake that is driven by heat from a hypothesized deep intrusive body.

The thermal structure of Newberry Volcano, an eruptive center 95 km to the northeast of Mount Mazama, can be used as an analogue to the Crater Lake/Mount Mazama system. Although Newberry is more shield-like than the Mazama stratocone, the volcano has a collapsed caldera, which now contains two lakes, and a volcanic history which extends from 500,000 years to 1,300 years before present (Fitterman, 1988). Consequently, Newberry has some of the same structural features and volcanic history as Mount Mazama, but its thermal structure has been documented by deep drilling data. Drilling on the volcanic slopes outside the Newberry caldera revealed a shallow isothermal zone (Swanberg et al., 1988), which may reflect meteoric recharge near the summit and through the flanks of the volcano. Nevertheless, vertical advection of thermal waters at Newberry Volcano is also indicated by the presence of thermal springs on the margins of the caldera lakes (Mariner et al., 1990) and the existence of temperatures as high as 265°C at depths less than one kilometer below the caldera floor (Sammel, 1981; Sammel et al., 1988). Hydrothermal modeling suggests that upward convection in the Newberry Volcano takes place only in localized zones of high vertical permeability, such as intrusive conduits or ring fractures (Sammel et al., 1988). These modeling results are similar to numerical simulations for Mount Mazama (Sammel and Benson, 1987)

In summary, the available thermal gradient data and ground-water flow simulations indicate that there are few hydrothermal outflows at the crests of the most recent Cascade volcanic centers. Much of the upper crust is characterized by near-isothermal conditions except where structural features provide conduits which favor the vertical advection of water heated by underlying magmatic bodies. At these sites of enhanced permeability, upward flow of thermal fluids results in exceptional thermal gradients and, in some cases, thermal springs. Such patterns are consistent with the possibility of hydrothermal inputs into the deep basins of Crater Lake.

General Bathymetry.

The original caldera morphology of Mount Mazama has been modified by the subsequent development of volcanic edifices, by erosion of the caldera wall, and by basin sedimentation. Wizard Island, the submerged Miriam Cone, and a shallow area to the east of Wizard Island (the Central Platform) are the major constructional volcanic features within the basin (Figure 57). The South Basin and the North Basin are the major depositional basins of the lake. These basins form large areas of low relief which are covered by 30 to 60 meters of volcanoclastics, turbidites, and fine lacustrine sediments (Barber and Nelson, 1990).

The Detailed Study Area is located in a geologically complex portion of the Crater Lake basin. The base of the relatively shallow Wizard Island platform bounds the northern edge of the area. Crossing diagonally through the study area with a NE-SW orientation is a zone of rather steep topography which descends from local high spots of 380 to 405 meters depth in the southern part of the study area to basin depths of 450 to 475 meters in the center of the area (Figures 1 and 2). The entire Detailed Study Area and much of the South Basin lie within a proposed ring fracture zone (Figure 57). This feature was first identified by Bacon (1983) as a zone of volcanism during caldera collapse. Wizard Island and Miriam Cone fall within the fracture zone. More recently Nelson et al. (1988) pointed out that this zone marked the maximum depths of acoustic basement and included the two areas of high heat flow that were defined by Williams and Von Herzen (1983). A saddle between the South Basin and the deeper North Basin of Crater Lake is formed by the elevated topography on the north and south margins of the area. This saddle lies within the ring fracture zone. It may be significant that anomalous bottom waters, bacterial mats, pools of

more saline water, and siliceous deposits of probable hydrothermal origin all are found within or close to the proposed ring fracture zone. Many of these features are found within a few meters to a few tens of meters from the change in slope that occurs at the base of the steep caldera wall.

Chaski Slide.

The elevated topography on the south side of the Detailed Study Area may be an extension of a subaqueous portion of the Chaski Bay Slide, a prominent catastrophic feature on the south caldera wall. An acoustic profile across the southern edge of our Detailed Study Area shows the presence of chaotic beds beneath the flat-lying turbidites and slowly accumulating lake sediments (Nelson et al., 1988). The lake bathymetry (Byrne, 1965) exhibits a deflection of the depth contours into the South Basin away from the subaerial portion of the Chaski Bay Slide. Nelson et al. (1988), use the bathymetry and the chaotic acoustic stratigraphy as evidence of debris flow and avalanche deposits at this location. They suggest that deposits of this type formed in response to seismic activity in association with post-caldera volcanism that began soon after the caldera collapsed. The hummocky topography, which is revealed by our finer-scale bathymetry (Figure 2, Figure 7), is also compatible with a debris flow.

The area identified as a possible debris flow terminates near the middle of our Detailed Study Area. Its northern limit may coincide with escarpments and steep rock outcrops which we observed in the region from the submersible. Some of the bacterial mats were found on the face of one of the escarpments, and other mats were found on flat lying sediments near the base of cliffs. The association of the escarpments with the bacterial mats suggests that these cliffs may be related to the origin of the anomalous fluids that provide a chemosynthetic energy source for the bacteria. If the escarpments mark a fault, perhaps part of a ring-fracture zone that has continued to subside since the original caldera collapse, then the association may simply be due to the fact that faults provide a conduit for convecting waters. Movement on this hypothetical fault would maintain the conduit and prevent the blockage of flow by crack-filling precipitation of hydrothermal minerals. From a seismic reflection record through our Detailed Study Area (Nelson et al., 1988), it is possible to infer that normal faulting has occurred in the region where we observe scarps. However, because of the difficulty in interpreting chaotic beds in the record, such an interpretation is equivocal. Nonetheless, faulting does provide a mechanism for maintaining the exposure of the chaotic beds despite the deposition of a relatively thick sequence of turbidites and more slowly deposited sediments.

Semi-consolidated sediments within the Detailed Study Area have vertical displacements of 0.5 to 2 meters (Plate 4) which appear to mark the locations of recent normal faulting. For three of these features, our navigation and documentation was sufficient to define their alignment. All three have a general northeast-southwest trend and are down-dropped to the northwest. Two of the apparent faults are located within the general area where the high temperature mats are located (Figures 8, 9, and 43). The third is near the north wall mats. Although bacterial mats were not observed directly on these zones of vertical displacement, the proximity of the mats, the elevated temperatures, and the apparent faults are all consistent with a fault-induced permeability that allows vertical convection of fluids through the crust. As indicated by the hydrologic modeling of Crater Lake (Sammel and Benson, 1987) and Newberry Volcano (Sammel et al., 1988), enhanced permeability zones beneath the caldera floor will result in vertical convection of waters that have been heated by intrusive magmatic features in the cores of these volcanoes.

The escarpments and rock outcrops in the middle of the Detailed Study Area could also mark the northern limit of the debris flow comprising the Chaski Slide. If this is the case, any causal or spatial relationship between the possible hydrothermal activity and the debris flow is less clear. Possibly, the debris flow forms a cap over the ring-fracture zone and directs hydrothermal flow to the face of the cliff that marks the termination of the chaotic beds. It is more reasonable, however, to think that the debris flow, if it is composed of large blocks, is more permeable than horizontally-bedded lake sediments that have accumulated over the past 5000 to 6000 years of lake history. If this is the case, deposition of the debris flow on top of a ring-fracture zone may provide pathways for fluid flow that extend from deep within the volcano to the lake floor (Barber and Nelson, 1990). In any case, the chaotic beds in the deeper parts of our Detailed Study Area are overlain by 20 to 25 meters of flat-lying lake sediments (Nelson et al., 1988). This indicates the landslide event must have taken place early in lake history.

The visual and photographic evidence suggests that the cliff faces where bacterial mats are found and the outcrops common on the steeper portions of the Detailed Study Area are composed of hydrothermally-altered rock. The fact that much of the rock making up the south caldera wall and the Chaski Slide is also hydrothermally altered and similar in appearance to the the submerged outcrops (C. Bacon, personal communication), supports the concept that many of the submerged outcrops are exposures of an earlier debris flow. Because the Chaski Slide rocks are at least 200,000 years old (C. Bacon, personal communication), the alteration predates the climactic eruption considerably. However, in some cases, the sediments adjacent to the subaqueous cliff faces appeared to be highly altered, an observation which may indicate that at least some *in situ* alteration has also occurred there.

Implications of the Palisades Point Thermal-Chemical Features.

The presence of bacterial mats, pools, and elevated temperatures at Palisades Point indicates that thermal features are not limited to the portion of the lake affected by the large landslide events, such as the Chaski Slide. The subaqueous topography extending off Palisades Point is among the steepest found within the lake (Figure 1). There is no bathymetric evidence for major slumping or landslide features. The steep topography at this site is a consequence of a step-like pattern of sequential vertical wall and talus slope couplets. This topography is probably what should be expected from normal faulting following the climactic eruption, and not the result of catastrophic failure of portions of the caldera wall.

The Palisades Point area and the Detailed Study Area do share a proximity to what has been identified as a ring fracture zone (Figure 57). This zone was previously defined by the existence of intercaldera volcanic features, Wizard Island and Miriam Cone, as well as by the high heat flow sites found by Williams and von Herzen (1983). In fact, the studies of Williams and Von Herzen (1983) defined an area of anomalous heat flow less than one kilometer southwest of our Palisades Point thermal features. It is possible that both observations are related to the ring fracture zone.

A linkage between the fracture zone and the Palisades Point features is reasonable if the source of the fluids which supply the thermally and chemically enriched inputs to the mats and pools is deep beneath the lake. As discussed above, occasional movements on the fracture zone would help maintain a conduit for convecting fluids. Likewise, the Skell Head spires, which have morphologies and chemical compositions similar to hydrothermal deposits, are also located just shoreward of the ring fracture zone. Since very little of the area near the break in slope has been

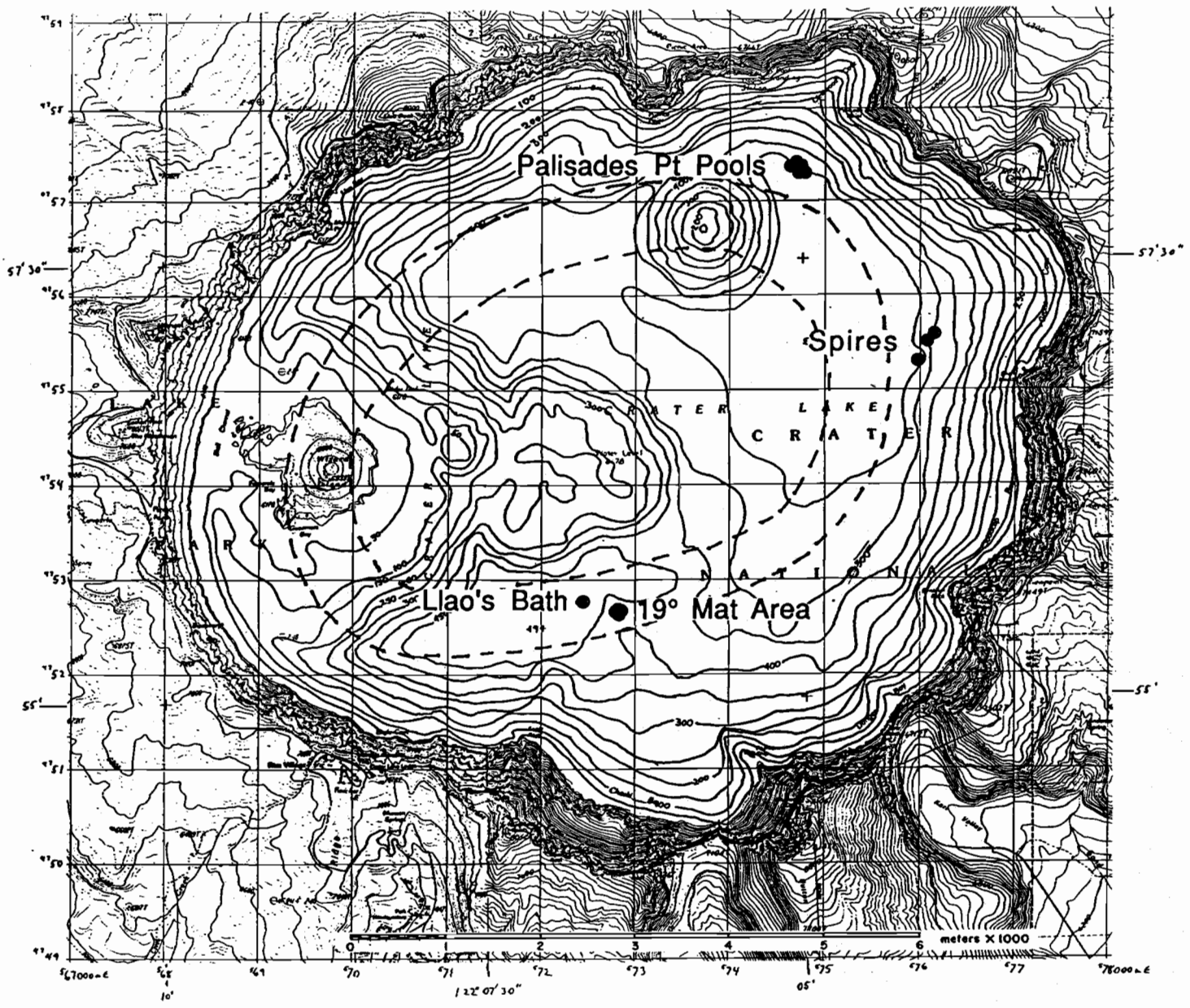

Figure 57. General locations of the thermal-chemical features discovered in Crater Lake. Also shown is the ring fracture zone after Nelson et al. 1988.

explored by submersible, it is possible that other active and inactive thermal features remain to be discovered within this portion of the lake. Alternatively, the location of the thermal-chemical features may not be controlled by the hypothesized ring-fracture zone, but rather by proximity to the caldera wall. La Fleur (1990) has hypothesized that the flow of meteoric water through caldera wall rocks is the source of anomalous fluids observed in the lake. Although in previous sections we have shown that this hypothesis is not supported by our thermal and chemical data, all of the hypotheses will be discussed more thoroughly later in the report.

IV.2. Geochemistry of Fluids

Composition of Sampled "End-Member" Fluids.

During the 1988 summer field program we were able to retrieve a bacterial mat sample and its associated *in situ* "pore water" during dive CD179. The sample was collected by closing a Niskin-type water sampler within the mat. Because of the method of collecting this sample, we cannot be sure of the extent of dilution of the actual bacterial mat fluids by the background lake water. However, a visual estimate made during sampling suggests that the sample is composed of 10% to 20% mat water and 80% to 90% bottom water. The water in this mat sample was the most thermally and chemically enriched water taken during the 1988 field program (sample CD179BT in Table 8). The thermistor probe registered a temperature of 5.7°C in this mat surrounded by a background water temperature of 3.60°C. The chemistry of this sample can be contrasted with "normal" deep lake water (sample 7.3 in Table 8) and with a South Basin sample which has anomalous temperature and ionic composition (sample 2.2-7 in Table 8). Many of the concentrations of the major ions are nearly a factor of two higher in the mat fluids and Mn concentrations are 2-3 thousand times higher than surrounding lake waters. These compositions document the major thermal and chemical gradients across the mat interface.

Table 8. Chemical composition of bacterial mat water sampled in 1988

sample	Na	K	Ca	Mg	SO_4	Cl	SiO_2	Li	Mn
	(mmoles/liter) --->						(μM)	(μM)	(nM) .
7.3 (hydrocast, 1987, 351m)	0.452	0.044	0.168	0.111	-	-	288	6.35	0.6
2.2-7 (hydrocast, 1988, 429m)	0.474	0.045	0.171	0.114	0.106	0.309	303	-	4.1
CD179BT (bacterial mat water)	0.840	0.077	0.314	-	0.209	0.443	478	11.12	590

In 1989, we were able to sample a variety of new fluids including the warm brines collecting in pools at the bottom of the lake ("Llao's Bath" and "Palisade Pool", Plates 9,10,13,14) and pore water samples from a number of locations throughout the lake. We also sampled several more bacterial mat pore fluids. Table 9 shows a composite list of these various fluids which appear to be the "least diluted" by lake water during sampling and best represent the "end-member" composition of fluids entering the lake. The concentration of dissolved oxygen in the Palisade Pool sample was very nearly zero (Table 9) indicating that this sample could have only a small amount of "contamination" from the well-oxygenated bottom water. Furthermore, the pool fluids resemble the pore water concentrations indicating that the pool brines represent relatively undiluted chemical end-members. We will use these end-member compositions in a variety of geochemical and mass balance calculations in our discussions below.

The composition of these end-members is quite different than that of most *cold* springs in the Crater Lake area, which attain their composition through normal low temperature weathering processes (Nathenson and Thompson, 1990). Also, for comparison to the Crater Lake samples, we have included our analyses of the thermal spring at East Lake within the Newberry Caldera located 95 km to the northeast. Analyses of this sample, collected in September, 1989, are similar to the concentrations reported by Mariner et al. (1990) for an East Lake hot spring sample collected in June, 1982. The spring has an outlet temperature of 57°C and is associated with a complex hydrothermal system which reaches temperatures of at least 265°C at 932 meters below the caldera floor (Sammel et al., 1988). The major cation concentrations in this hot spring are quite similar to the Llao's Bath and Palisades Pool samples (Table 9). While springs at both Crater Lake and Newberry Crater have relatively high concentrations of Mg, their other cation concentrations are generally included within the wide range of compositions of thermal springs in Oregon and Washington (Mariner et al., 1990). The concentration of chloride in the East Lake spring is anomalously low compared to the Crater Lake warm springs and other regional thermal springs. The anion charge balance for both sites is dominated by bicarbonate.

The pore waters, sampled for the first time in 1989, significantly expanded our list of sampled end-members. A first order similarity between pore water compositions and pool waters is suggested by their comparable Cl and Na concentrations and proportions (Figure 22). However, variability that seems to exceed analytical precision exists both between pools and pore waters and among the pore waters. Because this variability is relatively subtle, it is best observed by examination of elemental ratios. For example, variations in the Ca/Na contents appear to distinguish between both sediment-pore water reaction effects and advection of a relatively homogeneous fluid (Figure 24c). Reaction is indicated by the increase in Ca/Na with little increase in Cl contents in GC1, a trend which reflects the relative immobility of Na and low abundance of Cl in the aluminosilicates that comprise the sediments. In contrast, cores whose pore water gradients indicate appreciable advection, have somewhat lower Ca/Na than lake waters and appreciable enrichments in Cl. Variations of similar scale exist for other element pairs reflecting differences in the enrichments of the different ions in advecting fluids as well as their reactivity during low temperature weathering. We emphasize that the reaction effects are subtle and only apparent by examining elemental ratios and only then by contrasting cores with different apparent advection rates.

As discussed by Wheat (Appendix F), gravity cores GC8 and GC13 have the most non-linear concentration-depth profiles and thus the highest apparent advection rates of all of the gravity cores. The deeper portions of these cores tend to have the highest ion concentrations of any fluids observed in the lake and appear to have distinctive elemental ratios for the less reactive elements. For example, the Li/Na values of GC8 and GC13 are higher than either the lake values or those for

Table 9. Chemical compositions of representative "end-member" fluids.

sample	deep lake	bacterial mat	Llao's Bath	Llao's mat	Palisades Pool	Palisades mat	gravity core	box core	East Lake
ID	(composite)	CD179BT	(composite)	CD226 S3	CD228 S1	CD228 S3	GC8- 72cm	BC8- 10/11 cm	Spring
temp °C	3.673	5.7	4.4		5				57
pH	6.95		7.6	7.59	8.91	7.97	8.97	8.1	6.1
ΣCO2 (mM)	0.64		4.96		8.70	2.70	7.06	4.30	9.00
Na	0.47	0.84	2.80	2.22	5.14	1.47	4.63	2.31	2.4
K	0.047	0.077	0.225	0.176	0.124	0.064	0.427	0.179	0.18
Mg	0.12		1.12	0.93	2.21	0.62	0.98	1.08	1.8
Ca	0.18	0.31	0.94	0.77	0.64	0.23	0.91	0.82	2.0
Cl	0.29	0.44	1.03	0.87	1.15		1.99	1.13	0.06
SO4	0.10	0.22	0.69	0.55	0.84		0.00	0.89	0.91
O2 (µM)	295				17				
Si	327	478	1189	980	762	540	1118	822	3700
NO3	1.39		0.59	2.96	1.31	1.57	6.62	0.887	
PO4	0.52		0.21	3.43	10.7	11.3	1.28	2.64	
Li	7	11	35	29	30	12	78	33	4
Ba (nM)	48		312	130	227		1345		
Fe	0.2		41	30421	553		147000	617000	
Mn	3		12300	15272	5100		80800	308000	
Br					60		140		
Rb	16		86	60	49		96		
Sr	190		1150	950	1200		950		
I					30		160		
Cs	2		25	14	6		5		
Rn (dpm/100L)	9.4		9961		659				5725
He-3 (cc/ml)	3.78E-13		271E-13		44.8E-13				

Llao and Palisades Point pools. Likewise, GC8 has lower Na/Cl values than either of the pool locations; however, Na/Cl both in these pore waters and the pools are still higher than those observed in the lake. It is tempting to view the deeper fluids in GC8 and GC13 as an advecting pore water end-member. Since both cores are from approximately the same location near the high-temperature mat region (Wheat, Appendix F, Figure 1), the regional significance of this fluid end-member is uncertain.

Geothermometry.

If we assume that the brine fluids were at equilibrium with a solid mineral phase or authigenic precipitate in a geothermal system below the lake floor, then we can consider applying any of a variety of empirical chemical geothermometers to estimate the temperature at which this chemical equilibrium was reached (Fournier, 1981). In general, however, the approach to equilibrium is kinetically favorable only at relatively high temperatures (>150°C). The application of geothermometers at lower temperatures must be carried out with caution. In order for any geothermometer model to work, a geothermal fluid must reach equilibrium with a solid phase at *in situ* temperatures, and then it must retain that equilibrium composition during conductive cooling. These conditions are only possible if the kinetics of re-equilibration with secondary phases is slow with respect to the rate of cooling such that the water preserves a "memory" of the higher equilibration temperature. Obviously, mixing of a high temperature geothermal water with any low temperature meteoric water can also affect the composition and therefore the predicted temperatures given by many geothermometers. This is absolutely the case for any single-variable geothermometers (e.g. the various SiO_2 solubility systems), and *any* mixing will invalidate their direct application. Other geothermometers describe exchange equilibria through *ratios* of ions (e.g. Na/Li). *In principle*, these are less sensitive to mixing as long as the diluting fluid has insignificant concentrations of the geothermometer's ions.

It is important to contrast the way that the quartz (silica) geothermometers have been used in marine hydrothermal systems with their common application in continental geothermal wells. The first active marine hydrothermal vents discovered, located at the Galapagos Spreading Center, were sampled in 1977 and the chemical compositions and quartz geothermometry of these fluids were discussed by Edmond et al. (1979). A more detailed discussion of various SiO_2 - T systematics applied to the Galapagos system is given by Herzig et al. (1988). The primary difference in this system is that it is *dominated by mixing* of the high temperature end-member with cool seawater - *not by conductive cooling*. All the samples fall along a single mixing line between the warmest sample collected (12.1°C, 775 μM Si) and background seawater (2.0°C, 165 μM Si). Mixing is the dominant control on the range of Si concentrations in the samples; not the end-member temperature. Applying a closed system quartz geothermometer to any of these individual fluids is meaningless: the direct calculation of the quartz geothermometer temperature for the warmest end-member sampled at the Galapagos would predict an equilibrium temperature of less than 100°C. Independent evidence shows that these fluids equilibrated at temperatures near 350°C. However, by *incorporating* mixing in the model, geothermometry can still be used. Because of the tight mixing line, we are able to extrapolate the Si-T relationship to the point where it intersects the quartz solubility curve above 300°C. Once the hydrothermal fluid reaches these high temperatures, equilibrium with quartz is rapidly established and subsequent mixtures with cold seawater retain this Si/T ratio - but not the Si concentration.

The compositions of fluids sampled at Crater Lake generally suggest relatively low to intermediate temperatures. Consequently, the application of geothermometry is subject to the errors noted above. Thus, we will use these tools only as a first-order indication of the temperature history of the fluid. Because the predicted temperatures appear to be relatively low, we have chosen a set of geothermometers that have been constrained by low temperature data in their calibration. These include: chalcedony as a controlling silica phase (Fournier, 1981); the Mg-corrected Na-K-Ca geothermometer (Fournier and Truesdell, 1973; Fournier and Potter, 1979); the Na/Li geothermometer (Fouillac and Michard, 1981); and the Mg-Li geothermometer (Kharaka and Mariner, 1989). Some of these geothermometers were also discussed by Nathenson and Thompson et al. (1990) in application to low temperature water samples from the Wood River area, southeast of Crater Lake. Below (Table 10) we present a summary of the temperature predictions from these geothermometers.

The data in Table 10 show that the geothermometers do not provide a "consensus" temperature. As noted above, relatively low temperature equilibria apparently dominate the final concentration of most elements in the sampled Crater Lake end-members, and mixing of any primary fluid with colder fluids in the system may further complicate a geothermometric interpretation. While we cannot yet assess the amount of mixing that occurs between a higher temperature geothermal fluid and a sub-lakefloor aquifer, the very low concentration of ^{14}C in the pool fluids and pore waters (see table below) indicate that the ratio of mixing is not large. This would suggest that the temperatures of our system have primarily been affected by conductive cooling. Ingebritsen et al. (1989) show that this is also the case for many hot springs throughout the Cascades. These springs have been shown to contain very low concentrations of ^{3}H (tritium) which indicates they have not mixed significantly with shallow ground water aquifers.

The Na/Li geothermometer (Table 10) suggests that the fluid may have equilibrated at temperatures of up to 165°C and that the fluid has not re-equilibrated, with respect to these ions, at lower temperatures (Fouillac and Michard, 1981). The chalcedony geothermometer suggests an intermediate temperature and the Mg-Li and the Mg-corrected Na-K-Ca geothermometers suggest lower equilibration temperatures between 40-50°C. These may reflect the lower temperatures of secondary mineral alteration controlling the composition of the cooling fluids, and are primarily driven by the very high Mg^{2+} in the fluids. Finally, it may be significant that all of the applicable geothermometers predict that the Palisades Pool fluids equilibrated at a lower temperature than water from Llao's Bath in the South Basin.

The same geothermometers have been applied to the fluid at the East Lake hot spring and these also predict a wide range of temperatures (Table 10). While the Mg-corrected Na-K-Ca and silica geothermometers both yield temperatures near 160°C, the deepest parts of this system, which have been drilled for geothermal resource exploration, have measured temperatures of 265°C (Carothers et al., 1987). The surface outflow of the spring is 57°C (Mariner et al., 1990). Carothers et al. (1987) and Sammel et al. (1988) have discussed the hydrology of this system and included extensive subsurface mixing with meteoric water in their models. The concentration of Li in the East Lake spring is remarkably low which yields an anomalously low temperature using the Li-based geothermometers.

Table 10. Summary of Geothermometry

end-member samples (compositions from Table 7):

	Llao's Bath	Palisades Pool	East Lake Spring[4]
geothermometer:			
Chalcedony[1]	90°C	67	158
Na-K-Ca[2] with Mg-corr.	41[3]	NA[3]	162
Mg-Li[5]	50	40	8
Na/Li[6]	165	110	43

Notes:

1) The chalcedony (micro-crystalline quartz) geothermometer is often applied at lower temperatures since quartz equilibria are very slow below 150°C. (Fournier, 1981).

2) Na-K-Ca geothermometer with a correction applied for high Mg concentrations (Fornier,1981). As noted by Fornier, high concentrations of Mg in the water suggest that low temperature reactions have probably occurred and the application of any geothermometers should be cautioned.

3) The percentage of Mg in the sum of Mg+Ca+K (equivalents) determined the temperature correction to be applied (for percentages less than 50). This value is equal to 50 for Llao's Pool (at the limits of application of the geothermometer) and results in a downward temperature correction of 39°C. The value is over 70 for Palisades Pool and the geothermometer cannot be applied.

4) East Lake spring is located on the south shore of East Lake in Newberry Caldera, 95 km to the northeast of Crater Lake. The water temperature at the spring is 57°C and there are components of the deep hydrothermal system which reach temperatures of at least 265°C (Carothers et al., 1987).

5) Mg-Li geothermometer as introduced by Kharaka and Mariner (1989). We have applied the two Li geothermometers because the anomalously high concentrations of Li in Crater Lake have been attributed to geothermal input (Thompson et al., 1990). The Mg-Li model has been developed to describe the equilibria of an exchange reaction between Li^+ and Mg^{2+}. The concentration of Li in the East Lake spring is very low such that both Li geothermometers give anomalously low temperatures for this fluid.

6) Na/Li geothermometer as developed by Fouillac and Michard (1981). This is an empirical relationship which may not be based on any specific exchange reaction between Na^+ and Li^+.

Stable Isotope Measurements.

Isotopic measurements of water are useful as source tracers and can provide information on water-rock reaction temperatures. Thompson et al. (1990) reported hydrogen (∂D) and oxygen ($\partial^{18}O$) isotopic compositions of Crater Lake water and Mount Mazama springs. The relationship between ∂D and $\partial^{18}O$ in their spring water data fall on a line (Figure 58) which is very close to the universal meteoric water line of Craig (1966). Thompson et al. (1990) suggested that the isotopic composition of Crater Lake waters, which are isotopically heavier and lie off the meteoric line, can be accounted for by evaporation of the local meteoric water. Evaporation preferentially removes the lighter isotopes from the lake and causes the residual lake water to become heavier. Within the errors of their data, the lake appears to be isotopically well mixed.

High and low temperature water-rock interactions can cause changes in the isotopic composition of both rock and water. The extent of the isotopic shifts is linked to both the water-rock ratio and the temperature of interactions. High temperature geothermal waters commonly have higher $\partial^{18}O$ values and similar ∂D values compared to their meteoric precursors (Craig 1966). While ∂D of meteoric water is largely unaffected during hydrothermal alteration, the shift to higher $\partial^{18}O$ values is caused by equilibrium isotope-exchange reactions. The magnitude of the $\partial^{18}O$ shift is directly proportional to the temperature and inversely proportional to the water-rock ratio (Ohmoto and Rye 1974).

For this research project we selected samples for analysis which would be representative of various lake and pool end-members (Table 11). In addition, we analyzed a sample from an intercaldera Spring #30 near the lake surface on the south shore. The samples had been refrigerated in plastic bottles for 18 months prior to analysis. Although this storage is not ideal and could have resulted in some evaporation, our previous experience suggests these effects should be less than a few percent. Also, evaporation should affect all samples to the same degree and would not result in isotopic shifts that would affect a comparison among the samples. ∂D was measured in Dr. Paul Quay's laboratory at the University of Washington, and $\partial^{18}O$ was measured at Dr. Minze Stuiver's laboratory, also at the University of Washington. The precision of the ∂D measurements is $\pm$ 1 ‰ and that for the oxygen is $\pm$ 0.06 ‰. The values shown in Table 11 are per mil deviations from the Standard Mean Ocean Water (SMOW) standard.

The isotopic variability for all Crater Lake waters is very small. The total range of variability for ∂D is approximately 2 ‰ and for $\partial^{18}O$ is approximately 0.4 ‰. The small variations in the water column data are not statistically significant. Deep lake (>263 m) samples have a mean isotopic composition ($\partial^{18}O$ = -9.23 $\pm$ 0.07 ‰; ∂D = -81.0 $\pm$ 0.6 ‰) which is indistinguishable from the mean of the pool samples ($\partial^{18}O$ = -9.33 $\pm$ 0.12 ‰; ∂D = -81.4 $\pm$ 0.6 ‰). Although it is not statistically significant, there is a tendency toward more negative (isotopically lighter) values at greater water depths and in the pools. In contrast, the isotopic composition of Spring #30 ($\partial^{18}O$ = -13.34 ‰; ∂D = -98.3 ‰) is distinct from lake values and falls within the range of the meteoric water observed by Thompson et al. (1990) in Mount Mazama springs. Our lake water values average about 0.5 ‰ enriched in ^{18}O and about 1 ‰ lower in deuterium than the measurements of Thompson et al. (Figure 58). We believe these differences may reflect interlaboratory calibration effects, but they do not affect our interpretations which are drawn from our data set.

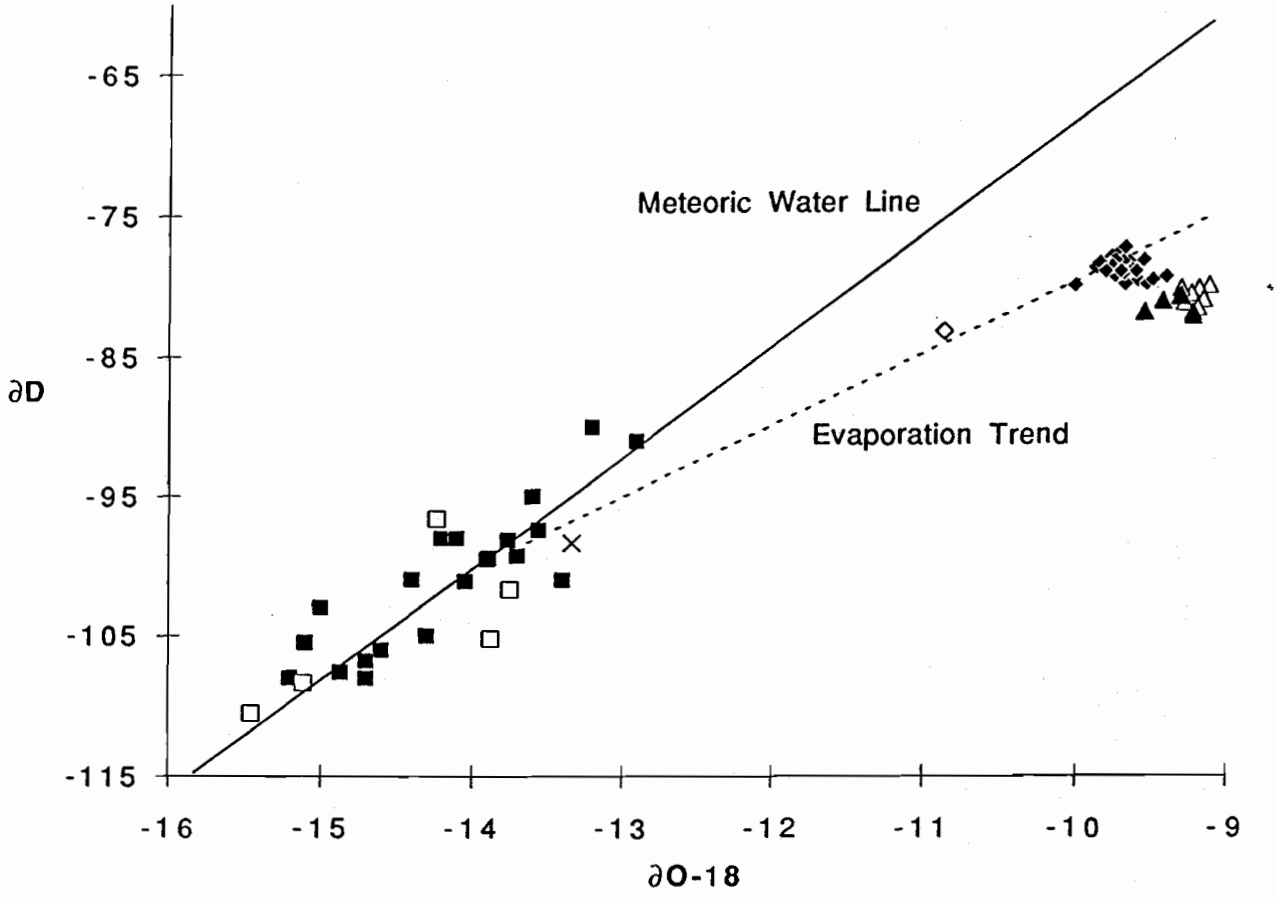

Figure 58. The stable isotopic composition of waters from Crater Lake and the vicinity. Data from both Thompson et al. 1990 and this study are shown. The Thompson et al. data include: filled squares = Mount Mazama springs from below the lake level; open squares = Mount Mazama springs from above lake level; filled diamonds = Crater Lake waters; open diamond = Diamond Lake, a lower elevation lake, 20 kilometers north of Crater Lake. Data from this study include: cross = Spring 30, a spring near lake level in the Chaski Slide area on the south shore; open triangles = Crater Lake water column samples; filled triangles = pool and mat samples collected by submersible. The meteoric water line and the evaporation trend are taken from Thompson et al. (1990).

Table 11. Stable Isotopic Measurements of Crater Lake Waters

Sample	$\partial^{18}O$	∂D
906 water column, 0 m depth	- 9.11	- 80.0
908 water column, 132 m depth	- 9.18	- 80.2
910 water column, 263 m depth	- 9.23	- 80.6
904 water column, 388 m depth	- 9.15	- 81.0
903 water column, 449 m depth	- 9.28	- 81.2
902 water column, 520 m depth	- 9.19	- 81.6
901 water column, 580 m depth	- 9.30	- 80.2
CD223 S1, Llao's Bath	- 9.22	- 82.2
CD226 S1, Llao's Bath	- 9.42	- 81.1
CD226 S3, Brain mat	- 9.54	- 81.9
CD 228 S1, pool from Palisades Pt.	- 9.31	- 80.8
CD228 S3, mat from Palisades Pt.	- 9.22	- 81.9
CD 230 S1, Llao's Bath	- 9.30	- 80.7
Spring #30	- 13.34	- 98.3

Source of the Thermal Waters—the ∂D Results.

The equivalence of ∂D in pool and lake waters is an important finding. Since hydrogen isotopic composition is not shifted significantly by water-rock interactions, this variable is an important tracer of the origin of the water. The distinctive isotopic composition of Crater Lake compared to all Mazama springs and Cascade meteoric water in general (Ingebritsen et al., 1989), provides very strong evidence that the pool and mat fluids originated within Crater Lake. The data of Thompson et al., 1990 (Figure 58) show that all springs — those low on the flanks as well as those within the Mount Mazama caldera — have ∂D values that are 10 to 30 ‰ lower than those of Crater Lake. The correlation between ∂D and elevation in the western Cascades (Ingebritsen et al., 1989) indicates that only at elevations below 700 m above sea level would meteoric waters with Crater Lake's isotopic composition be found. This elevation is nearly 1200 m below the elevation of the lake surface and 600 m below the bottom of the lake. Meteoric waters with hydrogen isotopic compositions similar to those observed in Crater Lake occur only at elevations which are several tens of kilometers away.

Consequently, the hydrogen isotopic data provide strong evidence that the thermally and chemically enriched pools and mat fluids originated as Crater Lake waters. This inference, when combined with the enrichments of dead carbon, mantle helium, and various ions, places important constraints on the processes which lead to the formation of these fluids. We can say with assurance that the fluids are not the result of springs that draw their fluids from precipitation on Mount Mazama. The very low concentration of ^{14}C in the pools (see below) places constraints on the amount of dilution of pool samples by normal lake water. Therefore, the isotopes document that the lake fluids sink into the crust beneath the caldera, participate in hydrothermal alteration, and ascend back into the lake.

Geothermometry—the Oxygen Isotopic Results.

Because the oxygen isotopic composition of water is much more strongly affected by interaction with rock, these data have the potential to clarify the conditions under which the sinking fluids have interacted with rocks. There are, however, complications to the use of oxygen isotopic composition. Although waters may initially undergo shifts toward heavier ^{18}O values through high temperature reaction with rocks, lower temperature re-equilibration may modify the signal. Also, the amount of $\partial^{18}O$ shift is dependent on the water-to-rock ratio (i.e., the amount of rock altered by a given amount of water). The magnitude of the $\partial^{18}O$ change also depends on the specific isotopic exchange reactions which dominate the water-rock interactions. As we discussed above, the end-member fluids represented by the Crater Lake pool waters are indicative of lower temperature water-rock interactions rather than the high ionic strength fluids that are observed in geothermal systems with temperatures greater than 200°C. Consequently, isotopic equilibration resulting in large changes of the fluid isotopic composition is not expected. In addition, with temperatures below 200°C isotopic exchange equilibrium is slow to achieve (Cole et al. 1987).

Despite these uncertainties, the measured $\partial^{18}O$ values of the pools and their similarity to lake waters allow an evaluation of the range of possible conditions which constrain the observed pool and mat fluid compositions. For a closed system the isotopic composition of water after equilibration with rock ($\partial_{f,w}$) is given by the relationship (Ohmoto and Rye, 1974):

$$\partial_{f,w} = \frac{\partial_{i,r} - \Delta_{r\text{-}w} + [\,(w/r)\ (\partial_{i,w})\,]}{1 + (w/r)}$$

where,

$\partial_{i,r}$ is the initial (unaltered) composition of the rock, which we assume to be 6.5 ‰, a typical value for Crater Lake volcanics (Bacon et al. 1989);

$\partial_{i,w}$ is the initial composition of the water, which we assume to be -9.2‰, the deep lake value;

$\Delta_{r\text{-}w}$ is the temperature-dependent fractionation factor for rock and water, which we will assume to be the plagioclase (An_{30}-H_2O) relationship of O'Neil and Taylor (1967);

w/r is the ratio of exchanged oxygen atoms in the water to those in the rock (we assume the rocks have about 50 weight percent oxygen, typical for andesites to rhyolites).

Figure 59 shows the results of this calculation for various temperatures and water-rock ratios. These calculations suggest $\partial^{18}O$ values similar to those observed in the pools could result from high water rock ratios (>10) over a range of temperatures. Low water rock ratios require temperatures of approximately 100°C. For the isotopic fractionation chosen (plagioclase-water), the change from an increase to a decrease in the $\partial^{18}O$ of the water occurs at approximately 100°C. Regardless of the water-rock ratio, at temperatures of approximately 100°C, there will be essentially no change in the isotopic composition of Crater Lake water by interaction with the typical Mazama rocks. Although the lack of change in the $\partial^{18}O$ of pool fluids could simply be a consequence of slow isotopic equilibration in a relatively low-temperature hydrothermal system, the data are compatible with isotopic exchange with rocks at approximately 100°C. This temperature is compatible with estimates of alteration temperature from chemical geothermometry calculations which range from 40°C to 165°C. The result is also comparable to data for a 57°C thermal spring in Newberry Caldera (Mariner et al., 1989). The $\partial^{18}O$ of that spring is nearly identical to that of the local meteoric water (Carothers et al., 1987).

The lack of shift in the $\partial^{18}O$, however, could also be the result of high water-rock ratios in the hydrothermal system. For a water-rock ratio of 10 (Figure 59), there would be only a 0.6 ‰ shift in Crater Lake water at a temperature of 300°C. That shift, however, is toward more positive $\partial^{18}O$ values. Although the variations aren't statistically significant, it appears that if there is any $\partial^{18}O$ shift in Crater Lake pools it is toward more negative values. Fine distinctions, however, are unwise since we do not know the specific equilibrium fractionation which controls the isotopic composition of the water. We have chosen the plagioclase-water fractionation in our example (Figure 59) because it is intermediate between other mineral fractionations that have been used to estimate water-rock $\partial^{18}O$ shifts (Field and Fifarek, 1985), and because positive europium anomalies in Crater Lake fluids indicate feldspar alteration probably has affected the fluid composition. The plagioclase-water fractionation is very similar to the basalt-water fractionation and is a good choice when the specific mineral-water fractionations are not known (Cole et al. 1987).

Another way of looking at these oxygen isotopic results is to consider that the water in the lake is in isotopic balance with the underlying volcanic crust. Water which circulates deeply into the crust and undergoes isotopic exchange at >200°C will become enriched in ^{18}O. In contrast, shallow circulation and reactions at temperatures <100°C will produce ^{18}O depletions in the water. Deeply circulating fluids must necessarily pass through cooler crust both during recharge and the upward portions of their flow path. The net result could be a balance between ^{18}O depletions in the water in the upper levels and ^{18}O enrichments lower in the crust. If such a balance does exist, it would also be appropriate to consider whether the oxygen isotopic composition of the entire lake is a consequence both of hydrothermal circulation and the evaporative effects. In order to evaluate this possibility, we must have better estimates for the mean isotopic composition of precipitation sources and the evaporative shifts in the oxygen isotopic composition. Such an evaluation is beyond this study, but is worthy of future consideration.

In summary, the stable isotope data provide some constraints on the source and conditions which form the thermally and chemically enriched fluids that are associated with the mats and pools. Hydrogen isotopic data indicate that these fluids are chemically altered lake waters. Oxygen isotopic data are compatible with water-rock interactions at approximately 100°C. Higher temperature reactions would require a geothermal system with high water-rock ratios or subsequent low temperature re-equilibration of the isotopes.

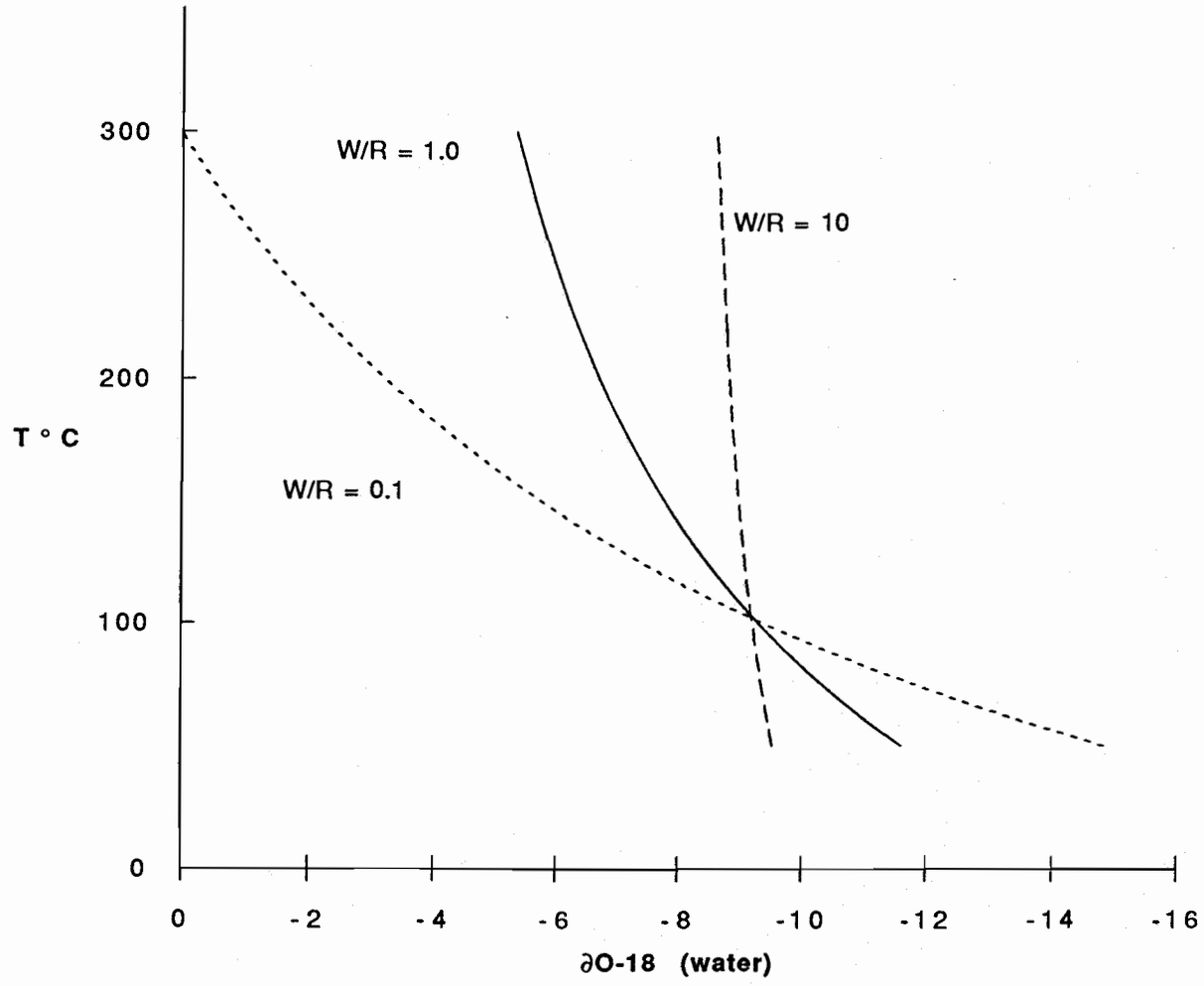

Figure 59. The oxygen isotopic composition of Crater Lake water which would be in exchange equilibrium with plagioclase at various temperatures. The lines shown track the isotopic composition of a water with an original composition that is equivalent to our measured deep lake value (-9.2 ‰), assuming exchange with Mount Mazama rocks ($\partial^{18}O$ = -6.5 ‰; Bacon et al. 1989) under differing water-rock ratios. Above a temperature of approximately 100 °C this mineral-water fractionation results in an increase in the $\partial^{18}O$ of the water; below this temperature the equilibrated water becomes isotopically lighter (more negative $\partial^{18}O$ values).

Rare Earth Elements.

Measurements of Lake Fluids.

The rare earth elements (REE) tend to be a chemically coherent group of elements which have been useful in studying of a broad range of petrological and geochemical problems. Most of the REEs occur only in the +3 oxidation state, but cerium and europium each have two oxidation states. Cerium can occur in either the +3 or +4 oxidation state, while Eu can exist in either the +2 or +3 oxidation state. Consequently, these two REEs behave somewhat anomalously in nature.

The occurrence of large positive Eu anomalies relative to Sm and Gd, its adjacent REEs, in seawater hydrothermal fluids (Michard et al., 1983; Campbell et al., 1988) is of particular interest to our Crater Lake studies. Because the REE abundance patterns in these high-temperature fluids are similar to plagioclase/magma partition coefficients (Schnetzler and Philpotts, 1970), it is generally believed that the hydrothermal pattern results from high temperature hydrothermal alteration (albitization) and leaching of plagioclase. (i.e., Eu in the +2 oxidation state can substitute for calcium in plagioclase.) REE measurements of hydrothermal solutions from continental geothermal systems (Michard, 1989) exhibit variable REE contents and abundance patterns. Low-temperature and alkaline geothermal fluids tend to have small or, in some cases, even negative Eu anomalies despite high concentrations of REE in some of these fluids. High temperature ($t > 230°C$) acidic systems ($pH < 6.0$) have large Eu anomalies and overall REE abundance patterns that are very similar to those observed in seawater hydrothermal systems.

Dr. Gary Klinkhammer (OSU) measured the REE abundances in a few Crater Lake water samples (Table 12; Figure 60) using inductively coupled plasma mass spectrometry (ICPMS). The REE abundance patterns of these samples, when normalized to chondritic meteorites (this normalization is used to document variations from bulk Earth REE composition), bear a strong resemblance to those observed in continental geothermal fluids and in seawater hydrothermal systems. Crater Lake waters have both light REE enrichments and a marked positive Eu anomaly. The highest REE concentrations were observed in the pore water sample (BC5), which is from a core with high major ion concentrations (Appendix F). REE concentrations of Llao's Bath water (CD226 S1) are similar to those observed in open lake water. If positive Eu anomalies are characteristic of aqueous fluids which have interacted with igneous rocks at elevated temperatures, these data could be important evidence that the REE chemistry of Crater Lake waters is dominated by high-temperature water-rock reactions.

Table 12. The REE Contents of Crater Lake Fluids

Sample	La	Ce	Pr	Nd	Sm	Eu	Gd	Dy	Ho	Er
Lake 399 m.	57	39	4.4	21	7	31	12	8.0	1.0	3.0
CD222,S1	190	97	17	73	20	29	23	26	4.8	14
CD230,S1	33	35	4.5	18	8	24	6.0	6.4	1.5	3.5
BC5, 10cm	1000	2700	265	1200	250	250	179	171	41	102

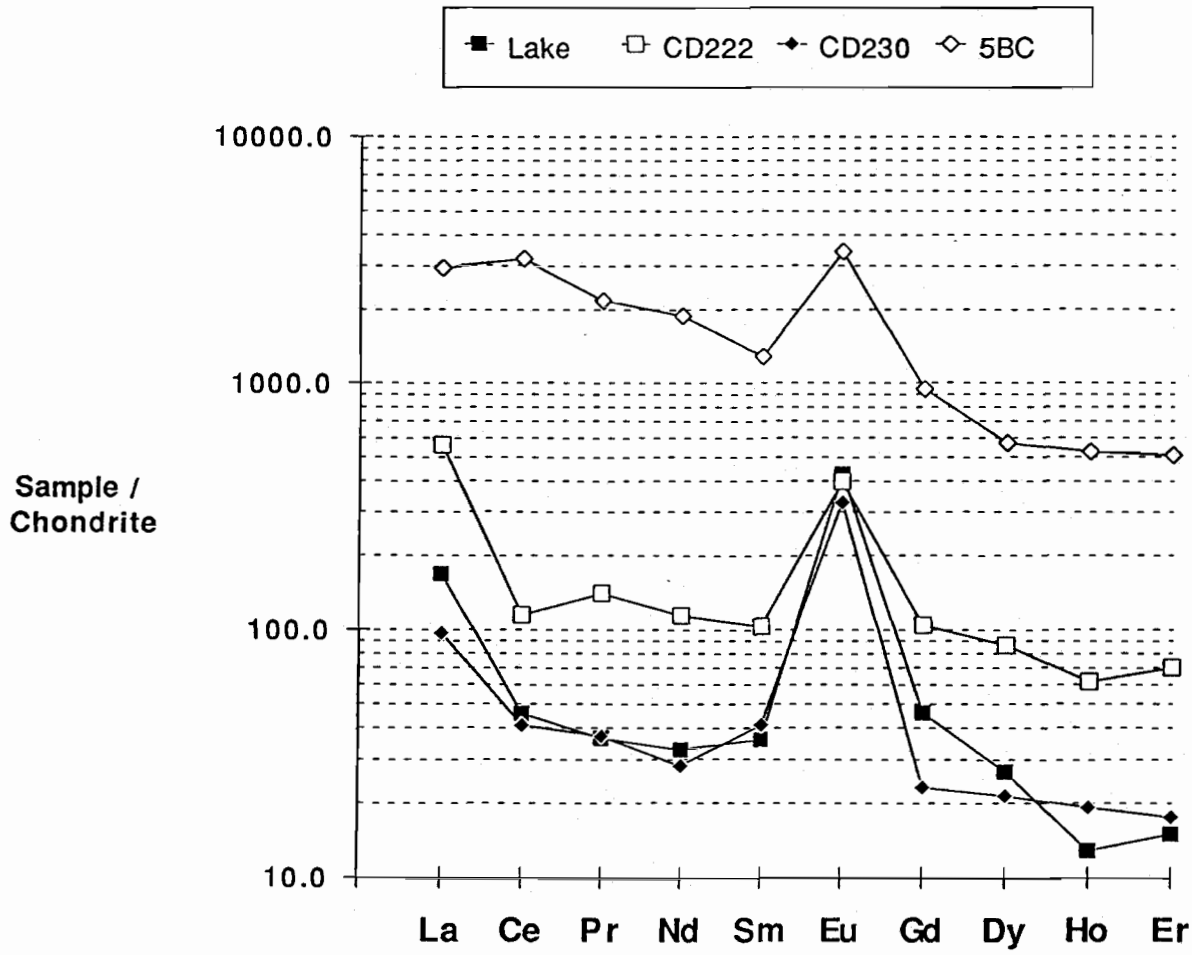

Figure 60. The abundances of rare earth elements in Crater Lake samples normalized to chondritic meteoritic abundances (Haskin et al. 1966). The lake sample is from 399 m depth in the South Basin. CD222 and CD230 are submersible samples taken from the high temperature mat area and Llao's Bath respectively. BC 5 refers to a pore water sample taken from a depth of 10 centimeters in a box core. The core was deployed in a large pool near Llao's bath and sampled the pool bottom sediments.

Several lines of evidence suggest that low-temperature alteration of igneous rocks will not generate positive Eu anomalies. In general, the REE are considered refractory elements which are resistant to leaching by both low and high temperature alteration (Ludden and Thompson, 1979; Michard, 1989). Nonetheless, the low concentrations of REEs expected in cold ground waters and other meteoric waters should reflect the composition of the rocks they weather. Analyses of REE abundances in Mt. Mazama volcanics reveal only light REE enrichments and no positive Eu anomalies, which is typical of andesites (Bacon and Druit, 1988). Therefore, anomalous REE patterns in ground waters, if they exist, could only occur by selective alteration of different volcanic phases. Although plagioclase phenocrysts within these rocks may have positive Eu anomalies, the feldspars are not likely to be leached of their REEs as rapidly as the fine-grained groundmass and glass that comprise most of the Mount Mazama lavas and ash. Thus, the REE abundance patterns of cold waters in contact with Mt. Mazama volcanics are probably similar to the bulk rock composition. Although we do not have measurements of REEs in Mt. Mazama cold springs, our conclusion is supported by measurements of the REE contents of Oregon rivers that drain volcanic terrain (Keasler and Loveland, 1982), which reveal only light REE enrichments and no Eu anomalies when normalized to chondrites. REEs from rivers around the world do not exhibit positive Eu anomalies (Goldstein and Jacobsen, 1988; Elderfield et al., 1990). Additional evidence that Eu is not selectively leached by low-temperature reactions comes from studies of ocean floor basalts. Ludden and Thompson (1979) observed that basalts altered by low temperature interaction with seawater do not have negative Eu anomalies, which would be expected if Eu was being leached relative to the other REEs.

Consequently, it appears that the REE patterns of Crater Lake fluids reflect high-temperature hydrothermal alteration rather than low temperature alteration processes. We propose two mechanisms to account for these patterns, both of which involve the convection of lake waters through the volcanic crust beneath Crater Lake: (1) the REE contents are controlled by high-temperature interaction between primary igneous rocks and deeply circulating lake waters; (2) the REE contents reflect dissolution of secondary alteration phases that were deposited in Mount Mazama volcanics during an earlier stage of hydrothermal alteration. The first mechanism can account for the observed REE patterns as well as the other chemical and thermal enrichments in lake fluids through processes similar to those which form continental geothermal fluids and seawater hydrothermal fluids. The second mechanism is based on the fact that precipitation of minerals from hydrothermal fluids can reflect the Eu anomalies in these fluids (Sverjensky, 1984). Because Eu^{+2} has an ionic radius nearly identical to Ba^{+2}, hydrothermal barites have large positive Eu anomalies (Guichard et al., 1979; Morgan and Wandless, 1980). Dissolution of barite, carbonate veins, and other secondary minerals by waters which circulate into zones of earlier hydrothermal alteration beneath the lake could produce the observed REE patterns. The REE results alone cannot distinguish between these two possibilities. We will discuss additional evidence which bears on the two hypotheses later in the report.

Solid Phase Rare-Earth Element Analyses.

We measured the rare earth element (REE) abundances of selected mat, crust, and pool samples (Tables 6 and 7; Appendix I). The iron-rich crusts and bacterial mats have low REE concentrations (Figure 61) however, these samples have significant variations in the relative abundances of the different REEs. For example, the La/Eu values in most iron-rich mat and crust samples range from 16 to 38 (Figure 62). The data shown in Figures 62 and 63 suggest that there are three end-members: First, an aluminosilicate component which has low iron contents, high Al contents, and

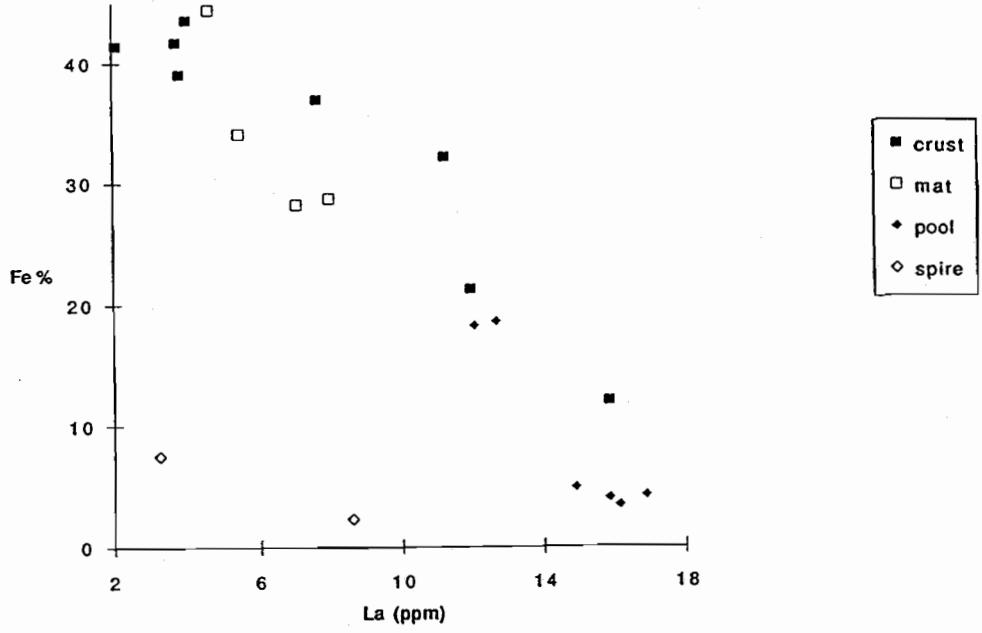

Figure 61. Iron vs. lanthanum concentration in various solid-phase samples from Crater Lake that show strong inverse correlation. Samples with a low abundance of iron are enriched in aluminosilicate debris. Note that the spire compositions are distinct and do not fall on the mixing line defined by the other samples.

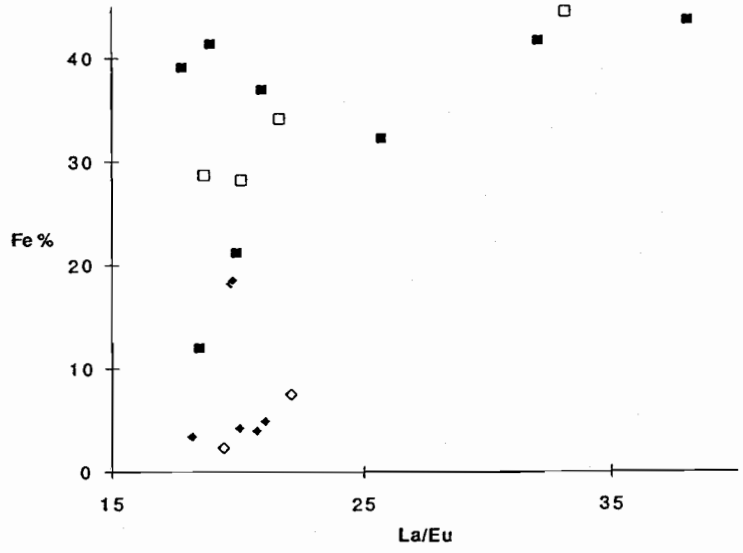

Figure 62. The iron abundances vs. La/Eu ratios in Crater Lake solid phase samples. The different symbols refer to the same sample types as in the previous figure. Note the range in La/Eu for samples with high iron abundances.

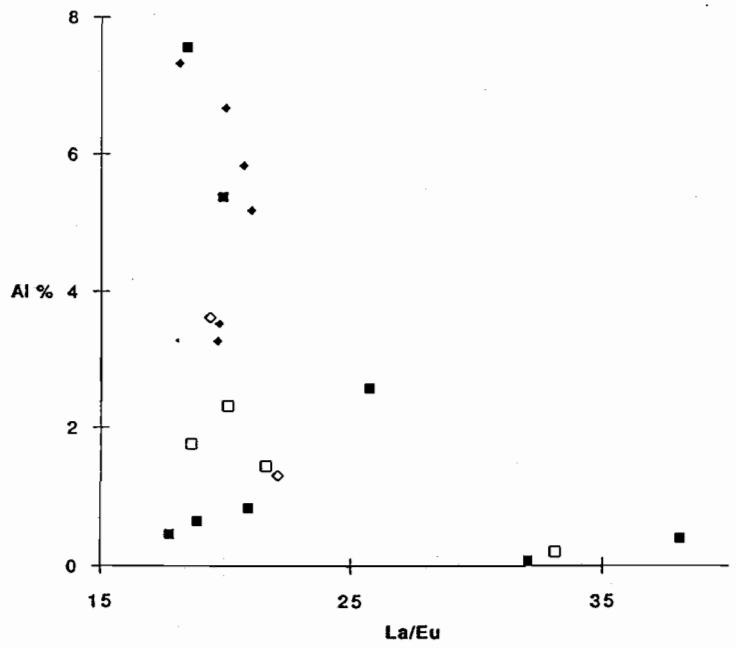

Figure 63. The Al abundances vs. La/Eu ratios in Crater Lake samples. The different symbols refer to the same sample types as in the previous figures. Aluminosilicate material has a well defined low ratio of La/Eu.

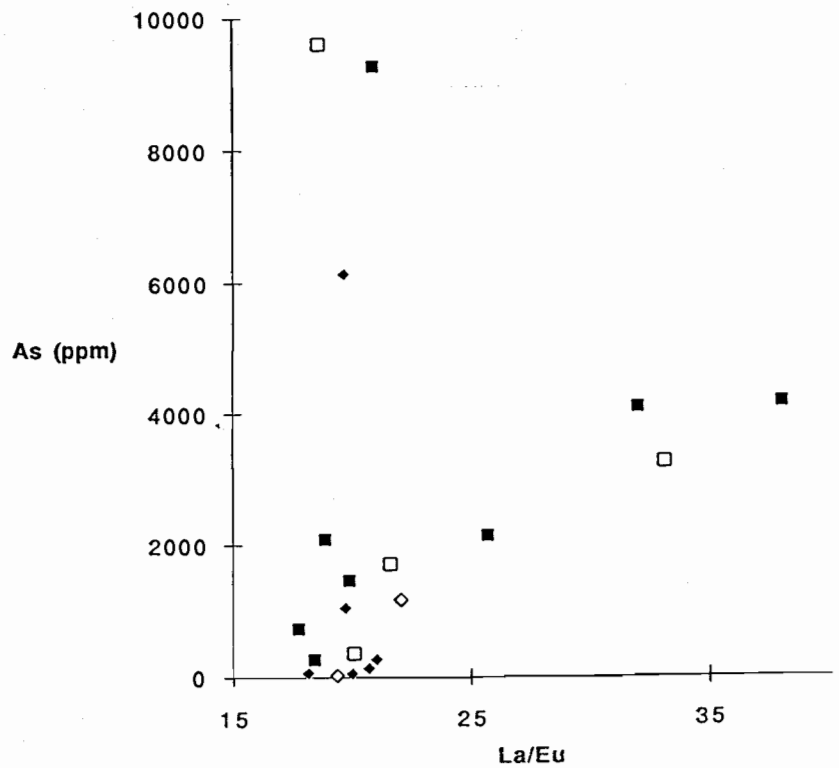

Figure 64. Arsenic concentrations vs La/Eu ratios in Crater Lake samples. The different symbols refer to the same sample types as in the previous figures. Note that the samples with the highest As abundances have low La/Eu values.

relatively low La/Eu values; second is an end-member with high iron and high La/Eu; and third, an end-member with high iron and low La/Eu.

It is probable that the minor element contents of iron oxyhydroxide precipitates reflect the composition of the surrounding fluids. Co-precipitation of dissolved REEs with iron hydroxide is a standard analytical technique for quantitative stripping of these elements from aqueous solution. In nature this process occurs during precipitation of iron oxyhydroxides from marine hydrothermal fluids. The scavenging and co-precipitation of seawater REEs by these oxyhydroxides result in metalliferous sediments with a distinctive seawater REE pattern (Dymond et al., 1973; Ruhlin and Owen, 1986). Consequently, we suggest that variations in the REE abundances of the mat and crust samples reflect distinct venting fluids. Although all the fluids from which these deposits form are enriched in iron, some are apparently more enriched in As and Eu in comparison with other fluids. It is noteworthy that those mats and crusts with relatively high Eu (low La/Eu) are also enriched in As (Figure 64). The association of arsenic with hydrothermal systems suggests that these crusts and mats have precipitated from fluids with a stronger hydrothermal signal. This suggestion is compatible with the recent finding that continental geothermal systems can have strong Eu enrichments (Michard, 1989) and with the data of Klinkhammer (Table 12) which document Eu anomalies in Crater Lake fluids.

The Distribution of Dissolved Carbon-14.

Introduction.

As discussed earlier, ΣCO_2 in the deep lake is enriched by approximately 10 % over values measured in the upper water column. In addition, the thermally and chemically enriched pools have ΣCO_2 contents ranging from 7 to 14 times higher than deep lake water values (Appendix I). The sources of this carbon enrichment can be clarified through isotopic measurements of the fluids. Carbon-14, a cosmogenic isotope produced in the upper atmosphere, has a half-life of approximately 5700 years. Rapid mixing of ^{14}C within the atmospheric CO_2 reservoir makes this isotope useful both for tracer studies and for age determinations of organic material. The global ^{14}C system has been affected by both nuclear weapons testing and fossil fuel burning. The net effect of these two inputs is to increase the present-day ^{14}C content of the atmosphere over what it would be in an unperturbed system. Because of the large dynamic range of ^{14}C for natural waters, we collected samples during the 1989 field program which would enable us to evaluate this isotopic system and address the source of the carbon enrichments observed in the pool fluids.

In part, our measurements were stimulated by the earlier studies of Simpson (1970) who measured ^{14}C in a few large water samples collected from the surface and deep waters of Crater Lake. His data revealed ^{14}C "ages" of the deep lake carbon that were incompatible with an atmospheric source of the CO_2 and with rapid lake mixing implied by other tracers. Simpson suggested that fumarole or hot spring inputs near the bottom could account for "old" ^{14}C ages of deep-lake water. In addition, Simpson measured ^{14}C ages of surface sediments that had apparent ages of approximately 1,800 years. He suggested these surprisingly old ages reflected the mean ^{14}C age of lake water which was affected by the input of old carbon. His sediment results are similar to the more recent unpublished data of S. Trumbore (personal communication, 1991), who found that the bulk organic carbon age of a sediment sample in a core from the Wizard Island platform is roughly 11,000 years (i.e., older than the 6,900 year age of Crater Lake caldera). Since the true age of

sediment at this core depth is 5-6,000 years, Trumbore's data suggest that the carbon present in the lake water 5-6,000 years ago was even more strongly affected by dead carbon inputs.

We collected samples for ^{14}C analyses in evacuated one-liter Pyrex® bottles containing 2 ml of concentrated $HgCl_2$ as a biocide. The samples were shipped to Dr. Bernd Kromer at the University of Heidelberg where graphite targets were prepared. The $^{14}C/^{12}C$ ratios were measured at the ETH Honggerber accelerator facility in Zurich, Switzerland. The results are listed in Table 13, expressed as per mil deviations from "modern" carbon (i.e., 0.95 times the NBS oxalic acid standard) and corrected for isotopic fractionation effects.

We have also converted the data to ^{14}C "ages" (Table 13) using the relationship:

$$T \text{ (years)} = 1/\lambda \ln (1 + \Delta\, ^{14}C/1000)$$

The decay constant, λ, is based on the ^{14}C half-life of 5,568 years (Libby, 1955). It is important to recognize that the "ages" are not the true ages of the fluids, but are actually artifacts of the mixing of fluids with varying ^{14}C activities.

Results.

The large variability in $\Delta^{14}C$ in the different lake samples is the most dramatic aspect of the data (Table 13). Since"dead" carbon has a $\Delta^{14}C$ of -1000‰, the carbon in Llao's Bath is almost entirely non-radioactive. Llao's Bath has a $\sum CO_2$ which is enriched by a factor of ~7 over the South Basin bottom water (Appendix I). If the carbon in this sample is a mixture of deep South Basin water (-140‰) and dead carbon, the mass balance requires that approximately 95% of Llao's Bath carbon is derived from a "dead" carbon source. Deep lake water has unusually old carbon ($\Delta^{14}C$ = - 89‰ to -140‰) for a system that exchanges with the atmosphere every few years. Our North Basin value of - 89‰ compares favorably with the Simpson (1970) measurement of $\Delta^{14}C$ = - 79‰ for a North Basin sample. The more negative $\Delta^{14}C$ value for the South Basin is consistent with our other data that show an enhanced thermal and chemical signal in this part of the lake.

Table 13. ^{14}C Results

Sample	Location	$\Delta\, ^{14}C$ ‰	Age (years)†
Spring 42	South shore of Lake	70.8 ± 8	+ 550 ± 60
CD228 S2	Deep Lake, N. Basin	- 89.1 ± 7	- 750 ± 60
CD226 S2	Deep Lake, S. Basin	- 139.9 ± 6.6	- 1210 ± 60
CD226 S1	Llao's Bath, S. Basin	- 955.1 ± 16	- 25,000 ± 3000
Benthic Barrel	South Basin (see Fig.3)	- 265.7 ± 5.8	- 2,480 ± 60
East Lake	south shore of lake	- 875.1 ± 21	- 16,700 ± 1350

† A positive number indicates a future age and indicates an input of bomb carbon.

Assuming the deep lake values are the result of mixing between modern atmospheric carbon, which has a $\Delta^{14}C$ of approximately +105‰ (Berger et al., 1987) and a source of "dead" carbon such as that observed in Llao's Bath, the fraction of "dead" carbon can be estimated. This mixing calculation indicates that approximately 20% of the deep lake carbon is free of ^{14}C. Consequently, the $\Delta^{14}C$ value of the deep lake is maintained both by lake mixing processes, which transfer atmospherically equilibrated surface waters to the deep lake, and by deep injection of "dead" carbon, which our data shows is associated with the thermally and chemically enriched pools.

Table 13 also shows the $\Delta^{14}C$ content of the caldera wall spring #42. The caldera spring measurement is similar to the current $\Delta^{14}C$ value for the atmosphere, indicating that this water exchanged relatively recently with with atmospheric carbon dioxide. Because atmospheric $\Delta^{14}C$ values have varied greatly during the past 40 years as a result of atmospheric testing of nuclear bombs (Berger and Libby, 1966; Berger et al., 1987), refined estimates of the equilibration age of the spring water or of possible"dead" carbon inputs are not possible. In general, however, the Spring #42 concentration is comparable to the $\Delta^{14}C$ measurements made by Simpson (1970) on Annie Springs and Murchison Springs. Simpson measured values of approximately +170‰ for these two Mt. Mazama springs. This was very similar to Crater Lake surface water and a little lower than the ^{14}C content of the atmosphere at that time. The Spring #42 result is compatible with the He data (Figure 26) from this spring which also indicate equilibration with the atmosphere.

The ΣCO_2 content of the Benthic Barrel sample increased by 18% during the 6.7 days that the barrel water was isolated from the lake (Section IV.3) Table 13 shows its $\Delta^{14}C$ equaled -265.7 ± 5.8‰ after 6.7 days. Mass balance mixing calculations indicate that nearly all of theΣCO_2 increase resulted from the input of "dead" carbon. This is an important result because it indicates that the sediment pore waters, which have migrated into the barrel, also have predominantly dead carbon. Since there are no feasible dead carbon sources within the sediments, such a finding cannot be explained by any possible reactions within the sediments. Only water advection through the sediments can supply the ΣCO_2 (as bicarbonate ions) added to the Benthic Barrel, and this same process must be contributing "dead" carbon-bearing fluids to the lake bottom waters.

In addition, a sample of water from an East Lake thermal spring was analyzed, because of its proximity to Crater Lake (95 km northeast of Crater Lake) and its similar geologic setting within Newberry Caldera. The ^{14}C sample was collected at the thermal spring location on the south shore of East Lake. Like the Llao's Bath sample, the carbon in the East Lake sample has very little ^{14}C. If the sample contains a mixture of "dead", hydrothermal carbon and atmospheric carbon, the $\Delta^{14}C$ measurement indicates that 89% of the total carbon is hydrothermal.

Discussion.

The $\Delta^{14}C$ data clearly demonstrate that there are active inputs of "dead" carbon into the deep lake and that the sources of this carbon could be pore water advection and mixing of thermally and chemically-enriched pool waters with deep lake water. The stable hydrogen isotopic data discussed above show that it is not possible for the anomalous pool fluids to have been derived from an aquifer source. As a result, the concept that the "dead" carbon is derived from deep aquifers with an atmospheric equilibration age of more than 25,000 years is untenable. Therefore, we will consider three possible sources of the dead carbon: (1) the carbon is a non-condensible magmatic gases which may evolve from deep-seated magmatic sources beneath Mt. Mazama; (2)

the carbon is carried in hydrothermal fluids that have interacted with primary igneous rocks at high temperatures; and (3) the carbon is carried by fluids that have dissolved carbonate vein material that was deposited in Mazama volcanics during an earlier stage of hydrothermal alteration.

The first hypothesis requires the mobility of magmatic CO_2 through Mazama volcanics and into the deep lake or into ground waters that enter the lake. Although such a mechanism could explain the ΣCO_2 enrichments of "dead" carbon in the deep lake and pools, it does not account for the close association of these enrichments with the thermal anomalies observed in the deep lake. It also does not account for the advection of carbon-enriched fluids which is indicated by the Benthic Barrel data. The input of carbon to the Benthic Barrel cannot occur except by fluid transport which brings both bicarbonate ion and other ions into the bottom of the lake. The observation that three Mazama springs (spring #42 in Table 13 and the two springs measured by Simpson, 1970) all have carbon contents which are essentially in equilibrium with the atmosphere is evidence that a transfer of magmatic volatiles to these aquifers does not occur. The lack of "dead" carbon in these springs does not preclude gaseous transfers into some Mount Mazama aquifers, but it does demonstrate that the process is not a pervasive influence on springs either inside or outside the Crater Lake caldera. Finally, if CO_2 were entering the lake as a noncondensable gas, the pH of Crater Lake water would be much more acid than is observed. The ΣCO_2 of the lake is dominantly in the form of bicarbonate ion, which must form by interaction of CO_2-bearing waters with volcanic rocks.

Nonetheless, it is known that CO_2 is a major gaseous component in magmatic systems. Meteoric waters circulate through cracks that form in cooling magmatic bodies. The waters become enriched in "dead", magmatic carbon. The interaction of these fluids with hot igneous rocks results in a hydrothermal fluid which has a high ionic content and whose ΣCO_2 will predominantly be of magmatic origin. This process can explain the "dead" carbon and associated thermal and chemical enrichments of the pool and pore water samples. As discussed above, the hydrogen isotopic data indicate that the anomalous water collected from the pools was originally lake water. Since mass balance calculations indicate that only 5% of the carbon in the pool samples can have a modern source, the hypothesized hydrothermal process must result in re-equilibration between a large magmatic carbon reservoir and any atmospheric carbon which was originally in the circulating lake water. In effect magmatic carbon sources completely dominate any initial atmospheric carbon from lake waters.

The third hypothesis requires the dissolution of secondary carbonate minerals by water circulating through the rocks which lie beneath Crater Lake. This process requires that the dissolved carbonates either be old (>40,000 years) or the result of precipitation from "dead", magmatic carbon. Mount Mazama has a 300,000 to 400,000 year history of volcanism, and hydrothermal alteration was a common feature of that volcanic activity. We cannot ascertain the extent of the hydrothermal alteration of the crust beneath Crater Lake from the few surficial rocks collected by the submersible; however, hydrothermal alteration of rocks near the current lake surface has been reported (Bacon and Lanphere, 1990). Although the presence of carbonate veins in these rocks has not been documented (C. Bacon, personal communication, 1991), the common association of carbonate precipitation with hydrothermal alteration indicates that carbonate minerals probably exist in some of the Crater Lake rocks.

The dissolution of carbonates by meteoric water would normally be driven by dissolved CO_2 originally derived from the atmosphere. This is typically represented by the following reaction:

$$CO_2 + H_2O + CaCO_3 = Ca^{++} + 2HCO_3^-$$

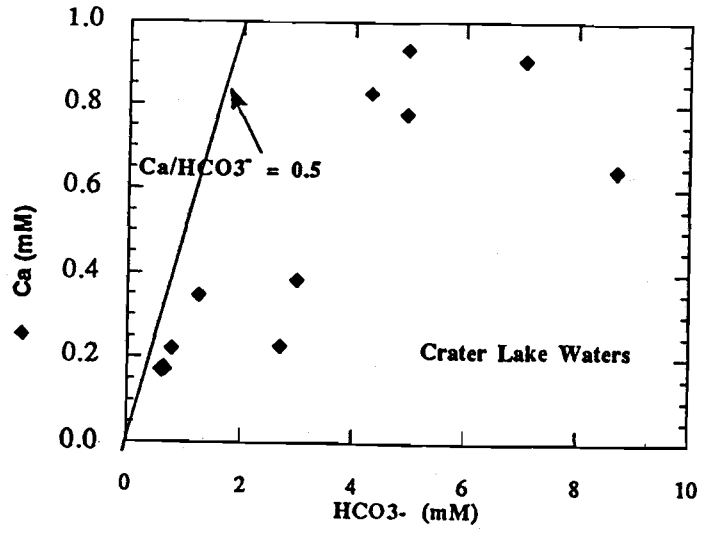

(a)

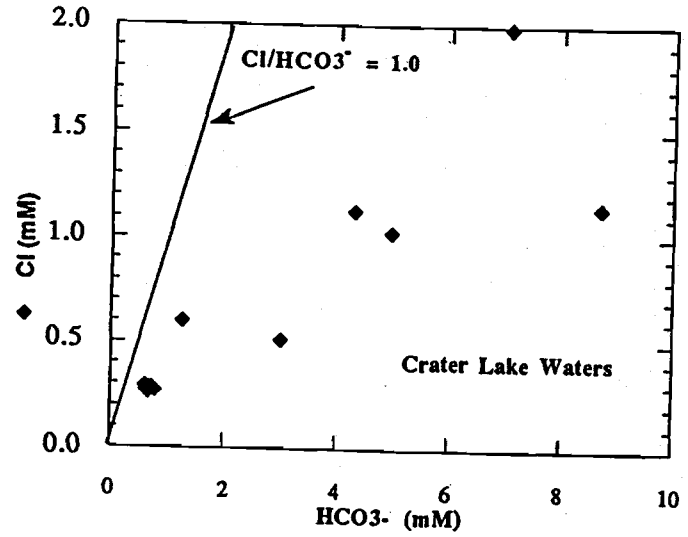

(b)

Figure 65. (a) The bicarbonate ion content vs. the calcium ion content in Crater Lake water column and pool samples. Lake waters fall in a small field of samples with less than 0.2 mM of Ca^{++} and about 0.6 mM of HCO_3^-. The line shows the stoichiometry expected if the Ca^{++} and HCO_3^- contents of the fluids were caused by carbonic acid dissolution of calcium carbonate. (b) The bicarbonate ion content vs. chloride ion content in Crater Lake water column and pool samples. The line shows the stoichiometry expected if the HCO_3^- contents of the fluids were the result of dissolution of calcium carbonate by hydrochloric acid.

Significantly, this equation demonstrates that one mole of atmospheric carbon is required to dissolve one mole of carbon from a calcium carbonate precipitate. The impact of this dissolution process would be to increase the ΣCO_2 content of the circulating fluid, but the $\Delta^{14}C$ of those fluids would not be -1000‰ (i.e., dead carbon). After dissolution of a carbonate precipitate containing only "dead" carbon, the $\Delta^{14}C$ in the water (the bicarbonate) would be approximately -500‰ which is clearly distinct from that observed in Llao's Bath and from the value inferred for pore waters by the benthic barrel sampling. In addition, the equation suggests that the molar ratio of Ca to HCO_3 should be 0.5. However, as shown in Figure 65a, the thermally and chemically enriched fluids sampled in the deep lake have much greater proportions of bicarbonate ion. Thus, it is highly unlikely that this process could be responsible for the observed increase in ΣCO_2 concentrations of the saline pools and the advected pore water.

In an alternative process, pre-existing carbonates could be dissolved by a strong acid such as HCl. HCl could be injected into crustal waters from a cooling magma body that may exist beneath Mount Mazama. The appropriate equation for this reaction is:

$$HCl + CaCO_3 = Ca^{++} + HCO_3^- + Cl^-$$

With this process the molar ratios of calcium, carbon, and chloride should be 1:1:1. However, as shown in Figure 65b, Llao's Bath and other pool samples have HCO_3/Cl ratios which are significantly greater than 1.0. Consequently, the abundance of bicarbonate in these thermally and chemically enriched waters also cannot be accounted for by dissolution of calcium carbonate by HCl.

From the combination of ^{14}C and ΣCO_2 measurements, we can compute the amount of admixed lake water present in our pool sample (CD226 S1; Table 13). If we assume that the pool sample is composed of a mixture of lake water and thermal water with a mantle carbon signature (i.e. dead carbon) the following equation describes the isotope ratio in the sample:

$$R_{sample} = (R_{lake} \times C_{lake} \times L) + (R_{thermal} \times C_{thermal} \times T)$$

where:

R_{sample} is the $^{14}C/^{12}C$ ratio in the sample mixture;

R_{lake} is the $^{14}C/^{12}C$ ratio in the lake;

$R_{thermal}$ is the $^{14}C/^{12}C$ ratio in thermal waters (assumed to be equal to zero);

C_{lake} is the ΣCO_2 concentration of the lake in moles per liter;

$C_{thermal}$ is the ΣCO_2 concentration of thermal waters;

L is the fraction of lake water in the mixture;

T is the fraction of thermal water in the mixture (where $L + T = 1$);

Since $R_{thermal}$ is zero for dead (magmatic) carbon, this equation can be rearranged to solve for L and reduced to:

$$L = R_{sample} / (R_{lake} \times C_{lake})$$

By converting our measured $\Delta^{14}C$ values (Table 13) to $^{14}C/^{12}C$ ratios and using the deep lake ΣCO_2 concentration (0.6 mM), we can solve for the fraction of lake water (L) in any sample. For the pool sample (CD226 S1) with a $\Delta^{14}C$ value of -955 ‰, the equation indicates 43% of the sample is lake water.

It is also possible to compute the concentration of ΣCO_2 in the unmixed thermal waters by solving the carbon balance equation:

$$C_{pool} = C_{thermal} \times T + C_{lake} \times L$$

Since T = 1 - L, we can solve this equation using our computed value of L (43%) and the measured ΣCO_2 in the pools (5 mM) and lake (0.6 mM). From this calculation we find the estimated ΣCO_2 (i.e., $C_{thermal}$) for an undiluted thermal fluid is 8.3 mM. This concentration is similar to the highest values measured in Palisades Pool (Table 9) and in pore waters which have the highest computed advection rates (Appendix F).

Our estimate of admixed lake water in Llao's Bath places important constraints on the evolution of the thermally and chemically enriched fluids found in the lake. As we discussed in the stable isotope section, the hydrogen isotopic composition indicates that the fluid sampled in the pools is lake water. By itself, the ∂D composition could be explained by major dilution of a primary thermal water source with bottom waters, and we would not have been able to constrain the ultimate source of the pool waters. However, the ^{14}C data indicate that the thermal waters in the pools are no more than 50 % diluted with lake water. Consequently, the pool fluids must have been lake waters that were incorporated into a convection system which operates within the volcanic crust beneath Crater Lake. This circulation adds heat, "dead" carbon, magmatic helium, and various ions to the fluid. During their buoyant ascent through fractured volcanic crust, the hydrothermal fluids have mixed with roughly equal parts of deep lake water to form chemically enriched pools on the lake bottom.

This scenario further implies that the concentrations of ions in primary hydrothermal fluids before mixing with lake water were not more than a factor of two higher than the values we measured in the pools. It is possible, however, that the warmest temperatures in the primary convecting fluids are higher than would be expected from simple mixing with cold lake water. Conductive heat loss can also result in major changes in the temperature of the hydrothermal waters. The importance of conductive heat loss in many thermal springs has been pointed out by Ingebritsen et al. (1989). Many Cascade thermal springs have temperatures in the 20°C to 60°C range, despite rock-equilibration temperatures based on geothermometry that are much higher (Mariner et al., 1990). Ingebritsen et al.(1989) point out that these springs have very low tritium (^3H) concentrations, an observation which, like our ^{14}C data for a Crater Lake saline pool, strongly limits the extent of mixing with cold, ambient waters. Apparently these lower temperature Cascade thermal springs have lost considerable heat by conductive cooling.

In summary, the presence of "dead" carbon in lake bottom waters, pore waters, and pool samples is not consistent with a direct input of CO_2 gas from a cooling igneous intrusive body or from the dissolution of secondary carbonate minerals within the rocks that underlie Crater Lake. The interaction of aqueous fluids with cooling igneous rocks within the volcano, i.e., hydrothermal processes, appears to offer the best explanation for the observed "dead" carbon as well as its association with thermal and chemical enrichments. The extremely low concentrations of ^{14}C in

the fluids entering the deep lake limit the extent to which these fluids could have mixed with lake waters or other modern aquifers.

IV.3. Fluxes of Materials Through the Lake System

Mixing Rates of Lake Water.

To this point, we have identified a set of variables that document the active input of thermally and chemically enriched fluids to the bottom of Crater Lake. These observations range from samples of concentrated fluid "end-members" to more dilute signals seen in the water column. Then, in order to evaluate how these inputs are dispersed through the system, we must discuss the overall mixing rates of fluids in different portions of the lake. Furthermore, based upon an understanding of the vertical and horizontal mixing rates in the lake, we are able to constrain the input rates for the hydrothermal fluids which have generated gradients in dissolved concentrations within the lake. Our discussion below will first focus on the local-scale processes which are associated with the initial introduction of these fluids into the lake. We will then summarize the observations which directly constrain the mixing rates within the water column.

Modes of Introduction.

Our combined submersible and porewater sampling program has delineated the following characteristics of the thermally and chemically enriched fluids found in Crater Lake:

(1) the initial source of the fluids is from within Crater Lake (from ∂D composition);
(2) measured temperatures vary from approximately 4°C to 19°C;
(3) pore waters from sediment cores are the most saline fluids, however, pools such as Llao's Bath have salinities which approach pore water values;
(4) despite their high salinities, the pool samples are much cooler than bacterial mats from cliff areas and nearby sediments from these areas;
(5) various geothermometers suggest rock-water equilibration temperatures ranging from 40°C to 165°C for fluids from the Detailed Study Area;
(6) fluids from the Detailed Study Area exhibit a range of heat-to-salt ratios;
(7) the chemically enriched fluids from the Palisades Point area have elemental relationships which are distinct from those within the Detailed Study Area, and geothermometry suggests a lower temperature of water-rock equilibration.;
(8) the low concentration of ^{14}C in the pools suggests that these fluids do not contain significant mixtures of deep lake or meteoric water.

Definition of these characteristics challenges us to formulate the processes which introduce and modify these enriched lake fluids. We proceed with this task under the assumption that the chemical evidence for a geothermal origin of these fluids is convincing. We will review this evidence and the alternative explanations later in the report. Our effort here is to examine whether a geothermal source can account for the full range of compositions and temperatures observed in the lake.

Within the Detailed Study Area the variations in salinity range from 0.1 g/kg in the background lake water to approximately 0.6 g/kg in the pools and pore waters. The generally consistent inter-element relationships between pools, mats, and pore waters implies that the range of salinity seen in the deep lake may represent variations in dilution with the background lake water rather than distinct compositional differences in the venting fluids. Any mixing prior to or during sampling of the fluids can explain the observed salinities within the Detailed Study Area.

Simple end-member mixing, however, cannot explain the distinct heat-to-salt ratios of the different near-bottom waters (Figure 16 in Appendix A) or the pool, mat, and pore fluids. However, since thermal diffusion is approximately 100 times faster than molecular diffusion of salt, conductive heat loss from various fluid reservoirs can account for these variations. Thus, venting of fluids with the maximum temperature and salinity observed in the deep lake (19°C and 0.6 g/kg) can produce any other fluids or deep lake waters by a combination of mixing and conductive heat loss (Appendix A).

As discussed in Appendix A, fluids with salinities of 0.6 g/kg are buoyant relative to lake water if they have temperatures >12°C. Thus, many of the bacterial mat fluids whose temperatures we measured would be buoyant if they have salinities similar to pools or the enriched porewaters. Unfortunately, we were not able to obtain an unmixed sample of the warmest mat fluids to document their salinity. Their buoyancy, however, is confirmed by heat probe measurements which suggest convection rates in the mats of 15 to 40 m/year (Section III.9 Lakefloor Temperature Data). Consequently, these fluids can ascend to the lakefloor, whereupon mixing and conductive cooling can produce fluids with both lower salinities and lower heat-to-salt ratios.

These mixed fluids can become non-buoyant as a result of conductive heat loss, which lowers their heat-to-salt ratio. Due to the non-linearities in the equation of state of water for the temperature range of the deep lake waters, mixtures of the warm saline fluids with lake water can result in a fluid that is more dense than either of the end-member fluids (Appendix A; Turner and Gustafson, 1978; Turner and Campbell, 1987). These dense mixtures may flow downslope as density currents resulting in the wide distribution of thermally and chemically enriched fluids at the bottom of the South Basin.

Because the saline fluids found within Llao's Bath and the Palisades Point pools have temperatures of less than 6°C, these fluids are currently non-buoyant and we must consider how they initially entered the pools. We suggest that the filling of these small pools could occur by down slope density flows, or through episodic or steady state input of buoyant fluids from below the pools.

Density flows have been deduced from the rills and channels at the Palisades Pool site. Such features are not present in the Llao's Bath region. Because some of these pools are locally elevated one to two meters above the surrounding terrain, they appear to fill from below. There may also be downslope sub-lake floor flow from the more elevated topography to the east where high temperature mats and sediments occur (Figure 9). Conductive heat loss during this type of lateral flow would account for their lack of buoyancy. However, we cannot yet further constrain the nature of this input.

Episodic buoyant input could contribute fluids to the pools. Such a process could hypothetically be associated with a thermal buildup of crustal fluids which would produce an intermittently buoyant fluid column. The fluid parcel would then rise to the lakefloor. However, conductive cooling and/or mixing could reduce the buoyancy and then end the convection. The rills at

Palisades Point, which had no observable flow during the submersible dive, may be evidence of episodic input at this site. As discussed in the Radon and Radium section, the observed ^{222}Rn values in the pools could be modeled as a batch inflow which occurred 15 to 30 days prior to our sampling. Since we have shown that a small, nearly unobservable flow of fluid could maintain these pools, there is no inherent reason to choose this model over a steady state input model (section III.8).

Continuous vertical flow of denser waters could be occurring if the complete fluid column underlying the pools has an integrated density less than an equivalent column of lake bottom water. Buoyant forces would move the column upward, even though continuous conductive heat losses in the upper parts of the crust or sediments could result in a non-buoyant fluid at the top of the column. The observation that the pore fluids in a core taken a few meters from the brain mat/Llao's Bath complex appear to be advecting at a rate of 1 meter per year, suggest continuous input at the site. Given an estimated area of Llao's Bath of 3 to 12 m^2, this advection rate results in a throughput of fluid at Llao's Bath of 3 to 12 m^3/year. Our continuous input model of Llao's Bath required an input of 8 to 30 m^3/year to account for the ^{222}Rn inventory. These two estimates of fluid flow into the pools, which are derived from totally independent models are in satisfactory agreement. This result serves to emphasize that slow vertical advection could account for some of the dramatic thermal features observed on the lake floor.

In summary, very reasonable physical processes can account for the major thermal and chemical characteristics of waters found within the deep lake. Hydrothermal convection can provide the thermally and chemically enriched fluids. Simple mixing can account for the observed range in salt contents in the deep lake, whereas conductive cooling of fluids will produce variable heat-to-salt ratios. Several processes could account for the emplacement of relatively dense, saline pools in the deep lake. While we cannot definitively choose among the possibilities, all are compatible with a hydrothermal fluid source.

Vertical and Horizontal Mixing Rates.

In this report and its appendices, several lines of evidence have been discussed to demonstrate a relatively high rate of mixing for the water in Crater Lake. We will summarize these important results here because the mixing rate determines the degree to which the hydrothermal inputs are further diluted and dispersed throughout the lake. This information will let us reconcile the general homogeneity of the water column with the observation of near-bottom gradients in thermal and chemical properties. Finally, a knowledge of the mixing rate coupled with these observed gradients provides one of our most direct estimates for the input rate of hydrothermal materials and heat to Crater Lake. The mechanisms and rates of lake mixing are discussed in more detail in Appendices A and G.

The upper 200 meters of the lake are completely homogenized twice each year. This is confirmed by many observations of an isothermal and isohaline water column to this depth and atmospheric saturation of this layer for oxygen, helium, and chlorofluorocarbons. While the gradients that begin to develop below this layer document incomplete mixing with the surface lake, the annual exchange of materials and heat down to at least 350 meters is significant.

The mixing rates between the upper and lower lake have been estimated using several techniques. Simpson (1970a) examined the vertical distribution of tritium (^3H) and first showed that the lake

mixes with a characteristic time of 1-2 years. Through the use of thermistor chains and CTD casts we have directly observed the vertical exchange of heat from the bottom of the lake (see Figures 3, 4, 5 and 10 in Appendix A). The steady state mixing rate we derive from these observations is consistent with a 2-3 year exchange rate with surface water. When this vertical mixing occurs each year, we have observed the partial reaeration of oxygen in the deep lake (see Figure 9 in Appendix A). The observed flux of this new oxygen into the deep basins predicts a vertical exchange rate with surface waters on the order of 2.5-3.5 years. Finally, our CTD measurements in the various basins of the lake demonstrate the rapid horizontal dispersion of materials with a characteristic time of several weeks (see Figure 12 in Appendix A).

The chlorofluorocarbons (i.e. CFC's or freons) in the global atmosphere have roughly doubled over the past 15 years. The concentration of these atmospheric pollutants in the water column of Crater Lake provides an unambiguous estimate of the vertical mixing rate (Appendix G). The concentrations in the upper 200 meters are at equilibrium with today's atmosphere. Below 200 meters, there is a steady decrease in concentration of CFC's to values which were in equilibrium with the atmosphere three years earlier (see Figure 2 in Appendix G). The derived mixing rate between the upper and lower lake using both freons (CFC-12 and CFC-13) averages 2 years. There is a steady increase in freon "age" between the winter mixed layer and the lake bottom. This is consistent with our hypothesis that the primary mode of vertical mixing in the deep lake is best modeled as a small- to intermediate-scale turbulent mixing process as opposed to a "complete" overturn of the water column.

In summary, all our data are consistent with a rapid vertical mixing rate of two years. This rapid mixing explains the first-order observation of a chemically homogeneous water column. Significantly, all the chemical and thermal gradients that we observe must be actively maintained in spite of these rapid homogeneous mixing processes. Below we will use these gradients and mixing rates to help quantify the active input rates of heat and salt.

Mass Balances of Materials.

Introduction.

Before we re-examine the observations of *active* inputs, we will evaluate an inventory of the total flux or "mass balance" of materials through the lake system. Since the lake is a closed basin with a relatively simple hydrologic budget, many investigators have evaluated geochemical budgets for various materials in this system (Simpson, 1970a; Volchok et al., 1970; Reilly et al., 1989; Nathenson, 1990a). During discussion of our 1987 and 1988 results (Collier and Dymond, 1988a and 1989), we also applied a geochemical mass balance model to the lake. As noted by all previous investigators, we identified a major imbalance in the dissolved ion budget of the lake if precipitation and runoff from the caldera wall are assumed to be the only inputs. We hypothesized that the input of a thermally and chemically enriched fluid balanced the lake's composition at "steady state".

The mass balance inventory of material moving into and out of a system like Crater Lake can be stated in terms of the change in mass (dM) in the lake over time (dt):

$$\frac{dM}{dt} = \sum \text{input rate} - \sum \text{output rate} + \text{internal processes} = 0 \text{ (at steady state)} \qquad \text{[eq.IV.3.1]}$$

The input of materials in the lake can occur through:

1. direct precipitation
2. caldera wall runoff and springs
3. cold springs
4. thermal springs
5. atmospheric exchange (gases)

The processes removing materials from the lake can include:

1. seepage
2. evaporation (water only)
3. atmospheric exchange (gases)

In addition there are internal processes which add (+) or remove (-) materials from the lake:

1. *in situ* dissolution (+) or precipitation (-) of solids
2. biological growth (-)
3. radioactive decay (-)

We will primarily apply our mass balance model to dissolved ions in the lake and will consider precipitation, runoff, and springs as the major inputs. The only output considered for the major dissolved ions is seepage of bulk lake water. We have not been able to identify any significant internal processes that affect the balance of the major dissolved ions. As noted by others, biological uptake of silicon by the phytoplankton (diatoms) in the lake has some effect on the removal of silica from the system (Reilly et al., 1989; Nathenson, 1990a).

The Hydrologic Budget.

The first step in developing a mass balance inventory of material fluxes through the system requires an understanding of the hydrologic budget. The hydrology of Crater Lake has been the focus of numerous investigations which are summarized below in Table 14. The input of water is primarily through direct precipitation on the lake surface (78%) or from streams draining the steep caldera walls surrounding the lake. Since there are no surface outflows, the output of water is through seepage and evaporation. The hydrologic parameters given in Table 14 summarize the work of three investigations (Phillips, 1968; Simpson, 1970; Redmond, 1990). We will use the most recent estimates of Redmond (1990) which have the highest rate of total water input and evaporation rate, but the primary conclusions drawn from our modelling effort would be essentially the same if we used the estimates of other investigators. Also, our use of this budget represents a maximum estimate for the "non-hydrothermal" factors which operate to control the concentration of dissolved salts in the lake: i.e. - evaporation and the input of ions via caldera wall runoff.

Table 14. Physiographic and Hydrologic Parameters of Crater Lake

Area	- lake surface(km^2)	53.1
	- drainage basin	67.8
Ratio of lake surface area to total basin		0.782
Lake volume (km^3)		17.3

(Phillips, 1968)

Hydrologic Budget:	Phillips(1968)	Simpson(1970)	Redmond(1990)
precipitation (cm/yr)			
- at Park HQ	175	171	170
- "expressed" in lake*	208	(217)	247
- caldera wall runoff (maximum value)	(33)	(46)	(77)
Seepage Rate (cm/yr)	147	138	127
Evaporation Rate (cm/yr)	61	69	120
(% of total water input)	(29%)	(33%)	(49%)
Residence time (years)			
water (with respect to total input)	156		132
solutes (with respect to seepage)			256

* The observed difference between the value measured at Park Headquarters and the response (or "expression") at the lake surface is due to differences in actual precipitation between the gauge and the lake surface, the drainage basin ratio (1.28), and possible enhanced precipitation or evaporation on the caldera wall.

The Model.

Figure 66 is a schematic diagram of the mass balance or "box model" for Crater Lake. The upper diagram represents the mass balance of ions; the lower diagram represents the hydrologic budget (the mass balance of water). The two parallel models are directly coupled through the calculation of concentration (mass/volume) in the lake. Boxes represent the reservoirs with flows in and out represented by the large arrows. Rates of flow ("valves" on flow arrows) are determined by initial conditions (constants) or by auxiliary first order equations. We have chosen to evaluate the evolution of concentrations in the lake using finite difference methods but an analytical solution to the differential equation is also possible (used by Nathenson,1990a). The system of equations represented by the diagram in Figure 66 is presented in Table 15 with an example of the initial values used for the chloride budget in the lake.

Evaluation of steady state assumptions.

Since the "age" of the lake is more than twenty times greater than the residence time of solutes (Table 14), it is a reasonable first-order assumption that the lake has reached a steady-state composition. However, if the various input or output terms in the mass balance have also changed over this time (such as a progressive decrease in a hydrothermal input), then the lake may not be at steady state. We will evaluate this possibility.

A qualitative evaluation by Phillips (1968) suggested that there was a lack of "appreciable chemical change" in the lake during the 52 year period over which data was available. Nathenson (1990a) extended this observation through 1986 and discussed the lack of changes within the analytical precision of the data set. Our data set continues this constant composition "trend" through 1990. Therefore, for a 90 year period (~1/3 of the residence time for solutes in the lake) there is no direct evidence to suggest that the lake is not at steady state. In addition to the observational support for steady state, we will apply the box model under various assumed conditions to further test the sensitivity of the system to changing inputs.

It has been suggested that the lake is *not* at steady state and that the elevated concentrations of ions such as chloride and lithium remaining in the lake can be traced back to the lake's early volcanic history (La Fleur, 1987). One implication of this hypothesis is that the concentration of these ions is still decreasing. We can demonstrate, however, that the modern lake has essentially no "memory" of the initial concentrations present when the lake was first formed in the young caldera. This result follows from the contrast between the age of the lake (approximately 6,000 years) to the residence time of solutes in the lake (~250 years).

The model (Figure 67) has been run to demonstrate how much of the signal from massive, early hydrothermal and fumarolic inputs associated with the formation of the caldera would still be present in the lake. The two examples are run with very high initial concentration conditions and they assume no active hydrothermal inputs beyond the initial pulse. These test the hypothesis that the high concentrations of certain solutes in Crater Lake are residual from very early in lake history. Two modern-day analogs of the formation stages of Crater Lake (Oregon) were considered for initial chemical conditions: Lake Öskjuvatn, Iceland and the crater lake in Soufriere volcano, St. Vincent Island. Lake Öskjuvatn is a 217m deep caldera lake formed after an eruption in 1875 with further eruptions in 1921 and 1926 (Olafsson, 1980). The crater lake in Soufriere volcano, St. Vincent Island, is a 200 m deep caldera lake which was reduced to 1/3 of its original

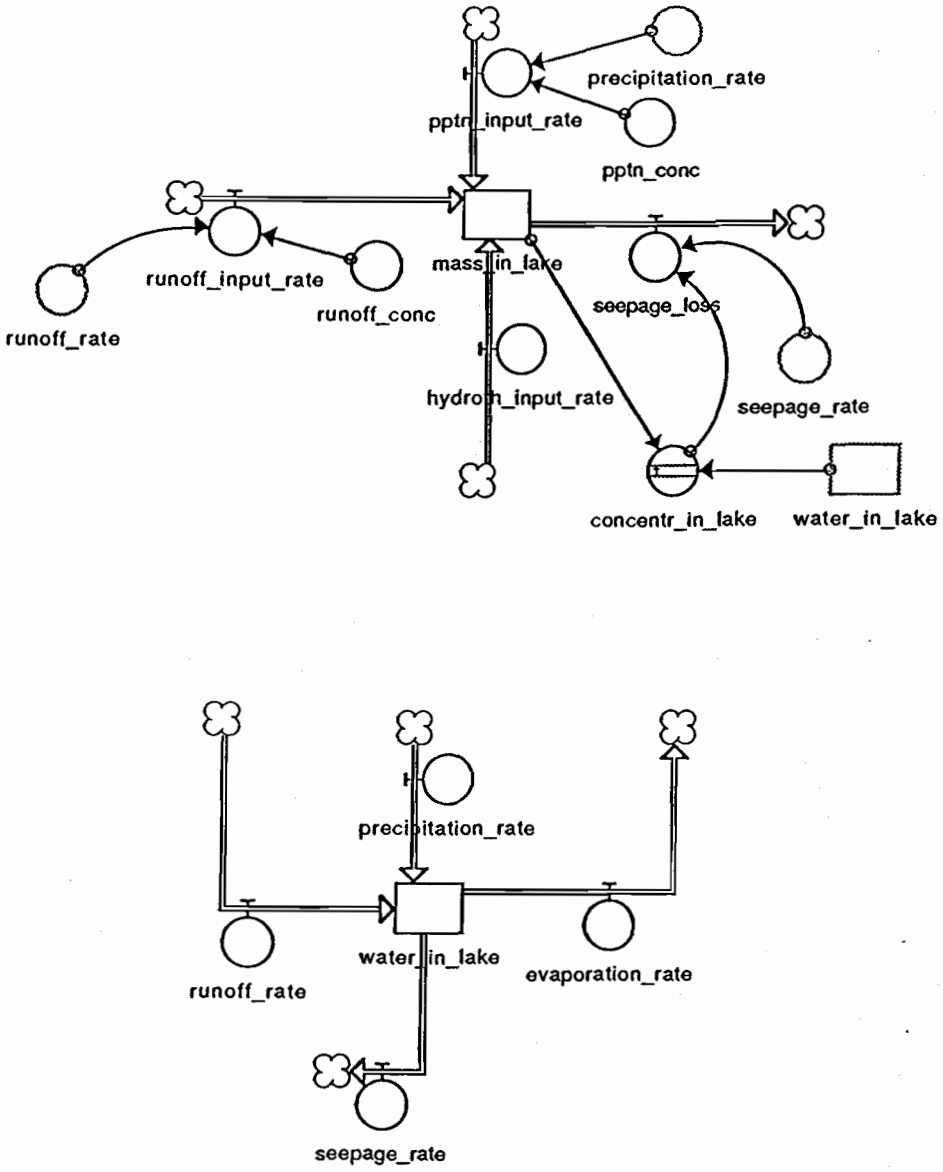

Figure 66. A schematic diagram representing a simple box model for dissolved ions in Crater Lake. The left hand diagram represents the mass balance of ions: the right hand diagram represents the hydrologic budget (the mass balance of water). The two parallel models are coupled through the calculation of concentration (mass/volume) in the lake. Boxes represent the reservoirs with flows in and out represented by the large arrows. Rates of flow ("valves" on flow arrows) are determined by initial conditions (constants) or by auxiliary first order equations. The system of equations is presented in Table 14. A form of this model was used by Collier and Dymond (1988a) in their discussion of geochemical balances in the lake. This model is essentially identical to those used by Simpson (1970a), Nathenson (1990), and Reilly (1989) with updates to the hydrologic budget by Redmond (1990).

Table 15. Crater Lake Box Model -- (chloride example)

SYSTEM OF EQUATIONS

(see Figure 57 for schematic relationships and Figure 58 for results)

Initialization equations:

INITIAL (mass_in_lake) = 1.24×10^{10} kg (results in an initial chloride concentration of 718 mg/liter)

INITIAL (water_in_lake) = 17.3×10^{12} liters (ref. 1)

concentr_in_lake = (mass_in_lake) / (water_in_lake)

evaporation_rate = 6.38×10^{10} liters/yr (ref. 2)

hydroth_input_rate = 0 (assumed for demonstration purposes)

pptn_conc = 3.75×10^{-7} kg/liter (ref. 3)

precipitation_rate = 9.51×10^{10} liters/yr (ref. 2)

pptn_input_rate =(precipitation_rate) x (pptn_conc)

runoff_conc = 5.79×10^{-7} kg/year (ref. 3)

runoff_rate = 3.62×10^{10} liters/yr (ref. 2)

runoff_input_rate = (runoff_rate) * (runoff_conc)

seepage_rate = 6.75×10^{10} liters/yr (ref . 2)

seepage_loss = (seepage_rate) x (concentr_in_lake)

Structure equations:

• mass_in_lake = *(element mass budget)*

(mass_in_lake) + (Δt) x [pptn_input_rate + runoff_input_rate + hydroth_input_rate - seepage_loss]

• water_in_lake = *(hydrologic budget)*

(water_in_lake) + (Δt) x [precipitation_rate + runoff_rate - seepage_rate - evaporation_rate]

Auxiliary equations:

concentr_in_lake = (mass_in_lake) / (water_in_lake)

pptn_input_rate =(precipitation_rate) x (pptn_conc)

runoff_input_rate = (runoff_rate) x (runoff_conc)

seepage_loss = (seepage_rate) x (concentr_in_lake)

References: (1) Phillips, 1968; (2) Redmond, 1990; (3) Reilly et al., 1989.

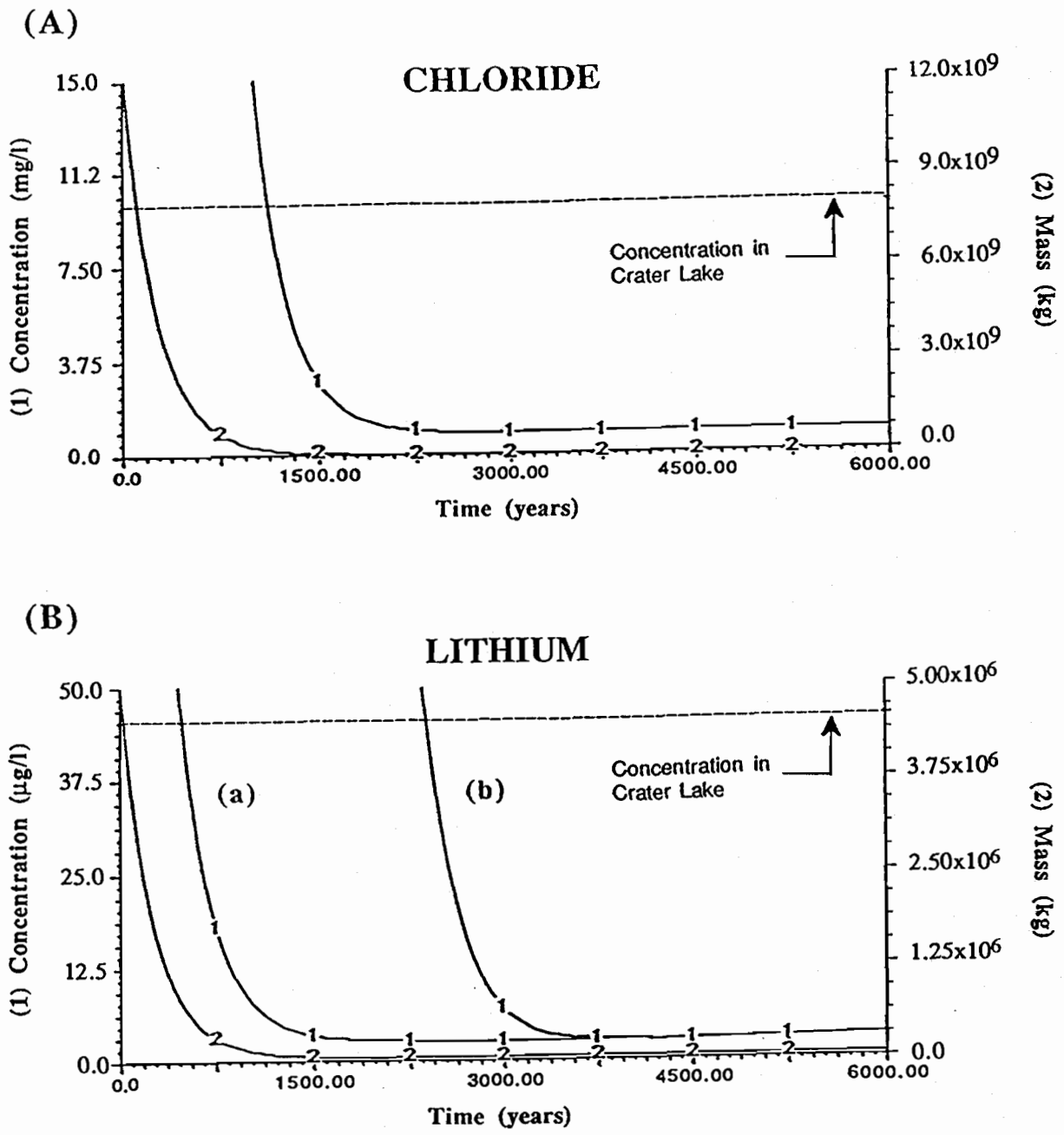

Figure 67. Results from the box model (Figure 66) applied to chloride (A) and lithium (B). Curves with a 1 represent concentration in units labelled to the left and those with a 2 represent mass in units labelled to the right. The overall residence time of ions in the model, with respect to seepage, is approximately 250 years. The initial chloride concentration (A) is chosen to be 718 mg/liter (Soufriere volcano). The concentration in the lake reaches 101% of the steady state value determined by precipitation and runoff (0.84 mg/liter) within 3000 years. The actual chloride concentration in Crater Lake is shown with a dotted line. The initial lithium concentration (B) was chosen to be 0.29 mg/liter (Soufriere volcano) and the concentration falls off even more rapidly (B - curve a). The actual concentration of Li in Crater Lake is shown by the dotted line. As an extreme example, an initial Li concentration of 1 gram/liter still falls to the same steady state within 3600 years (B - curve b).

volume in 1971-72 by the eruption of 80 x 10^6 m^3 of lava up through the lake floor (Sigurdsson, 1977). We have chosen the higher concentration for any element between these two caldera lakes as the initial conditions for Crater Lake, Oregon.

The models are run for 6,000 years - the approximate age of the lake, but the time axis can be considered as any point in time since the termination of volcanism. There is no evidence of volcanic eruptions inside the caldera within the last 4,000 years (Bacon and Lanphere, 1990). The initial chloride concentration (Figure 67A) is chosen to be 718 mg/liter (Soufriere). The concentration in the Crater Lake model reaches 101% of a steady state value (0.84 mg/liter) within 3,000 years. At this point in time, the model predicts a chloride concentration which is less than 10% of the actual chloride concentration in Crater Lake (shown with a dotted line). The initial lithium concentration (Figure 67B) was chosen to be 0.29 mg/liter (Soufriere), and the concentration falls below the Crater Lake value even more rapidly (Figure 67B - curve a). The actual concentration of Li is shown by the dotted line. As an extreme example, an initial concentration of 1 gram Li/liter, five times higher than the Salton Sea Brines (Thompson and Fournier, 1988), still falls to the same steady state within 3,600 years.

In order to reach steady state at the observed sodium concentration in the lake, an additional source of approximately 10^6 kg/year of sodium must be added to balance the outflow. This is nearly ten times higher than the inputs derived from the atmosphere and caldera wall runoff and documents the "need" for another major source to account for the steady state flux. A reasonable source for the missing ion fluxes is the input of the hydrothermal fluids at the lakefloor. If this "hydrothermal" source had stopped early this century (for instance at the time of the first chemical analyses of Crater Lake water), we would have seen nearly a 25% decrease in lake concentration by today. Obviously, we do not have the analytical sensitivity to detect much shorter term variability in the input fluxes, but the data are entirely consistent with steady state.

Summary of Steady State Model Results.

We have evaluated the steady state model for nine ions in the lake assuming that the mass of these materials is not changing with time (equation IV.3.1 = 0 such that Σ input rate = Σ output rate). The input is the sum of the precipitation, wall runoff, and lakefloor springs. The only output considered is seepage of bulk lake water. Precipitation and runoff sources are independently estimated using the concentrations of ions in precipitation and intercaldera wall springs summarized by Reilly et al. (1989). The total output rate is the product of the seepage rate for water and our data for bulk lake concentrations (Table 9 and Appendix I). The input flux from the lakefloor springs (also referred to as the hydrothermal flux) is calculated as the difference between the other inputs and the output. Table 16 presents the results of these steady-state calculations.

The budget for Si developed in Table 16 assumes the seepage loss is the only output for dissolved Si (at these pH values Si is present in solution as $Si(OH)_4$). However, this element is a significant nutrient for the diatoms in the lake which dominate the phytoplankton assemblage (Larson, 1988), and its removal to the sediments with biogenic debris must be included in a proper mass balance (Reilly et al., 1989; Nathenson, 1990a). Using unpublished results from our sediment trap program and sediment core analyses, we have estimated the burial rate of biogenic opal (as distinct from the burial of total SiO_2 which is dominated by aluminosilicates). Approximately 28 x 10^6 moles Si year per year are buried as opal which represents an additional output from the dissolved reservoir. Because the seepage flux (Table 16) is 20 x 10^6 moles Si year per year, the burial of

opal accounts for approximately 50% of the output. Consequently, the output term in the mass balance will increase. This causes an increase in the predicted hydrothermal flux of Si to rates equivalent to 67% to 77% of the total input rate.

The steady-state model (Table 16) documents that the hydrothermal input, calculated as the deficit in the mass balance, *is the dominant input* for dissolved components in the lake and accounts for greater than 90% of the Na^+, Cl^- and Li^+ fluxes. If we sum the mass of all elements in the hydrothermal input, we calculate a net flux of 3.4 to 4.2 x 10^6 kg/year as total dissolved solids or about 5-6 $\mu g/m^2 \cdot sec$ (integrated over the area of the lake deeper than 350 meters). Direct observations of salt accumulation based on a time-series of CTD measurements (Figure 68), leads to an estimate of the active salt flux (5 ± 2 $\mu g/m^2 \cdot sec$) which is indistinguishable from the steady state value estimated by our mass balance model.

TABLE 16. Steady State Mass Flux Calculations.

Component	Precipitation plus runoff inputs[1] (x 10^6 moles/year)	Seepage output (x 10^6 moles/year)	Hydrothermal flux (difference) (x 10^6 moles/year)	% of total input
Na^+	3.4–4.2	28.3	24.1–24.9	85–88%
K^+	0.71–0.96	2.8	1.8–2.1	66–74%
Ca^{2+}	1.9–5.1[2]	10.7	5.6–8.8	52–82%
Mg^{2+}	0.8–2.4	6.9	4.5–6.1	65–88%
HCO_3^-	8.7–10.4	36.8	26.4–28.1	72–76%
Cl^-	1.5–1.6	17.1	15.5–15.7	90–91%
SO_4^{2-}	0.6–4.3[2]	6.4	2.0–5.8	32–91%
Si	11.7–16.1	20.2[3]	4.0–8.5	20–42%
Li^+	0	0.43	0.43	100%

[1]Estimates based on the hydrologic budget of Redmond (1990) and concentrations in the atmospheric and runoff sources from Reilly et al. (1989). The range in fluxes is derived from the first and third quartile for the mean annual concentrations of various intercaldera wall springs (the runoff term).

[2]The large range for Ca^{2+} and SO_4^{2-} reflect the high concentration of these ions in springs draining Chaski Slide. Although we have no quantitative method of weighting the concentration of any particular spring in the net input, we believe the high values of the input range are driven by over-representing these Chaski Slide springs.

[3]The output term for Si listed is based only on seepage, as are all the other outputs in this calculation. Due to Si removal by diatoms, this output rate may be approximately 2 times larger, requiring a higher hydrothermal input flux. See text.

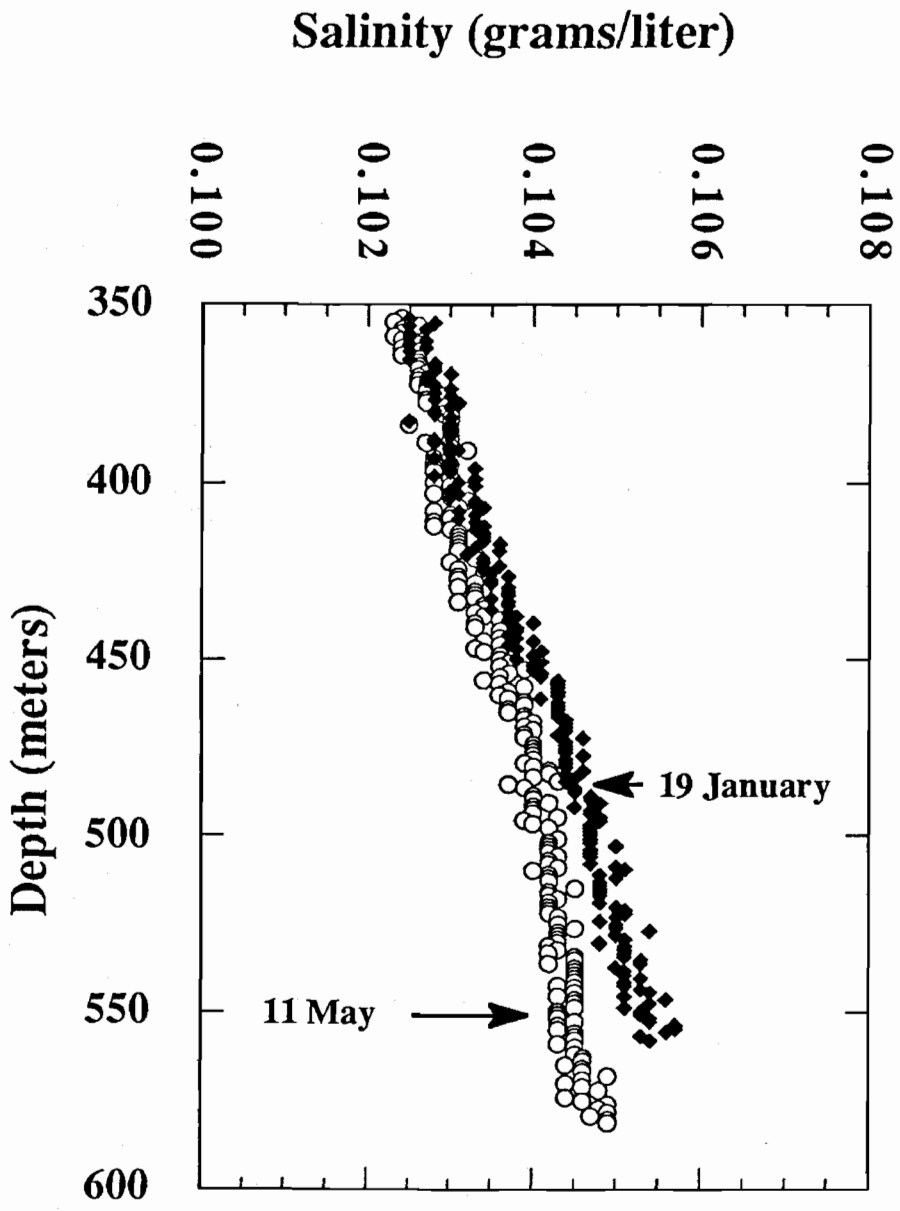

Figure 68. Salinity vs. Depth. Data from time series CTD measurements in the north basin (NPS station 13).

We can divide these steady state hydrothermal fluxes (moles/year, Table 16) by the composition of our hypothesized source end-members (moles/liter; Table 9) to arrive at an estimate of the actual fluid flux (liters/year). Separate calculations can be done for each individual ion measured in the various end-members (e.g., Llao's Bath, the Palisades Pool, and porewaters from GC8 and BC8; Table 9). The average of all these flow rate estimates is 265 liters/second with a standard deviation of 115 liters/second. This value may be compared to the ranges of 80-1,900 liters/second discussed by Nathenson (1990a), 120 liters/second estimated by Reilly et al. (1989) and 200-400 liters/second reported by McManus and Collier (Appendix A, this report).

The standard deviation in the mean flow is largely a consequence of different inter-element relationships between the lake water and the end-members. The flow estimates for a particular ion tend to have smaller variability (standard deviations ~50 liters/sec) than the variation of the mean estimates derived by including all the different ions. In particular, the flow rates needed to balance the Cl^- mass balance are nearly 400 liters/sec while the flows needed for the Na^+ model are only 230 liters/sec. This difference reflects the fact that the sampled end-members do not exactly account for the lake composition - the Na/Cl ratio in the lake is 1.6 while the ratio in all the sampled end-members ranges from 2 to over 4. This is a significant problem for which we have no definitive answer. Several possibilities can be suggested: the steady-state mass balance may be inaccurate for particular ions; a significant input or output source or process may have been overlooked; the lake is not at steady state with respect to our sampled end-members or other input estimates. In spite of the uncertainty, the mass balance approach and the direct sampling of the composition of the thermally and chemically enriched fluids entering the lake has given us a much better estimate of the integrated significance of hydrothermal inputs to the overall chemistry of the lake.

Since we have hypothesized that some or all of this flux might be in the form of diffuse flow through sediments, it is useful to evaluate the vertical velocity of porewaters that could carry this flux. For demonstration purposes, we can assume that an area the same size as the high heat and salt "anomaly" area (approximately 3×10^6 m^2 - Figure 12) has a flow rate of 3 meters/year as predicted from box cores near the site (see Appendix F). This would result in a flow of 30 liters/second. If we further assume that the remaining lake sediment floor (below 400 meters) has a flow rate of 0.1 meters/year (based on the gravity cores), we obtain an additional fluid flow rate of 70 liters/second. If we assume that 20 meters/year represents the flow through the mat sites and we assume that this flow occurs over an area one tenth of the size of the high heat/salt anomaly area, then we obtain an additional 190 liters/second of flow. These estimates yield a total flow of hydrothermal fluid of approximately 290 liters/second. These hypothetical calculations demonstrate that reasonable porewater flows can account for the necessary flux of heat and salt to the lake. However, considerably more data would be needed to constrain this further (see Appendix F).

Fluid Flows Through Sediments.

Flows deduced from sediment pore water distributions.

The pore water studies of Crater Lake sediments demonstrate a broad range of gradients and major differences in the dissolved ion content from different sites of the lake (Figure 69). Wheat (Appendix F) has shown that the non-linear gradients cannot be explained by sediment reactions, diffusion, or changes in lake composition. Only advection rates of a few centimeters/year to more than 100 centimeters/year appears capable of accounting for the observed gradients.

Since Crater Lake sedimentation is the result a variety of mixing processes which introduce volcanic debris from the summit and caldera wall, the solid phase sediment composition is relatively uniform. Except for variations in the biogenic opal and iron-rich precipitate content, the chemical composition of cores reflects a relatively uniform aluminosilicate input (Dymond and Collier 1990). Consequently, the differences in pore water concentrations cannot be the result of reactions. For example, GC8 has >5 times higher Na and Cl contents than are observed in GC1 (Appendix F). Any low temperature alteration of the aluminosilicate material in the core would produce similar pore water concentrations. The strong differences in the pore water concentrations in the GC8 core can only be maintained by advection of enriched pore fluids.

Comparisons of the compositions of caldera wall debris, sediment trap material, and buried sediments also document the inadequacy of low temperature alteration processes as an explanation of pore fluid compositions. The composition of caldera wall debris, sediment trap samples, and sediments are statistically indistinguishable (Figure 70). Because calcium is a relatively mobile element compared to aluminum, low temperature alteration is expected to decrease the Ca/Al values systematically from caldera wall debris to sediment traps to progressively deeper sediments. No such trend is observed, suggesting low temperature alteration does not mobilize major amounts of calcium. However, if we assume opposing two standard deviations of error on the Ca/Al means for sediments and traps, we estimate a maximum amount of Ca leached:

$$[(Ca/Al)_{traps} / (Ca/Al)_{sediment} - 1] \times 100 = \%\ \text{Ca lost by low temperature alteration}$$

This equation assumes no Al is lost after deposition. For the data shown in Figure 70, this calculation indicates that a maximum of 40% of the Ca could go into solution through reaction in the sediments. The trap data also indicate that the flux of particulate material to the bottom is approximately 40 $\mu g/cm^2/y$. Thus, an upper limit to the alteration loss is: 40 $\mu g/cm^2/y$ x 0.4 = 16 $\mu g/cm^2/y$.

To set this estimate in context, Wheat (Appendix F) estimates an advection rate of 8 cm/y would account for the pore water gradients in the GC8 core. Since pore water Ca contents are approximately 32 mg/l in this core, 256 $\mu g/cm^2/y$ of Ca is being removed from this core by advection of pore fluids. Consequently, the advective loss is 16 times our maximum possible estimate of low temperature reaction loss of Ca and 7 times the total flux of particulate Ca which reaches the bottom of the lake. Clearly, the estimated advective fluxes of Ca are impossible to explain by alteration reactions in the sediments. Similar conclusions can be documented for other ions.

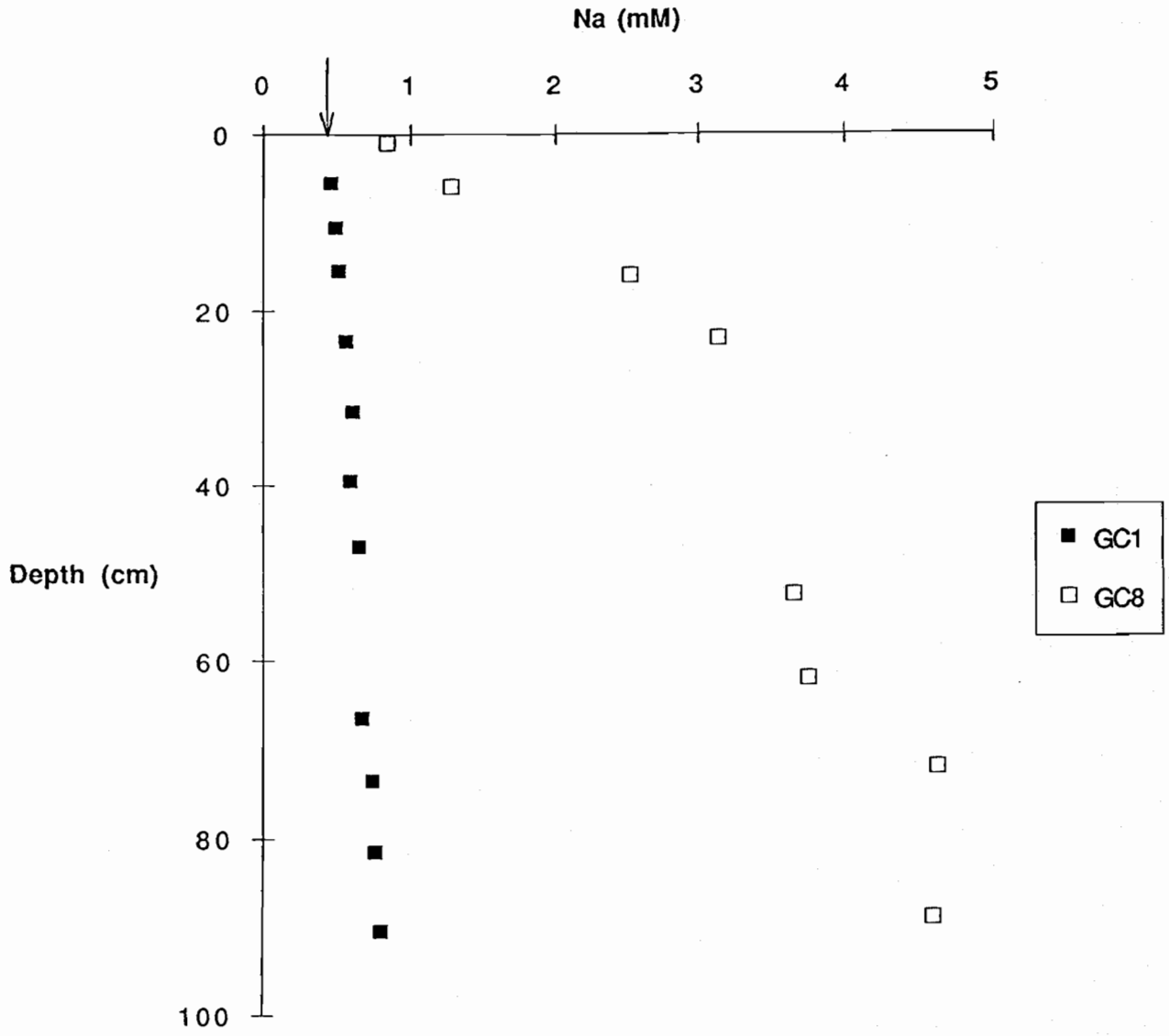

Figure 69. Pore water concentrations of sodium as a function of depth for two South Basin cores. Core locations are shown in Appendix F, Figure 1. The arrow on the x-axis marks bottom water concentrations. The low concentrations and linear gradients in GC1 can largely be explained by reaction between pore waters and sediments. In contrast, the higher concentrations and non-linear gradients in GC8 can only be accounted for by pore fluid advection (Appendix F).

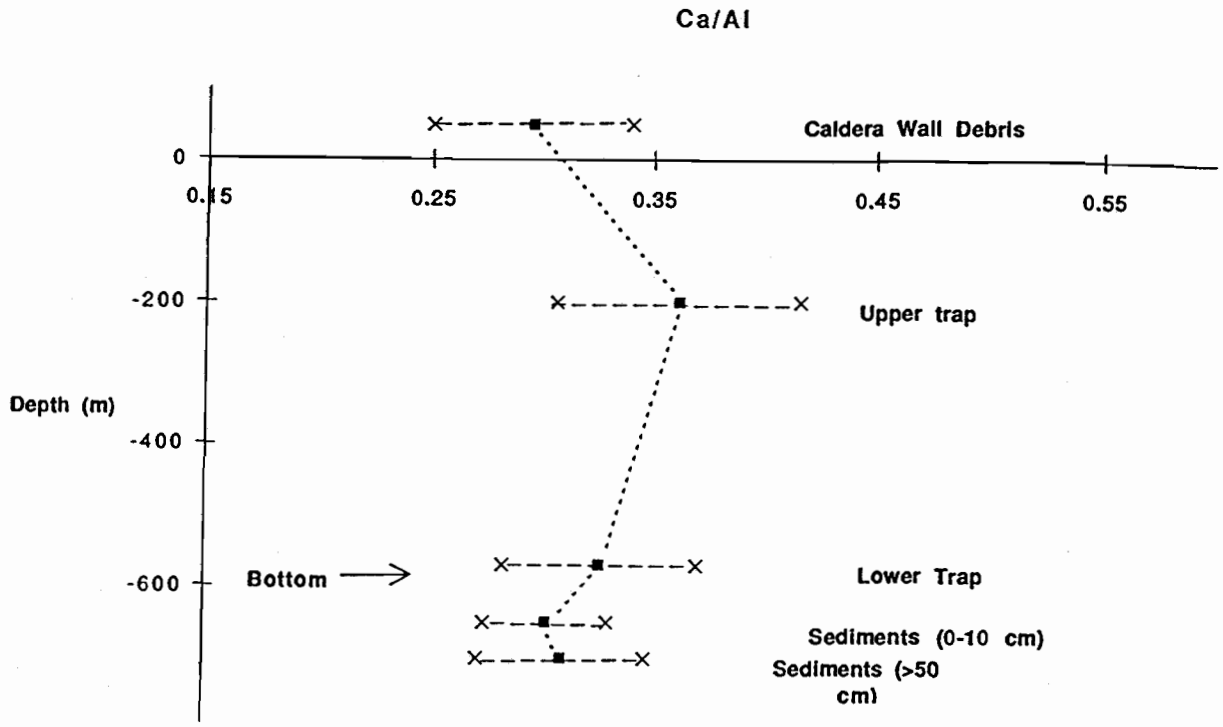

Figure 70. Ca/Al values for various Crater Lake solid materials. The ratio for caldera wall debris is indicated by the symbol above the zero depth line. Compositions for sediment trap depths at 200 m and 580 m depths are shown. The data represent the average and two deviations of unpublished results from five years of trap deployments. The sediment ratios are shown as symbols plotted below 600 m depth. These data are from Dymond and Collier (1990).

Flux Through the Sediments Collected by the Benthic Chamber.

A benthic chamber ("barrel") was deployed in the South Basin thermal area for 6.7 days. The barrel, with a 2.5 cm-diameter hole at the top to allow the passage of fluids, accumulates pore water moving upwards through the sediments. Only three of the six time-sequenced water samplers operated properly within the barrel which limits our ability to discern the functionality of the concentration increase within the chamber. For initial conditions inside the barrel at the time of deployment, we will assume the composition of a bottom water sample collected by the sub. The time series of water samples collected within the barrel clearly defines an accumulation of dissolved materials within the barrel. This observation is a direct confirmation of the upward flux of porewater through the sediments (Figure 71). The concentrations of Na, K, Li, Mg, Ca, Si, ΣCO_2 and Mn all increased (SO_4, Cl and temperature were not determined) while the concentration of O_2 decreased. The concentration of ^3He also increased from 2.8 to 8.5 x 10^{-13} cc/g and the fraction of "dead" carbon in the ΣCO_2 increased with $\Delta^{14}C$ dropping from -140‰ to -266‰ during the 6.7 day deployment.

In theory, the change in concentration in the open barrel over time can be described by the differential equation :

$$\frac{dC}{dt} = \frac{M}{V} - \frac{Q}{V} \cdot C$$

where:

M = mass flux (grams/sec)

Q = advective fluid flow (in = out; liters/sec)

V = volume of the chamber (208 liters)

C = concentration (grams/liter)

t = time (sec)

The solution is of the form:

$$C(t) = \frac{M}{Q}\left(1 - \exp\left(-\frac{Q}{V} \cdot t\right)\right)$$

If we choose a concentration for the pore water fluid entering the barrel (e.g. one of the pore water end-members from near the barrel), then the time series of data applied to this equation would ideally determine the advection rate. Conversely, if we use a fluid flow rate estimated from the pore water profile models (Appendix F), the concentration of the end-member is determined. Unfortunately, when we attempt to apply this model to the data in Figure 71, we find that no reasonable selection of flows or end-member concentrations properly describe the data. The primary problem is the shape of the curves in Figure 71, suggesting a rapid approach to some steady state value. This requires a very large flow rate (many meters/year) and projects to a very low end-member concentration. We believe that our estimate of the initial conditions within the

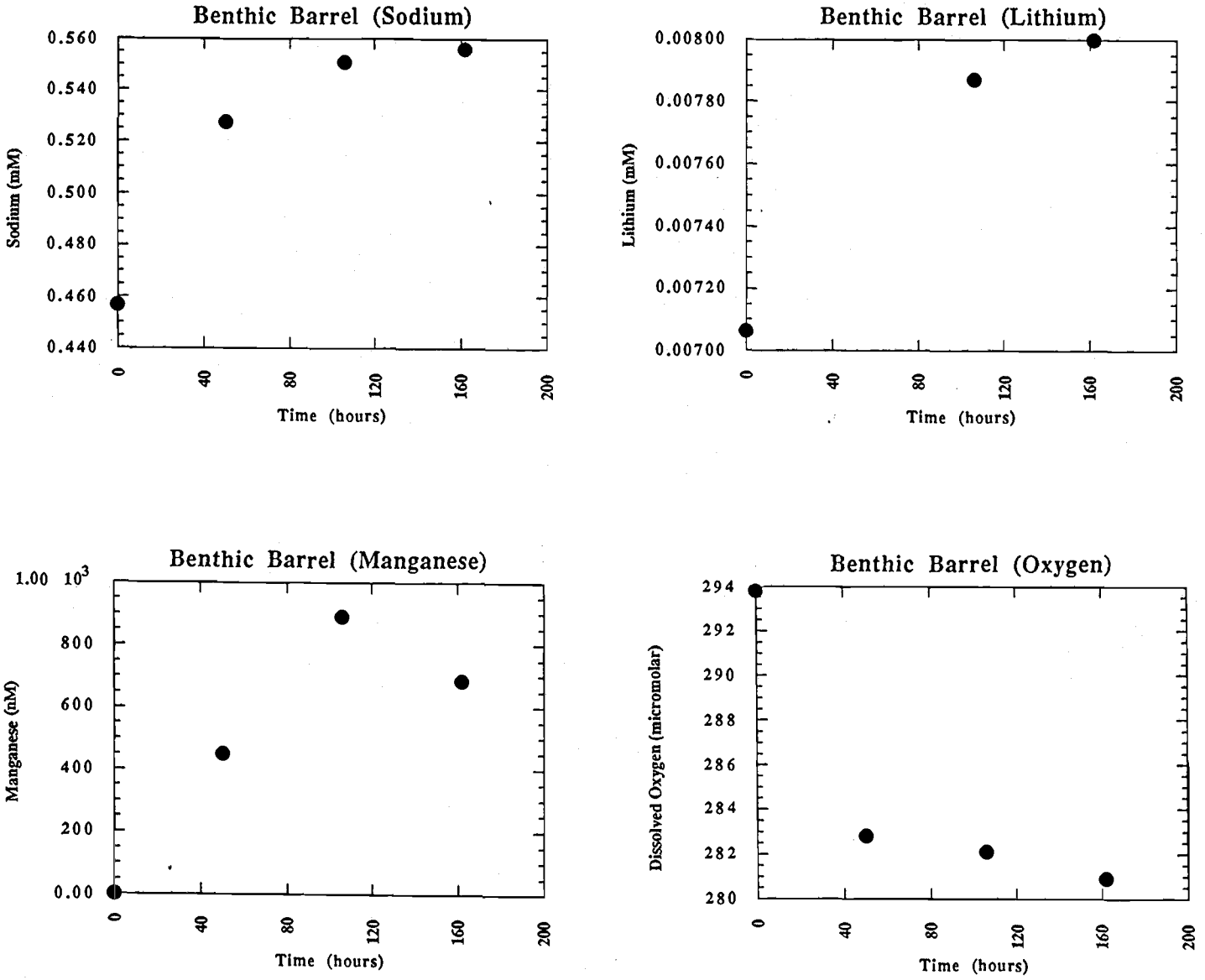

Figure 71. Benthic barrel data; sodium vs. time; lithium vs. time; managanese vs. time; and dissolved oxygen vs. time.

barrel probably too low, which largely forces the apparent shape. If we drop this point from the time series, there is insufficient data to constrain any functionality, although the observation of an increase with time is still clear. Therefore, we do not believe we can refine our estimates of sediment advection rates or the end-member concentrations with this experiment. However, the observed fluxes are consistent with the upward advection of the chemically and thermally enriched fluids predicted by the direct porewater analyses.

IV.4. Fluxes of Heat

Using various techniques and models as part of our research we have made estimates of the rate of heat input associated with the observed flux of anomalous fluids to Crater Lake. We will summarize these estimates here and compare them to the estimates made by Williams and Von Herzen (1983) and to other convective heat flows associated with hydrothermal springs in the Cascade Range (Ingebritsen et al., 1989; Mariner et al., 1990).

Direct Observations of the Accumulation of Heat.

As noted during our discussion of the temperature distribution of Crater Lake (section III.3), there is a clear increase in temperature in the bottom 200 meters of the lake. One of the significant contributions of our work are the estimates of heat fluxes which are needed to maintain these thermal gradients (section IV.3). In addition to this "steady-state" model of heat flux, we have *directly observed* an increase in the temperature of the deep lake over several field seasons. These observations, which are discussed in detail in Appendix A, are summarized below in order to emphasize this important result (Figure 72).

The observation of temporal changes require the application of precise instrumentation and collection of time series data. Time series of CTD profiles (Figure 72a) show the increase in temperature in the North Basin over a four month period in the summer. Although most of this heat is added in the South Basin, horizontal mixing is effective, and the warming is expressed throughout the deep lake. Due to the seasonal thermocline that develops during this period, there is very little exchange between the upper and lower lake. Consequently, there is little temperature change between 325 and 375 m. The deep lake isolation means that the origin of the observed heat increase is *not* the lake surface. Instead it must be derived from the input of geothermal heat from below. The time series of temperature can be integrated to estimate the total heat flux into the deep lake.

In addition to our CTD time series, we collected a continuous record of temperature at 10 meter intervals in the water column using a moored thermistor chain. The instrument was deployed in the South Basin between September, 1989 and July, 1990. Figure 72b shows the record for one depth, and the data for more than 20 depths in the lake is discussed in Appendix A. The data clearly document the seasonal cycle of geothermal heating when the lake is stratified followed by vertical mixing in the winter which results in a heat exchange with the deep water.

The observed temperatures changes can be integrated to yield estimates of the net input of heat (Appendix A). Assuming horizontal homogeneity and integrating over the deep basin area (~21km^2), we estimate a heat flux of 20 to 30 megawatts into the whole lake is required to produce the observed temperature increases.

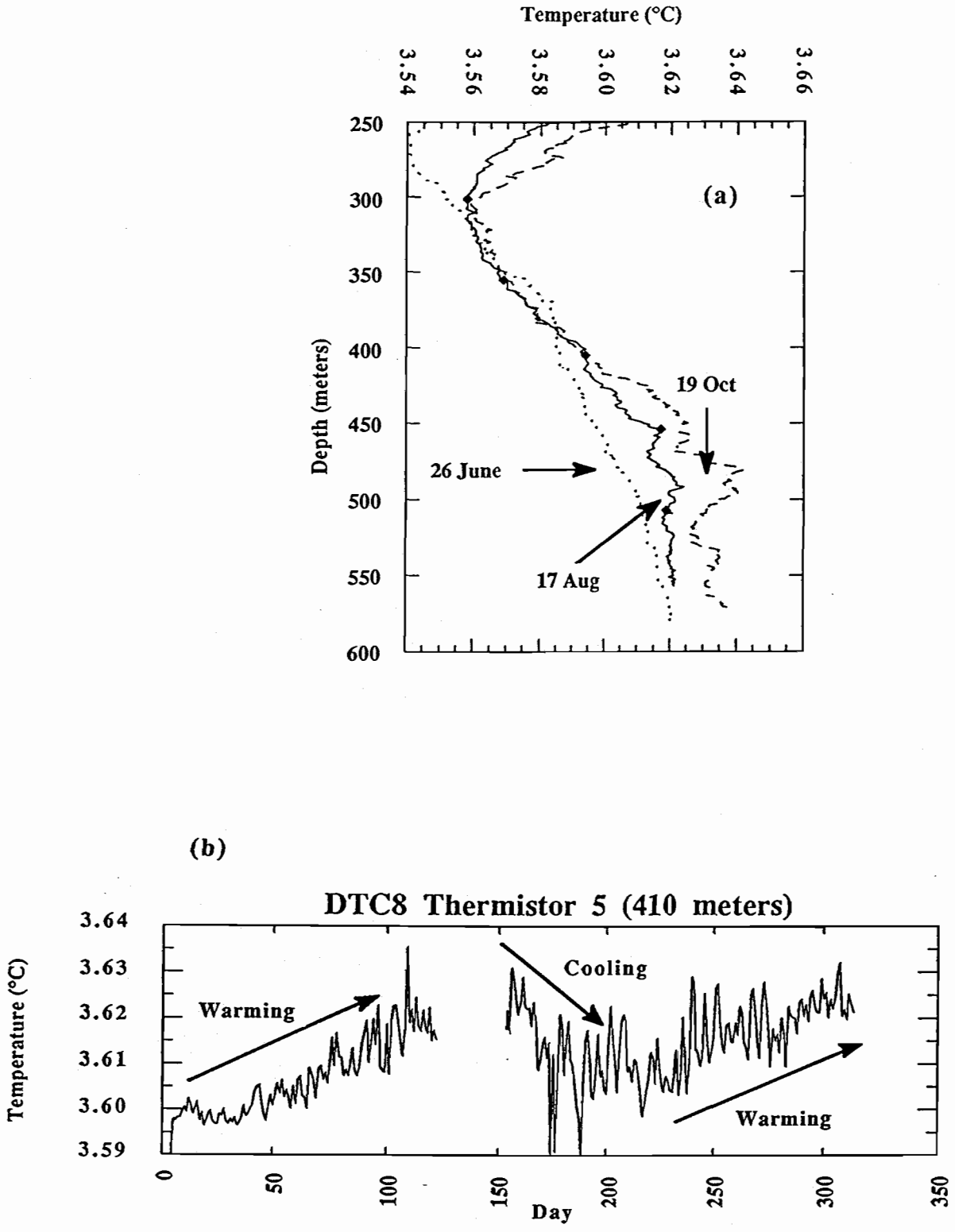

Figure 72. (a) Temperature versus depth. Data is from time series CTD taken from the north basin. (b) Temperature versus time from thermistor deployed in the south basin. Both figures demonstrate warming in the deep lake due to active inputs of thermally enriched fluids.

Helium-based Estimates of Heat Fluxes.

In section III.6 we discussed the large enrichments of ^3He over the concentration in equilibrium with the atmosphere. We have also discussed that the atmospheric gases dissolved in the lake equilibrate with a characteristic time of two years. Therefore, an amount equivalent to the complete inventory of "excess" ^3He (1.8×10^{22} atoms ^3He) must be added to the deep lake every two years. This would require a flux of 9×10^{21} atoms ^3He/year. The strong correlation of ^3He with temperature (Figure 21a) implies that the heat and ^3He have a common carrier. Consequently, we can divide the ^3He flux by the ratio of $^3He/\Delta T$ (1.5×10^{-12} cc ^3He/gram °C) to get an estimate of the heat flux which is associated with the thermal flows that carry the ^3He. The result is 29 megawatts which is comparable to the estimates based on the direct observations of temperature increases in the deep lake.

Using the same approach as our other steady state mass balance calculations (Table 16), we can estimate the flow rate of this hydrothermal fluid carrying the ^3He. We assume that the concentration of ^3He in the end-member is equal to that measured in Llao's Bath (271×10^{-13} cc/ml; Table 9) and divide this into the total ^3He flux (9×10^{21} atoms ^3He/year) and calculate a flow rate for the fluid of 400 liters/sec. We can also estimate the temperature of the end-member by dividing the end-member ^3He concentration by the water column ratio of $^3He/\Delta T$ (1.5×10^{-12} cc ^3He/gram °C). This calculation predicts an end-member temperature of 18°C which is very close to the highest lake bottom temperature measured during the submersible program.

Ion-based Estimates of Heat Flux.

Finally, we can make use of the estimates for the hydrothermal fluxes of ions derived from the mass balance model (Table 16) to estimate the total convective heat flux into the lake (Collier and Dymond, 1988a and 1989). Since these fluids are also warmer than deep lake water, this cation flux is associated with a heat flux. We compute the heat-to-cation ratio from the cation/^3He ratios derived from Figure 27b-f and the $^3He/\Delta T$ ratio used above. A total convective heat flux into the deep lake can be estimated from the product of the cation flux (deficit) and the heat-to-cation ratio. The average of the estimates from different cations is 15 megawatts (Table 17).

In summary, three methods, which are based on very different data sets and assumptions, predict heat fluxes ranging from 15-30 megawatts. The relatively close agreement gives us confidence in the quality of this estimate. Williams and Von Herzen (1983) estimate a net heat flux into the lake equivalent to 15-28 megawatts based on sediment heat flow measurements and water column temperature distributions. Our flux estimates could also be compared to the heat flux associated with other Cascade thermal springs. Mariner et al. (1990) estimate the convective heat flux of thermal springs and aquifers in the Cascade Range. The total direct discharge of thermal springs is 82 megawatts, and the total aquifer flux is estimated to be 190 megawatts based on a "chloride inventory" model. A summary of all fluid and heat flux estimates for the Crater Lake system is presented in Table 18.

Table 17. Cation-based heat flux estimates.

	$\frac{\text{cation}}{^3\text{He}}$	• $\frac{^3\text{He}}{\text{temp.}}$	= $\frac{\text{cation}}{\text{temp.}}$	=> $\frac{\text{heat}}{\text{cation}}$	• cation flux	= heat flux
units	$\frac{\text{mg/liter}}{\text{cc/gram}}$	$\frac{\text{cc/gram}}{°C}$	$\frac{\text{mg/liter}}{°C}$	$\frac{\text{calorie}}{\text{kg}}$	$\frac{\text{kg}}{\text{year}}$	$\frac{\text{calorie}}{\text{year}}$
sodium	27×10^{11}	1.5×10^{-12}	4.1	2.4×10^{8}	$5.5\text{-}5.7 \times 10^{5}$	$1.3\text{-}1.4 \times 10^{14}$
calcium	17	"	2.6	3.8	$2.3\text{-}3.5 \times 10^{5}$	$0.9\text{-}1.3 \times 10^{14}$
magnesium	8.4	"	1.3	7.7	$1.1\text{-}1.4 \times 10^{5}$	$0.9\text{-}1.1 \times 10^{14}$
potassium	4.5	"	0.68	15	$7.2\text{-}8.1 \times 10^{4}$	$1.1\text{-}1.2 \times 10^{14}$
lithium	0.20	"	0.030	330	3.0×10^{3}	1.0×10^{14}
	==> **average heat flux estimate =**				**1.1×10^{14} $\frac{\text{calories}}{\text{year}}$**	**(15 MWatts)**
(footnote)	(1)	(2)	(3)	(4)	(5)	(6)

(1) Cation / ^{3}He ratio derived from the correlations of these parameters shown in Figure 27.
(2) ^{3}He / temperature ratio derived from data in Figure 27a (Lupton et al., 1987).
(3) The product of (1) and (2) yields the slope of the cation / temperature relationship. This quantity was also calculated by Collier and Dymond (1988a).
(4) Conversion of (3) yields the heat flux associated with each kg of cation input.
(5) The cation flux into the lake to balance the steady state box model. The value for lithium is derived from our box model (Figures 57,58) with values based on our lake and spring analyses (assumes that the Li concentration in precipitation is very low). All the other cation fluxes are estimates of the "hydrothermal flux" calculated from our box model using direct estimates of atmospheric and runoff inputs taken from Reilly et al. (1989).
(6) If we assume as a hypothesis that the measured heat/cation relationship (4) is driven by the input of cation-rich thermal fluids, then the product of (4) and (5) yields an estimate of the convective heat flux carried by these fluids.

Table 18. Summary of Heat and Salt Flux Estimates for Crater Lake

Flowrate estimates for the hydrothermal "end-member":

Model Basis	
Excess Helium-3 Flux Balance	400 liters/second
Ion Fluxes (Table 15)	265 ± 115
Observed water column salt increase (Appendix A)	300 ± 100

Heat flow estimates:

Model Basis	
Excess Helium-3 / ΔT (section III.6)	29 megawatts
Ion balance estimates (Table 16)	15
Observed water column heat increase (Appendix A)	20-30
Williams and VonHerzen (1983)	15-28

IV.5. Significance of Fluxes to Other Lake Processes

Relationship to Other Lake Processes.

We have documented that an active input of thermally and chemically enriched fluids is necessary to (1) account for the presence of anomalous features on the lake floor, (2) understand the distribution of heat and salt in the deep lake (Appendix A), and (3) satisfy a chemical budget for the lake. We have not, however, attempted to describe the influence that this fluid influx has on the lake ecology. Because the input of heat and salt into the deep lake changes the density structure, lake mixing is affected by thermal fluid inputs. Since the extent of mixing in deep lakes is known to influence productivity (e.g. Goldman and Jassby 1990), a link between the input of thermally and chemically enriched fluids and lake ecology is plausible. Moving beyond this qualitative linkage, however, requires an assessment of multiple lake ecological factors which are beyond the scope of our research program. Nevertheless, we will review some general concepts concerning the influence of thermal and chemical inputs on lake mixing and productivity. More complete evaluation of these factors is the subject of the ten year limnological study of Crater Lake which is currently being conducted by the National Park Service and scheduled for completion in 1992.

Hydrothermal inputs to Crater Lake could either increase or decreases lake stability. Thermal inputs alone would destabilize the water column, but the addition of salt increases density and stability. Net stability enhancement by hydrothermal activity is suggested by the observation that the most dense lake waters are found near the lake bottom in the South Basin where chemical and thermal inputs appear to be greatest (Appendix A). The bulk water column, however, is only marginally stable , and this condition may reflect the combined influence of thermally and chemically enriched fluid inputs to the basin. These fluid inputs enhance the horizontal mixing of the whole lake as the more dense South Basin fluids mix horizontally across the sill connecting the two basins (Appendix A). The advection of South Basin fluids across the sill necessarily requires displacement of North Basin fluids, and the overall process must contribute to the turbulent energy and mixing of the entire lake.

Although perfect analogs to Crater Lake without the thermal and chemical enrichments do not exist, inter-lake comparisons may have some value. Goldman and Jassby (1990) suggest basin morphology, as defined by Z_T, the maximum depth as a percentage of mean surface diameter, is a predictor of ease of mixing. Higher Z_T indicates greater depth and lower wind fetch, both of which could decrease the rate of vertical mixing Consequently, Crater Lake with a Z_T of 7.2 might be expected to mix more slowly than Lake Tahoe with a Z_T of 2.0. The available data, however, suggest both lakes have a characteristic mixing time of two to three years (Pearl et al. 1975; Appendix G). This comparison, however, does not establish that the enhanced mixing in Crater Lake is due to thermally and chemically enriched inputs. Two significant features of lake mixing not considered in the calculation of Z_T are the temperature of maximum density and the timing of atmospheric mixing forces. Fresh water has a density maximum around 4°C, and this basic feature supplements mixing of lakes (Farmer and Carmack, 1981; Carmack and Farmer, 1982; Weiss et. al., 1991). The timing of maximum wind forcing with respect to the period when much of the water column is near this temperature of maximum density can determine the effectiveness of vertical mixing. Although basin morphology is certainly related to wind mixing effectiveness, it does not provide a quantitative measure of lake mixing.

It should also be recognized that the water column of Crater Lake has a total change in the vertical density structure which may be similar to other deep lakes — independent of hydrothermal activity. Unfortunately, the precise temperature and salinity measurements, necessary for accurate assessment of lake stability, do not exist for other deep lakes — e.g. Lake Baikal or Lake Tahoe. Thus, inter-lake stability comparisons based on the existing data are difficult.

Although we cannot definitively say what the influence of a hydrothermal input would be on lake mixing, exchange between the upper and deeper levels of Crater Lake undoubtedly alters the lake's productivity and overall ecology. Current estimates suggest 80% of the nitrate flux to the euphotic zone is a result of deep mixing, with the remaining fraction coming from atmospheric, and runoff sources (Reilly et al. 1989; McManus et al. in prep.). Clearly, a decrease in the rate of vertical mixing of the lake would result in relatively rapid decrease in the productivity, assuming the extent of nutrient recycling in the euphotic zone remains constant. The long term effects of a hypothesized decrease in mixing are not so clear because of possible shifts in lake ecology and feed-back processes which will tend to increase the deep lake nitrate pool. Without detailed modeling of the nutrient dynamics, the complexity of the system allows only qualitative views of the long-term changes in productivity.

IV.6. Evaluation of Hypotheses for the Thermal and Chemical Features

As we have shown throughout this report, Crater Lake has a number of physical, chemical, and biological features which are not typical of Cascade lakes or deep lakes in general. We have attempted in this study to collect the essential data which can account for these features. In our report on field studies conducted in 1988 (Collier and Dymond, 1988a), we considered seven hypotheses to account for the chemical composition of the bulk lake, the thermal and chemical variability in near-bottom waters, and the chemical variability in deep lake sediments:

(1) The high salt content of the lake is a consequence of fumarolic and thermal spring inputs that occurred soon after the collapse of Mt. Mazama.

(2) The evaporation rates in the lake are greater than previous estimates and can account for its high salt content.

(3) The chemical alteration of Mazama ash could introduce chloride and other elements into the lake, thereby accounting for the high content of these elements compared to other Cascade lakes which are dominantly fed by precipitation.

(4) The anomalous volatile contents (helium and radon) are a consequence of gaseous injection (i.e., non-condensable volatiles) and do not require a hot water source.

(5) The observed temperature pattern of the deep lake is a consequence of conductive heat flux through the lake bottom and does not involve any fluid injection.

(6) The near-bottom increases in major-ion content and the observed metal-rich deposits are the consequence of cold, saline spring input.

(7) There are hydrothermal inputs to the lake which are driven by convection of waters through cooling magmatic bodies that underlie Crater Lake.

In this section of the report we will evaluate the data which support or contradict each of these hypotheses.

(1) Early Fumarolic Input Hypothesis.

This hypothesis has been put forth by La Fleur (1987) as a means of explaining the elevated salt content of Crater Lake relative to other nearby lakes in the Cascade Range. The early stages of caldera lake evolution are often associated with continued volcanism, hot springs, and fumarolic inputs. As a consequence, these lakes can become extremely concentrated in dissolved ions and gases. For instance, in our discussion of the mass balance and residence time of ions, we used two such lakes as possible analogues for the young Crater Lake, Lake Öskjuvatn in Iceland (Olafsson, 1980) and the crater lake in the Soufriere volcano (Sigurdsson, 1977). We then applied simple mass balance calculations using the current hydrologic model for Crater Lake and demonstrated that Crater Lake (or any reservoir) has relatively little residual "memory" of events occurring more than ten residence times in the past. Therefore, dissolved chloride or soluble

materials added to Crater Lake following the collapse of Mount Mazama (La Fleur, 1987) would have been effectively purged from the lake within 2,500 years. Thus, if hydrothermal input had declined and ceased shortly after caldera collapse, ion concentrations would have declined to a relatively low, steady-state level maintained by precipitation and weathering. On the other hand, if there were continuous hydrothermal inputs into the lake, ion concentrations would achieve a steady-state balance between loss and new input. It is clearly more difficult to evaluate steady state conditions over time scales which are short compared to the response time of the system. Nonetheless, because the current concentration of ions in Crater Lake remains high compared to the concentration supported by precipitation and weathering, the exponential drop in ion concentrations toward a precipitation/weathering steady state should still be easily visible (Figure 58). Nathenson (1990a) has shown that there have been no such significant changes discernable in the chemical composition data for Crater Lake since 1912.

Consequently, although this hypothesis might potentially affect the very earliest phases of lake evolution, early fumarolic sources of dissolved ions cannot be significant at the present time.

(2) Evaporation hypothesis.

If a major fraction of the waters which have entered the lake evaporated, this would concentrate the ions dissolved in the lake and increase its salt content above that predicted by losses due to seepage outflow alone. A high evaporation rate has been proposed to explain the anomalously high chloride in the lake (La Fleur, 1987).

It has long been recognized that a significant fraction of the water in Crater Lake evaporates (Diller, 1902; Phillips, 1968; Simpson, 1970a; Redmond, 1990). Therefore, all of the hydrologic budgets used in examining the mass balance of ions in the lake include evaporation effects (Simpson, 1970a; Nathenson, 1990a). The hydrogen and oxygen isotope ratios in Crater Lake water fall off the meteoric trend and follow a reasonable evaporation trend (Thompson et al., 1987; 1990) (Figure 58). As discussed by Redmond (1990), direct measurements of evaporation are inaccurate and cannot represent an annual average until observations are made in the winter. Therefore, most estimates of evaporative losses from the lake have been based on water budget considerations. The values most frequently used for evaporation are quoted or derived from Phillips (1968). His water budget indicates that approximately 28% of the water entering the lake evaporates. The value chosen by Simpson (1970a,b) results in 33% loss by evaporation. In a detailed analysis of extensive records of climate and lake-level variations, Redmond (1990) proposes an evaporation rate equivalent to 50% of the total water input and shows that this rate is consistent with the long-term data record.

We have used the hydrologic data set of Redmond (1990) and the high evaporation rate he proposes in our application of the mass balance model for chloride and lithium (Figure 67a,b). Our mass balance calculation demonstrates that the steady-state concentration of chloride in the lake, assuming zero hydrothermal input, would be less than 10% of the observed level. Even if the evaporation accounted for 60% of the net water loss, the steady-state chloride value would be barely 10% of the concentration present in Crater Lake.

During evaporation, the ionic ratios between conservative salts remain constant - i.e., the final brine has the same ionic ratio as the parent fluids. If the source of these ions in the lake is primarily the weathering products carried by runoff, then the lake would have the same ion ratios

as those seen in that runoff. Figure 24 shows that this is not the case; ratios measured in the lake are markedly different from those in the caldera springs. Although evaporation removes approximately half of the annual inflow of water, it cannot account for the observed pattern of ion abundances or the magnitude of the ion concentrations in Crater Lake.

(3) The Ash Alteration Hypothesis.

Volcanic ash is reactive and can be readily altered to various hydrous phases. The classic rock-weathering reactions of Garrels and MacKenzie (1967) release cations and silicon to solution and produce alkalinity. Because of the abundance of fine, glassy pumice debris on the rim and caldera walls of Crater Lake, this debris weathering could provide a source of cations to Crater Lake waters. This hypothesis has been proposed by La Fleur (1987) as a source of chloride to the lake.

The weathering of volcanic phases as a source of elements in Crater Lake waters and Mazama springs has been discussed in detail by Nathenson and Thompson (1990). They found that simple weathering reactions involving the transformation of glass and clinopyroxene to kaolinite could account for the composition of most Mazama cold springs. However, the computed and observed contents of most cations dissolved in spring water were 25% to 35% of those observed in Crater Lake. In addition, Nathenson and Thompson (1990) computed the Cl contribution to spring waters from weathering by using measured ratios of chloride to sodium and assuming that all the chloride would dissolve with the sodium. The resulting value is more than 100 times less than the observed chloride contents in Crater Lake. Their data demonstrate that weathering of volcanic materials cannot account for the observed chloride concentration. At best, weathering contributes a small fraction of the other ionic constituents of Crater Lake waters. Alternative mass balance approaches have also come to similar conclusions (Reilly et al. 1989).

In addition, pore water studies conducted in 1989 (Appendix F) show that low temperature reactions between Crater Lake sediments and pore fluids produce only small changes in pore fluid oomposition. For sediment cores with slow advection rates(<1 cm/y), these changes can be explained by small amounts of fluid-solid reaction and molecular diffusion. In contrast, cores with moderate advection rates (approximately 10 cm/y) have as much as 10 times the ionic content of lake water.

Finally, chemical comparisons among caldera wall debris, sediment trap particles, and sediments recovered by coring reveal similar compositions (Figure 70). Thus, the weathering and low-temperature alteration processes, which transform caldera volcanic material into settling particles and finally into buried sediments, does not produce major changes in the chemical composition of the material. Mass balance estimates based on this observation indicate that the low temperature release of ions into the lake is minor relative to the fluxes of ions carried by pore water advection.

Consequently, mass balance studies and pore water data indicate that alteration of sedimentary volcanic debris cannot account for the elevated concentrations of salts in Crater Lake.

(4) Volatile Transport Hypothesis.

Because volcanic gases are enriched in ^3He, it might be possible that volatile transport of helium into the deep lake, independent of advecting thermal waters, could account for the observed ^3He

anomalies (La Fleur, 1990). For example, magmatic degassing has been suggested for the CO_2 buildup of Lake Monoun and Lake Nyos in Cameroon which led to a lethal gas burst (Sigurdsson, 1987). At these lakes, the SO_4 and Cl levels are very low, suggesting that there is little fumarolic or hydrothermal input. The $^3He/^4He$ values in these lakes, however, are similar to mantle values (Sano et al., 1987; 1990). If volcanic emanations carry HCl, this process could also account for the high concentration of chloride that is observed in Crater Lake (La Fleur, 1987) relative to precipitation-dominated lakes in the Cascades. An input of volatile CO_2 to the lake could account for the "dead" carbon inputs that are necessary to account for the gradients in ^{14}C observed by Simpson (1970a) in the deep lake.

Evidence against the volatile injection hypothesis comes from evaluation of the lake's pH and alkalinity budget. Thompson et al. (1990) argue that because Crater Lake is a near neutral lake (pH ~7.5), acidic gases such as HCl and H_2S are not the source of chloride and sulfate in the lake. They suggest that Na and Cl are entering the lake together in aqueous solution. Because precipitation and runoff can account for only a small fraction of the chloride in the lake, any injection of gaseous HCl to balance the chloride deficit (Simpson, 1970a; Nathenson, 1990a; Reilly et al., 1989) must produce a major impact on the observed pH and the alkalinity of the lake. If volatile CO_2 were injected to the lake, it would also result in a lower pH and would not directly account for Crater Lake's bicarbonate content, which is high relative to the precipitation-dominated lakes in the Cascades. The alkalinity deficit, which is needed to supplement inputs from precipitation and caldera spring sources (Reilly et al., 1989), requires sources of bicarbonate ion, not dissolved CO_2.

The volatile input hypothesis also does not account for the correlation between the helium concentrations and the thermal-chemical anomalies that are observed in the deep lake. In order to account for the observed correlation between these features, the volatile inputs must be interwoven with thermal sources (perhaps conductive heating from the lake floor) and chemical sources (perhaps cold springs) in such a way that the volcanic degassing would impact only those sites in the lake that receive cold spring input and experience high conductive heating. The fact that the ^3He-to-heat ratio measured in the bottom of Crater Lake is very similar to values measured in hydrothermal systems at oceanic hot springs (Lupton et al., 1989) suggests that only by remarkable coincidence could the heat and helium correlation be due to a combination of conductive heating and volatile degassing.

Finally, the observation that cold springs have atmospheric rather than mantle helium and carbon isotopic compositions, indicates that volatile inputs of helium are <u>not</u> an ubiquitous feature of cold spring sources.

In summary, non-condensible gas inputs cannot account for the necessary sources of Cl, SO_4, or ΣCO_2 needed to balance the elemental budgets of Crater Lake waters. The volatile transport hypothesis also fails to explain the consistent relationship among helium enrichments, bottom water temperatures, and salt contents in Crater Lake water. These same interrelationships which are observed in highly enriched saline pools and in bacterial mats. This can only be explained by advection of thermally and chemically enriched fluids.

(5) The Conductive Heat Hypothesis.

Conductive heating may be able to explain the gradual increase in temperature in the deep lake, but, an expansion of the hypothesis is required to explain the variability in the horizontal and vertical thermal gradients found at the lake bottom. Conductive heat transport into the lake should produce monotonic decreases in temperature with increasing height above the bottom. This is observed in some cases; however, a number of profiles in the Detailed Study Area have complex patterns, with warmer water overlying colder water (Collier and Dymond, 1988a). Moreover, conductive input of heat alone cannot explain the horizontal gradients in bottom water temperature except by even stronger gradients in the conductive heat flux. Variability in conductive heat flow is present in Crater Lake, but this variability has been interpreted to be a consequence of variable proximity to a convective heat source (Williams and Von Herzen, 1983).

The measurements of temperature gradients made with the submersible document the existence of convective heat transport (Figures 41,42,and 43). Non-linear thermal gradients imply advective flow in the range of 10 to 100 meters per year. The convective heat fluxes are heterogeneous and probably reflect localized pathways for fluid input.

In summary, because Crater Lake sits within a volcanic center, conductive heat transport into the bottom water must be occurring. However, this mechanism by itself cannot explain the most significant patterns of heat distribution within the lake. Documented convective sources are located within the areas of generalized thermal anomalies in bottom waters. The presence of convective sources can explain the bottom water temperature anomalies and the highly variable conductive heat flow found by Williams and Von Herzen (1983).

(6) The Cold Spring Hypothesis.

Input of cold spring water has been proposed to explain the increase in ionic content seen near the bottom of Crater Lake (La Fleur, 1990). Cold saline springs entering the deep lake would be denser than ambient lake water and could form a near-bottom layer. La Fleur (1990) developed this hypothesis to explain the association of unique thermal-chemical features with Chaski Slide on the south side of the lake. La Fleur (1990) suggests that ground waters flow through Chaski Slide and into the lake because of hydraulic forces. His model calls upon dissolution of iron and sulfate within Chaski Slide rocks to explain the observed enrichments of these species in bacterial mat fluids sampled in 1988. La Fleur (1990) also suggests that the temperature of ground waters within the area is typically about 10°C and that these ground waters could explain the maximum temperatures noted in the 1988 study.

Because some low-temperature processes can mobilize metals, the metal-rich deposits and sediments observed in the Detailed Study Area and recovered in cores (Dymond and Collier, 1990) do not in themselves prove that there are thermal spring inputs to the lake. Consequently, precipitation of metals from cold springs is possible, especially if a change in pH or oxygen content accompanies the mixing of spring and lake water. La Fleur (1990) suggested that cold springs might also provide iron for the observed bacterial mats. Although the particular bacterial genera described from samples of the Crater Lake mats have been observed in geothermal waters, they are not obligate thermophyllic bacteria. All that is required for their growth (particularly the genus *Gallionella*) is a continuous source of reduced iron and a redox boundary. Anoxic cold springs might provide such a source.

Although La Fleur (1990) makes a reasonable case for cold springs as an explanation of the thermal-chemical enrichments observed in the 1985-88 studies, certain observations made in the 1989 field program rule out this mechanism. The 1989 program discovered bacterial mats that had temperatures of approximately 19°C. These temperatures are not within typical ground water values as suggested by La Fleur (1990). In fact, data for Mazama cold spring temperatures (Nathenson, 1990b) directly contradict La Fleur's (1990) contention of 10°C ground water temperatures. Nathenson (1990b) has shown that cold springs at the elevation of the surface of Crater lake have temperatures which are very similar to the cold deep lake waters (4°C) and that these spring temperatures appear to be related to the mean annual air temperatures. Our measurements of fluid temperatures on the bottom of Crater Lake, which are more than 15°C above ambient water temperatures, clearly lie outside known values for cold water springs in the region.

In addition, the most saline fluids recovered in 1989 from pools and advecting sediment pore waters are 6 to 10 times enriched in major elements and 500 times enriched in certain minor species. The larger thermal-chemical anomalies measured in 1989 make the cold springs hypothesis less tenable. For cold springs to supply Crater Lake's ionic concentrations and the "missing" source of elements needed for mass balance considerations (Nathenson, 1990a; Reilly et al., 1989), the springs must either be very saline or of high volume. Springs from the Chaski Slide area, which are relatively close to the Detailed Study Area, have Mg, Ca, and SO_4 concentrations that are sufficiently enriched (Nathenson and Thompson, 1990) to account for the observed anomalies in the most chemically-altered water sample collected at the bacterial mat in 1988. Even for these elements, however, springs of a Chaski Slide composition would have to be a major source of water to the lake in order to account for the abundance of Mg, Ca, and SO_4 observed in the lake. Chaski Slide springs, however, are far more dilute than the pools and enriched porewaters sampled in 1989. The alternative of voluminous cold spring input would require major modification to the water budget of the lake which would contradict the findings of numerous researchers (Van Denburgh, 1968; Simpson, 1970b; Redmond, 1990; Nathenson, 1990a).

Significantly, Chaski Slide spring samples are no more enriched in Na, K, Li, and Cl than other Mazama springs. Thus, these springs could not account for these elemental enrichments in pools and mat samples or their abundance in the lake in general. In other words, neither the Chaski Slide springs nor any of the low-temperature Mazama springs have the appropriate composition to account for the anomalous fluids sampled in 1988 and 1989 nor to sustain the overall composition of Crater Lake.

Theoretically, cold anoxic springs might deposit metals in the form of bacterial mats and their possible fossil equivalents, the iron-rich crusts. However, we know these features are directly associated with fluids having the highest temperatures recorded in the deep lake. As we have demonstrated (Dymond and Collier, 1989), these temperatures cannot be maintained by metabolic iron oxidation in the associated bacterial communities. The strong enrichment of arsenic and antimony observed in the mats and crusts is additional evidence that these features are precipitating from fluids that have a high-temperature origin. Furthermore, the presence of silica-rich deposits in the lake (siliceous spires) is strong evidence of past hydrothermal inputs, although the age of these deposits has not been documented.

In addition, the cold spring hypothesis is inconsistent with ^{14}C measurements of pool waters, advecting pore fluids (Benthic Barrel), and deep lake waters. These data document the influx of a fluid which carries essentially no ^{14}C. In contrast, aquifer sources would be expected to have carbon with a modern ^{14}C signature. Measurements from caldera springs confirm a recent atmospheric equilibration of aquifers which feed Mount Mazama springs and indicate that these sources could not account for the dead carbon observed in the deep lake.

Finally, our hydrogen isotopic data in themselves eliminate the cold spring hypothesis. The hydrogen isotopic similarity between deep lake waters and the pool and mat fluids are unequivocal evidence that these anomalous fluids originated from within the lake and not from the meteoric waters found in local aquifers.

In summary, the cold spring hypothesis fails to account for either the elevated temperatures or the chemical and isotopic compositions of fluids observed in the deep lake. These thermally and chemically enriched fluids are the source of reduced chemical species used by bacterial communities and the metals which form other deposits present in the deep lake.

(7) The Hydrothermal Hypothesis.

As we have seen, none of the previous six hypotheses can account for all of the observed thermal and chemical anomalies found in Crater Lake. While each can explain a few of the features, each of the six has serious flaws. The major appeal of the hydrothermal hypothesis is that it can account for many and probably all of the unusual thermal and chemical features of Crater Lake.

The high ionic content of the lake compared to other precipitation-dominated Cascade lakes can be accounted for by input from thermal springs which are known to carry elevated concentrations of many elements relative to precipitation sources or cold-spring sources (Mariner et al. 1982). The concentrations of several elements in Crater Lake are high compared to those in most other Cascade lakes. East Lake, which has concentrations that are even higher.than Crater Lake, is an exception. However, East Lake is known to have hot spring inputs. These comparisons suggest that thermal springs can dominate the ion content of lakes. Similar conclusions have come from studies of lakes found in the volcanically active region of the North Island of New Zealand (Timperly and Vigor-Brown, 1986; Hoare, 1985: McColl, 1975 ; Forsyth, 1977).

Hydrothermal sources can explain the elevated concentrations of elements in Crater Lake, and can also account for the first-order features of the lake's inter-element relationships. As shown in Figures 22 and 23, a mixture of waters from precipitation and the anomalous fluids sampled in pools, bacterial mats, and sediment pore waters can account in a general way for the major element relationships in the lake.

The enrichments of certain minor elements in Crater Lake fluids also are evidence for a hydrothermal source. Thompson et al. (1990) have reported that boron is enriched by a factor of two and that lithium is enriched by a factor of ten in Crater Lake compared to the average waters from Mazama cold springs. Both elements are typically enriched in geothermal waters (White et al., 1976; Ellis and Mahon, 1977). Moreover, Cl/Li values in Crater Lake lie within the range of those observed for typical thermal waters, but outside the values measured in Mazama cold springs (Thompson et al., 1990). Thompson et al.(1990) suggest that both the chloride and lithium concentrations in the lake are controlled by hydrothermal input.

Our results show that lithium is correlated with temperature in near-bottom samples from the South Basin (Collier and Dymond, 1988a), and the data from submersible sampling show that these enrichments in pool and pore fluids are nearly 10 times greater than the bulk lake composition (Table 9). Lithium enrichments are particularly relevant because low-temperature weathering of rocks does not extract Li efficiently (Thompson, 1973), whereas high temperature, hydrothermal alteration can remove much of the Li from rocks, thereby strongly enriching the hydrothermal fluid (Von Damm et al., 1985). This temperature influence is illustrated by the relatively low concentrations of Li in all inter-caldera springs (J. McManus, unpublished data) and in Mazama springs in general (Thompson et al., 1990).

Two other highly successful tracers of hydrothermal activity in the oceans, manganese and radon–222, cannot be unequivocally linked to this source in Crater Lake because other processes might also cause enrichments. However, enrichments of these species are a necessary, but not sufficient, evidence for hydrothermal inputs. Thus, the hydrothermal hypothesis can account for the localized, strong enrichments of these tracers observed in the Detailed Study Area.

^{3}He is a primordial isotope which is a distinctive tracer of mantle origin; our measurements of elevated concentrations of ^{3}He are rigorous evidence for the injection of magmatic volatiles into the deep lake. The observation that this isotopic tracer positively correlates with temperature and with major element content in the deep lake waters is consistent with helium injection by a hydrothermal fluid. Further support for a hydrothermal input to the lake is provided by a ratio of ^{3}He to heat which is very similar to that observed in known deep-ocean hydrothermal vents (Lupton et al., 1989). Although the 1989 sampling program extended the known enrichments of ^{3}He in Crater Lake to 500 times the atmospheric equilibration value, these highly enriched samples have the same correlation with major element composition as found in deep lake water.

Thermal spring inputs can also account for the surprisingly low abundances of ^{14}C in the near-bottom waters of the lake and the predominantly "dead" carbon observed in pool samples. Magmatic carbon, released as CO_2 to circulating hydrothermal fluids, could be a source of dead carbon. Reaction of the hydrothermal fluids with wall rock will result in leaching of cations, neutralization of the acidity of the fluids, and an increase in carbonate alkalinity. Consequently, hydrothermal fluids generally have high bicarbonate ion content (Mariner et al., 1982). Bicarbonate is the major anion in Crater Lake waters and is in greater concentration than can be accounted for by low-temperature weathering reactions (Nathenson, 1990a). Pool and pore water samples collected in 1989 from the deep lake have ΣCO_2 values that are more than 10 times greater than the ambient deep lake values. Consequently, these values are a source for the "missing" alkalinity identified by mass balance studies (Nathenson, 1990a; Reilly et al., 1989).

The presence of bacterial mats and the measurements of elevated temperatures and chemical anomalies associated with these communities are perhaps the most direct evidence of hydrothermal fluid venting into the lake. Temperatures within the mats are 15°C above background lake values and are compatible with a diffuse flow of hydrothermal fluids. Hydrothermal advection of chemically enriched fluids can supply the necessary continuous source of reduced chemicals to the bacterial communities in the mats. We have deduced flow rates of 10 m/y to 100 m/y in these bacterial mats from temperature measurements made from the submersible in 1989.

The bacterial mats have a composition similar to the metal-rich crusts and pebbles that have been observed at a number of locations in the Detailed Study Area. Such deposits have been observed

nowhere else in the lake. These deposits may be the fossilized equivalents of the mats and may represent previous sites of hydrothermal fluid venting. Arsenic and antimony enrichments in these iron oxyhydroxides imply that they were precipitated from a fluid which was enriched in these elements. Such fluid enrichments are commonly observed in hydrothermal solutions.

Chemical geothermometers based on empirical data have been applied to our enriched pore-water and pool samples to define the possible rock-water equilibration temperatures. These results indicate that the enriched fluids found at the bottom of Crater Lake could have equilibrated at temperatures ranging from 40°C to 165°C consistent with a hydrothermal hypothesis. These elevated equilibration temperatures suggest that the enriched, lower-temperature fluids sampled in the deep lake are either diluted with normal lake water by a factor of 10 or that these enriched fluids have lost most of their heat by conduction to surrounding rocks and sediments. The predominance of isotopically "dead" carbon in pool samples indicates mixing of roughly equal parts of thermal fluids and deep lake water and suggests the importance of conductive heat losses.

Hydrothermal fluids can also account for the small thermal and chemical enrichments of bottom waters and the highly enriched pools at certain locations in Crater Lake. Calculated densities for waters with the highest temperatures observed (19°C) indicate these fluids are buoyant with respect to lake bottom water. However, conductive heat loss from these fluids can result in the formation of fluids which are more dense than ambient waters, thereby creating chemically enriched pools.

In addition, time-series measurements of temperature and conductivity document the continued accumulation of heat and salt in the deep lake. These measurements are used to compute a total heat input to the lake ranging between 20 and 30 megawatts and the total flux of chemically-enriched fluids of approximately 300 liters per second. These estimates, based on direct measurements, compare favorably with model-based estimates of heat and salt fluxes which predict a heat flux of 15 to 29 megawatts and a hydrothermal fluid input of 200 to 400 liters per second. Consequently, diverse approaches, which use very different data and assumptions, all indicate a similar flux of heat and salt into the deep-waters of Crater Lake. This flux is compatible with a common carrier — hydrothermal fluids.

Summary of Hypothesis Testing.

We summarize the seven hypotheses and their tests in an abbreviated form in Table 19. Despite the collection of a broad range of chemical and physical data, we have not been able to disprove the hydrothermal hypothesis. This hypothesis is completely compatible with the isotopic measurements, the major element compositions, the mass balance constraints, the minor element data, the temperature observations, the fluid advection rates, and the biological communities in Crater Lake. Consequently, the evidence strongly supports the concept of hydrothermal activity as an important Crater Lake process.

Table 19. Hypothesis Testing

Null Hypothesis:	Observation:	Status*
1. Early stage fumarolic and hydrothermal inputs account for the salt content of Crater Lake.	The flushing rate of Crater Lake waters is so large that any "old" ionic inputs are no longer present.	(–)
	There has been no measurable change in the Crater Lake salt content over the past 80 years.	(–)
2. High evaporation rates explain the ion content of Crater Lake water.	Evaporation can only account for a small fraction of the enrichments observed in Crater Lake waters.	(–)
	Evaporation of runoff waters could not produce the distinctive ion composition of the lake.	(–)
3. Alteration of sedimented volcanic debris is a major source of ions to the lake.	Pore water profiles are not compatible with significant alteration.	(–)
	Caldera wall debris, sediment trap particles, and sediments are compositionally very similar showing that little alteration has occurred.	(–)
4. Conductive heating is a major source of heat to the deep lake.	Sharp horizontal and vertical gradients in bottom water cannot be explained by conductive heating.	(–)
	Correlations among temperature, salt, and helium cannot be explained by the hypothesis.	(–)
5. Degassing of non-condensible gases can account for the enrichments of CO_2, Cl, and He in the lake.	Significant CO_2 and HCl inputs are incompatible with the observed pH in Crater Lake.	(–)
	The carbon and helium isotopic composition of caldera wall springs are atmospheric, not magmatic.	(–)
6. Mineral-laden cold springs are a major source of ions to the lake and can have temperatures similar to anomalous deep lake fluids.	He and ΣCO_2 correlations with temperature and ion contents are not explained by the hypothesis.	(–)
	Mazama cold springs do not have sufficient enrichments, especially for Cl, Li, Ba, Eu, and As.	(–)
	The H, He and C isotopic composition of anomalous lake fluids is incompatible with an aquifer source.	(–)
7. Hydrothermal venting through sediments, cliff faces, and pools accounts for the major inputs of heat and salt to the lake.	Thermal fluids 15 °C warmer than background lake water are located on the lake floor.	(+)
	Pore water advection accounts for the temperature and salt gradients observed in sediments.	(+)
	Bacterial mats have high internal temperatures that cannot be maintained without convection.	(+)
	The isotopic composition of He and C document a magmatic source.	(+)
	The correlation between ΣCO_2, He, ions, and T indicates a common carrier - warm salty water.	(+)
	Multiple approaches all indicate advection of 200 to 400 liters/s of saline fluids and 15 to 20 Mw of heat energy.	(+)

* (+) observation supports hypothesis ; (–) observation contradicts hypothesis

V. Summary and Conclusions

Significant observations

Submersible observations within the South Basin have defined fine-scale variations in the temperature and salt content of the near-bottom waters. Temperature variations of up to 0.5°C and conductivity variations of more than 10 percent occur over distances of a few meters. The magnitude and spatial scale of these variations require a continuing input of warmer and more saline water to maintain the high gradients.

Deep-lake communities of bacteria, which produce impressive mat features on rock outcrops and sediment surfaces, mark the site of diffuse venting on the lake floor. Some of these features cover areas tens of meters across and have internal temperatures elevated over background water by more than 15°C. These communities apparently use the abundant reduced iron which occurs in the advecting fluids to fuel their metabolism. Although there were no visual indications of flow from the mats, advection is implied by the requirements of the prolific bacterial communities for continuous inputs of reduced chemical species. Furthermore, a flow of warm fluids is required to maintain the temperature gradients observed within the mats. Advection as high as 100 m/y are indicated. Consequently, the bacterial mats are aptly described as visual markers of thermally and chemically enriched fluid venting.

Pools of saline water with major element contents that are approximately ten times greater than background lake values have been discovered in two widely separated areas of the lake. Sediment pore waters are another source of enriched fluids in the lake system. Various lines of evidence show that the pore water enrichments in salt cannot be the result of sediment reaction with normal lake water. Significantly, the pore water measurements reveal non-linear gradients of the enriched pore fluids. Consequently, the concentration profiles in the core require vertical fluid advection rates of up to 2 m/y.

Although comparisons among the pool, mat, and pore water compositions reveal some differences, similarities in the overall elemental contents suggest that the fluids advecting through the sediments and supplying the pools and mats have a similar source. Chemical geothermometry suggest the fluids equilibrated with silicate rocks at temperatures ranging from 40°C to 165°C.

Sampling of mat fluids, pools, and pore waters has greatly extended the range of anomalous water compositions which are found within Crater Lake. For example, the anomalies with respect to background lake levels for major elements are approximately a factor of ten. Manganese and ^{222}Rn, which are important tracers of hydrothermal sources in the ocean have some of the strongest enrichments. Manganese in the end-member fluids is a million times more enriched than observed in normal lake water. ^{222}Rn is 100,000 times enriched over typical lake values. Helium-3, perhaps the most distinctive indicator of a magmatic source, is enriched 500 times over values for water that is in equilibrium with the atmosphere. Rare earth element concentrations in sediment pore water, pool fluid, and lake samples have a distinctive pattern. The abundance of europium is markedly enriched over the other rare earth elements, which is a pattern commonly observed observed in hydrothermal fluids.

Isotopic measurements of pool samples places important constraints on the origin and evolution of these anomalous fluids. The hydrogen isotopic composition indicates that the pool fluid was originally lake water. This observation is unequivocal evidence that meteoric fluids carried in regional cold springs could not be the source of the pool waters. In addition, the deep lake contains surprising amounts of "dead" carbon (i.e., carbon with no radioactive ^{14}C). Carbon-14 measurements of a pool sample reveal that the carbon in these fluids is almost entirely "dead". Pore waters also contain abundant "dead" carbon. Magmatic carbon, which is carried by fluids

that have interacted with rocks at elevated temperatures, is the best hypothesis for the source of this carbon. Mass balance calculations based on both total carbon and ^{14}C isotopic systematics, suggest the pool fluids are a mixture of approximately equal parts of a primary hydrothermal fluid and normal lake waters. Further mixing of pool and pore fluids in addition to conductive heat transfer can account for the range of heat-to-salt ratios observed in the deep lake.

These data have permitted us to recalculate the geochemical mass balances for the lake which include realistic estimates of composition of a hydrothermal input. A variety of models result in similar estimates of the hydrothermal flows into the lake. For example, a helium flux model predicts a heat flow of 29 megawatts (MW) with a temperature of 18°C for the fluid as it enters the lake. This can be compared with the maximum measured bacterial mat temperature of 18.9°C. The cation budget predicts a heat flow of 15 MW. Similarly, we calculate that the flow rate of this thermally and chemically enriched fluid is approximately 200-400 liters/sec. This estimate is derived from the helium budget (400 liters/sec), the ion mass balance budgets (265 ± 115 liters/sec).

Significantly, these model-based estimates are entirely consistent with direct observations of heat and salt accumulations in the deep lake. Time series observations of annual temperature changes in the deep lake predict a heat flow of 20 to 30 MW. In addition, an observed accumulation rate of salt in the bottom of the lake requires 200 to 400 liters/sec of chemically-enriched fluid input (Appendix A).

Conclusions

As a result of the past three years of field studies and our interpretation of these and other data from the literature, we conclude that there are inputs of hydrothermal fluids into the bottom of Crater Lake. The dissolved materials associated with these thermally and chemically enriched fluids, coupled with the overall hydrologic balance, control the observed chemical composition of the Lake. While other geochemical processes are certainly operative, these geothermal inputs are significant in that they dominate the material fluxes for most chemicals into Crater Lake. Furthermore, the geothermal inputs have a direct effect on the density structure of the deep lake and the character of vertical mixing. The vertical mixing rate determines the rate of redistribution of heat, salt, and nutrients.

Many young caldera lake systems have been studied during their early post eruption phases (McColl, 1975; Sigurdsson, 1977; Timperley and Vigor-Brown, 1986). Crater Lake represents a late-stage in the evolution of these lakes. It has recently become clear that other lakes from a range of tectonic settings experience hydrothermal activity including Yellowstone Lake (Klump et al., 1988) and Lake Baikal (Golubev, 1978, 1984 and personal communication). Taken together, these studies and our results from Crater Lake demonstrate a broad range of hydrothermal expressions in diverse limnological systems.

VI. References

Asikainen, M. 1981. State of disequilibrium between ^{238}U, ^{234}U, ^{226}Ra, and ^{222}Rn in groundwater from bedrock. Geochim. Cosmochim. Acta **45:**201-206.

Bacon, C. R. 1983. Eruptive history of Mount Mazama and Crater Lake Caldera, Cascade Range, U.S.A. J. Volcan. Geotherm. Res. **18:**57-115.

Bacon, C. R., and T. H. Druitt. 1988. Compositional evolution of the zoned calc-alkaline magma chamber of Mount Mazama, Crater Lake, Oregon. Contrib. Mineral. Petrol. **98:**224-256.

Bacon, C. R., and M. A. Lanphere. 1990. The geologic setting of Crater Lake, p. 19-28. *In* E. T. Drake, G. L. Larson, J. Dymond, and R. Collier [eds.], Crater Lake: An Ecosystem Study. American Association for the Advancement of Science, Pacific Division.

Bacon, C. R., L. H. Adami, and M. A. Lanphere. 1989. Direct evidence for the origin of low-^{18}O silicic magmas: quenched samples of a magma chamber's partially-fused granitoid walls, Crater Lake, Oregon. Earth Planet. Sci. Letts. **96**:199-208.

Barber, J. H., Jr., and C.H. Nelson. 1990. Sedimentary history of Crater Lake Caldera, Oregon., p. 29-40. *In* E. T. Drake, G. L. Larson, J. Dymond, and R. Collier [eds.], Crater Lake: An Ecosystem Study. American Association for the Advancement of Science, Pacific Division.

Bender, M., W. Martin, J. Hess, F. Sayles, L. Ball, and C. Lambert. 1987. A whole core squeezer for interfacial pore water sampling. Limnol. Oceanogr. **32:**1214-1225.

Bender, M. L. 1983. Pore water chemistry of the Mounds Hydrothermal Field, Galapagos Spreading Center: Results from Glomar Challenger piston coring. J. Geophys. Res. **88:**1049-1056.

Benson, B. B., and D. Krause Jr. 1980. The concentration and isotopic fractionation of gases dissolved in freshwater in equilibrium with the atmosphere. 1. Oxygen. Limnol. Oceanogr. **25:**662-671.

Berger, R., T.B. Jackson, R. Michael, and H.E. Suess. 1987. Radiocarbon content of tropospheric CO_2 at China Lake, California 1977-1983. Radiocarbon **29**:18-23.

Berger, R. and W.F. Libby. 1966. UCLA radiocarbon dates V. Radiocarbon **9**:477-504.

Blackwell, D.D., R.G. Bowen, D.A. Hull, J. Riccio, and J.L. Steele. 1982. Heat flow, volcanism and subduction in northern Oregon. J. Geophys. Res. **87**:8735-8754.

Blackwell, D.D., J.L. Steele, S. Kelley, and M.A. Korosec. 1990. Heat flow in the state of Washington and thermal conditions in the Cascade Range.J. Geophys. Res. **95**:19495-19516.

Blackwell, D. D., J. L. Steele, M. K. Frohme, C. F. Murphey, G. R. Priest, and G. L. Black. 1990. Heat flow in the Oregon Cascade Range and its Correlation with Regional Gravity, Curie Point Depths, and Geology. J. Geophys. Res. **95:**19475-19493.

Bostrom, K., and L. Widenfalk. 1984. The origin of iron-rich muds at the Kameni Islands, Santorini, Greece. Chem. Geol. **42:**203-218.

Bredehoeft, J. D., and I. S. Papadopulos. 1965. Rates of vertical groundwater movement estimated from the earth's thermal profile. Water Resources Res. **1:**325-328.

Broecker, W. S., J. Cromwell, and Y. H. Li. 1968. Rates of vertical eddy diffusion near the ocean floor based on measurements of the distribution of excess Rn-222. Earth Planet. Sci. Lett. **5:**101.

Bruland, K. W. 1983. Trace elements in seawater, p. 157-220. *In* J. P. Riley and G. Skirrow [eds.], Chemical Oceanography, 2nd edition, V. 8. Academic Press.

Bruland, K. W., R. P. Franks, G. A. Knauer, and J. H. Martin. 1979. Sampling and analytical methods for the determination of copper, cadmium, zinc, and nickel at the nanogram per liter level in sea water. Analyt. Chim. Acta **105:**233-245.

Bullister, J. L., and R. F. Weiss. 1983. Anthropogenic chlorofluoromethanes in the Greenland and Norwegian Seas. Science **221:**265-221.

Bullister, J. L., and R. F. Weiss. 1988. Determinations of CCl3F and CCl2F2 in seawater and air. Deep-Sea Res **35:**839-853.

Byrne, J. V. 1962. Bathymetry of Crater Lake, Oregon. The Ore Bin **24:**161-164.

Byrne, J. V. 1965. Morphometry of Crater Lake, Oregon. Limnol. Oceanogr. **10(3):**462-465.

Campbell, A. C., M. R. Palmer, G. P. Klinkhammer, T. S. Bowers, J. M. Edmond, J. R. Lawrence, J. F. Casey, G. Thompson, S. Humphris, P. Rona, and J.A Karson. 1988. Chemistry of hot springs on the Mid-Atlantic Ridge. Nature, **335**:514-519.

Carmack, E.C., and D.M. Farmer. 1982. Cooling processes in deep, temperate lakes: A review with examples from two lakes in British Columbia. J. Mar. Res. **40:**85-111.

Carmack, E.C., R.F. Weiss, and V.M. Koropalov. 1989. Physical studies of mixing processes in Lake Baikal [abstr.]. EOS **70:**1136.

Carothers, W. W., R. H. Mariner, and T. E. C. Keith. 1987. Isotope geochemistry of minerals and fluids from Newberry Volcano, Oregon. J. Volcan. Geotherm. Res. **31**:47-63.

Carpenter, J. H. 1965a. The Chesapeake Bay Institute technique for the Winkler dissolved oxygen method. Limnol. Oceanogr. **10:**141-143.

Carpenter, J. H. 1965b. The accuracy of the Winkler method for dissolved oxygen analysis. Limnol. Oceanogr. **10:**135-140.

Chen, C. T., and F. J. Millero. 1986. Precise thermodynamic properties for natural waters covering only the limnological range. Limnol. Oceanogr. **3(3):**657-662.

Clark, E.E. 1953. Indian Legends of the Pacific Northwest. University of California Press. 225p, quoting Applegate, O.C. January 1907, The Klamath Legend of La-o, Steel Points I:75-76.

Cole, D.R., M.J. Mottl, and H. Ohmoto. 1987. Isotopic exchange in mineral-fluid systems. II. Oxygen and hydrogen isotopic investigation of the experimental basalt-seawater system. Geochim. Cosmochim. Acta **51**:1523-1538.

Collier, R., and J. Dymond. 1988a. Studies of hydrothermal processes in Crater Lake. A preliminary report of field studies conducted in 1987 for the Crater Lake National Park. Oregon State University, College of Oceanography Reference #88-5, 49 pp.

Collier, R., and J. Dymond. 1988b. Observations of bacterial mats associated with thermal springs at 450 meters depth in Crater Lake, OR [abstr.]. EOS **69:**1138.

Collier, R., and J. Dymond. 1989. Studies of hydrothermal processes in Crater Lake. A report of field studies conducted in 1988 for the National Park Service. Oregon State University, College of Oceanography Reference #89-2, 79 pp.

Collier, R., J. Dymond, J. Lupton, A. Chen, M. Lilley, and M. Thompson. 1987. Effects of hydrothermal inputs on the chemistry and physics of Crater Lake, OR [abstr.]. EOS **68:**1721.

Collier, R. W. 1985. Molybdenum in the northeast Pacific Ocean. Limnol. Oceanogr. **30:**1351-1354.

Collier, R. W., J. Dymond, J. McManus, and J. Lupton. 1990. Chemical and physical properties of the water column at Crater Lake, OR., p. 69-80. *In* E. T. Drake, G. L. Larson, J. Dymond, and R. Collier [eds.], Crater Lake: An Ecosystem Study. American Association for the Advancement of Science, Pacific Division.

Conway, B. E. 1952. Electrochemical Data. Butterworths.

Corliss, J. B., M. Lyle, J. Dymond, and K. Crane. 1978. The chemistry of hydrothermal mounds near the Galapagos Rift. Earth Planet. Sci. Lett. **40:**12-24.

Cox, R. A., F. Culkin, and J. P. Riley. 1967. The electrical conductivity/chlorinity relationship in natural seawater. Deep-Sea Res. **14:**203-220.

Craig, H. 1966. Isotopic composition and origin of the Red Sea and Salton Sea geothermal brines. Science **154**:1544-1548.

Derry, L.A., and S.B. Jacobsen. 1990. The chemical evolution of Precambrian seawater: Evidence form REEs in banded iron formations. Geochim. Cosmochim. Acta **54**:2965-2977.

Diller, J. S. 1902. The geology and petrography of Crater Lake National Park. U.S. Geological Survey Prof. Paper No. 3, Part I, 62 pp.

Dymond, J., J.B. Corliss, G.R.Heath, C.W. Field, E.J. Dasch, H.H. Veeh. 1973. Origin of metalliferous sediments from the Pacific Ocean. GSA Bull. **84**:3355-3372.

Dymond, J. 1981. Geochemistry of Nazca Plate surface sediments: An evaluation of hydrothermal, biogenic, detrital, and hydrogenous sources, p. 133-173. *In* L.D. Kulm, J. Dymond, E.J. Dasch, D.M. Hussong, and R. Roderick [eds.], The Nazca Plate. Geol. Soc. Amer. Memoir 154.

Dymond, J., E. Baker, and J. Lupton. 1988. Plumes: The oceanic limb of seafloor hydrothermal systems. Proceedings of the Salishan Meeting, The National Academy of Sciences.

Dymond, J., R. Cobler, L. Gordon, P. Biscaye, and G. Mathieu. 1983. ^{226}Ra and ^{222}Ra contents of Galapagos Rift hydrothermal waters - the importance of low-temperature interactions with crustal rocks. Earth Planet. Sci. Lett. **64:**417-429.

Dymond, J., and R. Collier. 1990. The chemistry of Crater Lake sediments: Definition of sources and implications for hydrothermal activity, p. 41-60. *In* E. T. Drake, G. L. Larson, J. Dymond, and R. Collier [eds.], Crater Lake: An Ecosystem Study. American Association for the Advancement of Science, Pacific Division,.

Dymond, J., R. W. Collier, and M. E. Watwood. 1989. Bacterial mats from Crater Lake, Oregon, and their relationship to possible deep-lake hydrothermal venting. Nature **342:**673-675.

Dymond, J., J. B. Corliss, R. Cobler, C. M. Muratli, C. Chou, and R. Conard. 1980. Composition and origin of sediments recovered by deep drilling of sediment mounds, Galapagos Spreading Center, p. 377-385. In B.R. Rosendahl, R. Hekinian, et.al. [eds.], Initial Reports of the Deep Sea Drilling Project, Vol. LIV.

Dymond, J., M. Lyle, B. Finney, D. Z. Piper, K. Murphy, R. Conard, and N. Pisias. 1984. Ferromanganese nodules from MANOP Sites H, S, and R - Control of mineralogical and chemical composition by multiple accretionary processes. Geochim. Cosmochim. Acta **48:**931-949.

Dymond, J., C. Perhats, R. Conard, and R. Collier. 1987. Hydrothermal activity in Crater Lake: Evidence from sediments [abstr.]. EOS **68:**1721.

Dyrssen, D. and L.G. Sillen. 1967. Alkalinity and total carbonate in sea water; a plea for P-T-independent data. Tellus **19**:113-121.

Edmond, J.M. 1970. High precision determination of titration alkalinity and total carbon dioxide content of sea water by potentiometric titration. Deep-Sea Res.**17**:737-750.

Edmond, J. M., C. I. Measures, R. E. McDuff, L. H. Chan, R. Collier, B. Grant, L. I. Gordon, and J. B. Corliss. 1979. Ridge Crest hydrothermal activity and the balance of the major and minor elements in the ocean; the Galapagos data. Earth Planet. Sci. Lett. **46:**1-18.

Ehrenberg, C. G. 1836. Vorlaufige Mitteilungen über das wirkliche Vorkommen fossiler Infusorien und ihre grosse Verbreitung. Poggendorf's Annalen **38:**213-227.

Elder, J. 1981. Geothermal Systems. Academic Press. London. 508pp.

Elderfield, H., R. Upstill-Goddard, and E. R. Sholkovitz. 1990. The rare earth elements in rivers, estuaries, and coastal seas and their significance to the composition of ocean waters. Geochimica et Cosmochimica Acta **54**:971-991.

Ellis, A. J., and W. A. J. Mahon. 1977. Chemistry and geothermal systems. Academic Press.

Emerson, S. 1976. Early diagenesis in anaerobic lake sediments: chemical equilibria in interstitial waters. Geochim. Cosmochim. Acta **40**:925-934.

EPA. 1979. Methods for Chemical Analysis of Water and Wastes. EPA-600/4-79-020.

Erlich, H. L. 1981. The geomicrobiology of iron, p. 393. [eds.], Geomicrobiology. Marcel Dekker, Inc.

Farmer, D.M., and E. Carmack. 1981. Wind mixing and restratification in a lake near the temperature of maximum density. J. of Phys. Ocean. **11:**1516-1533.

Feely, R.A., G.J. Massoth, E.T. Baker, J.P. Cowen, M.F. Lamb, and K.A. Krogslund. 1990. The effect of hydrothermal processes on midwater phosphorus distributions in the northeast Pacific. Earth Planet. Sci. Letts. **96**:305-318.

Field, C. W., and R. H. Fifarek. 1985. Light stable-isotope systematics in the epithermal environment. *In* Berger, B. R., and P. M. Bethke [eds.], Reviews in Economic Geology, Volume 2 p. 99-128.

Fine, R. A., M. J. Warner, and R. F. Weiss. 1988. Water mass modification at the Agulhas Retroflection: chlorofluoromethane studies. Deep-Sea Res **35:**311-332.

Fitterman, D. V. 1988. Overview of the structure and geothermal potential of Newberry Volcano, Oregon. J. Geophys. Res. **93:**10059-10066.

Forsyth, D. J. 1977. Limnology of Lake Rotokawa and its outlet stream. New Zealand Journal of Marine and Freshwater Research **11(3):**525-539.

Fouillac, C., and G. Michard. Sodium/Lithium ratio in water applied to geothermometry of geothermal reservoirs. Geothermics **10(1)**:55-70.

Fournier, R. O. 1981. Application of water geochemistry to geothermal exploration and reservoir engineering, p. *In* L. Rybach and L. P. J. Muffler [eds.], Geothermal Systems: Principles and Case Histories. J. Wiley and Sons.

Fournier, R.O.,and A.H. Truesdell. 1973. An empirical Na-K-Ca geothermometer for natural waters. Geochim. Cosmochim. Acta **37**:1255-1275.

Fournier, R. O., and R. W. Potter II. 1979. Magnesium correction to the Na-K-Ca chemical geothermometer. Geochim. Cosmochim. Acta **43:**1543-1550.

Froelich, P.N., G.P. Klinkhammer, M.L. Bender, N.A. Luedtki, G.R. Heath, D. Cullen, P. Dauphin, D. Hammond, and B. Hartman. 1979. Early oxidation of organic matter in pelagic sediments of the eastern equatorial Atlantic: Suboxic diagenesis. Geochim. Cosmochim. Acta **43**:1075.

Garrels, R. M., and C. L. Christ. 1965. Solutions, Minerals, and Equilibria. Harper and Row.

Garrels, R. M., and F. T. MacKenzie. 1967. Origin of the chemical compositions of some springs and lakes, p. 222-242. Equilibrium Concepts in Natural Water Systems. 151st Meeting of the American Chemical Society, 1966, American Chemical Society.

German, C.R., G.P. Klinkhammer, J.M. Edmond, A. Mitra, and H. Elderfield. 1990. Hydrothermal scavenging of rare-earth elements in the ocean. Nature **345**:516-518.

Goldman, C.R., and A. Jassby. 1990. Spring mixing depth as a determinant of annual primary production in lakes. *In* M.M. Tilzer, and C. Serruya [eds.], Large Lakes Ecological Structure and Function. Springer-Verlag. 125-132.

Goldman, J. C., D. A. Caron, and M. R. Dennett. 1987. Regulation of gross growth efficiency and ammonium regeneration in bacteria by substrate C:N ratio. Limnol. Oceanogr. **32(6):**1239-1252.

Goldstein, S.J., and S.B. Jacobsen. 1988. Rare earth elements in river waters. Earth Planet. Sci. Letts. **89**:35-47.

Golubev, V.A. 1978. Geothermal investigations on Lake Baikal using a cable probe-thermometer. Izvestiya **14(3)**: 235- 238.

Gran, G. 1952. Determination of the equivalence point in potentiometeric titrations. Part II. Analyst **77**:661-671.

Guichard, F., R.M. Church, M. Treuil, and H. Jaffrezic. 1979. Rare earths in barites: distribution and effects on aqueous partitioning. Geochim. Cosmochim. Acta **43**:983-997.

Hanert , H. H. 1981. The Genus *Gallionella*, p. 509-515. *In* M. P. Starr, H. Stolp, H. G. Truper, A. Balows, and H. G. Schlegel [eds.], The Prokaryotes: A Handbook on Habitats, Isolation, and Identification of Bacteria. Springer-Verlag.

Hanert, H. H. 1973. Rezente marine Eisenerze auf Santorin, Griechenland. II. Bakterogenese von Eisenhydroxidsedimenten. Geologische Rundschau **62:**786-812.

Harned, H. S., and B. B. Owen. 1958. The Physical Chemistry of Electrolyte Solutions, 3rd Edition. Reinhold.

Haskin, L.A., F.A. Frey, R.A. Schmitt, and R.H. Smith. 1966. Meteoritic, solar and terrestrial rare earth distribution, in *Physics and Chemistry of the Earth, VII* (L. II. Ahrens, F. Press, S.K. Runcorn, and H.C. Urey, eds.), Pergamon Press, London.

Herczeg, A.L., and D.M. Imboden. 1988. Tritium hydrologic studies in four closed-basin lakes in the Great Basin, U.S.A. Limnol. Oceanogr. **33(2)**:157-173.

Herzig, P.M., K.P. Becker, P. Stoffers, H. Bäcker, and N. Blum. 1988. Hydrothermal silica chimney fields in the Galapagos Spreading Center at 86°W. Earth Planet. Sci. Letts. **89**:261-272.

Hoare, R. A. 1985. Inferred geothermal inflows to Lake Rotorua. New Zealand Journal of Marine and Freshwater Research **19:**151-156.

Holbrook, S., R. Collier, and J. Dymond. 1985. Dissolved and particulate trace metal distributions in Crater Lake, Oregon [abstr.]. EOS **66:**1326.

Honeyman, B.D., L.S. Balistrieri, and J.W. Murray. 1988. Oceanic trace metal scavenging: the importance of particle concentration. Deep-Sea Res. **35**:227-246.

Huppert, H. E. 1971. On the stability of a series of double diffusive layers. Deep-Sea Res. **18:**1005-1021.

Hurst, A. W., and R. R. Dibble. 1981. Bathymetry, heat output and convection in Ruapehu Crater Lake, New Zealand. J. Volcanol. Geotherm. Res. **9:**215-236.

Hutchinson, G. E. 1957. A Treatise on Limnology, Vol. 1. Wiley.

Imboden, D.M.,R.F. Weiss, H. Craig, R.L. Michel, and C.R. Goldman. 1977. Lake Tahoe geochemical study. 1. Lake chemistry and tritium mixing study. Limnol. Oceanogr, **22**:1039-1051.

Ingebritsen, S. E., D. R. Sherrod, and R. H. Mariner. 1989. Heat flow and hydrothermal circulation in the Cascade Range, North-Central Oregon. Science **243**:1458-243.

Jahnke, R. A. 1988. A simple, reliable, and inexpensive pore-water sampler. Limnol. Oceanogr. **33:**483-487.

Jenkins, W.J. 1988. The use of anthropogenic tritium and helium-3 to study subtropical gyre ventilation and circulation. *In* Charnock, H., F.R.S., J.E. Lovelock, F.R.S., P.S. Liss, and M. Whitfield [eds.], Tracers in the Ocean. 43-61.

Johnson, D. M., R. R. Petersen, D. R. Lycan, J. W. Sweet, M. E. Neuhaus, and A. L. Schaedel. 1985. Atlas of Oregon Lakes. Oregon State University Press.

Juniper, S. K., and Y. Fouquet. 1988. Filamentous iron-silica deposits from modern and ancient hydrothermal sites. Canadian Minerologist **26:**859-869.

Kadko, D.C., N.D. Rosenberg, J.E. Lupton, R.W. Collier, and M.D. Lilley. 1990. Chemical reaction rates and entrainment within the Endeavour Ridge hydrothermal plume. Eart Planet. Sci. Letts. **99**:315-335.

Kadko, D., J. E. Lupton, R. Collier, M. D. Lilley, and H. Pak. 1986. Endeavour Ridge hydrothermal plume study [abstr.]. EOS **67:**1027.

Kadko, D. C. 1981. A detailed study of uranium series nuclides for several sedimentary regimes of the Pacific. Ph.D. Thesis, Columbia University, 312 p.

Karl, D. M., A. Brittain, and B. Tilbrook. In press. Initial microbiological investigations of Pelee's vent, Loihi Seamount. NOAA Symposium Series for Undersea Research, 6.

Karl, D. M., G. M. McMurtry, A. Malahoff, and M. O. Garcia. 1988. Loihi Seamount, Hawaii: A mid-plate volcano with a distinctive hydrothermal system. Nature **335:**532-535.

Keasler, K. M., and W. D. Loveland. 1982. Rare earth elemental concentrations in some Pacific Northwest rivers. Earth Planet. Sci. Letts. **61**:68-72.

Kelley, D. E. 1984. Effective diffusivities within oceanic thermohaline staircases. J. Geophys. Res. **89:**10,484-10,488.

Kelley, D. E. 1988. Small-scale turbulence and mixing in the ocean, p. 481-502. *In* J. C. J. Nihouc and B. M. Jamart [eds.], Proceedings of the 19th International Liege Colloquium on Ocean Hydrodynamics, Elsevier Oceanography Series.

Kelley, D. E. 1990. Fluxes through diffusive staircases: A new formulation. J. Geophys. Res. **95:** 3365-3371.

Kharaka, Y.K., and R.H. Mariner. 1989. Chemical geothermometers and their application to formation waters from sedimentary basins. *In* N.D. Naeser and T.H. McCulloh [eds.], Thermal History of Sedimentary Basins Methods and Case Histories. Springer-Verlag 99-117.

Kibby, H. V., J. R. Donaldson, and C. E. Bond. 1968. Temperature and current observations in Crater Lake, Oregon. Limnol. Oceanogr. 363-366.

Klump, J.V., R. Paddock, P.A. Anderson, C.C. Remsen, and J. Maki. 1988. Hydrothermal activity in Yellowstone Lake, WY: Preliminary observations of a unique lacustrine environment. EOS **69:**1109.

Krauskopf, K. B. 1957. Separation of manganese from iron in sedimentary processes. Geochim. Cosmochim. Acta **12:**61-84.

Krishnaswami, S., W. C. Graustein, and K. K. Turekian. 1982. Radium, thorium and radioactive lead isotopes in groundwaters: Application to the *in situ* determination of adsorption-desorption rate constants and retardation factors. Water Resources Res. **18:**1633-1675.

Krishnaswami, S., and K. K. Turekian. 1982. ^{238}U, ^{226}Ra, and ^{210}Pb in some vent waters of the Galapagos spreading center. Geophys. Res. Lett. **9:**827-830.

La Fleur, J. G. 1987. Legend of the Crater Lake hot springs: A product of model mania. Geothermal Resources Council, Transactions **11:**267-279.

La Fleur, J. G. 1990. An alternative hypothesis to explain temperature anomaly and other data observed at Crater Lake, Oregon., p. 61-68. *In* E. T. Drake, G. L. Larson, J. Dymond, and R. Collier [eds.], Crater Lake: An Ecosystem Study. American Association for the Advancement of Science, Pacific Division.

Larson, G. L. 1986. Crater Lake Limnological Program. 1985 Annual Report, National Park Service Cooperative Studies Unit. Oregon State University.

Larson, G. L. 1987. A review of the Crater Lake limnological programs, p. 58-69. *In* T. P. Boyle [eds.], New Approaches to Monitoring Aquatic Ecosystems. ASTM.

Larson, G. L. 1988. Crater Lake Limnological Studies. 1987 Annual Report, National Park Service Cooperative Studies Unit. Oregon State University.

Larson, G. L. 1989. Geographical distribution, morphology and water quality of caldera lakes: A review. Hydrobiologia **171:**23-32.

Larson, G. L. 1990. Status of the ten-year limnological study of Crater Lake, Crater Lake National Park, p. 7-18. *In* E. T. Drake, G. L. Larson, J. Dymond, and R. Collier [eds.], Crater Lake: An Ecosystem Study. American Association for the Advancement of Science Special Volume, Pacific Division.

Leinen, M., R. McDuff, K. Becker, P. Schultheiss, K. Dadey, M. Yamano, N. Fujii, J. Delaney, C. G. Wheat, M. Robotham, B. Holmen, and A. Isley. Submitted. Off-axis hydrothermal activity near the Mariana Trough Spreading Center. Earth Planet. Sci. Lett.

Libby, W.F. 1955. Radioactive Dating, 2nd ed. University of Chicago Press, Chicago. 171p.

Ludden, J. N., and G. Thompson. 1979. An evaluation of the behavior of the rare earth elements during the weathering of sea-floor basalt. Earth Planet. Sci. Letts. **43**:85-91.

Lupton, J. E., E. T. Baker, and G. J. Massoth. 1989. Variable ^{3}He/heat ratios in submarine hydrothermal systems: Evidence from two plumes over the Juan de Fuca ridge. Nature **337:**161-164.

Lupton, J. E., R. Collier, and J. Dymond. 1987. Excess ^{3}He in Crater Lake, Oregon: Evidence for geothermal input [abstr.]. EOS **68:**1722.

Lupton, J.E., and H. Craig. 1985. A major helium-3 source at 15S on the East Pacific Rise. Science **214**:13-18.

Lupton, J. E., R. Collier, and J. Dymond. In preparation. Evidence for hydrothermal inputs to Crater Lake, OR. II. -The Helium isotopes. Limnol. Oceanogr.

Lupton, J. E., G. P. Klinkhammer, W. R. Normark, R. Haymon, K. C. MacDonald, R. F. Weiss, and H. Craig. 1980. Helium-3 and manganese at the 21°N East Pacific Rise hydrothermal site. Earth Planet. Sci. Lett. **50:**115-127.

Mariner, R. H., T. S. Presser, and W. C. Evans. 1982. Chemical and isotopic composition of water from thermal and mineral springs of Washington. U.S. Geological Survey Open-File Report 82-98.

Mariner, R. H., T. S. Presser, W. C. Evans, and M. K. W. Pringle. 1990. Discharge rates of fluid and heat by thermal springs of the Cascade Range, Washington, Oregon, and northern California. J. Geophys. Res. **95:**19517-19531.

Mariner, R. H., J. R. Swanson, G. J. Orris, T. S. Presser, and W. C. Evans. 1980. Chemical and isotopic data for water from thermal springs and wells of Oregon. U.S. Geological Survey Open-File Report 80-737, 50p.

Maris, C. R. P. 1983. Chemical evidence for advection of hydrothermal solutions in ridge flank sediments. Ph.D. Thesis, University of Rhode Island, 264 p.

Maris, C. R. P., and M. L. Bender. 1982. Upwelling of hydrothermal solutions through ridge flank sediments shown by pore water profiles. Science **216:**623-626.

Maris, C. R. P., and M. L. Bender. 1984. Ridge flank hydrothermal solutions in the Galapagos Mounds Hydrothermal Field. Geochim. Cosmochim. Acta **48:**2331-2346.

Maris, C. R. P., M. L. Bender, P. N. Froelich, P. N. Barnes, and N. A. Luedtke. 1984. Chemical evidence for advection of hydrothermal solutions in the sediments of the Galapagos Mounds hydrothermal field. Geochim. Cosmochim. Acta **48:**2331-2346.

Marmorino, G. O., and D. R. Caldwell. 1976. Heat and salt transport through a diffusive thermohaline interface. Deep-Sea Res. **23:**59-67.

Marty, B., and A. Jambon. 1987. C/He^{3} in volatile fluxes from the solid Earth: implications for carbon geodynamics. Earth Planet. Sci. Lett. **83**:16-26.

Mathieu, G. G. 1977. ^{222}Rn-^{226}Ra technique of analysis, Annual Technical Report COO 2185-0 to ERDA. Lamont Doherty Geological Observatory, Palisades, NY.

McColl, R. H. S. 1975. Chemical and biological conditions in lakes of the volcanic plateau, p. 123-139. *In* V. H. Jolly and J. M. A. Brown [eds.], New Zealand Lakes. Aukland University Press.

McDuff, R. E. 1987. Chemistry of seafloor hydrothermal systems. Reviews of Geophysics **25:**1427-1429.

McManus, J., R. Collier, and J. Dymond. 1990. Heat and salt flux in Crater Lake, OR as deduced from water column CTD measurements. EOS **71:**

McManus, J., R. Collier, J. Dymond, and G. Larson. in prep. The role of mixing, carbon flux, and thermo-chemical inputs on the oxygen budget in Crater Lake, OR.

Michard, A. 1989. Rare earth element systematics in hydrothermal fluids. Geochimica et Cosmochimica Acta **53**:745-750.

Michard, A., F. Albarède, G. Michard, J.F. Minster, and J.L. Charlou. 1983. Rare-earth elements and uranium in high-temperature solutions form East Pacific Rise hydrothermal vent field (13°N). Nature **303**:795-797.

Morgan, J.W., and G.A. Wandless. 1980. Rare earth element distribution in some hydrothermal minerals: evidence for crystallographic control. Geochim. Cosmochim Acta **44**:973-980.

Mortimer, C. H. 1981. The oxygen content of air-saturated fresh waters over ranges of temperature and atmospheric pressure of limnological interest. Mitt. int. Ver. Limnol. **22:**23.

Mottl, M. J., and H. D. Holland. 1978. Chemical exchange during hydrothermal alteration by seawater, I. Experimental results for major and minor components of seawater: The role of seawater/basalt ratio. Geochim. Cosmochim. Acta **42:**1103-1115.

Mulder, E. G., and M. H. Deinema. 1981. The sheathed bacteria, p. 425-440. *In* M. P. Starr, H. Stolp, H. G. Truper, A. Balows, and H. G. Schlegel [eds.], The Prokaryotes: A Handbook on Habitats, Isolation, and Identification of Bacteria. Springer-Verlag.

Nathenson, M. 1990a. Chemical balance for major elements in water in Crater Lake, Oregon, p. *In* E. T. Drake, G. L. Larson, J. Dymond, and R. Collier [eds.], Crater Lake: An Ecosystem Study. American Association for the Advancement of Science, Pacific Division.

Nathenson, M. 1990b. Temperatures of springs versus elevation in the vicinity of Crater Lake, Oregon [abstr.]. EOS **71:**

Nathenson, M., and J. M. Thompson. 1990. Chemistry of Crater Lake, Oregon, and nearby springs in relation to weathering, p. *In* E. T. Drake, G. L. Larson, J. Dymond, and R. Collier [eds.], Crater Lake: An Ecosystem Study. American Association for the Advancement of Science, Pacific Division.

Neal, V. T., S. J. Neshyba, and W. W. Denner. 1971. Temperature microstructure in Crater Lake, Oregon. Limnol. Oceanogr. **16:**695-700.

Neal, V. T., S. J. Neshyba, and W. W. Denner. 1972. Vertical temperature structure in Crater Lake, Oregon. Limnol. Oceanogr. **17(3):**451-454.

Nelson, C. H., P. R. Carlson, and C. R. Bacon. 1988. The Mount Mazama climatic eruption (~6900 yr B.P.) and resulting convulsive sedimentation on the Crater Lake caldera floor, continent, and ocean basin. Geol. Soc. Amer. Special Paper **229:**37-57.

Nelson, C. H., A. W. Meyer, D. Thor, and M. Larsen. 1986. Crater Lake, Oregon: A restricted basin with base-of-slope aprons of nonchannelized turbidites. Geology **14:**238-241.

Newman, F.C. 1976. Temperature steps in Lake Kiva: A bottom heated saline lake. J. Phys. Ocean. **6:**157-163.

Ohmoyo, H., and R. O. Rye. 1974. Hydrogen and oxygen isotopic compositions of fluid inclusions in the Kuroko deposits, Japan. Economic Geology **69**:947-953.

Olafsson, J. 1980. Temperature structure and water chemistry of the caldera Lake Oskjuvatn, Iceland. Limnol. Oceanogr. **25:**779-788.

O'Neil, J. R., and H. P. Taylor Jr. 1967. The oxygen isotope and cation exchange chemistry of feldspars. American Mineralogist **52**:1414-1437.
Onishi, H. 1969. Arsenic, p. *In* K. H. Wedepohl [eds.], Handbook of Geochemistry, Section 33-I.
Padman, L., and T. M. Dillon. 1989. Thermal microstructure and internal waves in the Canada Basin diffusive staircase. Deep-Sea Res. **36(4)**:531-542.
Pearl, H. W., R. C. Richards, R. L. Leonard, and C. R. Goldman. 1975. Seasonal nitrate cycling as evidence for complete vertical mixing in Lake Tahoe, California-Nevada. Limnol. Oceanogr. **20(1)**:1-8.
Perkin Elmer. 1982. Analytical Methods for Atomic Absorption Spectrophotometry.
Phillips, K. N. 1968. Hydrology of Crater Lake, East Lake, and Davis Lakes, Oregon: U.S. U.S. Geological Survey.
Pond, S., and G. L. Pickard. 1978. Introductory Dynamic Oceanography. Pergamon Press.
Poreda, R. 1983. Helium, neon, water and carbon in volcanic rocks and gases. Ph.D. Thesis, University of California, San Diego.
Poreda, R., and H. Craig. 1989. Helium isotope ratios in Circum-Pacific volcanic arcs. Nature **338**:473-478.
Redmond, K. T. 1990. Crater Lake climate and lake level variability, p. *In* E. T. Drake, G. L. Larson, J. Dymond, and R. Collier [eds.], Crater Lake: An Ecosystem Study. American Association for the Advancement of Science, Pacific Division.
Reilly, J., P. Nelson, G. Larson, and M. Hurley. 1989. A chemical mass balance of Crater Lake, Oregon. Masters Thesis paper, Environmental Engineering, Oregon State University.
Robinson, R. A., and R. H. Stokes. 1959. Electrolyte Solutions: The Measurement and Interpretation of Conductance, Chemical Potential and Diffusion in Solutions of Simple Electrolytes. Butterworths.
Rosenberg, N. D., J. E. Lupton, D. Kadko, R. Collier, M. D. Lilley, and H. Pak. 1988. A geochemical method of estimating the heat and mass flux from a seafloor hydrothermal vent field [abstr.]. EOS **68:**1721.
Ruhlin, D.E. and R.M. Owen. 1986. The rare earth element geochemistry of hydrothermal sediments form the East Pacific Rise: Examination of a seawater scavenging mechanism. Geochim. Cosmochim. Acta **50**:393-400.
Ruttner, F. 1974. Fundamentals of Limnology. University of Toronto Press.
Sammel, E.A. 1981. Results of test drilling at Newberry Volcano, Oregon. Bull. Geotherm. Resour. Counc. **10**:3-8.
Sammel, E. A., S. E. Ingebritsen, and R. H. Mariner. 1988. The hydrothermal system at Newberry Volcano, Oregon. J. Geophys. Res. **93:**10149-10162.
Sammel, E. A., and S. Benson. 1987. An analysis of the hydrologic effects of proposed test drilling in the Winema National Forest near Crater Lake, Oregon. Internal Report - Bureau of Land Management, Oregon State Office, 33p.
Sano, Y., M. Kusakabe, J. Hirabayashi, Y. Nojiri, H. Shinohara, T. Njine, and G. Tanyileke. 1990. Helium and carbon fluxes in Lake Nyos, Cameroon: constraint on next gas burst. Earth Planet. Sci. Lett. **99:**303-314.
Sano, Y., Y. Nakamura, K.Notsu, and H. Wakita. 1988. Influence of volcanic eruptions on helium isotope ratios in hydrothermal systems induced by volcanic eruptions. Geochim. Cosmochim. Acta **52:**1305-1308.
Sano, Y., H. Wakita, T. Ohsumi, and M. Kusakabe. 1987. Helium isotope evidence for magmatic gases in Lake Nyos, Cameroon. Geophys. Res. Lett. **14(10):**1039-1041.
Sato, T. 1972. Behaviours of ore-forming solutions in sea water. Mining Geology **22:**31-42.

Sayles, F. L., and W. J. Jenkins. 1982. Advection of pore fluids through sediments in the Equatorial East Pacific. Science **217**:245-248.
Schnetzler, C.C., and J.A. Philpotts. 1970. Partition coefficients of rare-earth elements between igneous matrix material and rock-forming mineral phenocrysts-II. Geochim. Cosmochim. Acta **34**:331-340.
Schultheiss, P. J., and S. D. McPhail. 1986. Direct indication of pore-water advection from pore water measurements in Madeira abyssal plain sediments. Nature **320**:348-350.
Sherrod, D.R., and J.G. Smith. 1990. Quaternary extrusion rates of the Cascade Range, northwestern United States and southern British Columbia. J. Geophys. Res. **95**:19465-19474.
Sigurdsson, H. 1977. Chemistry of the crater lake during the 1971-72 Soufriere eruption. J. Vocanol. Geotherm. Res. **2**:165-186.
Sigurdsson, H. 1987. Lethal gas bursts from Cameroon Crater Lakes [abstr.]. EOS **68**:570-573.
Simpson, H. J. 1970a. Closed basin lakes as a tool in geochemistry. Ph.D. Dissertation, Columbia University, 325p.
Simpson, H. J. 1970b. Tritium in Crater Lake, Oregon. J. Geophys. Res. **75(27)**:5195-5207.
Sorey, M. L. 1985. Types of hydrothermal convection systems in the Cascade Range of California and Oregon, p. 63-67. *In* M. Guffanti and L. J. P. Muffler [eds.], Proceedings of the Workshop on Geothermal Resources of the Cascade Range. U.S. Geological Survey Open-file report 85-521.
Steele, J.L., D.D. Blackwell, and J.H. Robison. 1982. Heat flow in the vicinity of the Mt. Hood volcano, Oregon, Geology and Geothermal Resources of the Mt. Hood Area, Oregon, edited by G.R. Priest and B.F. Vogt. Spec. Pap. Oreg. State Dep. Geol. Mner. Ind. **14**:31-42.
Stumm, W., and J.J. Morgan. 1981. Aquatic Chemistry. An Introduction Emphasizing Chemical Equilibria in Natural Waters. John Wiley & Sons, Inc., New York. 780p.
Sverjensky, D. A. 1984. Europium redox equilibria in aqueous solution. Earth Planet. Sci Lett. **67**:70-78.
Swanberg, C.A., W.C. Walkey, and J. Combs. 1988. Core hole drilling and the "Rain Curtain" phenomenon at Newberry Volcano, Oregon. J. Geophys. Res. **93**:10163-10173.
Thompson, G. 1973. A geochemical study of the low-temperature interaction of sea-water and oceanic igneous rocks. EOS **54**:1015-1019.
Thompson, J. M., and R. O. Fournier. 1988. Chemistry and geothermometry of brine produced from the Salton Sea scientific drill hole, Imperial Valley, California. J. Geophys. Res. **93**:13,165-13,173.
Thompson, J. M., M. Nathenson, and L. D. White. 1990. Chemical and isotopic compositions of waters from Crater Lake and nearby vicinity, p. *In* E. T. Drake, G. L. Larson, J. Dymond, and R. Collier [eds.], Crater Lake: An Ecosystem Study. American Association for the Advancement of Science, Pacific Division.
Thompson, J. M., L. D. White, and M. Nathenson. 1987. Chemical analyses of waters from Crater Lake, Oregon, and nearby springs. U.S. Geological Survey Open-File Report 87-587.
Timperley, M. H., and R. J. Vigor-Brown. 1985. Weathering of pumice in the sediments as a possible source of major ions for the waters of Lake Taupo, New Zealand. Chem. Geol. **49**:43-52.
Timperley, M. H., and R. J. Vigor-Brown. 1986. Water chemistry of lakes in the Taupo Volcanic Zone, New Zealand. New Zealand Journal of Marine and Freshwater Research **20(2)**:173-184.

Trefry, J.H. and S. Metz. 1989. Role of hydrothermal precipitates in the geochemical cycling of vanadium. Nature **342**:531-533.
Turner, J. S. 1965. The coupled turbulent transports of salt and heat across a sharp density interface. Int. J. Heat Mass Transfer **8**:759-767.
Turner, J. S. 1973. Bouyancy Effects in Fluids. Cambridge University Press.
Turner, J. S., and I. H. Campbell. 1987. Temperature, density and buoyancy fluxes in "black smoker" plumes, and the criterion for buoyancy reversal. Earth. Planet. Sci. Lett. **86**:85-92.
Turner, J. S., and L. B. Gustafson. 1978. The flow of hot saline solutions from vents in the sea floor--some implications for exhalative massive sulfide and other ore deposits. Economic Geology **73**:1082-1100.
Van Denburgh, A. S. 1968. Chemistry of the Lakes, p. 41-45. *In* K. N. Phillips [eds.], Hydrology of Crater, East, and Davis Lakes, Oregon. U.S. Geological Survey.
Volchok, H. L., M. Feiner, H. J. Simpson, W. S. Broecker, V. E. Noshkin, V. T. Bowen, and E. Willis. 1970. Ocean fallout-the Crater Lake experiment. J. Geophys. Res. **75**:1084-1091.
Von Damm, K. L., J. M. Edmond, B. Grant, C. I. Measures, B. Walden, and R. F. Weiss. 1985. Chemistry of submarine hydrothermal solutions at 21°N, East Pacific Rise. Geochim. Cosmochim. Acta **49**:2197-2220.
Weiss, R. F., J. L. Bullister, R. H. Gammon, and M. J. Warner. 1985. Atmospheric chlorofluoromethanes in the deep equatorial Atlantic. Nature **314**:608-610.
Weiss, R. F., E. C. Carmack, and V. M. Koropalov. 1991. Deep water renewal and biological production in Lake Baikal. Nature **349**:665-669.
Wheat, C. G., and R. E. McDuff. 1988. Fluid circulation and water-rock interaction in the Mariana Mounds hydrothermal region [abstr.]. EOS **69**:1499.
Wheat, C. G., and R. E. McDuff. submitted. Fluid circulation in the Mariana Mounds Hydrothermal Region: Chemical tracers. Earth Planet. Sci. Lett.
White, D. E., J. M. Thompson, and R. O. Fournier. 1976. Lithium contents of thermal and mineral springs, p. 58-60. *In* J. D. Vine [eds.], Lithium Resources and Requirements by the Year 2000. U.S. Geological Survey Professional Paper 1005.
Williams, D.L., and C. Finn. 1985. Analysis of gravity data in volcanic terrain and gravity anomalies and subvolcanic intrusions in the Cascade Range. U.S.A. and at other selected volcanoes, in W.J. Hinze, ed., The utility of regional gravity and magnetic anomaly maps. Soc. Explor. Geophys. 52nd Annual Mtg. 1982, Proc. **13**:361-374.
Williams, D. L., K. Green, T. H. van Andel, R. P. Von Herzen, J. R. Dymond, and K. Crane. 1979. The hydrothermal mounds of the Galapagos Rift: Observations with DSRV ALVIN and detailed heat flow studies. J. Geophys. Res. **84(B13)**:7467-7484.
Williams, D. L., and R. P. Von Herzen. 1983. On the terrestrial heat flow and physical limnology of Crater Lake, Oregon. J. Geophys. Res. **88(B2)**:1094-1104.
Williams, S., Y. Sano, and H. Wakita. 1987. Helium-3 emission from Nevado Del Ruiz volcano, Colombia. Geophys. Res. Lett. **14(10)**:1035-1038.
Wolfe, R. S. 1964. Iron and manganese, p. 82-97. *In* H. Heukelakian and N. C. Dondero [eds.], Principles and Applications in Aquatic Microbiology. Wiley.

Appendix A.

On the Physical Limnology of Crater Lake, Oregon: Mechanisms for the redistribution of heat and salt in the water column.

James McManus, Robert Collier, and Jack Dymond
College of Oceanography
Oregon State University

Abstract

Introduction

Methods

Results and Discussion

1. Heat and Salt flux into the deep lake.

   CTD data
   Thermistor data

2. Full water column mixing of heat and salt.

   Mixing and heat exchange in the upper water column during periods of minimum vertical stability.
   Surface to deep lake exchange.

3. Observations on the horizontal and vertical transport of heat and salt through the hypolimnion.

   Analysis of the significance of double diffusive convection
   Basin to Basin exchange.
   Vertical mixing processes in the deep lake.

4. T-S properties of the hypolimnion.

   A conceptual model describing the near-bottom distribution of temperature and salinity in the South Basin.

5. The influence of hydrothermal activity on the physics of the water column in Crater Lake.

Conclusions

Abstract

The heat and salt budgets of the deep lake in Crater Lake, OR appear to be dominated by subsurface hydrothermal activity. Based on time series CTD data and data from a thermistor chain mooring, we estimate that the total conductive and convective heat flow, due to hydrothermal activity, is ~1W/m^2 and the corresponding salt flux is ~5 $\mu g/m^2 \cdot$second. This paper discusses the observation of these fluxes and the mechanisms and timescales of mixing responsible for the redistribution of these properties through the water column.

In Crater Lake, like many temperature lakes, annual vertical exchange of surface waters with waters from the lake's hypolimnion occurs during the early winter and possibly during late spring. This exchange mixes the heat and salt from the deep lake to the surface. Likewise, oxygen rich waters from the surface are mixed with the deep waters, resulting in a net increase in the deep lake dissolved oxygen content at the time of mixing. This mixing process is not complete, that is, the deep lake does not reach equilibrium saturation with respect to dissolved oxygen at any time during the year.

The active input of thermally and chemically enriched fluids produces heterogeneities and instabilities in the density structure of the deep lake which drive deep lake mixing. Horizontal advection, turbulent diffusion, and a variety of other physical mechanisms contribute to the relatively rapid mixing of heat and salt from their origin in the South Basin to the rest of the deep lake. The result of this rapid mixing is that, over timescales of several weeks to months, heat and salt are mixed horizontally.

Our data suggests that the South Basin of Crater Lake is the dominant region of active hydrothermal input. Detailed mapping of the near-bottom temperature and salinity structure, in the South Basin, has allowed us to propose a conceptual model which describes the entry of the enriched fluids into the deep lake. It is clear from our data set that simple linear mixing of warm, salty waters with ambient waters does not accurately account for the distribution of temperature and salinity observed near the sediment-water interface. It is possible that there are multiple fluid sources, each with their own temperature and salinity characteristics; however, it is more reasonable that there is one source which undergoes a variety of mixing processes. These processes must include the preferential loss of heat over salt, coupled with linear mixing with ambient waters. Since the observed changes in the heat to salt ratio of near-bottom waters follow the local bathymetry, the preferential loss of heat over salt may be occurring prior to the fluid's entry into the lake, i.e. while the fluid travels through the sediment/debris which covers the caldera basement rock.

Introduction

Crater Lake is a closed basin lake with a surface area of 53.2 km^2, which covers 78.5% of its total drainage basin. It is situated at an elevation of 1882 meters and has a volume of 17.3 km^3 (Phillips, 1968). The lake has two semi-enclosed basins, one in the northeastern portion of the lake (referred to here as the North Basin) which has a maximum depth of approximately 590 meters and the second in the southwestern section of the lake which has a maximum depth of approximately 485 meters (South Basin). There is a station buoy situated in the northeastern portion of the North Basin (NPS station 13), where much of our time series hydrographic data was collected. Some of the time series data presented in this paper was also collected in the South Basin, NPS station 23, and in the northwestern portion of the lake, NPS station 11 (see map Figure 1).

An understanding of the physical processes which control the redistribution of heat and salt in Crater Lake are essential to modeling the biogeochemical cycling of elements in the lake. Relatively little has been documented about the physical limnology of Crater Lake. Kibby et. al. (1968) reported surface current observations as well as vertical and horizontal temperature measurements in the upper water column. Data from Simpson (1970a &b) and Volchok et. al. (1970) indicate that the characteristic time-scale of surface to bottom exchange is approximately one year. Neal et. al. (1971, 1972) provided early temperature microstructure measurements which indicated the hyperadiabatic nature of the thermal gradient of the deep lake. Williams and Von Herzen (1983) provided the first empirical treatment of the water column physics in Crater Lake. Although the work of Williams and Von Herzen (1983) served as a catalyst to the current work, the lack of high precision salt determinations limited their ability to interpret the temperature microstructure of the hypolimnion in Crater Lake. Our research has provided the necessary high precision salinity data which when coupled with the temperature data, allows for the accurate determination of the physical properties and the mixing dynamics of the lake (McManus et. al, submitted).

To a first approximation Crater Lake is well mixed with respect to major ions (Collier et. al., 1990a; Nathenson, 1990; Thompson et. al., 1990; Nathenson and Thompson, 1990; McManus et. al., submitted). The upper water column (top 200 meters) is nearly isohaline, and this observation holds throughout most of the year (Figure 2). Due to evaporation, small increases in surface salinity are often observed by late summer/early fall. Below 200 meters the salinity increases with depth at all times (Figure 2). This increase is observed throughout the lake; however, there are small-scale spatial and temporal variations in the salt as well as the heat distribution of the deep lake. These variations in the heat and salt distribution of the deep lake can create vertical and horizontal heterogeneities in the density structure of the hypolimnion (McManus et. al., submitted). These density heterogeneities may act to drive mixing processes in the waters of the hypolimnion.

In section I of the results and discussion we will present the heat and salt budget for the deep (>350 meters) hypolimnion of Crater Lake. The remaining focus of this paper will be on identifying the processes, both large and small scale, which govern the redistribution of this heat and salt through the water column of Crater Lake. Our research has demonstrated that the mechanisms governing the redistribution of heat and salt in Crater Lake may be grouped into two categories; large scale vertical exchange of surface waters with bottom waters and small scale mixing processes. Annual exchange of surface waters with bottom waters affects the distribution of temperature and salinity throughout the entire water column. This mixing is due to conditional "thermobaric instabilities" which are generated during periods of lowered vertical stability. During periods of high surface stratification the deep lake is dominated by small scale horizontal and vertical mixing processes driven

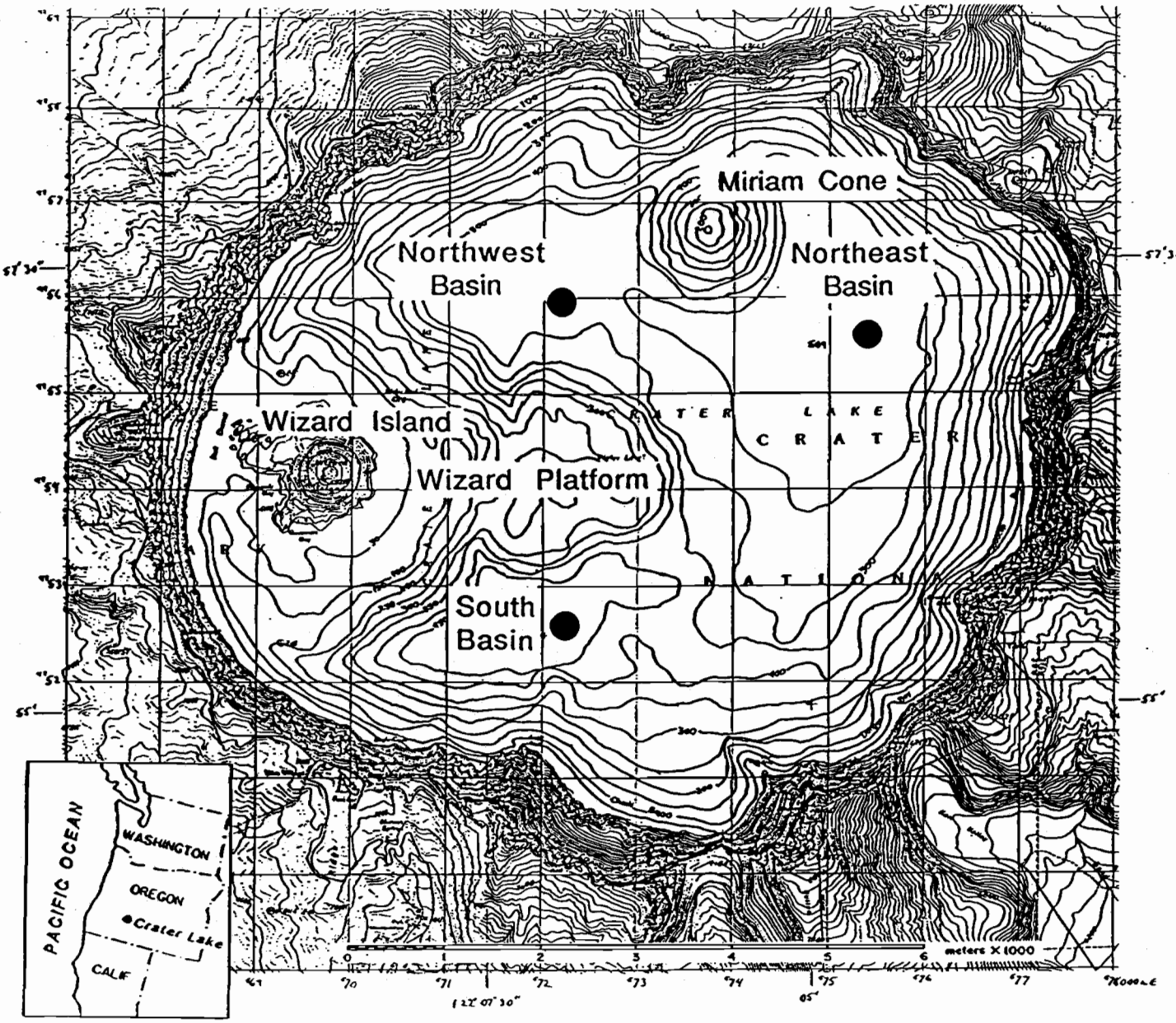

Figure 1.

Figure 1. Bathymetric/ topographic map of Crater Lake, OR with geologic features. Large dots represent approximate locations of time series monitoring stations: Station 23 located in the South Basin; Station 13 located in the North Basin; Station 11 located in the north west portion of the lake. The bathymetry (Byrne, 1965) has been projected onto the USGS 7.5-minute quadrangles for Crater lake East and West (provisional, 1985).

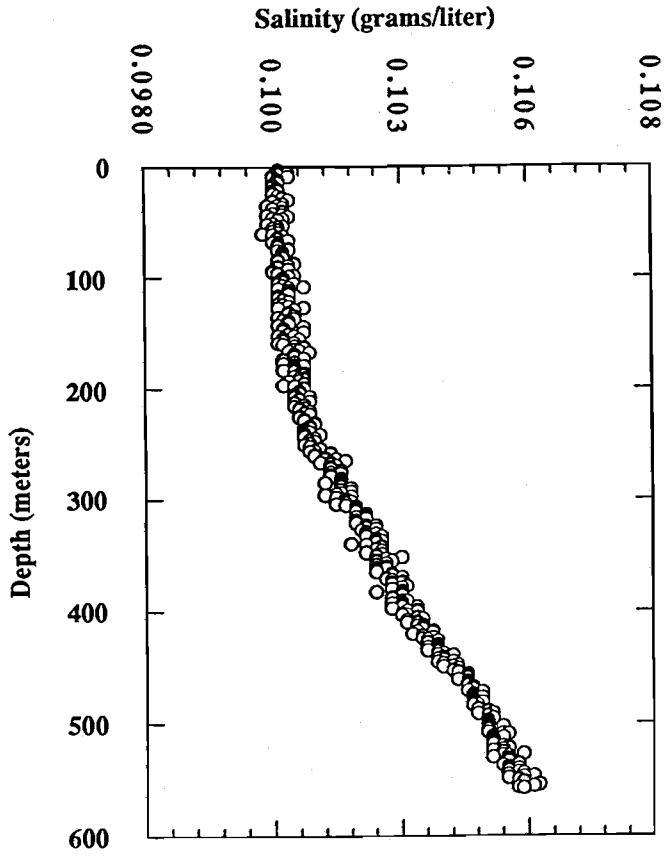

Figure 2. Depth versus salinity (grams/liter). Data was taken from station 13 on 19 January 1990. Note the near-uniform salinity of the upper 200 meters.

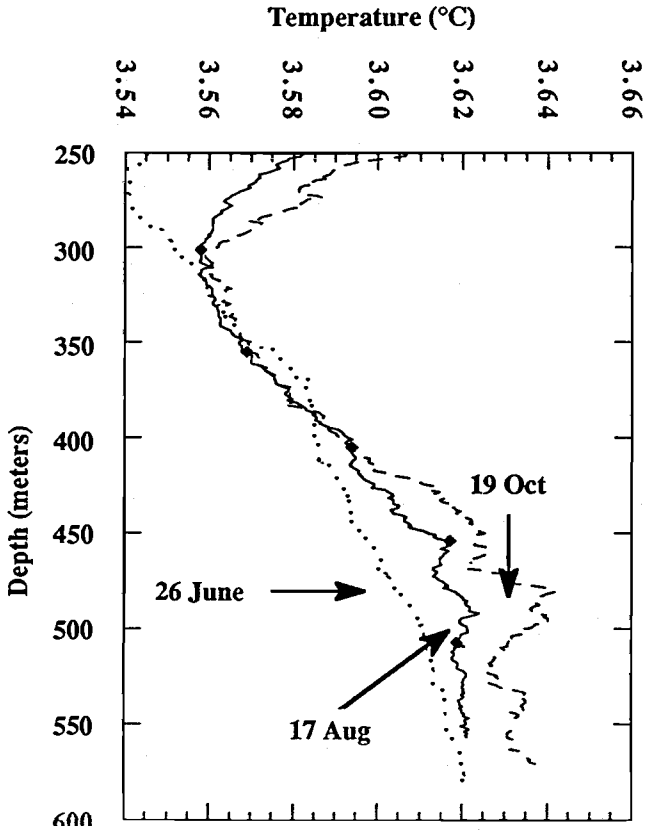

Figure 3. Depth versus temperature in time series. Figure demonstrates the accumulation of heat in the hypolimnion throughout the summer months.

by the active input of heat and salt into the lake's hypolimnion. The small scale physical mechanisms for the mixing of heat and salt include; horizontal advection, turbulent diffusion, and the periodic formation of convective cells and other water column density instabilities.

Methods

Temperature, pressure, conductivity, and light transmission were measured using a "CTD" (SEACAT® model SBE19, Sea-Bird Electronics Inc.) modified for low conductivity waters and equipped with a 25 cm path length light beam transmissometer (Sea Tech. Inc.). The CTD records all data internally at 2 scans per second. Temperature resolution is ±0.0005°C and, based on laboratory triple point calibrations of the temperature sensor, the absolute accuracy of the temperature sensor was better than 0.001°C from 1987 to 1989. Most of the CTD data presented in this paper was acquired with the profiler deployed on a hydrographic wire which was lowered from the NPS research boat. However, data describing the near-bottom distribution of temperature and salinity were collected with the CTD mounted on an "arm" of a one-man submersible (Dymond et. al., 1989).

Laboratory calibration of the conductivity sensor using Crater Lake water and subsequent chemical analysis of this water provided us with sufficient salinity, conductivity, and temperature data to obtain an expression for salinity as a function of *in situ* conductivity and temperature (McManus et. al., submitted). The expression was derived using a multiple regression analysis package and is similar in form to the expression for salinity used in seawater (Cox et. al., 1967). Salinities calculated from this expression are 25% greater than would be predicted from strong electrolytes alone; this is due to the fact that silicic acid accounts for approximately 25% of the total dissolved solids load in the lake. The rationale for including silicic acid as part of the total "salt" content is that in order to accurately calculate the physical properties of the water column (e.g. density), an accurate measure of the total dissolved solids is necessary. Our work has indicated that silicic acid is proportional to the total salt content and specific conductance in Crater Lake. The details of the experiments and further explanation of the affects of silicic acid on the density of lake water are presented in McManus et. al. (submitted).

Time series temperature data was also collected using two moored thermistor chains, one located in the upper water column, 50-150 meters, and the other extended from 350 to 450 meters -- where 450 meters is the approximate bottom depth at this location. The chains had 11 thermistors spaced at 10 meter intervals. Temperature data was recorded every three hours throughout deployment and the thermistors were calibrated at the OSU calibration facility both before and after deployment. From this calibration, the absolute accuracy of the thermistors was found to be ±0.010°C and the in-field precision, based on daily temperature measurements from the deep lake, was ±0.005°C.

Oxygen samples were analyzed according to a whole-flask Winkler titration method with the modifications of Carpenter (1965a &b). The overall precision of the oxygen measurement is based on the percent difference between duplicate sample analysis and appears to be better than 0.5%. To calculate oxygen solubility for Crater Lake the equations presented in Benson and Krause (1980) were employed. The mean barometric pressure was calculated from the altitude dependent equation given by Mortimer (1981).

Results and Discussion

1. Heat and salt flux into the deep lake.

Time series CTD data and data from a thermistor chain mooring indicate that there is a consistent input of heat and salt into the deep hypolimnion of Crater Lake. This is evinced in the deep lake by the gradual increase in temperature over time observed during periods of high surface stratification (Figure 3).

Table 1. Heat Flux, Salt Flux, and Fluid Flow

Year/ season**	Method	Heat Flux (W/m^2)	Salt Flux ($\mu g/m^2 \cdot sec$)	Fluid flow (liters/sec)
1989/S	CTD	0.92 ± 0.47	4.2 ± 2.5	141±84
1989/F	Thermistor	1.00 ± 0.28	N/A	N/A
1990/Sp	Thermistor	1.20 ± 0.59	N/A	N/A
1990/ES	CTD	0.94 ± 0.18	5.2 ± 3.0	254±146
1990/LS	CTD	1.03 ± 0.38	5.7 ± 3.0	278±146

***S, F, and Sp represent summer, fall, and spring respectively where E and L are early and late respectively.*
For 1989, we used 22.9 km^2 as the surface area of the lake over which the integration was calculated, and for 1990 we used 20.2 km^2.

CTD Data. Integrated values for the flux of heat and salt are calculated from the time series CTD data (McManus et. al. 1990). This is accomplished by integrating the area under a vertical profile (either salinity or temperature) and subtracting the area under a profile taken at the same location at an earlier time. (e.g. The difference in the area under the vertical profiles of temperature in Figure 3, between June '89 and August '89, will yield a "temperature flux" over that time period. This is then converted to heat flux.) The integration is done below the depth where a time series of profiles intersects, below 350 (Figure 3) or 400 meters, for 1989 and 1990 respectively (see Table 1 for surface areas). Each flux calculation represents an average of the three monitoring stations. The profiles are also broken up into depth intervals and volume-weighted to account for the different volumes of the basins. The results of these calculations for heat and salt flux are presented in Table 1. The heat and salt flux values presented in Table 1 are for discrete time intervals during a given year and the flux values represent differences between two profiles separated in time by several weeks. We chose this time spacing in order to avoid any large seasonal fluctuations in the "apparent" budgets of heat and salt, as measured by the CTD. Over shorter time scales, fluctuations in the property flux estimates are due to non-steady state physical processes in the water column which mix the heat and salt from the location of input through the water column. Also, over periods of several weeks to months the heat and salt fluxes appear to be at steady-state. Our calculated values for heat flux agree with those of Williams and Von Herzen (1983) who cited values between 0.7 and 1.4 Wm^{-2}.

Fluid flow values are derived directly from the salt flux values. In calculating the fluid flow, we have assumed that the salinity of the fluids as they enter the South Basin is 0.6 grams/kg. This salinity value is based on pore water chemistry data (Wheat, unpublished) and the chemical composition of brines which are found at the bottom of the South Basin (Collier et. al., 1990b). Our estimates for fluid flow and salt flux (Table 1) are consistent with other values suggested by Reilly (1990), 121 liters/second and 6-7 $\mu g/m^2 \cdot sec$, and Nathenson (1990), 80-1900 liters/second.

Thermistor Data. Using deep lake temperature data from a thermistor chain moored from the bottom of the South Basin (~450 meters) extending up through the water column to a depth of approximately 350 meters we can estimate the rate of deep lake warming. This is accomplished by determining the slope of the line which represents the change in temperature over time in the deep lake during periods of high surface stratification. We do this calculation for the thermistors below 350 meters and above 440 meters on the chain and obtain an average of all the resulting heat fluxes. The results are presented in Table 1. To demonstrate the warming of the deep lake we show an expanded-scale plot of temperature versus time for the thermistor deployed at 410 meters (Figure 4). The arrows indicate deep lake warming during periods of relatively high water column stability (fall and late spring/early summer). During winter there is some cooling of the deep waters which is associated with vertical mixing of surface waters with deep lake waters; these processes will be discussed later in the text. The absence of data apparent in Figure 4 marks a period of time when a large offset occurred in each thermistor record.

The "steady state" flux of heat and salt is difficult to precisely ascertain because the physical processes that transport these properties, through the water column, are not necessarily at steady state. The tendency of the thermally and chemically enriched fluids to "pond" along the bottom of the lake as suggested by the work of Williams and Von Herzen (1983) and Collier et. al. (1990) will result in the trapping of heat and salt within these fluids. Despite the uncertainty in our calculations, our method for estimating heat flux, salt flux and fluid flow confirm and refine the previously reported values.

2. Full water column mixing of heat and salt.

Annual vertical exchange of surface waters with waters from the deep lake mixes heat and salt during periods of reduced vertical stability of the water column. Since deep lake water is rich in biochemically important nutrients, particularly dissolved nitrate, this exchange is critical to new biological productivity in the upper 200 meters. Such exchange also carries cooler, oxygen rich waters from the surface to the hypolimnion. Therefore, the dissolved oxygen content of the deep lake allows us to estimate the degree to which surface to bottom exchange has occurred. For example, if the entire lake were to reach saturation with respect to dissolved oxygen, we would then conclude that all of the waters have come into contact with the surface during a single mixing period.

In the following section we will discuss surface mixing using data obtained from a thermistor chain mooring deployed at depths between 50 and 150 meters in the South Basin. Since we do not have the supporting data to develop a detailed model of upper water column physical processes, our discussion of this thermistor data will be limited to general observations on this part of the lake. We then examine the results from a near-bottom thermistor chain deployed between 350 and 450 meters, also in the South Basin, in relation to the exchange of surface water with deep lake water. In addition to the thermistor chain data, CTD data and dissolved oxygen data are also presented as evidence for vertical exchange. Once we have established the data base supporting our hypothesis, that the

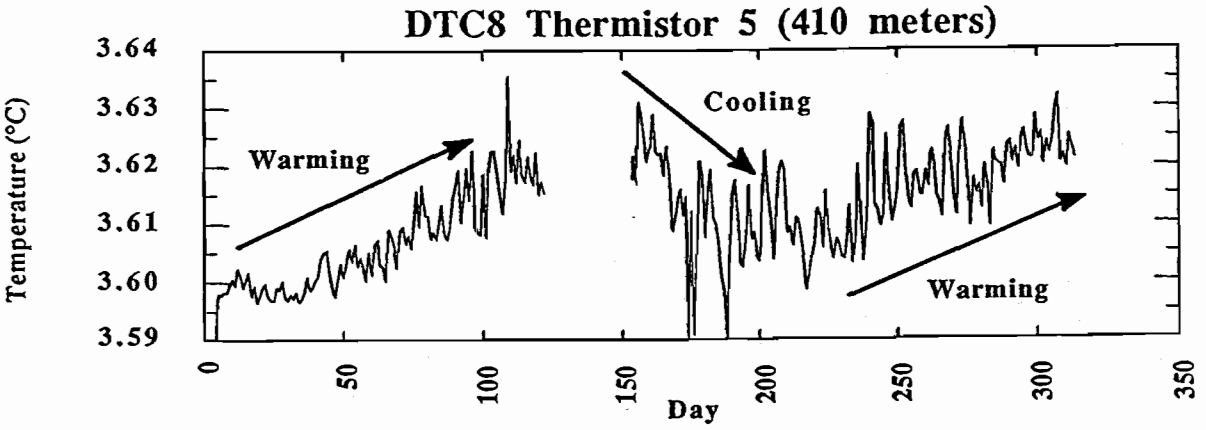

Figure 4. Temperature versus day from the bottom thermistor chain. Demonstrates the warming due to the constant input of heat from hydrothermal activity and the cooling due to winter mixing.

water column undergoes annual vertical mixing, we will attempt to elucidate the mechanism for this exchange.

Mixing and heat exchange in the upper water column during periods of minimum vertical stability. Results from two thermistor chains deployed in the South Basin from 3 September 1989 until 11 July 1990 reveal information on both surface and deep lake heat exchange. The chains are both 100 meters in length with thermistors spaced at 10 meter intervals. TC1084 was moored from 50 to 150 meters and thermistor chain TC8 was moored from 350 meters to 450 meters (the approximate bottom depth at this particular location in the South Basin).

TC1084 provides a record of upper water column temperatures (Figure 5). The upper water column begins to undergo destratification in late fall as the density of the surface waters increases due to cooling. Forcing due to wind mixing at the surface and cold-water convection allow the surface water to be transferred down the water column and mixed with the ambient water at depth. The result of this process is seen as an increase in temperature at 90 meters by late December (Figure 6a). By mid-January the deep thermistors show an increase in temperature due to this process (Figure 6b). At this time the entire upper 150 meters is isothermal. The rate that the initial warming signal is transferred through this upper water column mostly reflects the stronger stratification in the upper 100 meters as compared to the 100-150 meter depth range. From 50 to 90 meters this warm water signal (Figures 5 and 6) descends through the water column at a rate of 1.0 meter/day ±10%. From 100 meters to 130 meters the rate of transfer of this signal is much higher, 7.7 meters/day ±10%. After the initial increase in temperature down the water column, there is a gradual decrease in temperature of the upper 200 meters over time due to continued cooling. From mid-February to mid-March the upper water column is at its minimum in temperature and is nearly isothermal and isopycnal.

By early April, spring warming has begun to influence the temperature structure at 150 meters. Initial warming of the cold surface water produces water of greater density (e.g. the temperature of maximum density is greater than ambient water); hence, unstable parcels of surface water form and drive convection. This process is best demonstrated by temperature profiles obtained with the CTD from early May 1989 (Figure 7). As shown in Figure 7, the surface waters are heated during the day, forming convective cells which sink throughout the course of the day (solid line Figure 7). This continued process warms the entire water column through which convection may occur leaving a warmer column of near-uniform temperature water at the end of the day (dashed line Figure 7). The three profiles in Figure 7 were taken from the three different monitoring stations in the late afternoon to early evening on 11 May. Therefore, the net warming apparent between the three profiles does not reflect the total, one-dimensional heat input into the upper lake. Differential heating at the three stations causes STN 11 (the heavy dashed line) to receive more solar input than either of the other two stations.

During the spring warming process described above, a diurnal cycle of heating during the day and cooling at night appears to be established (Figure 8 a-d). The maximum in daily water temperature at 50 meters during the month of April is recorded at 1300 and the minimum between 0100 and 0500. The problem with this simple one-dimensional concept is that if this daily heating-cooling cycle were to be going on in the entire upper 50 meters (i.e. a daily change in temperature of the upper 50 meters of approximately 0.1°C), then the upper water column would be exchanging approximately 550 W/m^2 of heat, which is an unreasonably large amount of heat. It is more likely that this diurnal cycle is due to increases in the temperature of the convective plumes until mid-day followed by a decrease in temperature of the plumes. After these plumes cease forming (after sunset), diffusive

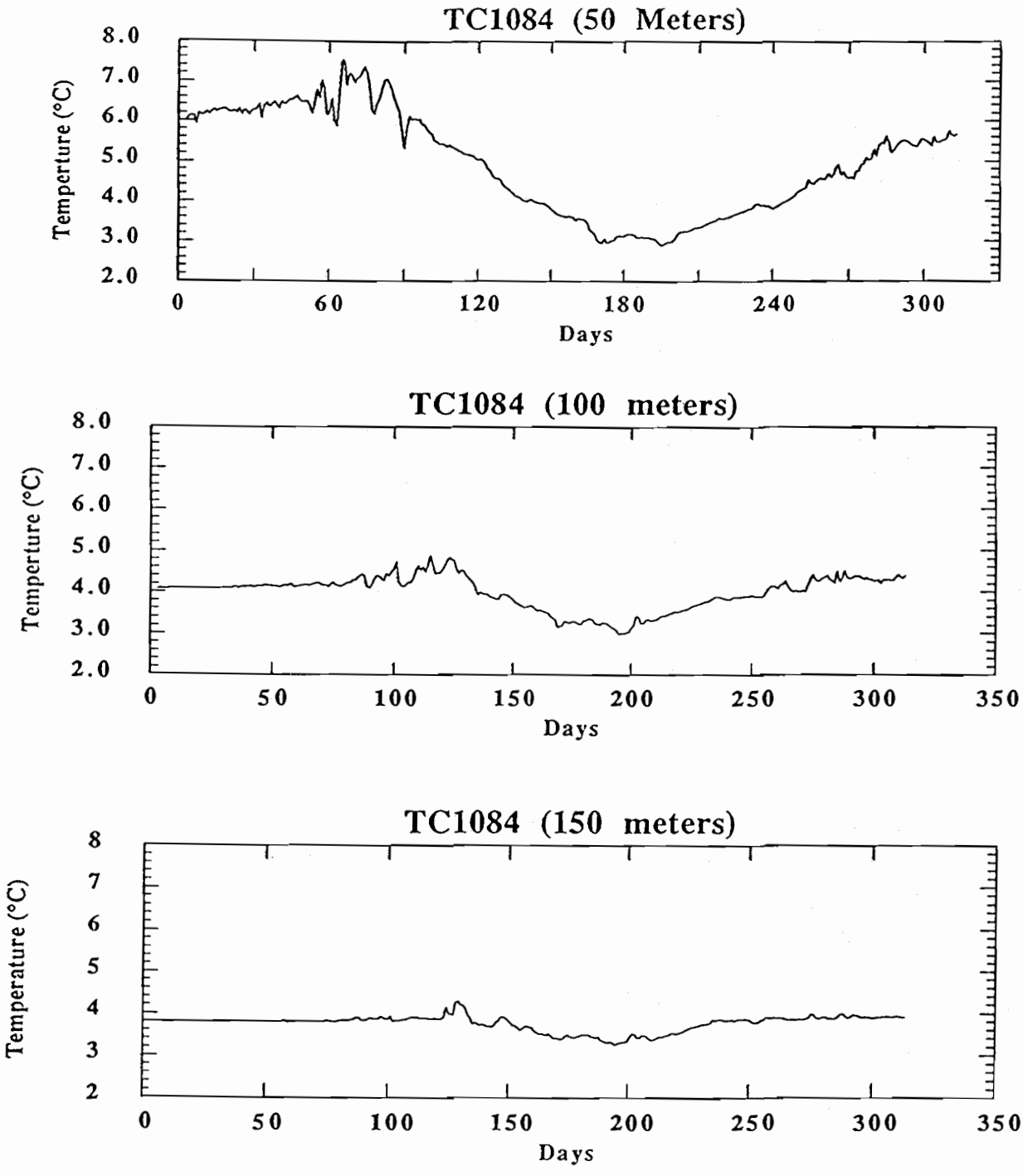

Figure 5. Upper water column thermistors showing the change in temperature over time. Thermistors were spaced at 10 meter intervals between 50 and 150 meters; here we show the 50, 100, and 150 meter thermistor as examples.

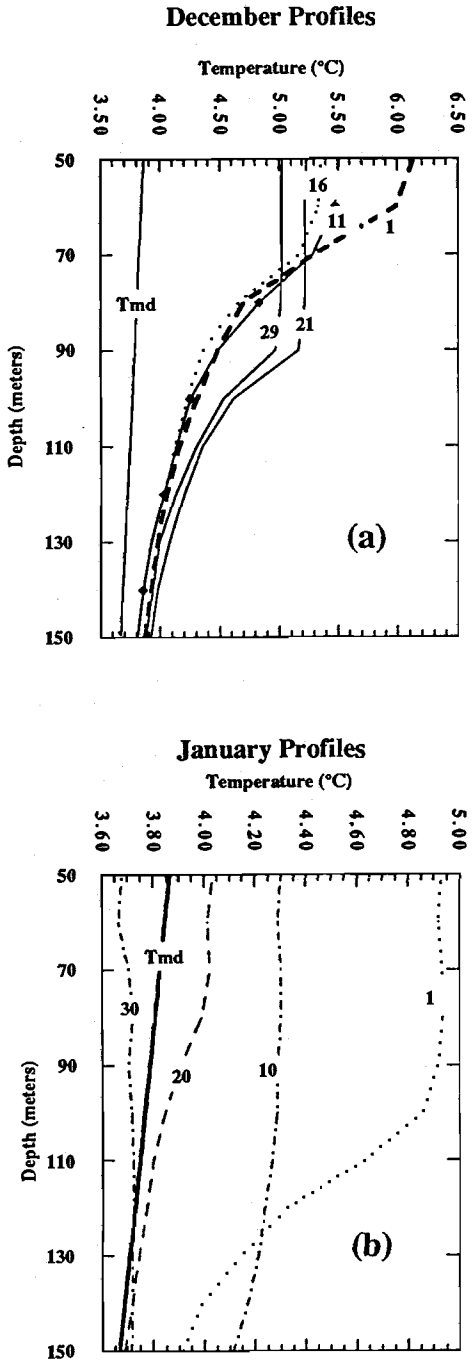

Figure 6. Depth versus temperature in the upper part of the water column for (a) December and (b) January. Data is taken from the thermistor chains as in Figure 5.

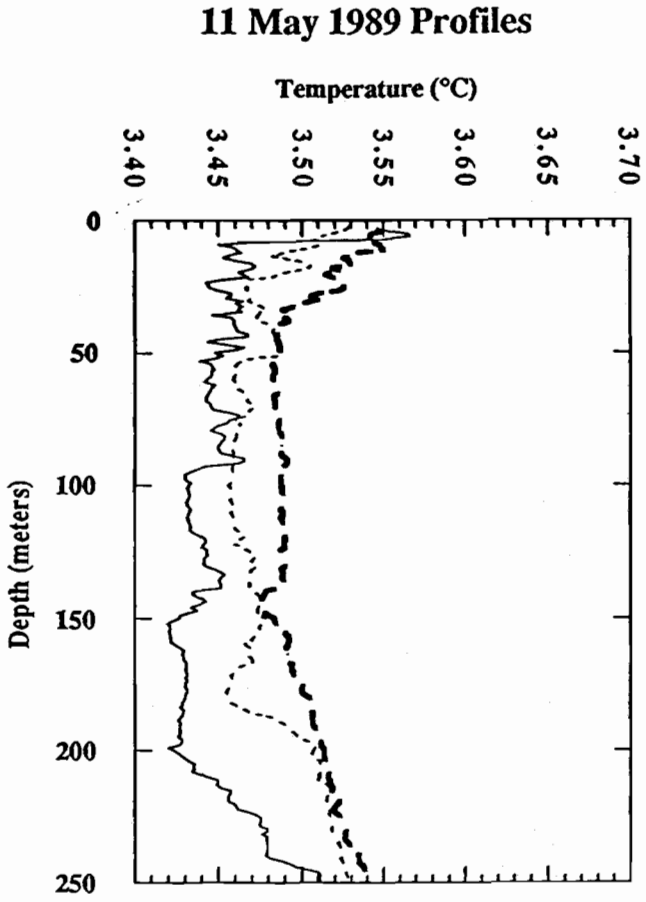

Figure 7. One day time series of depth versus temperature for Crater Lake. The figure demonstrates convective warming in the late afternoon (solid line), the gradual slowing of the convection by early evening (dotted line), and the near-uniform temperature profile by sunset (heavy dashed line).

processes mix the heat from these features with the ambient colder waters, this mixing process reduces the temperature seen by the thermistors to a minimum by early morning. Horizontal heterogeneity in the upper water column heat content will tend to enhance this apparent cycle as waters heated more at one end of the lake are transported to the other "cooler" side of the lake. In order to evaluate the total heat budget of the upper lake, longer term (days to weeks) averages of heat input should be evaluated.

Based on the thermistor at 50 meters depth, we calculate a net heat input from 1 April to 20 April and from 1 May to 20 May of approximately 55 W/m^2. This represents a reasonable heat flux due to the input of solar energy, at this time of year. As the temperature of the upper water column approaches the temperature of maximum density at 50 meters (line of T_{md} in Figure 8a-d), the upper water column becomes nearly isothermal at about 3.9°C. After this point (approximately 1 May), rapid warming of the surface waters stratifies the water column, thereby isolating the deeper waters as suggested by the near-constant water temperature at 100 meters until approximately 12 May. After approximately 10 May, we observe large variations in the daily water column temperatures. Our calculations suggest that these large changes in the "apparent" daily heat input, seen in Figure 8c & d, are on the order of hundreds of W/m^2, as measured by all the thermistors between 50-150 meters. These fluctuations are likely being driven by storms, surface driven convection due to cooling, strong horizontal thermal gradients, and other upper water column mixing processes.

A more detailed study of the upper water column-atmosphere interactions needs to include thermistors which extend to the surface as well as detailed meteorological data. Of particular importance to this work is the observation that the surface mixing processes described here yield an upper water column (top 200 meters) which is well-mixed with respect to dissolved ions (Figure 2) and oxygen (Figure 9) throughout the year. This upper region of the lake is also generally deplete of dissolved nitrate, suggesting that this entire region of the water column supports at least some biological productivity.

Mixing of surface water with deep lake water. Time series oxygen data, CTD data, and thermistor chain data all indicate that some exchange of surface water with deep water occurs in Crater Lake at least once a year. The data suggests that this annual mixing process is likely to be incomplete. As a result, progressively "older" water mixtures are found deeper in the lake.

As discussed above, the upper 200 meters of the lake becomes isothermal and isopycnal twice annually. The formation of this isothermal-isopycnal layer results in the near-saturation of dissolved oxygen in these upper waters (Figure 9). Oxygen data collected from July 1988 through July 1990 reveal that there is annual mixing of well-oxygenated (surface) water with bottom water. Our data collected from September 1988 and April 1989 demonstrate an increase in dissolved oxygen, measured at 550 meters, of nearly 10 μmoles/liter (Figure 9). Likewise, from January 1990 to July 1990 we observe another increase in deep lake dissolved oxygen indicating that the reaeration process was again repeated during the winter and/or spring of 1990. This mixing is, however, incomplete, leaving the deep lake undersaturated with respect to atmospheric saturation of oxygen at all times sampled. Simple mass balance calculations and some assumptions on the organic matter oxidation rate within the deep lake suggest that for the 1988-89 field season 30-45% of deep lake water was exchanged with well aerated surface water. This implies that it takes approximately 2 to 4 years for the deep lake to undergo complete ventilation.

CTD data collected at the same time as the dissolved oxygen data and thermistor chain data also provide evidence for the exchange of surface waters with waters from the

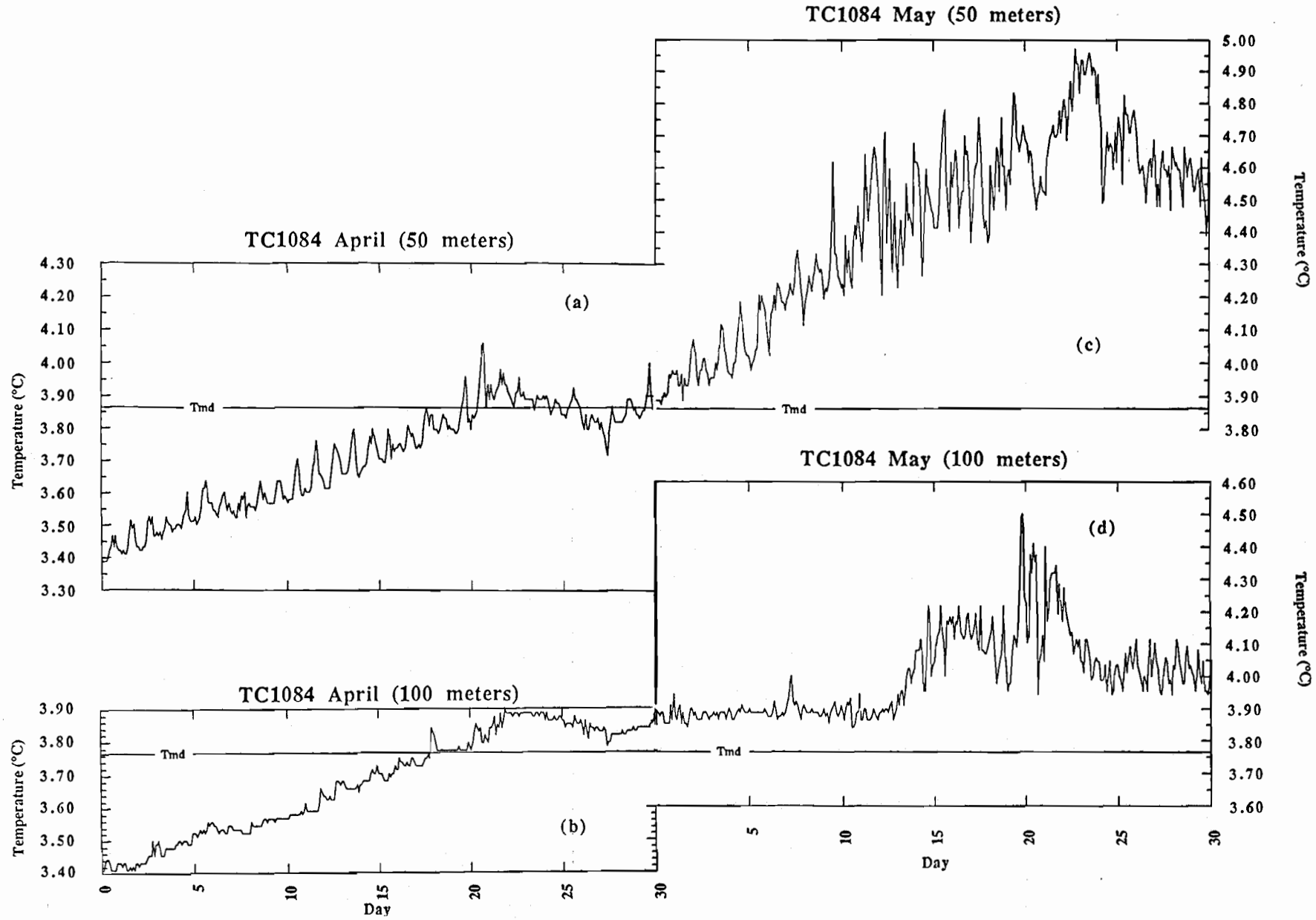

Figure 8. April - May expanded scale thermistor chain data (TC1084). Data is from 50 (top) and 100 meters (bottom). The temperature of maximum density (Tmd) was calculated from the equation presented in Chen and Millero (1986).

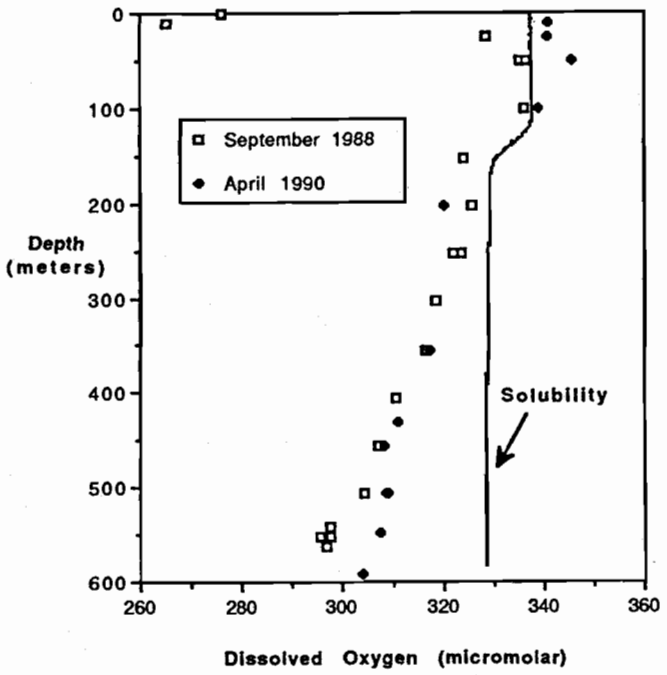

Figure 9. Depth versus dissolved oxygen for September 1988 and April 1989. The figure demonstrates the increase in deep lake oxygen from fall/winter to spring/summer. The line of oxygen solubility is for April and is calculated from equations presented in Benson and Krause (1980).

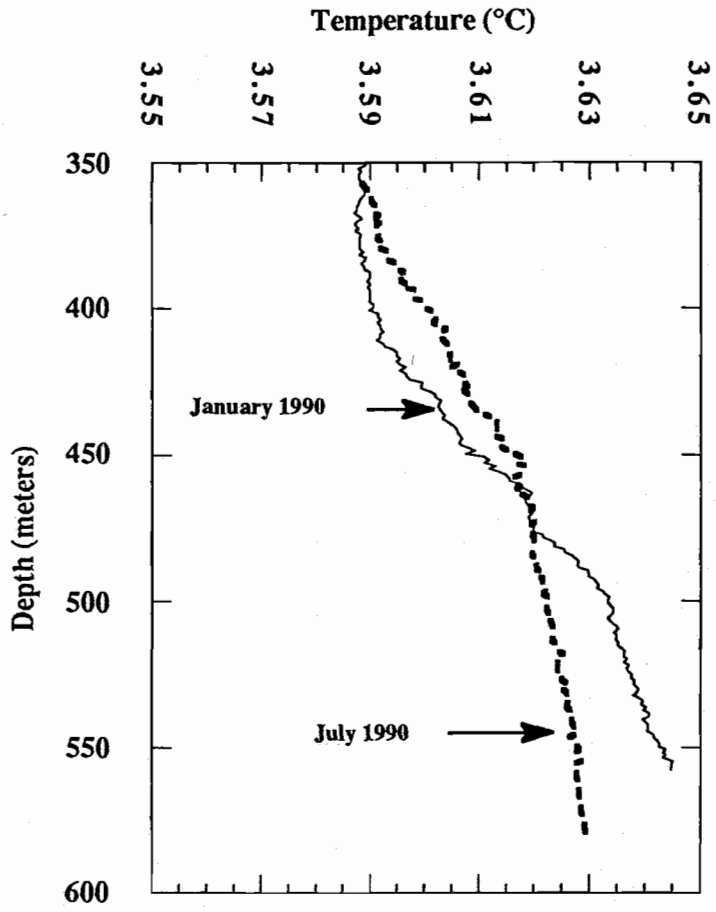

Figure 10. Depth versus temperature for January 1990 and July 1990. The figure illustrates the results of the cooling of the deep water column (from January to July) due to exchange of surface water with deep lake water.

hypolimnion. A one dimensional approximation of the heat budget in the deep North Basin from January 1990 to July 1990 (Figure 10) indicates that a net loss of heat (225 kcal/m^2) occurred between January 1990 and July 1990 in the North Basin deep water (350-550 meters). This loss of heat is presumably due to the mixing of cooler surface waters with bottom waters, providing further evidence for exchange between surface and deep waters. These findings are also consistent with the deep water cooling evident in the thermistor chain data collected from the South Basin (Figure 4).

The magnitude or effectiveness of this type of mixing will likely vary form year to year. As surface waters cool below the temperature of maximum density, the upper waters become restratified. The faster the upper waters cool and become restratified the less time available for deep water reaeration, hence influencing the "completeness" of vertical exchange. Year to year climate variations will therefore affect the extent of annual vertical exchange. This exchange is more likely to occur during the winter mixing phase rather than in the spring. Calmer weather conditions at Crater Lake typically dominate during spring, and heating of surface waters occurs fairly rapidly thereby making vertical exchange less likely or less efficient during this period.

The deep lake thermistor chain data imply that the deep lake reaeration process lasted at least one month (Figure 4). Most of the thermistors in this chain recorded the maximum in deep lake temperature shortly after day 150 (early February). After this time the deep lake undergoes some cooling, for about one month, until it again begins to warm. Water column cooling is caused by a reduction in water column stability whereby cold waters from the upper 200-300 meters can mix with the deep warmer waters. This mixing takes the form of both turbulent diffusion and a sudden or episodic mixing event. This latter process provides the impetus for the majority of the deep lake reaeration.

We hypothesize that the actual mixing "mechanism" for the majority of the exchange between surface and deep water is similar to that proposed by Farmer and Carmack (1981), Carmack and Farmer (1982), Carmack et. al., (1989), and Weiss et. al., (1991). This mechanism relies on the effects of pressure on the temperature of maximum density and has therefore been termed "thermobaric instability". Since the temperature of maximum density decreases with increasing pressure, colder water overlying warmer water becomes "conditionally unstable" with respect to water immediately below. Wind forcing and/or internal waves displace a water parcel vertically to a depth where its temperature is closer to the temperature of maximum density than the ambient water at that depth. Once the parcel is displaced it will continue to descend through the water column, because of its greater density relative to the surrounding water, until it reaches a point of neutral stability. For our purposes, water parcel stability is assessed with respect to the density gradient where depth (z) increases from the surface to the bottom and the density (ρ) is taken to be the density a fluid would have at some reference pressure which is in close proximity to the depth interval of interest. For the model of thermobaric instability, density is considered as a function of pressure and temperature ($\rho = \rho\ [T,P]$). Where z increases with depth and $\Delta\rho/\Delta z > 0$ between two water parcels over distances of approximately 10 meters (the distance between our thermistors) the parcels at those two positions are stable relative to each other, and if $\Delta\rho/\Delta z < 0$ the parcels are unstable with respect to each other.

A requirement for the deep penetration of a water parcel is that $\Delta S/\Delta z$ (the vertical salinity gradient) is approximately equal to zero or is negligible compared to the temperature and pressure effects on density. In Lake Baikal, U.S.S.R., where the results of this process have been dramatically demonstrated (Carmack, 1989; Weiss et. al., 1991), this requirement is satisfied. The result, in Lake Baikal, is that surface water descends through

the water column to near-bottom depths with a well-preserved surface signature in temperature, dissolved oxygen, and other geochemical tracers. In Crater Lake, over short vertical distances between the depths of 200 and 400 meters, the approximation of $\Delta S/\Delta z = 0$ may hold; however, below this depth increases in salinity with depth will increase the density of the ambient fluid making exchange of the colder, less salty fluids (upper waters) with the warmer, saltier fluids more difficult. Therefore, we have a situation in Crater Lake where two of the components of density, temperature and salinity, must be evaluated for their affect on the stability of the fluid and we must consider density as a function of temperature, pressure, and salinity.

Using estimates of the salinity gradient obtained from January 1990 CTD data and the thermistor data presented in Figure 11a, we calculate that the densities, relative to 400 decibars, of the waters above 390 meters are more dense than the waters at 400 meters. The result is a density profile which is schematically represented in Figure 11b. Figure 11c demonstrates the temperature profile for the following day. Here, there has been some apparent exchange between the colder water from above and the warmer water below, resulting in colder waters now underlying warmer water. In the subsequent days there are rapid changes in the vertical temperature distribution in this part of the water column, eventually resulting in a stable density gradient. It is also apparent from the figure that the near-bottom waters have not been mixed to the same degree as the waters above 420 meters. The net effect of mixing dense cold waters from above with warm, salty waters from below, is that any instability-driven mixing decreases in effectiveness with increasing depth in Crater Lake due to the resisting force of the salinity gradient.

Prior to the development of the instability and subsequent overturn described above, mixing through the hypolimnion appears to be dominated by the diffusion of cold water from above. This is seen in Figure 11a as a gradual decrease in temperature between 1 February and 20 February, over the depth interval 350 to 420 meters. This mixing of cold water from above with warm water from below can be modeled according to a simple diffusion model where the heat flux (F_H) can be calculated by

$$F_H(z,t) = \rho C \left(\partial T[z,t]/\partial t\right)_z dz \qquad (2a)$$

and

$$F_H(z,t) = -\rho C K(z,t) \left(\partial T[z,t]/\partial z\right)_t \qquad (2b)$$

where $\partial T/\partial z$ and $\partial T/\partial t$ are the slopes of the temperature versus depth and temperature versus time relationships respectively (Li, 1973), ρ and C are the density and the specific heat capacity respectively. The vertical diffusion coefficient (K) evaluated from this data is $1.5 - 2 \times 10^{-3}$ m^2/sec, which reflects relatively rapid vertical transfer. (We will compare this diffusion coefficient to the effective diffusion coefficient calculated for the hypolimnion during periods of high surface stratification, later in the text.)

The oxygen and temperature data presented here suggests that the annual exchange of surface water with deep water is an important process for the vertical redistribution of heat and salt in the lake. It is difficult to predict the annual magnitude or extent of this mixing process in the water column without yearly time series data collection. It is likely that a comprehensive model of surface-to-bottom exchange is impossible without detailed meteorological data as well as water column chemistry and temperature data. The use of time-dependent chemical tracers (e.g. tritium, Lupton [unpublished], and CFC's, Weiss

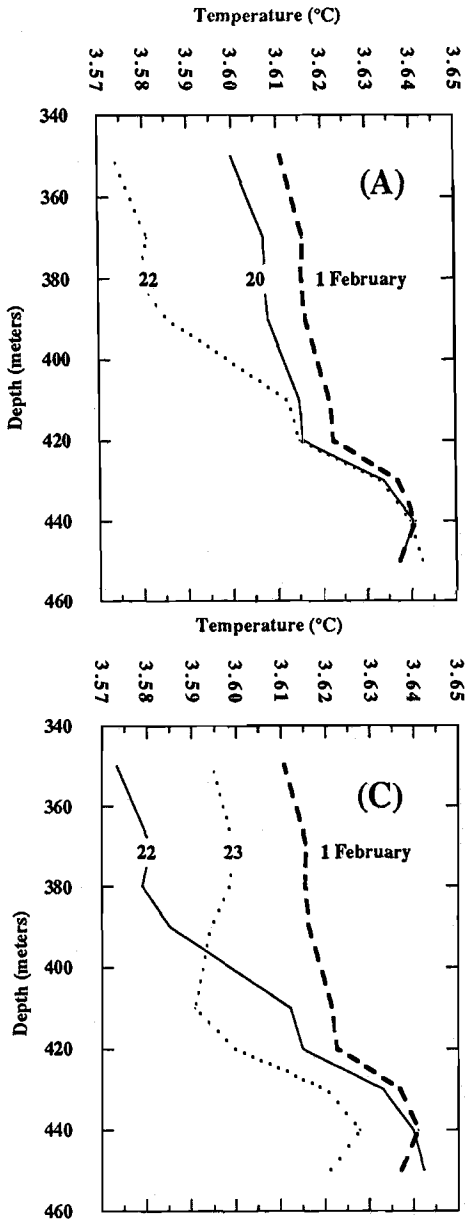

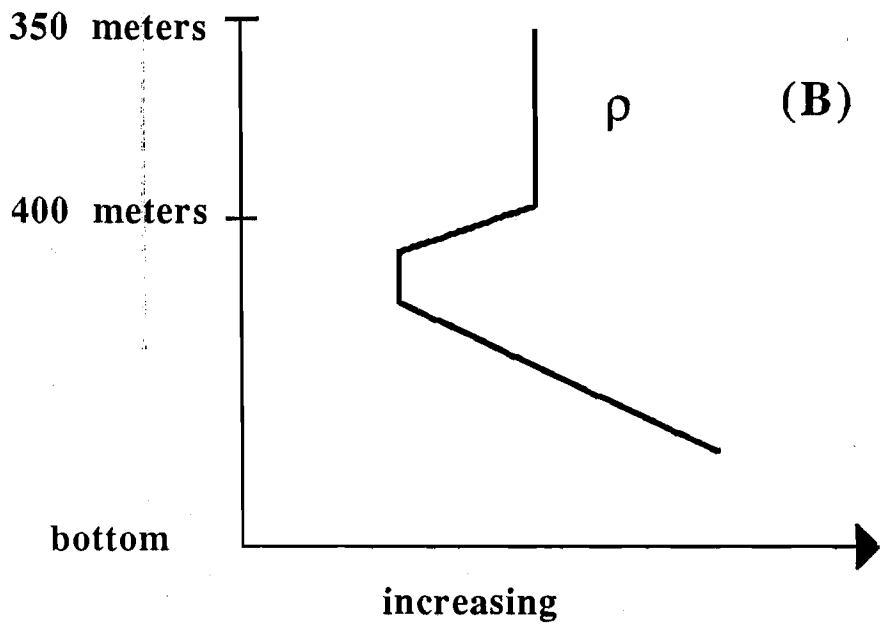

Figure 11. (a) Depth versus temperature for 1, 20, and 22 February.
(b) Schematic representation of depth versus density on 22 February.
(c) Depth versus temperature for 1, 22, and 23 February.

In (a) the diffusion of cold water from above dominates the mixing process from 1 February to 20 February. This is followed by the development of an unstable deep water column due to the accelerated (sudden) mixing of cold water from above. The density instability is schematically represented in (b) and is quickly mixed out as in (c).

[unpublished]) will provide a good integrated rate of deep lake renewal. The approach of Pearle et. al. (1975) of observing the sudden enrichment of nitrate in the surface waters as a measure of turnover can not be applied to the Crater Lake system without data which has been collected more frequently throughout the year. Some enrichments in surface nitrate have been observed during early April in the upper isothermal layer (G. Larson, unpublished data); however, it is not clear if these observed surface enrichments are due to bottom water upwelling, atmospheric inputs, or some combination of the two.

3. Observations on the horizontal and vertical transport of heat and salt through the deep lake.

This section deals with the processes of heat and salt transport through the hypolimnion during periods of high surface stratification. Because Crater Lake is a bottom heated, salt stabilized system we will first explore double diffusive convection as a possible mechanism for the transport of heat and salt through the water column. Parameterization of the vertical fluxes of heat and salt using equations developed by Kelley (1984, 1988, and 1990) are compared with the observed heat and salt flux measurements which are based on our time series experiments. It is found that double diffusion, as a mechanism for heat and salt transport, can not account for the heat and salt flux observed in Crater Lake. Having evaluated the significance of double diffusion within Crater Lake, we will suggest alternative mixing mechanisms that can account for the necessary extent of mixing.

Analysis of the significance of double diffusive convection in the water column. In this section we examine the theory behind the evaluation of double diffusive fluxes, how this flux is associated with layering, and compare the theory with observations in Crater Lake.

In cases where the vertical gradients of temperature (T) and salt (S) both increase with depth "staircase" features in T and S are often observed (Newman, 1976). These staircase features, which are dependent on the differing molecular diffusivities of heat and salt, are turbulent layers where T and S are well-mixed vertically, separated by sharp density interfaces above and below each layer (Turner, 1965). The fluxes of heat and salt across the interfaces between the layers rely on molecular diffusion (Huppert, 1971; Marmorino and Caldwell, 1976; Padman and Dillon, 1989).

The evaluation of double diffusive convection relies on the differing molecular diffusivities between heat and salt in lake water and the density ratio

$$R\rho = \beta\Delta S_z/\alpha\Delta T_z \qquad (3a)$$

(Kelley, 1990) where $\beta = \rho^{-1}(\partial\rho/\partial S)$, $\alpha = -\rho^{-1}(\partial\rho/\partial T)$, and ΔS_z and ΔT_z are the observed salinity and temperature gradients respectively. Although the increase in temperature with increasing depth provides a destablizing force on the density profile, the density profile in Crater Lake is statically stable. This is because increases in salt with depth provide sufficient stabilization for the density to increase with increasing depth (i.e. $R\rho > 1$).

Reformulation of the double diffusive flux laws and their components is the subject of on-going research (see Kelley, 1990). For the purposes of this study we will employ the traditional 4/3 flux law of Turner (1973)

$$\alpha F_T = c(g\kappa/\nu)^{1/3}(\alpha\Delta T)^{4/3} \qquad (3b)$$

$$\beta F_S = \alpha F_T \gamma \qquad (3c)$$

where F_T (°C m sec^{-1}) is the vertical flux of temperature associated with double diffusion and is easily converted to heat flux F_H (W m^{-2}) by $F_H = \rho C F_T$, where ρ is the density and C is the heat capacity of the fluid, F_S is the vertical flux of salt (g m^{-2} s^{-1}), c is the thermal flux factor which is an empirically derived quantity and is a function of the density ratio, g the gravitational constant, κ the thermal diffusivity, ν the kinematic viscosity, and γ the diffusive flux ratio which is empirically derived as a function of the density ratio. The variation of γ with the density ratio expresses the changes in the ratio of salt diffusivity to thermal diffusivity with increased mechanical mixing. Kelley (1988, 1990) points out that the 4/3 flux law of Turner (1973) could overestimate the actual property flux by 34%, this will prove to be of little consequence to the arguments developed here. We employ Kelley's (1990) formulations of c and γ for calculating diffusive fluxes where

$$\gamma = \frac{R\rho + 1.4(R\rho - 1)^{1.5}}{1+14(R\rho - 1)^{1.5}} \qquad (3d)$$

$$c = 0.0032 \exp(4.8/R\rho^{0.72}). \qquad (3e)$$

Table 2 presents data showing the flux of temperature over time as measured by the CTD and the temperature flux that is calculated by the 4/3 flux law. Heat (temperature) fluxes are calculated from the CTD by integrating the area under a vertical profile, below a depth of noted increase over time (see Table 2 for depth intervals). We then subtract the area under a profile taken at the same location at an earlier time. Since no obvious "step-like" features are evident for any prolonged period in the water column of Crater Lake, the criterion used for application of the flux law was that the temperature gradient, over the depth interval chosen, was relatively constant in time. The rationale behind this criterion is that, changes in the temperature and salinity gradients may be caused by advective processes and if double diffusion were the only mechanism for vertical mixing of heat and salt then the vertical gradients in temperature and salinity should not vary much over short time periods. Comparison of the CTD data with the calculated flux data (Table 2) shows that double diffusive convection does not account for the observed heat flux through the water column. For example, in Table 2 we see that between May and June from 409 to 544 meters (the depth interval over which the temperature gradient remained relatively constant) there was a net heat flux of 0.63 Wm^{-2} as measured by the CTD; however, based on the thermal gradient and equation 3b we calculate a double diffusive heat flux of 0.025 Wm^{-2}.

Double diffusive fluxes are related to the thickness of the convecting layers (Turner, 1973; Kelley, 1984). It is therefore useful for our purposes to estimate the height that these layers would need to be if double diffusion were the acting mechanism for the vertical transport of heat and salt through the water column. The parameterization of the layer thicknesses are carried out according to Kelley (1984, 1988) where the intrinsic layer thickness scale is

$$H_o = (\kappa_T/N)^{1/2} \qquad (3f)$$

and the layer thickness is given by

$$H = GH_o = G(\kappa_T/N)^{1/2} \qquad (3g)$$

where G is the scaled layer thickness and is a function of the density ratio ($R\rho$), the Prandtl number ($Pr = \nu/\kappa$), and the Lewis number ($Le = \kappa_S/\kappa_T$).

Table 2 Calculation of Heat Flux based on CTD data and model

Time period (1989)	Depth Range (meters)	CTD Flux (F_H) (W m^{-2})	Model (F_H) (W m^{-2})
May-June	409-544	0.63	0.025
June-July	400-500	0.46	0.024
July-Aug	400-500	1.20	0.038
Aug-Sept	400-500	0.14	0.028
Sept-Oct	400-500	2.00	0.026

Using equations 3b, 3f, and 3g we can estimate the ΔT (the change in temperature between the layers) and H (the layer thickness) required for double diffusion in the lake. The prescribed flux (F_T) is based on the CTD data in Table 2 (Flux (CTD)$^*_{obs.}$). Rearranging equation (3b) yields an expression for ΔT between two "steps" as a function of the prescribed flux [i.e. $\Delta T \propto (F_T)^{3/4}$]. By dimensional analysis the layer thicknesses would be dependent on the change in temperature at the interface (ΔT) divided by the temperature gradient ($\Delta T/\Delta z$). For the calculations of the layer thicknesses we use the observed temperature gradient ($(dT/dZ)_{obs.}$) presented in Table 3. The results of our calculations are summarized in Table 3. The modeled layer thicknesses (H_{model}) and ΔT's (ΔT_{model}) presented in Table 3 reflect reasonable estimates of what would be observed if double diffusion were the dominant mechanism for the transport of heat and salt through the water column in Crater Lake.

Table 3 ΔT and Layer Thicknesses based on Observed Fluxes

Time period (1989)	Flux (CTD)$^*_{obs.}$ (°C m s^{-1})	$(dT/dZ)_{obs.}$ (°C/m)	ΔT_{model} (°C)	H_{model} (meters)
June-July	10.9×10^{-8}	0.00024	0.002	8.9
July-Aug	28.5×10^{-8}	0.00032	0.004	13.2
Aug-Sept	3.3×10^{-8}	0.00042	0.001	3.3
Sept-Oct	47.6×10^{-8}	0.00027	0.007	25.4

**For purposes of dimensional consistency we have chosen to express the prescribed flux in units (°C m s^{-1}).*

It should be pointed out that the CTD fluxes presented in Table 2 are minimum values as they do not represent the full, deep lake water column (i.e. the bottom depth in the deep lake is approximately 590 meters). The total heat flux through the water column will be higher in each case; however, since the thermal and saline gradients change above and below the depths which were specified in Table 2, modeling of double diffusive convection in these regions of the water column would be inappropriate.

In summary it is apparent that double diffusive convection, as a mechanism for the transfer of heat and salt through the water column in Crater Lake, underestimates the total heat flux by one to two orders of magnitude. Double diffusion may, however, be important on small spatial and temporal scales, and may ultimately contribute to the T-S distribution near the sediment-water interface. This will be considered in Section 4 of the text. Processes contributing to the variations in the observed heat flux, as measured by the CTD (Table 2), will be discussed in the following section.

Horizontal mixing in the deep lake. When the upper water column is highly stratified ($N > 10^{-3}$), deep lake mixing is dominated by horizontal basin-to-basin exchange processes.

Our data suggests that the thermally and chemically enriched fluids derived from the the South Basin are frequently mixed with waters from the rest of the deep lake. Data used to support the contention of deep lake horizontal exchange include, time series CTD data and other geochemical data (e.g. dissolved gases and trace elements).

Temperature and salinity data taken from the North Basin in September 1988 shows dramatic mid-water column microstructure variations in temperature and salinity (Figure 12 a & b). We propose that these microstructure variations are due to the lateral flow of South Basin thermally and chemically enriched water. As the South Basin fills with warm, salty water, it will "spill over" into the deeper portions of the lake because of its greater density relative to non-enriched fluids. The sill depth between these two basins is between 425 and 450 meters depth. This is consistent with the data from the South Basin in that there was thermal and saline microstructure observed at approximately 425 meters depth in this basin (Figure 12a). (The term "microstructure" refers to small changes in the vertical gradients of temperature and salt.)

In order to accurately assess the stability of the deep water column in September 1988, we computed sigma$_{0.5}$ ($\sigma_{0.5}$). Where $\sigma_{0.5} = (\rho_{0.5} - 1) \times 1000$ and $\rho_{0.5}$ is the density a fluid would have at 500 decibars. In deep freshwater systems, sigma$_\theta$ does not accurately represent the local "stability" of the water column (Figure 12d). Conceptually, this is because of the changes in the temperature of maximum density with pressure where at the surface the T_{md} is nearly 4°C in Crater Lake, whereas at 500 decibars it is less than 3°C. Most of the water throughout the water column appears to be statically stable with respect to 500 decibars (Figure 12c); however, the calculation of the stability of discrete points within the water column reveals that there are some unstable parcels of water (arrows in Figure 12c). The parcels are unstable over vertical distances of 5-10 meters. These are difficult to see with the naked eye because of the apparent scatter in the data. The dynamic nature of these parcels is further suggested by the rapid (hours-days) changes in the vertical temperature and salinity structure of the deep lake.

^{222}Rn and Fe (dissolved and particulate) measurements further illustrate the basin to basin exchange process as water high in ^{222}Rn and Fe may often overlay water of lower ^{222}Rn and Fe content in the North Basin. Figure 13a demonstrates that the horizontal transport of iron leads to a maximum in dissolved and particulate Fe between 450 and 500 meters in the North Basin. ^{222}Rn also exhibits a deep-water maximum at 475 meters in the North Basin (Figure 13b). Although not on the graph, the deepest ^{222}Rn value from that particular South Basin hydrocast was 35 dpm/100 liters. The net effect of the proposed horizontal movement of waters from the South Basin to the North Basin is that "younger" (^{222}Rn enriched) waters overlie the "older" (^{222}Rn depleted) waters in the North Basin. Although we do not have the time series ^{222}Rn data to demonstrate it, we do not expect to always observe this pattern. As already suggested, the influx of South Basin waters to the North Basin is variable; therefore, sometimes a more uniform ^{222}Rn distribution in the deep water of the North Basin may exist due to the vertical mixing and decay of these South Basin waters after transport to the North Basin.

The timing of these horizontal mixing "events" also seems to be somewhat consistent from year to year. Although it is clear from the data set that these events may potentially occur at any time during the year; it seems that the events of greatest magnitude are consistently occurring in late summer/early fall (September-October). These periods of more intense horizontal exchange are characterized by the largest observed changes in the deep lake microstructure. Since September and October are periods which have strong stratification at the surface, it would seem that surface disturbances could not supply the necessary

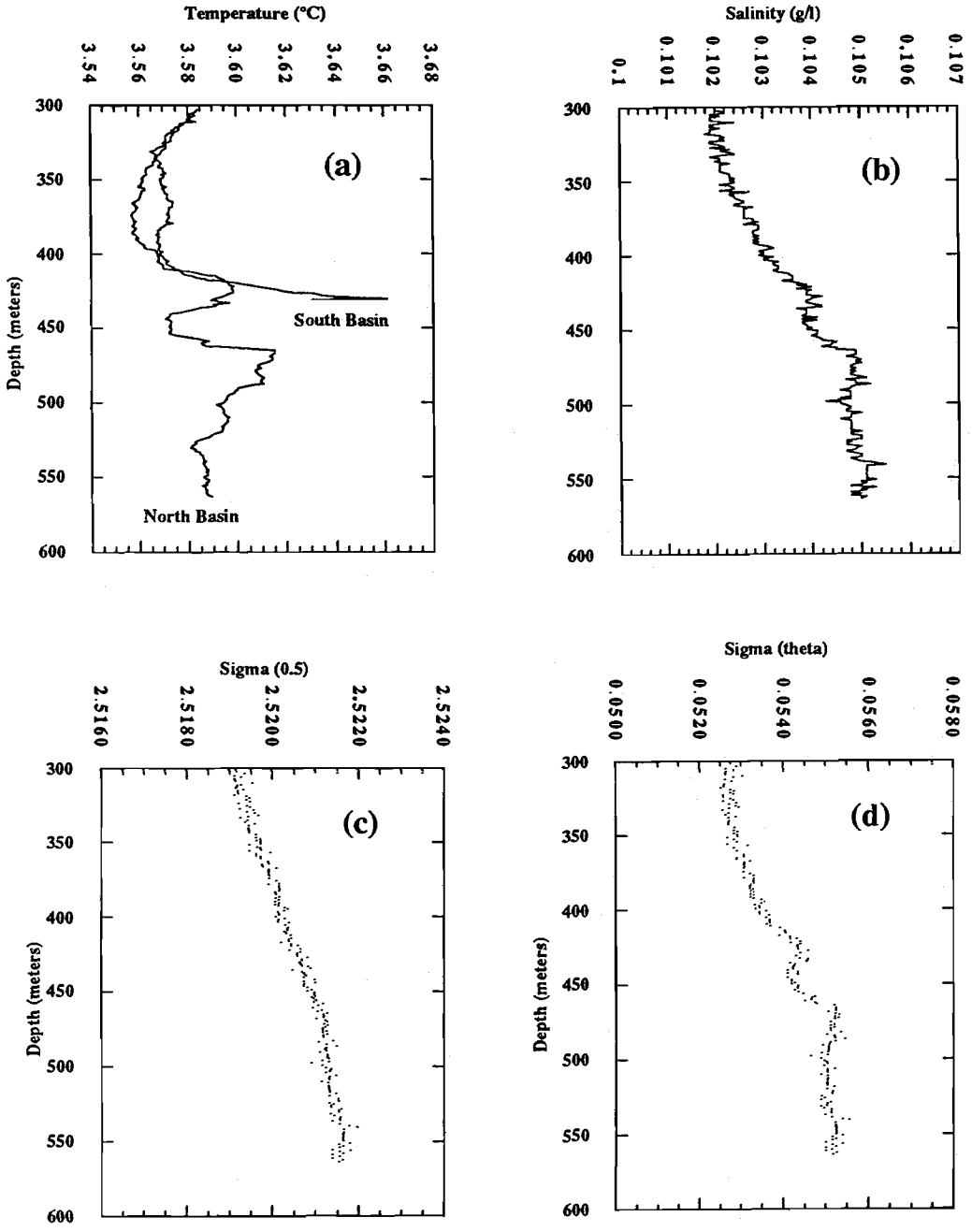

Figure 12. Hydrographic data taken 19 September 1988. (a) Depth versus temperature for both the South and the North basins, (b) depth versus salinity for the North Basin, (c) depth versus $sigma_{0.5}$ for the North Basin, (d) depth versus $sigma_{\theta}$ for the North Basin. The densities are calculated from equations presented in Chen and Millero (1986).

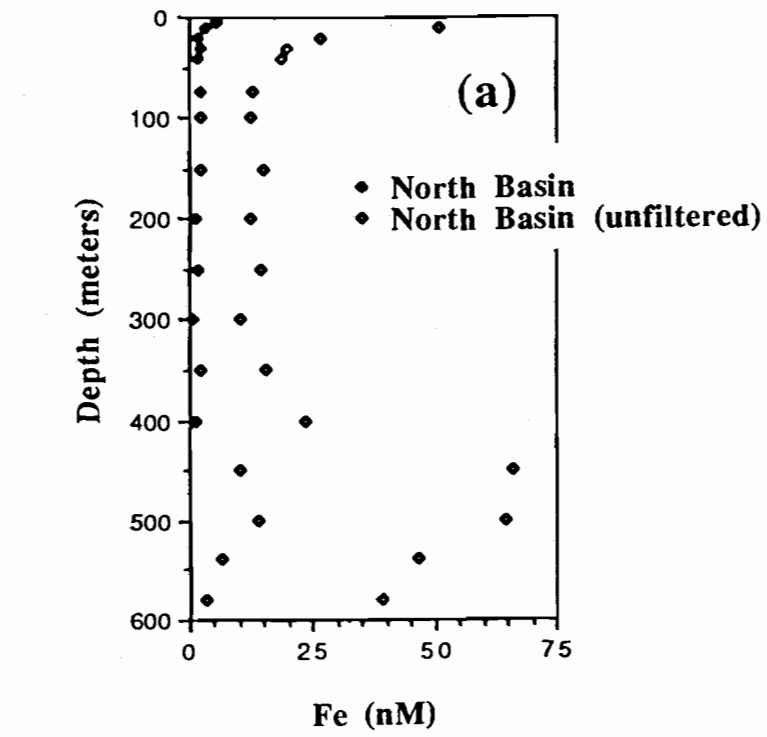

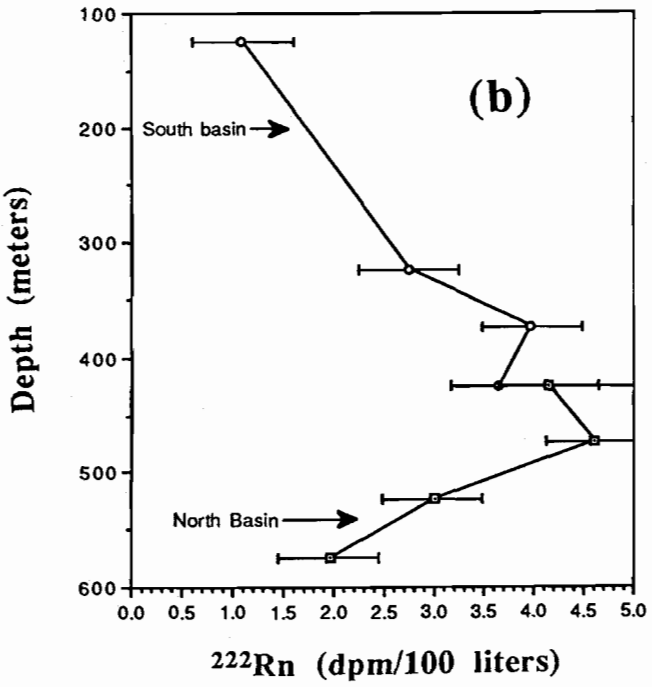

Figure 13. (a) Depth versus dissolved (closed symbols) and particulate (open symbols) iron from the North Basin (data from Collier et. al., 1990). (b) Depth versus ^{222}Rn for the North (open boxes) and the South (filled circles) Basin.

forcing for the initiation of this mixing process. We suggest that once the enriched water in the South Basin reaches a depth where inter-basin exchange may occur (approximately 425-450 meters) the South Basin enriched waters may, in effect, "spill over" into the North Basin. To demonstrate the plausibility of this process we take an average inflow of fluid, with a salinity of 0.6 grams/kg, of 0.2 m^3/second (Table 1). This fluid is diluted many times with background lake water, which has a salinity of 0.104 grams/kg, to make South Basin bottom water which has a salinity of 0.106 grams/kg. This yields a net inflow rate of 50 m^3/second for a fluid containing 0.106 grams/kg of salt. If we suppose that the South Basin can be represented by a box with the dimensions of 1000m x 2000m x 50m deep then it takes approximately 23 days for the enriched fluid to fill this box. This rather simple representation of the process simply demonstrates that, given our current knowledge of inflow and salt distribution, frequent "spillovers" are possible and are even likely.

The basin to basin exchange process proposed here is not a steady state process and one of the results of this non-steady state horizontal exchange of heat and salt is that there are noticeable variations in the heat flux estimates over short time scales (Table 2).

Vertical mixing processes in the deep lake. In addition to horizontal advection playing a large role in the transport of heat and salt through the deep lake, additional mechanisms also contribute to the vertical transport of these properties through the hypolimnion. We propose that turbulent diffusion coupled with vertical convection are likely contributing mechanisms for heat and salt transport through the hypolimnion, and we base this hypothesis on two observations: (1) since the calculated effective diffusivities for both heat and salt in Crater Lake are the same order of magnitude and are many orders of magnitude larger than the molecular values, the mixing process can not simply be driven by molecular diffusion (or double diffusion) (2) there are small-scale vertical instabilities in the water column which do not appear to be due to the horizontal transport of heat and salt.

The effective diffusivities for heat (K_{eT}) and salt (K_{eS}) can be modeled according to a simple diffusion model (see equations 2a and 2b for the development)

$$F_T = K_{eT} \ (dT/dz) \qquad (3h)$$

and

$$F_S = K_{eS} \ (dS/dz) \qquad (3i)$$

where F_T and F_S are the measured flux of temperature (°C m s^{-1}) and salt (g m kg^{-1} s^{-1}) respectively (for dimensional simplicity we use F_T as opposed to F_H -- the heat flux). These measurements are again based on time series CTD measurements (Table 1). Our calculations reveal that the effective diffusivities for heat and salt are approximately 6 to 8 x 10^{-4} m^2 s^{-1}. If molecular diffusion was an important mechanism for the transport of heat and salt through the water column, we would expect that the effective diffusivity for heat would be two orders of magnitude larger than the effective diffusivity for salt (e.g. molecular diffusivities for heat and salt are O(10^{-7} m^2 s^{-1}) and O(10^{-9} m^2 s^{-1}) respectively). This effective diffusion coefficient is approximately a factor of two smaller than the diffusion coefficient calculated for diffusion during the month of February ~2 x 10^{-3} m^2 s^{-1}. This observation suggests that the intensity of deep lake mixing during winter is greater than during the summer, which is not surprising since the overall stability of the upper water column is greater during the summer. However, both winter and summer diffusion processes will obviously be smaller in magnitude than the instability-driven convection described in Section 2.

Observations of small temperature inversions through the mid-water column suggest the presence of small, upwardly moving convective "plumes". Examples of potential convective cells are presented in Figure 14 where the unstable plumes are indicated by the arrows. In Figure 14 we only show the temperature profile, because the salinity profile lacks the resolution of the temperature profile. We therefore can not accurately calculate the stability of these thermal features; however, our data suggest that they are transient features which are not uncommon in the mid-to-deep lake. These "plumes" could be caused by either of two processes (or some combination of the two). The plumes may be caused by direct inputs of buoyant water into the South Basin. Alternatively, they may be generated by conductive heating of thermally and chemically enriched waters which are resting at the sediment-water interface. This latter process would eventually lead to instability and formation of thermal convection cells that vertically mix the excess heat and salt.

As discussed in the previous section, the horizontal transport of fluids with anomalous heat and salt content, followed by their sinking or their buoyant rise through the water column, is also important to the vertical mixing of these properties in the hypolimnion. However, the magnitude of this two-dimensional process is not constant in time, which leads to varying fluxes of heat and salt through the water column.

Another dimension of mixing heat and salt through the water column, is presented as a large temperature anomaly in the middle of the water column (Figure 15a). This temperature anomaly was measured in the South Basin of Crater Lake on 11 September 1987 and is greater than 0.1°C between 225 and 275 meters, relative to the North Basin profile. This corresponds to a total heat anomaly of 9600 kcal/m2, which is a factor of five to ten larger than typical near bottom thermal anomalies measured in the South Basin as compared to the North Basin (McManus and Collier, unpublished data). Shown with this data (Figure 15a) are temperature profiles taken from the South Basin approximately 6 hours earlier (solid line) and the North Basin approximately 3 hours earlier (dotted line). The earlier South Basin profile was taken in the same general location of the South Basin as the profile showing the dramatic temperature anomaly (dashed line); however, there is some uncertainty as to the relative location of the two South Basin temperature profiles and they may be separated in space by as much as 500-1000 meters. T-S diagrams (Figure 15b) of the three hydrocasts (below 100 meters) demonstrate the dramatic change in the T-S characteristics in the hydrocast with the large thermal anomaly (SBE028) as compared to the earlier South Basin diagram (SBE026) and the North Basin diagram (SBE027). However, the T-S diagrams of SBE026 and SBE027 both show some influence of the warmer, more saline water found in SBE028, suggesting that the heat and salt from SBE028 may be spreading horizontally along an isopycnal surface.

The large thermal anomaly demonstrated in Figure 15a is hydrostatically stable with respect to 250 decibars and is buoyant relative to 450 decibars. This suggests that perhaps the water column anomaly represents a "plume" which originated at the sediment-water interface and has risen to neutral buoyancy. Alternatively, there could be a source of thermally and chemically enriched water along the caldera wall at this depth, which we consider to be unlikely. It is apparent that this feature is anomalous in both time and space, and since we have not seen such an anomaly again it is difficult to ascertain the origin or significance of this feature.

In summary, the one dimensional calculation of an "effective" turbulent diffusion coefficient shows that the transport of heat and salt through the water column is several orders of magnitude faster than would be expected by molecular diffusion. The turbulent diffusion coefficient calculated here does not discriminate between the variety of

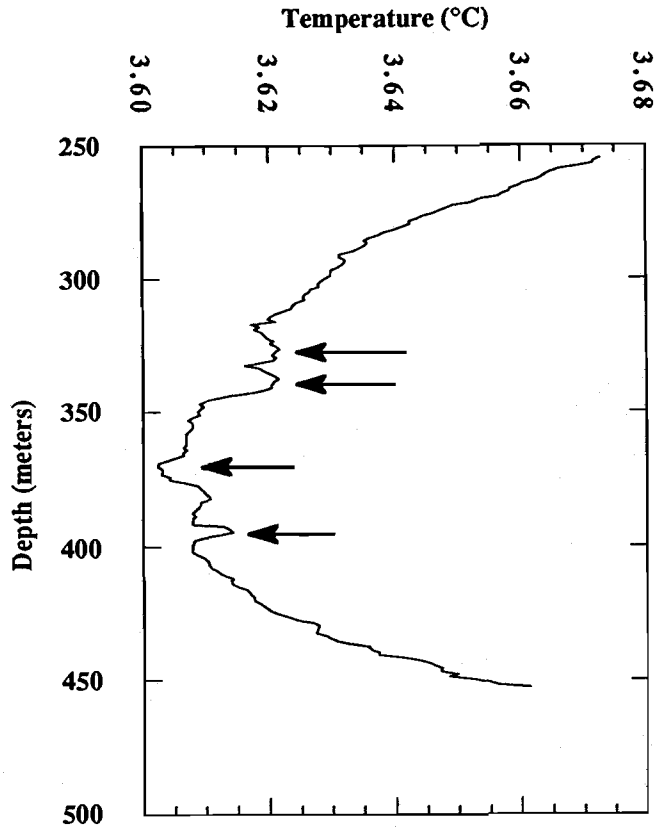

Figure 14. Examples of convective cells (arrows). Data is from 18 September 1990 from the South Basin.

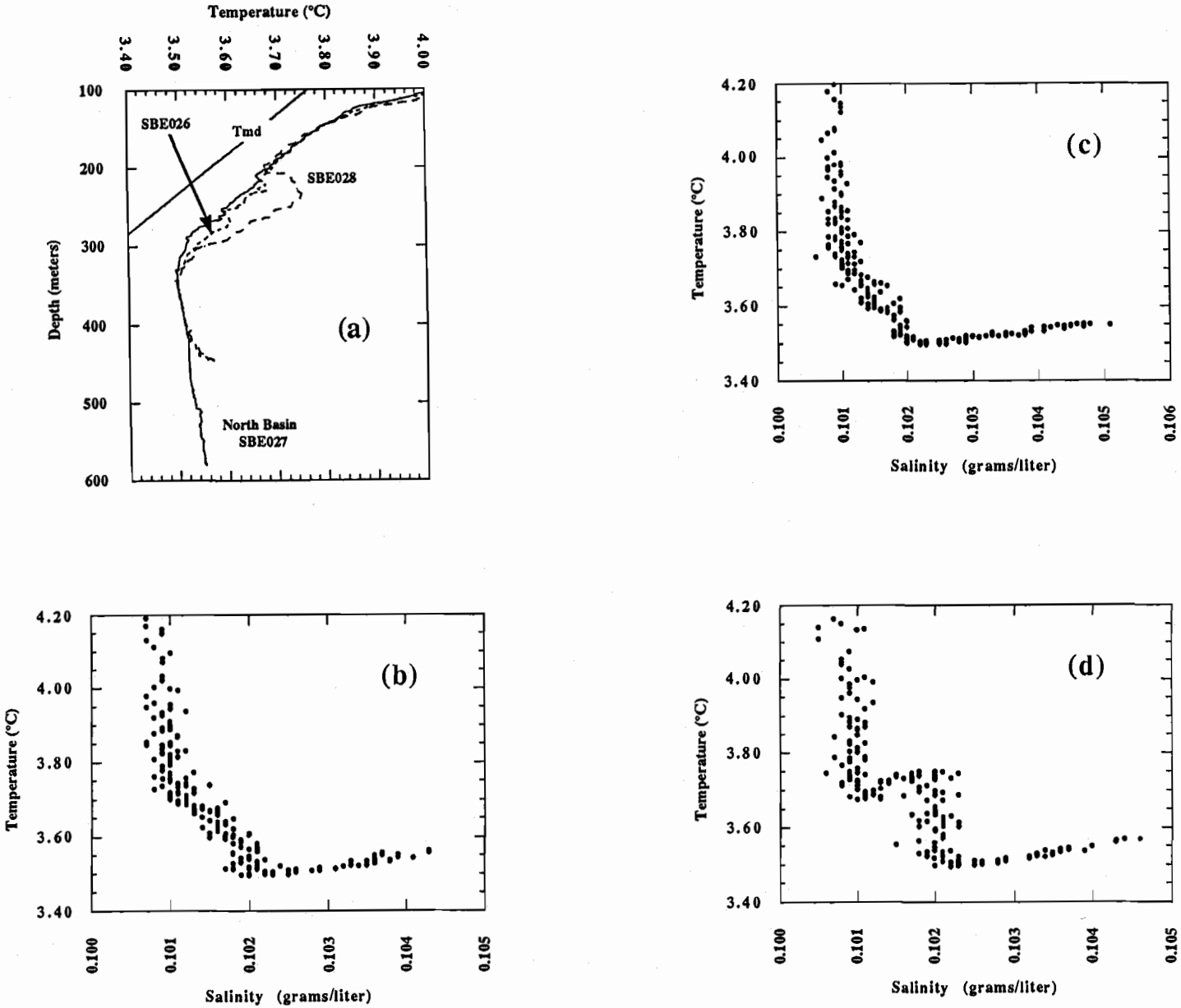

Figure 15. (a) Depth versus temperature for SBE026 (solid line, South Basin), SBE027 (dotted line, North Basin), and SBE027 (dashed line, South Basin). (b-d) T-S diagrams for the three hydrocasts. Data shows the T-S anomaly in all three hydrocasts, but particularly in SBE027.

mechanisms which physically transport the heat and salt through the hypolimnion, rather the diffusion coefficient reflects the net effect of all the mixing mechanisms operating in the hypolimnion. Such mechanisms include vertical convection, turbulent diffusion, and horizontal transport (advection) followed by the vertical mixing of these advected waters. Although there is also a potential for enhanced mixing along the sides of the basin, our calculations suggest that such mixing will be insignificant compared to the other mechanisms. The physical processes described here are directly tied to the active inputs of thermally and chemically enriched waters and because of these processes the deep lake remains relatively well mixed.

4. T-S properties of the hypolimnion.

The bulk T-S properties of the hypolimnion of Crater Lake document the warmer, more saline nature of South Basin deep water as compared to North Basin deep water. Figure 16a demonstrates the differences in the T-S properties between the two basins during the summer 1989 sampling period. Data to the left of the temperature minimum represent the T-S characteristics from 150-350 meters. Below this depth, after the temperature minimum on the diagram, the influence of the active input of thermally and chemically enriched fluids is seen as increases in both these properties (McManus et. al., submitted). In general, the North Basin and the north west portion of the lake have nearly identical T-S relationships which reflect background lake water (open circles in Figure 16a). Therefore, we will focus this section on the spatial distribution of the T-S properties in the deep South Basin and we will suggest a physical mechanism for the observed distribution of these properties.

CTD data from South Basin submersible dives demonstrate the heterogeneous nature of the near-bottom waters of the South Basin. Figure 16a presents a T-S diagram which includes data from the South Basin from submersible dives CD216, CD218, and CD222. Most South Basin submersible data is taken within 3 meters of the lake bottom. The curved lines represent isopycnals relative to 465 decibars. Three T-S "end-member" trends are apparent in the figure, (a) a high temperature-low salinity trend (CD218), (b) a high temperature-high salinity trend (CD222), and (c) a low temperature-high salinity trend (CD216), additionally, (d) represents background deep lake water. Water column temperature and salinity data from other dives in the South Basin all lie somewhere between the (a) and (c) end-member "arms" (Figure 16a); henc, his diagram represents the full range of T-S properties in this location of the South Basin.

Figure 16b presents an expansion of Figure 16a. Using Figure 16b we can extrapolate the points in 16a to hydrothermal fluid end-member compositions. This will allow us to formulate mixing models which explain the near bottom distribution of temperature and salinity in the South Basin. For modeling purposes we assume an end-member salinity of 0.6 grams/kg, which derives from the salinities of brine samples and pore water samples taken from the South Basin (Collier, et. al., 1990; Wheat, unpublished). The linear extrapolation from background lake water, (d), along the (a) end-member salinity should yield the original temperature of this fluid (Figure 16b). A linear mixing line is also shown for the (b) trend for comparison. The important point to be considered from Figure 16 is that end-members (b) and (c) when mixed with (d) will not generate fluids that would fall along the (a)-(d) trend; however, we will demonstrate that end-member (a) can undergo a variety of mixing and cooling processes which will result in any T-S combination found in Figure 16a.

Before pursuing a model which describes the near-bottom T-S distribution of the South Basin, it is important to introduce two other observations upon which we base our model. The first is that the heat to salt ratio in the water column above the bottom of the South

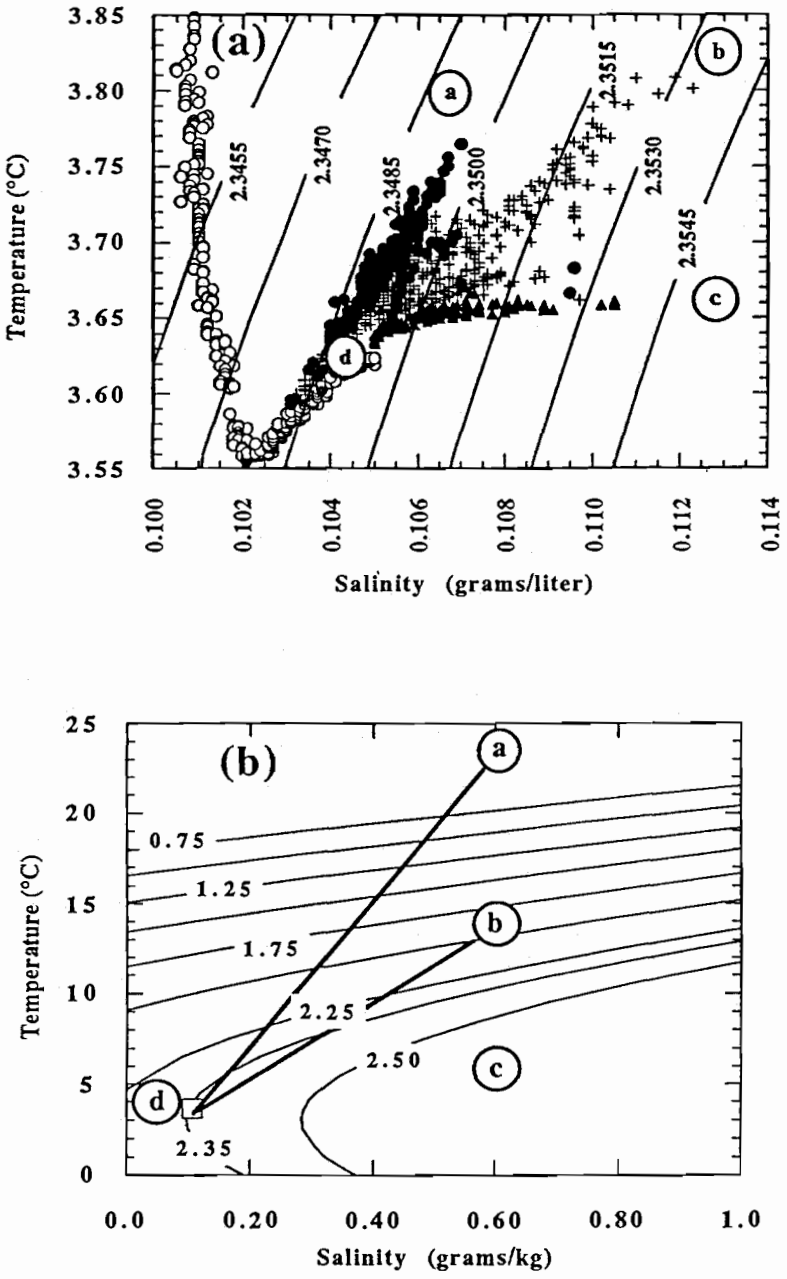

Figure 16. (a) T-S diagram of the hypolimnion of Crater Lake showing four T-S extremes: high heat to salt ratio; low heat to salt ratio; intermediate heat to salt ratio; background lake water. The lettering in the figure corresponds to the various heat to salt ratios. The open circles represent CTD hydrocast data taken from the North Basin. All the other symbols represent CTD data taken from submersible dives in the South Basin as described in the text. (b) Extrapolations of points in (a) to a salinity of 0.6 grams/kg.

Basin generally follows the bathymetry. At bathymetric highs the heat to salt ratio is high, (a) in Figure 16a. Likewise, at bathymetric lows the heat to salt ratio is low, (c) in Figure 16a. Intermediate bottom depths have intermediate heat to salt ratios. Furthermore, we observe higher-temperature hydrothermal "features" (e.g. bacterial mats) at bathymetric highs whereas at bathymetric lows we observe lower temperature bacterial mats and brines. (It is important to elucidate that "high" temperature indicates 15-19 °C and "low" temperature 4-10°C.) These observations indicate the need for models which recognize the relationship between the bathymetry and the distribution of the near-bottom temperature and salinity in the South Basin.

A conceptual model describing the near-bottom distribution of temperature and salinity in the South Basin. Based on near bottom T-S observations in the South Basin of Crater Lake, we have developed conceptual models which describe the mechanisms for entry of the thermally and chemically enriched fluids into the deep lake. We assume that the source fluid enters the system as a buoyant plume, represented, for instance, by (b) in Figure 16b. Here the "system" may be the highly porous sediments/debris overlying the basement (Barber and Nelson, 1990) or it may be the water column. In the case where the source fluid enters the system as a buoyant plume, non-linear density behavior may occur during linear T-S mixing, as demonstrated by the (d) to (b) line in Figure 16b (Turner and Gustafson, 1978; McDougall, 1983; McDougall, 1984; Campbell et. al., 1984; Turner and Campbell, 1987). Also, if the fluid flow from the source and the initial density difference between the source fluid and ambient lake water is small (such that the buoyant plume would not undergo rapid convection), double-diffusive effects may dominate fluid behavior (McDougall, 1983) leading to a decrease in the heat to salt ratio as the fluid travels away from its source.

In Figure 17 we present a conceptual model which describes how the fluids of varying heat to salt ratios, observed near the sediment-water interface in the South Basin, can be achieved. The lettering on the model corresponds to the lettering of end-members in Figure 16. At (a) a source of thermally and chemically enriched fluid enters the system with a high heat to salt ratio and is buoyant. The initial temperature and salinity of the entering fluid are greater than the ambient water; therefore, there is a density maximum for some intermediate dilution, such that the new mixture will be heavier than either of the components from which it formed (Sato, 1982; Turner and Gustafson, 1987). This mixing process will cause the newly formed mixture to flow in a downward direction, either within the debris column or along the sediment-water interface. If some or all of this mixing occurs in the debris column, the fluids may exit the system at a variety of locations down-slope of the initial source mixing region. Additionally, heat may be lost from the fluid due to the larger molecular diffusivity of heat relative to salt or due to direct conductive heat losses with the surrounding rocks/debris. This process will result in a reduction of the heat to salt ratio of the fluid as it travels through the system. This would explain the observed variation in the heat to salt ratio with bathymetry.

Although this kind of process could result in the observed near-bottom distribution of heat and salt, it is unlikely that such a process would result in highly dense saline brines located at the bottom of the lake, particularly with what we have established about the mixing time scale of the deep lake. We suggest that the brines represent a feature representative of active inputs of thermally and chemically enriched fluids. Thus, a buoyant source fluid travels through the sediment/debris column, and as it enters the lake it encounters a cooler, dense fluid in the form of the brines, (c) in Figure 17. The mixture of brine water with source fluid is denser than bulk lake water thus it will remain in the pool. At steady state, the flux of fluid into the pool must equal the flux out and flux of heat and salt from the pool is accomplished by double diffusive convection (McDougall,1984). Before steady state is reached, the buoyant source fluid must first travel through a cold sediment/debris column.

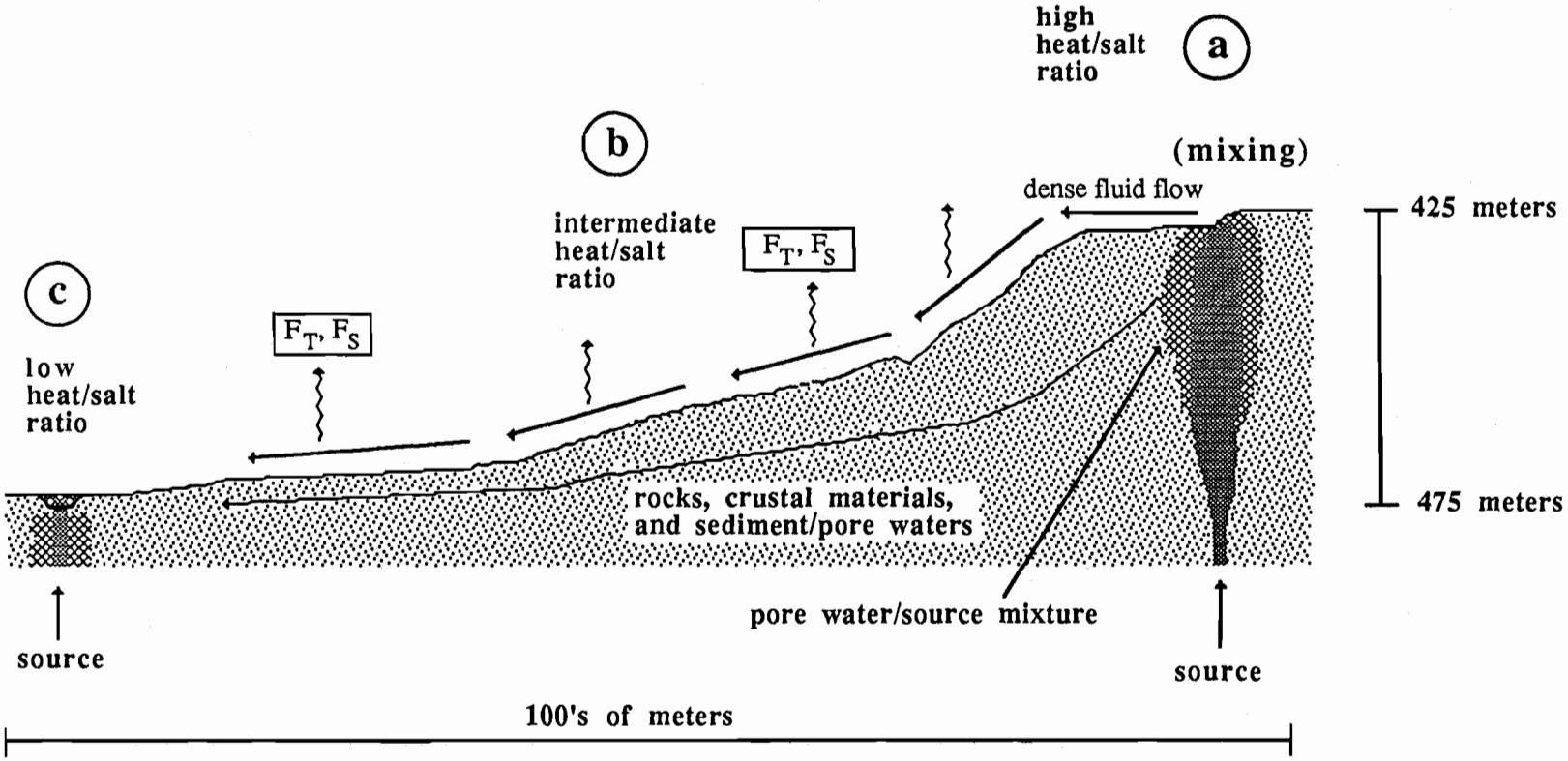

Figure 17. Conceptual model which describes how the varying heat to salt ratios (Figure 16a,b) observed near the sediment-water interface in the South Basin, may be achieved. The lettering on the cartoon corresponds to the lettering in Figure16.

The fluid will loose heat by conduction with the surrounding debris during its buoyant phase and by the time the fluid reaches the sediment-water interface it is no longer buoyant and therefore "ponds" along the bottom of the lake (McDougall,1984).

If preferential loss of heat over salt is occurring somewhere within the system, then we would expect to find curved T-S profiles as opposed to lines in T and S (Ingham, 1966; Schmitt, 1981; McDougall, 1983). In Figure 16a we note that the T-S trend from (d) to (c) is a curve rather than a line which suggests that the water in this region has undergone double diffusive loss of heat. In contrast, the data that extends to (a) in Figure 16a appears to fall along a line rather than a curve, indicating that linear mixing is occurring in this area of the South Basin. Because the scales of mixing (Section 3) suggest that double-diffusive convection is not a dominant mechanism for the redistribution of heat and salt in the bulk water column, we expect that the affects of any double diffusive convection on the overall T-S properties of the hypolimnion of Crater Lake will be confined to these small or local scales. It should also be pointed out that although curvature in the T-S relationships may be indicative of multiple sources of varing composition, we have no physical or chemical evidence that this may be the case.

Another mechanism for changing the heat to salt ratio of near bottom waters is through reactions within the sediments. This would tend to change the heat to salt ratio by increasing the salinty of the pore fluids. However, our observations indicate that there are no systematic changes in fluid chemistry throughout the system. In general, changes in fluid composition are primarily due to dilution with lake water and not reaction.

In this section, we have attempted to describe the likely processes which govern the near-bottom distribution of temperature and salinity, additionally, we have postulated a mechanism whereby dense saline pools can be maintained on the floor of the lake. Our proposed mechanisms rely on the non-linear density behavior of fluids during linear T-S mixing and on the preferential loss of heat from a fluid due to the larger molecular diffusivity of heat over salt [$O(10^2)$] and due to conductive losses of heat with the surrounding rock/debris. In order to better elucidate the physical mechanisms influencing the T-S distribution, we would need more extensive pore water chemistry and temperature data from the sediments and other hydrothermal features.

5. The influence of hydrothermal activity on the physics of the water column in Crater Lake.

The hypolimnion of Crater Lake is only marginally stable. This is reflected by the buoyancy frequency (N), which for the hypolimnion of Crater Lake is $O(10^{-4}$ second$^{-1})$ (Collier et. al., 1990; McManus, et. al., submitted). Correspondingly, the turbulent diffusion coefficient ranges between 10^{-4} and 10^{-3} m^2/sec, which reflects relatively rapid vertical exchange through the the deep lake. The question is then, if there were not active inputs of heat and salt into the hypolimnion what would be the scales of mixing? Without the input of heat into the hypolimnion there would be no destabilizing force acting on the water column. The addition of salt to the hypolimnion through the reminerialization of biogenic materials in the deep lake would tend to stabilize the deep water column; therefore, we might expect the magnitude of the diffusion coefficients to decrease. Alternatively, if Crater Lake were conductively heated from the bottom (due to the fact that it rests in a caldera) yet there were no fluid inputs, we might expect the lake to undergo thermal convection which would result in a more rapid mixing time scale.

The overall stability of the water column also has some influence on the effectiveness of the conditional convective overturn described in Section 2. If the change in the salinity

gradient were to be dominated only by reminerialization, it may, in principle, be easier to develop the thermobaric instabilities due to a reduced salinity gradient. Hence, the surface signal carried by this mixing process could be carried all the way to the bottom as in Lake Baikal (Carmack et. al, 1989; Weiss et. al, 1991); however, because of the conditional nature of the instability, it is likely that annual exchange would rely much more heavily on the severity of winter storms, as in Lake Tahoe (Pearl, et. al., 1975). Also because of the relatively small fetch of the lake, wind forcing may be relatively less significant and will make this kind of mixing more difficult.

It is difficult to ascertain the precise effect of hydrothermal activity on the overall physics of Crater Lake; however, there are a variety of unique physical features of the water column which can only be attributed to the active input of heat and salt near the bottom of the lake. It is clear that the active inputs of hydrothermal fluids generate both vertical and horizontal density instabilities. These instabilities contribute to the rapid mixing of deep lake water, both horizontally and vertically. It follows then, that hydrothermal activity is important to the relatively rapid vertical mixing that occurs in Crater Lake, OR (characteristic time-scale of mixing ~2 years). This mixing brings biologically important nutrients from the deep lake to the surface lake at least once a year. Without such nutrients, principally dissolved nitrate, the new production which relies on these nutrients would be lower.

Conclusions

Our estimations of the deep lake heat budget of Crater Lake confirms the previous estimates of Williams and Von Herzen (1983). Since our method for estimating heat flow differs from that of Williams and Von Herzen (1983), who used sediment heat flow measurements, the agreement between the two data sets lends credence to both estimates. The salt flux and fluid flow estimates offer additional constraints on these estimates which were first proposed by Reilley (1990) and Nathenson (1990).

Time series dissolved oxygen data, data from a thermistor chain mooring, and CTD data all indicate that annual surface to bottom exchange is an important mechanism for the redistribution of heat and salt in the hypolimnion of Crater Lake. Our data also indicate that this exchange process is incomplete, resulting in undersaturation of dissolved oxygen at all times in the hypolimnion.

During periods of high surface stratification, deep lake mixing is dominated by small-scale vertical and horizontal exchange processes. Our data suggests that vertical convection is a mechanism for the transport of heat and salt through the hypolimnion; however, the relative importance of this type of mixing process is not clear. Calculation of a turbulent diffusion coefficient for heat and salt confirms that the mixing mechanisms which transport the bulk of the heat and salt through the hypolimnion are turbulent as opposed to molecular. The diffusion coefficient will allow us to model the transport of biochemically important nutrients/elements during periods of high surface stratification. Horizontal exchange processes allow the thermally and chemically enriched fluids from the South Basin to be mixed with the deep water from the rest of the lake. The varying fluxes of heat and salt, as deduced from CTD data, suggest that the mixing processes acting in the hypolimnion are non-steady state.

The T-S properties of the hypolimnion reveal that the waters in the South Basin are warmer and saltier than those in the rest of the hypolimnion. Three T-S end-member fluids are apparent in the South Basin of Crater Lake. (1) Background deep lake water which is similar to deep water found elsewhere in the lake. (2) Water of high heat to salt ratio. (3) Water of low heat to salt ratio. We hypothesize that the formation and mixing of these three end-members is due to the buoyant rise of the thermally and chemically enriched fluids

through the debris/sediment column, mixing of these fluids with pore fluids, followed by molecular diffusion above and/or below the sediment-water interface, and finally advective processes once the fluid enters the water column. The preferential loss of heat over salt through thermal diffusion and/or conductive heat loss allows for the formation of waters with varying heat to salt ratios. Subsequent advective transport through the water column allows for the mixing of these waters with waters from the rest of the lake.

Appendix B. National Geographic Dive Report

H. Phinney, D. McIntire, G. Larson, and M. Buktenica

Biology (and a few USGS) Dives

Dives 219, 221, 224, 225, and 227 (Fig. 1) were supported by the National Geographic Society and were designed to locate and collect biological specimens from deep-water benthic communities. In particular, we were interested in the distribution and abundance of a deep-water aquatic moss (*Drepanocladus*) and its associated epiphytic algae. Samples also were obtained from rocks collected during three USGS dives (Dives 210, 212, and 214). All biological materials obtained from Dives 210, 212, 214, 219, 221, 224, 225, and 227 were examined under the supervision of Harry K. Phinney, Department of Botany & Plant Pathology, Oregon State University. Preserved specimens of *Drepanocladus* will be deposited in the Oregon State University Herbarium and in the Natural History Collection at Crater Lake National Park. In addition, permanent slides of epiphytic and epilithic diatoms are now available for examination from C. David McIntire (Department of Botany & Plant Pathology, OSU).

Field observations and samples obtained during Dives 219, 212, 214, and 227 indicate that the upper limit of distribution for *Drepanocladus* is approximately 27 m below the water surface. The lower distribution limit for this moss is less certain, as detrital fragments were found in small patches as deep as 545 m (Dive 227). However, all collections indicated that the optimum zone for the development of dense beds of moss and associated epiphytes is between 30 m and 80 m below the water surface. This depth range also corresponds to the zone of maximum primary production in the water column (i.e., primary production associated with phytoplankton), indicating that the distribution of *Drepanocladus* may be controlled by an interaction between light and nutrient limitation. An alternative hypothesis suggests that temperature may determine the upper limit of distribution. This limit corresponds to the position of the metalimnion during the period of thermal stratification in the summer; below this depth water temperature remains low ($< 8^{\circ}$ C) and much less variable than in the epilimnion. Unfortunately, it is not yet possible to attach a species name to the *Drepanocladus* found in Crater Lake, as the moss has been collected in the vegetative stage only, without sporophytes. This means that comparisons with distributional records for other lentic systems are inconclusive. In any case, it appears that *Drepanocladus* can generate enough plant biomass in the upper hypolimnion to have an influence on the nutrient dynamics of Crater Lake. Moreover, samples obtained in August 1989 from depths below 100 m suggest that the moss beds produce a cascade of detrital materials that are slow to decompose as they are translocated to the cold, deep-water regions of the lake.

The deep-water benthic algae in Crater Lake include numerous species representing the divisions Chlorophyta (green algae), Chrysophyta (yellow-green algae and diatoms), and Cyanophyta (blue-green algae or cyanobacteria) which grow on rocks and as epiphytes on *Drepanocladus*. Prominent epiphytic green algae found in the 1989 samples included species of *Oedogonium, Bulbochaete, Zygnema, Spirogyra, Mougeotia, Rhizoclonium,* and *Cladophora.* Most of these genera also have been observed in shallow water areas in the vicinity of Wizard Island and at locations where spring water enters the lake. The yellow-green algae were represented by epiphytic species of *Vaucneria* and *Tribonema*, while diatoms were found growing on rock, sediment, and as epiphytes on the moss and filamentous algae. *Melosira undulata* was a deep-water diatom of particular interest, as it has not been observed in any other Oregon lake and exhibits an unusual mechanism for attachment to various substrates. Other abundant diatoms associated with *Drepanocladus* included stalked species of *Gomphonema* and *Cymbella*, and *Epithemia*, a heavily silicified member of the Bacillariales. Many diatom taxa also were found in samples scraped from rocks collected during the USGS dives (Dives 210, 212, and 214). Colonies of *Nostoc* were found with the moss samples and were the only conspicuous representatives of the cyanobacteria. *Nostoc* also was observed growing on rocks in the shallow water area around Wizard Island.

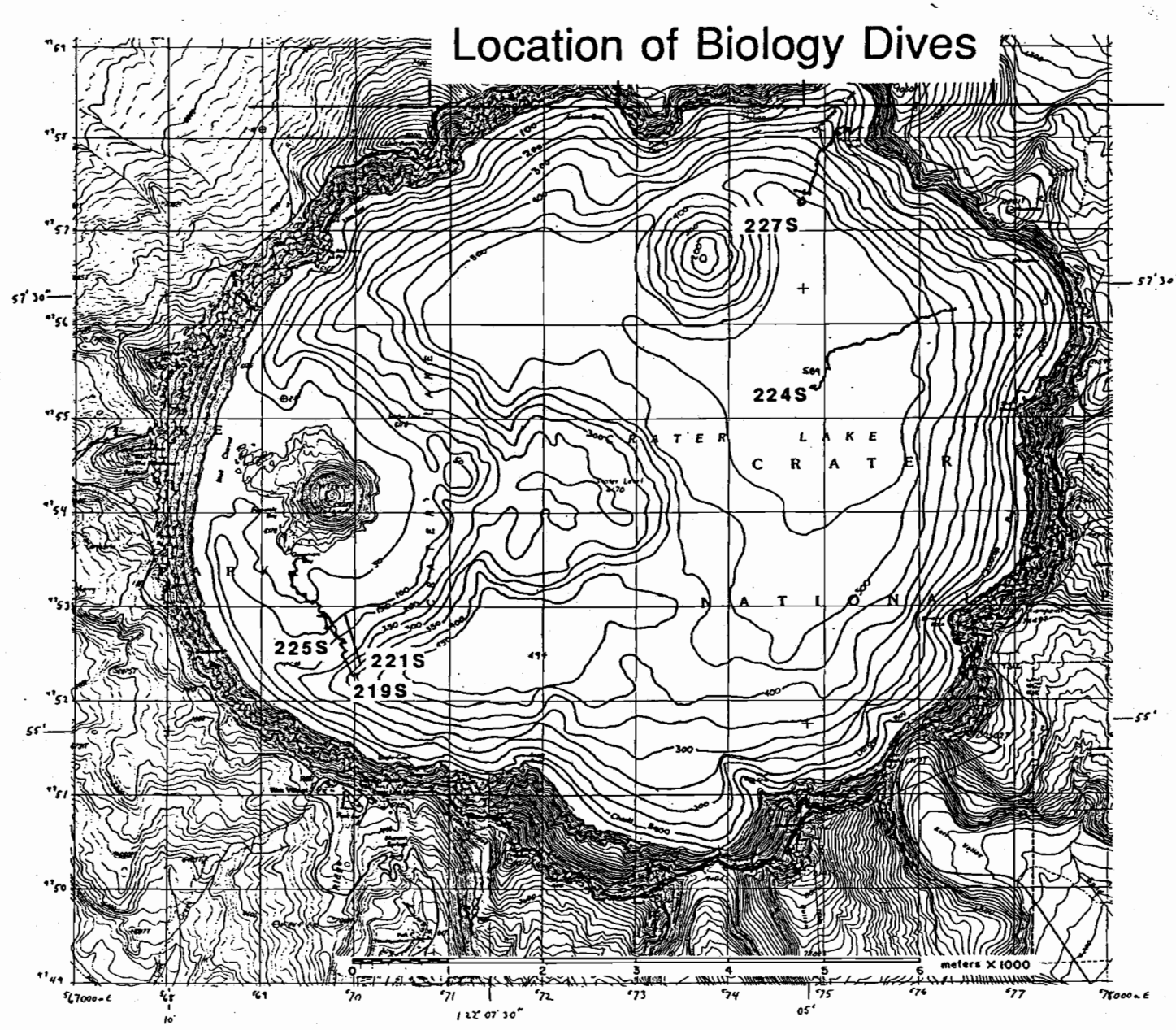

Figure 1. Dive tracks for biology dives (219, 221, 224, 225, and 227)

Appendix C. Geological Observations and Sampling

Charles R. Bacon
U.S. Geological Survey
Menlo Park, CA 94025

Nine dives with the submersible Deep Rover were dedicated to geologic studies. The major objectives of this program were to characterize the submerged caldera walls and postcaldera volcanic rocks. A secondary objective was to observe features related to sediment transport from the caldera walls to the deep basins of the lake.

Postcaldera volcanic rocks

The post caldera volcanics are those lavas and pyroclastic rocks that were erupted after collapse of Crater Lake caldera 6,845 +/- 50 yr B.P. All postcaldera volcanic activity in the Crater Lake area occurred within the caldera. Use of Deep Rover provided access to volcanic features on the lake floor. Postcaldera volcanic rocks previously were known only from limited video coverage obtained with an ROV, from a few dredge samples, and from the exposed part of Wizard Island. Observations made during four dives with Deep Rover in 1988 coupled with morphologic features of rock samples have allowed us to determine, with varying degrees of confidence, which postcaldera lava flows were emplaced beneath lake water and which were subaerial. This is important because it helps to constrain the relative ages of volcanic features, using filling of the lake as a timing device to supplement relative age information based on morphology and superposition of features (i.e., younger lava overlies older lava).

All postcaldera volcanic rocks, with the exception of the little rhyodacite dome east of Wizard Island, are andesites. These form the central platform (east of Wizard Island) and lava flows beneath it on the north and probably east sides (covered by sediment), Merriam Cone, and the Wizard Island edifice, only the tip of which projects above the lake surface. The oldest postcaldera andesite from which a sample was recovered is a flow north of the central platform. Domes or thick flows that form the central platform rest on this lava and were erupted before the lake filled to their level. Low ridges east-southeast of the central platform appear to be landslide material derived from the south caldera wall that was deflected eastward into the deep basin when the slide encountered the south side of the platform. Merriam Cone and the lava flows that form most of the surface of the submerged part of the Wizard Island volcano cooled under lake water, the Wizard Island lavas when the lake level was approximately 250' lower than at present. The rhyodacite dome east of Wizard Island is the youngest postcaldera volcanic feature on the basis of other work. The dome may have been emplaced when the lake surface was close to its present level.

Petrographic features of the volcanic rocks give information on the igneous processes responsible for the chemical compositions of the lavas. Thin sections were cut from about thirty postcaldera lava samples collected with Deep Rover. Samples from the central platform have relatively large (1-3 mm) plagioclase phenocrysts set in a glassy groundmass containing comparatively few small crystals, while lavas of Wizard Island and Merriam Cone have plagioclase phenocrysts generally less than 2 mm and abundant microphenocrysts in glassy groundmasses. Plagioclase, pyroxene, titanomagnetite, and olivine phenocrysts in nine representative samples were analyzed with the electron microprobe. Cores of plagioclase phenocrysts form three compositional populations that reflect different origins: (1) the majority of phenocrysts have anorthite contents of 50-60 mol % and probably crystallized from the andesitic liquids; (2) virtually all samples also contain phenocrysts with anorthite contents near 80 mol % that indicate a basaltic source; (3) most samples also contain more sodic plagioclase, around anothite 40 or less, that crystallized from silicic magma. The plagioclase data suggest that the andesites formed, at least in part, by mixing of basaltic and silicic magma, followed by precipitation of phenocrysts (population 1) from the hybrid liquid. Alternatively, the sodic and calcic plagioclase crystals are xenocrysts derived from cumulate crystal mush or subvolcanic pulutonic rocks that crystallized from both

basaltic and silicic magmas. Plagioclase of all groups tends to be zoned toward rims, anorthite 40-50 mol %, that apparently were in equilibrium with the groundmass glass as the lava cooled. Augite and orthopyroxene phenocrysts have compositions that suggest crystallization from andesitic and more silicic liquids. The more Fe-rich pyroxenes commonly are reversely zoned to relatively magnesian rims, as would be the case if crystals from silicic magma were introduced into andesitic liquid; normally zoned pyroxene phenocrysts probably grew in the andesitic liquid. Olivine phenocrysts are rare and appear to be xenocrysts from basaltic sources. Most titanomagnetite phenocrysts crystallized from, or at least equilibrated with, the hybrid andesitic magmas. In summary, the mineralogic data indicate that the postcaldera andesites do not represent liquid compositions related by crystal fractionation alone but also include material that crystallized from more mafic and more silicic magmas.

Fifteen postcaldera andesite whole-rock samples collected with deep rover were analyzed for major and trace elements by x-ray fluorescence, instrumental neutron activation, and inductively-coupled plasma techniques. Results of this work and earlier analysis of dredge and Wizard Island samples show that: (1) SiO_2 content ranges from 58.3 to 62.7 wt % among unaltered andesites; (2) central platform lavas have relatively high K/Na, Mg/Fe, and SiO_2; (3) Merriam Cone and the earliest Wizard Island lavas are more differentiated than later Wizard Island flows, and there is continuous variation between compositional extremes; (4) the morphology of the central platform, which suggests a group of coalescing domes, is consistent with the more SiO_2-rich compositions of its lavas that imply somewhat higher viscosities than for other postcaldera andesites.

Seven postcaldera andesite samples were analyzed for rare earth elements (REE) by isotope-dilution mass spectrometry in order to provide more precise data than obtained by neutron activation analysis. Six of the samples have very similar, negatively sloping chondrite-normalized REE patterns. Among these, three show no Eu anomaly, two have slight positive anomalies, and one has a small negative anomaly. As Eu is preferentially incorporated into plagioclase, the positive anomalies may be explained by contamination with xenocrysts, as suggested by the microprobe data. Negative Eu anomalies are traditionally interpreted as being due to plagioclase fractionation. The seventh sample, from the central platform, has a REE pattern parallel to the others but higher REE abundances and a distinct negative Eu anomaly. This is the most differentiated andesite sample on other chemical grounds, so it is not surprising that its REE pattern is suggestive of fractionation of an assemblage of REE-excluding (except Eu) phases dominated by plagioclase.

Volatile element concentrations in glassy lava would be expected to be abnormally high if eruption took place under the confining pressure of a deep body of water instead of at atmospheric pressure. Contents of H_2O, Cl, and F in subaerial and submerged Wizard Island andesites are similar, implying that the submerged lavas were erupted from the subaerial vent, degassed, and flowed into the lake. Two dredge samples from Merriam Cone (minimum depth about 180 m) have volatile-element contents like the Wizard Island andesites; as Merriam Cone andesites have morphologies that suggest cooling under water, we tentatively suggest that the lake was shallower when Merriam Cone formed.

In addition to the postcaldera andesite lava samples, a number of xenoliths in Wizard Island subaerial lavas were collected. The xenoliths are fragments of cumulates from andesitic magma and partially-fused basaltic hornfels. Minerals in representative xenoliths have been analyzed with the electron microprobe. One lava sample collected with Deep Rover contains partially-fused granodiorite similar to blocks ejected in the climactic eruption. These materials may be important components in the genesis of the postcaldera magmas. The next phase of the postcaldera lava study will be to model the lava compositions using the complete set of mineral and whole-rock compositional data.

Submerged caldera walls

The submerged caldera walls were studied and sampled during five dives in 1989 and at the beginning of one of the 1988 dives. The dives traversed from the lake bottom up the wall at five

points off Llao Rock, Palisade Point, Skell Head, Sentinel Rock, and Eagle Point. These localities were chosen in order to obtain the widest possible geographic coverage and to maximize opportunities to sample outcrops. The nature of this work is different from the postcaldera lava study in that outcrops on the deep caldera walls represent many different times in the history of Mount Mazama and consist of volcanic rocks from several eruptive centers. The following results are preliminary and are based on examination of thin sections and chemical analyses of approximately thirty-five samples.

The dive off Llao Rock yielded ten lava samples from outcrops between depths of 1064' and 193'. The four deepest samples (1064', 895', 639', 568') are compositionally similar silicic andesites that contain chlorite or clay alteration minerals in their groundmasses. These lavas may correlate with flows near lake level on the southwest side of the caldera. Between 500' and 300' we recovered relatively fresh andesites and one dacite (445'). The shallowest sample (193') is low-silica andesite that has clay alteration and probably belongs to the same set of flows as those exposed at the shore.

Eight samples were collected between 1530' and 318' below Palisade Point. None of these rocks has been significantly affected by hydrothermal alteration. The sample from the greatest depth is an andesite block from a large outcrop of probable flow-top breccia. Glassy rhyodacite was collected at 1495'. It is possible that this remarkably fresh sample is related to pre-Mazama rhyodacites to the east. However, there remains some question as to whether either this or the underlying andesite outcrops may be landslide blocks. The remaining six samples were collected at 1020' and above. These are andesite, silicic andesite, and dacite.

The dive opposite Skell Head netted one sample of vesicular andesite from 700'. Of greater interest were spires of siliceous sinter observed between about 1800' and 1500'. These are described elsewhere in the report.

Ten samples were collected below Sentinel Rock between 975' and 62'. Samples collected from between 975' and 528' are rather similar silicic andesites with clay alteration. One sample from this interval (955'), however, is distinctive, altered hornblende dacite that resembles rocks significantly older than Mount Mazama. The four shallowest samples are notably less altered than the deeper ones. They are dacite and silicic andesite collected from 386' and above. Most of the samples from this dive probably can be correlated with rocks above lake level to the southwest, below Dutton Cliff, and were erupted early in the history of Mount Mazama.

A total of seven samples were obtained between 1445' and 1290' during two dives near Eagle Point. These are the most altered rocks collected. All appear to have andesitic compositions. Some of the samples may be lava flow materials and some may be intrusive rocks. Epidote, chlorite, calcite, and quartz are alteration or secondary phases present in varying amounts. Hydrothermal alteration of these samples occurred before collapse of the caldera but the age of this alteration is unknown. The presence of epidote indicates alteration at temperatures above 200 °C. These apparently are Mazama lavas that are older than those of the exposed caldera wall, although we cannot say with certainty that the approximately 400'-high steeply-sloping pile of lava flows from which the samples were collected is not a large landslide block.

Continuing studies

Video coverage of the dives made in 1989 is yet to be thoroughly analyzed. Hence, we do not report here on observations related to sediment transport or possible geologic relationships between bedrock outcrops in the caldera walls. Attempts will be made to date by the K-Ar method selected, relatively fresh samples from the submerged caldera walls. In the future, we intend to publish the results of the postcaldera lava study in a scientific journal and to incorporate the information on the geology of the submerged caldera walls in other publications on Mount Mazama.

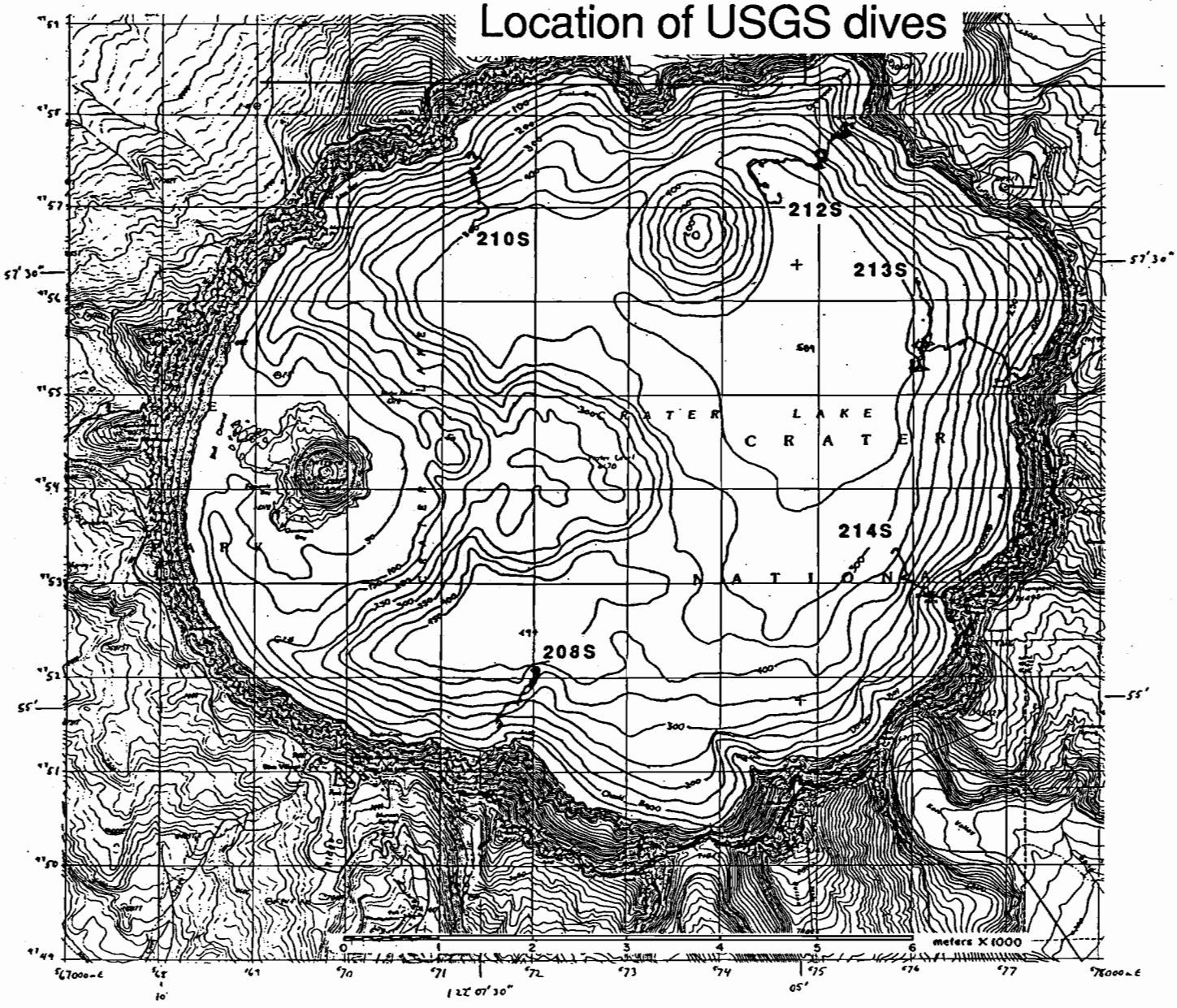

Figure 1. 1989 dive tracks for USGS dives (CD208, CD210, CD212, CD213, CD214)

Appendix D. Geological Observations and Sampling

C. Hans Nelson and John H. Barber, Jr.
Branch of Pacific Marine Geology
U.S. Geological Survey
Menlo Park, CA 94025

The Ring Fracture Zone and its Association with Continuing Geologic Activity

Bacon (1983) suggests that multiple vents formed along a ring fracture as the caldera collapsed. Observation of a number of geologic features led to the hypothesis by Nelson et al. (1988) that the expression of a ring fracture zone associated with the caldera collapse was evident in the acoustic basement as defined by continuous seismic reflection profiling. In the seismic profiles, this zone at the base of the caldera wall slopes is characterized by a ring of closed depressions in the acoustic basement surface, which are thought to be phreatic explosion craters, and by maximum thicknesses of subaerial and lake sediment. The main post-caldera vents of Merriam Cone and Wizard Island also lie along this ring fracture zone. The zones of warmer water from apparent lake-floor hydrothermal vents originally defined by Williams and Von Herzen (1983) also occur in the proposed ring fracture zone.

Examination of seismic records (Barber and Nelson, 1990), bottom samples, and *Deep Rover* observations suggests that deposits of the largest observed landslide off the caldera wall underlie the main vent site in the south basin of the lake floor. This extensive caldera wall failure consists of thick deposits of very coarse debris that cover the ring fracture zone. These deposits are likely to be relatively permeable, which may help explain the presence of the most extensive continuing hydrothermal activity in the southern ring fracture area. Elsewhere, hydrothermal plumes may be inhibited from reaching the lake floor by the thick lake sediment deposits that typically cover the ring fracture zone.

Further study of diving observations will permit more detailed mapping of sediment cover over the ring fracture area. This in turn may provide more evidence for defining the association of the ring fracture zone, sediment cover, and presence of thermal springs.

Appendix E

Bacterial Studies of Materials Collected at Crater Lake Vent Locations

Status Report, September 1990

David Karl, University of Hawaii

Introduction

My involvement in the 1989 Crater Lake hydrothermal processes study was by invitation of Drs. Jack Dymond and Robert Collier. Although I was unable to participate in the field expedition due to a previous commitment, I did provide the co-P.I.s with a list of basic research objectives and sampling instructions. In September 1989, I received the following samples: (1) live and preserved bacterial mats collected from a variety of sites for direct microscopy and pure culture isolation, (2) unpreserved, frozen bacterial mats for chemical, isotopic and enzymatic (carboxylase) determinations and (3) frozen porewaters for measurement of DOC, DON, DOP and specific organic constituents (amino acids and nucleic acids). No formal funding was provided, and none has been solicited since receiving the samples. Consequently, my progress towards the completion of sample analysis has been uncharacteristically (for me, at least) slow. Below I summarize our progress to date and prospectus for future work.

I. Pure Culture Isolations

Results from the 1988 submersible expedition revealed the presence of large concentrations of what the authors tentatively identified as iron-oxidizing bacteria of the genera, Gallionella and Leptothrix (Dymond et al. 1989, Nature 342: 673-675). These bacterial mats appear to be similar to the iron-oxidizing bacteria recently discovered at Loihi Seamount, a deep-sea, hot-spot volcano near Hawaii (Karl et al. 1988, Nature 335: 532-535). We attempted to isolate pure cultures of these putative iron-oxidizing bacteria using enrichment culture procedures. Media were prepared for the following "target" organisms: Leptothrix discophera, Gallionella sp., Sphaerotilus natans, Thiobacillus ferroxidans, T. intermedius and T. thioxidans. Of these, Gallionella, T. ferroxidans and T. thioxidans were "obligate autotroph" enrichments. Each medium type was prepared with a bottom plug of either ferrous iron (as ferrous ammonium sulfate), ferrous iron plus sulfide (as ferrous sulfide) or sulfide (as sodium sulfide) in 1.5-2% agar as the lithotrophic energy source, with a 0.2% soft agar plus medium overlay. A redox gradient was allowed to establish before primary inoculation was made throughout each tube. Eleven separate samples from a variety of sites were used for these enrichment studies. Positive enrichments were common. All samples tested were positive on Sphaerotilus medium; all but one (CD215) were positive on Leptothrix medium; all but one were positive on Gallionella medium (CD223); and all but two on T. intermedius medium (CD228, CD230). There was no growth on T. ferroxidans medium and no consistent growth on T. thioxidans medium. At present these cultures have survived several transfers without loss of viability. To date we have not had an opportunity to further characterize any of the isolates.

II. Enzyme Assays

A primary objective of our involvement in the Crater Lake project was to examine the bacterial mat assemblage for evidence of chemolithotrophic activity. This was to have been done in two ways: by C isotopic analysis of the organic matter and by measurement of RuBPCase (ribulose 1,5-bisphosphate carboxylase- oxygenase) enzyme activity.

RuBPCase is found in all photosynthetic and chemolithoautotrophic organisms where it catalyzes a dual reaction: (1) carboxylation of ribulose-1,5-bisphosphate to yield two molecules of glycerate 3-phosphate and (2) oxygenation of ribulose-1,5-bisphosphate to form phosphoglycolate and

glycerate 3-phosphate. Previous studies of deep-sea hydrothermal vent ecosystems have revealed the presence of RuBPCase thus providing supportive evidence for chemolithoautotrophic bacterial production (Tuttle 1985, Biol. Soc. Wash. Bull 6: 335-343).

Ms. Lara Asato, an undergraduate student in my laboratory, spent approximately 6 mo. of hard work refining these enzymatic methods for use in our laboratory. In particular, we were concerned with improving the detection limit of the existing methods for application to the Crater Lake samples. Before leaving Hawaii to start a graduate career at U.S.C. Lara made a preliminary analysis of the bacterial mat samples. RuBPCase was undetectable by our procedures. Addition of commercially available RuBPCase to subsamples of the mat had little effect on activity (relative to controls) so we conclude that the samples do not have any specific inhibitors which might otherwise complicate these quantitative assays. Although one interpretation is simply that RuBPCase and therefore, chemolithoautotrophic bacteria are not present in the Crater Lake samples, we feel that conclusion is premature. The main reason for our caution is that we were also unable to detect the heterotrophic carboxylating enzyme phosphoenolpyruvate carboxylase (PEPCase) in these samples which implies that we are simply below the detection limit for these measurements. From our previous work at Loihi Seamount we know that the majority of the iron-oxidizing bacterial mat is non-living and that the organic carbon content is low (1-3% by weight). Consequently we need to either improve the sensitivity of the carboxylase assay systems, find some method of separating and concentrating intact cells from the bacterial mats or try a different type of detection system. Regarding the latter, we are currently investigating the possible use of gene probes and polymerase chain reaction (PCR) technology as a mechanism for the sensitive detection of these specific enzymes.

III. Dissolved Substrate Analyses

The measurement of dissolved organic substrates in aquatic environments has recently become very controversial, again (Williams and Druffel 1988, The Oceanography Magazine 1: 14-17). We currently have the capability of measuring total dissolved organic nitrogen (DON) in small sample volumes using a commercially available, high temperature combustion instrument (Antek Instrument Co., Model #703C; Walsh 1989, Marine Chemistry 26: 295-311). We also have on order a commercially available, high-temperature dissolved organic carbon (DOC) analyzer (Ionics Model #555). In order to provide the most up-to-date methods possible, we are awaiting the arrival and complete set-up of these instruments before committing the Crater Lake porewater samples to analysis.

Appendix F. Fluid Circulation and Diagenesis in the Basement of Crater Lake, Oregon: Pore water Constraints

C. Geoffrey Wheat
SOEST, 1000 Pope Road
University of Hawaii
Honolulu, Hawaii, 96822

1. INTRODUCTION

Crater Lake is located in the caldera of Mt. Mazama, an andesidic volcano in the southern section of the Cascade mountain range of Oregon (Fig. 1). The caldera was produced by a cataclysmic eruption roughly 6850 y b.p. (Bacon, 1983), and is completely enclosed by steep walls that rise several thousand feet above the caldera floor. Crater Lake formed shortly after the formation of the caldera from inputs of meteoritic waters. Volcanic activity in the caldera continued for several thousand years after formation of the lake with the last eruption happening 4000 y b.p. (Bacon and Lanphere, 1990). Based on the geologic structure in which Crater Lake resides, it would not be surprising to find active hydrothermal venting through the lake floor.

Several studies of Crater Lake, Oregon, support the hypotheses that hydrothermal fluids issue from the lake floor. Inputs of hydrothermal fluids to Crater Lake were first postulated by Van Denburgh (1968) after discovering high concentrations of chloride and sulfate relative to concentrations measured in neighboring lakes. Since this discovery, chemical gradients have been measured in the water column that support the presence of hydrothermal inputs (Simpson, 1970a and 1970b; Dymond et al., 1989; Dymond and Collier, 1990; Collier et al., 1990a and 1990b; McManus et al., 1990). Further support for hydrothermal inputs to the lake are based on mass balance calculations of dissolved ions. These calculations are constrained by the hydrologic budget and require subsurface inputs of dissolved ions, presumably from subsurface hydrothermal springs (Nathenson, 1990; Reilly, 1989).

Physical measurements taken in Crater Lake also support the presence of hydrothermal inputs. Numerous temperature profiles have been measured in the upper 2.5 m of the sediment column (Williams and Von Herzen, 1983) and in the water column (Appendix A). All of the measured profiles in the sediment column were linear with an average conductive heat flow of 0.14 W/m^2; however, some heat flow values are as high as 5 W/m^2 (Williams and Von Herzen, 1983). These data suggest that fluid flow into the lake is either confined to zones of focused upflow, which were not sampled, or fluid flow is less than 1.3 m/y for profiles measured with a 2.5 m probe or less than 6.3 m/y for profiles measured with a 0.5 m probe (Bredehoeft and Papadopulos, 1965). Further support for hydrothermal inputs is from calculations of excess heat and salt in the water column (Appendix A).

The first direct evidence of hydrothermal flow through the sediments of Crater Lake based on systematic variations in pore water chemical and thermal properties is presented. These data were collected from a surface vessel and from a one-person submersible *Deep Rover*. By fitting these data to models that account for time dependant, advective, diffusive, and reactive processes (Wheat, 1990; Wheat and McDuff, submitted A), we estimate where and how fast fluids are flowing through the sediments. Other models based on systematic variations in the chemical composition of pore fluids allow us to constrain the general pattern of fluid circulation through basement, the composition of the fluid in basement, and the flux of ions and fluid from basement to the deep lake.

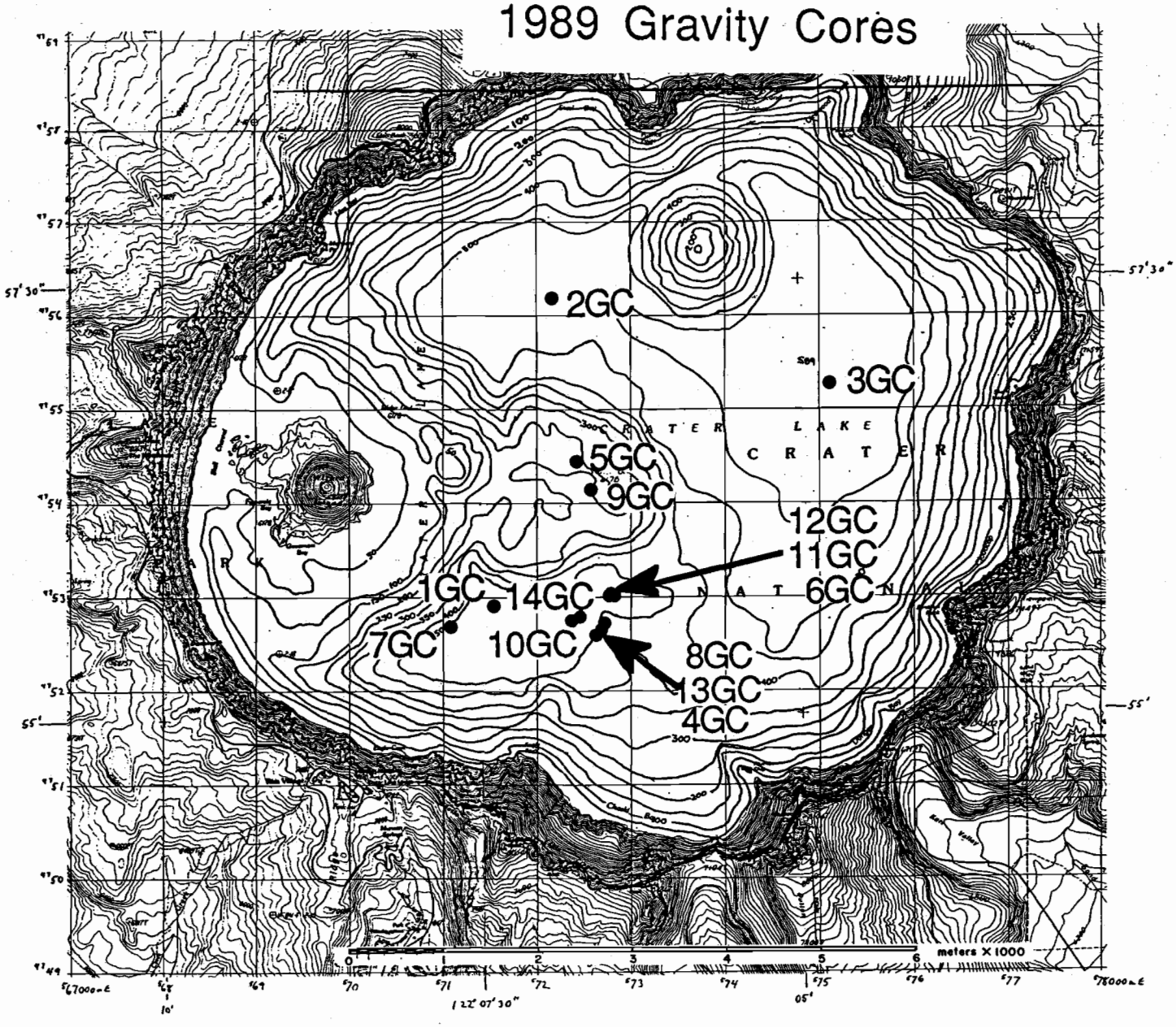

Fig. 1: Location of gravity cores taken from Crater Lake, Oregon, plotted with respect to bathymetry.

2. GEOLOGIC SETTING AND METHODS

The composition and accumulation of sediments in Crater Lake are controlled by the lake's geologic setting. Crater Lake represents about 78% of its own drainage area (Phillips, 1968). The remaining drainage area consists of the steep caldera walls, which limit sedimentary inputs to the lake. Sediments in Crater Lake are comprised of aluminosilicate debris from the caldera wall, biogenic debris from the euphotic zone, and iron-manganese rich precipitates from inputs of hydrothermal fluids at the lake bottom (Dymond and Collier, 1990). Net sediment accumulations in the lake differ from tens of centimeters on the slopes of the caldera walls to several meters on Wizard Platform to about 100 meters in basement depressions (Barber and Nelson, 1990).

The aluminosilicate debris is derived from the caldera wall and has an average aluminum content of 8.9% ±0.5% and an iron content of about 3.5% (Dymond and Collier, 1990). These measurements are consistent with the concentration of aluminum in the rhyodacite that was ejected during the climatic eruption (8.1%, McBirney, 1968). In contrast to the alimnosilicate debris, biogenic debris contains no measurable iron or aluminum, and appears to be largely comprised of biogenic opal (Dymond and Collier, 1990).

Iron-manganese rich crusts are enriched in iron, manganese, phosphorus, and barium and are depleted in aluminum, silica, potassium, and calcium compared with weathered material from the caldera wall (Dymond and Collier, 1990). These crusts contain about 35% iron and less than 1% aluminum and are found in three settings: (1) pavements of multicolored (ochre to dark brown) crusts that cover ten to hundreds of m^2; (2) fields of pebbles that also cover tens to hundreds of m^2; and (3) multiple ochre-colored layers that are visible in areas of sediment slumping (Dymond and Collier, 1990). These crusts are located in areas with high heat flow and are associated with bacterial mats and saline pools (Fig. 2). Bacterial mats are 2 to 20 m in length and several meters across and are mostly comprised of iron oxidizing sheath-forming bacteria of the genera, Gallionella and Leptothrix (Dymond et al., 1989). Most pools have salinities and temperatures that are greater than that measured in the surrounding bottom water and located in areas with little or no basement relief (Fig. 2). A more detailed physical, chemical, and thermal description of the mats and pools are found within the body of the report.

Sediments, crusts, bacterial mats, and pools were sampled with a gravity corer, a box corer, and peepers. These sampling devices provided a means to obtain pore fluids, which were analyzed for their chemical composition. Temperature profiles in the sediments were measured with two probes.

Fourteen gravity cores were retrieved from Crater Lake in 1989 (Fig. 1). Gravity coring provided the means to recover the longest section of the sediment column, 0.5 to 1.5 m in length, and targeted general areas of interest. Gravity cores were kept cold and split, described, and sampled for pore water analysis within twelve hours. Sediment samples for pore water analysis were centrifuged in a van held at 3-5°C and the supernatant was filtered through 0.45 micron filters.

A Soutar box corer was deployed from the submersible *Deep Rover* to retrieve sediments close to or in specific geologic features (Fig. 2). Five box cores were retrieved with core lengths ranging from 0.06 to 0.2 m. Box cores were sampled by whole core squeezing (Bender et al., 1987) immediately upon retrieval, and discrete samples were taken at the base of the cores. These discrete samples were kept cold until they could be centrifuged and filtered, within 3-15 hours after the cores were retrieved.

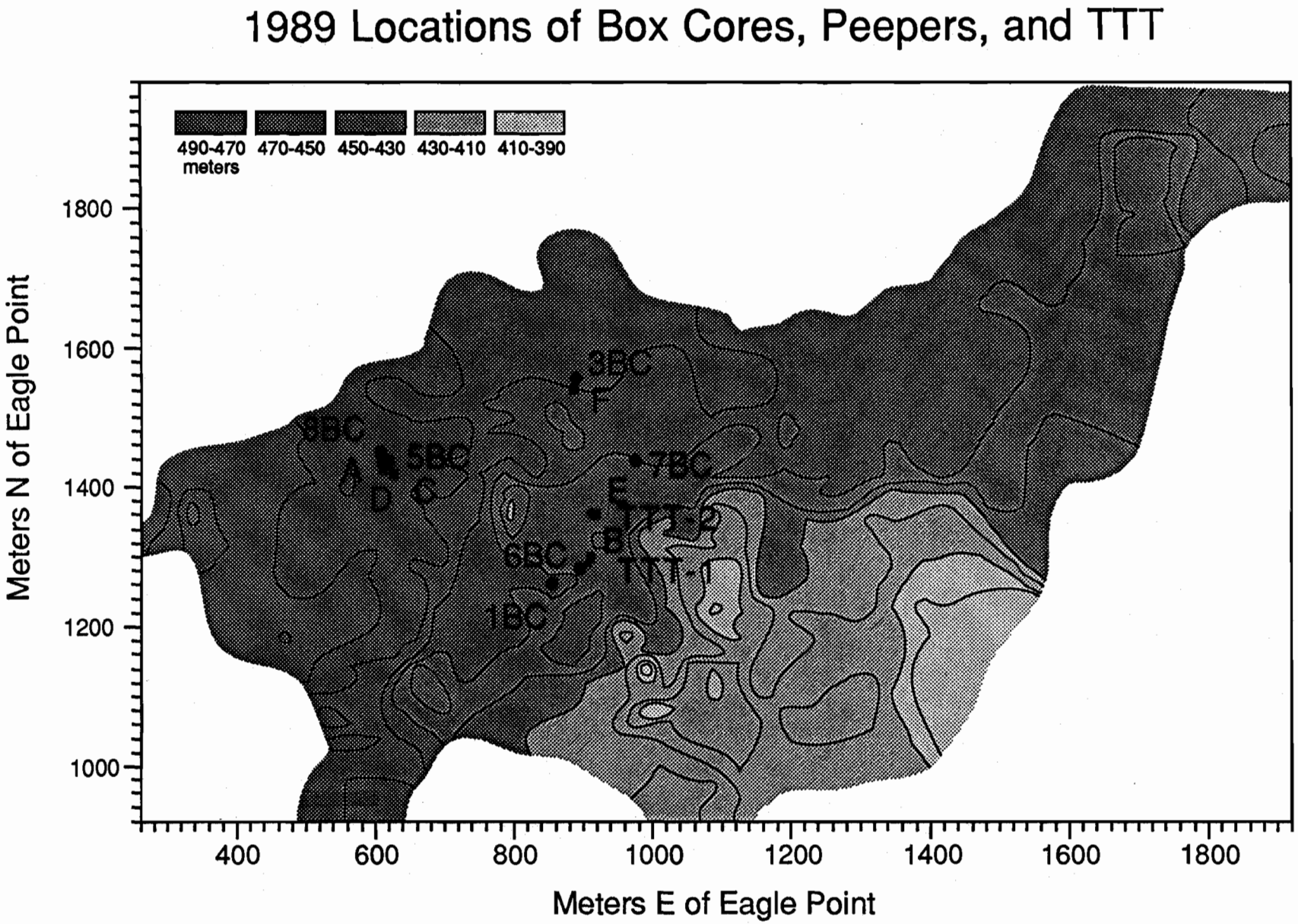

Fig. 2: Location of box cores, peepers, TTT, and bacterial mats in the south basin of Crater Lake plotted with respect to bathymetry.

Fluids extracted from gravity and box cores were divided into four aliquots. One aliquot was stored in polystyrene test tubes for analysis of nutrients, pH and total CO_2 within several days after the cores were retrieved. Chloride, sulfate and the stable isotopes of oxygen were analyzed on an aliquot sealed in a glass ampule. A 4-6 ml aliquot was spiked with 10 µL of redistilled 1N hydrochloric acid and stored in an acid washed polyethylene bottle. This aliquot was used for determining the concentrations of several metals. The remaining fluid was frozen for later determination of dissolved organic carbon (DOC).

Peepers were made of polycarbonate and were deployed by the submersible in specific features. Peepers provide a means to obtain pore fluids that are not chemically altered by sampling procedures. Cavities 1 cm in length were milled every two centimeters down the length of the sampler. These cavities held about 4.5 ml of fluid and two cavities were milled at each sample depth. Cavities were filled with deoxygenated distilled water and covered by a 0.45 micron dialysis membrane. Peepers were stored in deoxygenated distilled water until they were deployed by the submersible. A plastic T-handle was added to the peeper to aid in deployment and the bottom edge of the peeper was bevelled to cause minimal disturbance of the sediments. Four peepers with twenty cavities and one peeper with thirty-six cavities were deployed by the submersible for about one week (Fig. 2), allowing the fluid in the cavities to equilibrate with adjacent pore fluids via diffusion. Aliquots of pore fluids from the peepers were taken upon retrieval and stored in vacutainers. One aliquot was analyzed for nutrients, pH and total CO_2. The other aliquot was spiked with 10 µL of redistilled 1N hydrochloric acid and analyzed for several metals.

Chemical compositions of pore waters from representative cores are reported in Tables 1 and 2. Dissolved silica was measured using a standard colorimetric technique with a precision of about 2% (1s) (Parsons et al., 1984). Concentrations of chloride were determined by ion chromatography with a precision of <2% (1s) and oxygen isotopic compositions were determined by mass spectrometry with a precision of 0.1 per mil (1s). Atomic absorption spectrometry techniques were used to measure the concentration of sodium, calcium, magnesium, potassium, and lithium with precisions better than 5% and typically less than 2% (1s). Sampling artifacts increased the concentration of sodium by 0.3 mM in samples stored in vacutainers. Centrifuging the sediments for pore water adds 0.02 mM potassium to pore fluids. These sampling artifacts are inferred from offsets in property-property relationships of pore fluids collected by different techniques.

Two temperature probes were used, each requiring the submersible for deployment. One probe is 60 cm in length with thermistors mounted at 20, 40 and 60 cm along the probe. The resolution of each thermistor is 0.01°C with an accuracy of ±0.2°C which was calibrated against known resistance values periodically throughout the sampling program. This probe was connected to an Omega Model 5830 Thermistor Thermometer in the submersible. Temperature measurements were recorded on a video record of the operation, which allowed us to determine the depth of penetration. Forty-eight temperature profiles were recorded in discrete features (Table 3); however, twenty-eight of these measurements were made with only one thermistor inserted into a particular feature. Impenetrable crusts or underlying rocks prevented complete penetration of the probe.

The other temperature probe is a Sea-Bird Electronics SeaCat SBE 19 Profiler (TTT) with three thermistors epoxy-potted inside a 24-inch long, 0.25-inch diameter stainless steel tube. When fully inserted into the sediment, thermistor depths are 35 and 5 cm below the sediment-water interface and 5 cm above the sediment-water interface. The SeaCat profiler recorded temperature profiles two times a second with a resolution of 0.001°C and an accuracy of ±0.01°C over a

Table 1: Chemical composition of pore waters from box cores. Fluids were obtained by whole core squeezing and by centrifugation of one cm sections[1]. Negative depths are the distance above the sediment-water interface.

	Depth cm	Cl^- mM	Na^+ mM	Mg^{2+} mM	Ca^{2+} mM	K^+ mM	Li^+ mM	SiO_2 uM
BC 1								
	-3.91		0.520	0.122	0.176	0.051	0.0077	320
	-2.77							319
	-1.63		0.514	0.119	0.171	0.051	0.0074	323
	-1.33							334
	-1.06							310
	-0.93		0.529	0.120	0.170	0.051	0.0078	
	-0.52							336
	-0.39		0.503	0.130	0.128	0.051	0.0080	
	-0.27							336
	-0.14		0.574	0.173	0.125	0.060	0.0089	
	0.00							399
	0.49		0.818	0.324	0.125	0.083	0.0134	
	0.67							482
	0.98							483
	1.30							515
	1.46		0.911	0.386	0.161	0.091	0.0146	
	1.62							515
	1.78		0.912	0.395	0.139	0.094	0.0150	
	1.93							524
	2.09		0.918	0.393	0.128	0.097	0.0147	
	2.65							524
	2.85		0.947	0.412	0.429	0.103	0.0151	
	3.04							525
	3.44							543
	3.63		0.991	0.431	0.438	0.108	0.0156	
	4.22							575
	4.42		1.03	0.459	0.465	0.119	0.0164	
	5.21		1.10	0.506	0.507	0.129	0.0175	
	5.80							667
	6.03		1.16	0.555	0.581	0.137	0.0183	
	6.52					0.111		
	7.01		1.23	0.599	0.626	0.144	0.0197	
	12.5[1]		1.43	0.485	0.450	0.116	0.0234	587
	13.5[1]	0.840	1.50	0.487	0.439	0.119	0.0246	581
	14.5[1]		1.57	0.511	0.463	0.121	0.0260	572
	15.5[1]	0.910	1.63	0.517	0.449	0.120	0.0293	564
	16.5[1]		1.64	0.470	0.417	0.131	0.0270	564
	17.5[1]	0.900	1.57	0.458	0.397	0.129	0.0266	610
BC 3								
	0.08		1.01	0.373	0.323	0.100	0.0139	
	0.26							468
	0.45		1.09	0.467	0.345	0.108	0.0155	
	0.62							475
	0.78		1.13	0.493	0.469	0.111	0.0160	
	0.95							519
	1.13		1.14	0.501	0.475	0.112	0.0161	
	1.29							485
	1.46					0.116	0.0163	
	1.65							480
	1.86		1.16	0.494	0.471	0.119		
	2.11							496
	2.48		1.12	0.474	0.457	0.123		
	3.02							470
BC 5[3]								
	BC 5-1							240
	BC 5-2		1.67	0.691	0.523	0.142	0.0055	
	BC 5-3							344
	BC 5-4		1.69	0.688	0.524	0.137	0.0198	243
	BC 5-5					0.139	0.0200	299
	BC 5-6		1.68	0.680	0.522	0.137	0.0202	
	BC 5-7							252
	BC 5-8		1.68	0.689	0.522	0.138	0.0199	
	BC 5-9							279
	BC 5-10		1.65	0.691	0.515	0.137	0.0200	
	BC 5-11							249
	BC 5-12							191
	BC 5-13							221
	BC 5-14		1.67	0.684	0.514	0.137	0.0207	
	BC 5-15							219
	BC 5-17							298
	BC 5-18		1.83	0.729	0.564	0.184	0.0224	313

	1 BC 5	1.28	2.57	1.161	0.911	0.234	0.0339	753
	2 BC 5	1.52						537
	3 BC 5	1.54	2.78	1.156	0.903	0.246	0.0352	751
	4 BC 5	1.37						808
	5 BC 5		2.47	1.090	0.848	0.215	0.0318	768
	6 BC 5	1.32						810
	7 BC 5	1.35	2.50	1.035	0.799	0.254	0.0300	646
	8 BC 5	1.63	2.91	1.424	1.045	0.241	0.0370	799
BC 6								
	-8.27							336
	-8.02	0.356	0.509	0.130	0.201	0.058	0.0075	
	-7.77							336
	-6.81							339
	-5.73		0.508	0.136	0.206	0.058	0.0073	
	-4.72							337
	-2.50							341
	-1.48		0.505	0.136	0.207	0.060	0.0077	
	-0.79							343
	-0.45		0.520	0.135	0.212	0.059	0.0081	
	-0.24							348
	0.00	0.355	0.530	0.143	0.211	0.062	0.0090	
	0.24							387
	0.47		0.658	0.198	0.259	0.080	0.0106	
	0.73							496
	1.00		0.751	0.221	0.291	0.087	0.0131	
	1.28							505
	1.79							534
	2.04		0.791	0.242		0.093	0.0139	
	2.30							550
	2.55		0.815	0.244	0.313	0.097	0.0148	
	2.83							570
	3.10	0.542	0.811	0.257	0.314	0.102		
	3.34							578
	3.58		0.830	0.254	0.321			
	3.81							593
	4.07					0.102	0.0152	
	4.32							591
	4.58		0.842	0.258	0.325			
	4.83							604
	5.66		0.848	0.261	0.327	0.109	0.0150	621
	8[1]		0.730	0.110	0.167	0.092	0.0122	632
	9[1]		0.729	0.126	0.179	0.098	0.0119	591
	10[1]		0.774	0.115	0.164	0.103	0.0132	571
	11[1]	0.571	0.856	0.173	0.233	0.112	0.0135	597
	12[1]		0.874	0.173	0.245	0.123	0.0141	589
BC 7								
	-1.12							306
	-0.96		0.438	0.106	0.162	0.046	0.0073	
	-0.8	0.286						306
	-0.64							307
	-0.48		0.442	0.110	0.159	0.051	0.0072	
	-0.32							314
	-0.16	0.277						310
	0		0.442	0.113	0.162	0.050	0.0071	
	0.16							391
	0.29		0.520		0.170	0.065	0.0085	
	0.67							496
	0.86		0.553	0.126	0.186	0.071	0.0094	
	1.05	0.364						515
	1.54					0.074	0.0099	539
	1.82		0.595	0.139	0.200	0.075	0.0100	
	2.11	0.348						541
	2.39					0.078	0.0108	
	2.66							561
	2.98		0.621	0.148	0.207	0.079	0.0108	
	3.33							568
	3.76		0.630	0.152	0.212	0.080	0.0106	
	4.23	0.353						581
	6[1]	0.364	0.612	0.122	0.159			606
	7[1]		0.686	0.149	0.192	0.098	0.0117	598
	8[1]	0.387	0.739	0.173	0.210	0.105	0.0128	600
	9[1]		0.759	0.163	0.201	0.105	0.0128	595
	10[1]	0.468	0.898	0.216	0.262	0.121	0.0158	591
BC 8								
	-1.8		0.514	0.148	0.196	0.068	0.0081	
	-1.6					0.066	0.0080	320
	-1.4	0.325						324
	-1.2		0.545	0.166	0.209	0.067	0.0084	
	-1	0.457						346
	-0.8		0.597	0.205	0.233	0.072	0.0095	
	-0.6	0.393						356
	-0.4							373

	-0.2		0.689	0.259	0.271	0.074	0.0103	
	0.00							380
	0.19		0.720	0.269		0.076		
	0.38	0.550						431
	0.57		1.18	0.639	0.492	0.122	0.0176	
	0.76	0.747						607
	0.95		1.53	0.909	0.639	0.123	0.0232	
	1.11							652
	1.27		1.62	0.992	0.690	0.130	0.0240	
	1.46	0.890						667
	1.90							678
	2.09		1.67	1.043	0.722	0.137	0.0248	
	2.28							685
	2.51					0.140	0.0256	
	2.73	0.910						700
	2.92		1.80	1.227	0.812	0.145	0.0270	
	3.14	0.950						711
	3.55	0.787				0.154	0.0284	733
	3.74		1.99	1.301	0.934	0.156	0.0283	
	3.93							736
	4.12		2.01	1.433	0.978	0.159	0.0294	
	4.31							756
	4.70							754
	4.89		2.07	1.522	1.033	0.171	0.0303	
	5.04							781
	5.39							782
	5.77	1.14						799
	6.00		2.22	1.545		0.179	0.0324	
	9[1]	1.06	2.30	1.092	0.835	0.174	0.0311	814
	10[1]		2.31	1.083	0.817	0.179	0.0334	882
	11[1]	1.13						822
	12[1]		2.39	1.035	0.764	0.194	0.0348	894
	13[1]	1.20	2.37	1.029	0.782	0.186	0.0340	893
	14[1]							862
	15[1]	1.17	2.51	1.029	0.786	0.207	0.0359	865
	16[1]		2.63	1.049	0.795	0.211	0.0375	903
BC 10[4]								
	BC 10-1		0.456	0.107	0.173	0.054	0.0070	322
	BC 10-2		0.461	0.107	0.176	0.053	0.0071	324
	BC 10-4		0.458	0.109	0.176	0.053	0.0068	322
	BC 10-6		0.464	0.113	0.180	0.053	0.0068	322
	BC 10-7			0.107	0.174	0.053	0.0068	327
	BC 10-8							395
	BC 10-9		0.585	0.090	0.138	0.078	0.0098	374
	BC 10-10	0.412	0.614	0.097	0.144	0.081	0.0107	349
	BC 10-11		0.603	0.102	0.147	0.077	0.0098	348
BC 11[5]								
	BC 11-1		1.41	0.576	0.215	0.074	0.0106	398
	BC 11-2		1.40	0.579	0.214	0.076	0.0104	
	BC 11-3							385
	BC 11-4		1.36	0.563	0.206	0.073	0.0100	
	BC 11-6		4.14	2.554			0.0256	

[3] We sampled a pool with BC 5, which produced a soupy black sediment that lacked any definition of depth from the sediment-water interface.

[4] Problem with box corer that did not allow us to define sample depths.

[5] Same as BC 5.

Table 2: Chemical composition of pore waters from peepers. Cavities extend for 1 cm and are spaced every 2 cm downcore.

	Cavity number	Cl^- mM	Na^+ mM	Mg^{2+} mM	Ca^{2+} mM	K^+ mM	Li mM	SiO_2 uM
PA								
	1		1.86	0.743	0.608	0.133	0.0225	656
	2		2.07	0.772	0.637	0.144	0.0241	812
	3		2.08	0.846	0.654	0.150	0.0257	958
	4		2.10	0.828	0.657	0.149	0.0251	935
	5		2.13	0.832	0.670	0.146	0.0253	943
	6		2.16	0.795	0.664	0.148	0.0244	947
	7		2.06	0.799	0.659	0.154	0.0248	939
	8		1.99	0.712	0.618	0.144	0.0232	939
	9		2.14	0.827	0.697	0.145	0.0252	859
	10		2.06	0.816	0.687	0.145	0.0247	1014
PB								
	1		0.929	0.177	0.262	0.067	0.0093	407
	2		0.900	0.171	0.244	0.076	0.0093	391
	3		0.893	0.184	0.246	0.067	0.0097	407
	4		0.904	0.183	0.256	0.068	0.0100	407
	5		0.915	0.175	0.256	0.081	0.0092	429
	6		1.00	0.193	0.284	0.069	0.0113	471
	7		0.944	0.200	0.295	0.072	0.0113	491
	8		1.06	0.208	0.333	0.079	0.0113	489
	9		0.882	0.163	0.270	0.076	0.0092	479
	10		1.18	0.244	0.357	0.092	0.0142	395
PC								
	1							321
	2		0.970	0.327	0.354	0.073	0.0114	385
	3		1.06	0.330	0.370	0.077	0.0116	492
	4		1.22	0.377	0.431	0.082	0.0133	501
	5		0.883	0.285	0.315	0.075	0.0105	494
	6		1.09	0.354	0.387	0.075	0.0125	511
	7		1.04	0.311	0.346	0.072	0.0112	514
	8		1.03	0.320	0.330	0.076	0.0114	526
	9		1.14	0.348	0.394		0.0127	527
	10		1.15	0.360	0.377	0.080	0.0126	520
PD								
	1		0.788	0.128	0.210	0.062	0.0068	333
	2		0.740	0.128	0.195	0.060	0.0070	331
	3		0.774	0.135	0.211	0.067	0.0072	344
	4		0.849	0.171	0.232	0.068	0.0080	353
	5		1.76	0.737	0.586	0.127	0.0212	414
	6		1.97	0.868	0.666	0.143	0.0248	769
	7		2.07	0.902	0.677	0.140	0.0249	793
	8		2.21	0.959	0.738	0.159	0.0268	775
	9		2.08	0.794	0.676	0.135	0.0228	803
PE								
	1		0.860	0.187	0.237	0.076	0.0091	433
	2		1.33	0.346	0.386	0.115	0.0132	521
	3		1.24	0.356	0.396	0.092	0.0146	569
	4		1.20	0.311	0.374		0.0138	567
	5		1.08	0.272	0.331	0.085	0.0127	553
	6		1.09	0.242	0.318	0.089	0.0127	561
	7		1.15	0.236	0.319	0.089	0.0126	558
	8		1.13	0.246	0.342	0.087	0.0125	572
	9		1.12	0.253	0.337	0.093	0.0132	579
	10		1.07	0.267	0.335	0.088	0.0135	592
	11		1.08	0.273	0.340	0.088	0.0131	628
	12		1.17	0.278	0.362	0.096	0.0135	629
	13		1.12	0.283	0.350	0.096	0.0136	620
	14		1.20	0.289	0.354	0.103	0.0145	611
	15		1.18	0.289	0.352	0.096	0.0146	615
	16		1.22	0.287	0.367	0.099	0.0142	637
	17		1.17	0.282	0.368	0.095	0.0138	608
	18		1.21	0.282	0.366	0.108	0.0145	588

Table 3: Chemical composition of pore waters from gravity cores. Samples were obtained by centrifugation of 1 cm (GC 1 thru 6) or 2 cm (GC 7 thru 14) sediment sections.

	Depth cm	Cl^- mM	Na^+ mM	Mg^{2+} mM	Ca^{2+} mM	K^+ mM	Li^+ mM	SiO_2 uM
GC 1								
	5.5		0.458	0.124	0.248	0.072	0.0058	514
	10.5	0.315	0.487	0.138	0.283	0.080	0.0055	540
	15.5		0.507	0.153	0.309	0.083	0.0058	584
	23.5	0.337	0.557	0.193	0.357	0.091	0.0059	664
	31.5		0.602	0.207	0.381	0.105	0.0059	681
	39.5	0.333	0.588	0.233	0.452		0.0056	669
	47		0.649	0.256	0.483	0.112	0.0056	694
	56.5	0.359	0.670	0.312		0.112		762
	66.5		0.743	0.338	0.617	0.131	0.0054	778
	73.5	0.400	0.758	0.331	0.574	0.141	0.0057	676
	81.5		0.801	0.366	0.632	0.147	0.0051	739
	90.5	0.385	0.844	0.399	0.684	0.154	0.0053	862
GC 2								
	5.5		0.413		0.174	0.073	0.0063	533
	10.5		0.501		0.232	0.064	0.0065	648
	18.5	0.281	0.548	0.145	0.233	0.079	0.0064	684
	26.5							754
	34.5	0.323	0.662	0.170	0.270	0.093		797
	42.5		0.669	0.180	0.278	0.094	0.0072	757
	50.5	0.298	0.690	0.187	0.290	0.101	0.0071	774
	58.5		0.713	0.199	0.296	0.104	0.0073	775
	66.5	0.321	0.774	0.206	0.319	0.108	0.0069	798
	74.5		0.783	0.202	0.308	0.115	0.0075	754
	82.5		0.766		0.325	0.116	0.0073	760
	92.5		0.862	0.238	0.357	0.107	0.0073	791
	102.5	0.325	0.917	0.246	0.375	0.127	0.0079	764
	112.5		0.975	0.276	0.428	0.114	0.0081	772
	122.5	0.375	1.01	0.300	0.439	0.118	0.0084	795
GC 3								
	5.5		0.531	0.112	0.192	0.077	0.0066	648
	10.5	0.456	0.579	0.143	0.230	0.084	0.0066	686
	15.5		0.690	0.192	0.289	0.105	0.0067	691
	23.5	0.399	0.796	0.243	0.365	0.106		731
	31.5		0.860	0.254	0.381	0.117	0.0063	704
	39.5		0.920	0.253	0.397	0.141	0.0079	773
	58.5	0.486	1.14	0.340	0.490	0.142	0.0068	677
	67.5		1.24	0.409	0.572	0.151	0.0075	654
	76.5	0.520	1.33	0.445	0.610	0.145	0.0074	681
	85.5		1.43	0.429	0.601	0.180		
	94.5		1.39	0.432	0.594	0.162	0.0075	522
GC 4								
	2.5		0.854	0.288	0.345	0.116	0.0138	
	5	0.401	0.726	0.239	0.312	0.102		656
	7.5							606
	10.5	0.391	0.828	0.288	0.367	0.115		706
	15.5		0.968	0.350	0.433	0.139	0.0150	764
	20.5	0.540	1.08	0.413	0.483	0.157	0.0155	810
	28.5		1.23	0.483	0.532	0.181	0.0197	869
	36.5	0.668	1.38	0.549	0.587	0.188	0.0205	890
	42.5		1.42	0.575	0.612	0.194	0.0225	1030
	50.5	0.674	1.46	0.573	0.599	0.219	0.0244	1060
	58.5		1.61	0.605	0.625	0.219	0.0256	1060
	66.5	0.792	1.69	0.694	0.675	0.246	0.0278	1060
	74		2.09	0.841	0.770	0.294	0.0337	
	82.5	0.821	1.95	0.802	0.738	0.293	0.0322	1090
	90.5		1.87	0.779	0.726	0.258	0.0303	1130
	97	0.804	1.80	0.720	0.689	0.253	0.0294	1130
	102.5	0.603	2.12	0.873	0.795	0.257	0.0336	1220
	110.5	0.980	2.21	0.972	0.851	0.274	0.0292	1260
	118.5							1280
	129.5	1.07						1210
	137.5		2.51	1.109	0.918	0.282	0.0389	1330
	145.5	1.225	2.58	1.141	0.944	0.299		1350
GC 5								
	2.5		0.439	0.104	0.177	0.068	0.0067	400
	6.5	0.275	0.457	0.118	0.197	0.073	0.0068	463
	10.5		0.477	0.125	0.216	0.077	0.0068	512
	15.5		0.484	0.131	0.226	0.075	0.0067	554
	20.5		0.495	0.133	0.236		0.0067	613
	25.5	0.283	0.527	0.144	0.248	0.086	0.0061	623
	30.5		0.521	0.127	0.234	0.092	0.0070	652

	38.5	0.287	0.537	0.120	0.223	0.087	0.0072	689
	46.5		0.545	0.120	0.224	0.093	0.0073	721
	54.5	0.383	0.554	0.112	0.214	0.099	0.0071	
	62.5		0.565	0.118	0.223	0.099	0.0071	699
	70.5	0.325	0.556	0.114	0.216	0.096		716
	78.5		0.574	0.115	0.224	0.099	0.0068	682
	86.5	0.298	0.521	0.094	0.181	0.076		
	94.5		0.531	0.098	0.189	0.071	0.0060	715
	98.5	0.314	0.538	0.098	0.188	0.072	0.0061	711
GC 6								
	3.5		0.501	0.085	0.155	0.091	0.0064	479
	6.5	0.346	0.563	0.098	0.188	0.097	0.0074	562
	9.5		0.623	0.119	0.217	0.103	0.0082	680
	15.5	0.363	0.705	0.151	0.272	0.104	0.0081	728
	20.5		0.787	0.176	0.325	0.115	0.0088	804
	28.5		0.929	0.186	0.335	0.141		816
	37.5		1.05	0.216	0.390	0.142	0.0120	870
	46.5		1.22	0.243	0.434	0.168		864
	55.5		1.30	0.338	0.563	0.156	0.0151	840
	64.5	0.693						807
	82.5	0.782	1.69	0.448	0.711	0.179	0.0222	824
	91.5		1.82	0.488	0.766	0.199	0.0250	829
	100.5	0.920	2.02	0.550	0.852	0.209	0.0280	867
	109.5		2.14	0.526	0.801			
	118.5	1.07	2.25	0.627	0.922	0.232	0.0331	853
GC 7								
	3.75	0.295	0.527	0.086	0.159	0.091	0.0057	690
	12		0.576	0.101	0.191	0.102	0.0053	731
	17	0.341	0.748	0.156	0.273	0.122		776
	22.5	0.296	0.725	0.210	0.306	0.125		757
	31.5							699
	47		0.898	0.187	0.312	0.146		687
	56.5					0.175		665
	69		1.19	0.302	0.467			675
	80		0.955	0.187	0.319	0.157		647
	89		1.16	0.251	0.392	0.184		606
GC 8								
	1	0.492	0.841	0.143	0.212	0.111	0.0144	475
	6		1.28	0.143	0.226	0.162		792
	16	1.28	2.53	0.457	0.557		0.0523	893
	23.25		3.14	0.630	0.702	0.342	0.0647	1010
	32.5	1.59						1050
	42.5							1040
	52.5	1.85	3.65	0.927	0.928	0.419	0.0758	1070
	62		3.75	0.955	0.870	0.411	0.0775	1100
	72	1.99	4.63	0.983	0.907	0.427	0.0776	1120
	81	2.08						1090
	89		4.60	0.795	0.745	0.449	0.0778	1050
GC 9								
	1		0.478	0.085	0.144	0.079	0.0070	580
	7	0.299	0.492	0.091	0.163	0.083	0.0067	737
	14.25		0.495	0.097	0.179	0.083	0.0069	828
	21	0.300	0.513	0.105	0.197	0.084	0.0071	866
	28.75		0.524	0.111	0.203	0.087	0.0070	818
	36	0.286	0.518	0.111	0.197	0.090	0.0069	585
	45		0.422	0.110	0.170	0.070	0.0070	774
	53	0.344	0.486	0.104	0.172	0.072		539
GC 10								
	0.5	0.440	0.789	0.161	0.214	0.108	0.0113	670
	7.5							755
	14	0.497	1.17	0.297	0.438	0.164	0.0122	824
	20.5		1.37	0.321	0.454	0.193		819
	26.75	0.557	1.41	0.360	0.536	0.198	0.0149	850
	33.25		1.56	0.375	0.566	0.216		850
	43.5		1.85	0.380	0.588	0.251		832
	51	0.763						789
	61.5		2.17	0.426		0.301	0.0299	883
	76.5		2.09	0.364	0.544	0.298	0.0373	839
	91	0.900	2.34	0.497	0.702	0.308		950
	104.5		2.31	0.455	0.661		0.0450	936
	116		2.46	0.527	0.729	0.315		961
	128	0.973						975
	135		2.58	0.569	0.770			984
	148		2.68		0.748	0.341		964
	159							939
GC 11								
	0.75	0.335	0.510	0.082	0.139	0.082	0.0074	480
	5	0.347	0.608	0.108	0.196	0.109	0.0091	650
	12	0.375	0.729	0.122	0.259	0.116		744
	21		1.14	0.262	0.427	0.142	0.0136	823
	28		1.43	0.305	0.482	0.177		795
	38		1.63	0.393	0.601	0.188	0.0217	806

	46	0.752	1.77	0.415	0.634	0.199	0.0235	822
	57		1.91	0.490	0.742	0.212	0.0266	859
	68	0.885	2.00	0.521	0.794	0.226	0.0287	863
	79		2.09	0.510	0.797	0.234		866
	90.5	0.950	2.24	0.555	0.874	0.245	0.0321	869
	101.5		2.33	0.603	0.943	0.262	0.0345	903
	112	1.055	2.47	0.623	0.972	0.288	0.0373	852
	122							892
GC 12								
	2.5		0.528	0.105	0.168	0.078	0.0072	538
	8	0.343	0.640	0.131	0.217	0.095		643
	18.5		0.976	0.200	0.324	0.130		801
	28							786
	37.75		1.61	0.347	0.529	0.188		778
	47.5		1.78	0.419	0.634	0.202	0.0238	794
	56		1.85	0.426	0.668	0.209		828
	63		1.93	0.467	0.701	0.225		820
	73.5	0.980	2.23	0.537	0.831	0.251		863
	81.75		2.08	0.458	0.716	0.244	0.0307	813
	92.5		2.33	0.500	0.763	0.271		792
	102.75		2.44	0.584	0.921	0.278		922
GC 13								
	0.5		0.94	0.299	0.397	0.141	0.0126	488
	6	0.570	1.72	0.250	0.357	0.132	0.0154	696
	15							1080
	29		3.44	0.896	0.952	0.351	0.0673	1220
	38.25		3.77	1.045	1.002	0.377	0.0734	1160
	45.75	1.98						1210
	53.5		3.73	0.891	0.861		0.0722	1240
	58.5		3.78	0.931	0.870	0.422	0.0847	1220
GC 14								
	0.5		0.503	0.107	0.175	0.075	0.0074	478
	4.5	0.360	0.722	0.177	0.255	0.102		648
	12		0.868	0.269	0.369	0.126	0.0115	681
	27		2.21	0.660	0.560	0.293		976
	36							1060
	44		2.29	0.621	0.502	0.329	0.0345	957
	53		2.35	0.588				814
	59.5		2.40	0.549				860

temperature range of -5°C to 35°C. Intercalibration of the three temperature probes is shown in Fig. 3. All three thermistors registered identical temperatures during decent. Only after the initial penetration did the temperature readings diverge in response to the thermal gradients within the sediments. All three thermistors also registered identical temperature measurements during transit to the second area before the probe was inserted into the sediments and during assent. The TTT recorded data continuously at one site for three days and at a second site for four days (Fig. 2).

3. VELOCITIES OF FLUID FLOW THROUGH THE SEDIMENTS

3.1 Constraints from Chemical Profiles

Pore water profiles of sodium from representative cores are shown in Fig. 4. Some of the profiles increase linearly with depth. Other profiles are curved near the sediment-water interface and approach an asymptotic concentration with depth. Similar profiles exist for magnesium, calcium, chloride, lithium, and potassium. These ions are herein referred to as tracer ions. Profiles of dissolved silica from box cores and peepers are similar to profiles of the tracer ions, but profiles of dissolved silica from gravity cores are sometimes different than profiles of the tracer ions (Fig. 5). For example, the profile of dissolved silica from GC1 is curved, but the sodium profile is linear, suggesting that different processes control the shape of the profiles.

Chemical profiles of pore waters are influenced by time dependent, diffusive, advective, and reaction processes. For the one dimensional case, a mathematical representation of these processes is:

$$\frac{\partial(\phi,C)}{\partial t} = \frac{\partial(\phi D_s(\partial C/\partial z))}{\partial z} - \frac{\partial(\phi v C)}{\partial z} + \phi\Sigma \qquad (1)$$

where ϕ is porosity, C is concentration, t is time, D_S is the sediment diffusion coefficient, z is depth (positive downcore), v is velocity (upwelling is negative), and $\sum R$ includes all terms related to the chemical interactions influencing a particular solute. Before using this model, the importance of each term is evaluated. If a term proves to be insignificant or dominate, the model is simplified by eliminating needless terms. In the following discussion, arguments are presented that support an advection-diffusion model for tracer ions and an advection-diffusion-reaction model for dissolved silica.

Because chemical gradients are evident, a diffusive term must be included in the model. If diffusion is the dominate process that controls pore water profiles, the sediment diffusion coefficient must increase by an order of magnitude over the curved portion of the profile for the data to fit modeled profiles. Alternatively, one or more of the other processes must be included in modeling the profiles from Crater Lake. The sediment diffusion coefficient varies with temperature, tortuosity, and electrical effects (as reviewed in Berner, 1980). An increase of 25°C doubles the sediment diffusion coefficient (Li and Gregory, 1974) and thus, requires a temperature change of 75°C over the sampled section in order to change the sediment diffusion coefficient by an order of magnitude, in contrast to our temperature data (Table 3).

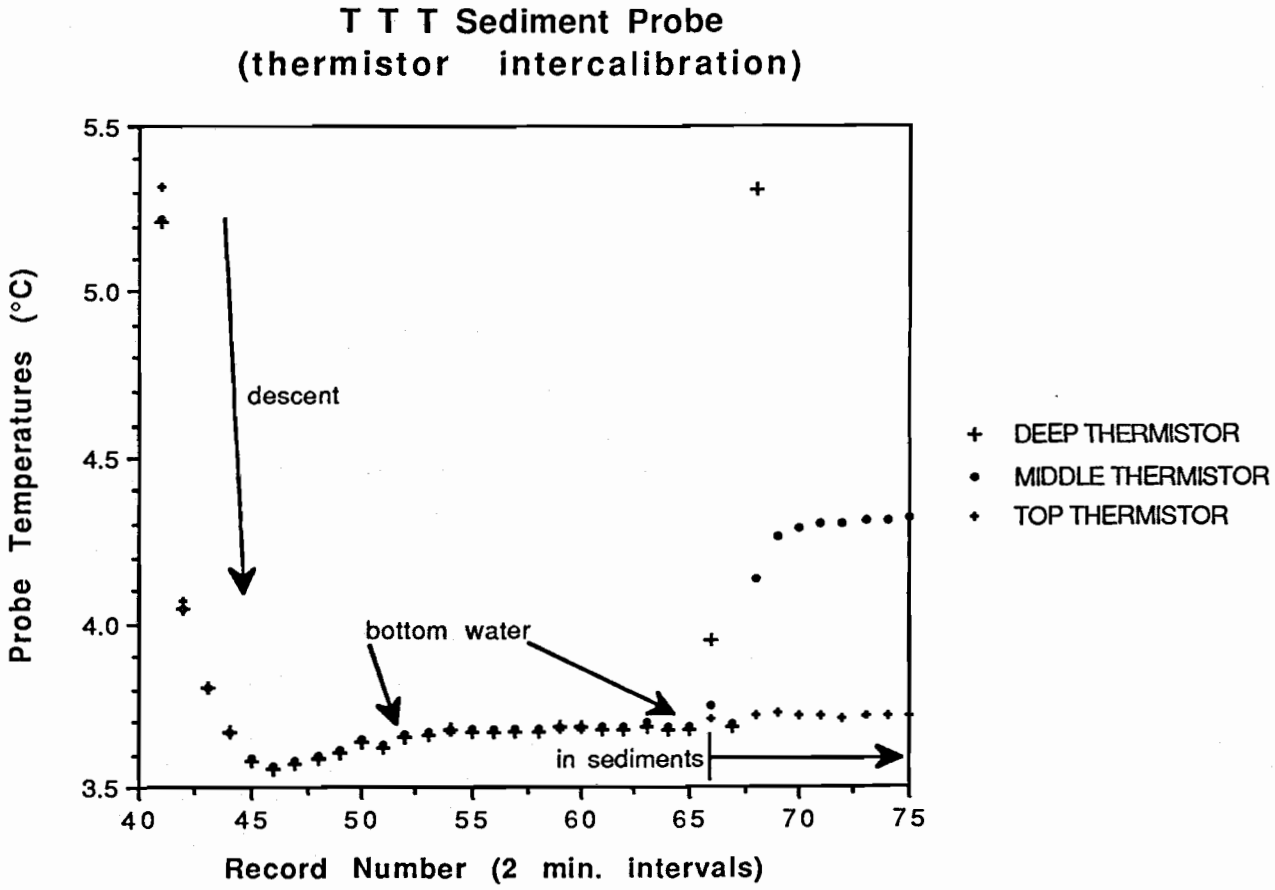

Fig. 3: Intercalibration of thermistors in the SeaCat TTT temperature probe. All three thermistors read exactly the same water temperature until the probe is inserted into the sediment. All three thermistors measured the same water temperature when the probe was moved and when the probe was retrieved.

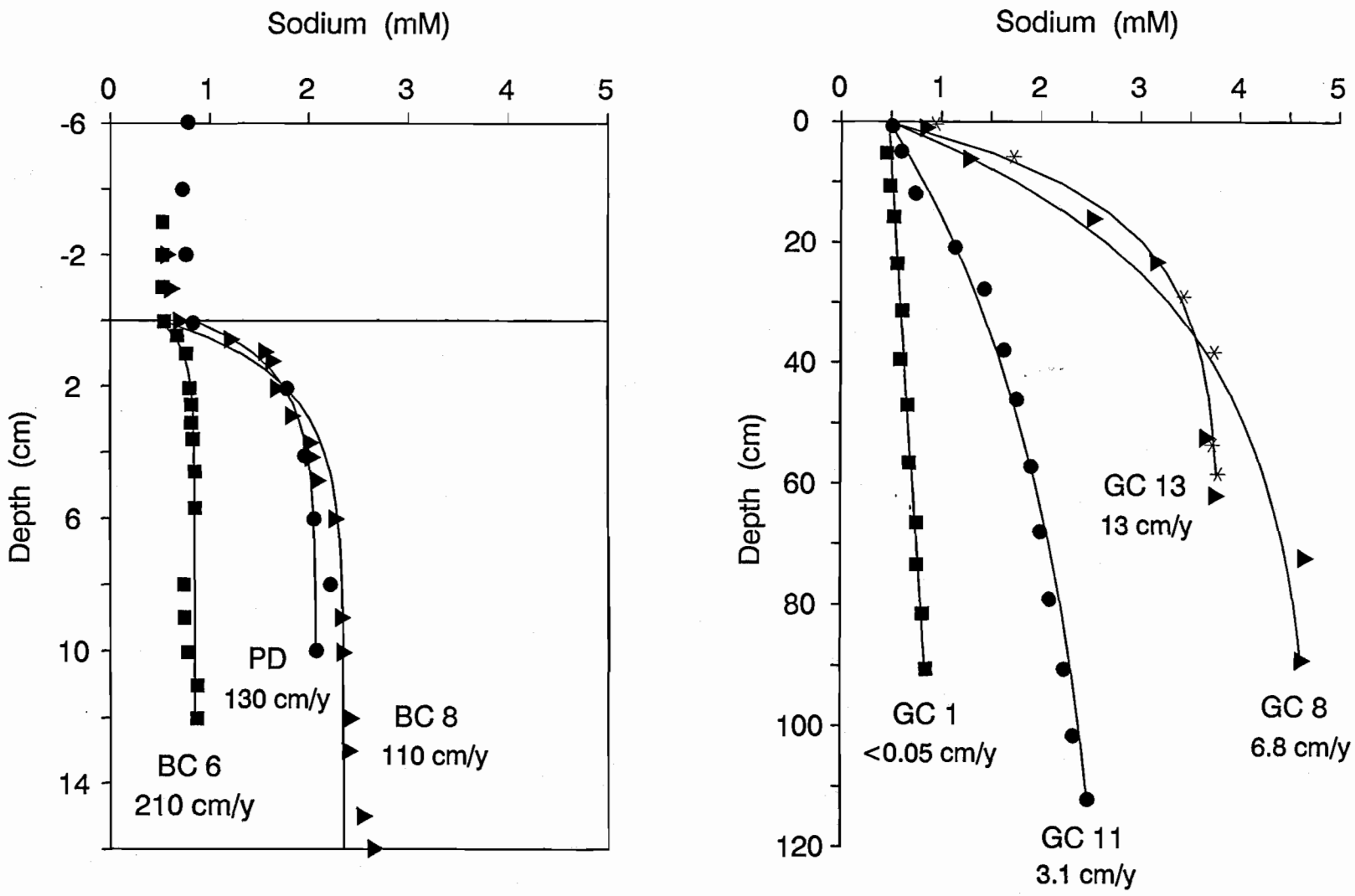

Fig. 4: Sodium profiles from representative cores plotted with modeled profiles. Modeled profiles are calculated from equation (9) using parameters that are defined in the text.

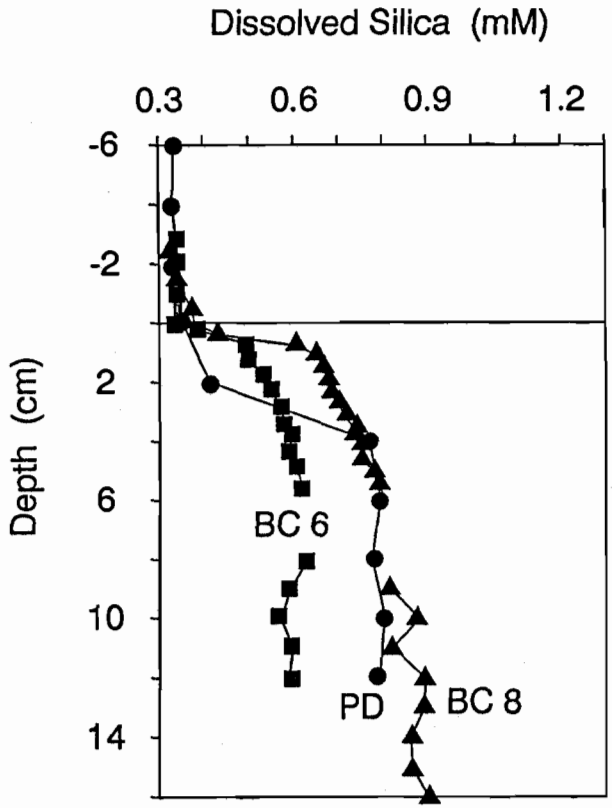

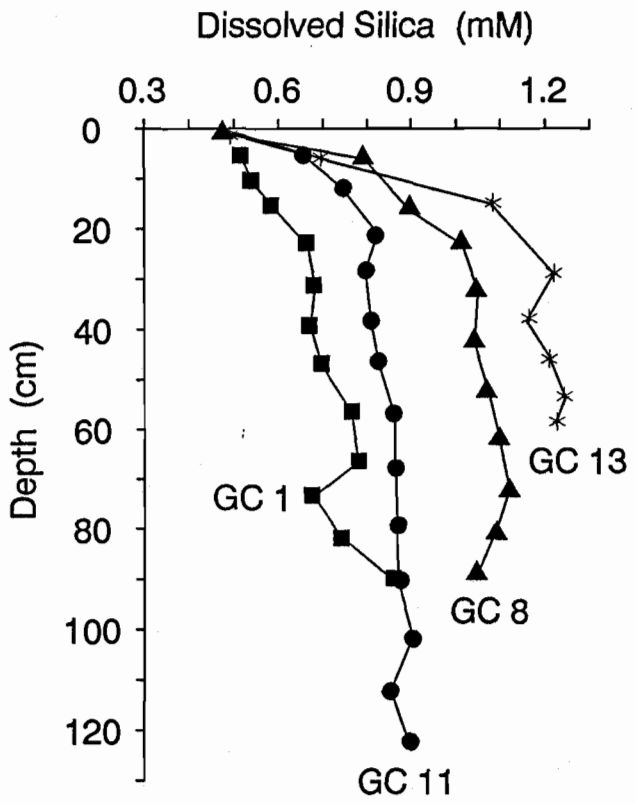

Fig. 5: Profiles of dissolved silica for representative cores.

The sediment diffusion coefficient is a function of tortuosity, which is a function of the formation factor and porosity. Although the formation factor was not measured, it is related to porosity by Archie's law (Berner, 1980), and thus, the tortuosity is a function of porosity. The average porosity decreases from 0.85 near the sediment-water interface to 0.65 at 1.7 m below the lake floor. This translates to a decrease in the sediment diffusion coefficient with depth.

Electrical effects influence the sediment diffusion coefficient by causing the more mobile ions to diffuse slower and the less mobile ions to diffuse faster. These effects are produced by gradients of charged ions generating an electrical potential while maintaining electroneutrality. Electrical effects alter the sediment diffusion coefficient by less than 25% in most cases, but approach 100% in some samples that have a measured charge balance that is not zero. Because we cannot justify an order of magnitude change in the sediment diffusion coefficient in the curved portion of the profile, other terms are needed to model chemical profiles from Crater Lake.

If we develop a time dependent-diffusion model, then for a well mixed lake, such as Crater Lake (Appendix A), all chemical profiles of pore waters would have the same curvature for a particular chemical species, in contrast to the data (Fig. 4). To generate some of the observed profiles, the concentration of lake water in the past year would have to be more than five times more concentrated than present values (Fig. 6), but the concentration of dissolved species in Crater Lake has been uniform for the past 100 years (Nathenson, 1990). A change in the composition of the fluid in basement with time will produce curved profiles, however these profiles will be concave-down and the measured profiles are concave-up. Therefore, diffusive and either reactive or advective processes or both are necessary in modeling the chemical profiles from Crater Lake.

Some profiles of dissolved species are influenced by fluid-sediment reactions. For example, dissolution of amorphous silica has been reported to increase the concentration of dissolved silica over bottom water values in the upper section of the sediment column. Once equilibrium is reached, the concentration of dissolved silica remains uniform with depth (Boudreau, 1990; Wheat and McDuff, submitted B). Similar profiles of dissolved silica are observed in Crater Lake (Fig. 5). These profiles are modeled with a reaction term that is first order with respect to the degree of undersaturation (Schink et al., 1975). If we assume fluid flow does not occur, profiles of dissolved silica are governed by the following equation:

$$D_S \frac{\partial^2 C}{\partial z^2} - K(C - C_{eq}) = 0 \qquad (2)$$

where k is the first order rate constant and C_{eq} is the pseudo equilibrium constant. Given the following boundary conditions:

$$C = C_o \quad \text{at} \quad z = 0 \qquad (3)$$

$$C = C_{bot} \quad \text{at} \quad Z = z_{bot} \qquad (4)$$

the solution is:

$$C = (C_o - C_{eq} - A_1)\exp(-\beta z) + A_1 \exp(\beta z) + C_{eq} \qquad (5)$$

where:

$$\beta = (k/d_s)^{0.5} \qquad A_1 = \frac{C_{bot} - C_{eq} + (C_{eq} - C_o)\exp(-\beta z_{bot})}{\exp(\beta z_{bot}) - \exp(-\beta z_{bot})}$$

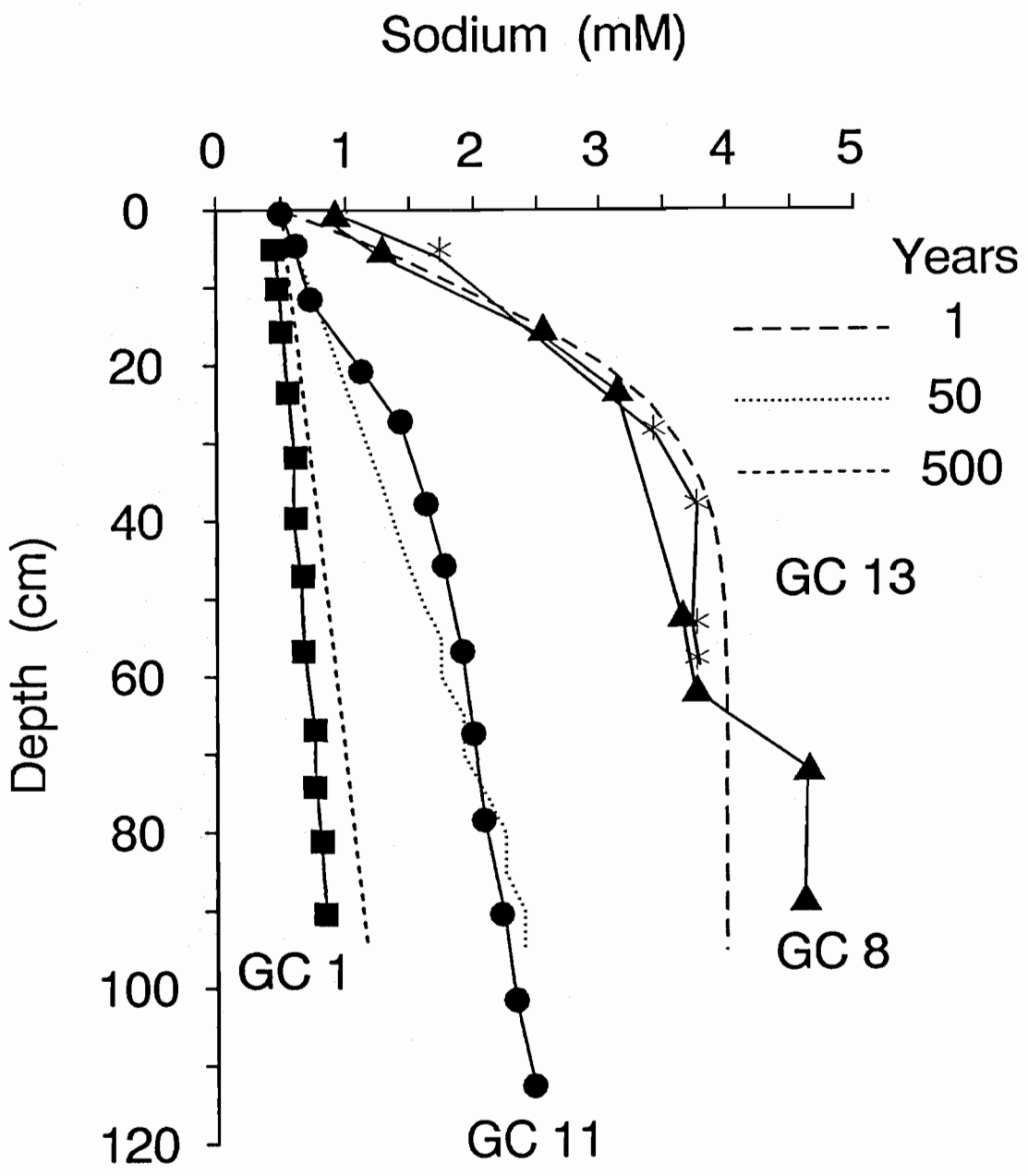

Fig. 6: Representative profiles of sodium plotted with modeled profiles from a time dependent-diffusion model for several intervals of time. For these modeled profiles, the initial concentration of sodium in lake fluids is 4 mM. The temporal variation required to fit the data precludes a time dependant process producing the observed profiles.

Some profiles of the tracer ions are similar to profiles of dissolved silica in that they increase in the upper section of the sediment column, then remain uniform with depth. These profiles suggest that the reaction term used in modeling dissolved silica could also be used to model the tracer ions. However, some evidence suggests that the tracer ions do not react in the sampled section, and therefore, advective processes must be included in modeling pore water profiles from Crater Lake.

First, let us assume that only reaction and diffusive terms influence chemical profiles of pore fluids. If the term for reaction is modeled with a first order rate equation that is proportional to the degree of undersaturation, then the best fits of the data to modeled profiles will require rates of reaction that differ from 10^{-14} s^{-1} in GC1, to 10^{-9} s^{-1} in GC11, to 10^{-8} s^{-1} in GC8 and GC13, to 10^{-6} s^{-1} in the box core and peeper samples. A range in the rate of reaction is consistent with reactions that occur at different temperatures or with different mineral assemblages. A 10°C increase in temperature approximately doubles the rate of reaction. Therefore, a four order of magnitude difference in the rate of reaction requires a difference of about 140°C, but no temperatures were measured above 20°C.

The calculated difference in the rate of reaction can not be explained by reaction with different mineral assemblages for two reasons. First, the source of the sediments is primarily weathered andesite from the caldera walls. These sediments are well mixed before being deposited on the lake floor. The other reason is that the reaction-diffusion model produces chemical fluxes from the sediments that are orders of magnitude greater than the burial fluxes (Table 4). Since the ratio of fluxes of chemical ions out of the sediments is different than the ratio of chemical fluxes due to burial, the model predicts that the sediments should have a measurable ratio of one chemical species to another that is different from material collected in sediment traps and from sediments. Comparisons between sediment trap compositions and those in sediment cores show this is not the case (Fig. 7).

Property-property plots also are useful in showing that the tracer ions are unreactive in the sampled section. Data from curved chloride and sodium profiles, when plotted against one another, plot along a single linear trend (Fig. 8). Linear property-property plots are typically associated with conservative mixing processes. Since diffusion alone cannot produce the observed profiles, either advection exists or the same mineral assemblages must be reacting throughout the lake at different rates, which is inconsistent with earlier reasoning.

In contrast to the chloride-sodium plot, if a chemical species is influenced by fluid-sediment interactions, such as dissolved silica, and another species is mixing conservatively, such as sodium, non-linear property-property trends will result (Fig. 8b). Plots of dissolved silica versus sodium for GC 11 produce a curved trend, which is the expected trend if amorphous silica dissolving as fluid from basement, upwells through the sediments. If GC1 was greater in length, a similar dissolved silica-sodium trend would exist once the equilibrium concentration of dissolved silica is reached. In contrast to GC11, plots of dissolved silica versus sodium for BC8, GC8, GC13, and PD show a linear dependance. This trend is expected if the speed of upwelling is fast enough so that dissolution of amorphous silica does not measurably alter the concentration of dissolved silica (Wheat and McDuff, submitted B).

Based on the rationale presented above, profiles of the tracer ions must be modeled using diffusive and advective terms. Although reaction may exist in some cases, as indicated from non-linear trends of ions plotted versus sodium or chloride, no reaction term is included. This was done for simplicity and does not alter the overall conclusions.

Table 4: Chemical fluxes (mg/cm^2y) from the sediments to the overlying water column compared to the burial rate (mg/cm^2y).

Chemical Species	BC 8	PD	BC 6	GC 13	Burial[1] Rate
Na^+	4.5	1.9	0.58	0.42	0.032
Ca^{2+}	2.0	0.77	0.23	0.11	0.035
Mg^{2+}	2.0	0.70	0.13	0.06	0.020
K^+	0.75	0.32	0.19	0.11	0.015
Li^+	1.6×10^{-2}	6.3×10^{-3}	3.2×10^{-3}	2×10^{-3}	4×10^{-5}
Si (as H_4SiO_4)	3.1	1.6	0.82	0.44	0.13

[1] unpublished data

Table 5: Vertical fluid velocities (cm/y) estimated from the chemical data. Upwelling is negative.

Core	Chemical Species Na^+	Ca^{2+}	Mg^{2+}	Cl^-	K^+	Li^+	Overall Rate
GC 1	±0.05	-0.6	±0.05	±0.05	±0.05	±0.05	±0.05
GC 8	-9.5	-5.2	-4	-11	-16	-10	-8
GC 11	-3.1	-1.5	-1.4	-3.6	-3.6	-1.5	-3
GC 13	-13	-9.6	-8	---	-12	-7	-11
PD	-130	-100	-80	---	-200	-110	-120
BC 6	-210	***	***	-220	-220	-240	-220
BC 8	-110	***	***	-150	-120	-80	-120

--- insufficient data

*** not determined because of sampling artifacts

Table 6: Average TTT measurements for each day of deployment. Fluid velocities are estimated from fits of the data to equation (13). The adjusted depth accounts for the depth that the probe over penetrated. Upwelling is negative and negative depths are the distance above the sediment-water interface.

Date	Area	Temperature (°C) of Probe at: -5 cm	5 cm	35 cm	Velocity (m/y)
8/24/91	1	3.80	4.35	5.62	-40
8/25/91	1	3.95	4.43	5.60	-37
8/26/91	1	4.03	4.43	5.60	-29
		Adjusted Depths 11 cm	21 cm	51 cm	
8/27/91	2	4.68	5.22	6.44	-11
8/28/91	2	4.68	5.22	6.44	-11
8/29/91	2	4.75	5.27	6.45	-14
8/30/91	2	4.63	5.19	6.44	-10
8/31/91	2	4.63	5.19	6.44	-10

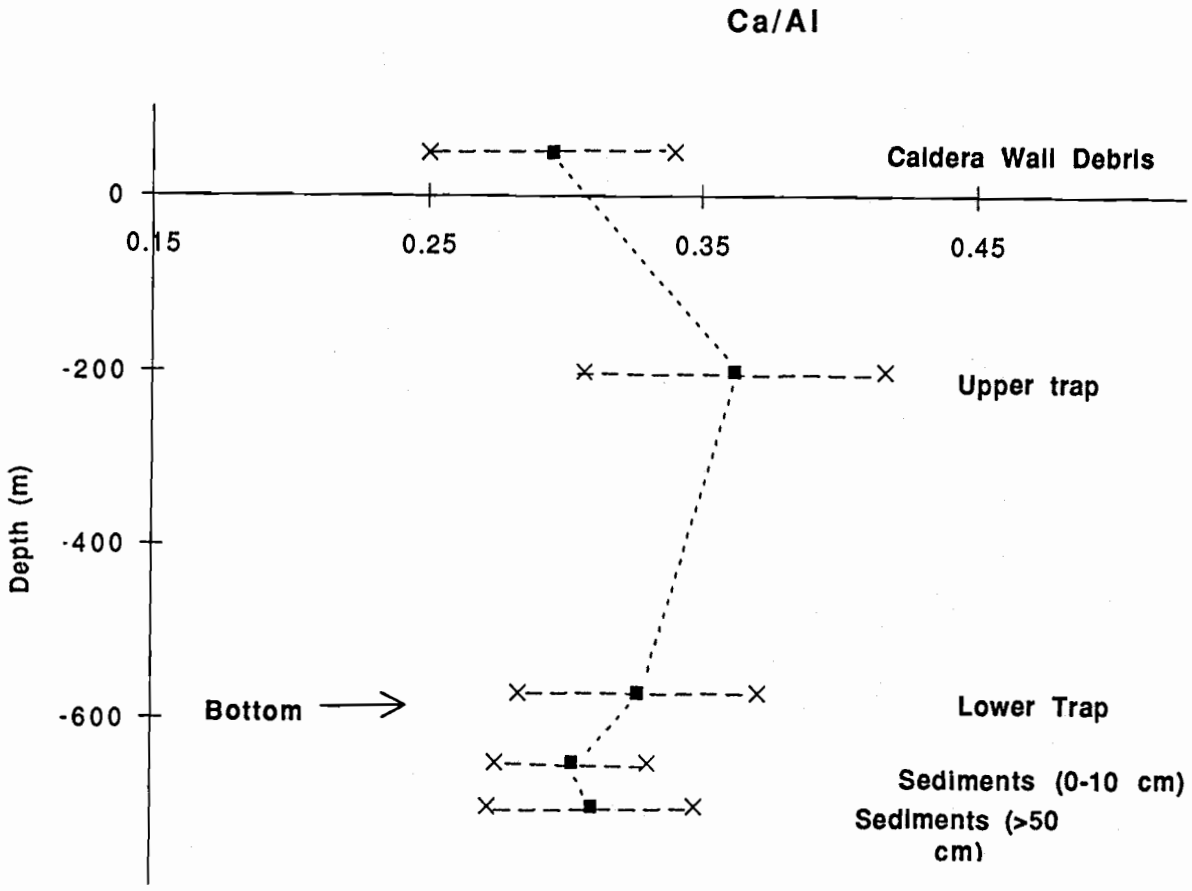

Fig. 7: Ca/Al values for various Crater Lake solid materials. The ratio for caldera wall debris is indicated by the symbol above the zero depth line. Compositions for sediment trap depths at 200 m and 580 m depths are shown. The data represent the average and two deviations of unpublished results from five years of trap deployments. The sediment ratios are shown as symbols plotted below 600 m depth. These data are from Dymond and Collier (1990).

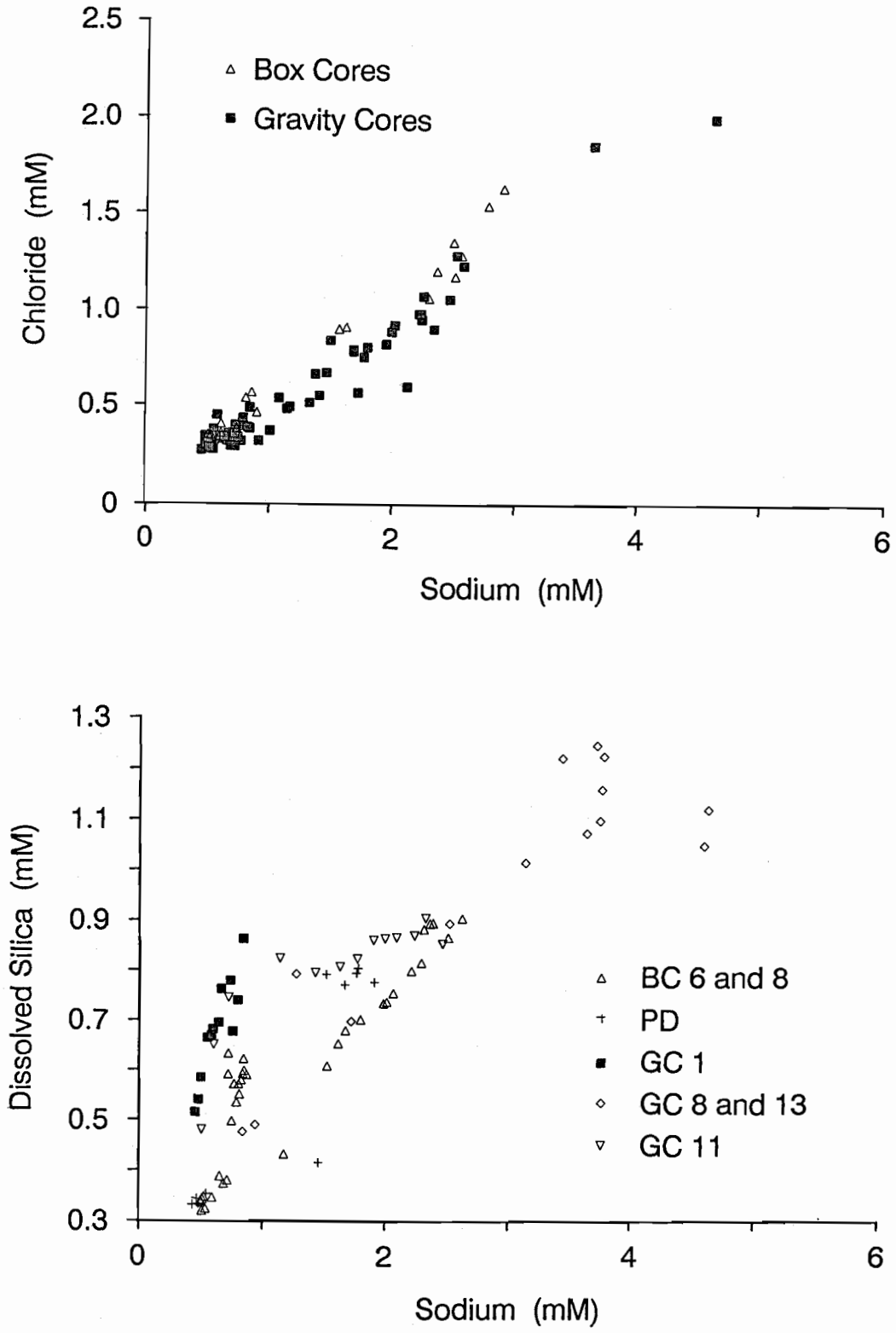

Fig. 8: Concentrations of chloride (a) and dissolved silica (b) plotted versus sodium. All of the data are shown in the plot of chloride versus sodium. For clarity, only data from representative cores are shown in the plot of dissolved silica versus sodium. BC 6 and 8, GC 8 and 13, and PD define a mixing line and GC 11 defines a reaction-mixing trend.

An advection-diffusion model was developed which considers a diffusive term that varies with tortuosity, temperature, and electrical effects. No temperature measurements were made where the cores were taken, however the range of temperatures recorded in hydrothermal features is about 4 to 15°C above ambient (Table 3). An increase of 15°C produces an increase in the sediment diffusion coefficient of 60%. Based on the data in Table 3 and in Williams and Von Herzen (1983), the sediment diffusion coefficient most likely increases by less than 30% downcore in cores taken in geologic features and even less in other cores. A decrease in the porosity of 14% over the sampled section produces a decrease in the sediment diffusion coefficient of 14% downcore. The use of electrical corrections to the sediment diffusion coefficient was not implemented, because the charge balance based on measured concentrations was not consistently zero. Therefore, because of the uncertainties in calculating profiles of the sediment diffusion coefficient, a uniform sediment diffusion coefficient with depth was assumed. These coefficients are calculated from those listed in Li and Gregory (1974) taking into account the temperature of bottom water 3.7°C, Archie's Law, and a uniform porosity of 0.85 downcore.

Based on a uniform diffusion coefficient with depth and allowing for only advective and diffusive processes, equation (1) reduces to:

$$D_s(\partial^2 C/\partial z^2) - v(\partial C/\partial z) = 0 \qquad (6)$$

Equation (6) is solved subject to the following conditions:

$$C = C_o \quad \text{at} \quad z = 0 \qquad (7)$$

$$C = C_{bot} \quad \text{at} \quad z = Z_{bot} \qquad (8)$$

where C_{bot} is the concentration of the pore fluid at the base of the core and z_{bot} is the length of the sampled section. The solution is:

$$C = C_o = A_1 + A_1 \exp(vz/D_s) \qquad (9)$$

where

$$A_1 = \{C_{bot} - C_o\}/\{\exp(vz_{bot}/D_s) - 1\}$$

Fluid velocities are calculated by fitting profiles of the tracer ions to calculations of equation (9) and minimizing the squared deviation (Figure 4 and Table 5). Differences in the calculated upwelling velocity for a particular core are a result of the method in which the diffusion coefficient is modeled, a result of the quality of analytical measurements, and a result of the number of measurements taken in the curved portion of the profile. The calculated advective rates may also differ if fluid-sediment interactions occur in the sampled section. For example, dissolution of calcite in GC1 produces a fit to the model with a faster upwelling speed than the speed estimated from the other tracer ions. Similarly, fluid-sediment interactions may influence the calculated upwelling speed that is estimated from the potassium profile from GC8. In both cases, plots of the ion versus sodium are non-linear, which is the expected trend if calcium and potassium are involved in fluid-sediment interactions and sodium is mixing conservatively. Differences in the calculated fluid velocities could be eliminated if a reaction term were included in equation (6) and if the rate of reaction were known.

Overall estimates of fluid velocities in representative cores are listed in Table 5. These velocities are based primarily on the sodium data, because sodium does not react in the sampled section.

Other ions, such as chloride and lithium, also do not react in the sampled section; however, chemical analyses of these ions are less sensitive and fewer in number than analyses of sodium. Fluid-sediment reactions involving the other tracer ions may exist in the sampled section of some cores, making these ions less reliable for use in estimating fluid velocities. Fluid velocities estimated from the box cores and peeper PD profiles are a minimum. Diffusion in the absence of advection after core retrieval and disturbance of the sediment-water interface produce a calculated velocity that is slower than the *in situ* velocity (Wheat and McDuff, submitted A). Velocities estimated from PD are a minimum because of the lack of any samples in the curved section of the profile.

Fluid velocities estimated from calcium and magnesium profiles from box cores are sometimes inconsistent with velocities estimated from the other profiles. This is a product of whole core squeezing. Whole core squeezing forces pore fluids to flow through overlying sediments. If fluid-sediment reactions are relatively quick, such as the dissolution of calcite or adsorption-exchange reactions (Bender et al., 1987), an artifact is introduced that increases the concentration of calcium and magnesium relative to sodium. This is illustrated in property-property plots and produces a calculated velocity that is different from the *in situ* velocity.

A measure of the uncertainty in estimating fluid velocities is the value of the reduced χ^2. Reduced χ^2 is calculated with variances that are estimated from concentrations of pore fluids in uniform sections of the profiles. For sodium, the variance is 0.0021 mM^2. Contours of reduced χ^2 are plotted as a function of the sediment diffusion coefficient and upwelling speed for BC6 and GC11 (Fig. 9). Reduced χ^2 values that are greater than 1.8, the 5% value, have a low probability of being the correct set of parameters that describes the observed profile. Note that a range of fluid velocities and diffusion coefficients provides a reduced χ^2 that is less than 1.8. The range of fluid velocities that fit BC6 for a particular diffusion coefficient is greater than the range calculated from fits of GC11 for the same parameters. This is a result of BC6 having only several data points in the curved section of the profile compared with thirteen points in GC11. Below the curved section of BC6, data and modeled profiles with fluid velocities greater than 1 m/y are uniform with depth. Thus, for any velocity greater than 1 m/y, reduced χ^2 values will be the same over the uniform section. These examples illustrate the uncertainty in modeling chemical profiles from areas with fluid velocities on the order of cm/y compared with larger uncertainties when estimating fluid velocities on the order of m/y. In areas with fluids upwelling at velocities greater than several m/y, a better method for estimating fluid velocities is to fit temperature profiles to advection-diffusion models.

3.2 Constraints from Temperature Profiles

Table 3 presents twenty temperature profiles taken in discrete locations. Temperature profiles are modeled with an advection-diffusion equation in one dimension:

$$D_T(\partial^2 T/\partial z^2) - v(\partial T/\partial z) = 0 \qquad (10)$$

where T is temperature (°C) and D_T is the thermal diffusivity (2×10^{-3} cm^2/s, Williams and Von Herzen, 1983). Given the following boundary conditions:

$$T = T_o \quad \text{at} \quad z = 0 \qquad (11)$$

$$T = T_{bot} \quad \text{at} \quad z = z_{bot} \qquad (12)$$

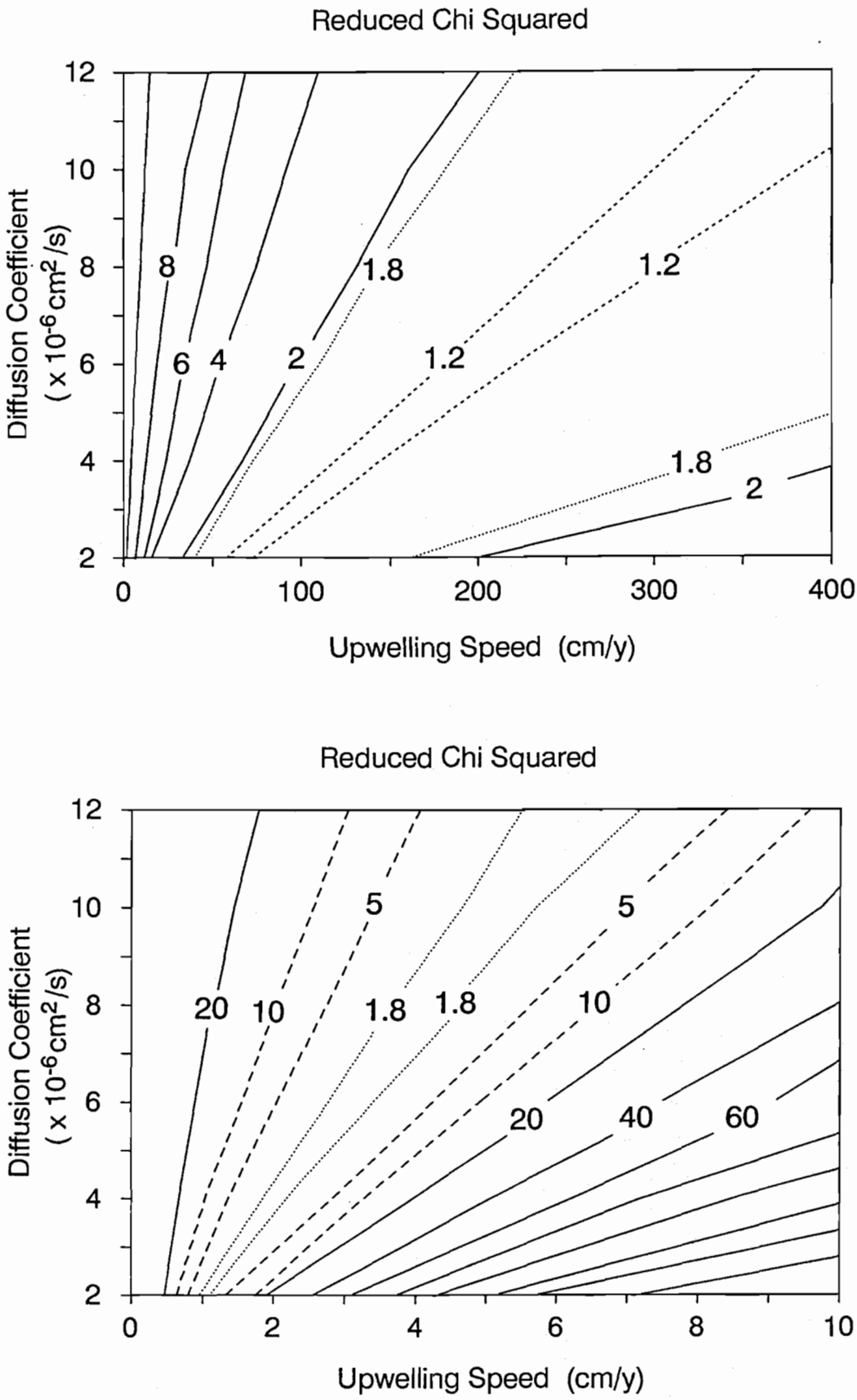

Fig. 9: Contour plots of reduced χ^2 as a function of the sediment diffusion coefficient and upwelling speed for representative cores. The 5% reduced χ^2 value is 1.8. Values greater than 1.8 represent a low probability for the given parameters to be the correct parameters for the profile, suggesting that the given parameters are inappropriate.

the solution to equation (10) is:

$$\frac{T - T_o}{T_{bot} - T_o} = \frac{1 - \exp(vz/D_T)}{1 - \exp(vz_{bot}/D_T)} \qquad (13)$$

Fluid velocities are estimated from the temperature data by minimizing the squared deviation of the data to calculations of equation (13) employing various fluid velocities (Fig. 10, Table 3). Fluid velocities listed in Table 3 are calculated with a temperature of 3.74°C in the bottom water. This temperature differs by at most 0.2°C over the area of study, as determined from temperature measurements that were made with a CTD mounted on the submersible (Appendix A). The range of fluid velocities calculated from the data is from less than several m/y to greater than 100 m/y. Uncertainties in the depth and angle of penetration, and uncertainties that result from lake water seeping into the sediments during insertion of the probe limit the precision of fluid velocities calculated from the temperature data. For example, if the depth of penetration of CD222 or CD230 is ±3 cm or the angle of penetration is 30°, the calculated fluid velocity is at most 25% different than the value listed in Table 3.

Twenty-eight temperature profiles have only one thermistor in the specific target. The highest temperature that was recorded is 18.9°C and was measured in a bacterial mat. Of the twenty-eight temperature profiles with a single measurement, eighteen were made in bacterial mats. Six of the eighteen measurements recorded temperatures greater than 10°C at a depth of less than 20 cm. Nine of the twenty-eight temperature profiles with only one temperature measurement were made in iron-manganese rich sediments. Three of these measurements are in the range of 10.5° to 11.2°C. A measurement of 6.45°C was made in a pool.

The other temperature probe was deployed for a week. An abbreviated time series record of the data is presented in Fig. 11 and listed in Table 6. For the first three days of deployment, fluctuations in the temperature of bottom water are less than 0.2°C, as recorded by the probe 5 cm above the sediment-water interface, and temperature measurements within the sediments are uniform. On the third day of deployment, higher temperature readings were recorded by the two thermistors near the sediment-water interface. These temperature changes reflect either a change in the upwelling speed or a change in the depth of penetration produced by settling of the probe.

After three days, the TTT probe was moved 30 m away to an area where higher temperatures were recorded in bottom waters and in the sediments. Temperatures were recorded at the second site for four days, during which time the three thermistors recorded temperatures that are about 0.8°C greater than temperatures recorded at the first site. The almost uniform increase in temperature of 0.8°C is not an instrument offset, because all of the thermistors measured 3.56°C in bottom water after retrieval of the instrument. Instead, the difference in the recorded temperatures is a product of the probe penetrating deeper into the sediment than planned. Assuming that the temperature of bottom waters above the probe is about 3.9°C, Table 6 lists fluid velocities that are estimated from the data by minimizing the least squared deviation to modeled profiles for various depths of penetration and fluid velocities.

4. Fluid Flow at the Sediment-Water Interface

Fluid flow at the sediment-water interface in Crater Lake is characterized by small areas with high heat flow and focused upflow, and by much larger areas with low heat flow and fluid velocities that are orders of magnitude less than velocities estimated in zones of focused upflow. Zones of

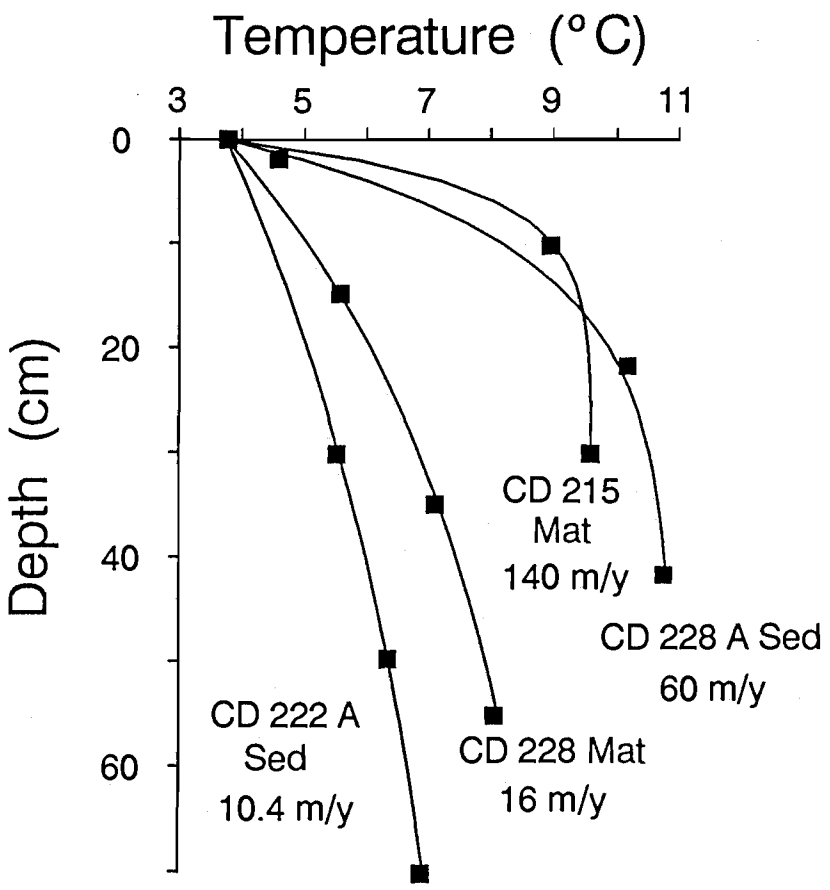

Fig. 10: Representative profiles of temperature plotted with modeled profiles. Modeled profiles are calculated from equation (13) and parameters listed in the text and in the figure.

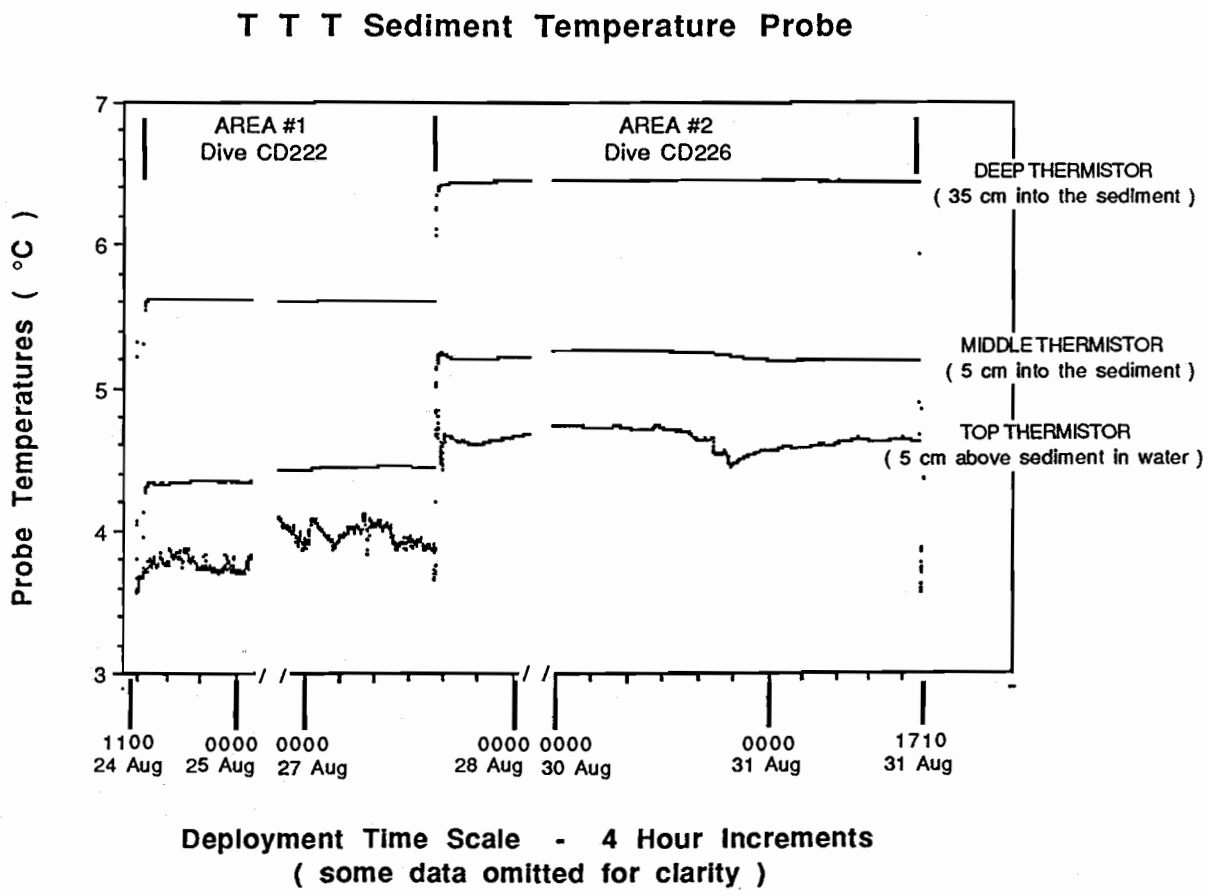

Fig. 11: Seven day time series record of the TTT temperature probe is shown. For clarity, we omitted data from 25-26 Aug. and from 28-29 Aug. 1989.

focused upflow occupy areas several m^2 to several hundreds of m^2 and are identified by iron-manganese rich crusts or by bacterial mats. Temperatures measured in zones with focused upflow and in areas with low heat flow differ by more than two times over a distance of less than 50 m. Fluid velocities also differ from less than 1 mm/y to greater than 100 m/y over a distance of 50 m. These differences are evident in velocities estimated from gravity cores, box cores, peepers, and temperature measurements that are within 40 m of one another. For example, GC13 and BC6 are located within 30 m of TTT-1, but the calculated fluid velocities differ by three orders of magnitude (Tables 3, 5, and 6). Differences between BC6 and TTT-1 may in part be due to continued diffusion and the absence of advection after BC6 was taken and before squeezing was commenced (Wheat, 1990). BC8, PD, two gravity cores (GC10 and GC14) and three heat flow measurements (CD216 sediment, CD230 mat, and CD230 pool) provide another example of a range in fluid velocities that are estimated from measurements within a radius of 50 m.

The temporal variability of fluid velocities in areas with fluid flow is evaluated from the time series data recorded by the TTT probe. The only other time series of this nature was recorded by Leinen et al., (submitted) in the Mariana Mounds, a ridge-flank hydrothermal system. Both data sets suggest that flow through the sediments is uniform for a period of at least several days. Longer deployments are required to define the time span over which variability occurs. Zones of focused upflow may be maintained for at least several years, as suggested by thriving bacterial mats observed in the same location during successive years.

The temporal variability of fluid velocities is also constrained by the chemical composition of pore fluids. Based on a 5 m sediment thickness, at least several tens of years are required for a fluid that is upwelling at a speed of 10 cm/y to establish a profile at steady state. More time is required to maintain profiles at steady state if upwelling speeds are slower than 10 cm/y or if the sediment column is deeper than 5 m. Because of the lack of data pertaining to the sediment thickness where samples were taken, the temporal variability of flow through the sediments is uncertain, but must persist for decades in areas with fluid velocities on the order of mm/y to several cm/y.

Redmond (1990) has identified the lake seepage rate to average ~1.3 m/y over the lake bottom. Of the numerous temperature profiles and cores taken in Crater Lake, only one core (GC6) has profiles of the tracer ions that are concave down, implying that lake fluids downwell in this area, or a time dependent process influences the shape of the profile. If downwelling occurs, a speed of about 1 cm/y is required for the data to fit modeled profiles. Because this core is located near other cores taken from a region with focused upflow, if fluids downwell in GC6, then these fluids are part of a local circulation cell and do not represent a pathway for mass seepage. Local circulation cells may develop from heterogeneities in lateral pressure gradients which are evident from measurements of surface heat flow (Wheat and McDuff, submitted A and B). If downwelling does not occur, then these profiles are influenced by a time dependent process that has recently increased the concentrations of dissolved species near the base of the core, presumably a result of opening and closing pathways for fluid flow.

5. CONCLUSIONS

Based on systematic variations in pore water chemical and thermal properties, evidence has been presented that supports the presence of fluid inputs to Crater Lake. These fluids issue from the lake floor at speeds of mm/y to hundreds of m/y in areas associated with iron-manganese rich crusts, bacterial mats, and pools. From extensive submersible and ROV surveys of the southern section of the south basin, most of the fluid flow from the sediments can be accounted for.

Acknowledgements

Many individuals contributed their time and effort during the field and laboratory portions of this work. The author is particularly appreciative of the generous help provided by Mark Buktenica, Jim Milestone, and the rest of the lake crew at Crater Lake National Park. Galen Whipple and Chi Meredith provided analytical assistance. The author is indebted to Russ McDuff for financial support during the field portion of this program. This research was funded by the U.S. National Park Service under cooperative agreement No. CA 9000-3-0003, CPSU, College of Forestry, Oregon State University.

6. REFERENCES

Bacon, C.R., Eruptive history of Mount Mazama and Crater Lake Caldera, Cascade Range, U.S.A., *J. Volcan. Geotherm. Res., 18,* 57-115, 1983.

Bacon, C.R., and M.A. Lamphere, The geologic setting of Crater Lake, Oregon, in *Crater Lake: An Ecosystem Study*, edited by E.T. Drake, G.L. Larson, J. Dymond, and R.W. Collier, pp. 19-27, American Association for the Advancement of Science, Pacific Division, 1990.

Barber, J.H., and C.H. Nelson, Sedimentary history of Crater Lake Caldera, Oregon, in *Crater Lake: An Ecosystem Study,* edited by E.T. Drake, G.L. Larson, J. Dymond, and R.W. Collier, pp. 29-39, American Association for the Advancement of Science, Pacific Division, 1990.

Bender, M., W. Martin, J. Hess, F. Sayles, and L. Ball, A whole core squeezer for interfacial pore water sampling, *Limnol. Oceanogr., 32,* 1214-1225, 1987.

Berner, R.A., *Early Diagenesis,* 241 pp., Princeton University Press, Princeton, NJ, 1980.

Boudreau, B.P., Asymptotic forms and solutions of the model for silica-opal diagenesis in bioturbated sediments, *J. Geophys. Res., 95,* 7367-7369, 1990.

Bredehoeft, J.D., and I.S. Papadopulos, Rates of vertical groundwater movement estimated from the earth's thermal profile, *Water Resources Research, 1,* 325-328, 1965.

Collier, R., J. Dymond, J. McManus, R. Conard, C. Meredith, and G. Wheat, Mass balances and geochemical fluxes derived from hydrothermal activity in Crater Lake, OR, *EOS Trans. AGU, 71,* 1674, 1990a.

Collier, R., J. Dymond, J. McManus, and J. Lupton, Chemical and physical properties of the water column at Crater Lake, Oregon, in *Crater Lake: An Ecosystem Study,* edited by E.T. Drake, G.L. Larson, J. Dymond, and R.W. Collier, pp. 69-79, American Association for the Advancement of Science, Pacific Division, 1990b.

Dymond J., R.W. Collier, and M.E. Watwood, Bacterial mats from Crater Lake, Oregon and their relationship to possible deep-lake hydrothermal venting, *Nature, 342,* 673-675, 1989.

Dymond, J., and R.W. Collier, The chemistry of Crater Lake sediments: Definition of sources and implications for hydrothermal activity, in *Crater Lake: An Ecosystem Study,* edited by E.T. Drake, G.L. Larson, J. Dymond, and R.W. Collier, pp. 41-60, American Association for the Advancement of Science, Pacific Division, 1990.

Leinen, M.L., R.E. McDuff, K. Becker, P. Schultheiss, K. Dadey, M. Yamano, H. Fujii, J.R. Delaney, C.G. Wheat, M. Robotham, B. Holmen, and A.E. Isley, Off-axis hydrothermal activity near the Mariana Trough spreading center, *Earth Planet. Sci. Letters,* submitted.

Li, Y.-H., and S. Gregory, Diffusion of ions in seawater and in deep-sea sediments, *Geochim. Cosmochim. Acta, 38,* 703-714, 1974.

McBirney, A.R., Compositional variations of the climatic eruption of Mount Mazama, in *Andesite Conference Guide Book*, edited by H.M. Dole, pp. 53-56, Oregon Dep. Geo. Mineral. Ind. Bull., 62, 1968.

McManus, J., R. Collier, and J. Dymond, Heat and salt flux in Crater Lake, OR as deduced from water column CTD measurements, *EOS Trans. AGU, 71,* 1674, 1990.

Nathenson, M., Chemical balance for the major elements in water in Crater Lake, Oregon, in

Crater Lake: An Ecosystem Study, edited by E.T. Drake, G.L. Larson, J. Dymond, and R.W. Collier, pp. 103-114, American Association for the Advancement of Science, Pacific Division, 1990.

Parsons, T.R., Y. Maita, and C.M. Lalli, *A Manual of Chemical and Biological Methods for Seawater Analysis*, 173 pp., Pergamon Press, New York, 1984.

Phillips, K.N., Hydrology of Crater, East, and Davis Lakes, Oregon, *U.S. Geol. Surv. Water-Supply Pap., 1859-E,* 66 pp., 1968.

Reilly, J., *A chemical mass balance of Crater Lake, Oregon,* Masters Thesis, Oregon State University, 1989.

Redmond, K.T., Crater Lake climate and lake level variability, in *Crater Lake: An Ecosystem Study,* edited by E.T. Drake, G.L. Larson, J. Dymond, and R.W. Collier, pp. 127-141, American Association for the Advancement of Science, Pacific Division, 1990.

Schink, D.R., N.L. Guinasso, and K.A. Fanning, Processes affecting the concentration of silica at the sediment-water interface of the Atlantic Ocean, *J. Geophys. Res., 80,* 3013-3031, 1975.

Simpson, H.J., *Closed basin lakes as a tool in geochemistry*, 325 pp., Ph.D. Dissertation, Columbia University, 1970a.

Simpson, H.J., Tridium in Crater Lake, Oregon, *J. Geophys. Res, 75,* 5195-5207, 1970b.

Van Denburg, A.S., Chemistry of the lakes, in *Hydrology of Crater, East, and Davis Lakes, Oregon,* edited by K.N. Phillips, pp. 41-45, U.S. Geological Survey, 1968.

Wheat, C.G., *Fluid circulation and diagenesis in an off-axis hydrothermal system: The Mariana Mounds,* 204 pp., Ph.D. Thesis, University of Washington, Seattle, WA, 1990.

Wheat, C.G., and R.E. McDuff, Mapping the fluid flow of the Mariana Mounds off-axis hydrothermal system: Power water chemical tracers, *Earth Planet. Sci. Lett.*, submitted A.

Wheat, C.G., and R.E. McDuff, Hydrothermal flow through the Mariana Mounds: Dissolution of amorphous silica and degradation of organic matter on a mid-ocean ridge flank, *Geochim. Cosmochim. Acta,* submitted B.

Williams, D.L., and R.P. Von Herzen, On the terrestrial heat flow and physical limnology of Crater Lake, Oregon, *J. Geophys. Res., 88,* 1094-1104, 1983.

Appendix G Deep water renewal rates in Crater Lake deduced from the distribution of anthropogenic chlorofluoromethanes (freons).

This appendix presents a brief summary of preliminary results from a study carried out by the laboratory of Dr. R. F. Weiss[1] in cooperation with our hydrothermal project. The study involves the determination by electron capture gas chromatography (Bullister and Weiss, 1988) of concentrations of anthropogenic chlorofluorocarbons ("Freons" or CFCs) dissolved in the deep lake which are then used to estimate the deep water renewal rate within the lake. Weiss and coworkers have used the distributions of these CFCs as time- dependent tracers of atmospheric exchange and vertical mixing rates in the oceans and in Lake Baikal (Bullister and Weiss, 1983; Weiss et al., 1985; Weiss et al., submitted). A complete discussion of the CFC results for Crater Lake will be published by Weiss and coworkers. A preliminary discussion is presented here because knowledge of the deep water renewal (or "ventilation") rate is a critical element in the estimation of the input rate of hydrothermal materials. The results of this study provide an unambiguous answer to this question.

The chlorofluorocarbons which were measured in Crater Lake, CCl_3F (CFC-11) and CCl_2F_2 (CFC-12), are distributed relatively homogeneously in the troposphere and are chemically stable in natural waters. The global atmospheric concentrations of these industrially produced compounds have roughly doubled over the past 1.5 decades and the time histories of these increases are relatively well documented (Weiss et al., 1985; Fine et al., 1988; Figure 1). The concentrations of these compounds in equilibrated surface waters are proportional to their known solubilities and to their current atmospheric concentrations (Henry's Law). Therefore, a water parcel leaving the surface due to convective overturn carries with it a signature of the time-dependent atmospheric CFC composition. Weiss et al. (submitted) have discussed models for the various mixing and diffusive processes which affect the concentrations of these tracers after they leave the surface in deep temperate lakes. In the following discussions, we approximate the mean mixing "CFC age" represented by the measured deep water CFC concentrations as equivalent to the age of the deep mixed layer source waters which had the same CFC concentrations.

The vertical profiles of CFC-11 and CFC-12 measured in August, 1989 are shown in Figure 2. In Crater Lake, roughly the upper 200 m is subject to complete convective and turbulent mixing every autumn and spring (see Appendix A). This deep mixed layer (at ~3.8 °C) is homogeneous in CFCs, as can be seen in Figure 2 at the top of each profile, and its CFC concentrations follow the atmospheric CFC increases over time. In Figure 2 the surface water points are off scale (low) due to reequilibration of the warm seasonal thermocline (CFC solubilities are lower at higher temperatures). The decrease below the deep mixed layer (i.e. below ~200 m) reflects the decreasing rate of deep water renewal with increasing depth. The volume-weighted mean CFC concentrations below this depth correspond to mean deep water renewal time of 2.1 years based on CFC-11, or 1.5 years based on CFC-12, for an average value of 1.8 years. Given a mean depth of the water column below the surface mixed layer of 213 meters, this mean renewal time results in an effective vertical exchange rate of 120 meters/year. The "oldest" or least-ventilated waters are found at the bottoms of the two deep basins. A maximum CFC age of about 3.2 years is found at the deepest point in the lake, at the bottom of the East (North) Basin.

In this report, and in our previous reports (Collier and Dymond, 1988; Collier and Dymond, 1989) we have used an approximate mean deep water renewal time of 2 years, which we derived from the tritium work of Simpson (1970). The CFC data confirm this choice and clearly determine the rapid vertical mixing rate against which all deep water concentration anomalies must be compared to obtain deep water hydrothermal, chemical and biogenic fluxes. In association with the CFC experiment, Dr. J. Lupton, UCSB, collected samples for the analysis of tritium and its radioactive decay daughter product helium-3. The results of these time-dependent tracer measurements will complement the CFC results and lead to a more quantitative determination of hydrothermal fluxes in Crater Lake.

---

[1] R.F. Weiss, Scripps Institution of Oceanography, University of California, San Diego, La Jolla, CA 92093-0220. Any reference to, or other use of these unpublished data should be referred to Dr. Weiss.

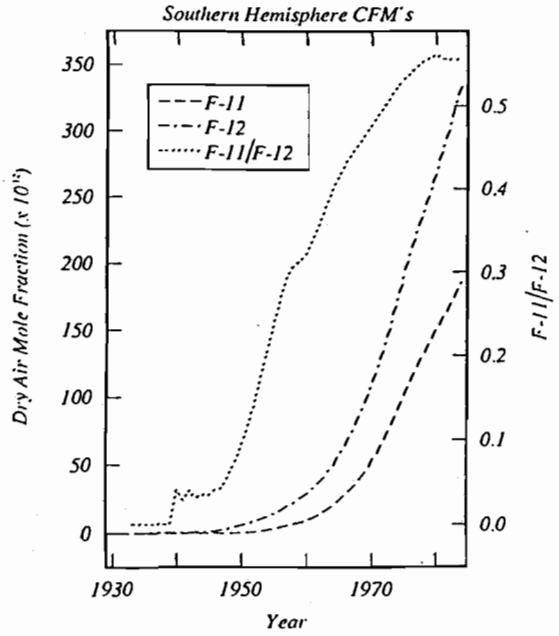

Figure 1. Dry air mole fractions of F-11 and F-12 (dashed curves) and the ratio of F-11/F-12 (dotted curve) in the atmosphere vs time in years.

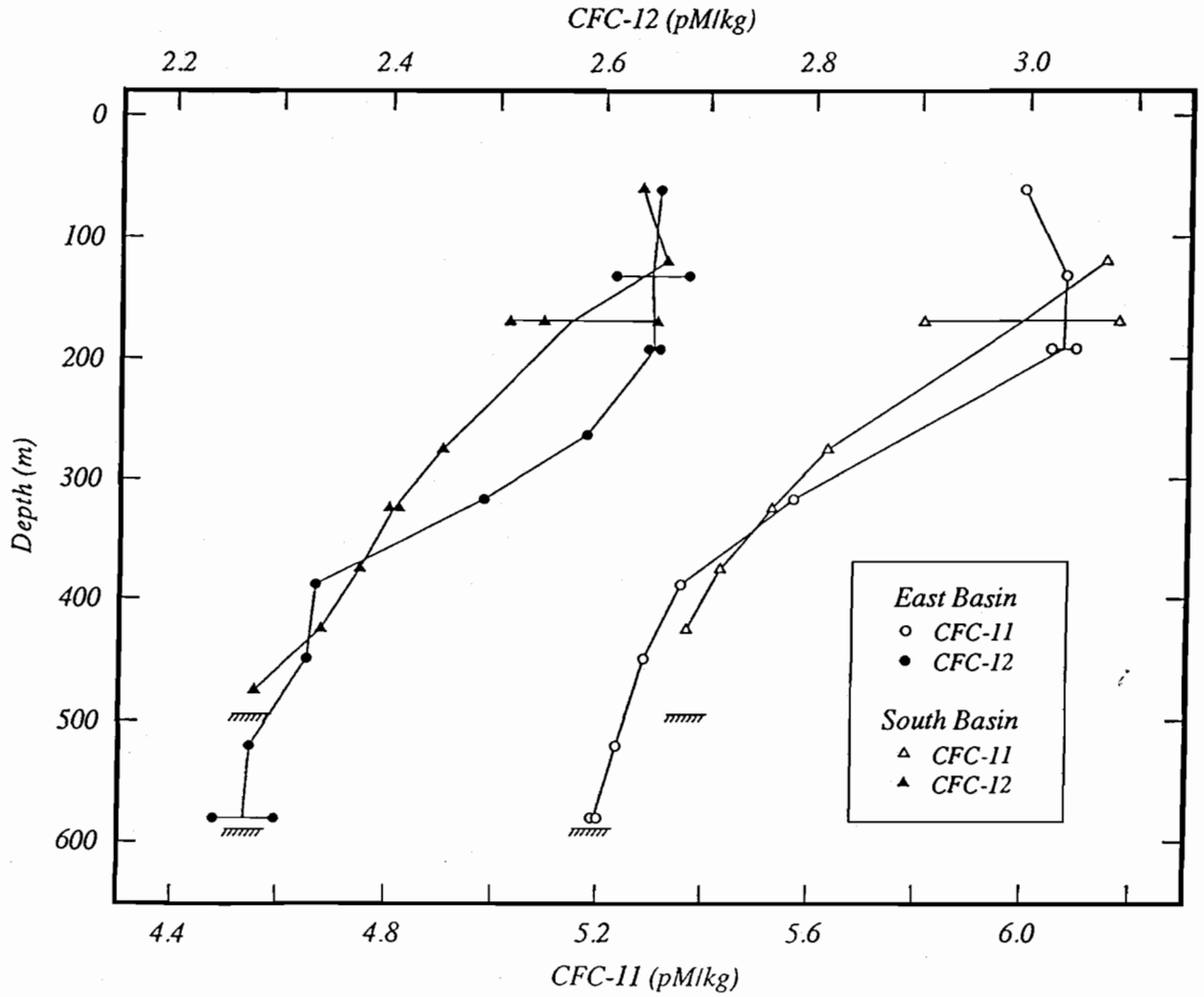

Figure 2. Vertical profiles of CFC-11 and CFC-12 in Crater Lake (August, 1989)

Appendix H. Submersible Locations and Dive Summaries

Table H1: 1987 ROV and 1988, 1989 Crater Lake Submersible Dive Summary

ROV #	Date	Location
1	8/10/87	Dacite Dome
2	8/10/87	Wizard Platform
3	8/11/87	Study Area
4	8/12/87	Study Area
5	8/13/87	Miriam Cone
6	8/13/87	Study Area
7	8/15/87	Study Area

Dive #	Date	Can-Dive #	Pilot	Location	Purpose
1	8/3/88	167	Fuzessery	S.of Wizard Is.	Systems Check
2	8/4/88	168	Dymond	Dacite Dome	Training
3	8/4/88	169	Collier	Wizard Platform	Training
4	8/5/88	170	Dymond	Study Area	Hydrothermal
5	8/6/88	171	Collier	Study Area	Hydrothermal
6	8/7/88	172	Buktenica	Eagle Point	Training/Biology
7	8/8/88	173	Dymond	Study Area	Hydrothermal
8	8/9/88	174	Collier	SW Miriam Cone	USGS
9	8/10/88	175	Dymond	N.Wizard Plat.	USGS
10	8/11/88	176	Buktenica	Eagle Pt.	USGS
11	8/12/88	177	Collier	Study Area	Hydrothermal
12	8/13/88	178	Dymond	Study Area	Hydrothermal
13	8/14/88	179	Collier	Study Area	Hydrothermal
14	8/17/88	180	Hawkes	Pumice Pt.	Systems Check
15	8/17/88	181	Earle	Palisades Pt.	Biology
16	8/18/88	182	Dymond	Study Area	Hydrothermal
17	8/19/88	183	Collier	Study Area	Hydrothermal
18	8/20/88	184	Dymond	Study Area	Hydrothermal
19	8/21/88	185	Buktenica	E.Wizard Plat.	USGS
20	8/22/88	186	Collier	Study Area	Hydrothermal
21	8/23/88	187	Dymond	Study Area	Hydrothermal
1	8/5/89	205	Robison		Training
2	8/5/89	206	Collier		Training
3	8/6/89	207	Collier	Study Area	Hydrothermal
4	8/7/89	208	Buktenica	Eagle Point	USGS
5	8/8/89	209	Dymond		Training
6	8/9/89	210	Buktenica	Llao Rock	USGS
7	8/10/89	211	Dymond	Study Area	Hydrothermal
8	8/11/89	212	Buktenica	Palisades Pt.	USGS
9	8/12/89	213	Collier	Skell Head	USGS
10	8/13/89	214	Buktenica	Sentinal Rock	USGS
11	8/14/89	215	Dymond	Study Area	Hydrothermal
12	8/15/89	216	Collier	Study Area	Hydrothermal
13	8/16/89	217	Dymond	Study Area	Hydrothermal
14	8/19/89	218	Collier	Study Area	Hydrothermal
15	8/20/89	219	Buktenica	S. of Wizard Is.	Biology
16	8/21/89	220	Dymond	Study Area	Hydrothermal
17	8/23/89	221	Robison	S. of Wizard Is.	Biology
18	8/24/89	222	Collier	Study Area	Hydrothermal
19	8/25/89	223	Dymond	Study Area	Hydrothermal
20	8/26/89	224	Buktenica	Skell Cove	Biology
21	8/26/89	225	Earle	S. of Wizard Is.	Biology
22	8/27/89	226	Collier	Study Area	Hydrothermal
23	8/28/89	227	Buktenica	Palisades Pt.	Biology
24	8/29/89	228	Dymond	NE Basin	Hydrothermal
25	8/30/89	229	Collier	Study Area	Hydrothermal
26	8/31/89	230	Dymond	Study Area	Hydrothermal

CD207

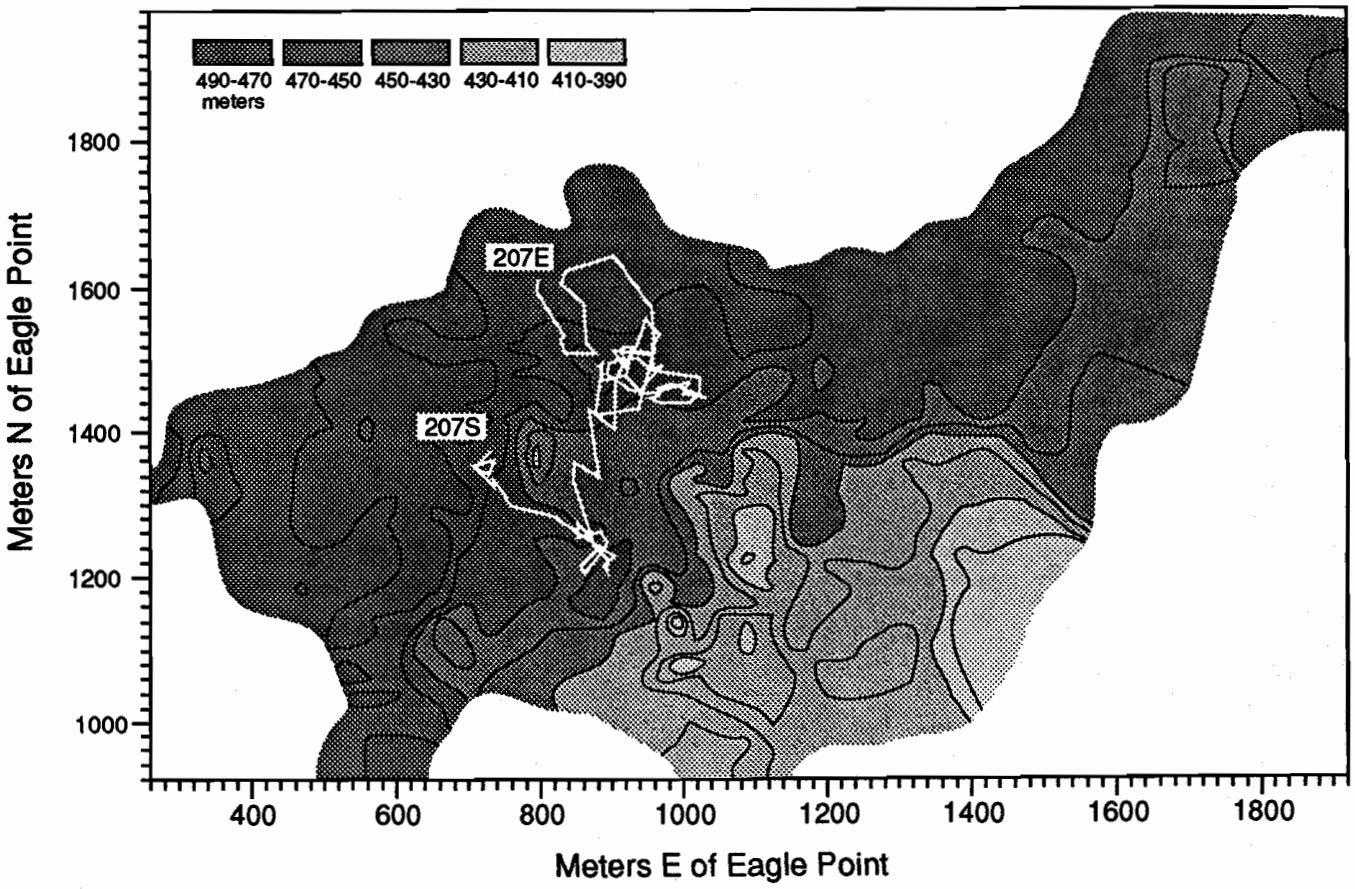

CD207

Pilot: Collier
Purpose: Hydrothermal
Location: Detailed study area

The dive began at x= 740, y = 1370. Proceeded southeast for approximately 100 meters where a box core was taken near mottled sediments. Observed bacterial mats on this track. After the core, traveled north 250m to the major bacterial mats that were discovered during CD179 in 1988. Made temperature measurements and took water samples at the 179 mats.

Samples collected:	1BC (x=860, y=1260)
	S1 between 1BC and CD179 site (x=950, y=1550)
	S2 at 179 mat
	S3 base of slope at 179 mat
Temperature probes:	at center of top mat (Tmax =10.0)
	in sediments above the mat (Tmax = 6.7)
	in sediments below the mat (Tmax = 4.38)
Markers Deployed:	#1 at 1BC
	#2 bottom of slope at CD179 mat (x=865, y=1570)

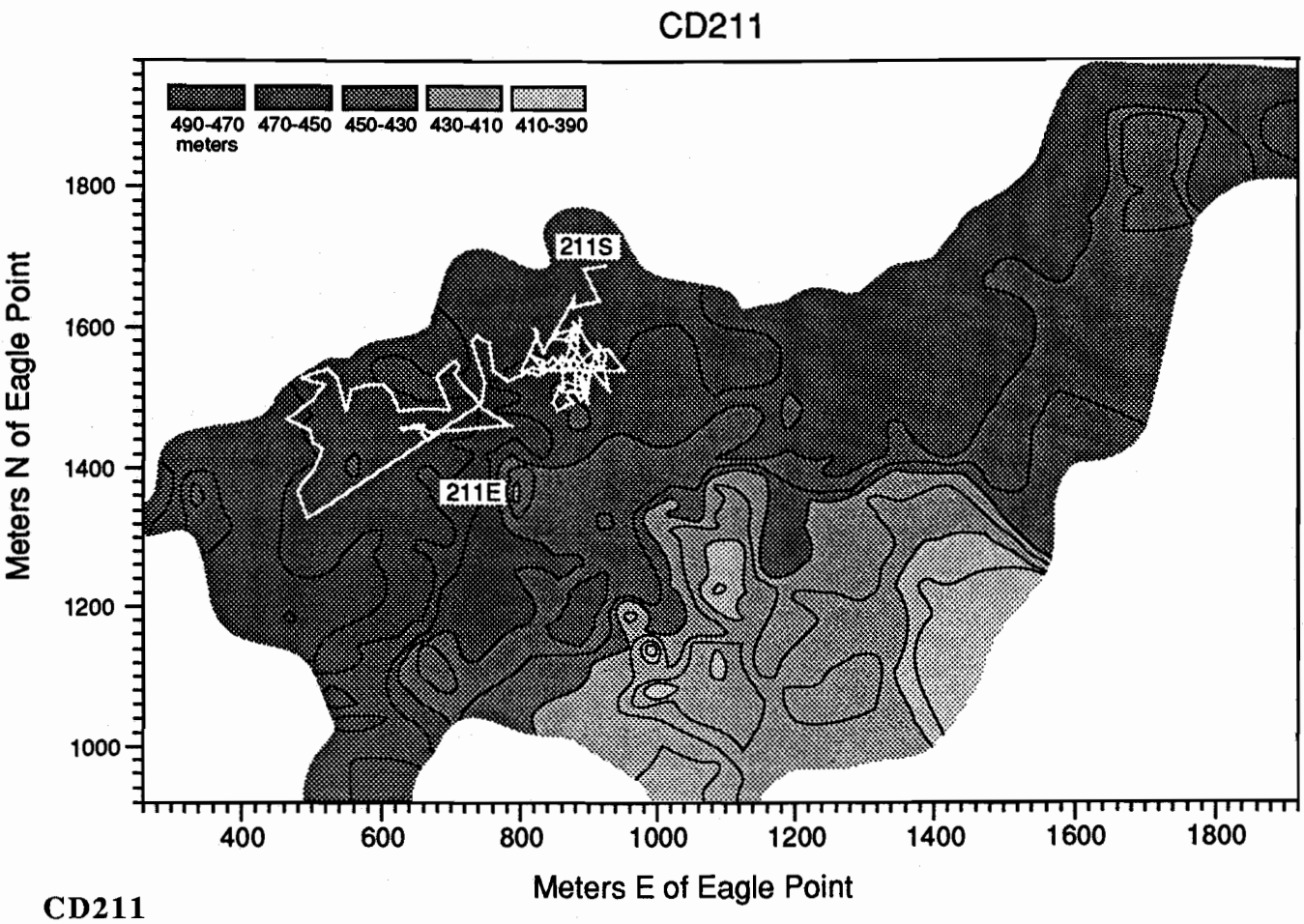

CD211

Pilot: Dymond
Purpose: Hydrothermal
Location: Detailed study area

The dive began at x = 940; y = 1690; depth = 1490 feet; near the CD 179 mats. Took box core (3BC) at the base of the slope near a mat feature on the bottom. Measured temperatures at BC site (4.18 °C). Deployed peeper in CD 179 mats (F). Took water sample (S3) near marker #2. Headed west for surveying. Surveyed on a zig-zag pattern in a southwestern direction. Discovered Llao's Bath about 300 meters from CD 179 mats. Surveyed the bath, took water samples (S1 and S2) above the pool, made temperature probe measurements of the pool (4.45 °C) and in sediments next to pool (4.35 °C). Deployed marker #4, SE of pool.

Samples Collected:	3BC (x=890, y=1550)
	S1 (Llao's Bath, x=625, y=1430)
	S2 (Llao's Bath)
	S3 (CD 179 mat)
Peepers Deployed	F (CD 179 mat)
Markers Deployed	#4

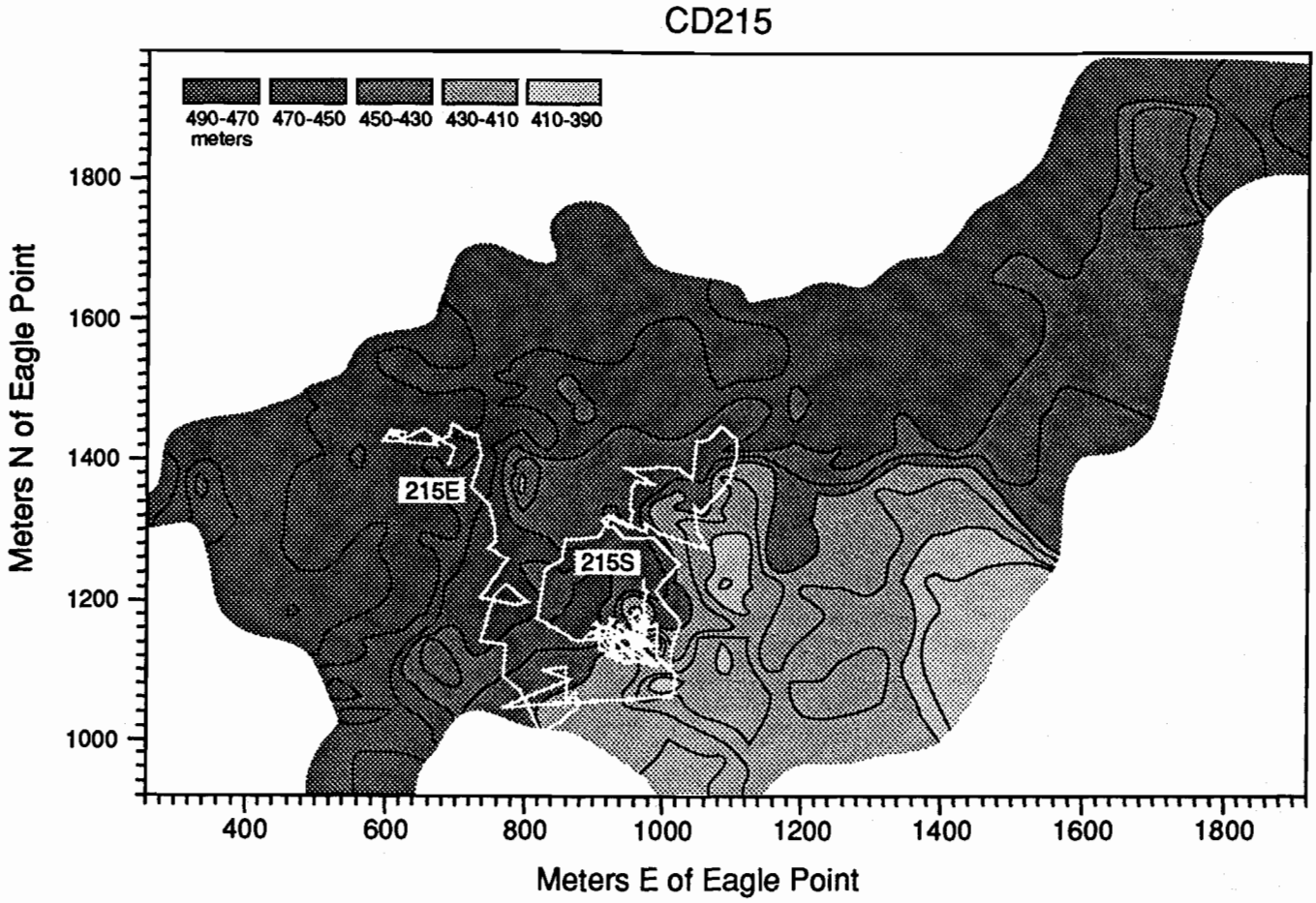

CD215

Pilot: Dymond
Purpose: Hydrothermal
Location: Detailed Study Area

Dive began at x = 980; y = 1200; depth = 1451 feet. Headed southwest. and then northwest. Observed mottled sediments. Many bacterial mats along cliff. Took water sample S1 in a bacterial mat. Temperature probe in the mat revealed 11.6 °C Tmax. Surveyed south and then northwest to Llao's Bath. Collected rock from an altered outcrop enroute to Bath. Circled around to the west side of Bath, observed small pools and mats. Observed brain mat and many small pools. Took water sample S2 in the brain mat area.

Samples Collected: S1 (high temperature mats on cliff, x=950, y=1150)
S2 (brain mat, x=615, y=1435)
1 rock

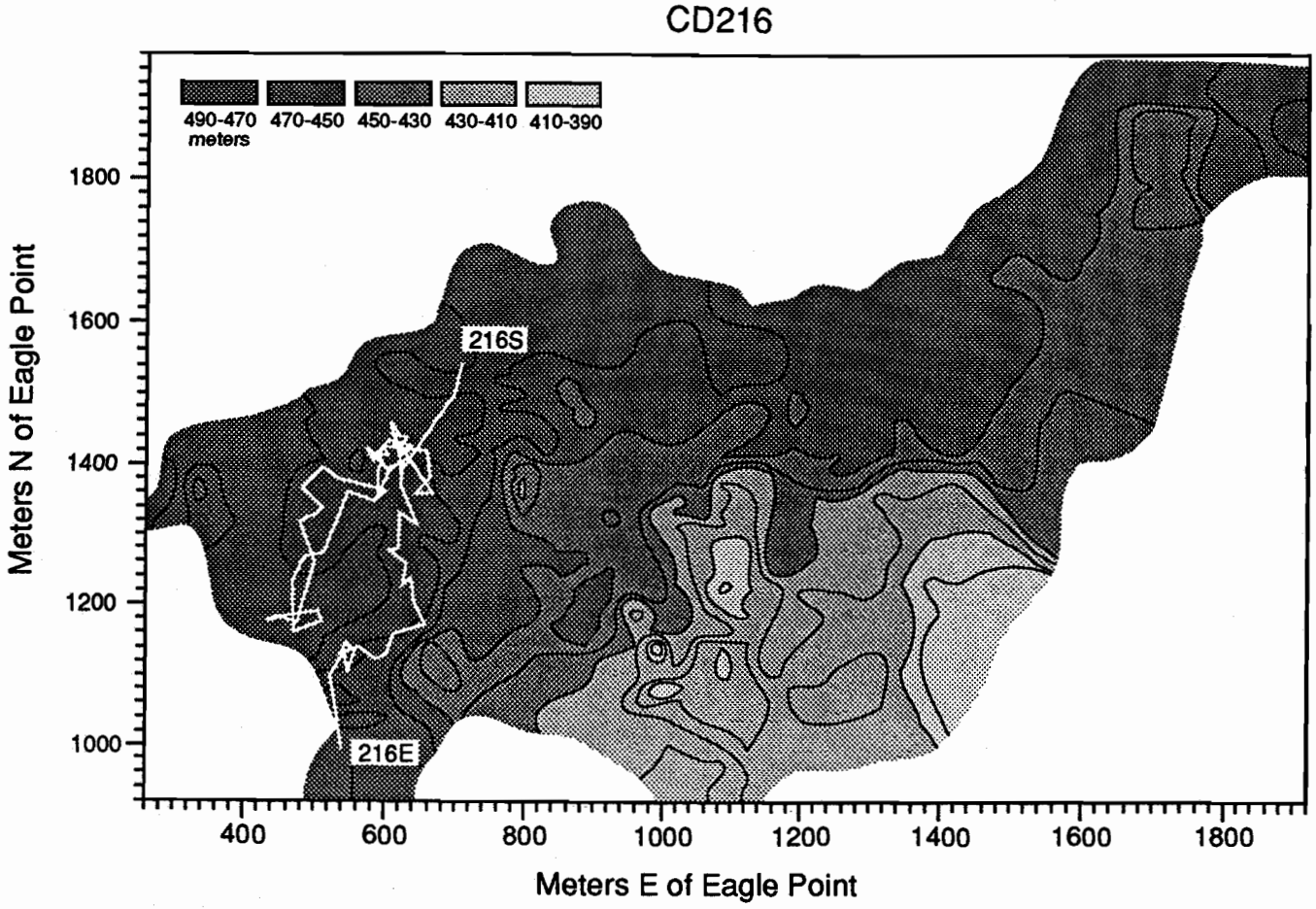

CD216

Pilot: Collier
Purpose: Hydrothermal
Location: Detailed Study Area

Dive began near Llao's Bath; depth = 1520 feet. Explored around Llao's Bath. Discovered a bath much larger than Llao's Bath and took a core (5BC in the pool). Took water and bacteria sample in brain mat. (S3). Temperature probing in the mat (Tmax = 4.54 °C). Took water sample at the brain mat (S1). Deployed peeper in Llao's Bath. Headed south from Llao's Bath for about 400 meters. Noted small bacterial mats on slope. Mats on the wall similar to the CD179 mats. Tmax in these mats was 6.85 °C with 7.2 °C in an adjacent metalliferous outcrop. Saw mottled sediments and additional mats a little farther south. Took water sample (S2) at end of dive.

Samples Collected:	S1 (brain mat + sediments)
	S2 (near southern mats, x=540, y=990)
	S3 (brain mat)
	5BC (bulk sample only, in large pool near Llao's bath)
Peeper deployed:	C (Llao's Bath)

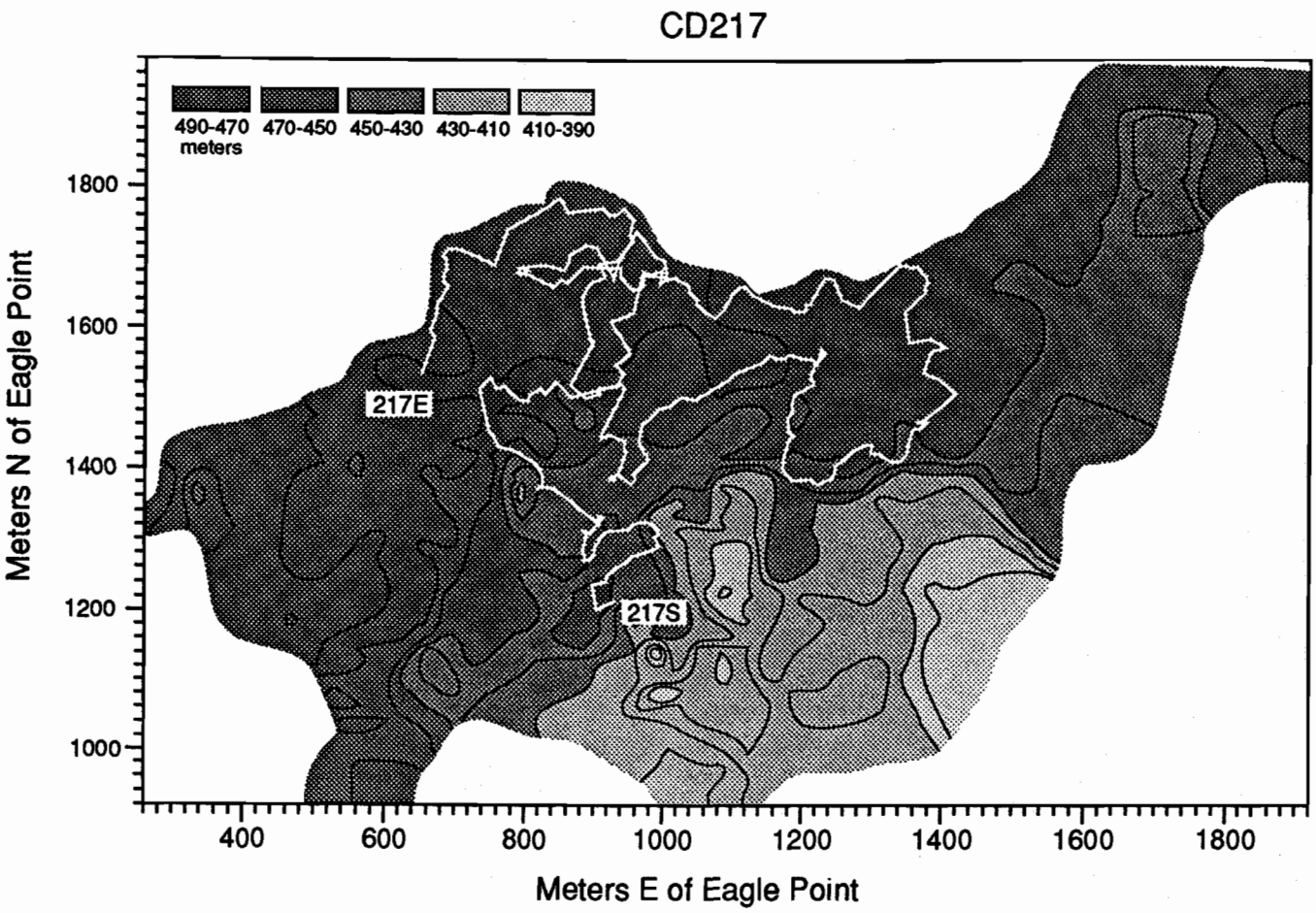

CD217

Pilot: Dymond
Purpose: Hydrothermal
Location: Detailed Study Area

A major goal of the dive was to deploy the benthic barrel in an area of mottled sediments. The dive began at x = 900, y=1235; depth = 1466 feet. Benthic barrel was deployed early in the dive on mottled sediments. Water sample was taken at barrel site (S2). Measured temperature of the sediments; Tmax = 5.68 °C. From the BB headed northwest for about 300m; then turned and headed east. Noted bacterial mats on this course and mottled sediments. Stayed on a generally easterly course for 650 meters. S1 bottle accidentally tripped in the basket during transect. Changed to northerly course. Noted mottled sediments. Changed to a westerly course; bottom water temperatures of 3.78 °C. Took water sample (S3) and made temperature probes in sediment (Tmax = 4.08 °C). Ended the dive with surveying to the north and west.

Samples Collected:	S1 (tripped in basket)
	S2 (at benthic barrel)
	S3 (general area of warmer water, x=1030, y=1660)
Sampler deployed:	Benthic Barrel (x=910, y=1210)

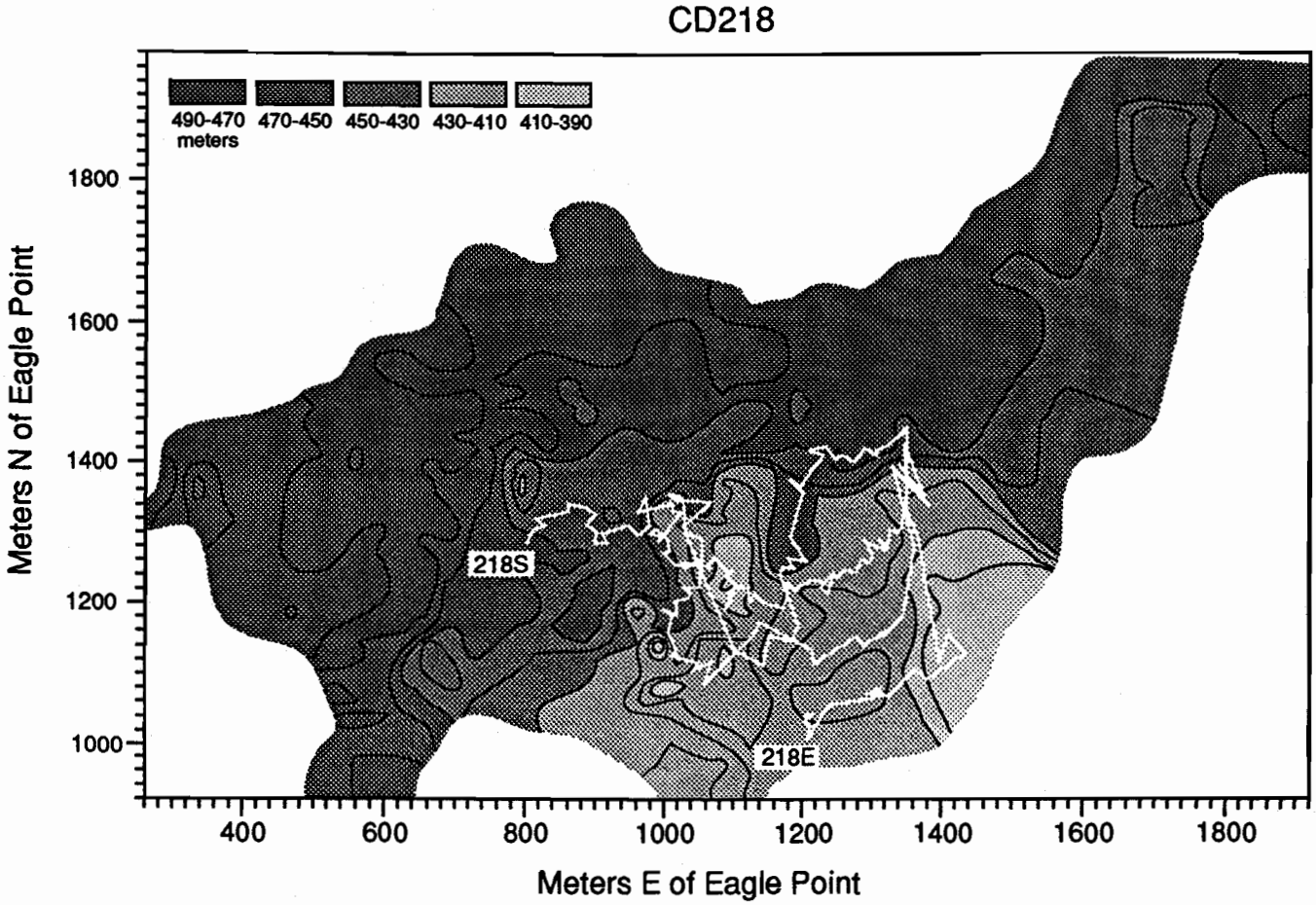

CD218

Pilot: Collier
Purpose: Hydrothermal
Location: Detailed Study Area

The purpose of the dive was to collect a box core at the benthic barrel site and conduct some general surveying for additional venting sites. Sub on the bottom at x = 800; y = 1270; depth = 1448 feet. Headed east to the benthic barrel where 6BC was taken. Deployed peeper (B) next to the barrel. Continued east. Observed the basketball mat and collected mat material and water sample (S1). Observed a linear feature that extended many ten's of meters; it may be an old vehicle track. Traveled 400 m east and changed course to ~010 ° for 250 meters. Changed course to 250 ° toward the general area that the dive began. Moving along slope found a number of bacterial mats and made temperature probes in them. Tmax = 16.1 °C. Tprobe in adjacent sediments = 8.6 °C. Deployed marker #3 near the 16.1 °C mats.

Samples Collected:	S1 (basketball mat, x=1015, y=1340)
	S2 (near the basketball (3.72 °C)
	6BC (next to barrel, x=910, y=1210)
Peepers Deployed	B (next to barrel)
Markers Deployed	#3 (x=1025, y=1360)

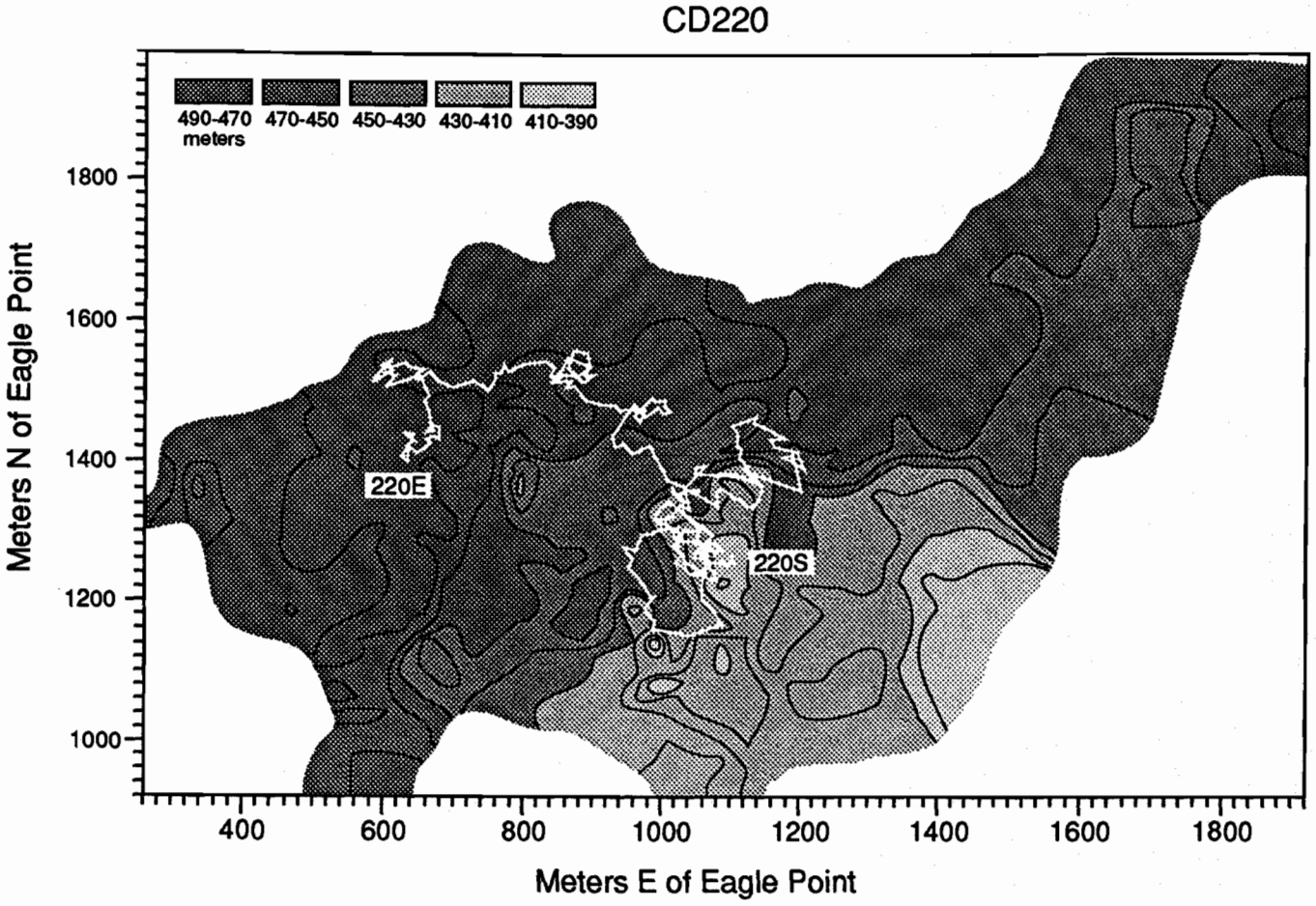

CD220

Pilot: Dymond
Purpose: Hydrothermal
Location: Detailed Study Area

The purpose of the dive was to collect a box core at the high temperature mat site, collect further samples at the CD179 mat site and deploy a peeper near Llao's Bath. Sub on the bottom at x = 1100; y = 1260; depth = 1340 feet. Headed west ~70m, stopped to probe a small mat (Tmax=7.5°) Continued west into mottled sediments. Changed course to east to go to high temperature mat area. Observed marker #3 and dropped corer. Corer caught on sub, no core. Continued southwest ~20m and probed a mat (Tmax=17.7°). Collected mat material and water sample (S2). Observed small stalagtites..Traveled 200m northeast to CD179 mat area observing mottled sediments along the way. Tripped S1 in mat. Headed southeasterly ~180 m to Llao's bath. Continue counterclockwise around pool. Deploy peeper A into bacterial mat next to a pool. Deployed Marker #5.

Samples Collected:	S1 (mat at CD179)
	S2 (at 17.7° mat, x=1030, y=1340)
Peepers Deployed	A (in mat)
Markers Deployed	#5, #11 (from surface boat, in Llao's Bath area)

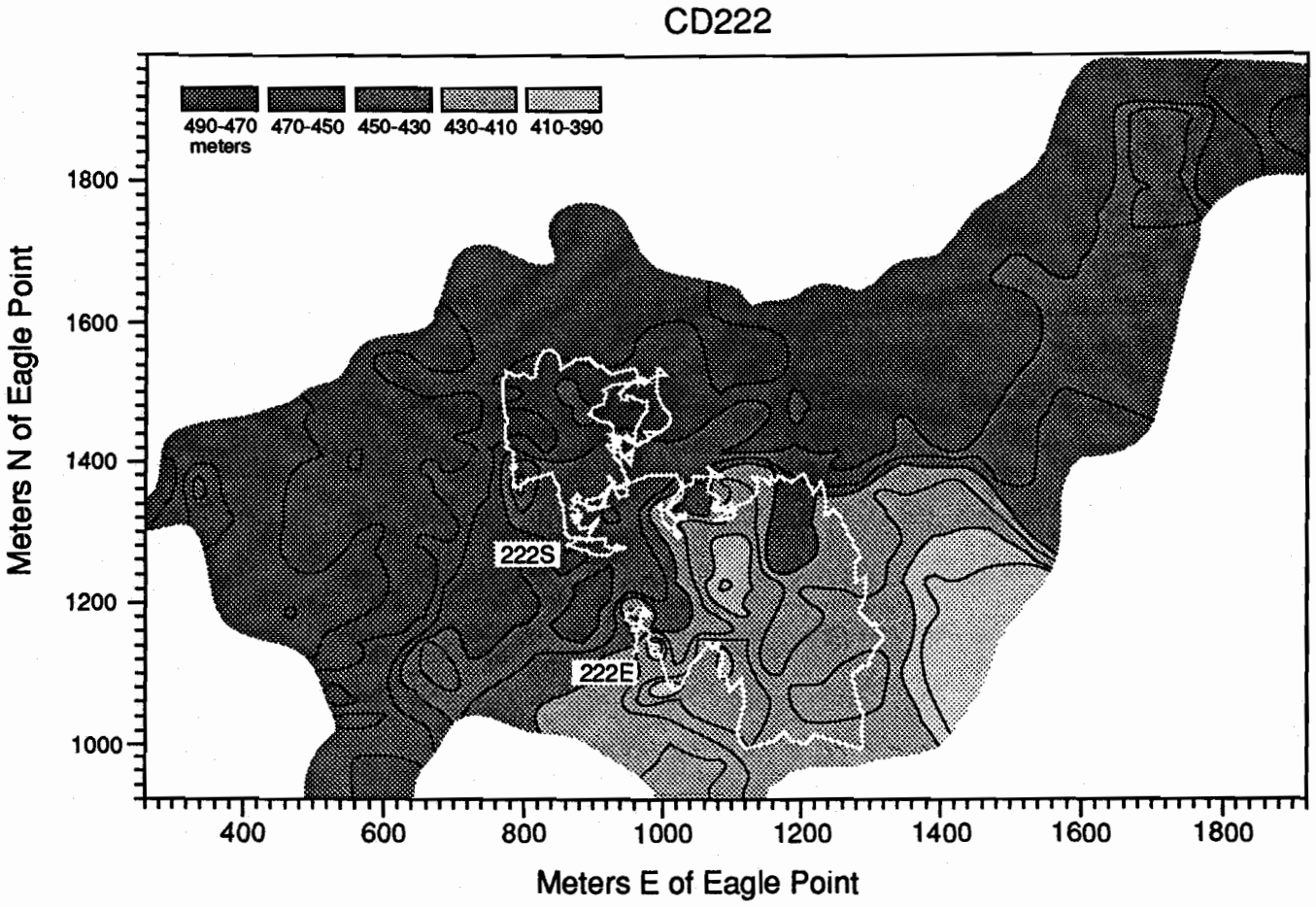

CD222

Pilot: Collier
Purpose: Hydrothermal
Location: Detailed Study Area

A major purpose of the dive was to deploy the TTT at the Benthic Barrel site. On bottom (x=860, y=1310, depth=405m). Started east ~20m, observed marker #12, then marker #13, ~30m further east to barrel. Deployed TTT ~20 feet east of Barrel. Do a general survey: head northeast ~300m, then east ~200m. Trip S2 in 3.80° water. Head south ~100m, observe mottled sediments, change to northwest direction for ~100m, east ~80m, south ~80m. T=3.82°, drop corer. T-probe in sediments (Tmax=5.33°). Continued south ~80m into very mottled sediments, take T-probe measurements in sediment (Tmax=6.92°), deploy peeper and marker. Head east 150m to high temperature mat area. Sample mat (S1) and T-probe in sediment (Tmax=11.2°). Continue survey northeast ~60m, east 150m, south 350m, and west 350m, observing several mats (Tmax=7.9°)

Samples Collected:	S2 (3.80° water, x=945, y=1495)
	S1 (mat near 11.2° sediment, x=1020, y=1350)
	7BC (mottled sediments, x=980, y=1430)
Peepers Deployed	E (mottled sediments)
Sampler Deployed	TTT (at Benthic Barrel site)
Markers Deployed	#6 (x=915, 1360),
	#12, #13 (deployed from boat near Benthic Barrel)

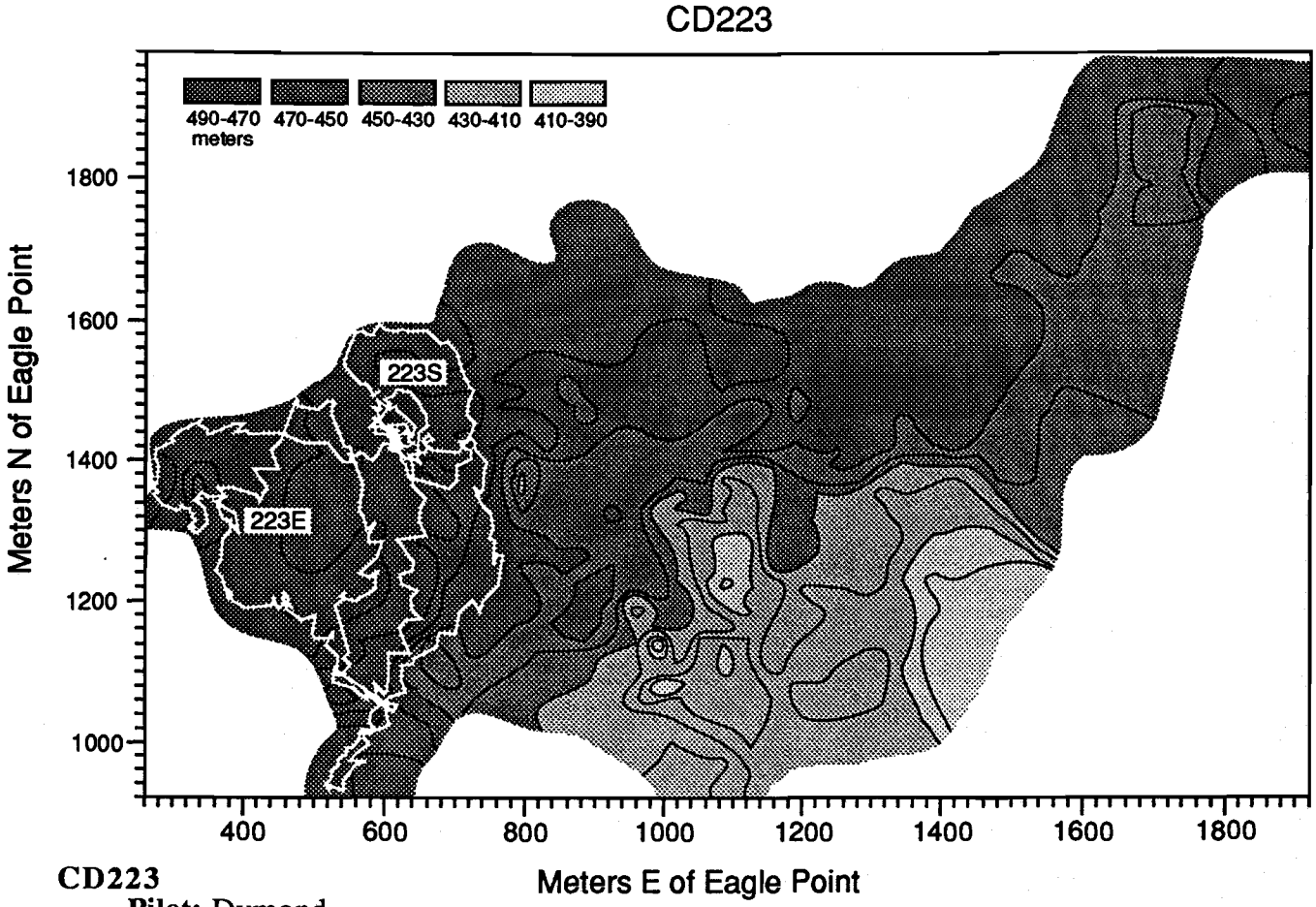

CD223

Pilot: Dymond
Purpose: Hydrothermal
Location: Detailed Study Area

The purpose of the dive was to collect samples from the Llao's Bath area and conduct some general surveying to the south and west for additional venting sites. Sub on the bottom at x = 590; y = 1500; depth = 1532 feet. Headed east toward pools, looped around south observing mat on cliff face (mat Tmax=5.75°, sediment Tmax=4.52°) then northwest to Llao's Bath . Circled around Llao's Bath clockwise, observing peepers set from previous dives. Deployed corer in mat-sediment area west of Llao's Bath. Returned to Llao's Bath observing that all pools now have debris settled on them. Sampled Llao's Bath (S1). Deployed peeper into a bacterial mat, clockwise from marker #4. Started survey, west ~400m, south 100m, east 100m. Observed laminated sediments, too soft to sample. Continued northeast ~250m. then south ~300m to discover "little pools" (in sediment, Tmax=4.24°) Took water sample (S2) and deployed marker #7. Continued south ~150m through mottled sediments and old pool features. Found small pool with bacterial mat around it. Surveyed south another 200m, then northeast 400m (observe mottled sediments), north ~150m. Tripped sample S3 above small mat and pool. (Llao's bath is <50m west of here). Surveyed south 350m. Sampled a short thick stalagmite (termed "elephant's foot"). Headed northeast ~250m to end dive. The CTD failed to collect any data other than the last 1.5 hour of the dive.

Samples Collected:	S1 (in Lao's Bath)
	S2 (little pools, x=540, y=1210)
	S3 (mat and pool east of Llao's Bath, x=660, y=1425)
	8BC (x=610, y=1445)
	Crust ("elephant's foot", x=600, y=1060)
Peepers Deployed	D (in mat near Llao's Bath)
Markers Deployed	#7 (x=540, y=1210)

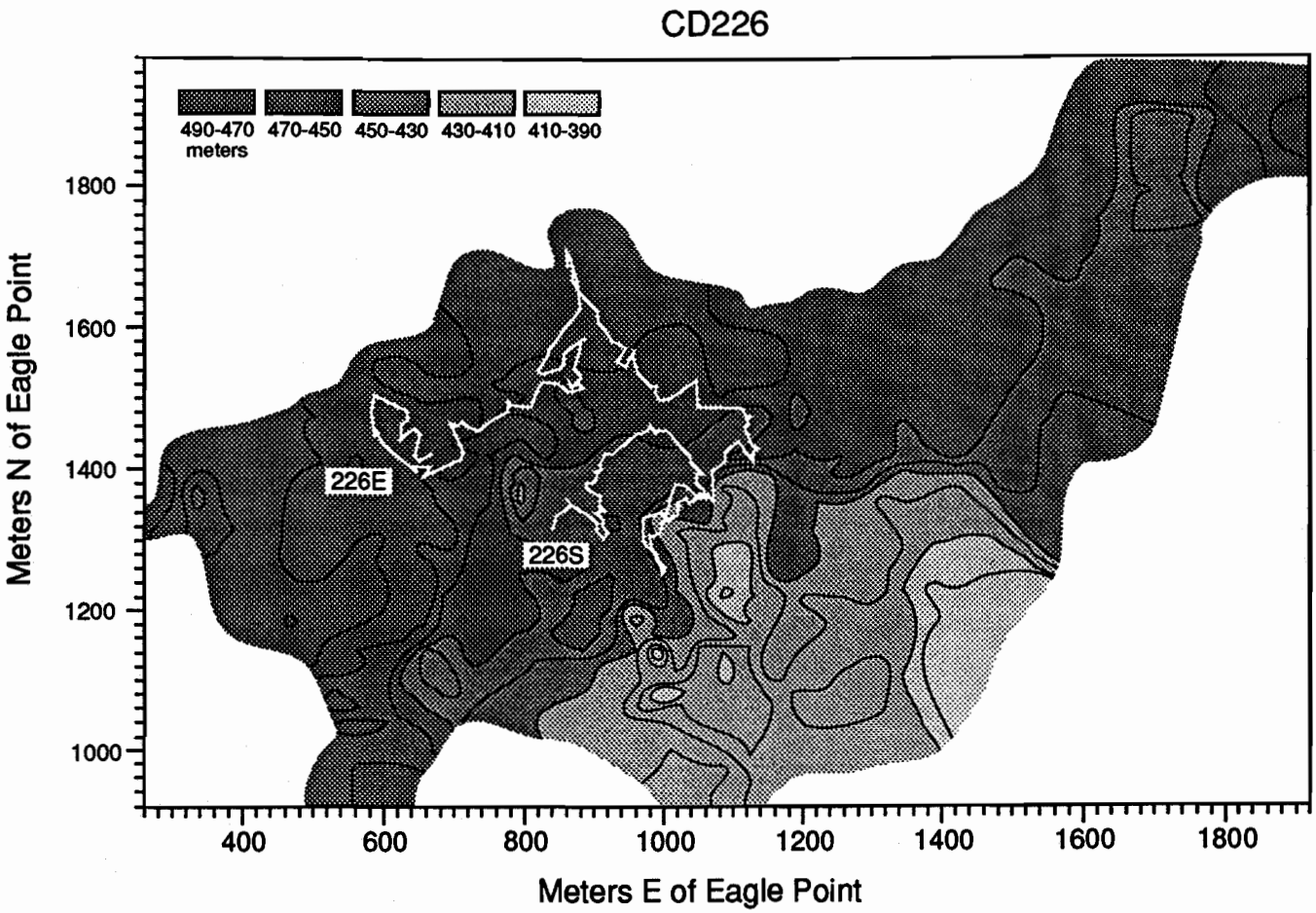

CD226

Pilot: Collier
Purpose: Hydrothermal
Location: Detailed Study Area

A major purpose of the dive was to remove the TTT from the barrel site and redeploy it at the warm mottled sediment area. (Start x=840, y=1315, depth=1470 feet) Went east ~70m to the Benthic Barrel site. Picked up the TTT, moved north ~70m to marker #6 and redeployed TTT. Deployed box corer. Continued ~125m east to marker #3, the high temperature mat area. Followed contour on slope generally southwest, observing bacterial mats and taking T-probe measurements (mat Tmax=13.6°, sediment Tmax=10.2°) Reddish outcrop at southern end of traverse (x=1010, y=1250) had a T=11.5°. Reversed direction along contour, continuing further northeast. Headed northwest ~250m to CD179 mat area. Observed marker #2, previously disturbed mats. Continued southwest ~250m to Llao's Bath. Pumped Llao's Bath with Go-flo sampler (S1), took water sample (S2) about 25 feet east of peeper. No CTD for this dive.

Samples Collected:
S1 (Llao's Bath)
S2 (near Llao's Bath)
10BC (at 2nd TTT site, x=915, y=1370)

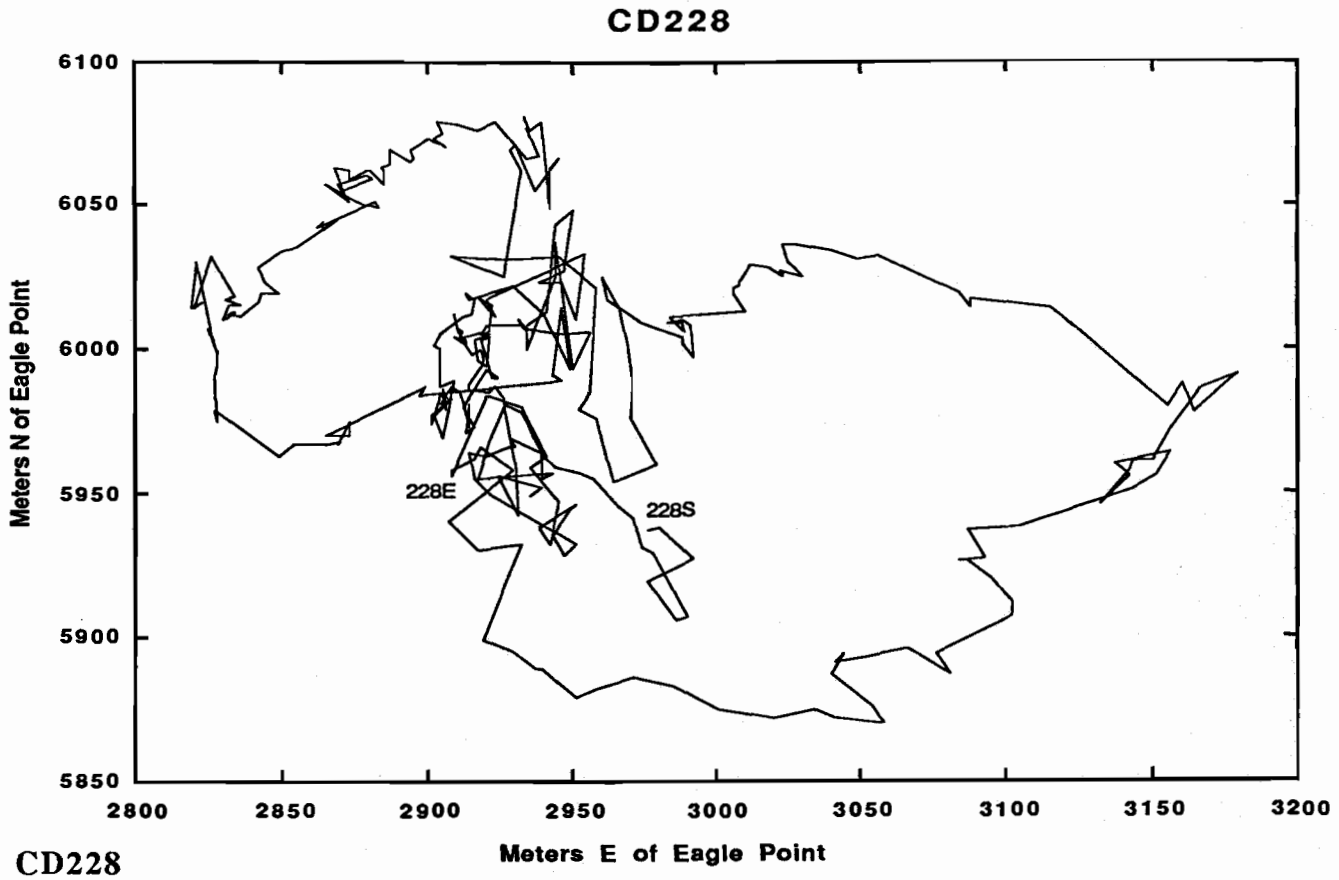

CD228

Pilot: Dymond
Purpose: Hydrothermal
Location: Palisades Point pool and mat area

The purpose of the dive was to further explore the pools and bacterial mats found in the northeast basin. (Start x= 2980, y=5940; depth = 1819 feet). Headed northwest ~90m to find small pools with crusts of bacteria around the edges. T=6.45° in a shallow pool. Followed depth contour (~80°), reversed course back to little mats and pools. Saw big pools with islands in them, drainage appeared to come from under a rock. T-probe in pool (Tmax =5.6°). Tripped sample S1 and dropped box corer in pool. Followed shore line, then long river to the south until in disappeared into a bacterial mat. Continued west, observed mottled sediments. Change course to northeast, observed more small pools with drainage channels. Took T-probe measurements (in mat Tmax=8.11°, in sediment Tmax=10.8°) Continued east ~300m, then southwest ~150m, then west ~120m through mottled sediments. Continued north (observed smooth sediment with bacteria on it) approx. 50m. T-probe measurement next to a boulder (Tmax=8.85°). Due to a severe thunderstorm, the Computer NAV was shut down and surface boat docked at Cleetwood Cove. The sub continued east, tripped water sampler on side of sub (S2) above a mat. Returned to the large pool observed at the beginning of the dive. Attempted T-probe measurements about 0.5m into pool, stirred up black material, bent the T-probe. Deployed marker #8. Surveyed west, then north, then east. T-probe in mat+ sediment material (Tmax=9.68°). Continued on, probably covered area found in CD227. Returned to large pool and marker #8, T-probe in mud (Tmax=4.31°). Tripped S3. Loaner CTD from Seabird used during this dive.

Samples Collected:	S1 (pumped large pool, x=2910, y=5985)
	S2 (above a mat)
	S3 (arm sample over large pool)
	11BC (no core, a little bulk material, x=2910, y=5985)
Markers Deployed	#8

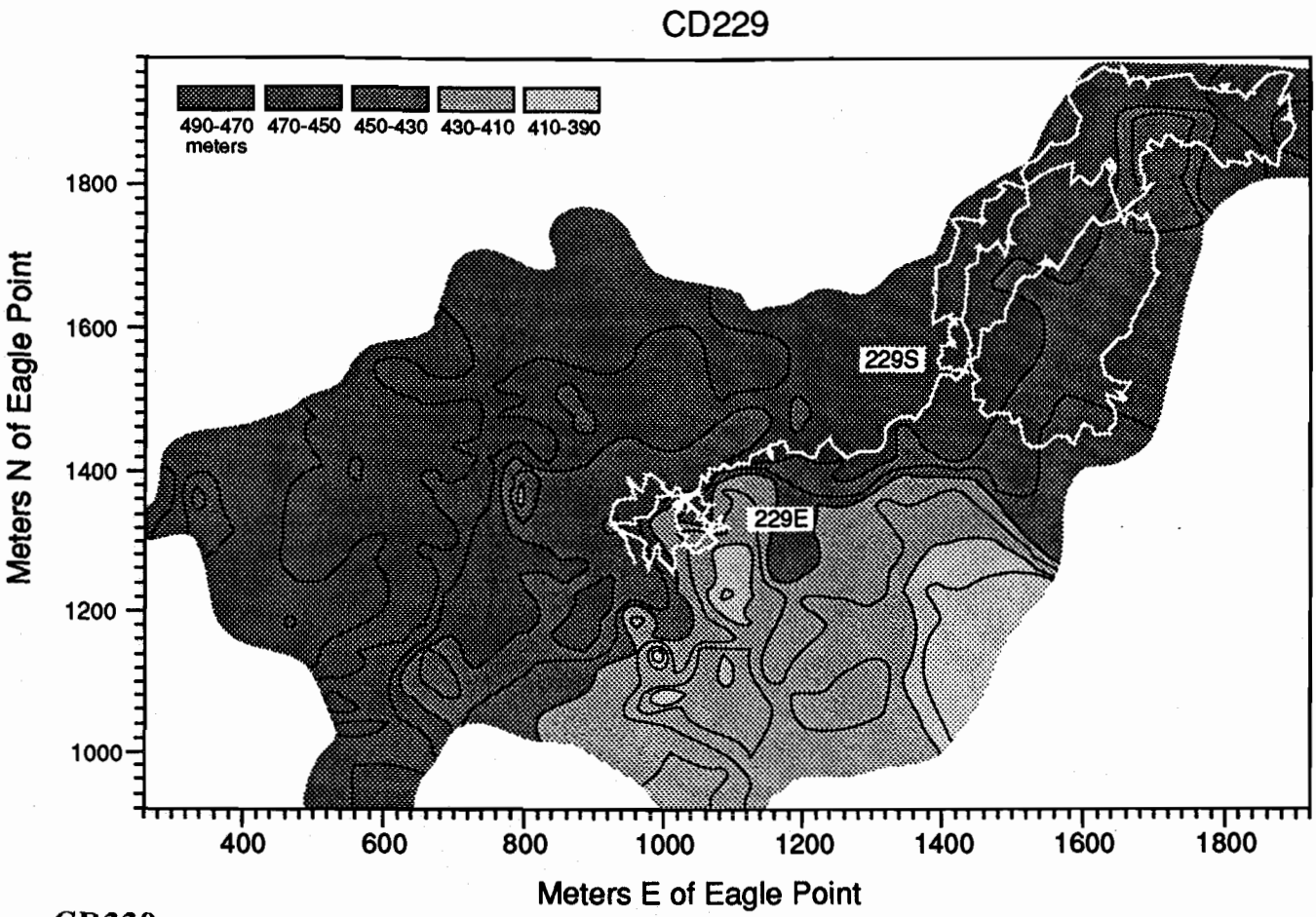

CD229

Pilot: Collier
Purpose: Hydrothermal
Location: Detailed Study Area

The purpose of the dive was to conduct a general survey to the east for additional venting sites. Sub on the bottom at x =1450; y = 1530; depth = 1476 feet. Started north for ~200m, then east ~250m, then south ~350m. Occasional mottled sediments found along this track. Changed course to west for ~170m, then northwest 500m. Traveled east 300m, then south 100m, then west, 200m, southwest 950m to marker #6 and TTT location. Drop box corer; floats are tangled. Headed east (~110m) to marker #3 and high temperature mats. T-probe in mat (Tmax=18.9°), Pumped mat with Go-flo sampler (S1). Head west to marker #6 and box corer. Tripped water sampler S3. Secured box corer in manipulator and lifted off bottom. Loaner CTD from Seabird used during this dive.

Samples Collected: S1 (mat (t=18.9°), x=1055, y=1335)
S3 (water in 2nd TTT location, mottled sediment)

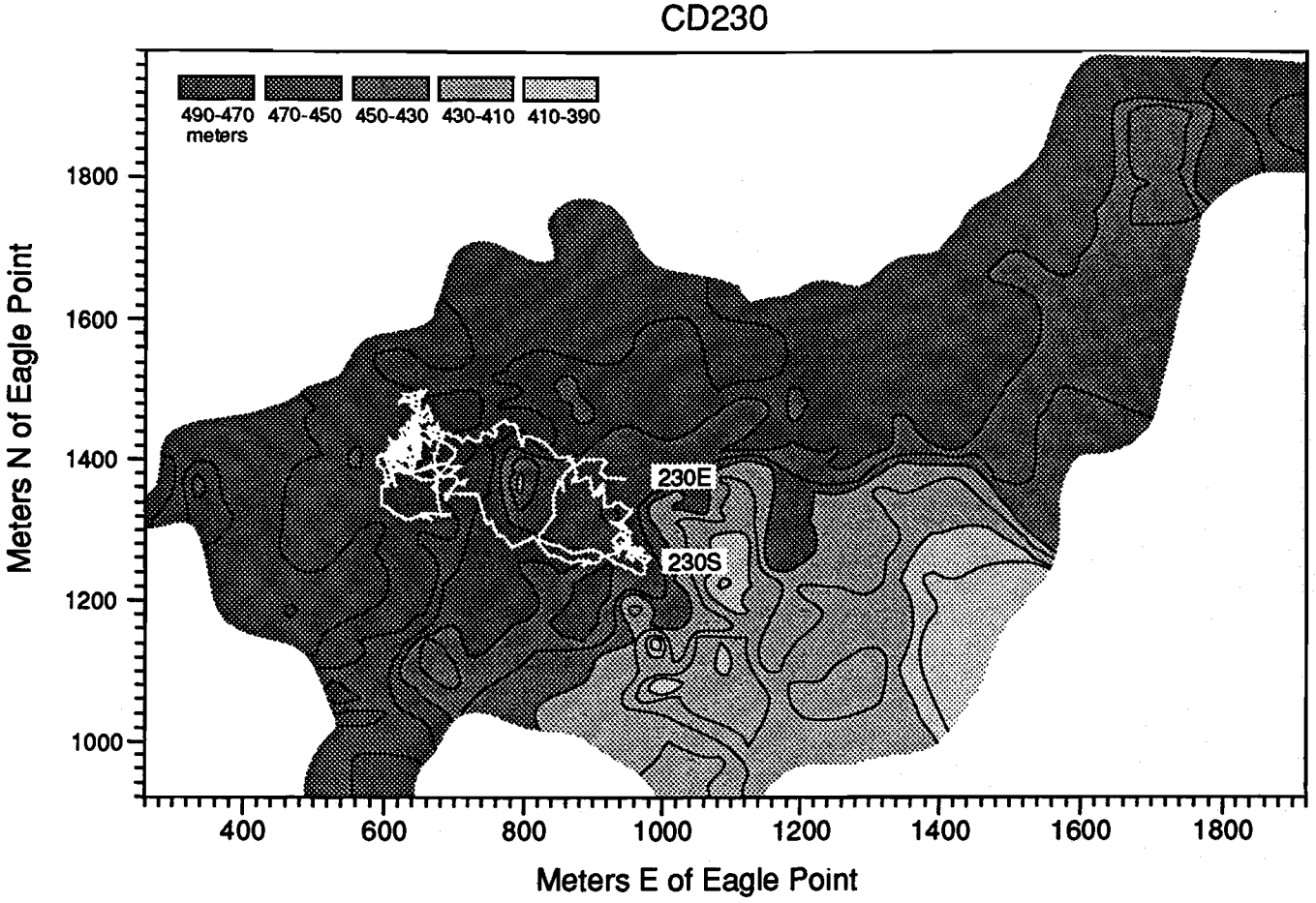

CD230

Pilot: Dymond
Purpose: Hydrothermal
Location: Detailed Study Area

The purpose of the last dive was to collect all of the samplers deployed on the lake floor. The dive began at the Benthic Barrel site (x=940, y=1310, depth=1453 feet.) Dropped box corer (no core recovered), picked up peeper B, released the Benthic Barrel, took water sample S2. Head northwest to Llao's Bath area. Observed two small bacterial mats along the transect. Arrived at marker #4, picked up peeper A at the edge of a small pool. Surveyed to the south and west of Llao's Bath. Returned east, T-probe in brain mat near peeper (Tmax=5.98°), recovered peeper D, suctioned sample one sub width from peeper (S1). Proceeded to Llao's Bath which had lost water since the last visit. Recovered peeper C from Llao's Bath. Circled around Llao's Bath, tripped S3 in small milky colored pool with large amounts of mat around it. Picked up a Fe crust on top of a big rock (too big to pick up). Headed east to TTT site, recovered peeper E and TTT. Loaner CTD from Seabird used during this dive.

Samples Collected:	S1 (brain mat)
	S2 (water at Benthic Barrel location)
	S3 (mat in milky pool)
Peepers Recovered:	A,B,C,D,E
Samplers Recovered:	Benthic Barrel
	TTT

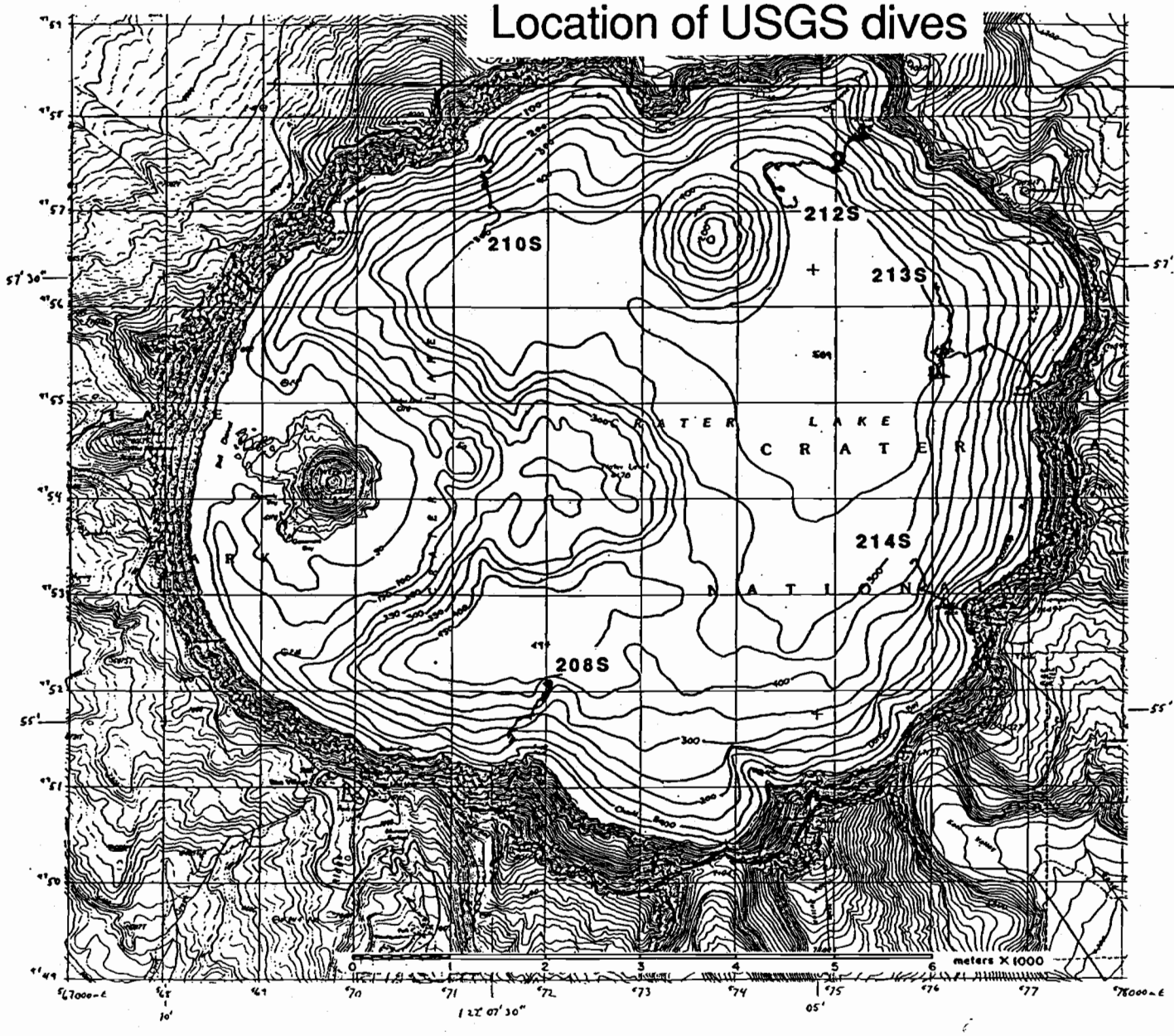
Location of USGS dives
210S
212S
213S
214S
208S
CRATER LAKE
NATIONAL PARK
meters X 1000

1989 Summary USGS Dives

CD208

Pilot: Buktenica **Location:** Eagle Point

The dive began at x = 100; y = 850; depth 1550 feet. Took a core in sediments at descent location. Moved upslope on a southwest heading, picking up rocks along the way. Total distance traveled was about 700 meters. Left the bottom at 350 feet depth.

Samples collected: 2BC
four rocks

CD210

Pilot: Buktenica **Location:** Llao Rock

The dive began at x = -550; y = 5440; depth = 1733. Traveled upslope and on a northerly course for approximately 1000 meters. Picked up rocks on this course. Saw periphyton at 500 feet. Collected moss between 300 and 200 feet depths. Dive ended at 50 foot depth.

Samples collected: 10 rocks
one moss sample

CD212

Pilot: Buktenica **Location:** Palisades Point

The dive began at x = 2750; y = 5840; depth = 1869 feet. This location is just to the east of Miriam Cone. Dropped a core at descent location. Traveled northwest for 450 meters and then east for 800 meters, looking for turbidite and channel features for Hans Nelson. From there the dive proceeded upslope in a northeast direction toward Palisades Point, collecting rocks along the way.

Samples Collected: 4BC
8 rocks
moss sample at 280 feet.

CD213

Pilot: Collier **Location:** Skell Head

The dive began at x = 4200; y = 4900; depth = 1782. Moved south from descent location 800 meters. Near the end of this traverse encountered siliceous spires. Took two samples within 35 meters from different spires. The dive continued upslope on an easterly direction for 1000 meters. The dive ended 550 feet.

Samples Collected: 2 spire samples
1 rock

CD214

Pilot: Buktenica **Location:** Sentinel Point

The dive began at x = 4000; y = 2050; depth = 1589 feet. Proceeded upslope on a general southeast direction, sampling rocks.along the way. Saw moss at 790 feet. Collected moss at 732 feet. Popped to the surface 3.5 hours into the dive to drop off moss. Traversed along a debris chute. Collected more moss. Generator failure resulted in a loss of navigation for the last two hours of the dive.

Samples Collected: 10 rocks
3 moss samples

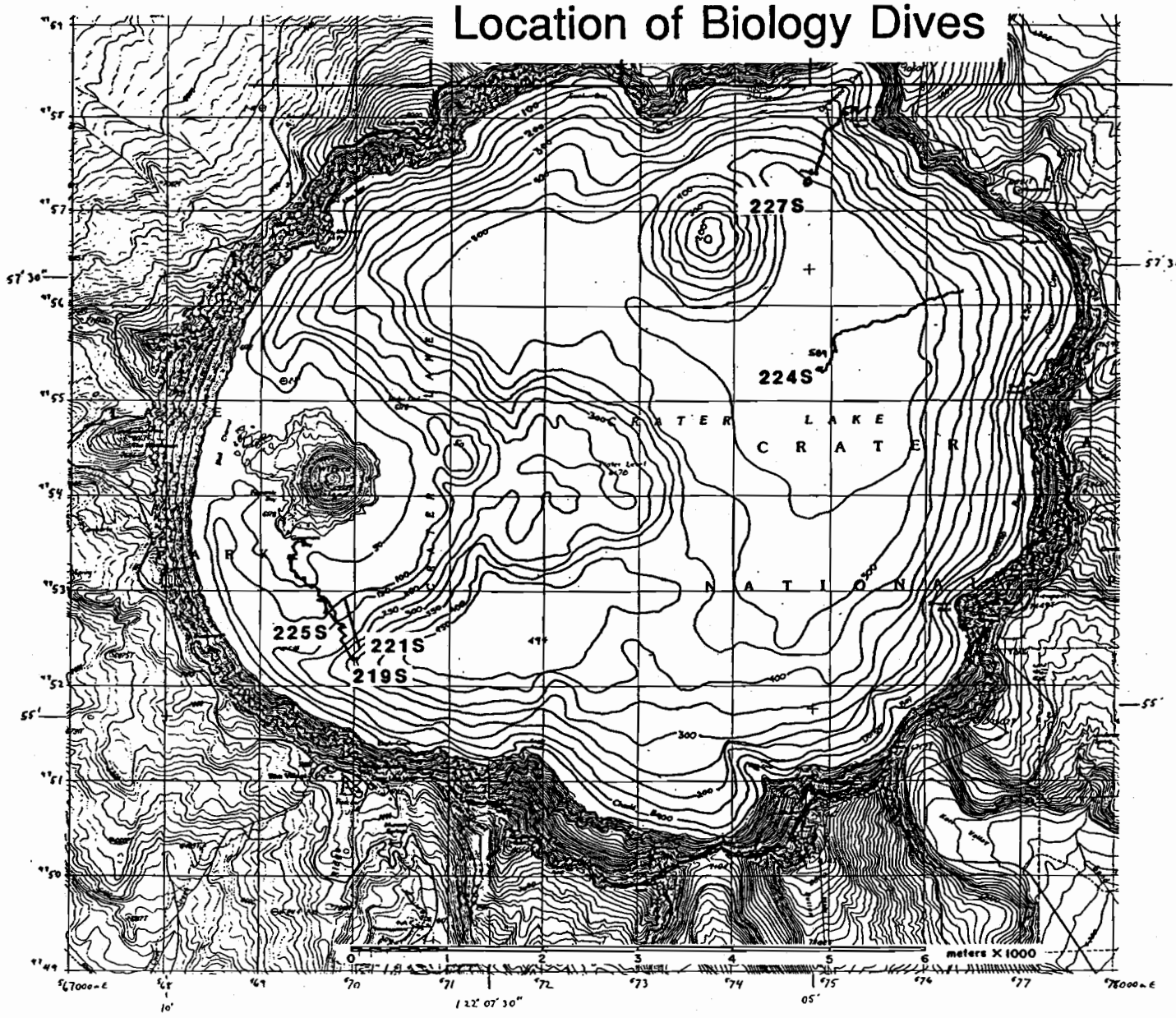
Location of Biology Dives
227S
224S
225S
221S
219S
CRATER LAKE
NATIONAL
meters X 1000

1989 Summary Biology Dives

CD219

Pilot: Buktenica **Location:** South of Wizard Island

Dive took place in the moss beds south of Wizard Island (Start x=-1750, y=950, Depth=1325 feet). Proceeded SW~50m, then NNW~380m to old moss bed, continued NW ~400m, collecting moss samples from dense fields of moss. Surfaced at x=-2240, y=700 to drop off samples. On bottom again at x=-2225m, y= 1710m, depth=200 feet. Continued NNW~500m. Reached upper edge of moss distribution at 95 feet.

Samples Collected: 1 rock
9 moss samples

CD221

Pilot: Robison **Location:** South of Wizard Island

Dive took place in the moss beds south of Wizard Island (Start x=-1725, y=1053, Depth=1350 feet). Proceeded NW, collected daphnia in suction sampler (below 500 feet), collected rock with moss at 515 feet. surfaced at x=-1880, y=1571. There was no computer navigation during this dive due to adverse weather conditions.

Samples Collected: 1 rock
Daphnia sample

CD224

Pilot: Buktenica **Location:** Skell Cove

Dive started at x=3060, y=3990, depth=1915 feet. Deployed box corer. Headed north ~400m, observing small depressions with black crater shaped colonies and taking several suction samples. Continued northeasterly ~650m, sediment is smoother, observed heavily sedimented trees and other debris, few large boulders. Final depth 1500 feet. No CTD for this dive.

Samples Collected: 9BC
sample from suction sampler

CD225

Pilot: Earle **Location:** South of Wizard Island

The purpose of this dive was to continue the transect started in CD221 over the moss beds south of Wizard Island (Start x=-1925, y=1240, Depth=550 feet). Proceeded NW, collected algae in suction sampler (454 feet). Collected moss at 294 feet, 255 feet, 230 feet. Surfaced at x=-2175, y=1560. No CTD for this dive.

Samples Collected: 3 moss samples
Algae sample

CD227

Pilot: Buktenica **Location:** Palisades Point

Dive started at x=2980, y=6020, depth=1793 feet. Headed east ~20m, then south 60m, collecting a moss sample. Changed course to west found bacterial mats and pools. Mat streams appeared to come out from under boulders and run downhill. Changed course to north to look for moss, leaving bacterial mat area. A leak in the backup air supply forced a return to surface for repair. Back on the bottom (x=2910, y=6095, depth=1767 feet). On course to east for ~160m, collected a moss sample. Course changed to northwest (~700m), then east ~250m, collecting moss samples along the traverse. Observed vertical rock face with drawing-like figures at the beginning of the east traverse. No CTD for this dive.

Samples Collected: 6 moss samples

Appendix I. Data Tables

1989 Water Data

SAMPLE NAME	DEPTH	CO2 (mM)	pH	O2 (µM)	Rn (dpm/100L)	Ra (dpm/100L)	Na (mM)	K (mM)	Mg (mM)	Ca (mM)	Li (µM)	Cl (mM)	SO4 (mM)	Ba (nM)	Fe (nM)	Mn (nM)	SiO2 (µM)	NO3 (µM)	PO4 (µM)
Mats																			
CD207 S3					129		.544	0.048	.126	0.176	6.8				1.9	16			
CD215 S1		.65			373	1.5	.473	0.047	.116	0.176	7.2	.27	0.11	47			317	1.03	.71
CD216 S1		1.26	7.13		771	232	1.152	0.098	.393	0.347	15.3	.60	0.31	73	380	3.9	469	1.17	1.2
CD216 S3		.73	7.31	294.2			.479		.126			.28	0.11		350	207	207	1.39	.53
CD220 S1					1887	877	.761	0.073	.247	0.253	10.3	.33	0.19	30			322		
CD226 S3			7.59				2.220	0.176	.925	0.771	28.6	.87	0.55	127	30400	15300	980	2.96	3.4
CD228 S3		2.70	7.97				1.469	0.064	.616	0.227	12.6				42	38	540	1.57	11.3
CD229 S1			7.50				.494	0.051	.121	0.174	7.4	.31	0.11	33				1.35	1.8
Pools																			
CD223 S1		3.00	6.27	228.2	3063	15.7	1.109	0.092	.406	0.384	14.7	.51	0.25	108	18	1680	350	1.44	.86
CD226 S1		4.96			9962	117	2.799	0.225	1.121	0.936	35.3	1.03	0.69	314	41	12300	1190	.59	.21
CD228 S1		8.70	8.91	17.5	659	124	5.138	0.124	2.211	0.645	30.0	1.15	0.84	224	554	5100	762	1.31	10.7
CD230 S1		4.95	7.23	17.7			2.355	0.189	.941	0.780	30.0		0.55	210	254	25200		.61	11.3
CD230 S3		.78	7.14	279.2			.608	0.058	.177	0.222	8.5	.27	0.15	77				2.55	
Misc Dive Samples																			
CD207 S2		.59	7.67				.464		.116								318	1.51	.84
CD211 S1		.68	7.19		46.2		.467		.116		6.8	.28	0.11				338	1.34	.63
CD215 S2		.71	7.17				.470		.118			.28	0.11				317	1.32	.57
CD216 S2		.64	7.52				.460		.112			.27	0.10				260	1.35	.48
CD217 S1		.62	7.18				.458	0.046	.109	0.169	6.9	.29	0.10	47			317	1.23	.55
CD217 S2		.62	7.18				.457		.112		6.9						322	1.38	.54
CD217 S3					243		.472	0.046	.115	0.178	6.9			43					
CD218 S2		.67	7.41		160		.467	0.046	.113	0.172	7.2			43				1.13	.54
CD220 S2		.67	7.17				.456		.112			.26	0.10				338	1.09	.55
CD222 S1		.60	7.35				.460		.110									1.16	.65
CD222 S2		.66	6.98	296.6			.472		.122			.27	0.11				594	1.41	.63
CD223 S2		.70	6.92		21.5		.469		.117		6.9	.27	0.11				334	1.47	.55
CD223 S3		.67	7.08	294.6								.27	0.10				314	1.48	.56
CD226 S2		.69	7.26	292.6			.464		.115			.27	0.11				318	1.91	.44
CD228 S2		.68	7.56	297.3			.468		.124			.28	0.11				330	1.51	.59
Porewaters																			
GC8-72		7.06	8.97				4.630	0.153	.980	0.910	27.8	1.99	0.00		147000	80800	1120	6.62	1.3
BC8-10/11		4.30	8.10				2.320		1.080	0.830		1.13	0.89		617000	308000	822	.89	2.6
Springs																			
SPRING 18							.097		.074										
SPRING 19							.183		.145										
SPRING 20							.109		.054			.01	0.84						
SPRING 30							.364		.158										
SPRING 42							.111		.052										

1989 Water Data continued.

SAMPLE NAME	DEPTH	CO2 (mM)	pH	O2 (µM)	Rn (dpm/100L)	Ra (dpm/100L)	Na (mM)	K (mM)	Mg (mM)	Ca (mM)	Li (µM)	Cl (mM)	SO4 (mM)	Ba (nM)	Fe (nM)	Mn (nM)	SiO2 (µM)	NO3 (µM)	PO4 (µM)
89 North Basin																			
89080901	580	.62	7.42	295.9	3.6		.456		.111		6.7						326	1.48	.54
89080902	520	.61	7.46	302.7	3.9		.455		.110		6.7						324	1.35	.53
89080903	449	.61	7.56	306.1	1.5		.452		.110		6.8						323	1.19	.52
89080904	388	.58	7.54	308.8	2.4		.447		.109		6.6						316	1.05	.53
89080905	317	.57	7.57	313.2	2.5		.445		.108		6.6						312	.72	.50
89080910	263	.57	7.60	316.7			.441		.105								310	.15	.48
89080909	192	.58	7.63	323.9			.446		.108								314	.04	.45
89080908	132	.57	7.63	326.8			.438		.108								310	.04	.45
89080907	61	.56	7.69	339.2			.438		.108								312	.04	.42
89080906		.55	7.76	270.9			.439		.108								312		.44
89 South Basin																			
89081001	475	.69	7.26		4.0		.443		.107						.2	13	338	1.32	.53
89081002	425	.60	7.49		3.5		.446		.106								323	1.12	.49
89081003	375	.58	7.50		1.3		.452		.108								327	.98	.49
89081004	325	.59	7.53		1.4		.451		.108								321	.80	.48
89081005	275	.59	7.58		1.2												320	.62	.49
89081010	230	.58	7.58														313	.31	.45
89081009	170	.55	7.61														314	.05	.43
89081008	120	.55	7.75														319	.04	.39
89081007	60	.55	7.79														316	.04	.39
89081006		.52	7.75														316	.01	.38
89081401	408	.58	7.54	309.4	1.2		.452		.109								314	1.08	.58
89081402	418	.59	7.58	306.2	6.6		.452		.109								315	1.10	.56
89081403	428	.59	7.46	304.9	4.8		.455		.109								319	1.13	.55
89081404	438	.59	7.30	302.6	6.7		.455		.110								320	1.21	.54
89081405	446	.54	7.83				.443		.106								311	.01	.53
89081905	440	.59	7.46	302.7	3.1		.454		.109								316	1.21	.52
89081904	450	.59	7.41	301.7	2.1		.454		.110								318	1.21	.56
89081903	460	.59	7.41	299.1	2.2		.455		.111								318	1.26	.55
89081902	470	.64	7.42	298.9	3.6		.458		.112								321	1.27	.57
89081901	480	.70	7.25	295.6	4.7		.462		.114								324	1.35	.61
89082301	437	.60	7.37	303.1	4.9		.453		.110		6.7							1.21	.49
89082302	447	.59	7.29	301.7	4.2		.453		.110		6.7						319	1.22	.50
89082303	457	.58	7.25	300.3	9.4		.454		.109		6.7						320	1.30	.50
89082304	467	.61	7.18	299.7	8.2		.458		.112		6.8						321	1.37	.50
89082305	477	.63	7.12	299.2	4.0		.462		.114		6.8						328	1.50	.50
89082306	439	.60	7.33	303.6	4.2		.453		.109		6.7						319	1.27	.49
89082307	449	.60	7.23	301.0	13.6		.454		.110		6.7						320	1.31	.49
89082308	459	.61	7.26	300.5	1.4		.457		.111		6.8						320	1.32	.49
89082309	469	.61	7.18	298.4	2.4		.460		.113		6.7						324	1.33	.50
89082310	479	.64	6.95	294.7	9.4		.467		.116		6.8						327	1.39	.52

1989 Water Data continued.

SAMPLE NAME	DEPTH	CO2 (mM)	pH	O2 (µM)	Rn (dpm/100L)	Ra (dpm/100L)	Na (mM)	K (mM)	Mg (mM)	Ca (mM)	Li (µM)	Cl (mM)	SO4 (mM)	Ba (nM)	Fe (nM)	Mn (nM)	SiO2 (µM)	NO3 (µM)	PO4 (µM)
89 South Basin (cont)																			
89082501	452	.60	7.23	299.6	1.2		.455		.111		6.7						327	1.31	.49
89082502	467	.62	7.09	295.9	4.8		.460		.113		6.8							1.37	.53
89082503	482	.64	6.90	290.5	16.9		.468		.117		6.8						326	1.46	.55
89082504	456	.60	7.25	299.2	2.5		.457		.111		6.8						328	1.29	.52
89082505	471	.63	7.16	296.1	3.5		.459		.114		6.7						313	1.38	.55
89082506	486	.55	7.02		2.1		.442		.106		6.5						321	.08	.37
89082510	74	.54	7.62	340.6			.439		.105								303	.34	.48
89082509	50	.57	7.62	339.3			.397		.095								313	.16	.39
89082508	25	.57	7.65	318.2			.437		.105								314	.29	.37
89082507		.55	7.70	264.5			.439		.107								303	.13	.42
89082701	420	.58		306.3	2.2		.452		.108									1.12	
89082702	430	.60		302.3	3.2		.456		.110								309	1.12	
89082703	435	.62		302.3	14.2		.457		.111								315	1.87	
89082704	451	.62		300.6	29.7		.463		.112								319	1.30	
89082705	425	.58		302.9	1.1		.452		.109								318	1.20	
89082706	441	.59		301.8	4.5		.451	0.044	.110	0.172	6.6						317	1.21	
89082707	451	.63		299.2	13.4		.458		.111		6.8						321	1.36	
89082708	99	.56	7.61	334.0			.439		.105								320	.04	.44
89082709	150	.57	7.62	324.3			.442		.106								308	.06	.44
89082710	200	.57	7.63	322.6			.437		.107								312	.14	.42
89082711	250	.57	7.62	318.2			.444		.107								315	.19	.38
89083001	463	.64	7.32	296.9	7.7		.462		.112		6.8						329		.56
89083002	453	.63	7.34	299.0	5.1		.457		.110		6.7						326	1.32	.53
89083003	443	.62	7.36	299.5	5.5		.454		.110		6.8						325	1.29	.53
89083004	432	.58	7.42	300.7	2.2		.452		.108		6.8						326	1.26	.54
89083005	407	.58	7.49	304.4													318	1.22	.54
89083006	382	.58	7.50	306.3													320	1.15	.54
89083007	356		7.50	309.7													319	1.05	.55
89083008	429	.59	7.47	305.5	45.1		.454		.109		7.0						333	.94	.56
89083009	414	.61	7.48	305.2	2.0		.449		.108		6.6						323	1.16	.58
89083010	399	.60	7.48	306.2	1.9		.450		.109		6.7						325	1.18	.55
89083011	313	.54	7.52	314.6													325	.86	.51
89083012	284	.54	7.51														320	.74	.59
89083013	259	.55	7.52														308	.64	.50
89083103	453	.61	7.48	301.2	3.2		.454		.110		6.7						318	1.28	.55
89083104	443	.60	7.49	301.4	1.8												318	1.23	.56
89083105	477	.68	7.33	294.5	6.1		.461		.114		6.7						320	1.42	.58
89083106	462	.62	7.49	299.6	2.4		.457		.111		6.6						312	1.33	.56
89083107	447	.59	7.70	300.7	2.3		.455		.109		6.6						315	1.29	.53

1988 Hydrocast Data

Sample	Depth	T (°C)	[Mg] (mM)	[K] (mM)	[Na] (mM)	[SiO2] (µM)	[Ca] (mM)	[Cl] (mM)	[SO4] (mM)	pH	Alk (meq/l)	[Mn] (nM)
2.2-5	441.3	3.619	0.112	0.0446	0.463	304	0.172					8.2
2.2-6	434.4	3.597	0.112	0.0448	0.463	303	0.172					4.9
2.2-7	428.8	3.580	0.114	0.0448	0.475	302	0.172					4.1
2.3-1	448.2	3.610	0.111	0.0446	0.460	305	0.172					4.3
2.3-2	408.1	3.564	0.110	0.0436	0.455	302	0.169					0.3
2.3-3	398.1	3.561	0.110	0.044	0.455	301	0.170					0.5
2.3-4	387.4	3.559	0.110	0.0439	0.457	299	0.169					0.6
81801	439.0	3.599	0.112	0.0445	0.467	303		9.74	10.04	7.10	0.583	1.8
81802	429.5	3.586	0.110	0.0444	0.461	301		9.75	10.03	7.20	0.626	1.2
81803	419.1	3.578	0.111	0.0438	0.460			9.76	10.01	7.11	0.627	
81804	408.8	3.568	0.110	0.0442	0.457	297		9.61	9.99	7.10	0.629	
81807	378.6	3.563	0.110	0.0439	0.455	296		9.59	9.89	7.14	0.622	
81809	347.6	3.570	0.110	0.0435	0.453	296		9.51	9.96	7.23	0.605	
81811	318.0	3.572	0.108	0.0435	4.524	294		9.55	9.94	7.31	0.624	
82501	445.1	3.609	0.111	0.0442	0.467	303	0.172	9.67	10.06	7.17	0.634	4.4
82502	434.8	3.607	0.111	0.0445	0.455	302	0.172	9.65	10.06	7.18	0.636	4.8
82503	424.1	3.598	0.111	0.0444	0.456	299	0.171	9.74	10.02	7.26	0.634	3.2
82504	415.3	3.581	0.110	0.0442	0.453	300	0.170	9.61	10.04	7.15	0.613	1.3
82505	302.2	3.595	0.109	0.0431	0.447	295	0.169	9.66	9.81			1.5
82506	262.4	3.659	0.108		0.445	294	0.169	9.60	9.93			0.4
82507	221.5	3.731	0.109	0.0439	0.448	293	0.168	9.58	9.79			1.7

1988 Dive Data

Dive	[Mg] (mM)	[K] (mM)	[Na] (mM)	[SiO2] (µM)	[Ca] (mM)	pH	Alk (meq/l)	[Mn] (nM)
CD179.1	0.120	0.0453	0.469	310	0.177			3.55
CD179.2	0.120	0.0454	0.473	309	0.177			10.21
CD179 BT		0.0770	0.839	477	0.314			589.70
CD182.1	0.162	0.0542	0.568	354	0.206			36.01
CD182.2	0.173	0.0576	0.605	382	0.210			9572.
CD183.2	0.114	0.0462	0.471	288	0.174			114.9
CD184.0	0.119	0.0453	0.472	309	0.176	6.501	0.696	10.66
CD185.1	0.113	0.0449	0.470	305	0.172			6.41
CD185.2	0.110	0.0437	0.451	296	0.169			5.40
CD186.1	0.113	0.0469	0.470	307	0.174	7.403	0.641	41.47
CD186.2	0.115	0.0459		306	0.174			45.43
CD187.0	0.113	0.0462	0.473	308	0.174	7.151	0.653	34.17

1988 Spring Data

Spring	[Mg] (mM)	[K] (mM)	[Na] (mM)	[Ca] (mM)	[SiO2] (µM)	[Mn] (nM)
20	0.0658	0.0239	0.130	0.164	423	
16		0.0422			444	5.7
48	0.0209	0.0348	0.110	0.058	587	
2	0.0359	0.0237	0.067	0.063	625	2.0
38	0.1174	0.0288	0.169	0.226	552	
42	0.0531	0.0438	0.122	0.114	619	
19	0.1405	0.0156		0.293	133	2.0
11	0.0416	0.0169	0.202	0.049	611	
39	0.0205	0.0192	0.087	0.062	431	5.7
24		0.0084		0.522	605	
35	0.0101	0.0318	0.121	0.205	518	76.0

1987 Hydrocast Data

Sample	Depth	T (°C)	[Na] (mM)	[Ca] (mM)	[Mg] (mM)	[K] (mM)	[Li] (μM)	[SiO2] (μM)	[Mn] (nM)
6.1	446.1	3.610	0.475	0.173	0.113	0.0456	6.7	302	17.82
6.3	427.0	3.592	0.471	0.170	0.113	0.0452	6.7	299	11.27
6.4	416.7	3.537	0.463	0.168	0.112	0.0445	6.5	297	2.78
6.5	407.5	3.530	0.452	0.169	0.111	0.0445	6.4	295	3.13
6.6	397.2	3.514	0.463	0.168	0.111	0.0442	6.4	294	1.03
7.1	385.3	3.508	0.460	0.168	0.111	0.0442	6.4	294	0.37
7.2	375.8	3.506	0.456	0.168	0.110	0.0441	6.4	294	0.49
7.3	350.9	3.501	0.451	0.168	0.111	0.0438	6.4	287	0.59
7.4	325.7	3.499	0.445	0.167	0.110	0.0437	6.4	292	0.33
7.5	300.9	3.514	0.456	0.166	0.109	0.0434	6.4	290	0.75
7.6	276.4	3.552	0.457	0.167	0.110	0.0435	6.4	290	0.51
18.1	418.5					0.0439	6.5	296	1.31
18.6	404.1	3.514	0.454	0.168	0.111	0.0442	6.4	296	1.05
18.2	433.5	3.517	0.455	0.168	0.110	0.0441	6.6	297	0.63
18.3	449.2	3.520	0.455	0.168	0.111	0.0441	6.6	297	1.16
18.5	464.1	3.521	0.451	0.168	0.111	0.0438	6.4	296	2.84
19.4	476.7	3.522	0.455	0.170	0.111	0.0441	6.6	298	0.55
20.1	486.7	3.612	0.473	0.178	0.119	0.0451	6.6	309	5.10
20.2	471.0	3.575	0.469	0.172	0.114	0.0445	6.5	302	2.50
20.3	456.8	3.553	0.453	0.171	0.112	0.0444	6.5	299	1.98
20.4	441.2	3.530	0.455	0.170	0.111	0.0440	6.5	297	0.78
20.5	427.0	3.526							
20.6	411.3	3.520	0.452	0.168	0.111	0.0438	6.5	298	0.75
21.6	456.5	3.591	0.462	0.172	0.114	0.0448	6.6	302	5.64
21.5	440.8	3.571	0.465	0.172	0.111	0.0446	6.5	298	8.26
26.1	443.3	3.558	0.458	0.171	0.111	0.0443	6.5	298	2.76
26.2	435.2	3.544	0.468	0.171	0.112	0.0441	6.4	293	1.85
26.3	424.9	3.530	0.462	0.171	0.111	0.0440	6.4	293	1.86
26.4	414.2	3.523	0.455	0.170	0.111	0.0441	6.4	293	1.18
26.5	405.4	3.524	0.441	0.169	0.111	0.0439	6.4	292	1.19
27.1	582.2	3.553	0.450	0.173	0.113	0.0444	6.4	300	5.03
27.2	533.3	3.540	0.468	0.170	0.112	0.0444	6.4	297	1.62
27.3	483.6	3.526	0.464	0.170	0.112	0.0444	6.4	295	1.74
27.4	434.3	3.520	0.455	0.170	0.111	0.0439	6.4	294	1.78
27.5	383.1	3.508	0.459	0.169	0.111	0.0437	6.4	295	1.45
28.1	447.7	3.577	0.458	0.172	0.112	0.0447	6.5	301	3.98
28.2	433.5	3.538	0.456	0.171	0.111	0.0444	6.5	298	1.48
28.3	417.5	3.526	0.466	0.170	0.110	0.0437	6.5	295	0.86
28.4	403.3	3.517	0.445	0.170	0.110	0.0437	6.3	294	0.77
28.5	388.0	3.509	0.456	0.170	0.110	0.0437	6.4	293	0.39
29.1	324.2	3.514	0.449	0.170	0.109	0.0435	6.4	290	0.47
29.2	250.4	3.727	0.445	0.169	0.109	0.0432	6.4	290	0.72
29.3	175.1	3.725	0.445	0.168	0.109	0.0430	6.3	289	0.61
29.4	100.5	4.102	0.454	0.169	0.109	0.0429	6.3	288	0.19
29.5	24.9	8.429	0.457	0.169	0.110	0.0436	6.3	289	4.13

1985-1989 He data in Crater Lake water samples

Sample	M east of Eagle point	M north	Sample D. M	Bottom D. M	3He cc/g	4He cc/g
1985						
CL85-H1-1	S. Basin		324	494	1.130E-13	4.690E-08
CL85-H1-2			374		1.364E-13	4.880E-08
CL85-H1-3			424		1.665E-13	5.180E-08
CL85-H1-4			474		2.961E-13	6.450E-08
CL85-H2-1	Central Basin		434	594	1.705E-13	5.210E-08
CL85-H2-2			474		1.968E-13	5.460E-08
CL85-H2-3			524		2.131E-13	5.640E-08
CL85-H2-4			574		2.284E-13	5.780E-08
CL85-H3-1	South Basin		122	492	6.768E-14	4.250E-08
CL85-H3-2			222		7.474E-14	4.310E-08
CL85-H3-3			472		2.572E-13	6.060E-08
CL85-H4-1	S.Basin Saddle		288	458	9.896E-14	4.560E-08
CL85-H4-2			338		1.204E-13	4.730E-08
CL85-H4-3			388		1.445E-13	4.960E-08
CL85-H4-4			438		1.792E-13	5.310E-08
1987						
CL87-H6-6	1444	1551	397	453	1.342E-13	4.811E-08
CL87-H6-5			408		1.428E-13	4.880E-08
CL87-H6-4			417		1.593E-13	5.043E-08
CL87-H6-3			427		1.949E-13	5.430E-08
CL87-H6-2			438		1.103E-13	4.476E-08
CL87-H6-1			446		2.212E-13	5.609E-08
CL87-H7-6	1437	1551	276	457	8.547E-14	4.242E-08
CL87-H7-5			301		9.562E-14	4.313E-08
CL87-H7-4			326		1.059E-13	4.440E-08
CL87-H7-3			351		1.146E-13	4.500E-08
CL87-H7-2			376		1.242E-13	4.646E-08
CL87-H7-1			385		1.286E-13	4.676E-08
CL87-H18-6	2386	1687	404	489	1.353E-13	4.825E-08
CL87-H18-1			418		1.369E-13	4.857E-08
CL87-H18-2			434		1.427E-13	4.807E-08
CL87-H18-3			449		1.479E-13	4.903E-08
CL87-H18-5			464		1.545E-13	4.979E-08
CL87-19-4	2401	1662	477	480	1.602E-13	4.966E-08
CL87-20-6	-62	1340	411	491	1.423E-13	4.780E-08
CL87-20-4			441		1.556E-13	4.837E-08
CL87-20-3			457		1.953E-13	5.289E-08
CL87-20-2			471		2.346E-13	5.714E-08
CL87-20-1			487		3.751E-13	7.145E-08
CL87-21-3	1254	1542	397	460	1.326E-13	4.641E-08
CL87-21-2			411		1.282E-13	4.596E-08
CL87-21-1			426		1.223E-13	4.456E-08
CL87-21-5			441		1.831E-13	5.048E-08
CL87-21-6			457		2.366E-13	5.683E-08
CL87-27-5	3133	3714	383	588	1.283E-13	4.698E-08
CL87-27-4			434		1.499E-13	4.925E-08
CL87-27-3			484		1.625E-13	5.028E-08
CL87-27-2			533		1.769E-13	5.166E-08
CL87-27-1			582		2.121E-13	5.532E-08

1985-1989 He data in Crater Lake water samples cont.

Sample	M east of Eagle point	M north	Sample D. M	Bottom D. M	3He cc/g	4He cc/g
1988 Hydrocast Samples						
CL8825-07	825	1210	221	450	7.389E-14	4.422E-08
CL8825-04			415		1.732E-13	5.325E-08
CL8825-03			424		1.819E-13	5.323E-08
CL8825-02			435		1.958E-13	5.476E-08
CL8825-01			445		2.177E-13	5.666E-08
1989 Hydrocast samples						
CL89.8.9-10	213	4850	0	580	5.345E-14	3.854E-08
CL89.8.9-9			60		6.260E-14	4.133E-08
CL89.8.9-8			130		6.415E-14	4.145E-08
CL89.8.9-7			190		6.563E-14	4.156E-08
CL89.8.9-6			260		8.740E-14	4.509E-06
CL89.8.9-5	133	4848	320	580	1.118E-13	4.853E-08
CL89.8.9-4			390		1.472E-13	5.153E-08
CL89.8.9-3			450		1.885E-13	5.576E-08
CL89.8.9-2			520		2.193E-13	5.893E-08
CL89.8.9-1			580		2.394E-13	6.113E-08
CL89.8.10-5	NE Basin		275	476	1.062E-13	4.785E-08
CL89.8.10-4			325		1.289E-13	5.103E-08
CL89.8.10-3			375		1.526E-13	5.276E-08
CL89.8.10-2			425		1.807E-13	5.536E-08
CL89.8.10-1			475		3.560E-13	7.282E-08
CL89.8.19-1	3150	942	474		3.423E-13	7.131E-08
CL89.8.23-5	3618	805	471		3.310E-13	6.937E-08
CL89.8.23-10	3078	921	473		3.783E-13	7.455E-08
1989 Spring Samples						
East Lake 11					1.267E-13	4.674E-08
EL (East Lake)					1.668E-13	5.081E-08
Spring 30					9.252E-14	5.728E-08
Spring 42+					6.716E-14	4.558E-08
1988 Dive samples						
CD179-2	1065	1660		455	3.354E-13	6.899E-08
CD184	1050	1575		455	3.604E-13	7.121E-08
CD186-1	1510	1340		420	2.841E-13	6.311E-08
1989 Dive Samples						
BBarrel S1	909	1290		453	9.092E-14	4.480E-08
BBarrel S5	909	1290		453	8.517E-13	1.200E-07
CD207 S1	953	1553		447	2.707E-13	6.391E-08
CD207 S2	843	1528		455	2.485E-13	6.126E-08
CD211 S1	634	1452		477	3.706E-13	7.390E-08
CD215 S2	614	1434		476	3.793E-13	7.455E-08
CD216 S1	633	1423		472	3.400E-12	3.782E-07
CD217 S3	1028	1663		460	3.944E-13	7.489E-08
CD220 S2	1030	1337		421	2.262E-13	5.891E-08
CD222 S1	1022	1351		424	2.546E-13	6.532E-08
CD222 S2	945	1495		448	4.410E-13	8.101E-08
CD223 S1	612	1416		477	9.866E-12	9.942E-07
CD228 S1	2907	5984		559	4.475E-12	4.915E-07
CD228 S2	NE Basin			559	2.505E-13	6.220E-08
CD229 S1	1055	1335		433	5.894E-13	9.469E-08
CD230 S1	612	1421		478	2.707E-11	2.666E-06
CD230 S2	909	1290		453	2.806E-13	6.561E-08

1985-1989 Rn data in Crater Lake water samples

Sample	M east of Eagle point	M north	Sample D. M	Bottom D. M	Rn dpm/100L	Ra dpm/100L
1985						
CL85-H1-1	S. Basin		324	494	2.74	
CL85-H1-2			374		3.97	
CL85-H1-3			424		3.65	
CL85-H2-1	Central Basin		434	594	4.14	
CL85-H2-2			474		4.61	
CL85-H2-3			524		2.99	
CL85-H2-4			574		1.95	
CL85-H3-1	South Basin		122	492	1.09	
CL85-H3-2			222		6.51	
CL85-H3-3			472		36.51	
CL85-H4-1	S.Basin Saddle		288	458	3.69	
CL85-H4-2			338		7.69	
CL85-H4-3			388		8.61	
CL85-H4-4			438		4.69	
1986						
CL86-H1-1	2457	1261	394	494	13.18	
CL86-H1-2			419		9.32	
CL86-H1-3			444		14.5	
CL86-H1-4			474		16.1	
CL86-H2-1	2087	1553	445	480	7.49	
CL86-H2-2			460		10.45	
CL86-H3-1	1745	1753	450	480	6.79	
CL86-H3-2			465		17.68	
CL86-H4-1	1403	1989	406	436	2.19	
CL86-H4-2			421		2.97	
CL86-H5-1	1570	1432	418	448	18.2	
CL86-H5-2			433		6.34	
CL86-H6-1	1646	1596	437	467	5.97	
CL86-H7-1	1814	2000	409	439	1.49	
CL86-H7-2			424		3.68	
CL86-H8-1	1759	1748	442	457	10.72	
CL86-H9-1	2436	1287	464	494	5.64	
CL86-H9-2			479		12.56	
1988 Hydrocast Data						
CL8820-03	880	1450	412	445	4.58	
CL8820-02			417		15.99	
CL8820-01			432		14.29	
CL8822-04	773	1203	396	440	12.81	
CL8822-03			412		6.98	
CL8822-02			427		3.89	
CL8822-01			439		16.33	
CL8825-04	825	1210	415		9.65	0.42
CL8825-02			435		29.4	1.46
CL8825-01			445		29.85	0.65
1989 Hydrocast Data						
CL89.8.9-5	133	4848	320	580	3.6	
CL89.8.9-4			390		3.91	
CL89.8.9-3			450		1.52	
CL89.8.9-2			520		2.4	
CL89.8.9-1			580		2.45	

1985-1989 Rn data in Crater Lake water samples cont.

Sample	M east of Eagle point	M north	Sample D. M	Bottom D. M	Rn dpm/100L	Ra dpm/100L
1989 Hydrocast Data cont.						
CL89.8.10-5	NE Basin		275	476	1.22	
CL89.8.10-4			325		1.38	
CL89.8.10-3			375		1.31	
CL89.8.10-2			425		3.53	
CL89.8.10-1			475		3.97	
CL89.8.14-5	1835	1242	403		1.16	
CL89.8.14-4			413		6.57	
CL89.8.14-3			423		4.84	
CL89.8.14-2			433		6.69	
CL89.8.19-5	3150	942	434		3.13	
CL89.8.19-4			444		2.08	
CL89.8.19-3			454		2.15	
CL89.8.19-2			464		3.58	
CL89.8.19-1			474		4.65	
CL89.8.23-1	3618	805	431	474	4.88	
CL89.8.23-2			441		4.17	
CL89.8.23-3			451		9.38	
CL89.8.23-4			461		8.23	
CL89.8.23-5			471		3.99	
CL89.8.23-6	3078	921	433	476	4.2	
CL89.8.23-7			443		13.63	
CL89.8.23-8			453		1.43	
CL89.8.23-9			463		2.36	
CL89.8.23-10			473		9.41	
CL89.8.25-1	2504	826	446	479	1.24	
CL89.8.25-2			461		4.76	
CL89.8.25-3			476		16.89	
CL89.8.25-4	2788	1431	450	483	2.49	
CL89.8.25-5			465		3.5	
CL89.8.25-6			480		2.13	
CL89.8.27-1	1194	1566	415	448	2.21	
CL89.8.27-2			425		3.22	
CL89.8.27-3			435		14.22	
CL89.8.27-4			445		29.69	
1988 Dive samples						
CD183	895	1210		405	36.13	
CD187	750	1100		430	202.3	4.71
1989 Dive samples						
BBarrel S6	909	1290		453	25.87	8.6
CD207 S3	843	1528		455	128.92	
CD211 S1	634	1452		477	46.19	
CD215 S1	951	1150		425	373.07	1.53
CD216 S1	633	1423		472	771.31	232.11
CD217 S3	1028	1663		460	242.7	
CD218 S2	982	1313			159.86	
CD220 S1	869	1524			1886.57	876.62
CD223 S1	612	1416		477	3063.2	15.71
CD223 S2	539	1207			21.51	
CD226 S1	663	1419			9961.51	117.42
CD228 S1	2907	5984		559	659.17	123.76

1988 Dive Program: Sediment, Crust, and Mat Data

Access #	Title	type	S-CNS %	C-CHN %	N %	P %	Ash %	Si %	Al %	Na %	Mg %
1988 Sediment core data											
CL32059	CL8808-2GC 71-72cm	sed								2.233	
CL32060	CL8808-2GC 78-79cm	sed								2.274	
CL32061	CL8808-2GC 91-92cm	sed								2.397	
CL32062	CL8808-2GC 101-102cm	sed								2.320	
1988 Crater Lake Shore Data											
CL31331	East slope of Wizard Island <325mesh	sed						18.86	14.23	0.787	1.08
CL31332	Cloud Cap <325mesh	sed						30.84	8.64	1.689	0.55
CL31333	Pumice Point <325mesh	sed						28.18	8.18	1.337	1.14
CL31334	Sentinal Rock Avalanch <325mesh	sed						29.37	8.78	1.296	1.30
CL31335	Chaski slide Snowfield Spring 27 <325mesh	sed						26.3	9.53	0.585	2.57
CL31336	Spring 23 <325mesh	sed						27.04	8.6	0.963	2.91
CL31337	Castle Rock <325mesh	sed						27.91	9.28	1.388	1.31
CL31338	Dutton Cliff <325mesh	sed						26.52	9.39	1.219	1.87
1988 Dive Data											
CL31519	CD171 Fe Crust	crust		1.25	0.2	3.01	92.2	10.88	2.58	0.573	
CL31520	CD 171 Gray Sed + Fe Crust	crust		1.56	0.21	1.73	94.1	17.59	5.28		
CL31522	CD176 Rock sample#4, brown-orange ppt	crust		0.87	0.21	0.78	96.1	22.39	7.56	1.898	
CL31523	CD177-1, Mn color	crust		2.3	0.36	0.15	93.9	25.71	7.85	1.769	
CL31526	CD 179 Fe lumps	crust		1.63	0.28	1.25	93.9	18.42	5.37	1.230	
CL31527	CD 179 Photo sea bulk	crust		1.54	0.25	0.11	94.7	25.02	7.72	1.820	
CL31528	CD182-B1 Black crust w/brown sed.	crust		0.11	0.08	0.08	97.1	27.06	10.98		
CL31529	CD 182-B2 Brown sediment	crust		0.065	0.18	0.08	97.5	27.41	10.71		
CL31530	CD 182-1 Bulk	crust		0.56	0.15	0.99	88.7	10.28	0.65	0.198	
CL31531	CD 182-2 Bulk	crust	nd	0.34	0.09	1.86	89.2	8.45	0.40	0.145	
CL31534	CD 182-4 Gray layered bulk	crust		0.84	0.12	2.51	93.4	17.93	5.48	1.196	
CL31535	CD 182-5 Bulk layered	crust		0.84	0.14	2.31	92.9	19.33	5.80		
CL31537	CD 185 cemented sediment	crust		0.14		0.07	97.3	27.01	9.51		
CL31538	CD 186 cemented bulk	crust		0.11		0.06	96.7	28.96	8.13		
CL31539	CD 187 Crust	crust	nd	0.573	0.13	1.96	89.7	11.66	0.46	0.144	
CL32058	CD 179 Bacterial Mat	mat	0.27	2.44	0.97	1.37	83.9	7.18	0.21	0.130	

1988 **Dive Program: Sediment, Crust, and Mat Data cont.**

Access #	K %	Ca %	Sc ppm	Cr ppm	Mn ppm	Fe %	Co ppm	Ni ppm	Cu ppm	Zn ppm	As ppm	Br ppm	Sr ppm	Sb ppm	Cs ppm
1988 Sediment core data															
CL32059			13.59	26.9		3.34	15.7				20.3	4		1.12	22.1
CL32060			13.25	29.0		4.26	14.2				73.2	3		0.99	14.1
CL32061			13.18	27.2		3.81	13.4				25.1	3		1.42	12.9
CL32062			13.42	24.9		3.83	15.9				20.6	6		0.47	11.6
1988 Crater Lake Shore Data															
CL31331	0.51	2.60			564	3.72		22	159	76			389		
CL31332	2.07	1.91			549	2.43		0	66	59			315		
CL31333	1.15	2.34			773	3.56		0	116	66			440		
CL31334	1.52	2.76			1268	3.92		0	110	63			435		
CL31335	1.05	2.40			884	5.25		48	91	77			395		
CL31336	0.9	3.01			902	4.74		32	74	80			529		
CL31337	1.4	2.90			676	3.74		21	106	63			424		
CL31338	1.05	3.08			909	4.38		43	124	71			462		
1988 Dive Data															
CL31519		1.40	4.22	19.8	4832	31.42	21.5		41	27	2151	29		1.85	8.0
CL31520		1.99			3697	19.66			62	45					
CL31522		2.92	11.41	43.8	5248	11.87	33.5		101	76	271	34		0.98	16.0
CL31523		2.69	12.80	35.9	19397	4.96	32.1		94	65	56.5	29		0.97	16.8
CL31526		1.88	8.56	27.9	3761	20.74	50.7		64	47	1474	22		1.29	9.8
CL31527		2.72	12.08	39.0	22213	7.45	165.6		70	62	54.6	15		0.67	12.6
CL31528		3.79			3473	2.56			24	123					
CL31529		3.74			380	2.83			25	117					
CL31530		0.85	1.32	9.9	1084	41.51	8.8		19	20	2094	4		1.97	4.3
CL31531		0.85	1.84	11.2	1077	43.43	16.3		12	13	4172	2		2.58	3.1
CL31534		2.17	8.62	27.2	855	18.50	17.2		104	55	3200	9		2.41	15.7
CL31535		2.18			532	16.64			96	53					
CL31537		3.08			748	4.36			49	38					
CL31538		1.24			568	2.76			44	48					
CL31539		0.87	0.87	14.9	4513	37.31	2.0		29	23	747	4		1.84	1.4
CL32058		0.78	1.84	9.9	137	41.21	1.9				3247	10		2.73	2.3

1988 Dive Program: Sediment, Crust, and Mat Data cont.

Access #	Ba ppm	La ppm	Ce ppm	Nd ppm	Sm ppm	Eu ppm	Tb ppm	Yb ppm	Lu ppm	Hf ppm	Ta ppm	Th ppm	U ppm	Li ppm
1988 Sediment core data														
CL32059	474	18.9	39.2	29	4.17	1.045	0.53	1.98	0.35	4.92	0.6	4.28	1.5	
CL32060	551	19.6	37.8	24	4.16	0.956	0.57	1.64	0.33	4.82	0.5	4.07	1.3	
CL32061	581	20.7	43.7	26	4.37	1.032	0.67	1.95	0.32	5.27	0.4	4.06	2.0	
CL32062	537	19.3	43.7	19	4.15	1.057	0.56	1.72	0.33	5.03	0.5	4.04	1.7	
1988 Crater Lake Shore Data														
CL31331	232													23
CL31332	722													41
CL31333	582													40
CL31334	679													40
CL31335	415													26
CL31336	485													25
CL31337	601													36
CL31338	502													38
1988 Dive Data														
CL31519	1939	11.2	14.9	8	1.92	0.437	0.23	0.86	0.14	1.61		1.37	0.68	
CL31520	1083													
CL31522	546	15.9	26.5	22	3.39	0.862	0.49	1.37	0.21	3.65		2.80	1.3	
CL31523	566	16.4	34.3	18	3.48	0.883	0.46	1.48	0.28	3.56	0.5	3.29	1.8	
CL31526	572	12.0	21.3	14	2.57	0.603	0.34	1.23	0.20	2.51	0.3	2.33	1.5	
CL31527	557	15.7	32.5	23	3.25	0.802	0.51	1.46	0.25	3.45	0.4	3.34	1.6	
CL31528	679													
CL31529	796													
CL31530	246	2.1	1.0		0.34	0.112		0.43	0.08	0.55		0.23	1.5	
CL31531	342	4.0	1.7		0.56	0.106	0.25	1.94	0.38	0.27		0.23	1.6	
CL31534	2509	13.4	20.8	21	2.64	0.643	0.30	1.37	0.21	2.59		2.18	1.8	
CL31535	2348													
CL31537	462													
CL31538	554													
CL31539	611	3.8	2.2		0.82	0.216		0.72	0.12					
CL32058	318	4.6	3.4		0.74	0.140	0.20	2.38	0.46				1.7	

1989 Dive Program: Sediment, Crust, and Mat Data

Access #	Title	type	S-CNS %	C-CNS %	N %	P %	Ash %	Si %	Al %	Na %	Ca %
1989 Dive Data											
CL32223	CD213 #1 spires	crust	nd	0.32	0.08	0.19	97.18	38.74	1.30	0.355	
CL32227	CD220 mat crusts CD179 area	crust	nd	0.42	0.1	1.61	86.19	6.29	0.08	0.0832	0.66
CL32229	CD223 Elephant's Foot	crust	nd	0.49	0.09	2.81	86.42	6.97	0.83	0.264	1.30
CL32237	CD230 crust	crust	nd	0.19	0.04	0.03	99.33	38.26	3.61	1.009	1.40
CL32224	CD215 S1 "mat"	mat						27.10	7.49	2.075	3.25
CL32225	CD216 #1 Niskin	mat	0.13	3.47	0.37	0.20	85.97	14.49	2.31	0.613	1.23
CL32226	CD218 Bottle #1	mat						8.58	1.76	0.667	1.26
CL32230	CD226 Llao's Bath Go-Flo	mat	0.38	2.76	0.29			27.60	7.34	1.79	
CL32231	CD228 S1 Go-Flo	mat	0.31	3.23	0.38			27.15	6.67	1.917	
CL32232	CD228 S2 arm sample	mat	0.12	4.21	0.43	1.84	85.86	16.19	3.26	0.956	2.05
CL32234	CD228 BC11 bottom water	mat						24.96	5.17	1.273	1.23
CL32235	CD230 Go-Flo	mat	nd	3.79	0.43			18.14	3.52	0.938	
CL32236	CD230 S3 "mat"	mat	0.17	1.86	0.22	1.09	86.59	11.73	1.43	0.639	1.33
CL32238	CD216 CL8908-5BC-3 sq.cake	sed	2.07	2.58	0.295	0.15	92.05	26.55	6.70	1.759	2.33
CL32239	CD216 CL8908-5BC-8 sq.cake	sed						25.28	6.73	1.718	
CL32240	CD218 CL8908-6BC 0.5-1.5cm	sed						27.32	7.23	1.875	
CL32241	CD218 CL8908-6BC 2-3cm	sed						24.57	6.41	1.687	
CL32242	CD218 CL8908-6BC 3-4cm	sed						26.35	7.25	2.036	
CL32243	CD218 CL8908-6BC 4-5cm	sed						25.87	6.91	1.81	
CL32244	CD218 CL8908-6BC 9-10cm	sed						28.62	8.28	1.973	
CL32228	CD223 Soutar Surface 8BC	sed						21.61	5.53	1.355	
CL32245	CD223 CL8908-8BC 0-1cm	sed						22.67	6.10	1.548	
CL32246	CD223 CL8908-8BC 2.5-3.5cm	sed						17.33	3.64	1.066	
CL32247	CD223 CL8908-8BC 5-6cm	sed						22.38	5.13	1.459	
CL32248	CD223 CL8908-8BC 10.5-11.5cm	sed						19.18	4.31	1.149	
CL32249	CD223 CL8908-8BC 14-15cm	sed						28.68	8.33	2.072	
CL32250	CD223 CL8908-8BC 17-18cm	sed						17.99	3.26	0.849	
CL32251	CD223 CL8908-8BC 21-22cm	sed						27.45	7.64	1.822	
CL32233	CD228 BC11 sludge at bottom	sed	1.10	5.18	0.52			26.26	5.83	1.619	1.76

1989 Dive Program: Sediment, Crust, and Mat Data cont.

Access #	Sc ppm	V ppm	Cr ppm	Mn ppm	Fe %	Co ppm	Ni ppm	Cu ppm	Zn ppm	As ppm	Br ppm	Sb ppm	Cs ppm	Ba ppm
1989 Dive Data														
CL32223	2.351		9.307	259	7.52	3.08	17	44.6	31.9	1180.8		60.50	4.5	145
CL32227	1.574		9.052	1844	41.73	23.41	18	16.7	9.9	4104		2.68	2.6	305
CL32229	3.644		11.35	1732	36.97	32.85	35	21.5	26.9	9277.3		11.60	6.1	537
CL32237	6.197		19.04	229	2.33	5.52	28	50.8	31.6	30.3	2	0.34	12.9	225
CL32224	11.23	133	43.93	3775	5.10	44.22	75	48.2	75.6	347.5		1.10	15.4	509
CL32225	4.721		18.13	3272	28.22	24.54	37	47.8	35.2	354.5	21	0.62	8.3	378
CL32226	5.334	225	28.97	1471	28.72	8.63	24	51.5	33.3	9604.1	32	21.20	6.5	569
CL32230	11.54		37.56	459	3.45	12.42	61	88.2	70.1	67.2	19	0.52	20.1	386
CL32231	11.53		31.27	1687	4.24	14.74	55	114.4	73.8	60	56	0.73	14.8	429
CL32232	6.686		21.89	6190	18.25	66.78	146	87.3	58.5	6139	45	1.12	6.8	716
CL32234	10.52	82.2	27.96	608	4.90	18.43	50	122.4	90.7	277.7	71	1.39	13.1	360
CL32235	7.538		25.2	2751	18.57	14.63	45	68.0	43.5	1053.7	24	0.77	13.6	852
CL32236	3.305		14	150.30	34.12	3.15	20	26.2	18.5	1710.4	14	0.63	7.6	376
CL32238	12.14		38.73	457	6.00	17.78	62	89.2	82.1	176.6	15	0.61	16.1	487
CL32239	11.48		33.26	466	5.68	16.47	66	89.2	73.6	175.4	16	0.52	15.2	438
CL32240	12.07		40	13165	3.55	16.88	78	76.1	68.4	26.1	23	0.60	17.1	486
CL32241	11.52		39.92	3946	9.07	31.31	56	72.0	61.1	354.3	24	0.60	17.8	409
CL32242	12.62		41.89	1135	5.37	15.23	56	69.3	64.4	161.2	17	0.70	17.2	416
CL32243	12.27		39.28	1969	7.68	20.63	56	79.1	64.7	406.8	18	0.73	17.4	556
CL32244	13.96		45.42	1234	3.95	19.83	64	92.0	69.7	21.6	19	0.98	20.5	468
CL32228	9.922		30.34	103083	4.48	124.64	138	77.2	76.5	97.8	19	0.75	15.3	830
CL32245	10.74		39.24	70927	4.23	79.73	116	70.2	64.6	74.1	18	0.97	15.6	838
CL32246	7.011		28.85	4215	23.97	78.93	49	58.2	42.0	75.7	17	0.81	8.6	724
CL32247	9.631		34.23	3256	15.52	60.01	55	69.5	54.2	119.7	19	0.73	10.9	697
CL32248	7.748		29.27	3125	19.74	51.52	47	60.3	46.7	220	12	0.83	9.9	695
CL32249	13.49		44.86	670	4.57	35.57	64	72.4	71.3	8.65	17	0.65	16.1	482
CL32250	6.544		23.46	2380	23.71	53.40	43	60.5	40.5	383.5	14	0.49	9.3	687
CL32251	13.15		39.24	895	6.35	34.05	59	82.0	66.7	84.2	10	0.63	17.2	503
CL32233	10.81	80.9	28.18	465	4.01	15.32	63	123.8	101.6	133.7	68	1.23	13.2	392

1989 Dive Program: Sediment, Crust, and Mat Data cont.

Access #	La ppm	Ce ppm	Nd ppm	Sm ppm	Eu ppm	Tb ppm	Yb ppm	Lu ppm	Hf ppm	Ta ppm	Th ppm	U ppm	Pb ppm	I ppm	Au ppm
1989 Dive Data															
CL32223	3.2	7.4		0.75	0.195	0.10	0.88	0.17	0.91		0.72	0.5	39.5		
CL32227	3.8	1.7		0.47	0.116	0.23	2.01	0.39				1.5	51.9		
CL32229	7.6	11.1		1.58	0.390	0.46	1.45	0.27	0.58		0.32	1.5	47.9		
CL32237	8.6	18.3	9	1.96	0.494	0.26	0.78	0.13	1.85	0.2	1.63	1.0	34.3		
CL32224	15.6	30.2	15	3.23	0.948	0.37	1.54	0.22	3.34	0.3	2.77	1.0	62.4	113	
CL32225	7.0	14.8	10	1.41	0.404	0.34	0.87	0.19	1.51	0.2	1.40	0.9	57.9		
CL32226	8.0	20.3		1.89	0.504	0.42	1.82	0.26	1.52	0.2	1.08		49.2	497	
CL32230	16.1	33.4	17	3.15	0.949	0.43	1.87	0.37	3.29	0.3	2.92	1.5	46.7		
CL32231	16.9	37.2	22	3.74	0.906	0.47	2.13	0.29	3.95	0.4	3.44	1.3	44.9		
CL32232	12.1	24.7	13	2.57	0.611	0.38	1.41	0.28	2.34	0.2	2.23	1.2	55.0		
CL32234	14.9	36.0		3.27	0.778	0.41	1.37	0.29	3.48	0.3	3.41	1.7	54.4	102	0.076
CL32235	12.7	23.9	11	1.77	0.645	0.37	2.51	0.42	2.22	0.2	2.13	1.5	44.7		
CL32236	5.4	8.7	7	1.07	0.279	0.21	1.37	0.27	0.85	0.1	0.85	1.3	47.8		
CL32238	16.3	35.5	23	3.30	0.927	0.50	1.73	0.24	3.68	0.3	3.21	1.3	52.8		
CL32239	16.0	35.1		3.44	0.935	0.44	1.49	0.26	3.23	0.3	3.08	1.1	50.9		
CL32240	16.6	33.9	20	3.10	0.901	0.51	1.49	0.24	3.52	0.5	3.01	1.8	60.1		
CL32241	15.5	31.0	20	3.17	0.842	0.43	1.35	0.22	3.27	0.3	2.96	2.0	62.0		
CL32242	15.6	32.8	19	3.29	0.953	0.50	1.63	0.28	3.61	0.3	3.02	1.9	51.1		
CL32243	16.8	35.3	20	3.46	0.912	0.35	1.83	0.26	3.53	0.3	3.16	1.7	52.3		
CL32244	19.2	39.6	23	3.73	1.012	0.42	1.89	0.30	3.97	0.4	3.57	1.6	49.3		
CL32228	14.2	30.6	14	2.73	0.785	0.40	1.43	0.20	2.82	0.3	2.49	1.4	57.3		0.017
CL32245	14.7	32.3	21	3.03	0.876	0.44	1.48	0.22	3.06	0.4	2.89	1.3	54.6		0.015
CL32246	9.9	22.3		1.98	0.572	0.28	1.17	0.17	2.15	0.2	2.22	1.0	57.9		
CL32247	13.4	27.7	12	2.53	0.710	0.33	1.58	0.21	2.53	0.3	2.40	1.5	57.0		
CL32248	11.0	21.5		2.21	0.637	0.28	1.31	0.24	2.67	0.2	2.14	0.4	57.5		
CL32249	16.6	32.6	21	3.41	0.981	0.60	1.44	0.29	3.68	0.4	3.49	1.7	53.5		
CL32250	8.7	17.9		1.82	0.501	0.32	1.00	0.19	1.96	0.2	1.84	0.6	55.2		
CL32251	18.3	38.4	27	3.44	0.994	0.57	2.42	0.35	4.13	0.4	3.47	1.2	53.6		
CL32233	15.9	38.4	19	3.86	0.867	0.58	1.28	0.27	3.59	0.3	3.43	1.6	49.6	49	0.039

Temperature Probe Stations

Dive	time	x	y	Depth(ft)	Station Type	Top Thermistor T (°C)	Top Thermistor Depth(cm)	Mid. Thermistor T (°C)	Mid. Thermistor Depth(cm)	Bot. Thermistor T (°C)	Bot. Thermistor Depth(cm)	comments
CD207	17:23	843	1528	1489	water	3.67	NA	3.71	NA	3.66	NA	
CD207	17:24	843	1528	1489	mat	—	—	—	—	6.00	60	left, upper side of top mat
CD207	17:26	843	1528	1486	mat	7.56	30	7.76	50	8.10	70	at the center of top mat; D=1486'
CD207	17:30	843	1528	1486	mat	—	—	—	—	9.12	70	right side of top mat
CD207	17:42	843	1528	1485	sed	—	—	—	—	6.70	?	lithified sediment; probe partially inser
CD207	18:04	813	1594	1498	sed	3.66	—	—	—	4.38	?	mottled seds
CD211	13:46	893	1550	1511	water	—	—	—	—	3.66	NA	
CD211	13:50	893	1550	1511	sed	—	—	—	—	4.18	20	at 3BC location
CD211	14:44	891	1540	1484	mat	3.66	in water	—	—	4.89	50	crusty, lithified old mats,10 cm out
CD211	16:34	634	1452	1547	sed			—	—	4.35	40	1M from pool; 2/3 inserted
CD211	16:34	634	1452	1547	water	—	—			3.67	NA	
CD211	16:36	634	1452	1547	pool	—	—	—	—	4.45	in pool	
CD215	13:45	951	1150	1402	mat	—	—	4.10	0	11.60	20	shallow mat; 1/3 in
CD215	13:46	951	1150	1397	mat	—	—	—	—	8.60	?	left of mat
CD215	13:50	951	1150	1394	mat	—	—	9.00	10	9.60	30	1m up; very rocky; 1/3 in
CD216	13:38	609	1431	1547	water	—	—	3.71	—	3.75	NA	
CD216	13:38	609	1431	1547	mat	—	—	4.46	40	4.54	60	base of mat/pool
CD216	15:49	547	1136	1519	mat	—	—	—	—	6.85	80	buried submersible arm in mat material
CD216	15:55	547	1136	1517	mat	—	—	—	—	7.20	?	metalliferous surface
CD217	14:14	891	1268	1464	sed	3.75	in water	3.79	20	5.68	40	
CD217	14:14	891	1268	1464	water	—	—	—	—	3.72	NA	
CD217	15:56	978	1664	1490	sed	3.78	20	3.96	40	4.08	60	
CD218	15:37	1040	1253	1392	water	—	—	—	—	3.74	NA	
CD218	15:37	1040	1253	1392	sed	4.16	20	—	—	5.86	60	
CD218	17:04	1032	1302	1407	mat	—	—	—	—	16.10	10	
CD218	17:04	1032	1302	1407	sed	—	—	—	—	8.60	?	sed next to mat
CD220	12:09	1030	1270	1370	mat	—	—	—	—	7.50	60	
CD222	14:47	949	1438	1490	water	—	—	—	—	3.79	NA	
CD222	14:48	949	1438	1490	sed	4.21	20	4.72	40	5.33	60	
CD222	15:04	945	1561	1477	water	—	—	—	—	3.94	NA	just above seds
CD222	15:06	945	1361	1477	sed	5.00	20	5.85	40	6.65	60	
CD222	15:06	945	1361	1477	sed	—	—	—	—	6.90	60+	a little deeper
CD222	15:13	924	1337	1476	sed	5.55	20	6.35	40	6.92	60	
CD222	16:03	1022	1351	1408	sed	—	—	—	—	10.50	?	
CD222	16:05	1022	1351	1405	sed	—	—	—	—	11.20	60	higher up the hill
CD222	16:16	1067	1383	1378	mat	—	—	—	—	6.20	60	
CD222	17:10	952	1178		mat	—	—	—	—	4.80	?	
CD222	17:17	964	1163	1425	mat	—	—	—	—	7.90	?	
CD223	12:55	614	1422	1551	water	—	—	—	—	3.71	NA	
CD223	12:56	614	1422	1551	sed	3.77	20	4.16	40	4.52	60	below mat; sed quivers
CD223	12:58	614	1422	1545	mat	4.39	20	5.10	40	5.75	60	
CD223	15:09	335	1327	1503	water	—	—	—	—	3.68	NA	
CD223	15:46	539	1207	1558	sed	3.80	15	4.05	35	4.24	55	next to southern small pools
CD226	15:00	1062	1363	1397	sed	5.30	20	7.90	40	10.20	60	
CD226	15:15	999	1327	1412	mat	7.50	10	11.08	30	12.90	50	
CD226	15:24	999	1327	1412	mat	—	—	—	—	13.60	?	
CD226	15:33	1006	1262	1396	sed	—	—	—	—	11.00	?	
CD226	15:41	1005	1338	1395	mat	—	—	—	—	11.50	?	
CD229	17:53	1055	1335	1410	mat	—	—	—	—	18.90	10	
CD228	13:50	2914	6005	1850	pool	—	—	3.73	0	6.45	20	shallow pool; only 1/3 in
CD228	14:13	2907	5984		pool	4.60	15	5.00	35	5.60	55	
CD228	14:58	2884	6062	1820	mat	5.60	20	7.15	40	8.11	60	
CD228	15:04	2884	6062	1820	sed	4.60	2	10.20	22	10.81	42	next to mat, 2/3 in
CD228	15:52	2917	5954	1845	sed	3.68	20	6.10	40	8.85	60	next to a boulder
CD228	17:02	no nav	no nav	1809	sed	3.68	in water	5.80	15	9.77	35	probe not far in; #3 in water
CD228	17:06	no nav	no nav	1807	mat	6.04	?	—	—	10.80	?	mat and sed
CD228	17:07	no nav	no nav	1807	sed	3.69	in water	6.37	20	9.66	40	hit rock, 2/3 in
CD230	14:54	612	1421	1547	mat	4.59	20	5.51	40	5.86	60	near peeper; brain mat area
CD230	14:55	612	1421	1547	mat	4.84	30	5.75	50	6.00	70	inserted deeper
CD230	15:57	618	1420	1546	pool	4.30	20	5.00	40	5.21	60	near pool of peeper-A